Morphologie mathématique pour des images multi-variées

Jesus Angulo

Université de Marne-la-Vallée

Mémoire pour l'obtention de

l'Habilitation à Diriger des Recherches

Spécialité : Mathématiques et STIC - Traitement du signal et des images

Morphologie mathématique pour des images multi-variées

Présentée par **Jesús ANGULO-LÓPEZ**

Habilitation soutenue le 15 Mars 2012

Jury composé de:

Isabelle Bloch *(examinateur)*, Professeur, TELECOM ParisTech
Jocelyn Chanussot *(rapporteur)*, Professeur, Institut Polytechnique de Grenoble
Michel Couprie *(rapporteur)*, Professeur, ESIEE (PRES Université Paris-Est)
Fernand Meyer *(examinateur)*, Directeur de Recherche, MINES ParisTech
Philippe Salembier *(rapporteur)*, Professeur, Universitat Politecnica de Catalunya
Michel Schmitt *(examinateur)*, Directeur de la Recherche, MINES ParisTech
Jean Serra *(directeur d'hdr)*, Professeur Emérite, ESIEE (PRES Université Paris-Est)
Alain Trémeau *(examinateur)*, Professeur Université Jean-Monnet Saint-Etienne

To Linda, my lovely wife

A mis adorables hijas Carmen y Bianca

Remerciements

Je remercie Messieurs les Professeurs Jocelyn Chanussot, Michel Couprie et Philippe Salembier d'avoir accepté l'effort de juger ce travail.

Je remercie également Madame le Professeur Isabelle Bloch et Messieurs les Professeurs Michel Schmitt et Alain Trémeau de m'avoir fait l'honneur de participer au jury.

J'ai choisi un jury de chercheurs que j'admire par leur créativité scientifique.

Je tiens à remercier tout particulièrement Fernand Meyer, directeur du CMM. Il m'a toujours encouragé, en m'accordant une grande liberté dans ma démarche scientifique. Je le remercie chaleureusement d'avoir soutenu fermement ma carrière.

J'ai une pensée particulière pour Jean Serra, qui une fois de plus a accepté généreusement de me guider dans la finalisation de mon HDR. Je suis honoré de son amitié et je me considérerai toujours l'un de ses disciples.

Les discussions enrichissantes, stimulantes et amicales avec Jean Serra et Fernand Meyer son pour moi une importante source d'inspiration.

Je pense à mes collaborateurs et mes étudiants qui se sont associés à ces travaux. La liste serait longue, mais je partage avec tous la satisfaction des travaux que nous avons accomplis. Merci de tout mon cœur. Je pense en particulier à mon ami Santiago Velasco-Forero, mon complice de ces dernières années ; j'aime penser que nous sommes la preuve qu'il y a un algèbre dans lequelle $1+1 > 2$.

Je remercie les membres présents et passés du CMM avec qui je partage mon quotidien : même dans les situations les plus adverses, ils savent créer une ambiance toujours positive. Je pense notamment à Catherine Moysan, une aide précieuse et généreuse qui facilite mon travail scientifique. Je pense également à Michel Bilodeau, un pilier central du CMM, sa capacité d'écoute et sa sagesse m'ont souvent aidé.

Finalement, je veux très spécialement remercier mon épouse Linda et nos filles Carmen et Bianca, pour leur amour, leur patience et leur soutien. Qu'elles me pardonnent d'être parfois trop absorbé par le travail. Je vous aime bien plus que la morphologie !

Fontainebleau, le 14 janvier 2012.

Résumé

Mes travaux de recherche, menés au Centre de Morphologie Mathématique de MINES ParisTech depuis 2000, se sont articulés autour de deux grands volets : l'un plus méthodologique, allant de la théorie aux algorithmes et comme thématique centrale l'extension de la morphologie aux images multi-variées, et l'autre, beaucoup plus applicatif et souvent lié à des contrats et projets partenariaux, consacré principalement à la microscopie quantitative en biomédecine.

Dans ce mémoire d'HDR, je présente de manière synthétique mes activités de recherche théorique et notamment :

- Travaux en modélisation et traitement morphologique des images couleur.
- Recherches encadrées en filtrage, exploration de la dimension et traitement morphologique des images multi/hyper-spectrales.
- Extension des opérateurs morphologiques à des images dans des espaces non-euclidiens : représentations hypercomplexes, images à valeurs sur la sphère et images à valeurs matricielles/tensorielles.
- Travaux sur des images multi-variées associées à une décomposition structure+texture ou bien celles qui sont associées à une famille de formes spatialement équivalentes.
- Résumé d'une série de travaux avec des contributions originales en morphologie mathématique, allant de la segmentation probabiliste (LPE stochastique), aux opérateurs régularisés (microviscosité, morphologie robuste) et passant par des liens avec l'adaptabilité et l'invariance (morphologie cyclique en coordonnées log-pol, morphologie anisotrope associée à un champ de gradient, morphologie bilatérale, morphologie structurellement adaptative). Mais aussi des travaux plus fondamentaux comme l'étude des connexions de la morphologie mathématique avec la non-linéarisation de la diffusion réelle et complexe ou la recherche de nouveaux paradigmes morphologiques comme les approximations morphologiques parcimonieuses.

Une dernière partie sera consacrée aux travaux à caractère plus applicatif ainsi qu'aux activités de valorisation. Notamment, d'une part, un rappel des applications que j'ai développées en traitement des images issues du domaine de la microscopie biomédicale (puces à ADN, cytologie hématologie et phénotypage cellulaire) ; d'autre part, un résumé de l'activité contractuelle et de valorisation industrielle menée en parallèle de travaux plus scientifiques.

Après avoir fait le point sur les activités de recherche passées, le mémoire inclut un projet de recherche avec les perspectives envisagées dans mes travaux pour les cinq prochaines années. Ce projet de recherche est relativement bien établi, avec quelques sujets plus théoriques/méthodologiques en imagerie multi-variée et imagerie non-euclidienne, mais aussi en considérant leur pertinence pour des applications.

Mots clés :
traitement non-linéaire d'image ; imagerie vectorielle ; imagerie non-euclidienne ; morphologie mathématique couleur ; morphologie mathématique hyperspectrale ; LPE stochastique ; morphologie mathématique spatialement adaptative ; morphologie mathématique parcimonieuse ; non-linéarisation de la diffusion

Abstract

My research work, carried out at the Center of Mathematical Morphology of MINES ParisTech since 2000, have been organized around two main aspects : the first one is more methodological, from theory to algorithms, with a core subject about the extension of mathematical morphology to multivariate images, and the second one, much more applicative and often linked to partnerships and industrial contracts, mainly dealing with quantitative microscopy in biomedicine.

In this HDR dissertation (French post-doctoral degree allowing its holder to fully supervise PhD students), my theoretical research activities are synthesized, and notably :

- My works on color modeling and morphological color image processing,
- My research activities in filtering, dimensionality reduction and morphological processing of multi/hyper-spectral images,
- My works on the extension of morphological operators to images valued in non-Euclidian spaces : hypercomplex representations, images valued on the sphere, matrix/tensor images.
- My studies on multivariate images associated to a structure+texture decomposition, or to those associated to a group of spatially equivalent shapes.
- The summary of a series of original contributions in mathematical morphology, including stochastic watershed segmentation, regularized operators (microviscosity, robust morphology), spatial adaptability and invariant operators (cyclic morphology in log-pol coordinates, anisotropic morphology based on a gradient field, bilateral morphology, structurally adaptive morphology). Other fundamental works, such as the connections of mathematical morphology with non-linear real and complex diffusion, or the notion of sparse morphology, are also summarized.

Another part of the document is devoted to more applicative works, together with industrial-oriented development of my research results. This part includes, on the one hand, a reminder of the applications I developed in image processing from the bio-medical microscopy field (DNA microarrays, quantitative cytology and hematology, cell-on-chip based high content screening) ; on the other hand, a summary of my activities of collaboration with the industry and the technological transfer of some scientific results.

After having taken stock of my past research, I include in my dissertation a research project for the next five years. It is quite clearly defined, with some more theoretical/methodological themes in multivariate and non-Euclidian imaging, but I have also envisaged them regarding their relevance towards more concrete applications.

Key words :
non-linear image processing ; vector image ; non-Euclidean image ; color mathematical morphology ; hyperspectral mathematical morphology ; stochastic watershed ; spatially adaptive mathematical morphology ; sparse mathematical morphology ; non-linearization of image

Resumen

Mis trabajos de investigación, realizados desde el año 2000 en el Centre de Morphologie Mathématique de MINES ParisTech, se articulan alrededor de dos ejes complementarios : uno más metodológico, que va de la teoría a los algoritmos, el otro, mucho más aplicativo y a menudo ligado a contratos con la industria o proyectos, dedicado principalmente a la microscopia cuantitativa en biomedicina.

En esta memoria de Habilitación a Dirigir la Investigación (HDR), presento de manera resumida mis actividades de investigación teórica y en particular :

- Mis trabajos en modelización y procesamiento morfológico de imágenes digitales en color.
- Mis investigaciones dirigidas en el marco del filtrado, exploración de la dimensión y procesamiento morfológico de imágenes multi/hyper-espectrales.
- Mis estudios sobre la extensión de los operadores morfológicos a imágenes con valores en espacios no-euclidianos : representaciones hypercomplejas, imágenes a valores sobre la esfera e imágenes a valores matriciales/tensoriales.
- Mis trabajos sobre las imágenes multi-variables asociadas a una descomposición estructura+textura o bien aquellas que son asociadas a una familia de formas espacialmente equivalentes.
- El resumen de una serie de trabajos con contribuciones originales en morfología matemática, yendo de la segmentación probabilista (*watershed* estocástico), a los operadores regularizados (microviscosidad, morfología robusta) y pasando por las nociones de adaptabilidad y la invarianza (morfología cíclica en coordenadas log-pol, morfología anisotrópica asociada a un campo de gradiente, morfología bilateral, morfología estructuralmente adaptable). Incluyendo también algunos trabajos màs fundamentales como el estudio sobre las conexiones de la morfología matemática con la no-linearización de la difusión real y compleja o bien la búsqueda de nuevos paradigmas morfológicos como las aproximaciones morfológicas parsimoniosas.

Una última parte tiene como objeto los trabajos de carácter más aplicativo así como las actividades de valorización. Específicamente se trata, por un lado, de un recapitulativo de las actividades que he desarrollado para el procesamiento de imágenes provenientes del dominio de la microscopia cuantitativa (*DNA microarrays*, citología hematológica y *screening* celular a alto contenido) ; por otro lado, de un resumen de la actividad contractual y de valorización industrial realizada en paralelo a los trabajos más científicos.

Después de haber realizado un análisis de mis actividades pasadas de investigación, este documento incluye mi proyecto de investigación con las perspectivas de mis trabajos para los próximos cinco años. Mi proyecto esta relativamente bien establecido, con varias líneas teóricas/metodológicas en imagen multi-variable e imagen no-euclidiana, pero también considerando la pertinencia para las aplicaciones.

Palabras clave :
procesamiento no-lineal de imagen digital ; imagen vectorial ; imagen no-euclidiana ; morfología matemática color ; morfología matemática hyperespectral ; *watershed* estocástico ; morfología matemática espacialmente adaptable ; morfología matemática parsimoniosa ; no-linearización de la difusión

Table des matières

Première partie

Introduction, CV, enseignement/encadrement et liste de publications

Chapitre 1

Introduction

J'introduis dans ce premier chapitre le contexte global et la motivation de mes travaux de recherche en morphologie mathématique que j'ai commencés il y a une douzaine d'années. Mon intérêt tout particulier pour le développement d'approches innovantes pour l'analyse et le traitement des images multi-variées sera illustré par quelques exemples de ce type d'images. Je mentionne aussi d'autres axes méthodologiques qui articulent le reste de mes recherches en morphologie mathématique avancée.

Je décris aussi très brièvement l'organisation du reste du manuscrit.

1.1 Quelques lignes d'histoire

Notre ambition dans cette section n'est pas de faire un état de l'art exhaustif en morphologie mathématique mais simplement de rappeler les principaux jalons dans son développement ; ceci nous permettra de mieux situer les travaux résumés dans ce manuscrit. Nous invitons le lecteur intéressé par l'Histoire de la morphologie mathématique à lire les deux articles [56, 36] écrits par les deux principaux protagonistes de l'histoire.

La morphologie mathématique est une méthodologie non-linéaire de traitement d'image initiée dans les années 60 par Matheron [34, 35] et Serra [52, 54] à l'Ecole des Mines de Paris. D'un point de vue théorique, le cadre axiomatique de la morphologie mathématique correspond initialement à une approche ensembliste (poursuite des travaux sur l'addition de Minkowski [37, 38] et sur la géométrie intégrale de Hadwiger [17, 18]) très bien adaptée aux images binaires et ayant des liens très proches avec la théorie de processus aléatoires dans l'espace. Les opérateurs morphologiques furent ensuite généralisés par Serra [53] et Sternberg [61] aux fonctions numériques (images à niveaux de gris) en ayant recours à différentes approches, telles que la transformation "umbra" ou la décomposition par ensembles des niveaux. Cependant, c'est au début des années 80 que Matheron et Serra ont proposé la formulation définitive de la théorie du filtrage morphologique dans le cadre algébrique des treillis complets [11]. S'appuyant sur une structure de treillis complet, qui suppose la définition d'une relation d'ordre et donc le calcul d'un supremum et d'un infimum, les opérateurs qui en découlent s'appliquent immédiatement aux images binaires ou à niveaux de gris. En effet, n'importe quel ensemble de pixels se trouve totalement ordonné en considérant l'ordre naturel sur leur intensité lumineuse. Cette formulation a été théoriquement enrichie notamment par les travaux des algébristes Heijmans and Ronse [20, 49, 21].

La Ligne de Partage des Eaux (LPE) est l'opérateur de segmentation morphologique par excellence. Introduit initialement par Beucher et Lantuéjoul [5] à partir de notions ensemblistes, la LPE a

fait ensuite l'objet d'importants développements méthodologiques et algorithmiques (e.g., approches hiérarchiques, implémentations optimales par files d'attente hiérarchiques, formulation dans la théorie de graphes, etc.), notamment par les travaux de Beucher et Meyer [6, 40, 42]. Mais la segmentation morphologique ne se limite pas à la LPE et d'autres techniques fondées sur la notion de connexion ont été aussi proposées ; voir à ce propos la théorie de la segmentation de Serra [57].

Ainsi, la morphologie mathématique dispose aujourd'hui d'un corpus méthodologique très riche dans le traitement des fonctions numériques scalaires, à 2D, 3D ou N dimensions, pour des tâches de filtrage, de segmentation et d'extraction/mesure de caractéristiques. Mais le monde ne se limite pas aux images scalaires : les images multi-variées et notamment les images couleur sont couramment utilisées dans tous les domaines. Or, la notion de supremum et d'infimum n'est pas naturellement définie pour les fonctions multi-variées et en conséquence, l'extension des opérateurs morphologiques n'est ni directe ni triviale.

Déjà au début des années 90, Serra [55] s'est intéressé à la construction d'opérateurs couleur en donnant les premières pistes. L'application de la LPE aux images couleur a aussi été introduite par Meyer [41] à la même époque. Depuis lors, un nombre important de travaux ont été publiés dans le domaine de la morphologie pour les images multi-variées, principalement les images couleur. Le lecteur intéressé par un état de l'art plus détaillé peut consulter les articles référencés dans ma liste de publications, pour certains en annexe de cette HDR, car c'est justement l'extension aux images multi-variées des opérateurs morphologiques pour le filtrage et la segmentation qui est l'objet d'une partie importante mes travaux de recherche méthodologique.

Le formalisme théorique de la morphologie mathématique établit un cadre solide fondé sur certaines lois de commutation et propriétés d'invariance sous-jacentes aux opérateurs : extensitivité (anti-extensitivité) et commutation de la dilatation (de l'érosion) avec le supremum (l'infimum), invariance aux changements de contraste pour les opérateurs plats, invariance par translation, etc. Cependant, ce cadre peut être aussi trop rigide lorsqu'on travaille sur des problèmes pratiques : sur des images entachées de bruit, on souhaite pouvoir dilater les structures mais pas le bruit ; dans beaucoup de situations, le choix d'un élément structurant global à toute l'image n'est pas pertinent et une adaptativité locale des éléments structurants à l'orientation ou à la taille des structures est plus intéressante. Dans une autre partie de mes travaux, je me suis intéressé à ce type de démarches qui permettent l'introduction d'opérateurs régularisés ou adaptatifs que bien que ne vérifiant pas toutes les propriétés algébriques d'une dilatation/érosion, elles produisent des traitements très performants.

D'autres ruptures que j'ai apportées avec mes travaux concernent d'une part la probabilisation de la LPE, en introduisant un schéma de génération de marqueurs aléatoires et d'estimation d'une densité de contours qui prend à contrepied le paradigme classique de la LPE où le choix déterministe des marqueurs constitue la clé des algorithmes. D'autre part, j'ai introduit récemment de nouveaux paradigmes morphologiques, comme la morphologique mathématique parcimonieuse ou l'utilisation de fonctions de profondeur statistique pour construire des ordres intrinsèques aux données, que j'espère permettront dans le futur proche apporter des solutions pour des applications intéressantes.

Par ailleurs, on sait bien que le filtrage d'image par des techniques de type diffusion (linéaire, non-linéaire, anisotrope, complexe) constituent une branche particulièrement féconde du traitement d'images. Ceci est dû au fait que les algorithmes s'inspirent de modèles physiques très puissants et que les méthodes de résolution numérique des EDP associées ont été très élaborées. Dans ce contexte, je m'intéresse aussi à l'élargissement des frontières de la morphologie mathématique, en explorant la non-linéarisation des différentes diffusions pour obtenir de nouveaux opérateurs qui se comportent asymptotiquement comme des opérateurs morphologiques tout en tirant partie des avantages de la diffusion.

Parmi les premières applications de la morphologie mathématique il faut citer la microscopie

biomédicale, et notamment les travaux en cytologie quantitative de Meyer [39]. Par la suite, la morphologie mathématique a démontré à de multiples reprises être une méthodologie très puissante pour l'étude des images tirées de la microscopie biomédicale. Comme je montre plus loin dans le manuscrit, jusqu'à présent, mes travaux de recherche plus applicatifs (liés à des projets industriels) ont été principalement consacrés à résoudre des problèmes pertinents en traitement d'image en microscopie biomédicale. Il est vrai que dans la dernière partie de mes travaux, j'ai commencé aussi à travailler sur d'autres thématiques applicatives, plus liées à la vision industrielle et à la télédétection.

1.2 Objet d'étude : les images multi-variées

Commençons tout d'abord par une définition formelle de l'objet d'étude principal de cette thèse d'HDR.

Définition. Une image multi-variée, notée $\mathbf{f}(\mathbf{x})$, est une fonction définie comme suit

$$\mathbf{f} : \left\{ \begin{array}{lcl} E & \rightarrow & \mathcal{V} \\ \mathbf{x} & \rightarrow & \mathbf{f}(\mathbf{x}) = (f_1(\mathbf{x}), f_2(\mathbf{x}) \cdots, f_L(\mathbf{x})) \end{array} \right.$$

où E est l'espace discret support des pixels et $\mathcal{V}$ est l'espace des valeurs de l'image. Tous les travaux présentés dans ce document sont illustrés avec des images à 2 dimensions spatiales, par conséquent $\mathbf{x} \in E \subset \mathbb{Z}^2$; $\mathbf{x}_i = (x_i, y_i)$ étant les coordonnées du pixel i. L'image est constituée de L variables, i.e., $\{f_j(\mathbf{x})\}_{j=1}^{L}$, que nous appelons généralement images composantes. Chaque variable est une image scalaire avec des valeurs dans l'espace $\mathcal{T}_j$, i.e., $f_j(\mathbf{x}) : E \rightarrow \mathcal{T}_j$; où l'espace final est $\mathcal{V} = \mathcal{T}_1 \times \mathcal{T}_2 \times \cdots \times \mathcal{T}_L$. Dans le cas le plus général, nous pouvons considerer des images à valeurs réelles, i.e., $\mathcal{T}_j \subset \mathbb{R}$; même si très souvent on travaille dans une intervalle discrète de niveaux de gris : $\mathcal{T}_j = \{t_{\min}, t_{\min+1}, \cdots, t_{\max}\}$. Dans le cas des images multi-variées homogènes, toutes les composantes sont définies dans le même espace scalaire $\mathcal{T}$ et donc nous avons $\mathcal{V} = \mathcal{T}^L$; cependant dans de nombreux cas, l'espace multi-varié produit est non homogène. Par ailleurs, à chaque point $\mathbf{x}$ de l'image, on associe le vecteur $\mathbf{v} = (v_1, v_2, \cdots, v_L) = \mathbf{f}(\mathbf{x})$, $\mathbf{v} \in \mathcal{V}$; ainsi $\mathbf{f}(\mathbf{x})$ peut aussi être considéré comme une image vectorielle.

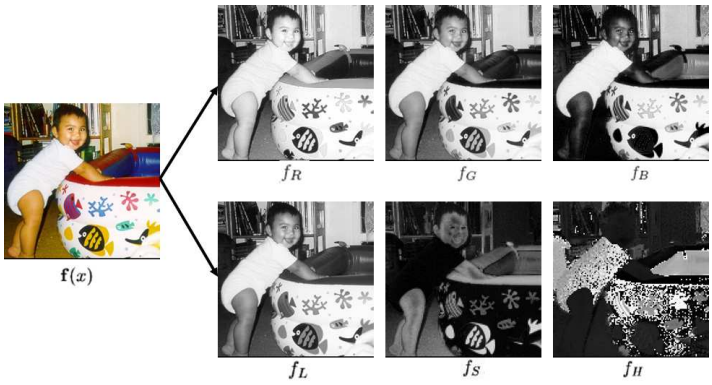

FIG. 1.1 – Image couleur.

Mais pourquoi nous intéresser aux images multi-variées ? Dans de très nombreuses applications (multimédia grand public, imagerie biomédicale, télésurveillance, etc.), l'imagerie couleur joue un rôle capital. L'information chromatique permet en effet souvent de lever des ambiguïtés subsistant sur les images à niveaux de gris et permet ainsi d'améliorer les performances des tâches classiques de

segmentation, d'analyse, de reconnaissance, de détection ou de classification. L'image couleur, voir l'exemple dans la Fig. 1.1, est constituée de trois composantes (trois images à niveaux de gris). Dans cet exemple, l'image couleur est représentée dans les coordonnées couleur cartésiennes homogènes (rouge, verte et bleue) et également, après transformation, dans les coordonnées polaires : luminance, saturation et teinte ; cette dernière composante est définie sur le cercle unité.

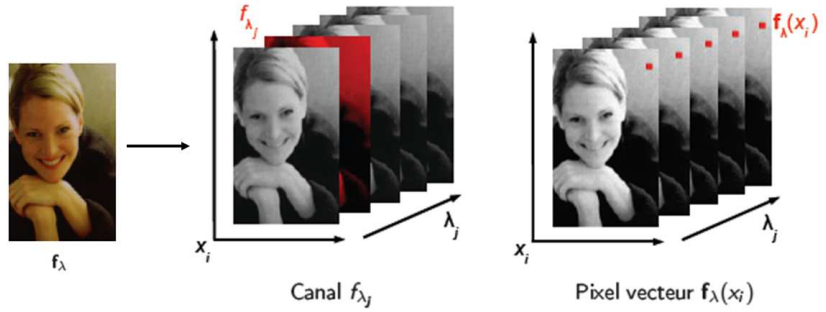

FIG. 1.2 – Image multispectrale.

L'image couleur est le cas le plus répandu d'image multi-variée. Néanmoins, une place prépondérante lui est attribuée dans l'état de l'art, et bien sûr aussi dans mes travaux, en raison de son caractère spécifique (interprétation physique des composantes et relation avec la perception humaine, omniprésence dans les applications). Parallèlement, d'autres applications impliquant différents types d'images multi-variées sont également devenues monnaie courante. On peut citer les images multi/hyperspectrales utilisées en télédétection (satellitaire ou aéroportée) ou en microscopie (en sciences des matériaux ou en biomédecine). En fait, les images multispectrales peuvent être vues comme une généralisation des images couleur, à trois composantes rouge, vert et bleu, où le nombre de composantes est maintenant de plusieurs dizaines, voire plusieurs centaines. La Fig. 1.2 présente un exemple d'image dans le domaine du visible constituée d'une soixantaine de composantes. En utilisant la terminologie "spectrale", chacune des composantes d'une image multi-variée représente un canal spectral (i.e., une variable), et la valeur associée à chaque pixel est appelée spectre (i.e., un vecteur).

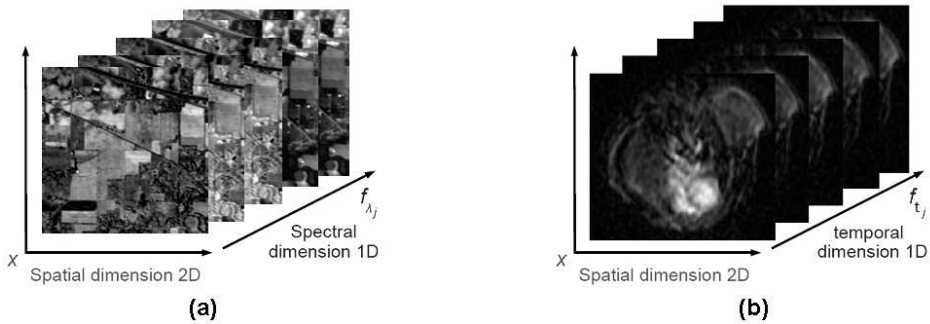

FIG. 1.3 – (a) Image hyperspectrale. (b) Image d'une série temporelle.

Dans la littérature des images spectrales, on parle soit des images multispectrales soit des images hyperspectrales (plus récemment, on commence aussi à parler d'images ultraspectrales). Grosso modo, une image multispectrale a quelques dizaines de bandes tandis qu'une image hyperspectrale en aurait quelques centaines. Mais plutôt que le nombre, la différence principale vient du fait que l'image hypersectrale correspond à un échantillonnage plus fin du spectre ; donc plus de résolution spectrale,

qui en contrepartie implique souvent une perte dans la résolution spatiale. Ainsi, l'exemple de la Fig. 1.3(a) est un cas classique d'image hyperspectrale de plus de 200 bandes issue du domaine de l'image satellitaire.

Dans un sens général, les images multi-variées vectorielles ne sont pas uniquement acquises dans le domaine des longueurs d'ondes mais peuvent correspondre à une description d'un pixel par un ensemble de valeurs : c'est-à-dire un vecteur qui peut être par exemple indexé dans le temps. La Fig. 1.3(b) montre un exemple d'image d'une série temporelle, plus précisément une image de suivi de perfusion d'un produit de contraste par IRM (pour la détection de la vascularisation tumorale). Evidemment, pour que ce type d'image multi-variée soit équivalent à une image spectrale nous faisons une hypothèse de cohérence spatiale dans le temps : c'est-à-dire qu'il n'y pas de mouvement (ou que celui-ci est négligeable) dans la période discrète de temps considérée.

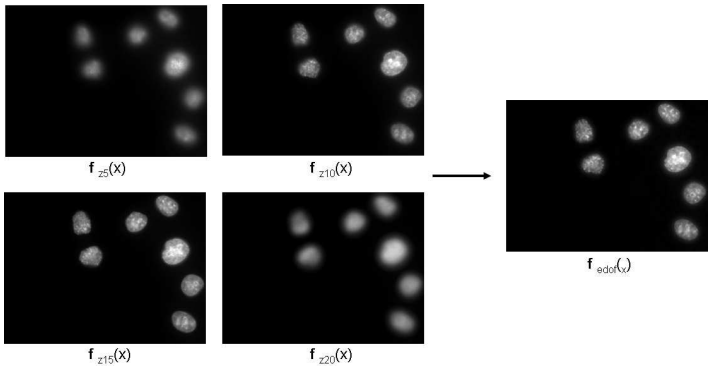

FIG. 1.4 – z-pile d'images à différents points de focalisation et image de profondeur de champ étendue.

Regardons un autre exemple donné dans la Fig. 1.4. Il s'agit d'une pile d'images cytologiques acquises avec un microscope à différentes hauteurs en z, et donc à différents degrés de focalisation pour chaque point : les valeurs sont ici l'intensité à chaque plan de focalisation. A partir de ces images, nous pouvons les combiner pour construire une image de profondeur de champ étendue. Il s'agit donc dans ce cas d'une image 3D au sens traditionnel d'une troisième dimension spatiale. Cependant, nous ne devons pas confondre le type de traitement que nous proposons pour les images temporelles et les piles d'images en z avec le traitement d'image 3D.

Aussi bien les images spectrales que les images de série temporelles ou les piles d'images en z sont des images intrinsèquement multi-variées, dans le sens où le système d'acquisition produit naturellement l'ensemble de variables. Or notre généralisation de la notion d'image multi-variée est plus large, car nous pouvons aussi considérer les images dont, à partir d'une image scalaire, les différentes variables sont introduites par traitement de l'image scalaire.

Un cas très étudié ces derniers temps dans la littérature est celui de la décomposition d'une image dans la somme d'une image qui représente les structures principales et une autre image qui correspond aux oscillations associées à la texture (et aux petits détails). Nous pouvons ensuite imaginer une deuxième décomposition qui fournira une série d'images avec les différentes échelles de texture ; ou bien une série d'image où la notion de texture est donnée sous forme d'une énergie locale indexée à l'échelle. L'exemple de la Fig. 1.5 correspond particulièrement à ce dernier cas. En produisant ces nouvelles variables extrinsèques pour chaque composante d'une image déjà multi-variée, nous obtenons des images avec une description très riche de leur structure spectrale et spatiale.

Une autre formalisation d'image multi-variée que j'ai considérée dans mes travaux est une approche probabiliste. Par exemple, la Fig. 1.6 montre une famille d'images dont chacune contient un objet similaire, des cellules dans ce cas-la, qui après segmentation, constitue un famille de formes. Si

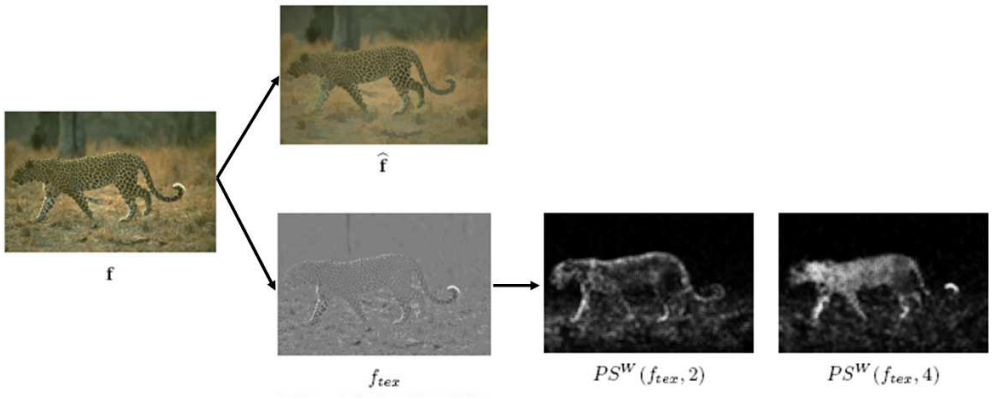

FIG. 1.5 – Images de Structure + d'Energie de texture.

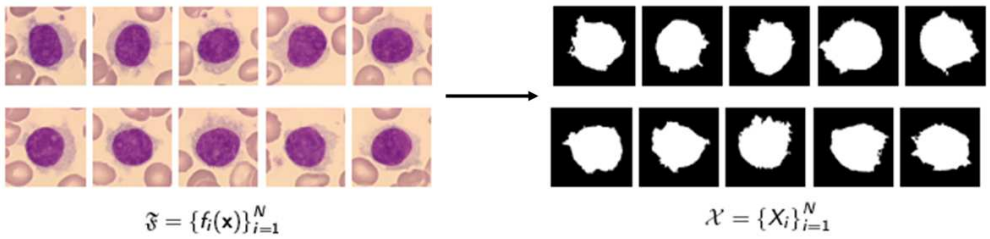

FIG. 1.6 – Famille d'images de formes.

les objets sont spatialement équivalents, c'est-à-dire si l'on élimine les variations en échelle, en translation et en orientation, la famille d'objets peut être vue comme une image multi-variée où chaque variable correspond à la réalisation d'un processus stochastique. A partir de ce type d'images il faut typiquement obtenir la moyenne et la variance de forme, interpoler de nouvelles formes, etc...

Le dernier exemple donné dans la Fig. 1.7 est aussi une image multi-variée probabiliste dont chaque variable est la réalisation d'une segmentation stochastique, i.e., contours associés à la LPE en utilisant des marqueurs aléatoires. Une fonction de densité de contours peut être obtenue à partir de ces simulations.

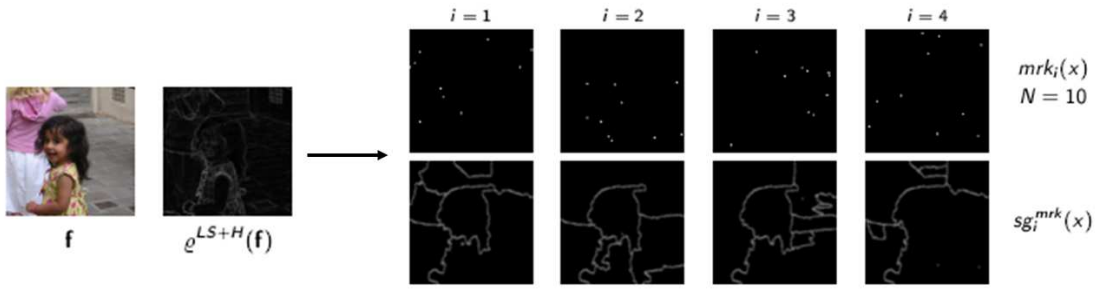

FIG. 1.7 – Images de réalisations d'une segmentation stochastique.

Toutes les images précédentes peuvent être considérées comme “euclidiennes” car elles sont à valeurs sur un sous-espace vectoriel, i.e., $\mathcal{V} \subset \mathbf{R}^L$. Plus récemment, dans une série de travaux encore en développement, j'ai commencé à m'intéresser aux images à valeurs sur des espaces non-euclidiens. En particulier, j'ai travaillé sur trois cas : images à valeurs hypercomplexes (quaternions réels) $\mathcal{V} \subset \mathbf{H}$; images à valeurs sur la sphère $\mathcal{V} \subset \mathbf{S}^2$; images à valeurs sur l'espace des matrices symétriques définies positives $\mathcal{V} \subset PDS(n)$. Je donnerai plus de détails dans le chapitre correspondant, mais il est évident que l'extension de la morphologie mathématique à ces images pose des questions théoriques et algorithmes difficiles qui nécessitent des approches innovantes.

D'autre part, le choix de ce type d'espaces n'est pas exclusivement lié aux enjeux théoriques, qui bien évidemment m'ont aussi motivé, mais également à des problèmes pratiques et à des applications que produisent (ou que produiront dans le futur proche) ce type d'image. Par exemple : la sphère est l'espace de représentation des images à données polarimétriques, images d'orientations, etc... ; les images à matrices PDS apparaissent déjà dans certaines modalités d'imagerie médicale comme l'IRM à diffusion ; des modalités de microscopie à phase quantitative produisent sur chaque pixel une valeur d'intensité et une valeur de phase de la lumière, donc un complexe, etc...

En résumé, on établit la taxonomie suivante pour les images multi-variées que j'ai étudiées dans mes travaux :

- Pixels multi-variés vectoriels par la nature intrinsèque des images : couleur, multi/hyper-spectrale ;
- Pixels multi-variés à valeurs dans un espace non-vectoriel : hypercomplexe, sphère, matrice définie positive :
- Apparition naturelle de plusieurs dimensions additionnelles dans l'espace de valeurs : séries temporelles, images multi-z ;
- Introduction de nouvelles dimensions par décomposition de l'image en plusieurs caractéristiques spatiales : espace-échelle de décomposition, énergies de texture ;
- Multiples réalisations d'un processus stochastique : familles de formes, segmentations aléatoires.

Plus, bien évidemment, tous mes travaux méthodologiques axés sur des fonctions scalaires (i.e., images à niveaux de gris).

Analyser morphologiquement tous ces types d'images, qui correspondent à la définition de $\mathbf{f}(\mathbf{x})$ donnée plus haut, implique non seulement définir des opérateurs multi-variés de filtrage ou de segmentation, mais aussi trouver les meilleur espace de représentation des variables. Ainsi, disposer des images multi-variées n'est pas seulement un *problème* pour la morphologie mathématique. En tirant partie des propriétés intrinsèques des espaces de valeurs et en s'appuyant sur des méthodes de géométrie euclidenne ou pas, de la statistique et de l'analyse de données, je montrerai dans les différents chapitres des techniques morphologiques qui n'ont pas d'équivalent pour les images scalaires.

Tels que précédemment évoqués, tous les exemples que j'ai utilisés pour illustrer mes travaux sont issus des images 2D dans l'espace support des pixels. Quoi qu'il en soit, la très grosse majorité des méthodes que j'ai développées sont applicables aux images 3D, voir nD ; la difficulté principale pour leur application aux images multidimensionnelles est liée aux questions informatiques de stockage et à la manipulation des espaces support à plus de deux dimensions.

1.3 Organisation de cette thèse d'HDR

Mes activités de recherche menées depuis 2000 se sont articulées autour de deux grands volets : l'un plus méthodologique, allant de la théorie aux algorithmes, et l'autre, beaucoup plus applicatif et souvent lié à des contrats et projets partenariaux, consacré principalement à la microscopie quantitative en biomédecine.

Dans la deuxième partie de cette thèse je vais donc présenter de manière synthétique mes activités de recherche théorique réalisées au cours de mes douze années de carrière scientifique.

- Je commence dans le chapitre 5 avec un résumé de mes travaux en modélisation et traitement morphologique des images couleur.
- Le chapitre 6 est ensuite consacré aux recherches que j'ai encadrées en filtrage, exploration de la dimension et traitement morphologiques des images multi/hyper-spectrales.
- L'objet du chapitre 7 est l'extension des opérateurs morphologiques à des images dans des espaces non-euclidiens : représentations hypercomplexes, images à valeurs sur la sphère et images à valeurs matricielles/tensorielles.
- Je présente ensuite, dans le chapitre 8, mes travaux sur des images multivariées associées à une décomposition structure+texture ou bien celles qui sont associées à une famille de formes spatialement équivalentes.
- Vient après le chapitre 9, où je résume une série de travaux avec des contributions originales en morphologie mathématique, allant de la segmentation probabiliste (LPE stochastique), aux opérateurs régularisés (microviscosité, morphologie robuste) et passant par liens avec l'adaptabilité et l'invariance (morphologie cyclique en coordonnées log-pol, morphologie anisotrope associée à un champ de gradient, morphologie bilatérale, morphologie structurellement adaptative). Mais aussi des travaux plus fondamentaux comme l'étude des connexions de la morphologie mathématique avec la diffusion réelle et complexe ou la recherche de nouveaux paradigmes morphologiques comme les approximations parcimonieuses.

Je résume ensuite dans la troisième partie mes travaux à caractère plus applicatif ainsi que les activités de valorisation industrielle.

- Le chapitre 10 est consacré au rappel des applications que j'ai développées en traitement des images issues du domaine de la microscopie biomédicale (puces à ADN, cytologie hématologie et phénotypage cellulaire).
- Ensuite, dans le chapitre 11, je rappelle l'activité contractuelle et de valorisation industrielle que j'ai menée en parallèle à mes travaux plus scientifiques. Je présenterai mon rôle dans chacun des projets, certains d'eux encore en cours.

La quatrième partie de mon HDR, dans le chapitre 12, est consacrée aux perspectives que j'envisage pour mes travaux dans les cinq prochaines années. Mon projet de recherche est relativement bien établi, avec quelques sujets plus théoriques/méthodologiques en imagerie multi-variée et imagerie non-euclidienne, mais aussi en considérant la pertinence pour des applications.

Finalement, dans la cinquième partie de la thèse j'inclus, dans le chapitre 13, une sélection de mes publications, représentatives des éléments les plus marquants de mes travaux.

Par ailleurs, en plus de ce chapitre 1 d'introduction, cette première partie du document d'HDR est complétée par,

- mon Curriculum Vitae dans le chapitre 2,
- une synthèse de mes activités d'enseignement ainsi que d'encadrement d'étudiants et post-doctorants dans le chapitre 3 et
- une liste complète de mes publications dans le chapitre 4.

Chapitre 2

Curriculum Vitæ

"In necessariis unitas, in dubiis libertas, in omnibus caritas". Saint Augustin.

Curriculum Vitae

Jesús Angulo

Chargé de Recherches

Centre de Morphologie Mathématique (CMM)
Département de Mathématiques et Systèmes
MINES ParisTech
35, rue Saint-Honoré
77305 Fontainebleau, FRANCE
Tel. : + 33 (0) 1 64 69 47 75
Fax. : + 33 (0) 1 64 69 47 07
E-mail : jesus.angulo@ensmp.fr
Web : http ://cmm.ensmp.fr/∼angulo/

ETAT CIVIL

- *Prénom :* **Jesús**
- *Nom :* **Angulo López**
- *Date de naissance et lieu :* **28 Avril 1975** à Cuenca, **ESPAGNE**
- *Adresse :*
  19, Paul Jozon,
  F-77300 Fontainebleau, FRANCE
- *Téléphone :* **+ 33 (0) 1 60 72 15 96**
- *Nationalité :* **espagnole**
- *Langues :*
  - **Espagnol :** langue maternelle
  - **Français :** courant
  - **Anglais :** courant
- *Situation de famille :* **Marié, deux enfants**

FORMATION

- **Thèse de doctorat en Traitement d'Image (Morphologie Mathématique)** ***(1999-2003)*** : Ecole des Mines de Paris, France, au Centre de Morphologie Mathématique. Mention Très Honorable avec les Félicitations du Jury.
  Directeur de thèse : Prof. Jean Serra
  Sujet : Morphologie Mathématique et indexation d'images couleur. Application à la microscopie en biomédecine.
  Membres du Jury : Prof. A. Albiol, Prof. A. Trémeau, Prof. G. Flandrin, Dr. J. Klossa, Dr. F. Vallet et Prof. J. Serra
- **Thèse de Master Recherche** ***(1999)*** : Universidad Politécnica de Valencia, Valencia, Espagne, au sein du Groupe de Traitement d'Image et de Vidéo. Mention Très Honorable ("Matricula de honor")
  Directeur de thèse : Prof. Antonio Albiol
  Thème de Recherche : Segmentation temporelle de séquences vidéo.
- **Ingénieur en Télécommunications** ***(1993-1999)*** : Ecole d'Ingénierie en Télécomunications, Universidad Politécnica de Valencia, Espagne, diplôme décerné en Octobre 1999.

- **Baccalauréat** ***(1989-1993)*** : "Instituto de Bachillerato C.E.I." à Albacete, Espagne. Diplôme avec mention.
- **Ecole primaire** ***(1981-1989)*** : "Colegio Público Juan Angel Sevilla" à Honrubia, Cuenca, Espagne. Diplôme avec mention.

NOMINATIONS

Participant à la finale du Prix ParisTech de la meilleure thèse, en 2003 (ParisTech est un regroupement des dix plus prestigieuses Ecoles Supérieures d'Ingénierie en France)

EXPERIENCE PROFESSIONNELLE ET RESPONSABILITES

Depuis Février 2008 **Chargé de Recherches au CMM, MINES ParisTech.**

- Recherche théorique/méthodologique en morphologie mathématique :
  - Extension de la morphologie mathématique aux images multi-variées vectorielles (couleur, multi/hyper-spectrale, séries temporelles).
  - Extension de la morphologie mathématique aux images à valeurs dans des espaces non-euclidiens (tensorielles/matricielles, polarimétriques).
  - Morphologie mathématique et géométrie (analyse dans des espaces de forme, morphologie adaptative, morphologie et théorie de groupes, morphologie pour des images à support sur une variété Riemannienne).
  - Approches stochastiques pour le filtrage et la segmentation morphologique (LPE stochastique, filtrage stochastique non-linéaire).
  - Nouveaux paradigmes morphologiques (dichotomique fond/objet et profondeur statistique, morphologique mathématique parcimonieuse).
  - Elargissement des frontières théoriques de la morphologie mathématique (EDP morphologiques, exploration des connexions asymptotiques avec la diffusion, exploration des connexions avec l'analyse idempotente de Maslov et l'analyse max-plus).
- Recherche appliquée et transfert technologique :
  - Chef de projet dans divers contrats : Développement d'algorithmes morphologiques de traitement du signal et d'image, transfert technologique aux partenaires, etc...
    Domaines d'applications principaux : microscopie quantitative pour des applications biomédicales en génotypage, phénotypage cellulaire et anatomo-pathologie ; contrôle industriel par vision ; télédétection à haute résolution spatiale et imagerie radar ; analyse en imagerie médicale non conventionnelle.
  - Recherche de financement, montage, suivi et gestion en tant qu'acteur principal de projets de collaborations : Projet PARTOX (Jan 08/Dec 08) (ANR), Projet RAMIS (Jan 08/Dec 10), Projet IMHO (Dec 07/Mai 11) (ANR), Projet ArcelorMittal/IDSIA/CMM (Sept 10/Sept 13).
- Encadrement d'étudiants en thèse et en stage de master M2 ainsi que des chercheurs post-doctorants.
- Activités d'enseignement dans le cadre de l'option "MAREVA " de MINES ParisTech et dans d'autres école d'ingénieurs (ENSTA, Ecole de Télécom. à Valencia et Ecole de Télécom à Cartagena en Espagne). Mise en place de plusieurs "enseignements à la clé" pour des industriels.
- Participation active à la vie scientifique du CMM (présentations dans les séminaires internes, suivi des travaux publiés par d'autres équipes dans les domaines de recherche du CMM, etc...)

Janvier 2004 - Janvier 2008 **Ingénieur ARMINES au CMM, Ecole des Mines de Paris.**

- Axes de recherche méthodologiques : Imagerie multi-variée (couleur, multi/hyper-spectrale, séries temporelles), segmentation morphologique, morphologie mathématique et géométrie.

- Recherche appliquée et transfert technologique. Développement d' algorithmes morphologiques de traitement du signal et d'image. Domaine d'application principal : microscopie quantitative pour des applications biomédicales en génotypage, phénotypage cellulaire et anatomopathologie.
- Depuis 2004 le CMM et le Centre de Bioinformatique (CBIO) de l'EMP ont noué une collaboration étroite à travers plusieurs projets de recherche ; le CMM prenant en charge le traitement d'images et le CBIO le traitement statistique et l'interprétation des données (cf. infra les projets GEMBIO, BIOTYPE, RAMIS et PARTOX). Outre le travail spécifique de traitement d'images, je servais d'interface entre les deux équipes.
- Montage, suivi, et coordination de contrats de recherche : Projet GEMBIO (Jan 04/Dec 06), Projet européen INDIGO (Août 05/Jul 08), Projet BIOTYPE (Oct 06/Mars 09).
- Valorisation : Transfert technologique du logiciel de lecture de puces à ADN à la société Genewave.
- Activités d'enseignement dans le cadre de l'option "Vision et Morphologie" de l'EMP et dans d'autres école d'ingénieurs (ENSTA, Ecole de Telecom. à Valencia en Espagne) ; et d'encadrement d'étudiants (thésards, post-doc).

Novembre 1999 - Décembre 2003 **Ingénieur de recherche au CMM, Ecole des Mines de Paris.**

- Doctorant en thèse au Centre de Morphologie Mathématique de l'Ecole des Mines de Paris.
- Activités liées au développement et à la programmation d'algorithmes de traitement morphologique d'image appliqués à la biomédecine et la biotechnologie,
  - Analyse de cellules sanguines dans des images couleur
  - Projet Matchcell dans le domaine de la cyto-hématologie : mise au point d'une plateforme de téléconsensus, d'un logiciel automatisé d'analyse et déploiement d'un réseau de télémédecine pour les affections sanguines
  - Logiciel pour la lecture d'images de puces à ADN.
- Travaux de recherche en imagerie couleur et morphologie mathématique.
- Assistant dans l'enseignement pour les travaux pratiques des cours donnés par les chercheurs du CMM.

COMPETENCES INFORMATIQUES

- **Outils de traitement d'image :** Morph-M, PDI32, Micromorph, Aphelion, Xlim3D
- **Langages de programmation :** C, C++, Python, Pascal, BASIC
- **Logiciels scientifiques :** MATLAB, R, Mathematica
- **Systèmes opératifs :** Windows, Linux/UNIX
- **Autres :** LaTex, HTML, Office Applications (MS and others), Professional Graphical Applications

AUTRES ACTIVITES PROFESSIONELLES ET ACADEMIQUES

- Membre du *Steering Committee* de l'"International Symposium on Mathematical Morphology(ISMM)"
- Membre de "The International Society for Stereology (ISS)" et membre de "Editorial Board" de la revue *Image Analysis & Stereology.*
- Membre de la Société de Mathématiques Appliquées Industrielles (SMAI), France
- Membre du Groupe Français de l'Image Numérique Couleur (French Color Imaging Group).
- Editeur associé de la série de livres "Research on computing science", Editée par l'Instituto Politécnico National, Mexico.

TRAVAIL EDITORAL DE RELECTURE

- IEEE Transactions on Pattern Analysis and Machine Intelligence Journal
- IEEE Transactions on Image Processing
- IEEE Signal Processing Letters
- Bioinformatics Journal
- Biostatistics Journal
- Machine Vision and Applications Journal
- Computer Vision and Image Understanding Journal
- International Journal of Computer Vision
- Image and Vision Computing Journal
- IEEE Transactions on Information Technology in Biomedicine
- BMC Bioinformatics
- BioTechniques Journal
- 5th conference on Applied Geometric Algebras in Computer Science and Engineering (AGACSE'2012) July 2012, La Rochelle, France : Member of Scientific Committee
- 1st International Conference on Pattern Recognition Applications and Methods (ICPRAM'2012), February 2012, Algarve, Portugal : Member of the International Program Committee
- 10th International Symposium on Mathematical Morphology (ISMM'11), July 2011, Intra, Lake Maggiore, Italy : Member of the Program Committee
- IASTED International Symposia on Imaging and Signal Processing in Healthcare and Technology (ISPHT'2011, ISPHT'2012), May 2011 Washington DC, USA : Member of the Advisory Board Committee
- IASTED International Conference on Computational Photography (CPhoto 2011), June 2011 Calgary, Canada : Member of International Program Committee
- 9th International Symposium on Mathematical Morphology (ISMM'09), August 2009, Groningen, The Netherlands : Member of the Program Committee
- 2009 Computational Color Imaging Workshop (CCIW'09), March 2009, Saint Etienne, France : Member of the Workshop Program Committee
- 15th ECMI (European Conference on Mathematics for Industry) 2008 (ECMI'2008) : Co-organiser of mini-symposium "Multivariate and/or multidimensional image processing in biomedical applications"
- IS&T's Fourth European Conference on Color in Graphics, Imaging and Vision (CGIV'08), June 2008, in Barcelona, Spain : Member of the Technical Program Committee
- 2007 Computational Color Imaging Workshop (CCIW'07), 2007, Modena, Italy : Member of the Workshop Program Committee
- IASTED International Conference on Visualization, Imaging, and Image Processing (VIIP'2005, 2006, 2007, 2008, 2009) : Member of the International Program Committee
- 7th International Symposium on Mathematical Morphology (ISMM'05), April 2005, in Paris, France : Reviewer
- Advanced Concepts for Intelligent Vision Systems (ACIVS'2005,2006,2007,2008) : Reviewer
- Signal Processing in Bio-engineering section of the IEEE 2005 Workshop on Signal Processing Systems (SIPS'05), November 2005, in Athens, Greece : Reviewer
- XII International Computing Conference 2003, Mexico : Reviewer
- International Workshop GEOPRO 2003 (Semantic Processing of Spatial Data), Mexico : Member of the International Program Committee

Chapitre 3

Activités d'enseignement et encadrement

"Assiduus usus uni rei deditus et ingenium et artem saepe vincit". Cicéron.

Dans ce chapitre de suite de mon CV, je détaille mes activités d'enseignement et de direction des travaux de recherche d'étudiants en thèse de doctorat et en stage de master, ainsi que d'encadrement de post-doctorants travaillant au CMM.

3.1 Expérience en enseignement

A l'exception des responsables d'option, la charge d'enseignement des chercheurs à MINES ParisTech est généralement assez limitée. Tel est mon cas. Or, je considère que l'enseignement de la discipline dans laquelle un chercheur mène ses travaux lui permet une consolidation des fondamentaux, par l'effort de simplification et d'adaptation pédagogique aux différents niveaux des élèves, ainsi qu'un approfondissement des points clés via le questionnement des élèves.

Pour ces raisons, en plus de ma participation à l'enseignement à MINES ParisTech, j'enseigne régulièrement la morphologie mathématique, à différents niveaux, dans d'autres écoles d'ingénieurs.

Avant d'énumérer ces différentes activités, je tiens à souligner que je souhaite continuer, et si possible élargir, ce volet d'enseignement de ma carrière. Ainsi, j'ai commencé à préparer le matériel pédagogique pour un cours théorique de morphologie mathématique d'une vingtaine d'heures (incluant 50% de TPs) en prenant le point de vue de l'analyse numérique (EDPs morphologiques, connexions avec l'analyse convexe, non-linéarisation de la diffusion, etc...) plutôt que le point de vue algébrique qui est privilégié dans l'enseignement classique de la morphologie mathématique au CMM. D'autre part, les aspects sur l'extension de la morphologie mathématique aux images multi-variées et notamment aux images multi/hyper-spectrales, font aussi l'objet d'un cours avancé que j'ai commencé à mettre en place.

Enseignement à MINES ParisTech

- Assistant de Travaux Pratiques : Lors de mes années en thèse au CMM (2000-2003), j'ai participé comme enseignant-assistant pour les travaux pratiques (deux après-midis par année) dans le cours *Morphological Image Processing in Practice* (Jean Serra) et *Ecole d'été de morphologie mathématique* (Serge Beucher).

- Participation à l'enseignement dans l'option *Vision & Morphologie* (plus tard, option *Mathématiques Appliquées : Robotique, Vision, Automatique*), 2ème du cycle Ingénieur Civil à MINES ParisTech : Depuis 2003 où j'avais préparé, dans le cadre de la semaine de cours *Introduction à la morphologie mathématique*, une séance dédiée à la morphologie mathématique pour les images couleur (3 heures de théorie + 3 heures de TP), je me suis occupé trois fois de cet enseignement. Actuellement, la partie morphologie couleur ne comprenant qu'une demi-matinée, elle est assurée par l'enseignant responsable du cours.
- D'autres cours dans le cadre de formations extérieures.
  - Ecole d'Hiver sur l'Image Numérique Couleur (EHINC'2007) (Poitiers, France, Janvier 2007) : *Apports de la morphologie mathématique couleur au filtrage et à la segmentation* (1h30)
  - Ecole d'Hiver sur l'Image Numérique Couleur (EHINC'2009) (Toulon, France ; Janvier 2009) : *Segmentation morphologique d'images multivariées : de la couleur aux images hyperspectrales* (1h30)
  - "Course on Mathematical Morphology" (Tsinghua University, Beijing, China ; October 2011) : *Mathematical morphology for colour and multi/hyper-spectral images* (1h30)
- "Formation à la carte" pour des industriels : Le CMM organise des formations *ad hoc* pour des chercheurs travaillant avec nos partenaires industriels. Dans ce cadre, j'ai preparé en 2008 le matériel et j'ai assuré l'enseignenemt des cours : *Analyse de formes et morphologie mathématique* (3h théorie + 3h TP), *Morphologie mathématique et segmentation d'images hyperspectrales* (3h théorie + 3h TP), *Filtrage d'image avec des opérateurs morphologiques visqueux* (1h théorie + 1h TP).
- Indépendamment de l'enseignement réglé, j'organise régulièrement des présentations pédagogiques pour les membres du CMM sur des sujets spécifiques : *Morphologie non-planaire*, *Morphologie adaptative*, etc... C'est un cadre qui permet de "tester" le contenu et le matériel pour des formations à la carte.

Enseignement à l'ENSTA ParisTech et à SUPELEC-Metz

J'ai été depuis 2002 et jusqu'en 2010 enseignant vacataire à l'Ecole Nationale Supérieure de Techniques Avancées (ENSTA ParisTech), intervenant dans le cours *Imagerie médicale* (un cours de 3h sur l'*Analyse et quantification de l'image en biomédecine et biotechnologie avec des opérateurs morphologiques*) et prenant en charge les travaux pratiques du cours *Morphologie Mathématique* (spécialisation 2ème année d'Ingénieur) organisé par Antoine Manzanera.

Pendant l'année scolaire *2004/2005*, j'ai été enseignant vacataire (en remplacement de Corinne Vachier) à l'école d'ingénieur SUPELEC-Metz (Ecole Supérieure d'Electricité), prenant en charge le cours *Analyse d'image et morphologie mathématique* (18 heures).

Enseignement dans des Universités Espagnoles

Dans le cadre du programme "Investigadores de Prestigio" du "Ministerio de Educación" d'Espagne j'ai été enseignant invité

- à l'Université Polytechnique de Valencia (une semaine chaque année depuis 2008) dans le cadre du " Máster en Tecnologías, Sistemas y Redes de Comunicaciones" : alternant le cours *Course on Morphological Signal/Image Processing* (10h théorie + 3 h TP) et le cours *Course on Advanced Morphological Signal/Image Processing* (10h théorie + 3 h TP)
- à l'Université Polytechnique de Cartagena (Espagne) (une semaine en 2011) dans le cadre du "Master Universitario en Tecnologías de la Información y Comunicaciones" : *Course on Mathematical Morphology for Nonlinear Signal/Image Processing* (10h théorie)

3.2 Encadrement d'étudiants en thèse de doctorat et master

- *Santiago Velasco-Forero*, Thèse de doctorat en cours (Feb 2009 –) : "Mathematical morphology in high dimensional spaces".
  Direction à 100 %.
- *Guillaume Noyel*, (co-supervisé avec Dominique Jeulin), Thèse de doctorat (Oct 2005 – Oct 2008) : "Filtering, dimensionality reduction, classification and morphological segmentation of hyperspectral images".
  Co-direction à 50 % avec Dominique Jeulin.
  Jury : Ch. Fernandez-Maloigne, F. Hamprecht, M. Jourlin, J. Angulo, J. Chanussot, Ch.-A. Cuenod and D. Jeulin.
  Mention : Très Honorable avec les Félicitations du Jury

- *Joana M. Frontera-Pons*, Thèse de Master (9 mois en 2010-2011) : "Mathematical morphology on the sphere : Application to Polarimetric Image processing" (collaboration F. Barbaresco/Thales). Diplôme avec mention.
- *Miguel A. Luengo-Oroz*, Thèse de Master (9 mois en 2004) : "Mathematical morphology in polar-logarithmic coordinates and geometrical methods of classification. Application to study the erythrocytes".
  Diplôme avec mention.
- *Gauravdeep Singh Sagar*, Stage (3 mois en 2004) : "Development of a GUI to pilot the cDNA microarray image analysis algorithms and research on a new algorithm to detect the skew of images".

3.3 Encadrement de post-doctorants

- *El Hadji S. DIOP*, Post-Doc (Juillet 2011 –Juin 2012) : "Adaptive morphological PDEs" et "Unmixing hyperspectral data" (ARCELOR Project).
- *Guillaume Thibault*, Post-Doc (Oct 2009 –Dec 2010) : "Advanced morphological analysis of fluoresce-markers cell assays for mitosis studies in pharmacology" (RAMIS Project).
- *Erik Urbach*, Post-Doc (Feb 2009 –Juillet 2009) : "Advanced morphological analysis of fluoresce-markers cell assays for mitosis studies in pharmacology" (RAMIS Project).
- *Dalila Benboudjema*, Post-Doc (Oct 2007 –Sept 2008) : "Advanced morphological analysis of fluoresce-markers cell assays for mitosis studies in pharmacology" (RAMIS Project).

3.4 Participation comme membre de jury de thèse

- *Silvia Valero Valbuena*, Ph. Thesis, Université de Grenoble (France) and Universitat Politècnica de Catalunya (Spain), December 2011. Dissertation title : "Hyperspectral image representation and processing using binary partition trees". Committee member : J. Serra, A. Plaza, J. Zerubia, C. Lopez-Martinez, H. Talbot, J. Angulo.
- *José Mennesson*, Thèse de doctorat, Université de La Rochelle (France), Novembre 2011. Titre : "Méthodes fréquentielles pour la reconnaissance d'images couleur - Une approche par les algèbres de Clifford". Membres du Jury : J. Mitéran, S.J. Sangwine, J. Angulo, L. Macaire, L. Mascarilla, Ch. Saint-Jean.
- *Arturo Aquino Martín*, Ph. Thesis, Universidad de Huelva (Spain), March 2011. Dissertation title : "Fundus Digital Image Processing : Automated Segmentation of the Main Retinal Anatomical Structures." (en Anglais). Committee members : J.M. Andújar, M. Aguilar, P. Real, E. Decencière, J. Angulo.

- *Myriam Oger*, Thèse de doctorat, Université de Caen/Basse-Normandie (France), Decembre 2008. Titre : "Indexation automatique d'images numériques : Application aux images histopathologiques du cancer du sein et hématologiques de leucémies lymphoïdes chroniques" (in French). Membres du Jury : M. Desvignes, H. Cardot, F. Meyer, P.J. Van Diest, J. Angulo, Ph. Belhomme, P. Herlin, A. Elmoataz, J.-J. Michels.
- *Patrice Denis*, Thèse de doctorat, Université de Poitiers (France), December 2007. Titre : "Quaternions et Algèbres Géométriques, de nouveaux outils pour les images numériques couleur" (in French). Membres du Jury : J.M. Chassery, P. Lambert, J. Angulo, M. Berthier, P. Carré, C. Fernandez-Maloigne.
- *Rafael Verdú Monedero*, Tesis doctoral, Universidad de Cartagena (Espagne), Diciembre 2005. Título : "Formulación de los contornos activos en el dominio de la frecuencia y análisis de convergencia en segmentación de imagen." (en Espagnol). Tribunal : A. Albiol, J. F. Zapata, J. Angulo, V. Naranjo, R. Molina.
- *Cristina Vicente Chicote*, Tesis doctoral, Universidad de Cartagena (Espagne), Diciembre 2005. Título : "Desarrollo integral de sistemas de procesamiento de información visual : un enfoque multi-paradigma basado en líneas de producto, componentes y generación automática de software". Tribunal : J.A. de la Puente, J. Vitrià, J. A. Toval, J. Angulo, D. Rogriguez.

Chapitre 4

Liste complète de publications

Thèses

1. J. Angulo. "**Morphologie mathématique et indexation d'images couleur. Application à la microscopie en biomédecine**" (in French). Ph.D. Thesis, 341 p., Centre de Morphologie Mathématique, Ecole des Mines de Paris, France, December 2003.
2. J. Angulo. "**Temporal segmentation of video sequences**" (in Spanish). Master thesis, 239 p., Polytechnic University of Valencia, Spain, October 1999.

Revues Internationales

1. J. Angulo. "**Morphological Bilateral Filtering**". Submitted to *SIAM Journal on Imaging Sciences*, 2011.
2. S. Velasco-Forero, J. Angulo, P. Soille. "**Conditional mathematical morphology for edge enhancement and salt-and-pepper noise reduction**". Submitted to *IEEE Transactions on Image Processing*, 2011.
3. J. Angulo. "**Generalised Morphological Image Diffusion**". Submitted to *Computer Vision and Image Understanding*, 2010.
4. K. Bernard, Y. Tarabalka, J. Angulo, J. Chanussot, J.A. Benediktsson. "**Spectral-Spatial Classification of Hyperspectral Data based on a Stochastic Minimum Spanning Forest Approach**". Accepted in *IEEE Transactions on Image Processing*, 2011.
5. S. Velasco-Forero and J. Angulo. "**Supervised ordering in R^n : Application to morphological processing of hyperspectral images**". *IEEE Transactions on Image Processing*, Vol. 20, No. 11, 3301–3308, 2011.
6. J. Larrey-Ruiz, R. Verdu-Monedero, J. Morales-Sanchez, J. Angulo. "**Frequency domain regularization of d-dimensional structure tensor-based directional fields**". *Image Vision and Computing*, Vol. 29, 620–630, 2011.
7. J. Angulo and S. Velasco-Forero. "**Structurally Adaptive Mathematical Morphology Based on Nonlinear Scale-Space Decompositions**". *Image Analysis and Stereology*, Vol. 30, 111–122, 2011.
8. J. Angulo. "**Hypercomplex mathematical morphology**". *Journal of Mathematical Imaging and Vision*, Volume 41, No. 1–2, 86–108, 2011.
9. G. Noyel, J. Angulo and D. Jeulin. "**Fast computation of all pairs of geodesic distances**". *Image Analysis and Stereology*, Vol. 30, 101–109, 2011.

10. F. Meyer and J. Angulo. "**Microviscosity and micromorphology**". Accepted for publication in *Image Vision and Computing*, 2011.

11. R. Verdú, J. Angulo, J. Serra. "**Anisotropic morphological filters with spatially-variant structuring elements based on image-dependent gradient fields**". *IEEE Trans. on Image Processing*, Vol. 20, No. 1, 200–212, 2011.

12. G. Noyel, J. Angulo and D. Jeulin. "**A new spatio-spectral morphological segmentation for multispectral remote sensing images**". *International Journal of Remote Sensing*, Vol. 31, No. 22, 5895-–5920, 2010.

13. J. Angulo. "**Geometric algebra colour image representations and derived total orderings for morphological operators - Part I : Colour Quaternions**". *Journal of Visual Communication and Image Representation*, Vol. 21, 33–48, 2010.

14. M. Luengo-Oroz, E. Faure and J. Angulo. "**Robust iris segmentation on uncalibrated noisy images using mathematical morphology**". *Image Vision and Computing*, Vol. 28, 278–284, 2009.

15. M. Luengo-Oroz and J. Angulo. "**Cyclic Mathematical Morphology in Polar-logarithmic Representation**". *IEEE Transactions on Image Processing*, Vol. 18, No. 5, 1090–1096, 2009.

16. J. Angulo. "**Polar modelling and segmentation of genomic microarray spots using mathematical morphology**". *Image Analysis and Stereology*, Vol. 27, 107–124, 2008.

17. G. Noyel, J. Angulo and D. Jeulin. "**Morphological segmentation of hyperspectral images**". *Image Analysis and Stereology*, Vol. 26, 1–9, 2007.

18. J. Angulo. "**Morphological colour operators in totally ordered lattices based on distances. Application to image filtering, enhancement and analysis**". *Computer Vision and Image Understanding*, Vol. 107, No. 2–3, 56–73, 2007.

19. V. Naranjo, J. Angulo, A. Albiol, J.M. Mossi, Al. Albiol and S. Gómez. "**Gradual transition detection for video partitioning using morphological operators**". *Image Analysis and Stereology*, Vol. 26, 51–61, 2007

20. J. Angulo and S. Matou. "**Application of mathematical morphology to the quantification of *in vitro* endothelial cell organization into tubular-like structures**". *Cellular and Molecular Biology*, Vol. 53, No. 2, 22–35, April 2007.

21. J. Angulo, J. Serra. "**Modelling and Segmentation of Colour Images in Polar Representations.**". *Image Vision and Computing*, Vol. 25, No. 4, 475–495, 2007.

22. F. Lemaire, C. Mandon, J. Reboud, A. Papine, J. Angulo, H. Pointu, C. Diaz-Latoud, C. Lajaunie, F. Chatelain, A.-P. Arrigo and B. Schaack. "**Toxicity Assays in Nanodrops Combining Bioassay and Morphometric Endpoints**" *PLOS One*, 2(1) : e163, 2007.

23. J. Angulo. "**Morphological colour image simplification by saturation-controlled regional levellings**". *International Journal of Pattern Recognition and Artificial Intelligence*, Vol. 20, No. 8, 1207–1223, December 2006.

24. J. Angulo, J. Klossa and G. Flandrin. "**Ontology-based lymphocyte population description using mathematical morphology on colour blood images**". *Cellular and Molecular Biology*, Vol. 52, No. 6, 2–15, May 2006.

25. O. Phan, O. Ivanovski, T. Nguyen-Khoa, N. Mothu, J. Angulo, R. Westenfeld, M. Ketteler, N. Meert, J. Maizel, N. Igor, R. Vanholder, B. Lacour, T.B. Drüeke, Z.A. Massy. "**Sevelamer prevents uremia-enhanced atherosclerosis progression in apolipoprotein E deficient (apoE-/-) mice**". *Circulation (Journal of the American Heart Association)*, Vol. 112, No. , pp. 2875–2882, November 2005.

26. J. Angulo and J. Serra. "**Image color segmentation using bivariate histograms in luminance/saturation/hue polar color spaces**" (in Spanish). *Computación y Sistemas*, Vol. 8, No. 4, pp. 303–316 June 2005.
27. Z.A. Massy, O. Ivanovski, T. Nguyen-Khoa, J. Angulo, D. Szumilak, N. Mothu, M. Daudon, B. Lacour, T.B. Drüeke and M.S. Muntzel. "**Uremia accelerates both atherosclerosis and arterial calcification in apolipoprotein-E knockout (apoE-/-) mice**". *Journal of the American Society of NEPHROLOGY*, Vol. 16, No. 1, pp. 109–116, 2005.
28. J. Angulo and J. Serra. "**Traitements des images de couleur en représentation luminance/saturation/teinte par norme L_1**" (in French). *Traitement du Signal*, Vol. 21, No. 6, pp 583–604, December 2004.
29. J. Angulo and J. Serra. "**Automatic analysis of DNA microarray images using mathematical morphology**". *Bioinformatics*, Vol. 19, No. 5, pp. 553–562, 2003.
30. J. Angulo, T. Nguyen-Khoa, Z.A. Massy, T. Drüeke and J. Serra. "**Morphological quantification of aortic calcification from low magnification images**". *Image Analysis and Stereology*, Vol. 22, pp. 81–89, 2003.
31. J. Angulo and G. Flandrin. "**Automated detection of working area of peripheral blood smears using mathematical morphology**". *Analytical Cellular Pathology*, Vol. 25, No. 1, pp. 37–49, 2003.

Chapitres de livre

1. J. Angulo, S. Lefèvre, O. Lezoray. "**Représentation et traitement couleur dans des espaces polaires intensité, teinte et saturation**". *Edited by*, "*Imagerie couleur numérique : avancées et perspectives*" (ISBN), Chapter, 40 pp., Collection IC2, Hermès, Paris, 2011.
2. J. Angulo and J. Chanussot. "**Color and Multivariate Images**". *Edited by L. Najman and H. Talbot*, "*Mathematical morphology : from theory to applications*" (ISBN 97-81848212152), Chapter 11, 321–356, ISTE-Wiley, June 2010.
3. J. Angulo and J. Chanussot. "**Couleur et images multi-variées**". *Edited by H. Talbot and L. Najman*, "*Morphologie Mathématique Vol II : estimation, choix et mise en œuvre*", Chapitre 5, 119–150, Collection IC2, Hermès, Paris, 2010.
4. J. Angulo and G. Flandrin. "**Microscopic image analysis using mathematical morphology : Application to haematological cytology**". In *Edited by A. Mendez-Vilas*, "*Science, Technology and Education of Microscopy : An overview*" (ISBN 84-607-6679-7), Vol. 1, pp. 304–312, FORMATEX Eds., Badajoz, Spain, 2003.
5. J. Angulo and J. Serra. "**A mathematical morphology contribution to the analysis of DNA microarray images**". In *V. Capasso, Editor*, "*Mathematical Modelling & Computing in Biology and Medicine*" (ISBN 88-7488-055-3), pp. 3–9, SOCIETÀ EDITRICE ESCULAPIO Eds., Bologna, Italy, 2003.

Conférences Internationales avec Comité de Lecture

1. J. Angulo. "**Parabolic Nonlinear Laplacian : Morphological Counterpart of Laplacian of Gaussian**". In *Proc. of 13th International Congress of Stereology (ICS-13)*, Beijing, China, October 2011.
2. J. Angulo, D. Reberioux, G. Thibault, C. Etievant, F. Meyer. "**Self-normalization of cell images in multifocus quantitative fluorescence**". In *Proc. of 13th International Congress of Stereology (ICS-13)*, Beijing, China, October 2011.

3. S. Koudoro, S. Velasco-Forero, J. Angulo. "**Morphological Snowflakes for Robust Nonlinear Filtering**". In *Proc. of 13th International Congress of Stereology (ICS-13)*, Beijing, China, October 2011.
4. S. Velasco-Forero, J. Angulo. "**Geodesic depth for description and retrieval of 2D/3D shapes**". In *Proc. of 13th International Congress of Stereology (ICS-13)*, Beijing, China, October 2011.
5. J. Angulo. "**Non-Linearization of Free Schrodinger Equation and Pseudo-Morphological Complex Diffusion Operators**". In *Proc. of IEEE ICIP'11 (2011 IEEE International Conference on Image Processing)*, Brussels, September 2011.
6. G.Thibault, J. Angulo, F. Meyer. "**Advanced Statistical Matrices for Texture Characterization : Application to DNA Chromatin and Microtubule Network Classification**". In *Proc. of IEEE ICIP'11 (2011 IEEE International Conference on Image Processing)*, Brussels, September 2011.
7. K. Bernard, Y. Tarabalka, J. Angulo, J. Chanussot, J. Benediktsson. "**Stochastic Minimum Spanning Forest Approach for Spectral-Spatial Classification of Hyperspectral Images**". In *Proc. of IEEE ICIP'11 (2011 IEEE International Conference on Image Processing)*, Brussels, September 2011.
8. F. López-Mir, V. Naranjo, J Angulo, E. Villanueva, M. Alcañiz, S. López-Celada. "**Aorta segmentation using the Watershed algorithm for an augmented reality system in laparoscopic surgery** ". In *Proc. of IEEE ICIP'11 (2011 IEEE International Conference on Image Processing)*, Brussels, September 2011.
9. J. Angulo and R. Verdú-Monedero. "**Multiscale local multiple orientation estimation using mathematical morphology and B-spline interpolation**". In *Proc. of 7th International Symposium on Image and Signal Processing and Analysis (ISPA 2011),* IEEE Proc., p. 575–578, Dubrovnik, Croatia, September 2011.
10. J. Angulo. "**Morphological bilateral filtering and spatially-variant adaptive structuring functions**". In *Proc. of ISMM'11 (2011 International Symposium on Mathematical Morphology)*, LNCS 6671, Springer-Verlag Berlin Heidelberg, p. 212–223, Intra (Lake Maggiore), Italy, July 2011.
11. J. Angulo and S. Velasco-Forero. "**Sparse Mathematical Morphology using Non-Negative Matrix Factorization**". In *Proc. of ISMM'11 (2011 International Symposium on Mathematical Morphology)*, LNCS 6671, Springer-Verlag Berlin Heidelberg, p. 1–12, Intra (Lake Maggiore), Italy, July 2011.
12. S. Velasco-Forero and J. Angulo. "**Mathematical Morphology for Vector Images using statistical depth**". In *Proc. of ISMM'11 (2011 International Symposium on Mathematical Morphology)*, LNCS 6671, Springer-Verlag Berlin Heidelberg, p. 355—366, Intra (Lake Maggiore), Italy, July 2011.
13. S. Velasco-Forero and J. Angulo. "**Multiclass ordering for filtering and classification of hyperspectral images**". In *IEEE WHISPERS'11 (3rd IEEE GRSS Workshop on Hyperspectral Image and Signal Processing)*, p. 1-4, Lisbon, Portugal, June 2011.
14. J. Angulo. "**Pseudo-Morphological Image Diffusion using the Counter-Harmonic Paradigm**". In *Proc. of Acivs'2010 (2010 Advanced Concepts for Intelligent Vision Systems)*, LNCS 6474, Springer-Verlag Berlin Heidelberg, Part I, p. 426–437, Sydney, Australia, December 2010.
15. S. Velasco-Forero and J. Angulo. "**Hit-or-miss transform in multivariate images**". In *Proc. of Acivs'2010 (2010 Advanced Concepts for Intelligent Vision Systems)*, LNCS 6474, Springer-Verlag Berlin Heidelberg, Part I, p. 452-463, Sydney, Australia, December 2010.

16. S. Velasco-Forero and J. Angulo. "**Morphological processing of hyperspectral images using kriging-based supervised ordering**". In *IEEE ICIP'10 (2010 IEEE International Conference on Image Processing)*, p. 1409-1412, Hong Kong, September 2010.
17. J. Angulo and S. Velasco-Forero. "**Structurally Adaptive Mathematical Morphology on Nonlinear Scale-Space Representations**". In *IEEE ICIP'10 (2010 IEEE International Conference on Image Processing)*, p. 121-124, Hong Kong, September 2010.
18. R. Verdu-Monedero, J. Angulo, J. Larrey-Ruiz, J. Morales-Sanchez. "**Comparison of orientated and spatially variant morphological filters vs mean/median filters for adaptive image denoising**". In *IEEE ICIP'10 (2010 IEEE International Conference on Image Processing)*, p. 113-116, Hong Kong, September 2010.
19. S. Velasco-Forero and J. Angulo. "**Statistical Shape Modeling using Morphological Representations**". In *IEEE ICPR'10 (20th IEEE International Conference on Pattern Recognition)*, p. 3537-3540, Istanbul, Turkey, August 2010.
20. S. Velasco-Forero and J. Angulo. "**Spatial structures detection in hyperspectral images using mathematical morphology**". In *IEEE WHISPERS'10 (2nd IEEE GRSS Workshop on Hyperspectral Image and Signal Processing)*, p. 1-4, Reykjavík, Iceland, June 2010.
21. J. Angulo, and S. Velasco-Forero. "**Semi-supervised hyperspectral image segmentation using regionalized stochastic watershed**". In *Proc. of SPIE symposium on Defense, Security, and Sensing : Algorithms and Technologies for Multispectral, Hyperspectral, and Ultraspectral Imagery XVI*, SPIE Vol. 7695, Orlando, United States, April 2010.
22. S. Velasco-Forero and J. Angulo. "**Parameters selection of morphological scale-space decomposition for hyperspectral images using tensor modeling**". In *Proc. of SPIE symposium on Defense, Security, and Sensing : Algorithms and Technologies for Multispectral, Hyperspectral, and Ultraspectral Imagery XVI*, SPIE Vol. 7695, Orlando, United States, April 2010.
23. J. Angulo. "**From Scalar-Valued Images to Hypercomplex Representations and Derived Total Orderings for Morphological Operators**". *Proc. of ISMM'09 (2009 International Symposium on Mathematical Morphology)*, LNCS 5720, Springer-Verlag Berlin Heidelberg, p. 238–249, Groningen, The Netherlands, August 2009.
24. J. Angulo and F. Meyer. "**Morphological Exploration of Shape Spaces**". *Proc. of ISMM'09 (2009 International Symposium on Mathematical Morphology)*, LNCS 5720, Springer-Verlag Berlin Heidelberg, p. 226—237, Groningen, The Netherlands, August 2009.
25. R. Verdú-Monedero, J. Angulo and J. Serra. "**Spatially-Variant Anisotropic Morphological Filters Driven by Gradient Fields**". *Proc. of ISMM'09 (2009 International Symposium on Mathematical Morphology)*, LNCS 5720, Springer-Verlag Berlin Heidelberg, p. 115-–125, Groningen, The Netherlands, August 2009.
26. S. Velasco-Forero and J. Angulo. "**Morphological scale-space for hyperspectral images and dimensionality exploration using tensor modeling**". *Proc. of IEEE WHISPERS'09 (First IEEE GRSS Workshop on Hyperspectral Image and Signal Processing)*, Grenoble, France, August 2009.
27. J. Angulo, S. Velasco-Forero, and J. Chanussot. "**Multiscale stochastic watershed for unsupervised hyperspectral image segmentation**". *Proc. of IEEE IGARSS'2009 (IEEE International Geoscience & Remote Sensing Symposium)*, Vol. III, 93–96, Cape Town, South Africa, July 2009.
28. S. Velasco-Forero, J. Angulo and J. Chanussot. "**Morphological image distances for hyperspectral dimensionality exploration using Kernel-PCA and ISOMAP**". *Proc. of*

IEEE IGARSS'2009 (IEEE International Geoscience & Remote Sensing Symposium), Vol. III, 109–112, Cape Town, South Africa, July 2009.

29. J. Angulo. "**Structure tensor of colour quaternion image representations for invariant feature extraction**". *Proc. of CCIW'09 (2009 Computational Color Imaging Workshop)*, LNCS 5646, Springer-Verlag Berlin Heidelberg, p. 91-–100, Saint-Etinne, France, March 2009.
30. R. Verdú-Monedero and J. Angulo. "**Spatially-variant directional mathematical morphology operators based on a diffused average squared gradient field**". *Proc. of ACIVS'2008 (Advanced Concepts for Intelligent Vision Systems)*, LNCS Vol. 5259, Springer-Verlag Berlin Heidelberg, p. 542–553, Juan-les-Pins, France, October 2008.
31. Y. Tarabalka, J. Chanussot, J.-A. Benediktsson, J. Angulo and M. Fauvel. "**Segmentation and classification of hyperspectral data using watershed**". *Proc. of IEEE IGARSS'2008 (IEEE International Geoscience & Remote Sensing Symposium)*, Vol. III, p. 652–655, Boston-Massachusetts, USA, July 2008.
32. J. Angulo. "**Morphological deterministic operators and stochastic models for image segmentation of multi-fluorescence labelled cell populations**". In (Eds. E. Wilson, A. Fitt, J. Norbury) *Progress in Industrial Mathematics at ECMI'2008 (Proc. of the 15th European Conference on Mathematics for Industry)*, London, UK, July 2008. Springer p. 217–222.
33. G. Noyel, J. Angulo and D. Jeulin. "**Regionalized random germs by a classification for probabilistic watershed. Application : angiogenesis imaging segmentation** ". In (Eds. E. Wilson, A. Fitt, J. Norbury) *Progress in Industrial Mathematics at ECMI'2008 (Proc. of the 15th European Conference on Mathematics for Industry)*, London, UK, July 2008. Springer p. 211–216.
34. J. Angulo. "**Quaternion colour representations and derived total orderings for morphological operators**". In *Proc. of the IS&T's Fourth European Conference on Color on Graphics, Imaging and Vision (CGIV'2008)*, p. 417–422, Terrasa-Barcelona, Spain, June 2008.
35. G. Noyel, J. Angulo and D. Jeulin. "**Classification-driven stochastic watershed. Application to multispectral segmentation**". In *Proc. of the IS&T's Fourth European Conference on Color on Graphics, Imaging and Vision (CGIV'2008)*, p. 471–476, Terrasa-Barcelona, Spain, June 2008.
36. F. Robert-Inacio, J. Angulo and E. Dinet. "**Contour and Detail Detection for Spatially Adaptive Color Median Filtering**". In *Proc. of the IS&T's Fourth European Conference on Color on Graphics, Imaging and Vision (CGIV'2008)*, p. 388–393, Terrasa-Barcelona, Spain, June 2008.
37. J. Angulo and B. Schaack. "**Morphological-based adaptive segmentation and quantification of cell assays in high content screening**". In *Proc. of the 5th IEEE International Symposium on Biomedical Imaging (ISBI'2008)*, p. 360–363, Paris, France, May 2008.
38. G. Noyel, J. Angulo, D. Jeulin, D. Balvay and C.-A. Cuenod. "**Filtering, segmentation and region classification by hyperspectral mathematical morphology of DCE-MRI series of angiogenesis imaging**". In *Proc. of the 5th IEEE International Symposium on Biomedical Imaging (ISBI'2008)*, p. 1517–1520, Paris, France, May 2008.
39. J. Angulo, C. Lajaunie, M. Bilodeau, L. Martinelli, F. Le Boulaire and F. Meyer. "**Preprocessing and analysis of microarray images from integrated lensless bio-photonic sensors**". In *Proc. of SPIE Photonics Europe 2008 : Optical and Digital Image Processing*, SPIE Vol. 7000, 12 p., Strasbourg, France, April 2008.
40. G. Noyel, J. Angulo, D. Jeulin. "**Random Germs and Stochastic Watershed for Unsupervised Multispectral Image Segmentation**", In *Proc. of 11th International Conference*

on Knowledge-based and Intelligent Information and Engineering Systems (KES 2007) (special session on Computational Learning Methods for Unsupervised Segmentation (CLeMUS)), Salerno, Italy, September 2007. Lecture Notes in Artificial Intelligence, Vol. LNAI 4694, Part III, p. 17–24, Springer, 2007.

41. J. Angulo, D. Jeulin. "**Stochastic watershed segmentation**", In *Proc. of the 8th International Symposium on Mathematical Morphology (ISMM'2007)*, Rio de Janeiro, Brazil, October 2007. p. 265–276, MCT/INPE, 2007.
42. F. Meyer, J. Angulo. "**Micro-viscous morphological operators**", In *Proc. of the 8th International Symposium on Mathematical Morphology (ISMM'2007)*, Rio de Janeiro, Brazil, October 2007. p. 165–176, MCT/INPE, 2007.
43. J. Angulo. "**Morphological texture gradients. Application to colour+texture watershed segmentation**", In *Proc. of the 8th International Symposium on Mathematical Morphology (ISMM'2007)*, Rio de Janeiro, Brazil, October 2007. p. 363–374, MCT/INPE, 2007.
44. G. Noyel, J. Angulo, D. Jeulin. "**On distances, paths and connections for hyperspectral image segmentation**", In *Proc. of the 8th International Symposium on Mathematical Morphology (ISMM'2007)*, Rio de Janeiro, Brazil, October 2007. p. 399–410, MCT/INPE, 2007.
45. G. Noyel, J. Angulo, D. Jeulin. "**Morphological segmentation of hyperspectral images**", In *Proc. of the ICS XII (International Conference in Stereology) 2007*, 8 p., Saint-Etienne, France, August 2007.
46. J. Angulo. "**Morphological model-based microarray spot classification and segmentation in polar coordinates**", In *Proc. of the ICS XII (International Conference in Stereology) 2007*, 8 p., Saint-Etienne, France, September 2007.
47. J. Angulo. "**Gradients morphologiques de texture. Application à la segmentation couleur+texture par LPE**" (in French). In *Actes de CORESA 2006 (Compression et Représentation des Signaux Audiovisuels)*, p. 42–47, Caen, France, November 2006.
48. J. Angulo. "**A mathematical morphology approach to the analysis of the shape of cells**". In (Eds. L.L. Bonilla, M. Moscoso, G. Platero, J.M. Vega) *Progress in Industrial Mathematics at ECMI'2006 (Proc. of the 14th European Conference on Mathematics for Industry)*, Leganes, Spain, July 2006. Springer, p. 543–547.
49. J. Angulo, B. Marcotegui. "**Sur l'influence des conditions d'éclairage dans la segmentation morphologique couleur par LPE**" (in French). In *Actes de CORESA 2005 (Compression et Représentation des Signaux Audiovisuels)*, p. 313–318, Rennes, France, November 2005.
50. J. Angulo. "**Morphological color processing based on distances. Application to color denoising and enhancement by centre and contrast operators**". In *Proc. of the IASTED International Conference on Visualization, Imaging, and Image Processing (VIIP'2005)*, p. 314–319, Benidorm, Spain, September 2005.
51. J. Angulo, S. Matou. "**Automatic quantification of *in vitro* endothelial cell networks using mathematical morphology**". In *Proc. of the IASTED International Conference on Visualization, Imaging, and Image Processing (VIIP'2005)*, p. 51–56, Benidorm, Spain, September 2005.
52. M.A. Luengo-Oroz, J. Angulo, G. Flandrin and J. Klossa. "**Mathematical morphology in polar-logarithmic coordinates. Application to erythrocyte shape analysis**". In *Proc. of the 2nd Iberian Conference on Pattern Recognition and Image Analysis (IbPRIA'2005)*, Estoril, Portugal, June 2005. Lecture Notes in Computer Science, Vol. LNCS 3523, p. 199–205, Springer, 2005.

53. J. Angulo. "**Unified morphological color processing framework in a lum/sat/hue representation**". In *Proc. of the International Symposium on Mathematical Morphology (ISMM'2005)*, Paris, France, April 2005. p. 387–396, Kluwer, 2005.
54. J. Angulo. "**Mathematical morphology operators for reading radioactivity DNA array images**". In *Proc. of the IASTED International Conference on Visualization, Imaging, and Image Processing (VIIP'2004)*, p. 802–807, Marbella, Spain, September 2004.
55. J. Angulo. "**Simplification morphologique d'images couleur par critères connectifs**" (in French). In *Actes de CORESA 2004 (Compression et Représentation des Signaux Audiovisuels)*, p. 149–152, Lille, France, May 2004.
56. J. Angulo and J. Serra. "**Mathematical morphology in color spaces applied to the analysis of cartographic images**". In *S. Levachkine, J. Serra and M. Egenhoger (Eds.) Semantic Processing of Spatial Data (Proc. of the GEOPRO 2003-International Workshop Semantic Processing of Spatial Data)*, p. 59–66, Mexico City, Mexico, November 2003.
57. J. Angulo and J. Serra. "**Color segmentation by ordered mergings**". In *Proc. of the IEEE International Conference on Image Processing (ICIP'2003)*, Vol. II, p. 125–128, Barcelona, Spain, September 2003.
58. F. Torres, J. Angulo and F. Ortiz. "**Automatic detection of specular reflectance in colour images using the MS diagram**". In *Proc. of the 10th International Conference on Computer Analysis of Images and Patterns (CAIP'2003)*, Groningen, The Netherlands, August 2003. Lecture Notes in Computer Science, Vol. LNCS 2756, p. 132–139, Springer, 2003.
59. J. Angulo and J. Serra. "**Morphological coding of color images by vector connected filters**". In *IEEE Proc. of the Seventh International Symposium on Signal Processing and Its Applications (ISSPA'2003)*, Vol. 1, p. 69–72, Paris, France, July 2003.
60. J. Serra and J. Angulo. "**Application of mathematical morphology to telemedicine and biotechnology : morphological characterisation of blood cells and analysis of cDNA microarrays**" (in Spanish). In *J. L. Díaz de León Santiago and C. Yañez Marquez (Eds.) Proc. of the CIARP 2002 (VII Congreso Iberoamericano en reconcimiento de patrones)*, p. 39–50, Mexico City, Mexico, November 2002.
61. J. Angulo, G. Flandrin and J. Klossa. "**Automated morphometric analysis of peripheral blood smears cells in microscopic large fields images**". In *Proc. of the 8th Congress of the European Society for Analytical Cellular Pathology*, p. 40-41, Heracliton Crete, Greece, September 2002.
62. J. Angulo and J. Serra. "**Morphological color size distributions for image classification and retrieval**". In *Proc. of ACIVS'2002 (Advanced Concepts for Intelligent Vision Systems)*, p. 46-53, Ghent, Belgium, September 2002.
63. J. Angulo and J. Serra. "**A mathematical morphology contribution to the analysis of DNA microarray images**". In *Proc. of the 5th ECMTB (European Society of Mathematical and Theoretical Biology) 2002 on Mathematical Modeling & Computing in Biology and Medecine*, p. 113, Milano, Italy, July 2002.
64. F. Ortiz, F. Torres, J. Angulo and S. Puente. "**Comparative study of vectorial morphological operations in different color spaces**". In *Proc. of Intelligent Robots and Computer Vision XX : Algorithms, Techniques, and Active Vision*, SPIE Vol. 4572, p. 259-268, Boston, Massachusetts, USA, November 2001.
65. J. Angulo, J. Serra and G. Flandrin. "**Haematological cytology image analysis and semantic indexing : Towards a global approach**". Special Presentation. In *Proc. of the XIVth Congress of the International Society of Diagnostic Quantitative Pathology*, p. 37, Oviedo, Spain, September 2001.

66. J. Angulo and J. Serra. "**Morphological texture study of the chromatin in lymphoid cells**". In *Proc. of the IX Spanish Symposium on Pattern Recognition and Image Analysis*, Vol II, p. 423-428, Benicàssim (Castellón), Spain, May 2001.
67. J. Angulo, J. Serra and G. Flandrin. "**Quantitative descriptors of the lymphocytes**". In *Proc. of the 7th Congress of the European Society for Analytical Cellular Pathology*, p. 69-70, Caen, France, April 2001.
68. A. Albiol, V. Naranjo and J. Angulo. "**Low complexity cut detection in the presence of flicker**". In *Proc. of the IEEE International Conference on Image Processing (ICIP'2000)*, Vol. III, p. 957-960, Vancouver, Canada, September 2000.

Autres (symposiums, séminaires, tutoriaux, cours, etc...)

1. J. Angulo. "**Mathematical Morphology for Matrix-Valued Images**". (Invited Speaker) In *Indo-French Workshop Matrix Information Geometries (MIG),* Ecole Polytechnique (Palaiseau), France, February 23rd-25th 2011.
2. J. Angulo. "**Counter-harmonic mean and pseudo-morphological image diffusion**". In *34ème Journée ISS (International Society for Stereology - France),* Paris, France, February 2011.
3. J. Angulo. "**Mathematical morphology for hyperspectral images : Filtering and segmentation in a supervised framework**". In *Séminaire "Morphologie mathématique, structures et connexions" - Le 70ème anniversaire de Jean Serra*, ESIEE (Marne-La-Vallée), France, April 2nd 2010.
4. J. Angulo and S. Velasco-Forero. "**Structurally adaptive mathematical morphology on nonlinear scale-space pyramids**". (in French) In *33ème Journée ISS (International Society for Stereology - France)*, Paris, France, February 2010.
5. J. Angulo. "**Hypercomplex Mathematical Morphology**". Invited Speaker to *Mathematics and Image Analysis 2009 (MIA'09)*, Paris, France, December 14-16, 2009.
6. J. Angulo. "**Morphologie mathématique multivariée appliquée aux images issues de la cytologie quantitative et du phenotypage cellulaire**" (in French). In *Séminaires du Département XLIM - SIC, Université de Poitiers*, Poitiers, France, March 2009.
7. J. Angulo. "**Segmentation morphologique d'images multivariées : de la couleur aux images hyperspectrales**" (in French), Lecture notes. In *Actes de l'Ecole d'Hiver sur l'Image Numérique Couleur (EHINC'2009)*, Toulon, France, January 13rd-16th 2009.
8. J. Angulo. "**Sur le calcul de la forme moyenne d'une famille d'objets**" (in French). In *31ème Journée ISS (International Society for Stereology - France)*, Paris, France, February 2008.
9. J. Angulo. "**Approche probabiliste à la segmentation morphologique par LPE, avec des exemples en imagerie multi-variée**" (in French). In *Séminaire au GIPSA-Lab, INP-Grenoble*, Grenoble, France, October 25th, 2007.
10. J. Angulo, D. Jeulin. "**Approche probabiliste à la segmentation morphologique par LPE**" (in French). In *30ème Journée ISS (International Society for Stereology - France)*, Paris, France, February 2007.
11. J. Angulo. "**Apports de la morphologie mathématique couleur au filtrage et à la segmentation**" (in French), Lecture notes. In *Actes de l'Ecole d'Hiver sur l'Image Numérique Couleur (EHINC'2007)*, Poitiers, France, January 9th-11th 2007.
12. J. Angulo. "**Morphologie mathématique en coordonnées (log-)polaires pour l'analyse des objets arrondis. Deux cas d'étude**" (in French). In *29ème Journée ISS (International Society for Stereology - France)*, Paris, France, February 2006.

13. J. Serra and J. Angulo. "**Etude sur la décomposition de cartes couleur en leurs différentes planches**" (in French). In *Journée GDR-ISIS traitements perceptifs couleur dédiés à l'image et à la vidéo*, Cergy-Pontoise, France, December 2005.
14. J. Angulo and S. Matou. "**Application of mathematical morphology to the quantification of *in vitro* endothelial cell organization into tubular-like structures**". In *4th World Congress on Cellular and Molecular Biology (CMB'05)*, Poitiers, France, October 2005.
15. J. Angulo and G. Flandrin. "**Ontology-based lymphocyte population description using mathematical morphology from colour blood images**". In *4th World Congress on Cellular and Molecular Biology (CMB'05)*, Poitiers, France, October 2005.
16. J. Klossa, J. Angulo, J.-C. Cordier, G. Flandrin, E. Jullien, G. Moebst and M.A. Luengo. "**VideoCell : a teleconsensual approach for cell semiology aimed at developing automated classifications tools ; application to peripheral blood cells**". In *7th European Congress on Telepathology*, Poznan, Poland, July 2004.
17. J. Angulo and J. Serra. "**Imagerie médicale et télémedecine**" (in French). *Revue des Ingénieurs-Mines*, No. 405, p. 37-38, Juillet-Septembre 2003.
18. J. Angulo. "**Rôle de l'analyse morphologique sur l'image biomédicale en télémédecine. Application à l'hématologie cellulaire**" (in French). In *12ème Forum des Jeunes Chercheurs en GBM - Journées de Recherche en Imagerie Médicale*, Nantes, France, May 2003.
19. J. Angulo. "**Analyse et quantification de l'image en biomédecine et biotechnologie avec des opérateurs morphologiques**" (in French). In *Cours d'imagerie médicale (2e année-2003), École Nationale Supérieur de Techniques Avancées*, Paris, France, April 2003.
20. J. Angulo and J. Serra. "**Segmentation d'images couleur, pyramides et fusion de partitions**" (in French). In *26ème Journée ISS (International Society for Stereology - France)*, Paris, France, February 2003.
21. J. Angulo and S. Matou. "**Quantification morphologique de l'organisation in vitro en réseau de type capillaire**" (in French). In *26ème Journée ISS (International Society for Stereology - France)*, Paris, France, February 2003.
22. F. Ortiz, F. Torres and J. Angulo. "**Aerial image segmentation using morphological color geodesy**" (in Spanish). In *XXIII Jornadas de Automática*, CD-ROM, paper $ja02_060$ (7 pp.), La Laguna (Santa Cruz de Tenerife), Spain, September 2002.
23. J. Angulo. "**Deux applications de la morphologie mathématique en imagerie biomédicale : puces à ADN et réorganisation in vitro de cellules endothéliales**" (in French). In *Cours de morphologie mathématique (2e année-2002), École Nationale Supérieur de Techniques Avancées*, Paris, France, April 2002.
24. J. Angulo and J. Serra. "**Application de la morphologie mathématique à l'analyse des images des puces à ADN**" (in French). In *25ème Journée ISS (International Society for Stereology - France)*, Paris, France, February 2002.
25. J. Angulo, G. Flandrin, J. Klossa and J. Serra. "**Le retour du microscope en hématologie : imagerie numérique et morphologie**" (in French) . In *Premier Colloque "Sang et Vin"*, Bordeaux, France, April 2001.
26. F. Meyer, M. Coster and J. Angulo. "**Tutorial on Image Analysis and Mathematical Morphology**". In *7th Congress of the European Society for Analytical Cellular Pathology*, Caen, France, April 2001.
27. J. Angulo and J. Serra. "**Etude morphologique de la texture de la chromatine des lymphocytes**" (in French). In *24ème Journée ISS (International Society for Stereology - France)*, Paris, France, February 2001.

28. J. Angulo. "**Cytologie quantitative et morphologie mathématique : Application aux syndromes lymphoprolifératifs**" (in French). In *Ecole d'été de Morphologie Mathématique 2000, Centre de Morphologie Mathématique - Ecole des Mines de Paris*, Fontainebleau, France, September 2000.
29. J. Klossa, J. Angulo, P. Hauri and G. Migliore. "**Instruments and Telepathology**". In *5th European Congress on Telepathology*, Aurich, Germany, July 2000.

Deuxième partie

Activités de recherche théorique et méthodologique

Chapitre 5

Modélisation et traitement morphologique des images couleur

Les travaux présentés dans ce chapitre sur l'extension de la morphologie mathématique aux images couleur ont été en partie l'objet de ma thèse de doctorat. Il s'agit notamment de mes recherches réalisées en étroite collaboration avec J. Serra sur le calcul approprié du changement des coordonnées cartésiennes rouge, verte, bleue aux coordonnées polaires luminance, saturation et teinte ainsi que l'intérêt de ce dernier espace de représentation pour la segmentation morphologique couleur. Nous avons en particulier montré le rôle que la saturation peut jouer pour une combinaison adaptative de l'information chromatique et de l'information achromatique (ou spectrale vs. géométrique-spatiale), soit pour la construction des gradients couleur utilisées avec la LPE, soit pour la combinaison de partitions associées à chaque magnitude de la couleur, soit finalement pour la généralisation de transformations résiduelles, type chapeau haut de forme, pour l'extraction de détails couleur. Par ailleurs, nous avons proposé un modèle linéaire d'illumination régionalisée qui permet une interprétation physique de la présence d'alignements dans les histogrammes luminance/saturation.

Dans la deuxième partie du chapitre, je me concentre plus sur la définition de la dilatation et l'érosion couleur. A partir des travaux préliminaires proposés par plusieurs chercheurs sur l'utilisation des ordres lexicographiques associés aux représentations type luminance, saturation et teinte, j'ai approfondi de manière systématique, également dans ma thèse de doctorat, les propriétés de filtrage pour la simplification par nivellements, pour le débruitage, pour l'extraction de détails, etc. J'ai ensuite poursuivi mes recherches en filtrage et segmentation morphologique couleur, et je continue à le faire, car les enjeux en termes d'applications sont très importants. L'image couleur reste le cadre d'étude privilégié pour explorer théoriquement les différentes alternatives de généralisation des approches morphologiques aux images multi-variées. Ainsi, j'ai ensuite étudié comment un pré-ordre associé à la distance couleur à une couleur de référence, complété de manière secondaire par une cascade lexicographique, permet de bâtir des opérateurs couleur très puissants pour le filtrage couleur. Plus récemment, en travaillant sur des représentations des couleurs par des quaternions, j'ai aussi proposé des ordres totaux pour l'extension des opérateurs couleur qui utilisent les propriétés de manipulation géométrique des quaternions (représentation polaire, projections, décompositions selon une référence, etc.) avec une formulation qui généralise mes travaux précédents.

5.1 Modélisation et segmentation morphologique des images couleur représentées dans des espaces couleur polaires

Luminance, saturation et teinte en norme L_1 ; alignements en lum/sat ; modèle linéaire régionalisé d'illumination

Parmi les représentations des images couleur les plus couramment utilisées, on trouve les représentations géométriques en coordonnées polaires de type Teinte-Luminance-Saturation (TLS). La luminance correspond à l'intensité lumineuse, la saturation mesure la pureté de la couleur et la teinte est un index représentant la longueur d'onde dominante ou couleur perçue. En accord avec l'interprétation humaine, les espaces TLS permettent une séparation de l'information chromatique et achromatique. Les représentations classiques sont limitées : les expressions de la luminance et de la saturation ne sont souvent pas des normes, conduisant à des résultats faux pour le calcul des valeurs moyennes ou de distances. De plus, ces deux composantes ne sont pas indépendantes.

Ces défauts peuvent être surmontés par diverses représentations alternatives, selon différentes normes employées pour définir la luminance et la saturation. Plus précisément, nous avons démontré grâce aux histogrammes bi-variables luminance/saturation et teinte/saturation que la diversité dans la définition des notions de saturation et de luminance fournit un ensemble de représentations complémentaires. Nous avons à ce sujet proposé une méthode simple de segmentation couleur, par clustering morphologique des histogrammes et combinaison des deux partitions associées.

Nous avons ensuite introduit une approche pour l'extraction de reflets, ombres portées et dégradés de lumière d'une image couleur en étudiant les alignements de l'histogramme luminance/saturation en norme L_1. Elle est fondé sur un modèle que nous avons introduit de variation spectrale régionalisée qui permet l'interprétation de ces alignements de l'histogramme luminance/saturation.

Rôle de la saturation dans la segmentation : gradients et top-hats couleur

Nous avons aussi abordé l'extension de certains opérateurs morphologiques pour le filtrage et la segmentation d'images couleur, le but principal étant de développer des opérateurs couleur, extension des opérateurs scalaires, qui soient adaptés aux caractéristiques avantageuses des espaces couleur type TLS. Notamment le fait d'avoir à notre disposition l'information chromatique et l'information achromatique d'une manière indépendante, ainsi qu'une information comme la saturation qui joue le rôle de poids de contrôle entre les deux, nous permet de proposer quelques façons différentes de filtrer/segmenter conjointement les structures chromatiques et achromatiques d'une image couleur.

Nous avons introduit une extension des opérateurs gradient et des chapeaux haut de forme pour les images couleur, en utilisant les opérateurs scalaires et angulaires classiques pour chacune des composantes de l'espace TLS, en les combinant intuitivement avec la saturation. Nous avons aussi caractérisé l'intérêt pratique de ces gradients couleurs pour la segmentation par LPE : segmentation combinée ou séparée des régions chromatiques et achromatiques, robustesse face aux variations des conditions d'illumination de la même scène, gradients associés à des invariants couleurs, etc...

Rôle de la saturation dans la segmentation : connexions scalaires et combinaison contrôlée par la saturation

Le fondement de l'approche est la formalisation de l'observation psycho-visuelle selon laquelle l'on segmente à l'aide des variations de teinte dans les régions saturées, et des variations de luminance dans les régions grises. Le principe mis en place est le suivant : i) segmenter séparément la luminance, la saturation et la teinte, ii) et combiner les partitions de la luminance et de la teinte à l'aide de la saturation, qu'on prendra comme critère pour choisir en chaque endroit l'une ou l'autre classe des segmentations de la luminance et de la teinte.

Il y a plusieurs façons de construire les segmentations séparées, ainsi que de les mixer (en seuillant ou non la saturation, par exemple). En particulier nous avons montré la pertinence de l'usage de critères connectifs scalaires ; comme par exemple, les connexions par sauts.

Principales publications

- J. Angulo and J. Serra. "**Color segmentation by ordered mergings**". In *Proc. of the IEEE International Conference on Image Processing (ICIP'2003)*, Vol. II, p. 125–128, Barcelona, Spain, September 2003.
- J. Angulo and J. Serra. "**Mathematical morphology in color spaces applied to the analysis of cartographic images**". In *S. Levachkine, J. Serra and M. Egenhoger (Eds.) Semantic Processing of Spatial Data (Proc. of the GEOPRO 2003-International Workshop Semantic Processing of Spatial Data)*, p. 59–66, Mexico City, Mexico, November 2003.
- J. Angulo, J. Serra. "**Modelling and Segmentation of Colour Images in Polar Representations.**". *Image Vision and Computing*, Vol. 25, No. 4, 475–495, 2007.

5.2 Treillis couleur et opérateurs morphologiques pour le filtrage et l'extraction de caractéristiques

Ordres totaux lexicographiques et priorité dans le choix des différentes variables couleur : approche adaptative régionale

Les opérateurs morphologiques ont besoin d'une structure de treillis complet. Nous rappelons qu'un treillis complet repose sur la définition d'un ordre partiel et l'existence d'un infimum (plus grand minorant associé à l'érosion) et d'un supremum (plus petit majorant associé à la dilation). Il existe un grand nombre de familles de méthodes pour ordonner les données vectorielles. Pour certains ordres vectoriels, le sup et l'inf d'un ensemble de vecteurs ne font pas toujours partie de cet ensemble. Ce problème se manifeste par l'introduction de fausses couleurs dans l'image filtrée. Une méthode intéressante (et la plus étudiée dans la littérature) pour définir le sup et l'inf de couleurs est l'ordre conditionnel, car il n'introduit pas de nouveaux points.

L'utilisation de l'ordre conditionnel ou lexicographique implique forcément l'attribution d'une priorité aux composantes, parce que dans la plupart des cas, la relation d'ordre de deux vecteurs sera décidée par la première condition de la cascade lexicographique. Il est souhaitable de pouvoir contrôler la dépendance vis-à-vis de la première composante en rendant plus flexible l'ordre lexicographique, tout en préservant le principe d'ordre total. Nous avons proposé une approche qui consiste à réduire d'une manière linéaire la marge dynamique de variation de la première composante : ordre lexicographique à module. Ensuite, nous avons caractérisé les différents ordres lexicographiques à module dans les espaces couleur TLS : priorité donnée à la luminance, priorité à la saturation et priorité à la teinte (pondérée par la saturation).

Par ailleurs, nous avons introduit une méthode pour la simplification morphologique des images couleur qui est basée sur l'application d'un nivellement couleur à chaque région significative, en adaptant le choix de l'ordre lexicographique à la nature de la région (chromatique ou achromatique), et qui a besoin évidemment d'une segmentation préalable de l'image.

Ordres réduits par distance à une couleur de référence, complétés avec cascades lexicographiques

Ensuite, dans une autre étude, nous avons généralisé l'approche précédente avec un cadre très riche pour la construction d'opérateurs morphologiques dérivés des érosions/dilations, qui consiste à définir un pré-ordre basé sur la distance de chaque point dans l'espace couleur à une couleur de référence.

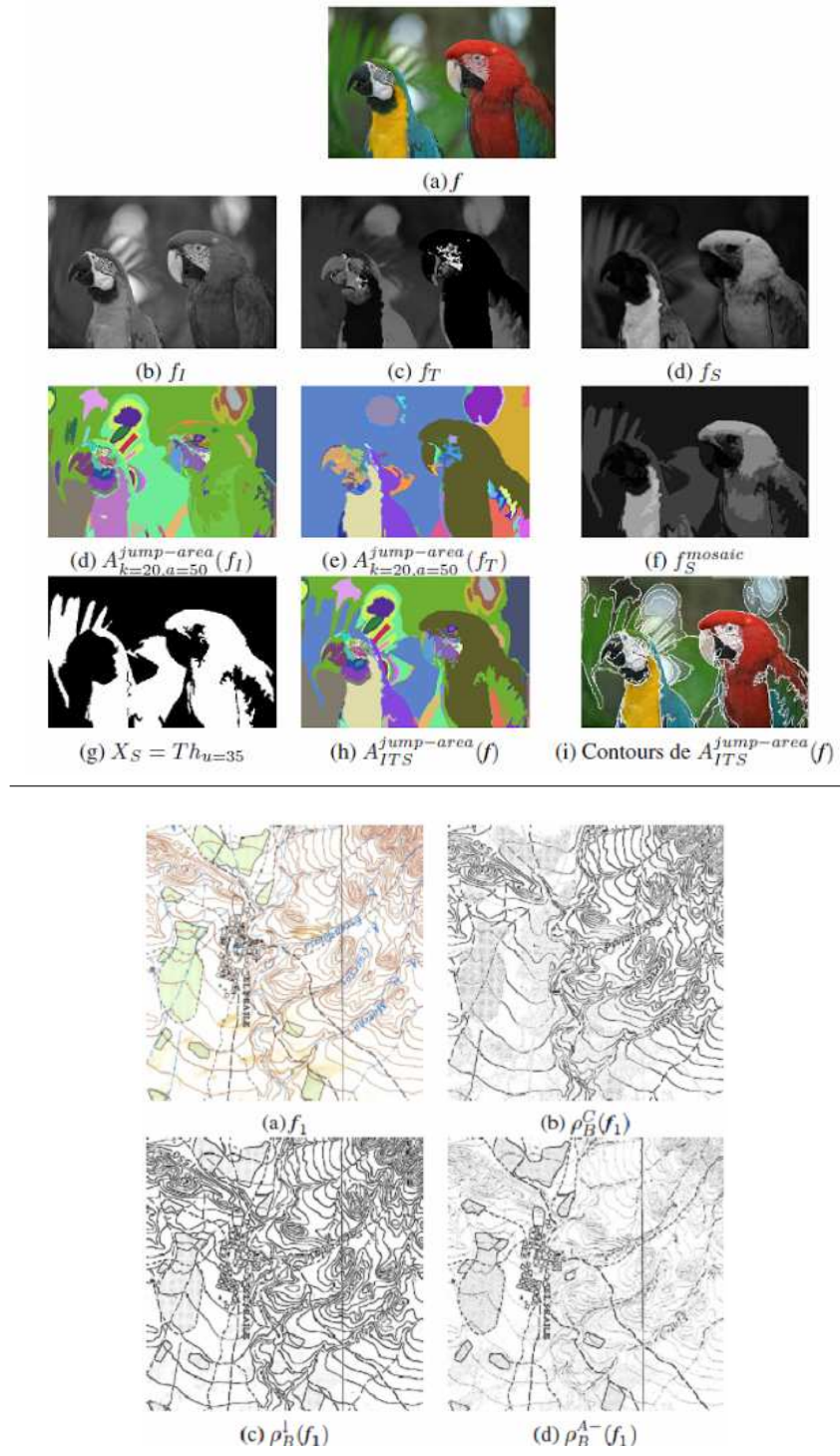

FIG. 5.1 – Segmentation morphologique des images couleur représentées dans des espaces couleur polaires : haut, segmentation marginale par connexions scalaires et combinaison des partitions de la luminance et de la teinte à l'aide de la saturation ; bas, chapeaux haut de forme chromatique et achromatique pour l'extraction des détails.

Ce type d'ordres réduits, par distance à une couleur de référence, doit être complété par une cascade lexicographique.

Cette méthode d'ordre est très générale et elle peut être utilisée avec toutes les représentations couleur, y compris celles qui n'ont pas des cascades lexicographiques évidentes (RVB et L*a*b*), car les points couleur sont principalement ordonnés par rapport à leur distance à la référence. Par ailleurs, nous avons montré avec différentes applications que le choix de la couleur de référence donne une grande flexibilité pour l'adaptation des effets d'un opérateur aux structures d'une couleur particulière proche de ou opposée à la couleur de référence.

Quaternions couleur, décompositions quaternioniques et ordres totaux

Les images couleur peuvent être représentées par différentes structures algébriques ; en particulier, nous avons abordé en profondeur l'intérêt des représentations couleur par des quaternions réels, et notamment l'apport de la partie scalaire pour introduire une dimension colorimétrique additionnelle au triplet RVB.

Nous avons ainsi étudié différentes alternatives de la partie scalaire, qui est nécessaire pour avoir un quaternion couleur complet. Il s'agit de trois variantes : une fonction de saturation, une fonction de masse associée à une couleur de référence, une fonction de potentiel associée à un ensemble de couleurs de référence. Nous avons ensuite considéré l'extension de la morphologie mathématique aux images quaternioniques couleur ; ce qui implique fondamentalement la construction des ordres totaux pour des quaternions réels. Ces ordres utiliseront différentes représentations des quaternions réels : hypercomplexe, polaire, parallèle/perpendiculaire. Nous avons étudié les propriétés des différents ordres et nous avons illustré les algorithmes avec des applications réelles des opérateurs quaternioniques couleur de type géodésique (associés à la reconstruction géodésique).

Par ailleurs, nous avons abordé l'extension de la notion de tenseur de structure, basé sur le produit dyadique des dérivées premières, aux images quaternioniques couleur. Ainsi, on a pu généraliser les détecteurs classiques de points d'intérêt et d'extraction de contours, qui sont obtenus à partir des valeurs propres du tenseur de structure quaternionique couleur. Les propriétés d'invariance des dérivées spatiales couleur ont été aussi considérées.

Principales publications

- J. Angulo. "**Unified morphological color processing framework in a lum/sat/hue representation**". In *Proc. of the International Symposium on Mathematical Morphology (ISMM'2005)*, Paris, France, April 2005. p. 387–396, Kluwer, 2005.
- J. Angulo. "**Morphological colour image simplification by saturation-controlled regional levellings**". *International Journal of Pattern Recognition and Artificial Intelligence*, Vol. 20, No. 8, 1207–1223, December 2006.
- J. Angulo. "**Morphological colour operators in totally ordered lattices based on distances. Application to image filtering, enhancement and analysis**". *Computer Vision and Image Understanding*, Vol. 107, No. 2–3, 56–73, 2007.
- J. Angulo. "**Geometric algebra colour image representations and derived total orderings for morphological operators - Part I : Colour Quaternions**". *Journal of Visual Communication and Image Representation*, Vol. 21, 33–48, 2010.
- J. Angulo. "**Structure tensor of colour quaternion image representations for invariant feature extraction**". *Proc. of CCIW'09 (2009 Computational Color Imaging Workshop)*, LNCS 5646, Springer-Verlag Berlin Heidelberg, p. 91-–100, Saint-Etinne, France, March 2009.

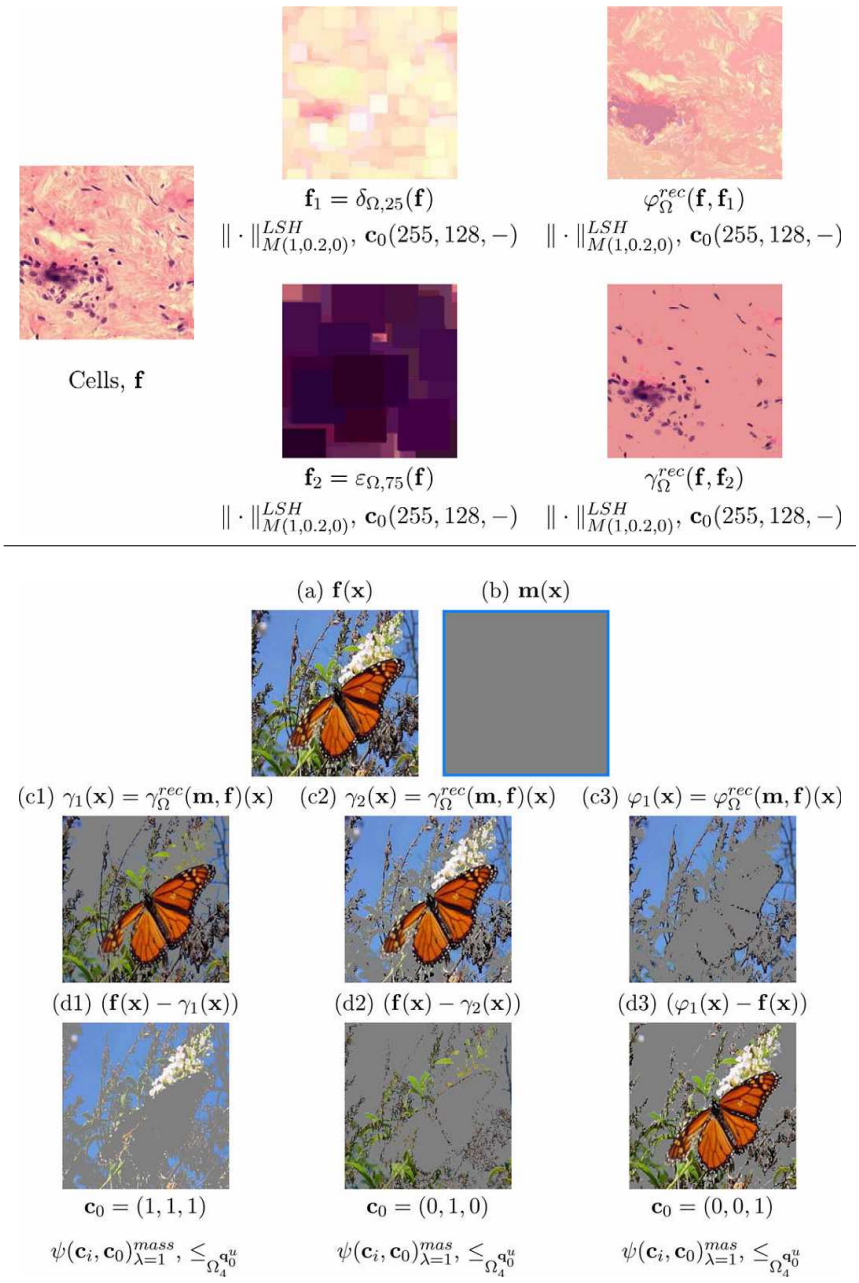

FIG. 5.2 – Filtrage morphologique couleur par des opérateurs géodésiques (ouvertures/fermetures par reconstruction) : haut, utilisation des ordres réduits par distance à une couleur de référence ; bas, représentation par des quaternions couleur et ordres totaux par décomposition parallèle/perpendiculaire selon une couleur de référence.

Chapitre 6

Filtrage, exploration de la dimension et morphologique mathématique pour des images multi/hyper-spectrales

De manière assez naturelle, après avoir étudié en profondeur les possibilités d'extension de la morphologie mathématique aux images couleur, je me suis intéressé au cas plus général des images multi/hyper-spectrales.

Dans la thèse de G. Noyel (2005-2008), que j'ai co-dirigé avec D. Jeulin, nous avons développé une chaîne complète de segmentation automatique des images hyperspectrales par des techniques morphologiques. Pour ce faire, nous avons mis au point une méthode efficace de débruitage spectral par Analyse Factorielle de Correspondances, qui permet de conserver les contours spatiaux des objets. Puis la dimension est réduite par des méthodes linéaires d'analyse de données ou par modélisation des spectres, afin d'obtenir une autre représentation de l'image avec un nombre restreint de canaux. A partir de cette image de plus faible dimension, des techniques de classification (non supervisée type k-means, ou supervisée type LDA) permettent de grouper les pixels en classes spectralement homogènes. Le résultat de la classification peut ensuite être utilisé pour construire les marqueurs d'une segmentation par LPE construite sur un gradient vectoriel. Nous avons montré en particulier l'intérêt de la LPE probabiliste, où le tirage des germes est conditionné par la classification spectrale ; ce qui produit à la fin des segmentations spatio-spectrales avec des contours réguliers et pertinents.

Pour valider la généralité de nos méthodes de traitement, nous les avons appliquées à plusieurs types d'imagerie correspondant aux images hyperspectrales les plus variées : des images multispectrales dans le visible avec quelques dizaines de longueurs d'ondes, des images satellites de télédétection, des séries temporelles d'imagerie thermique et des séries temporelles d'imagerie par résonance dynamique (DCE-MRI). En particulier, pour ce dernier type d'images, les méthodes développées ont permis d'établir une méthode automatique d'aide à la détection de tumeurs cancéreuses.

Par ailleurs, à partir des nouvelles connexions définies pour des fonctions multi-variées, nous avons proposé d'autres techniques géodésiques de segmentation des images hyperspectrales qui permettent de déterminer les régions homogènes selon des critères de variation

totale ou de distance géodésique. Le problème du calcul efficace du tableau de toutes les paires de distances géodésiques dans une image a été aussi considéré dans les travaux de thèse de G. Noyel. Ce type de représentation extrêmement riche, mais aussi très lourde à calculer, est indispensable pour certains algorithmes de réduction de la dimension et de segmentation d'image, particulièrement appropriés pour les images hyperspectrales.

La suite de ces travaux dans le domaine de l'imagerie hyperspectrale correspond à la thèse de S. Velasco-Forero (2009-), que je dirige actuellement. Dans la première année de la thèse, nous avons travaillé sur la façon d'introduire avec des outils morphologiques l'information structurelle dans la réduction de la dimension et dans la subséquente classification des pixels dans l'espace à dimension réduite. Nous avons notamment exploré deux pistes. La première approche consiste à représenter chaque composante spectrale selon la dérivée d'un espace-échelle non-linéaire, basé sur une famille de nivellements. Avec cette décomposition morphologique, les contours des structures sont bien préservés. Ensuite, l'ensemble des espaces-échelles de différentes composantes spectrales est considéré comme un tenseur d'ordre 4 : deux ordres spatiaux, un ordre spectral et un ordre structurel. A l'aide de techniques assez récentes de l'algèbre multilinéaire, nous pouvons réduire simultanément les différents ordres du tenseur et en conséquence, représenter les images dans des espaces où les points s'organisent selon les valeurs spectrales mais aussi leur position dans l'image ainsi que sur leur appartenance structurelle.

La deuxième approche s'appuie sur des techniques métriques non-linéaires de réduction de la dimension (e.g., ACP à noyau et ISOMAP). Cette fois-ci, la façon d'introduire l'information structurelle consiste à utiliser des distances de nature morphologique entre les composantes spectrales pour construire la matrice de Gramm des variables. Nous avons exploré deux familles de distances. La première est une généralisation de la métrique de Hausdorff pour des fonctions numériques ; la deuxième est de nouveau fondée sur l'opérateur nivellement et sur la mesure des distances dans le chemin géodésique constitué par les images intermédiaires du nivellement de chaque paire de composantes spectrales.

Les performances de ces techniques innovantes sont assez encourageantes et constituent une contribution notable par rapport à l'état de l'art.

Dans la deuxième phase de la thèse de S. Velasco-Forero, les recherches qu'il mène sous ma direction se sont focalisées sur l'extension des opérateurs dilation/érosion aux images hyperspectrales. Notre objectif étant d'introduire un cadre de traitement qui combine efficacement l'information spectrale et l'information spatiale/géométrique. Nous avons notamment proposé deux formalismes différents qui sont très originaux par rapport à l'état de l'art et qui permettent une extension correcte de la morphologie mathématique aux images hyperspectrales, tout en fournissant une méthodologie pour résoudre les problèmes typiques en analyse hyperspectrale.

La première approche considérée est fondée sur l'hypothèse que l'on dispose d'une information spectrale a priori sur les objets d'intérêt, ou plus généralement, que l'on dispose d'un training set pour chaque classe spectrale contenue dans l'image. Dans ce cadre, et en utilisant des techniques d'apprentissage comme le krigage et les SVM, il est possible de construire un ordre vectoriel supervisé. Le cas le plus intéressant est celui d'un ordre partiel (complété par une cascade lexicographique) associé à une paire d'ensembles (e.g., ensemble de "foreground" et ensemble de "background"). Nous avons aussi considéré les cas d'un ordre multi-classes. Les opérateurs morphologiques associés sont particulièrement utiles pour l'extraction d'objets selon leur morphologie et spectre (par résidus d'ouvertures/fermetures), la détection de cibles structurées (par transformé en tout-ou-rien), la

segmentation spatio-spectrale (par nivellement), etc...

Le deuxième formalisme est basé sur les fonctions de profondeur statistique, qui permettent de construire un ordre partiel dans les vecteurs selon leur structure spectrale intrinsèque. Les fonctions de profondeur statistique attribuent à chaque vecteur son degré de centralité par rapport à la distribution de tous les vecteurs spectraux présents dans l'image. Il y a des algorithmes très efficaces pour estimer la profondeur avec des projections aléatoires uni-variées. L'hypothèse fondamentale qui garantit l'intérêt des dilations/érosions associées à un ordre par profondeur et le fait d'avoir une image avec une distribution "foreground"/"background" relativement définie : le "centre" de la distribution correspond aux spectres du fond de l'image et les "outliers" étant associés aux objets spectralement différents du fond. Avec cette méthode, il est possible de résoudre des problèmes en imagerie hyperspectrale tels que la détection d'anomalies sur un background relativement hétérogène, le débruitage et la régularisation spatiale pour améliorer l'extraction d'endmembers, etc.

Finalement, S. Velasco-Forero et moi-même avons généralisé la notion de profondeur statistique aux espaces géodésiques ce qui permet son calcul pour des formes 2D/3D ; nous avons montré que la fonction de profondeur géodésique est un descripteur de formes avec de bonnes propriétés d'invariance.

6.1 Segmentation spatio-spectrale morphologique des images hyperspectrales

Filtrage spectral et réduction de la dimension par Analyse Factorielle de Correspondances

Généralement, les différents canaux (ou composantes spectrales), d'une image multi/hyper-spectrale sont fortement corrélés entre eux. La première étape consiste donc à réduire sa dimension pour trouver un espace de projection à dimension réduite qui représente au mieux l'information importante. En fait, cette réduction implique aussi un filtrage du bruit spectral de l'image et permet d'améliorer les étapes ultérieures de classification ou segmentation spatio-spectrale.

Nous avons considéré en détail des méthodes de réduction de dimension par Analyse Factorielle des Correspondances (AFC) et par Analyse en Composantes Principales (ACP). Les canaux de l'image multi/hyper-spectrale sont ainsi transformés pour obtenir un espace de dimension réduite composé de facteurs pixels (i.e. vecteurs propres de l'AFC ou de l'ACP) qui constituent une nouvelle représentation de l'image hyperspectrale de départ. Par ailleurs, une nouvelle méthode de sélection des axes factoriels par leur rapport signal à bruit a été développée, qui est fondé sur l'estimation de la matrice de covariance de chaque facteur pixel et l'étude de sa valeur à l'origine (effet pépite en géostatistique), pour séparer dans l'estimation le terme de variance de bruit et de variance de signal. Elle s'avère être particulièrement intéressante car elle prend en compte l'information spatiale portée par les axes et non plus un critère statistique d'inertie ou de variance comme c'est souvent le cas dans le choix des dimensions pertinentes.

Par ailleurs, en reconstruisant à partir des facteurs pixels retenus, nous avons montré la capacité de débruitage, à la fois pertinente et rapide. Cette méthode de débruitage spectral, qui conserve les contours spatiaux tout en réduisant le bruit, offre l'avantage d'avoir des contours les plus nets possibles en vue du traitement morphologique. Une étude très poussée sur des données simulées nous a permis de constater que la composition de deux AFC-reconstitutions (avec un décalage du tableau de données pour assurer la positivité) améliore notablement la qualité de débruitage. Cette question du "shift" du centre des données (qui pourrait se faire de manière stochastique en cherchant l'optimal) plus

l'itération de l'analyse reste ouverte et mérite sans doute un approfondissement.

Gradients vectoriels, marqueurs associés à une classification et segmentation hyperspectrale par LPE probabiliste

Dans les images multi/hyper-spectrales il existe souvent un ensemble d'entrainement qui décrive chacune des classes spectrales à segmenter. Ainsi, l'étape suivante à la réduction de la dimension/débruitage est la classification spectrale des pixels de l'image (qui sera supervisée avec des algorithmes type LDA ; ou non-supervisée s'il n'y a pas d'ensemble d'apprentissage, avec des techniques type k-means). Néanmoins cette classification ne tient pas compte de la cohérence spatiale entre les pixels et produit donc des résultats qui ne sont pas des régions homogènes spatialement/spectralement. Pour arriver à cet objectif nous avons utilisé la LPE.

L'approche par LPE nécessite une fonction à inonder scalaire (i.e. une image à niveaux de gris) et des marqueurs. Pour obtenir ces marqueurs, nous avons montré qu'il est possible d'utiliser les classes de la classification spectrale précédemment obtenues après quelques traitements mineurs (réduction de leur surface). Avec une distance spectrale adaptée à l'espace image de représentation, il est possible de construire un gradient de l'image multi/hyper-spectrale. Ce type de gradient généralise notre démarche introduite pour le calcul des gradients sur des images couleur.

D'autre part, dans ces travaux, nous avons fait apparaître que pour les images hyperspectrales, la LPE probabiliste est bien adaptée si l'on construit des densités de probabilités de contours (pdf) à partir de germes conditionnés par la classification spectrale. Le mécanisme de la LPE probabiliste sera décrit brièvement dans le chapitre 9. Dans ces conditions, la densité de probabilité de contours (pdf) obtenue prend donc à la fois en compte l'information spatiale et l'information spectrale. La segmentation de cette fonction est ensuite effectuée par LPE sur un critère morphologique permettant de sélectionner un nombre a priori de régions selon le volume du bassin versant associé. Nous avons également développé une approche plus robuste que le critère du nombre de régions. Il est en effet particulièrement intéressant d'utiliser des marqueurs issus de la classification spectrale, pour choisir les régions, puisque seul le nombre de classes est requis. Ce critère est plus robuste que le nombre de régions car il est le même pour des images similaires présentant le même nombre de classes spectrales alors que ce n'est pas le cas pour le nombre de régions.

Nous avons montré qu'une même chaîne de traitement (exactement les mêmes algorithmes et en considerant un cadre supervisé avec un ensemble d'entrainement pour chaque classe spectrale à segmenter) permet de segmenter de manière satisfaisante des images multi-variée issues de domaines aussi différents que la télédétection ou l'imagerie médicale : séries temporelles d'imagerie résonance magnétique dynamique utilisées pour la détection tumorale par injection de produit de contraste.

Principales publications

- G. Noyel, J. Angulo and D. Jeulin. "**Morphological segmentation of hyperspectral images**". *Image Analysis and Stereology*, Vol. 26, 1–9, 2007.
- G. Noyel, J. Angulo, D. Jeulin, D. Balvay and C.-A. Cuenod. "**Filtering, segmentation and region classification by hyperspectral mathematical morphology of DCE-MRI series of angiogenesis imaging**". In *Proc. of the 5th IEEE International Symposium on Biomedical Imaging (ISBI'2008)*, p. 1517–1520, Paris, France, May 2008.
- G. Noyel, J. Angulo and D. Jeulin. "**A new spatio-spectral morphological segmentation for multispectral remote sensing images**". *International Journal of Remote Sensing*, Vol. 31, No. 22, 5895-–5920, 2010.

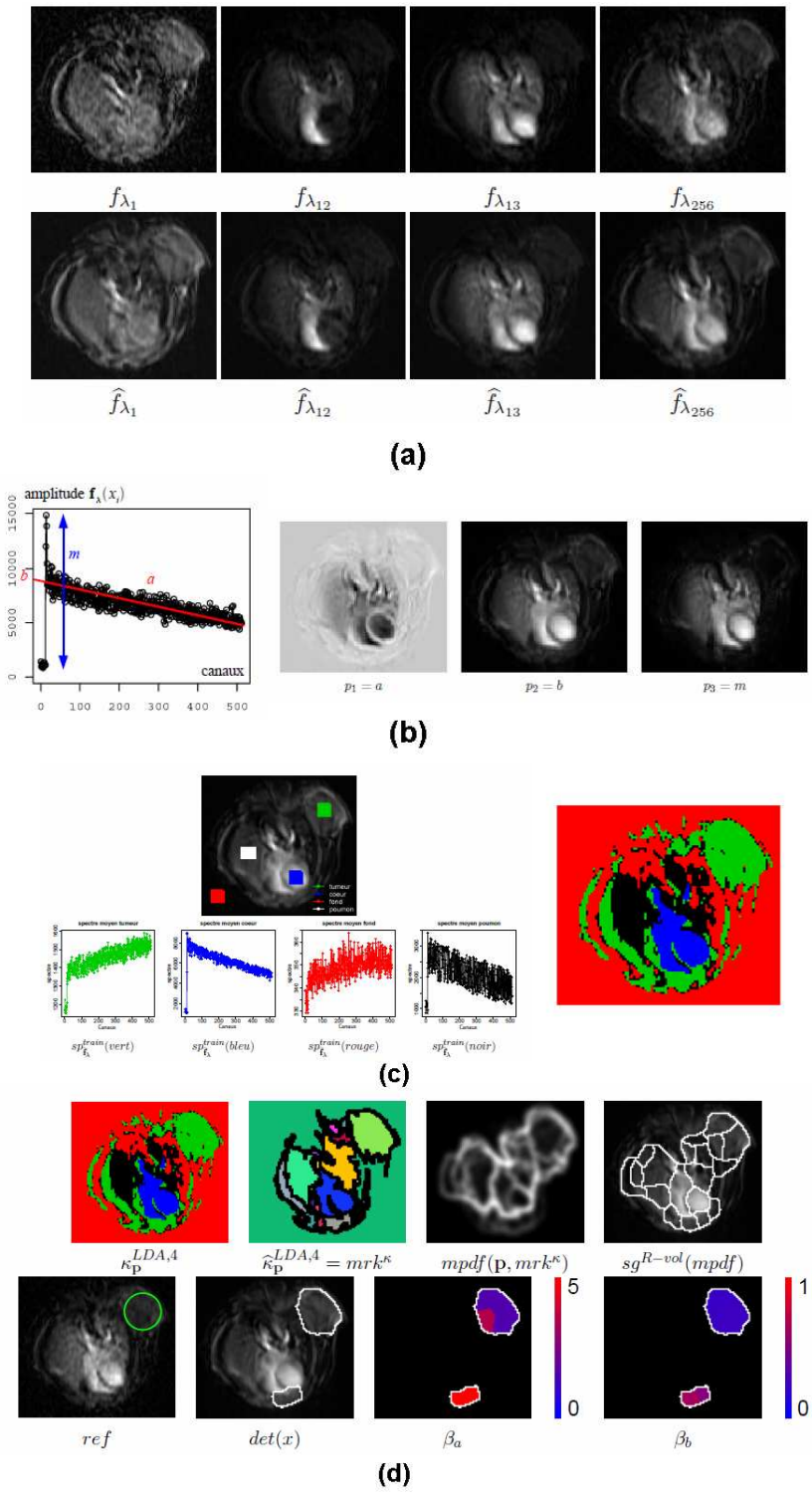

FIG. 6.1 – Segmentation spatio-spectrale morphologique appliquée à l'analyse de séries temporelles d'imagerie résonance magnétique dynamique utilisées pour la détection tumorale par injection de produit de contraste : (a) debruitage par réduction avec AFC ; (b) modélisation temporelle et images paramétriques ; (c) classification supervisée par LDA ; (d) gradients vectoriels, marqueurs associés à la classification, segmentation par LPE probabiliste et détection tumorale par analyse des zones de l'image.

6.2 Chemins géodésiques et connexions pour la segmentation des images hyperspectrales

Au-delà des $\lambda-$flat zones : régions $\eta-$bornées et boules $\mu-$géodésiques

Si l'on considère une distance spectrale pour comparer deux pixels d'une image hyperspectrale, il est possible de définir des critères connectifs pour construire une partition de l'image en zones connexes. Les zones $\lambda-$plates utilisent exclusivement un seuil local : un ensemble de pixels est consideré comme appartenant à la même zone $\lambda-$plate si pour toute paire de pixels il existe un chemin tel que l'écart entre deux pixels adjacents est inférieur à λ. Le paramètre croisant λ engendre une hiérarchie ou pyramide de partitions. L'inconvénient principal des zones $\lambda-$plates, pour la segmentation en zones pertinentes, vient du fait qu'elles sont très sensibles à des petites variations du paramètre λ. Pour pallier à cet effet, nous avons proposé des critères qui utilisent une information régionale par rapport à l'information locale des zones $\lambda-$plates.

Nous avons introduit les connexions η et μ, qui sont considérées de second ordre car elles sont incluses dans les zones connexes $\lambda-$plates. Afin de construire ces nouvelles zones, la méthode consiste à sélectionner un paramètre λ suffisamment élevé pour obtenir une sous-segmentation. Puis les régions $\eta-$bornées et les boules $\mu-$ géodésiques sont construites, conduisant à une segmentation par agrégation. Les régions $\eta-$bornées introduisent un paramètre qui contrôle les variations spectrales (i.e., le "dénivelé" spectral global) dans les zones $\lambda-$plates, tandis que les boules $\mu-$géodésiques introduisent un paramètre de contrôle de la taille géodésique des zones par la mesure de la distance spectrale cumulée dans les zones $\lambda-$plates. En outre, ces connexions du second ordre produisent des pyramides de partitions avec un nombre décroissant de régions quand la valeur de η ou μ croît, jusqu'à atteindre la partition associée au niveau qui correspond à celle des zones $\lambda-$plates. Cependant, il est intéressant de remarquer que cette pyramide ne constitue pas une hiérarchie ordonnée en raison des classes qui ne sont pas ordonnées par niveau croissant.

Les algorithmes proposés pour la construction des partitions associées à ces deux connexions η et μ utilisent des files d'attente avec un tri de germes selon leur distance cumulée à tous les autres points d'une zone $\lambda-$plate.

Calcul efficace du tableau de toutes les paires de distances géodésiques dans une image

Le tableau de paires de distances géodésiques entre les pixels d'une image hyperspectrale est la représentation la plus riche pour explorer la dimensionnalité spatio-spectrale de l'image, pour segmenter l'image avec des techniques de coupes de graphes, pour construire des voisinages adaptatifs, etc... Cependant, calculer toutes les paires de distances géodésiques entre les pixels d'une image est très coûteux en temps de calcul. L'approche naïve consiste à effectuer P fois, avec P le nombre de pixels, l'algorithme de propagation géodésique qui calcule la distance géodésique d'un pixel à tous les autres.

Dans ce contexte, nous avons exploré différents algorithmes efficaces pour le calcul de ce tableau. Pour ce faire, on exploite la redondance des propagations géodésiques grâces à l'utilisation d'un arbre géodésique. Ensuite, plusieurs stratégies de choix des points pour calculer la propagation géodésique ont été introduites. Nous avons comparé une méthode en spirale qui choisit les points de manière aléatoire sur les spirales concentriques de l'image avec d'autres approches plus élaborées : i) choix en priorité des extrema géodésiques (obtenus par propagation à partir du centroïde), ii) choix selon le taux de remplissage (sélectionner en priorité les points pour lesquels nous connaissons le moins de distances à tous les autres), iii) une méthode en spirale mais avec répulsion. Pour différentes images test, nous avons observé une diminution du nombre de propagations géodésiques pour remplir le tableau de 18 % à 50 % par rapport à l'approche naïve.

Principales publications

- G. Noyel, J. Angulo, D. Jeulin. "**On distances, paths and connections for hyperspectral image segmentation**", In *Proc. of the 8th International Symposium on Mathematical Morphology (ISMM'2007)*, Rio de Janeiro, Brazil, October 2007. p. 399–410, MCT/INPE, 2007.
- G. Noyel, J. Angulo and D. Jeulin. "**Fast computation of all pairs of geodesic distances**". *Image Analysis and Stereology*, Vol. 30, 101–109, 2011.

6.3 Contribution de la morphologie mathématique à des approches tensorielles et métriques pour la classification en images hyperspectrales

Décomposition par espace-échelle morphologiques, représentation tensorielle des images et réduction de la dimension par des méthodes multilinéaires

Les méthodes linéaires de réduction de la dimension pour des images hyperspectrales type ACP (ou AFC) commencent toujours par "vectoriser" les différentes composantes : on transforme chaque image scalaire dans un vecteur colonne de dimension égale au nombre de pixels. Ensuite, l'outil mathématique fondamental pour trouver la base orthogonale de projection est la SVD. Ainsi, l'organisation spatiale des pixels dans chaque variable est perdue. D'autre part, les opérateurs morphologiques géodésiques (ouvertures/fermetures par reconstruction, et nivellements) permettent la construction d'espaces-échelles qui décomposent les structures d'une image scalaire dans différentes échelles, tout en préservant les contours des structures qui apparaissent dans une échelle particulière.

Nous avons donc proposé une exploration/réduction de la dimension des images hyperspectrales qui, d'une part, considère la structure spatiale des images (chaque variable est un tenseur matrice et pas un vecteur), et d'autre part, considère chaque image spectrale représentée par sa décomposition en différentes échelles morphologiques (plutôt qu'une matrice, chaque composante spectrale est un tenseur d'ordre trois). Au final, chaque image hyperspectrale est représentée par un tenseur d'ordre 4 : les deux dimensions spatiales, la dimension liée à la décomposition multi-échelle et la dimension liée au spectre. Nous avons utilisé des outils mathématiques de l'algèbre linéaire proposés récemment (la SVD d'ordre supérieur) pour réduire, et donc filtrer, simultanément les différentes dimensions.

Nous avons montré que les résultats de classification obtenus dans ces espaces tensoriels spatiaux/spectraux/morphologiques sont comparables ou meilleurs que les méthodes proposées précédemment dans l'état-de-l'art. Pour bien maitriser ces outils puissants, nous avons étudié l'unicité de la représentation obtenue ainsi que caractérisé en profondeur les différents paramètres de l'approche ; par exemple, la discrétisation dans la décomposition morphologique par nivellement.

Distances morphologiques entre images pour la réduction de la dimension avec des méthodes nonlinéaires

L'autre approche à inspiration morphologique que nous avons proposée comme alternative pour réduire la dimension des images hyperspectrales s'appuie sur des méthodes nonlinéaires, et notamment l'ACP à noyau et ISOMAP (plongement isométrique). L'ingrédient principal de ces méthodes est une distance pour comparer les canaux spectraux ; à partir de cette distance on construit la matrice des paires de distances entre tous les canaux (matrice de Gramm). Avant notre étude, les deux familles de distances entre images qui avaient été considérées sont les distances pixels (e.g., distance euclidienne entre les images) et les distances entre les histogrammes des images (e.g., divergence de Kullback-Leibler).

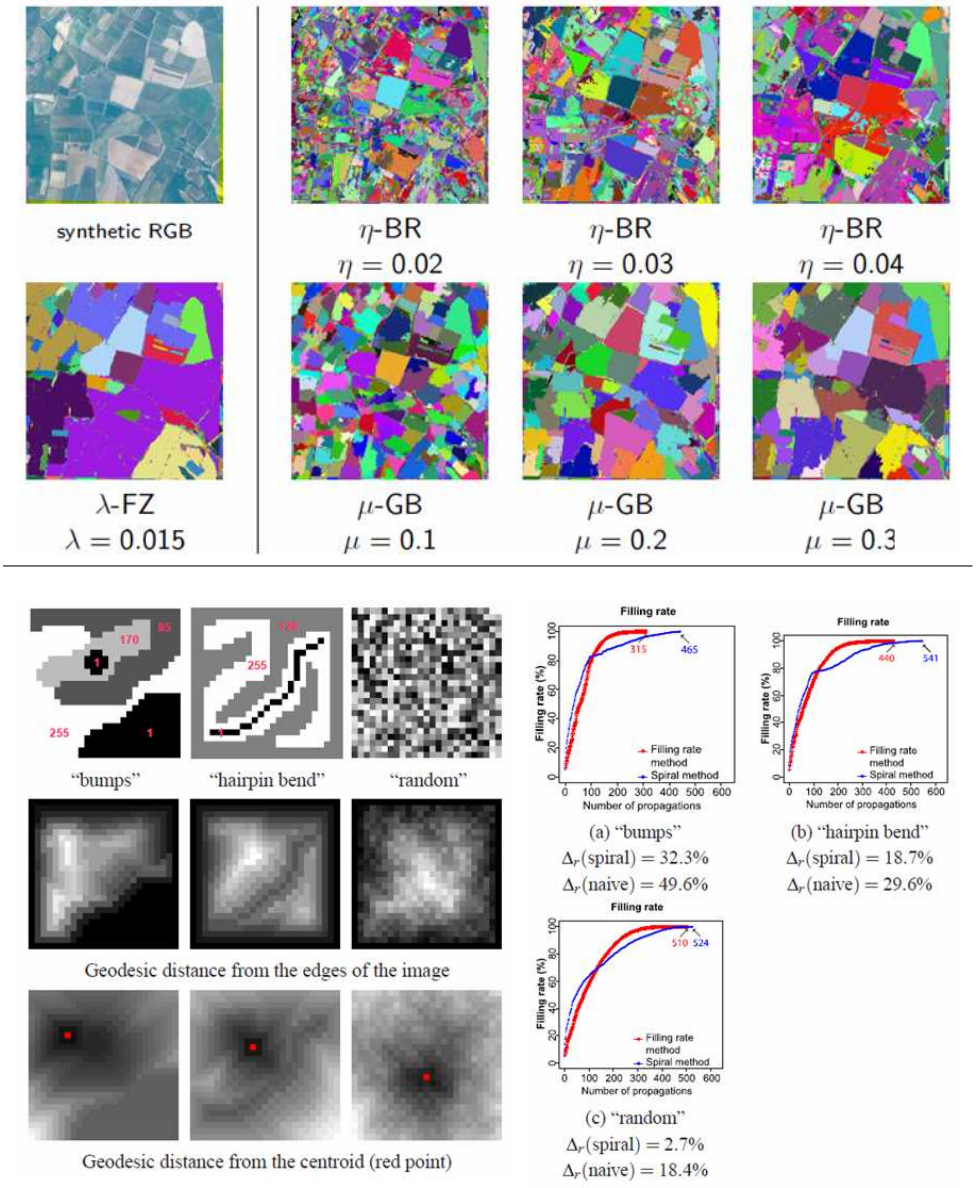

FIG. 6.2 – Chemins géodésiques et connexions pour la segmentation d'images hyperspectrales : haut, régions $\eta-$bornées et boules $\mu-$géodésiques ; bas, calcul efficace du tableau de toutes les paires de distances géodésiques.

Nous avons introduit deux nouvelles familles de distances de type morphologique pour comparer les composantes spectrales. Le premier type de distance entre images scalaires est une généralisation de la distance de Hausdorff (qui est définie pour des ensembles), écrite sous forme de dilatations. On calcule la distance de Hausdorff entre les ensembles de niveaux de la paire d'images, dont les histogrammes ont été au préalable normalisés, et finalement on prend la distance maximale entre toutes les paires. L'autre distance consiste à utiliser l'opérateur nivellement pour mettre chaque image dans le "repère" de l'autre (un nivellement de la première image avec la deuxième comme marqueur et un autre nivellement de la deuxième avec la première comme marqueur). Ensuite nous pouvons utiliser une distance entre pixels pour comparer les deux images nivelées. Dans une autre variante, nous avons considéré que les deux images se trouvent dans une variété topologique et que le nivellement partant de l'une vers l'autre, et vice-versa, définit un chemin dans la variété par les différentes étapes de dilatation/érosion géodésique du nivellement. Il est possible donc de définir une distance "géodésique" dans la variété qui correspond à la somme cumulée des distances des étapes.

En plus de pouvoir comparer structurellement les images, les deux motivations de nos distances morphologiques étaient, d'une part, d'avoir des distances qui soient invariantes à des transformations qui peuvent apparaitre en imagerie hyperspectrale (i.e., translation spatiale entre une bande spectrale et les autres, sensibilité variable entre les différentes bandes spectrales, etc...), et d'autre part, travailler avec des distances qui soient robustes au bruit (qui est aussi indépendant et variable entre les bandes). Nos résultats, en simulant sur les images réelles ce type de problèmes, ont montré que ces nouvelles distances sont justement plus performantes pour la classification que directement les distances entre pixels ou histogrammes.

Principales publications

- S. Velasco-Forero and J. Angulo. "**Morphological scale-space for hyperspectral images and dimensionality exploration using tensor modeling**". *Proc. of IEEE WHISPERS'09 (First IEEE GRSS Workshop on Hyperspectral Image and Signal Processing)*, Grenoble, France, August 2009.
- S. Velasco-Forero and J. Angulo. "**Parameters selection of morphological scale-space decomposition for hyperspectral images using tensor modeling**". In *Proc. of SPIE symposium on Defense, Security, and Sensing : Algorithms and Technologies for Multispectral, Hyperspectral, and Ultraspectral Imagery XVI*, SPIE Vol. 7695, Orlando, United States, April 2010.
- S. Velasco-Forero, J. Angulo and J. Chanussot. "**Morphological image distances for hyperspectral dimensionality exploration using Kernel-PCA and ISOMAP**". *Proc. of IEEE IGARSS'2009 (IEEE International Geoscience & Remote Sensing Symposium)*, Vol. III, 109–112, Cape Town, South Africa, July 2009.

6.4 Morphologie mathématique hyperspectrale : Ordre vectoriel supervisé par apprentissage statistique

Ordre supervisé selon un entrainement pour le "foreground" et "background" de l'image

Intuitivement, nous pouvons dire qu'en morphologie binaire (numérique) la dilatation élargit les particules (objets et structures claires) et rétrécit le fond (objets et structures sombres) ; l'érosion agissant de manière duale par le complément. Derrière ce principe se trouve la structure mathématique de treillis complet (totalement ordonné) où il existe une valeur maximale, associée au "foreground" et une valeur minimale pour le "background". Ainsi, la dilatation tend à rapprocher les valeurs vers la valeur du foreground, en les éloignant en même temps de la valeur du background. Dans nos travaux précédents sur l'extension de la morphologie aux images couleur, nous avons proposé un cadre où l'introduction d'un couleur de référence, correspondant au foreground, produisait des opérateurs très puissants pour les applications. Cependant, on avait déjà noté à l'époque que cela implique une certaine

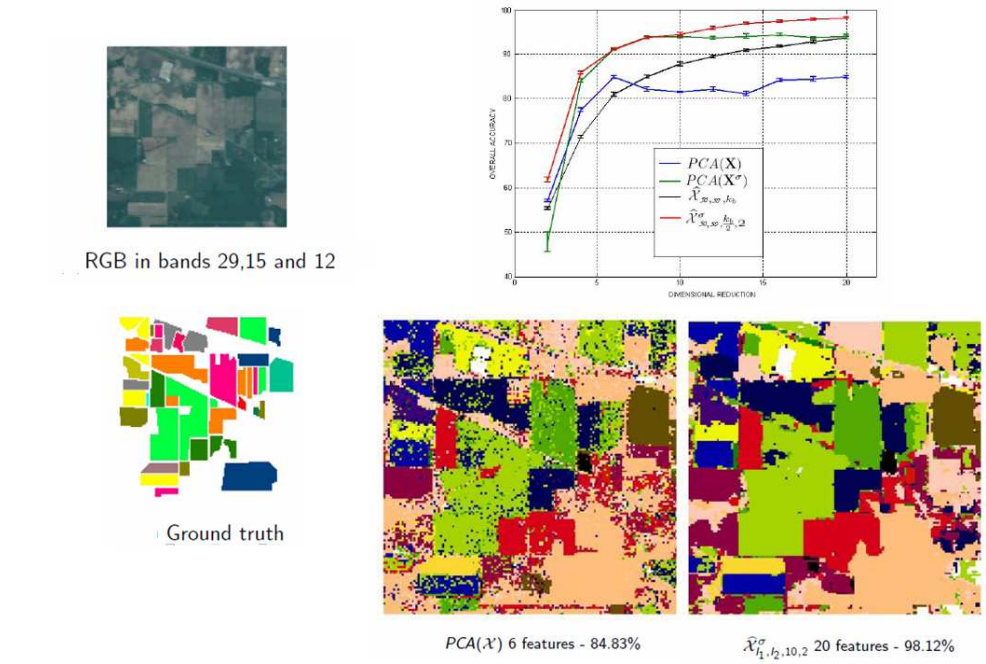

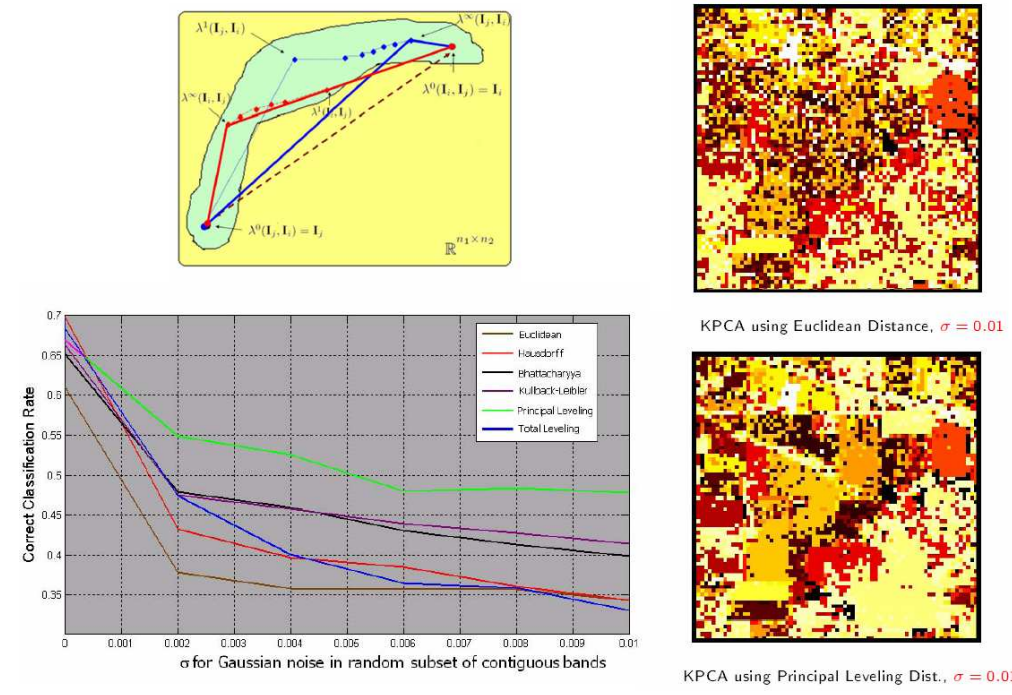

FIG. 6.3 – Contribution de la morphologie mathématique à la classification spatio-spectrale des images hyperspectrales : haut, décomposition par espace-échelle morphologique, représentation tensorielle des images et réduction de la dimension par des méthodes multilinéaires ; bas, distances morphologiques robustes au bruit par des nivellements et réduction de la dimension par des méthodes non-linaires.

asymétrie dans la définition du treillis car la valeur de référence pour le background n'apparaissait pas explicitement et par conséquent, la dualité par le complément posait de problèmes.

Dans ce contexte, nous avons introduit un formalisme plus cohérent pour construire de manière supervisée un treillis complet (totalement ordonné) sur des espaces vectoriels. Le cas le plus simple est celui où il y a un vecteur de référence associé au foreground (qui est le point le plus grand dans le treillis) et un autre vecteur différent au background (qui représente le plus petit) : la fonction d'ordre pour tout autre vecteur dépend de la distance aux références du foreground/background. Ceci peut se généraliser au cas où le foreground est donné par un ensemble de vecteurs et le background par un autre ensemble disjoint au premier. Nous avons montré que des algorithmes d'apprentissage supervisé permettent de prédire l'ordre de chaque vecteur par rapport aux distances aux ensembles d'apprentissage. Nous avons considéré notamment l'ordre par SVM (l'ordre est lié à la distance à l'hyperplan de séparation maximale) et l'ordre obtenu par le krigeage de la géostatistique (l'ordre est plus lié à une fonction d'"interpolation" entre les valeurs du foreground et ceux du background).

La question de l'ordre total est résolue en complétant cet ordre réduit supervisé par une cascade lexicographique des composantes spectrales. Il faut noter que l'influence dans l'ordre de cette dernière partie est très limité, spécialement si le nombre de composantes est élevée (dimensionnalité de l'espace) car en travaillant sur une précision numérique suffisante, la fonction de prédiction d'ordre produira très rarement la même valeur pour deux vecteurs différents présents sur l'image.

Généralisation de la Transformé en Tout-ou-Rien

Les ordres supervisés permettent donc la définition de la dilatation et l'érosion d'une image multi/hyper-spectrale selon les réponses spectrales que nous associons au foreground et au background : considérons une image hyperspectrale satellite d'un parc naturel, en prenant pour l'objet un ensemble de spectres représentatifs des zones d'eau et pour le fond des zones de végétation et de terre, l'ouverture morphologique de l'image avec un certain élément structurant supprimera dans l'image les régions d'eau (et donc son résidu pourra les extraire).

Nous avons voulu aller plus loin, et montrer comment pouvoir détecter sur des images hyperspectrales des objets qui ont une certaine forme et une certaine réponse spectrale sur l'objet, et une autre réponse spectrale dans le fond qui entoure l'objet. Pour cet objectif, nous avons généralisé la transformé en tout-ou-rien : un opérateur morphologique très puissant qui utilise l'érosion par deux éléments structurants disjoints. Notre formalisme d'ordre supervisé est parfaitement adapté à cette généralisation : l'intersection entre les deux érosions (une dans le treillis objet/fond et l'autre dans le treillis fond/objet) est facilement remplacé par un test de distance à la valeur minimale correspondant à chaque treillis. Cela permet donc d'introduire un paramètre de détection optimisable par rapport au bruit de l'image.

Apprentissage d'un ordre multi-classe

La dernière contribution dans cette série de travaux a eu pour objet le problème de l'apprentissage d'un ordre multi-classe. C'est-à-dire que nous considérons qu'il y a dans l'image K classes spectrales différentes, chacune caractérisée par un ensemble d'apprentissage de vecteurs spectraux. Comment définir une dilatation dans ce contexte, en sachant qu'aucune des classes n'a un rôle particulier de foreground ou background.

La solution que nous avons proposée utilise la fonction d'évaluation de K classifiers de type "one-vs-all SVM", dont chaque classifier prend une classe d'un côté et toutes les autres de l'autre côté. On a donc K fonctions d'ordre. L'ordre final est donné par la fonction la valeur max. des différentes fonctions d'ordre. Nous pouvons l'interpréter en disant qu'un vecteur pixel sera globalement plus grand qu'un autre si le premier est proche des pixels d'apprentissage que définissent l'une des classes spectrales. En sachant qu'en général ces pixels d'apprentissage doivent être pris comme étant des pixels "purs" de la

classe, une dilatation aura tendance à élargir les zones des pixels spectralement pures et une érosion à les supprimer.

Nous avons illustré ce principe en montrant comment cela permet de construire une distribution de taille (granulométrie) des structures d'une image ou bien comment utiliser des opérateurs nivellement pour régulariser spatialement une classification spectrale.

Principales publications

- S. Velasco-Forero and J. Angulo. "**Supervised ordering in R^n : Application to morphological processing of hyperspectral images**". *IEEE Transactions on Image Processing*, Vol. 20, No. 11, –, 2011.
- S. Velasco-Forero and J. Angulo. "**Hit-or-miss transform in multivariate images**". In *Proc. of Acivs'2010 (2010 Advanced Concepts for Intelligent Vision Systems)*, LNCS 6474, Springer-Verlag Berlin Heidelberg, Part I, p. 452-463, Sydney, Australia, December 2010.
- S. Velasco-Forero and J. Angulo. "**Multiclass ordering for filtering and classification of hyperspectral images**". In *IEEE WHISPERS'11 (3rd IEEE GRSS Workshop on Hyperspectral Image and Signal Processing)*, p. 1-4, Lisbon, Portugal, June 2011.

6.5 Morphologie mathématique hyperspectrale : Ordre vectoriel intrinsèque par profondeur statistique

Fonctions de profondeur statistique spectrale et leur calcul

Les fonctions de profondeur statistiques ont été introduites dans le domaine de l'analyse et l'inférence non-paramétrique robuste. Ces fonctions assignent à chaque point d'un espace vectoriel son "degré de centralité" par rapport à un certain nuage de points (ou plus généralement par rapport à une certaine distribution de probabilité). En fait les fonctions de profondeur sont des modélisations intrinsèquement adaptées aux données sans besoin de faire des hypothèses sur le type de distribution.

Dans le cas uni-varié, une fonction de profondeur statistique produit un ordre parmi les points qui va du centre du nuage vers la périphérie, où la médiane est la valeur la plus profonde. Lorsqu'on passe au cas multi-varié, la notion d'ordre du centre vers la périphérie se généralise. On peut le voir aussi comme une généralisation de la distance de Mahalanobis lorsque la distribution n'est pas gaussienne, et ceci sans besoin d'estimer la matrice de covariance.

Les fonctions de profondeur statistiques ont des propriétés très intéressantes de monotonie et d'invariance aux transformations affines du nuage de point ; et surtout elles sont très robustes aux outliers. En pratique, il existe plusieurs définitions précises de fonction de profondeur qui conduisent chacune à des méthodes de calcul plus au moins opérationnelles. Nous nous sommes intéressés à la profondeur par projection. Cette dernière introduit la non-centralité multi-variée comme la valeur de non-centralité la plus défavorable par rapport à toutes les projections uni-variées. Cela conduit à des algorithmes (intrinsèquement parallèles) d'exploration du nuage par projections aléatoires uni-variées qui, au fur et à mesure des réalisations, approximent de manière satisfaisante la profondeur.

Morphologie intrinsèque à l'image sur la dualité "foreground"/"background"

Dans le cas des images multi/hyper-spectrales, nous pouvons voir les spectres présents dans l'image comme un nuage de points dans l'espace de dimension le nombre de canaux. Nous pouvons calculer pour toute image vectorielle sa profondeur qui nous donne donc un ordre intrinsèque aux valeurs de l'image. La question est de savoir dans quel cas cette fonction d'ordre est pertinente pour faire des transformations morphologiques.

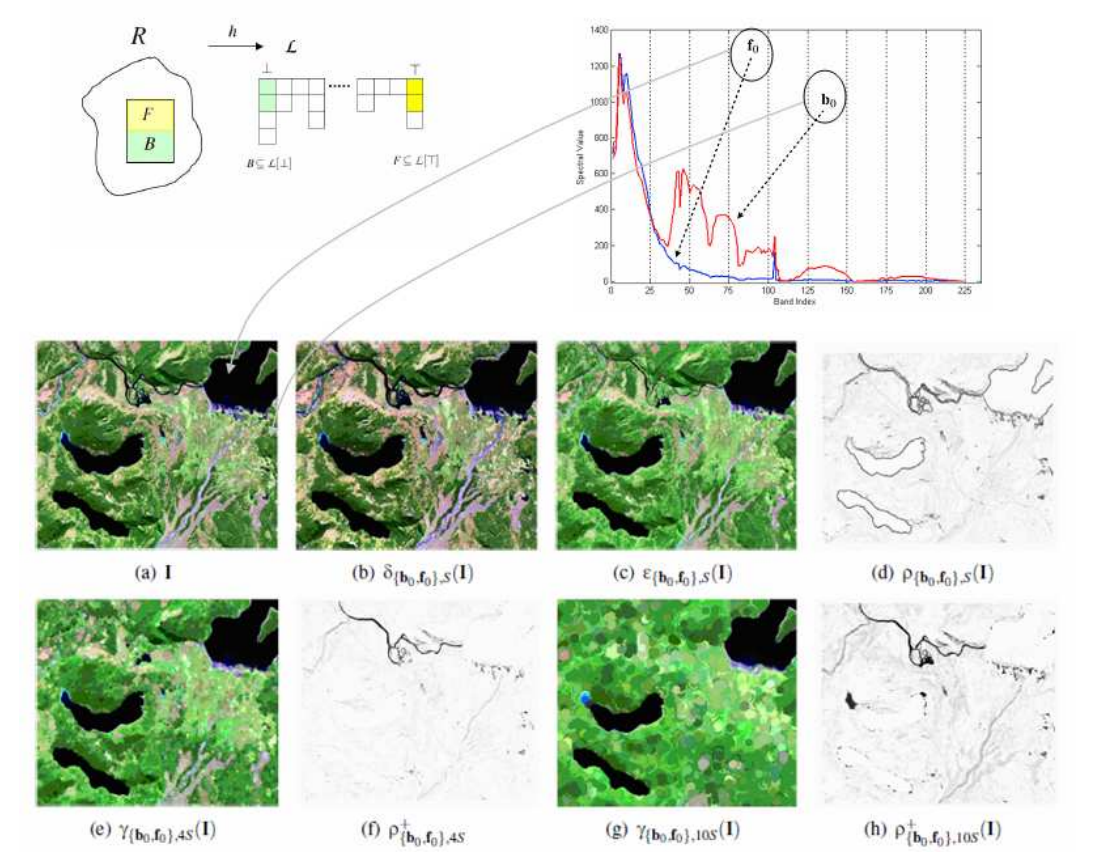

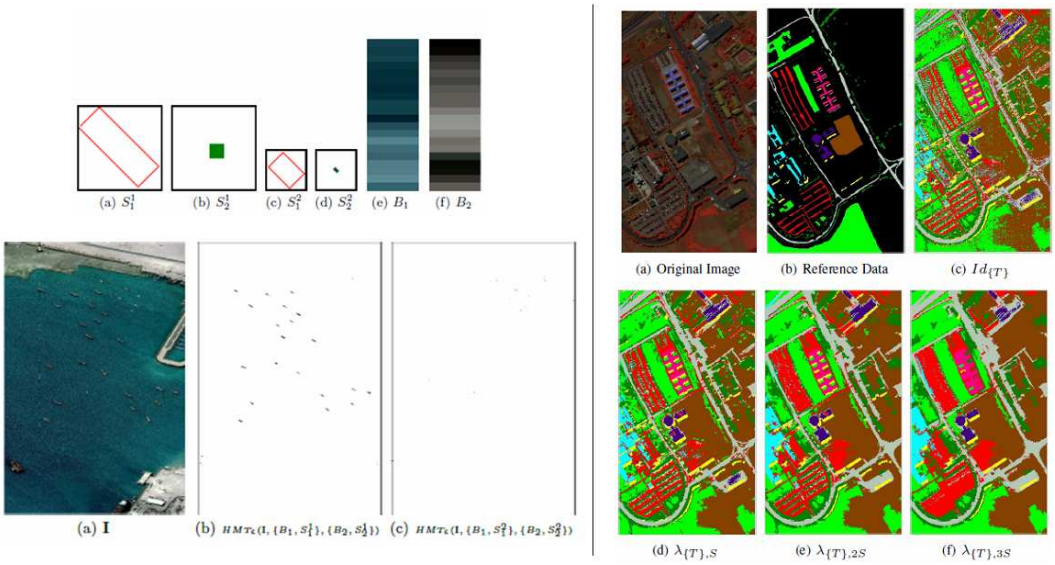

FIG. 6.4 – Morphologie mathématique hyperspectrale supervisée : haut, opérateurs dilatation/érosion, gradient, ouvertures et top-hats par ordre supervisé selon un entrainement pour le “foreground” et le “background” de l’image ; bas-gauche, généralisation de la transformé en tout-au-rien, bas-droite, apprentissage d’un ordre multi-classe et application à la classification spatiale par nivellement.

Nous avons montré que lorsque le contenu de l'image suit une configuration de type : présence majoritaire d'un fond plus au moins homogène (y compris texturé), qui contient certains objets moins représentés et spectralement différents du fond (et qui peuvent être de plusieurs natures spectrales) ; la fonction de profondeur statistique produit un ordre entre les valeurs spectrales qui reflète cette dichotomie. Si cette hypothèse se vérifie, ce qui arrive dans un grand nombre de situations pour des images issues de domaines très variés, la dilatation a une interprétation très intéressante : elle élargit des objets et rétrécit les zones du fond. Par conséquent, les ouvertures permettent d'extraire les objets spectralement saillants dans l'image sans aucun information a priori sur eux. Par opposition à l'approche que nous avons résumée dans la section précédente, les opérateurs morphologiques fondés sur la profondeur sont totalement non supervisés.

Il s'agit d'un paradigme de morphologie mathématique non-supervisé que nous considérons comme très prometteur et que nous allons poursuivre dans nos travaux futurs.

Notion de profondeur géodésique et son utilisation pour l'analyse de formes 2D/3D

Nous avons introduit récemment la notion de profondeur géodésique pour la caractérisation de formes 2D/3D ; cela ne concerne donc pas directement des images multi/hyperspectrales. En fait, l'idée consiste à considérer que les formes sont définies par son ensemble de points dans l'espace de dimension correspondante et à calculer la distance géodésique entre un point de la forme choisi aléatoirement et tous les autres. La profondeur géodésique est définie pour chaque point de la forme comme la valeur de distance géodésique (centrée et réduite) maximale parmi les différentes réalisations aléatoires considérées. On transforme donc la forme dans une fonction numérique normalisée qui décrit d'une certaine manière la distribution géodésique de l'objet.

Nous avons montré que ce descripteur est extrêmement puissant pour la reconnaissance de formes (classification et clustering) par ses propriétés d'invariance aux rotations, aux changements d'échelle, etc... ainsi que par son comportement de robustesse au bruit et aux déformations limitées de forme sans changement de topologie.

Principales publications

- S. Velasco-Forero and J. Angulo. "**Mathematical Morphology for Vector Images using statistical depth**". In *Proc. of ISMM'11 (2011 International Symposium on Mathematical Morphology)*, LNCS 6671, Springer-Verlag Berlin Heidelberg, p. 355—366, Intra (Lake Maggiore), Italy, July 2011.
- S. Velasco-Forero, J. Angulo. "**Geodesic depth for description and retrieval of 2D/3D shapes**". In *13th International Congress of Stereology (ICS-13)*, Beijing, China, October 2011.

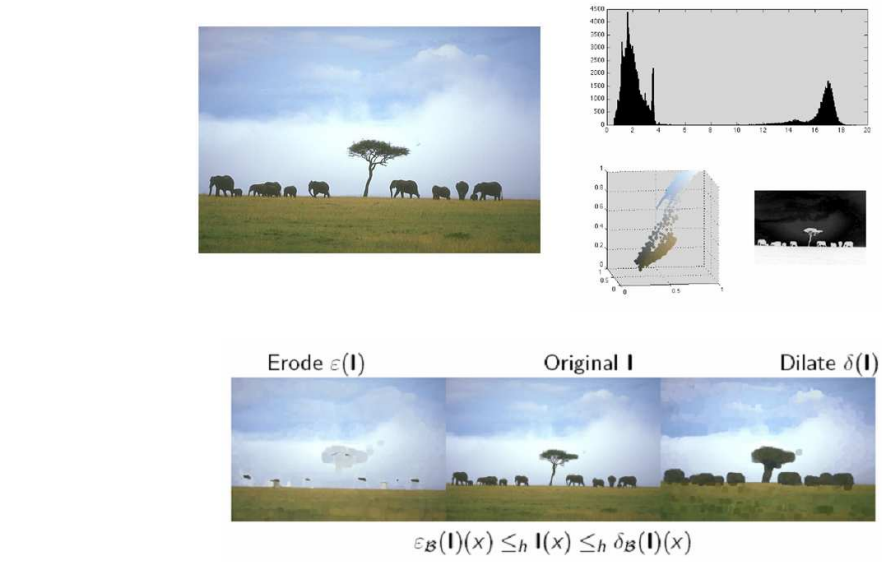

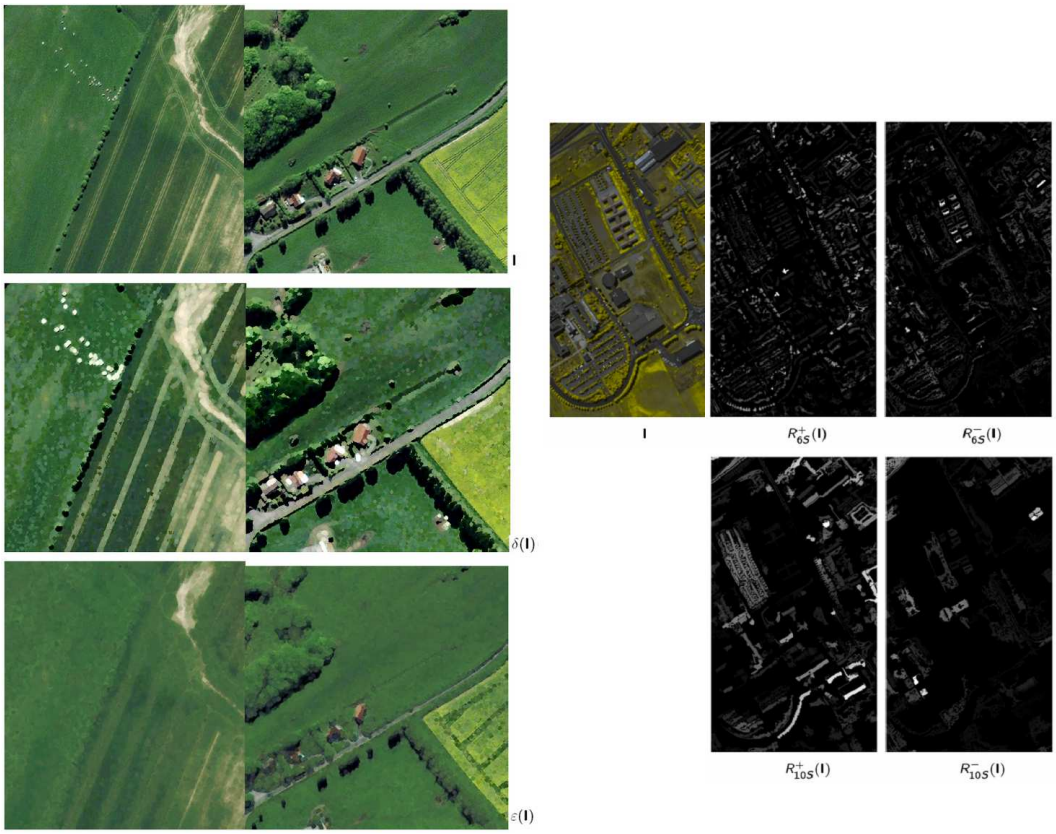

FIG. 6.5 – Morphologie mathématique hyperspectrale non-supervisée : haut, construction d'un ordre intrinsèque par calcul de fonction de profondeur statistique qui conduit à une morphologie sur la dualité "foreground"/"background" ; bas-gauche, exemples de dilatation (du foreground par rapport au background) et d'érosion (du foreground par rapport au background), bas-droite, décomposition des structures par résidus d'ouvertures.

Chapitre 7

Morphologie mathématique pour des images à valeurs dans des espaces non euclidiens

Dans ce chapitre je vais continuer à présenter mes travaux en imagerie multi-variée. Or cette fois-ci, je vais me focaliser sur mes recherches en morphologie mathématique lorsque les valeurs sur les pixels appartiennent à des espaces non euclidiens. Il s'agit de travaux que j'ai menés dans la période la plus récente et qui sont encore en cours.

Après m'être intéressé à la représentation des couleurs par des quaternions réels, en ajoutant une partie réelle associée à une couleur de référence, j'avais commencé aussi à étudier comment ces représentations hypercomplexes étaient utilisées par d'autres chercheurs pour généraliser la notion de signal analytique. C'est à partir de ces travaux que j'ai eu l'idée de construire des images morphologiques complexes et hypercomplexes, à partir d'une image à niveaux de gris comme partie réelle et des transformations morphologiques pour les composantes imaginaires. J'ai introduit ensuite des ordres totaux pour les hypercomplexes qui permettent donc de généraliser tous les opérateurs morphologiques à ce cadre. En plus de certaines propriétés théoriques intéressantes, ces nouveaux opérateurs permettent d'introduire des effets de deuxième ordre dans la dilatation/érosion selon le type de partie imaginaire utilisée.

Nous pouvons trouver aujourd'hui différents types d'images à valeurs matricielles ou tensorielles. On a, d'une part, des images scalaires dont une transformation produit un tenseur pour chaque pixel ; l'exemple classique est celui des images du tenseur de structure (qui correspond fondamentalement à l'orientation locale et à la cohérence dans le voisinage du pixel). D'autre part, on trouve des images de nature intrinsèquement tensorielle : des images d'IRM de diffusion, de cartographies 2D de matrices de covariance issues de différentes modalités d'imagerie radar, etc...

L'extension de la morphologie mathématique aux images à valeurs matricielles a été jusqu'à présent très peu considérée dans l'état de l'art qui se limite exclusivement aux travaux de Burgeth et autres [9, 10]. Les deux approches qu'ils ont considérées sont d'une part l'ordre partiel de Löwner (qui utilise des outils de l'analyse convexe pour les calculs de max./min.) et d'autre part la généralisation de l'EDP morphologique aux valeurs matricielles.

J'ai commencé à travailler sur la question en cherchant des alternatives à ces deux approches et qui soient inspirées par mon expérience préalable dans l'extension de la morphologie mathématique aux images vectorielles. J'ai proposé trois familles de nouvelles méthodes pour le calcul du supremum/infimum d'ensemble de matrices symétriques définies positives : i) à partir de la notion d'ordre partiel spectral et en proposant des sup/inf par solution d'un problème spectral inverse ; ii) en introduisant des ordres totaux entre les matrices qui choisissent comme sup/inf l'une des matrices de départ ; iii) par non-linéarisation des différents algorithmes de calcul de moyenne/médiane d'un ensemble de matrices.

Très récemment, dans le cadre du stage-Projet Fin d'Etudes de J. M. Frontera-Pons, que j'ai encadré en 2010-2011, nous avons travaillé sur l'extension de la morphologie mathématique pour des images à valeurs sur la sphère. Les valeurs sur la sphère unité peuvent représenter différents types d'informations physiques. Dans les applications d'imagerie, le cas le plus classique est celui de la carte des orientations, obtenues après l'estimation de la locale l'orientation de chaque pixel. Dans l'imagerie médicale moderne, la modalité HARDI (High Angular Resolution Imaging) produit également des images avec des valeurs sur la sphère. Nous nous sommes cependant intéressés aux images de polarimétrie, en particulier dans le domaine Radar. En effet, les états de polarisation se représentent sur la sphère de Poincaré qui correspond justement à $\mathbb{S}^2$.

Certaines de nos idées sont inspirées de la morphologie sur le cercle unité [19], mais la plupart des résultats donnent une généralisation à la sphère qui pourrait être plus féconde pour être transposée à d'autres variétés Riemanniennes que $\mathbb{S}^2$. *Nous avons considéré plusieurs relations d'ordre sur la sphère unité, qui conduisent à différentes formulations des opérateurs morphologiques adaptés à la géométrie intrinsèque de la sphère définie par sa métrique. Les notions de supremum et infimum locaux ont été introduites, qui permettent de définir les opérateurs de dilatation et d'érosion sur le plan tangent à des barycentres obtenus par l'algorithme de Fréchet-Karcher. Des opérateurs associés à des ordres supervisés, inspirés de mes travaux précédents sur l'ordre supervisé vectoriel, sont en particulier considérés pour les questions de reconnaissance de cibles. Nous avons proposé également différentes procédures de filtrage à des fins de débruitage. L'analyse effectuée conduit à une compréhension extensive des données polarimétriques, qui permet l'automatisation de la détection de cibles dans ce type d'images Radar.*

7.1 Morphologie mathématique hypercomplexe

Représentations complexes morphologiques et ordres totaux associés

Tout d'abord, nous avons introduit l'image complexe associée à un opérateur morphologique : une image où la partie réelle est l'image originale, et la partie imaginaire est l'image transformée par l'opérateur en question. On s'était bien évidemment inspiré de la notion de signal analytique, où la partie imaginaire est la transformée de Hilbert (changement de phase du signal original). Ensuite nous avons introduit des ordres totaux dans $\mathbb{C}$ (deux ordres lexicographiques avec le module, plus un ordre total sur le cercle unité par choix d'une phase de référence). A partir de ces ordres, nous avons introduit un treillis complet totalement ordonné pour la définition générique des opérateurs dilatation et érosion dans nos représentations complexes, en considérant les propriétés que nous imposons à ces opérateurs.

Dilatation et érosion complexes

L'étape suivante a donc consisté à étudier les opérateurs morphologiques qui sont les plus appropriés pour la construction des représentations complexes. Notre point de départ était de produire des paires de dilatation/érosion qui soient des adjonctions ; il est bien connu que si l'adjonction est vérifiée, les produits de la dilatation/érosion produisent l'ouverture et la fermeture complexe correspondante.

Nous avons considéré deux familles de dilatation/érosion complexes. Dans la première, la partie imaginaire de la représentation adaptée à la dilation complexe est une ouverture, et dans l'érosion adjointe, la partie imaginaire est une fermeture. Nous avons montré que ces deux opérateurs sont aussi duaux par le complément. Il faut aussi tenir compte du fait qu'il y a deux ordres totaux pour les complexes (à une phase de référence donnée) et que par conséquent, nous avons deux paires adjointes et duales de dilatation/érosion complexes avec ouverture/fermeture comme partie imaginaire. La deuxième famille considère comme parties imaginaires le résidu de l'ouverture (le top-hat) et minus le complément du résidu par fermeture. A nouveau, pour une origine de phase donnée, on obtient deux paires d'adjonctions.

En plus de ces propriétés théoriques intéressantes, ces nouveaux opérateurs permettent d'introduire des effets de deuxième ordre dans la dilatation/érosion selon le type de partie imaginaire utilisée. Par exemple, avec une partie imaginaire ouverture et selon que l'ordre soit en commençant par le module ou par la phase, la dilatation privilégie dans le calcul du supremum soit les pixels qui ont des intensités plus élevés avant et après l'ouverture (module plus élevé) ou ceux qui se trouvent dans des structures plus invariantes à l'ouverture indépendamment de leur intensité initiales (phase plus proche à $\pi/2$ qui la référence). Avec les top-hats, l'interprétation est similaire en termes de contraste local. Ces opérateurs complexes permettent donc d'être plus robuste au bruit dans le calcul des dilatations/érosions, mais aussi plus sélectif selon l'intensité locale dans un voisinage associé à l'élément structurant de l'ouverture/fermeture de la partie imaginaire.

Généralisation avec des quaternions réels

Nous avons finalement généralisé l'approche précédente aux représentations hypercomplexes (i.e., quaternions réels) : c'est-à-dire que, cette fois-ci, il y aura l'image originale dans la partie réelle (ou une première transformation qui peut être l'identité ou pas), et la partie imaginaire est composée de trois transformations morphologiques appliquées à l'image scalaire originale. Ce formalisme a été construit selon la même procédure. En commençant par définir des ordres totaux $\mathbb{H}$, selon les représentations quaternioniques polaire et décomposition parallèle/perpendiculaire à un quaternion de référence. Les transformations les plus pertinentes pour les dilatations/érosions quaternioniques ont été ensuite étudiées, spécialement pour les cas des ordres associés à une décomposition orthogonale selon un quaternion de référence. Ainsi, nous avons considéré le cas où le triplet de la partie imaginaire est associé à une ouverture/fermeture directionnelle selon les directions principales de la trame (dans le cas d'une image 3D) et la partie réelle à une ouverture isotrope. La dilatation hypercomplexe sur un élément structurant isotrope produira de résultats "directionnels" selon le choix de quaternion de référence qui joue le rôle de projecteur.

Nous avons montré par différents exemples que ces dilatations/érosions (hyper-)complexes semblent particulièrement intéressantes par rapport aux scalaires lorsqu'on construit des opérateurs géodésiques (ouvertures et fermetures par reconstruction).

Principales publications

– J. Angulo. "**From Scalar-Valued Images to Hypercomplex Representations and Derived Total Orderings for Morphological Operators**". *Proc. of ISMM'09 (2009 International Symposium on Mathematical Morphology)*, LNCS 5720, Springer-Verlag Berlin Heidelberg, p. 238-249, Groningen, The Netherlands, August 2009.

– J. Angulo. "**Hypercomplex mathematical morphology**". *Journal of Mathematical Imaging and Vision*, Volume 41, No. 1–2, 86–108, 2011.

7.2 Morphologie mathématique pour des matrices symétriques définies positives

Ordre partiel spectral et le problème inverse

Comme d'habitude dans nos travaux, nous devons trouver la manière de définir, pour un ensemble de matrices symétriques définies positives (SDP) (qui est l'espace tensoriel le plus intéressant aussi bien du point de vue théorique que des applications), la valeur supremum (infimum) qui est associée à la dilatation (l'érosion). Par ailleurs les matrices SDP peuvent être visualisées comme des ellipsoïdes, ce qui permet une interprétation géométrique des opérations de supremum et d'infimum.

Initialement, nous avons considéré l'ordre partiel basé sur une cascade lexicographique des valeurs propres. Ainsi, il est possible de définir le supremum (l'infimum) d'un ensemble de matrices comme la matrice ayant comme valeurs propres le supremum (l'infimum) marginalement des valeurs propres. Toutefois, la base orthogonale qui définit complètement la matrice SDP correspondante au supremum (a l'infimum) peut être obtenue par différentes solutions de ce problème spectral inverse. Une solution consiste à associer au supremum et à l'infimum la base orthogonale de la matrice moyenne de l'ensemble. Cette matrice moyenne peut s'obtenir par l'algorithme du barycentre de Fréchet-Kercher, qui est bien formulé dans le cadre de la variété Riemannienne associée aux matrices SDP. Une deuxième solution que nous avons proposée et utilise un algorithme de construction progressive de la base orthogonale. Le premier vecteur propre est celui associé à la plus grande des valeurs propres parmi toutes les matrices. Le deuxième est obtenu comme étant le vecteur le plus proche à la plus grande des deuxièmes valeurs propres, dans le sous-espace orthogonal à celui que nous avons déjà fixé. Et ainsi jusqu'à la construction complète.

Ordres totaux pour des matrices et sup/inf préservant la famille de valeurs

Tel que nous avions fait dans les espaces vectoriels, nous pouvons aussi définir des ordres totaux pour l'espace des matrices SDP. La conséquence fondamentale de ce type d'ordre est que le supremum et l'infimum d'un ensemble de matrices seraient justement l'une de ces matrices. Une méthodologie alternative à l'utilisation de l'ordre partiel spectrale consiste à définir comme supremum d'un ensemble de matrices la matrice qui est plus la plus grande en fonction de la priorité lexicographique des valeurs propres ou selon une priorité donnée entre certains invariants associés aux valeurs propres (polynômes symétriques fondamentaux ; paramètres géométriques liés aux ellipsoïdes).

Nous pouvons aussi prendre l'approche supervisée et définir deux ensembles de matrices de référence, comme d'habitude, l'un pour le "foreground" l'autre pour le "background". Ensuite à l'aide de la distance métrique associée à la variété des matrices SDP, nous pouvons calculer une fonction d'ordre pour chaque matrice selon l'ensemble d'apprentissage.

Non-linéarisation de la moyenne de matrices et opérateurs asymptotiquement morphologiques

La dernière approche que nous avons formalisée pour le calcul du supremum/infimum d'ensemble de matrices SDP utilisent un cadre de non-linéarisation fondé sur la moyenne contra-harmonique. Nous décrirons un peu plus en détails dans le chapitre 9 la manière dont la moyenne contra-harmonique nous permet d'introduire des opérateurs non-linéaires qui se comportent asymptotiquement comme la dilatation et l'érosion.

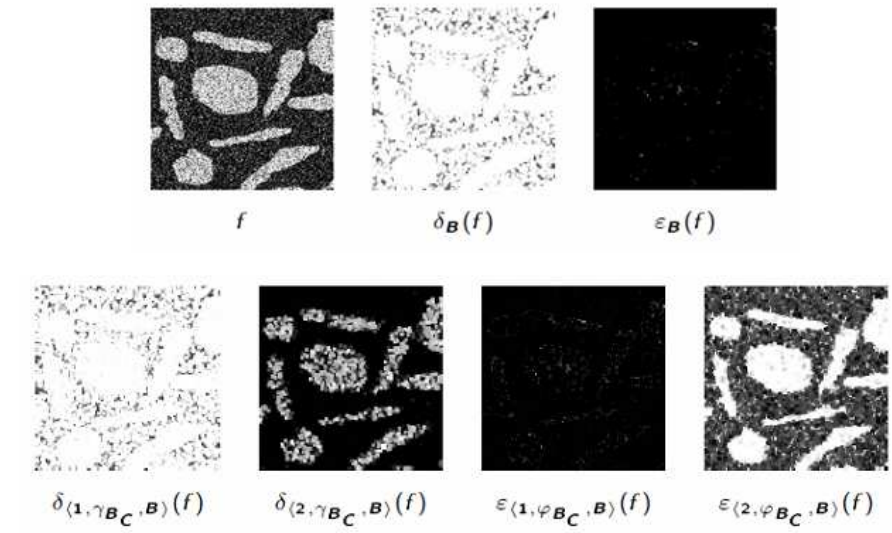

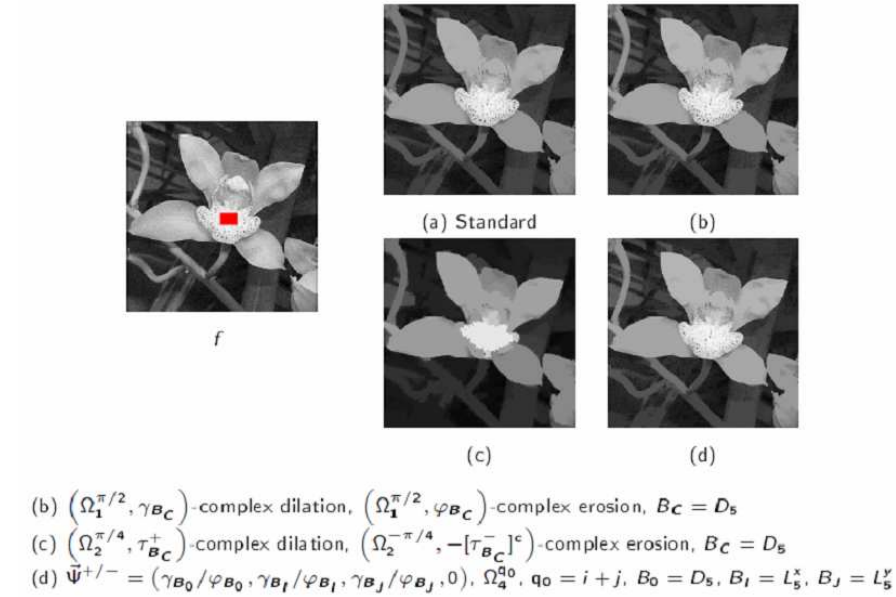

FIG. 7.1 – Morphologie mathématique hypercomplexe : haut, comparaison des dilatations/érosions complexes avec la dilatation/érosion scalaire ; bas, reconstruction géodésique (le marqueur correspond à la zone rouge) par des dilatations géodésiques (hyper)complexes.

Nous avons donc généralisé la moyenne contre-harmonique au cas des matrices SDP, ce qui produit une non-linéarisation de la moyenne euclidienne par rapport à un certain ordre de non-linéarité. Nous avons aussi proposé l'équivalent dans le cas de la moyenne log-euclidienne des matrices.

Nous espérons que cette approche pourra nous permettre aussi dans le futur la non-linéarisation de l'EDP de diffusion des matrices SDP.

Principales publications

– J. Angulo. "**Mathematical Morphology for Matrix-Valued Images**". In *Indo-French Workshop Matrix Information Geometries (MIG),* Ecole Polytechnique (Palaiseau), France, February 23rd-25th 2011.

7.3 Morphologie mathématique sur la sphère $\mathbb{S}^2$

Origine locale sur la sphère et calcul du sup/inf sur l'espace tangent

Par la géométrie de la sphère, le seul filtrage qui apparait naturellement pour un ensemble de points est celui qui donne sa valeur centrale : c'est-à-dire son barycentre. Il existe dans la géométrie Riemannienne une méthode qui permet de calculer cette valeur : le barycentre de Fréchet-Karcher ; qui dans le cas précis de la sphère produit un algorithme itératif très efficace. Cela consiste fondamentalement à projeter les points sur l'espace tangent à l'un des points, puis calculer sur cet espace euclidien le barycentre qui est ensuite ré-projeté sur la sphère pour définir un nouvel espace tangent et ainsi jusqu'à la convergence.

Etant donné un ensemble de points sur $\mathbb{S}^2$, nous avons introduit une notion de supremum qui se calcule justement sur l'espace tangent au pole nord (N) de la sphère comme l'un des quatre coins du rectangle cartésien minimal contenant les points, et ceci après une rotation de ces points sur la sphère de telle sorte que la valeur centrale de l'ensemble correspond à N. Plus précisément, pour calculer une pseudo-dilatation, nous commençons par définir une valeur barycentrique qui sera la référence locale à utiliser. Nous avons proposé de calculer cette valeur comme le barycentre de Fréchet-Karcher mais à partir d'un ensemble de points autour de la valeur à dilater qui doit être plus large que la taille de l'élément structurant (ceci garantit que la dilatation des points proches d'une image se réalise dans le même espace tangent et donc il y a une continuité garantie). A partir de ce barycentre, on applique une rotation aux points sur la sphère pour faire correspondre le barycentre avec N. Les points sont ensuite projetés sur l'espace tangent à N (espace euclidien 2D). On calcule la boîte rectangulière minimale contenant les points et on dit que le supremum correspond à celui qui a la norme la plus élevée. En faisant ensuite la projection de ce point sur la sphère, puis sa rotation inverse, nous obtenons la valeur de la dilatation sur $\mathbb{S}^2$. La pseudo-érosion est définie de manière similaire, où l'infimum est introduit selon une dualité qui correspond à l'inversion des coordonnées dans l'espace tangent à N : l'érosion sera l'un des coins de la boîte la plus grande qui contient l'origine et ne contient pas des points de l'ensemble. En fait, nous n'avons pas de dilatation/érosion strictement car les propriétés de distributivité de celles-ci ne sont pas vérifiées dans ce type d'ordre localement adapté.

Ordre supervisé sur la sphère : transformé tout-ou-rien et ouvertures

Dans une deuxième démarche nous avons abordé l'ordre sur la sphère par rapport à une distribution de valeurs de référence. Ceci entre donc dans le cadre des ordres supervisés.

Nous avons donné une interprétation des valeurs de référence comme des charges sur la sphère qui peuvent être positives (lorsqu'elles sont associées au "foreground") or négatives (associées au "background"). Nous avons ensuite considéré plusieurs alternatives dans la définition de la fonction qui donne une valeur d'ordre pour chaque point de la sphère à partir des charges de référence. Bien

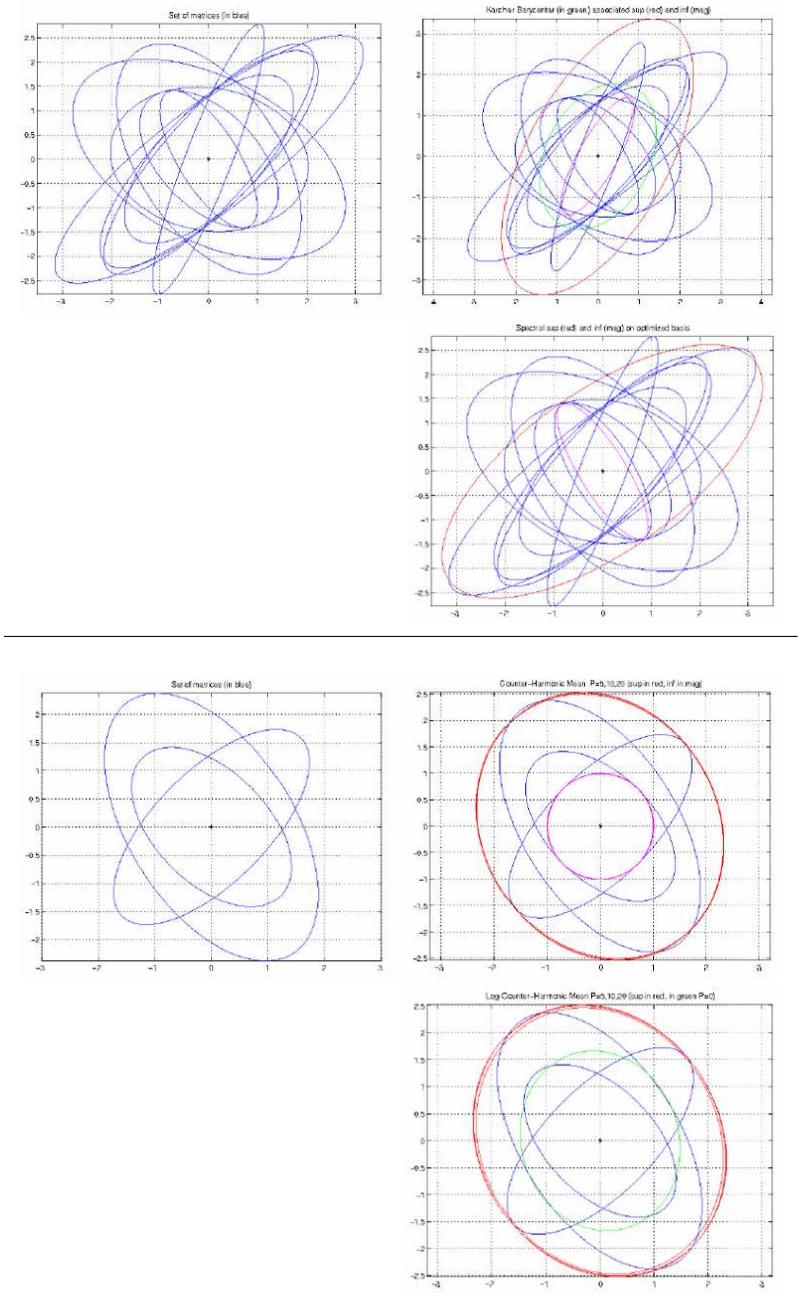

FIG. 7.2 – Supremum (rouge) et infimum (rose) pour des ensembles de matrices symétriques définies positives : haut, ordre partiel spectral et d'une part, sup/inf sur base orthogonale associée au barycentre de Fréchet-Karcher (vert), puis d'autre part, par construction progressive de la base orthogonale ; bas, non-linéarisation de la moyenne contra-harmonique pour des matrices SDP et de la moyenne log-euclidienne.

évidemment cela ne dépend que de la distance géodésique sur la sphère du point en question à la distribution de charges. Une approche directe consiste à considérer que cette fonction d'ordre est le potentiel donné par les charges. Mais nous avons aussi étudié d'autres alternatives : la valeur d'ordre dépend exclusivement du barycentre des charges positives et du barycentre des charges négatives ; la valeur d'ordre dépend simplement de la distance à la plus proche des charges positives et la plus proche des négatives.

Les opérateurs de dilatation et érosion sur la sphère, associés à ces ordres supervisés, forment des adjonctions qui vérifient toutes les propriétés requises pour une dilatation et une érosion.

Application à la détection de cibles sur des images Radar polarimétriques

Parmi les différentes modalités d'imagerie à valeurs sur la sphère, nous avons illustré nos algorithmes et étudié leurs performances (à l'aide des courbes ROC) dans le cas des images polarimétriques issues du domaine Radar. Il faut préciser que nous avons travaillé sur des images simulées car pour des raisons de confidentialité des données Radar réelles, celles-ci ne pouvaient pas illustrer nos travaux.

Une des questions clés en Radar est celle du bruit des images. Donc, en plus des opérateurs morphologiques que nous avons mentionnés plus haut, nous avons aussi introduit des filtres de débruitage adaptés aux données sur la sphère. Plus particulièrement, en utilisant l'algorithme du barycentre de Fréchet-Karcher sur la sphère, nous avons généralisé le filtre bilatéral pour le debruitage spatialement adaptatif de ce type d'images et même introduit la notion de filtre trilatéral avec un terme additionnel qui préserve les valeurs proches d'une cible que nous ne voulons par perdre sur l'image.

Nous avons ensuite utilisé pour les exemples d'application les opérateurs morphologiques sur la sphère qui sont appropriés à la détection de cibles sur des images polarimétriques, notamment le gradient morphologique, les résidus des ouvertures et la transformée en tout-ou-rien.

Principales publications

– J.M. Frontera-Pons. "**Mathematical morphology on the sphere : Application to Polarimetric Image processing**". *Rapport de Projet Fin d'Etudes (dirigé par J. Angulo)*, 87 p., CMM-Centre de Morphologie Mathématique, MINES ParisTech, Juillet 2011.

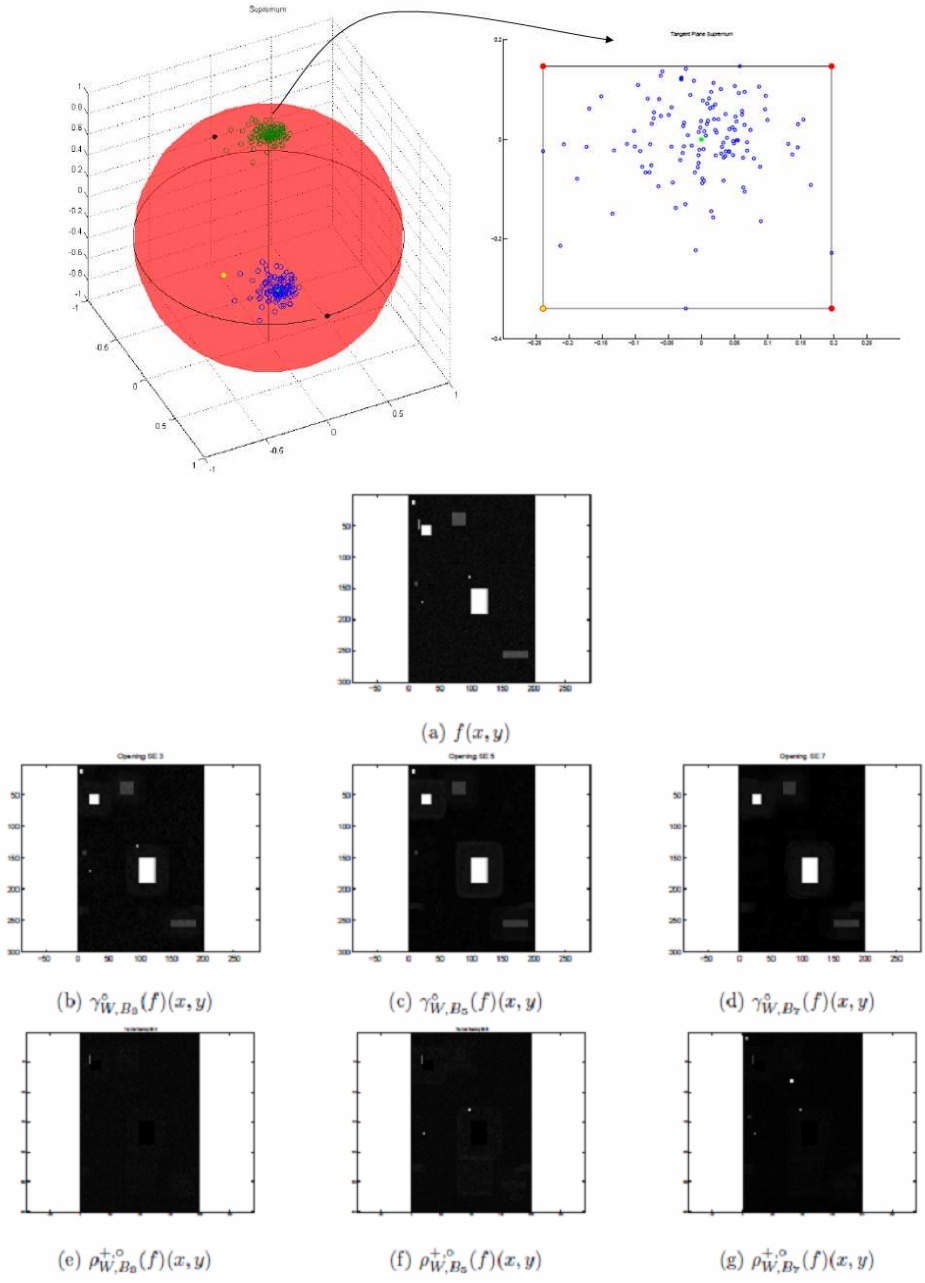

(a) $f(x,y)$

(b) $\gamma^{\circ}_{W,B_3}(f)(x,y)$ (c) $\gamma^{\circ}_{W,B_5}(f)(x,y)$ (d) $\gamma^{\circ}_{W,B_7}(f)(x,y)$

(e) $\rho^{+,\circ}_{W,B_3}(f)(x,y)$ (f) $\rho^{+,\circ}_{W,B_5}(f)(x,y)$ (g) $\rho^{+,\circ}_{W,B_7}(f)(x,y)$

FIG. 7.3 – Morphologie mathématique sur la sphère $\mathbb{S}^2$: haut, origine locale sur la sphère et calcul du sup/inf sur l'espace tangent ; bas, application des résidus d'ouvertures sur la sphère pour la détection de cibles sur des images Radar polarimétriques.

Chapitre 8

Images multi-variées de forme ou de texture et morphologie mathématique

Dans les trois chapitres précédents, j'ai présenté des travaux sur des images intrinsèquement multi-variées : on associe à chaque pixel une valeur vectorielle/matricielle, qui est produite généralement par le capteur de nature spectrale, polarimétrique, tensorielle, etc. Dans ce chapitre je ne parlerai pas de l'information spectrale au sens large, mais de la texture et de la forme, en considérant les deux cas comme des espaces de pixels multi-variés.

La texture est une information visuelle très précise mais relativement difficile à utiliser de manière quantitative pour l'analyse de bas niveau des images. Par exemple, dans certaines images complexes, les variations de texture permettent de définir les transitions entre régions ; cependant, il n'est pas de méthode directe pour introduire la texture dans la chaîne de segmentation morphologique par LPE. En fait, pour segmenter une image avec la LPE, on commence classiquement par simplifier l'image, typiquement avec un nivellement, avant de calculer le gradient de l'image. A partir d'une idée introduite par l'équipe de P. Maragos [51], si l'on récupère le résidu entre l'image originale et l'image nivelée on obtient la texture de l'image. Ainsi, le nivellement peut être considéré comme un outil pour décomposer l'image dans la composante de structure et la composante de texture. J'ai proposé une approche pour construire une image multi-variée d'énergie de texture, à partir du calcul d'une granulométrie locale. On peut donc calculer un gradient multi-varié de texture qui peut être ensuite combiné avec un gradient couleur. La construction et l'analyse d'espaces morphologiques de texture pour des images hyper-spectrales a été aussi exploré dans la thèse de S. Velasco-Forero. J'ai utilisé le même type de décomposition structure + différentes échelles de texture pour l'approche de morphologie structurellement adaptative présentée dans le chapitre 9.

Dans beaucoup d'applications, une fois la segmentation de l'image achevée, les objets sont définis par leur forme. Pour étudier l'espace de formes associé à une famille d'objets nous pouvons calculer des paramètres de forme et ensuite faire de l'analyse sur les valeurs des paramètres, ou bien, faire directement de l'analyse dans l'espace de formes. Pour que cette analyse soit pertinente, les formes des objets doivent être à la même échelle et être spatialement équivalente (i.e., centrées et orientées). Une famille d'objets peut maintenant

être considérée comme une image multi-variée, dont chaque variable est l'un des objets. On peut aussi faire une interprétation stochastique considérant chaque objet comme la réalisation d'une variable aléatoire. Ainsi, j'ai travaillé sur méthodes pour l'exploration morphologique dans des espaces de forme. Une partie de l'étude sur la statistique de formes (moyenne, médiane et variance de forme) a été réalisée en collaboration avec F. Meyer. J'ai aussi travaillé sur la projection de formes dans des espaces à dimension réduite et sur l'interpolation morphologique dans des variétés topologiques de forme. Dans la suite de cette étude, en collaboration avec S. Velasco-Forero, nous avons aussi travaillé sur l'inférence et la classification statistique dans des espaces morphologiques de formes.

8.1 Construction et analyse d'espaces morphologiques de texture

Décomposition structure+texture par nivellement

Depuis quelques années, un grand nombre de travaux se sont intéressés à la décomposition additive d'une image en deux termes : l'un représentant la composante de texture de l'image (partie "oscillante") et l'autre terme représentant les objets de l'image (partie "cartoon"). Le modèle original de décomposition, proposé par Y.Meyer [46] avec des EDPs non-linéaires et ondelettes, a conduit par la suite à des approches fondamentalement basées sur des algorithmes de minimisation de la variation totale.

En utilisant le nivellement, un filtre morphologique connexe qui simplifie symétriquement les structures claires/sombres (bruit, texture, etc...) d'une image tout en préservant les contours de celles qui ne sont pas filtrées, nous avons montré comment la morphologie mathématique permet une décomposition additive de l'image en deux termes : l'image de structure (objets principaux) et l'image de texture. Dans notre approche, la composante de "texture" n'est pas associée à la partie oscillante mais plutôt aux détails de l'image originale qui sont plus "petits" au sens du critère introduit par une image additionnelle qui joue le rôle du marqueur dans le nivellement. Les marqueurs les plus pertinents sont généralement des filtres Gaussiens ou des filtres morphologiques type alternés séquentiels. Le choix de la taille dans le filtre associée au marqueur détermine la "taille" de la texture dans la décomposition (ce type de paramètre apparait dans tous les algorithmes variationnels de décomposition cartoon+texture).

Dans le cas des images couleur, on applique un nivellement couleur pour obtenir l'image de structure, celle de texture étant donnée par la différence entre la luminance de l'image originale et celle de l'image nivelée.

Images d'énergie de texture et gradients de texture pour la segmentation

Les distributions granulométriques de taille peuvent être utilisées comme descripteurs dans des schémas de classification de textures. A partir du calcul d'une distribution granulométrique locale à chaque "patch" (une fenêtre autour de chaque pixel) de l'image de texture, nous avons introduit la notion d'image multi-variée d'énergie locale de texture, avec une image scalaire par taille de la granulométrie. D'autres types d'analyse multi-échelle morphologique à partir de nivellements a été aussi considéré pour la construction des images d'énergie multi-échelle de texture.

Ensuite, nous avons considéré les différentes façons de calculer une image de gradient associé à cette analyse multi-échelle et qui puisse permettre la détermination des contours des régions de textures différentes. Les deux formulations du gradient multi-varié de texture utilisent soit une approche marginale (un gradient pour l'image d'énergie de chaque échelle, puis la combinaison par sup ou somme) soit une approche vectorielle (à partir de la distance euclidienne entre deux pixels d'énergie

multi-variée, on calcule pour chaque pixel dans son voisinage la valeur maximale de distance entre le pixel en question et ses voisins.

Dans certaines images la texture est une information très discriminante pour la séparation des objets. Les gradients de textures que nous avons introduits pour les images d'énergie peuvent être utilisés avec la LPE pour segmenter l'image en régions homogènes selon la texture. Nous avons aussi montré que, si l'on combine le gradient de texture (par somme ou par sup) avec un gradient couleur obtenu à partir de l'image de structure, il est possible d'obtenir une segmentation mixte couleur+texture qui peut être plus pertinente que celle obtenue seulement avec des gradients couleur pour des images naturelles complexes.

Principales publications

– J. Angulo. "**Morphological texture gradients. Application to colour+texture watershed segmentation**", In *Proc. of the 8th International Symposium on Mathematical Morphology (ISMM'2007)*, Rio de Janeiro, Brazil, October 2007. p. 363–374, MCT/INPE, 2007.

8.2 Analyse statistique dans des espaces morphologiques de forme

Statistiques de formes : moyenne et variance de forme

Les approches les plus puissantes pour le calcul de la forme moyenne et variance de forme à partir d'une collection d'objets ont été étudiées dans la littérature par des méthodes issues soit de la géométrie différentielle soit d'analyse variationnelle.

Nous avons introduit différentes alternatives de "forme moyenne" fondées sur des outils classiques et puissants de la morphologie mathématique, notamment à partir de la médiane morphologique entre deux ensembles (notion à la base de l'interpolation morphologique) et de la fonction distance d'un ensemble. Nous pouvons mentionner en particulier l'algorithme qui produit exactement la forme moyenne au sens de la métrique L_2 par calcul d'une LPE sur la somme des fonctions distances des différentes formes ; ainsi, on obtient la forme optimale par une technique purement géométrique. Par ailleurs, il est aussi possible d'obtenir avec la même approche une image de variance locale de forme.

Projection de formes dans des espaces à dimension réduite et interpolation morphologique dans des variétés topologiques de forme

Les notions de moyenne et variance de forme ont du sens seulement dans le cas de familles homogènes de forme : dans une collection très hétérogène de formes d'objets, la forme moyenne est très probablement le cercle moyen. L'application de techniques d'analyse de données aide à explorer les familles de formes (trouver des sous-familles homogènes) et leur représentation sur des espaces à dimension réduite.

Nous avons considéré dans un premier temps l'Analyse en Composantes Principales (ACP) comme paradigme de l'analyse linéaire. Nous avons ainsi montré la manière dont l'ACP, combinée avec la LPE, permet la construction d'images des modes de variation de forme.

Dans un deuxième temps, nous avons considéré une approche non-linéaire très puissante de plongement isométrique (Isomap) qui, à partir d'une métrique entre deux formes, permet la construction d'une représentation de la famille de formes dans un graphe (projeté sur un espace à dimension réduite) où les distances géodésiques entre les formes sont préservées. L'intérêt dans l'analyse de formes vient du fait qu'Isomap produit des chemins géodésique entre paires de formes et par exemple, cela nous

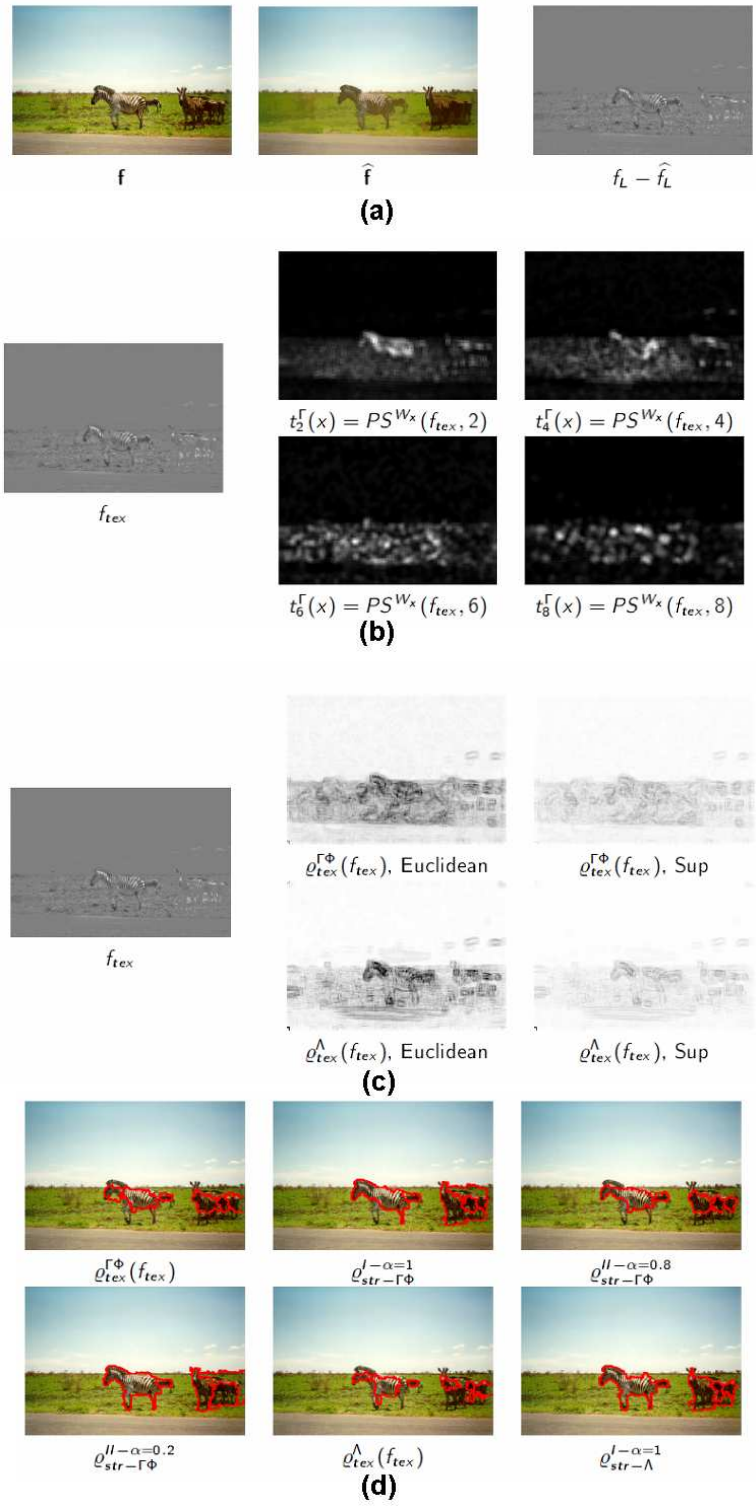

FIG. 8.1 – Construction et analyse d'espaces morphologiques de texture : (a) décomposition structure+texture par nivellement ; (b) image d'énergie de texture multi-échelle ; (c) gradient de texture pour la segmentation ; (d) segmentation des gradients par LPE avec marqueurs.

permet de construire des espaces d'interpolation entre deux formes contenant d'autres formes de la famille.

Inférence et classification statistique dans des espaces morphologiques de formes

Si l'on assume que la famille de formes suit une loi Gaussienne, nous pouvons utiliser les images de forme moyenne et de variance de forme pour construire une fonction de densité de probabilité de forme.

En se fondant sur cette fonction, nous avons introduit un algorithme pour le calcul des intervalles de confiance de la forme moyenne ainsi qu'un algorithme de simulation de formes aléatoires associées à une famille.

D'autre part, nous avons introduit une méthode pour calculer la probabilité conditionnelle d'une forme nouvelle par rapport à une famille de formes donnée. Si l'on dispose de plusieurs classes de formes, nous construisons facilement un algorithme de classification bayésienne de formes. Notre approche de classification bayésienne sur des espaces morphologiques a été validée sur une base standard de formes et les résultats obtenus sont comparables à d'autres méthodes computationnellement plus lourdes.

Principales publications

– J. Angulo and F. Meyer. "**Morphological Exploration of Shape Spaces**". In *Proc. of ISMM'09 (2009 International Symposium on Mathematical Morphology)*, LNCS 5720, Springer-Verlag Berlin Heidelberg, p. 226–237, Groningen, The Netherlands, August 2009.

– S. Velasco-Forero and J. Angulo. "**Statistical Shape Modeling using Morphological Representations**". In *IEEE ICPR'10 (20th IEEE International Conference on Pattern Recognition)*, p. 3537–3540, Istanbul, Turkey, August 2010.

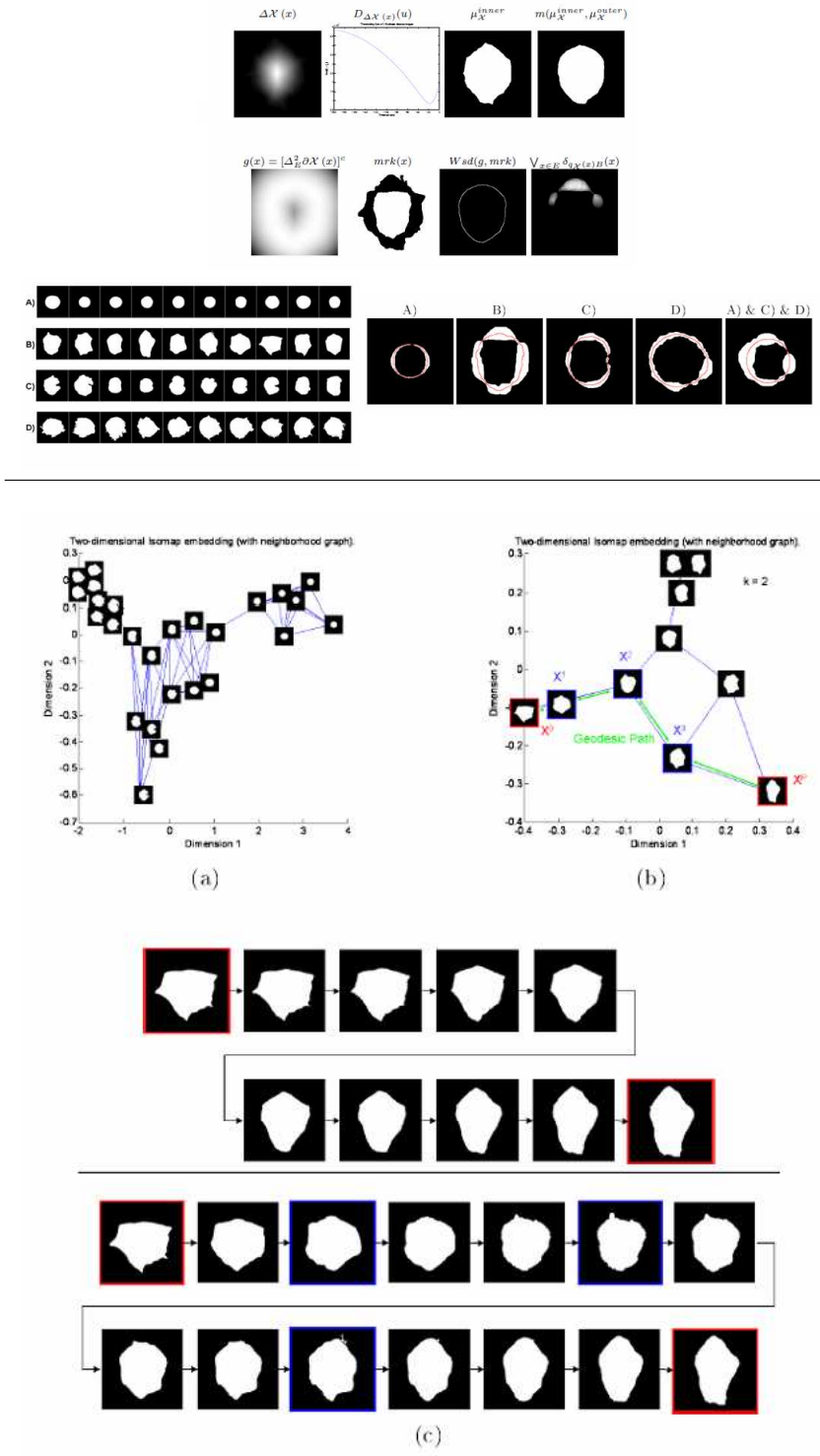

FIG. 8.2 – Analyse statistique dans des espaces morphologiques de forme : haut, moyenne et variance de formes ; bas, projection de formes dans des espaces à dimension réduite et interpolation morphologique dans des variétés topologiques de forme.

Chapitre 9

Avancées en morphologie mathématique : segmentation probabiliste, géométrie et invariance, opérateurs adaptatifs et régularisés

Malgré une maturité théorique certaine et un corpus méthodologique exceptionnellement riche, la morphologie mathématique reste une discipline féconde. Au cours de mes recherches, j'ai travaillé sur des points fondamentaux de la morphologie mathématique qui ne se limitent pas à leur extension aux images multi-variées.

Les contributions résumées dans ce chapitre s'inscrivent dans une réflexion que je mène atour de trois grands volets :

- *d'une part, la "régularisation" des effets des opérateurs de segmentation et de filtrage par des approches soit probabilistes soit basées sur l'utilisation de notions géométriques (symétries, changement d'espace de représentation des pixels, etc...) ;*
- *d'autre part, "l'adaptabilité" des opérateurs morphologiques aux propriétés locales (de nature spectrale, de nature géométrique ou de nature structurelle) de chaque pixel de l'image ;*
- *finalement, la "non-linéarisation" de méthodes et d'approches issues d'autres paradigmes du traitement d'image et l'analyse de données (généralisation de la diffusion, représentations parcimonieuses)*

Comme je mentionnerai après dans le chapitre des perspectives, j'envisage dans mon projet de recherche l'approfondissement de ces trois axes.

Dans une démarche de "probabilisation" de la segmentation morphologique, j'ai introduit à la fin 2006 la notion de LPE stochastique, par des simulations de LPE avec des germes aléatoires. Ce travail a été ensuite publié avec D. Jeulin. Dans la thèse de doctorat de G. Noyel, nous avons proposé des techniques pour le conditionnement des germes aléatoires selon une classification des pixels. F. Meyer s'est aussi intéressé à la méthode et il a proposé l'algorithme pour le calcul analytique des valuations d'arêtes d'un graphe qui est équivalent à la LPE stochastique, sans besoin de faire des simulations [45].

Je continue toutefois à développer la potentialité de la méthode par des algorithmes de simulation, en particulier pour la segmentation d'images multi-variées. Dans la suite de ces travaux, j'ai proposé avec S. Velasco-Forero et J. Chanussot, d'une part, une méthode multi-échelle probabiliste, où l'estimation de la pdf de contours tire partie, soit d'une représentation de l'image sous forme d'une pyramide, soit d'un schéma multi-échelle des germes aléatoires de différentes tailles. D'autre part, j'ai proposé aussi avec S. Velasco-Forero une approche semi-supervisée de segmentation d'images hyperspectrales qui est fondée sur la régionalisation des germes aléatoires selon des fonctions qui dépendent des différentes classes spectrales présentes dans l'image.

Les relations entre le filtrage linéaire (espaces-échelle associés au filtrage gaussien et à l'équation de la chaleur) et le filtrage morphologique (espaces-échelle associés aux dilatations/érosions non-plates) ont été étudiées précédemment par divers travaux de l'état-de-l'art. Ainsi, le parallélisme entre le monde linéaire et non-linéaire du traitement d'image et surtout l'établissement des ponts entre eux est un sujet qui me passionne. Dans une série d'études récentes, je suis en train d'étudier comment généraliser les approches de filtrage par diffusion dans le but d'introduire des filtres non-linéaires dont les effets imitent la dilatation et l'érosion morphologique. La méthodologie que j'ai suivie est basée dans la moyenne contre-harmonique. J'ai considéré la mise en œuvre numérique de différents cas de diffusion : diffusion isotrope, modèle de Perona-Malik, modèle de Weickert, diffusion complexe. Par ailleurs, nous avons étudié l'expression analytique des cas limites de non-linéarisation. J'ai pu ainsi redécouvrir le lien classique entre l'espace-échelle gaussien et le l'espace-échelle des dilatations /érosions par des fonctions structurantes quadratiques. Mais aussi découvrir l'opérateur morphologique équivalent au "laplacian of gaussian" (LoG), c'est-à-dire la dérivée seconde morphologique régularisée.

Avec l'objectif d'appliquer de manière optimisée des opérateurs morphologiques avec des éléments structurants adaptés aux objets circulaires, qui ont des symétries radiales et angulaires, M.A. Luengo-Oroz a introduit, dans le cadre de son stage-Projet Fin d'Etudes que j'ai encadré en 2004, la notion de morphologie mathématique cyclique en coordonnées log-pol. En plus de l'application initiale à l'analyse de forme des cellules, la méthode s'est montrée très efficace pour la modélisation et la segmentation des spots des puces à ADN. Plus récemment, aussi en collaboration avec M.A. Luengo-Oroz, nous avons utilisé la morphologie cyclique en polaires pour la segmentation automatique de l'iris sur des images non calibrées d'œil ; notre méthode a fini en huitième position dans la compétition internationale NICE-I, sur une centaine des meilleurs groupes de recherche du monde dans le domaine.

La morphologie cyclique est un exemple de morphologie variable dans l'espace : l'élément structurant appliqué dans chaque pixel n'est pas constant. Cette généralisation, avec la perte de l'invariance par translation dans l'espace des pixels, a des conséquences importantes dans l'implémentation des opérateurs. La théorie nécessaire au développement de la morphologie variable dans l'espace a été introduit par J. Serra dans les années 80, cependant l'application de ce type de techniques est restée très limitée. En collaboration avec R. Verdu-Monedero et J. Serra, nous avons justement étudié la manière de construire adéquatement des opérateurs morphologiques anisotropes, c'est-à-dire localement orientés selon l'information du gradient. Nous avons montré comment calculer un champ d'orientations dense et régulier ainsi que la façon de paramétrer, à partir de ce champ, en plus de l'orientation, la taille et l'anisotropie des éléments structurants.

Le développement de filtrage localement adaptatif est bien établi dans la théorie et la pratique du filtrage gaussien. En particulier, le filtrage bilatéral est une convolution gaussienne localement adaptative pour débruiter/lisser les images tout en préservant les contours : pour chaque pixel, les coefficients de noyau gaussien (liés à la distance spatiale) sont pondérés par la distance d'intensité avec ses voisins. Ses résultats sont généralement très acceptables, sa formulation est assez simple et ne nécessite que deux paramètres faciles à choisir : l'un pour la taille spatiale et l'autre pour le contraste afin de préserver les caractéristiques. Par ailleurs le filtrage bilatéral est fortement lié à la théorie du filtrage robuste (pondération par moindres carrés) et au filtrage par solution de l'EDP de diffusion de Perona et Malik.

Poursuivant notre intérêt pour les opérateurs morphologiques variables dans l'espace, j'ai généralisé ces approches de convolution gaussienne dans le but d'introduire des dilatations/érosions bilatérales.

En plus des opérateurs adaptatifs selon l'orientation des structures ou selon l'homogénéité, que j'ai considérés dans mes travaux, il y existe un autre type d'adaptabilité qui a été proposé dans l'état de l'art de la morphologie mathématique. Il s'agit des opérateurs adaptés à l'intensité du pixels qui ont été proposés par Vachier et Meyer [62]. Cela consiste à utiliser une décomposition de l'image numérique en ensembles de niveaux, suivie par le traitement de chaque niveau par un élément structurant plat dont la taille dépend du niveau de gris (selon une règle de taille particulière) et enfin la reconstitution d'image à partir des ensembles de niveaux traités. Dans cette approche, l'adaptabilité pour chaque point dépend de la valeur de l'intensité absolue ; ainsi, deux points de l'image associée à des structures d'échelle similaire mais d'intensité différente sont traitées différemment. Nous avons proposé, avec S. Velasco-Forero, un nouveau cadre d'opérateurs adaptatifs non-linéaires : la structure adaptative morphologie mathématique. Plus précisément, le raisonnement derrière notre approche est de travailler sur une décomposition non-linéaire multi-échelle de l'image basée sur une famille de nivellements. Ensuite, la taille de la fonction structurante à chaque pixel est intrinsèquement adaptée à l'échelle locale des structures sur ce pixel. En d'autres termes, deux régions de l'image apparaissant dans une échelle similaire vont suivre un filtrage morphologique de la même "taille", indépendamment des intensités absolues sur ces deux régions. La valeur de la transformation de l'image sera obtenue par la reconstitution des différentes échelles traitées séparément. Nous remarquons également que notre approche n'est pas limitée à des opérateurs morphologiques plats.

En travaillant en 2006 avec F. Meyer sur l'implémentation des bi-nivellements, qu'il avait proposé afin d'introduire des propriétés de micro-viscosité dans la reconstruction géodésique lorsqu'on travaille sur la trame hexagonale, nous avons eu l'idée d'utiliser le même type de mécanisme pour construire des dilatations et érosions micro-visqueuses, ainsi que leurs opérateurs évolués. Une théorie sur les adjonctions sur les éléments de la trame hexagonale (pixels et arêtes) a été ainsi développée par F. Meyer, qui permet de formaliser ces opérateurs qui fournissent d'excellents résultats pour le débruitage, y compris des images binaires, et pour l'obtention de gradients robustes face au bruit.

Plus récemment, j'ai poursuivi ces travaux avec S. Koudoro et S. Velasco-Forero, en introduisant une famille d'éléments structurants unitaires de symétrie hexagonale (plus grands que l'hexagone unitaire) que nous avons appelés des flocons de neige. Chaque flocon de neige étant composé de l'union d'un pixel central et six micro-voisinages. Il existe deux familles de filtres qui peuvent être définies : i) des opérateurs de second-ordre qui produisent du filtrage robuste au bruit par l'incorporation de micro-opérations de débruitage, ii) des opérateurs locaux sélectifs qui permettent une adaptabilité locale très simples à

implémenter.

Le dernier sujet inclus dans ce chapitre est celui de la morphologie parcimonieuse que j'ai introduite récemment avec S. Velasco-Forero. Le principe est assez simple. Imaginons qu'on doit appliquer un certain opérateur morphologique à chacune des images d'une collection de M images, définies sur le même espace support des pixels. Considérons aussi qu'il existe une représentation parcimonieuse des M images sous forme d'un dictionnaire de K images ($K < M$) ; c'est-à-dire chacune des M images initiales est codée par une combinaison des K images du dictionnaire. Dans ce contexte, la question que je me suis posée est donc : quel type de représentation parcimonieuse permet de dire qu'appliquer l'opérateur à une image de la collection initiale est approximativement égal à appliquer le même opérateur à chacun des K atomes du dictionnaire puis à les combiner en utilisant le codage initial de l'image en question. Ce questionnement dans le cadre des opérateurs morphologiques dilatation et érosion m'a conduit vers des représentations de type factorisation non-négative de matrices (NMF). Je travaille actuellement sur la suite de cette étude.

9.1 LPE stochastique

Principe : LPE sur marqueurs aléatoires et estimation d'une pdf des contours par simulations de MonteCarlo

La LPE est une méthode de segmentation morphologique très puissante. Différents types d'algorithmes de segmentation basés sur la LPE ont été proposée dans l'état de l'art : segmentation avec des marqueurs, pyramides non-paramétriques, hiérarchies selon des critères morphologiques (contraste, volume), etc... Dans tous ces algorithmes, la question clé pour réduire et contraindre la segmentation consiste en sélectionner de manière déterministe les bons marqueurs.

Nous avons introduit une méthodologie stochastique pour la segmentation par LPE. L'approche, par simulation de MonteCarlo, utilise M réalisations de N germes ou marqueurs aléatoires pour estimer selon la méthode de Parzen une fonction de densité de probabilité (pdf) de contours : les contours les plus importants de l'image apparaissent plus fréquemment et donc auront une probabilité élevée. La pdf de contours peut ensuite être segmentée hiérarchiquement en utilisant l'algorithme non-paramétrique des cascades ainsi que des algorithmes de seuillage basés sur des critères de probabilité. L'approche est valable pour des images à niveaux de gris et pour les images multi-variées. Nous avons prouvé par nos résultats que cette méthode améliore notablement les résultats lorsque l'objectif est la segmentation d'images complexes en peu de régions.

Nous avons considéré quelques variantes pour le tirage des marqueurs aléatoires : i) germes aléatoires uniformes, ii) germes régionalisés sur la fonction du gradient, et iii) germes aléatoires uniformes pour un nivellement avant de calculer le gradient sur lequel la LPE est calculée. Le dernier algorithme est plus complexe mais il rend les meilleurs résultats.

Calcul de la pdf dans le cas multi-échelle

Nous avons ensuite considéré le cas multi-échelle pour le calcul de la pdf des contours. Le schéma multi-échelle probabiliste est basé sur le calcul par des simulations Monte Carlo de la probabilité conditionnelle d'une échelle par rapport à la pdf d'une autre échelle préalablement obtenue. Nous pouvons donc obtenir une pdf marginale à chaque échelle, une pdf d'une échelle conjointement aux échelles précédentes.

Nous avons décliné ce formalisme en quelques algorithmes selon l'ingrédient utilisé pour construire la représentation multi-échelle considérée. Nous avons considéré notamment i) une pyramide linéaire

de l'image par un espace-échelle gaussien, ii) une pyramide morphologique en utilisant un espace-échelle par nivellements, iii) et une pyramide multi-échelle obtenue en modifiant la taille des germes aléatoires.

Segmentation semi-supervisée et régionalisation des germes

D'autre part, nous avons aussi proposé un algorithme de LPE stochastique semi-supervisée qui vise à segmenter les images en utilisant une information à priori sur son contenu, mais sans arriver à passer par une pré-classification de l'image en régions (qui correspondrait à une approche totalement supervisée). Par ailleurs, cette méthodologie est surtout pertinente dans le cas des images hyperspectrales car assez souvent cette information à priori est bien disponible.

L'idée est la suivante : à partir d'un ensemble d'entrainement consistant en une sélection de pixels représentatifs de chaque classe spectrale de l'image, l'algorithme commence par calculer pour chaque classe une carte de probabilité d'appartenance à la classe (MPM). Ensuite, chaque MPM est considérée comme une fonction de densité régionalisée qui est utilisée pour simuler les marqueurs aléatoires utilisés dans l'estimation MonteCarlo de la pdf des contours de la classe correspondante. Cette pdf privilégie les régions spatiales de l'image spectralement associées à la classe. Après, en appliquant la même technique pour chaque classe, une série de pdf est obtenue pour chaque image. Les pdf des contours peuvent être considérées soit séparément soit, après combinaison, comme une seule fonction globale à l'image.

Principales publications

- J. Angulo. "**Probabilistic approach to the morphological segmentation**," *Rapport Technique CMM-Ecole des Mines de Paris, N-/06/MM*, September 2006.
- J. Angulo, D. Jeulin. "**Stochastic watershed segmentation**", In *Proc. of the 8th International Symposium on Mathematical Morphology (ISMM'2007)*, Rio de Janeiro, Brazil, October 2007. p. 265–276, MCT/INPE, 2007.
- J. Angulo, S. Velasco-Forero, and J. Chanussot. "**Multiscale stochastic watershed for unsupervised hyperspectral image segmentation**". *Proc. of IEEE IGARSS'2009 (IEEE International Geoscience & Remote Sensing Symposium)*, Vol. III, 93–96, Cape Town, South Africa, July 2009.
- J. Angulo, and S. Velasco-Forero. "**Semi-supervised hyperspectral image segmentation using regionalized stochastic watershed**". In *Proc. of SPIE symposium on Defense, Security, and Sensing : Algorithms and Technologies for Multispectral, Hyperspectral, and Ultraspectral Imagery XVI*, SPIE Vol. 7695, Orlando, United States, April 2010.

9.2 Non-linéarisation de la diffusion réelle et complexe et filtrage asymptotiquement morphologique

De l'espace-échelle contra-harmonique gaussien à l'espace-échelle des dilatations/érosions paraboloïdales

La moyenne contra-harmonique d'ordre P est un estimateur de la valeur "représentative" d'un ensemble de valeurs réelles, qui selon le choix de P, sera biaisée vers les valeurs les plus hautes ($P > 0$) ou vers les valeurs les plus basses ($P < 0$). Ainsi, avec un P suffisamment élevé positif (négatif), la moyenne contra-harmonique donne le supremum (l'infimum) de l'ensemble des valeurs. Nous avons commencé par montrer que le comportement asymptotique de la moyenne contra-harmonique est plus intéressant que celui des $P-$normes (normes de Minkowski) pour approximer de manière robuste la valeur de la dilatation et érosion plates.

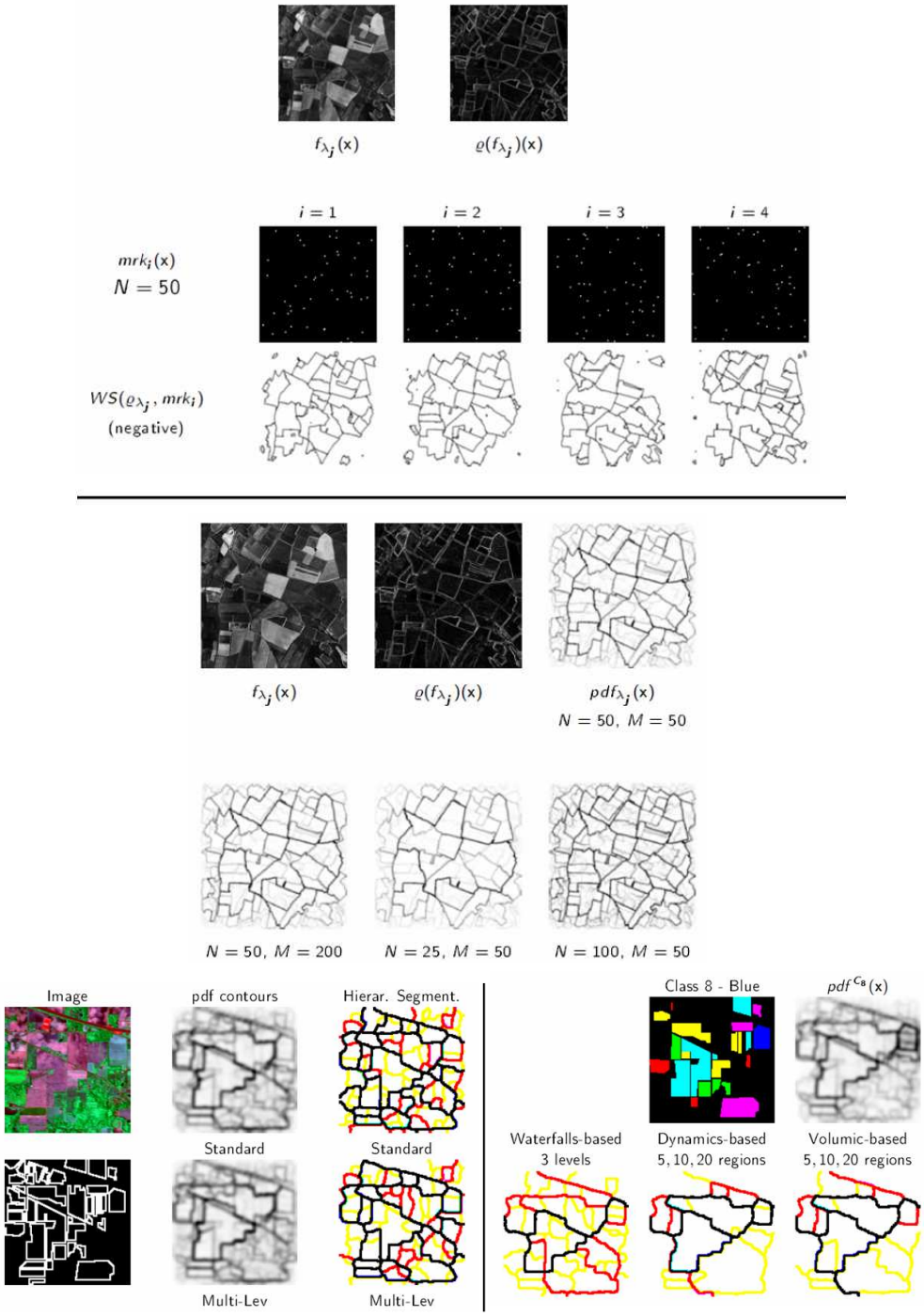

FIG. 9.1 – LPE stochastique : haut, segmentations par réalisations de marqueurs aléatoires ; milieu, estimation de la pdf des contours par le méthode de Parzen ; bas-gauche, calcul de la pdf dans le cas multi-échelle ; bas-droite, segmentation semi-supervisée par régionalisation des germes.

En utilisant le formalisme de la moyenne contra-harmonique, nous avons introduit la notion de convolution contra-harmonique et en particulier, nous avons étudié le cas des noyaux gaussiens de convolutions. Nous avons introduit donc la notion d'espace-échelle contra-harmonique gaussien qui dépend de manière monotone du paramètre de non-linéarité P. L'étude des cas limites nous a permit de montrer que pour une valeur de P positive (négative) très large nous obtenons une dilatation (une érosion) plate, le cas $P = 0$ est celui de la convolution linéaire, et pour $P > 0$ ($P < 0$) nous obtenons un opérateur non-linéaire qui se comporte asymptotiquement comme une dilatation (érosion) paraboloïdale. Nous avons donc redécouvert la connexion logarithmique qui existe entre la convolution linéaire par un certain kernel et la dilatation/érosion par une fonction structurante qui est le logarithme du kernel ; et qui avait été montré précédemment par d'autres approches.

Généralisation de la diffusion et solution numérique

Partant de l'équivalence qu'il y a entre l'espace-échelle gaussien et la résolution de l'équation de diffusion linéaire, nous avons montré comment la convolution contra-harmonique gaussienne peut être transposée à la solution numérique par différences finies de l'équation de diffusion, de manière à obtenir les pseudo-dilatations/érosions par la non-linéarisation de la solution numérique de l'EDP de diffusion. Par ailleurs, nous avons aussi introduit un schéma numérique alternatif où la non-linéarisation contra-harmonique a lieu à chaque temps d'intégration : même si nous ne l'avons pas encore prouvé, nous conjecturons que ce schéma doit correspondre asymptotiquement à celui utilisé pour résoudre l'EDP de type Hamilton-Jacobi associée à la dilatation/érosion quadratique.

Non-linéarisation des modèles de diffusion de Perona-Malik et de Weickert

Après avoir considéré la solution numérique de la diffusion isotrope, nous avons aussi montré la validité de notre approche pour la non-linéarisation de deux des modèles de diffusion adaptive les plus utilisés de l'état de l'art : la diffusion non-linéaire de Perona-Malik où le coefficient de diffusion est localement calculé pour chaque pixel par une fonction qui pénalise les valeurs fortes du gradient (les transition entre régions) et la diffusion anisotrope de Weickert qui adapte la diffusion localement selon un tenseur d'orientation qui permet de filtrer de manière directionnelle.

Nous avons montré qu'avec le cadre contra-harmonique, nous pouvons obtenir facilement, en utilisant les schémas numériques de différences finies, des pseudo-dilatations/érosions qui ne modifient pas les contours principaux de l'image (associés aux zones de fort gradient) ou qui suivent la cohérence directionnelle des structures.

Non-linéarisation de la diffusion complexe : Laplacien parabolique non-linéaire

Dans la dernière partie de cette série de travaux, nous avons considéré aussi le cas de la diffusion complexe : le coefficient de diffusion est un nombre complexe. Le modèle physique associé à cette équation est la forme la plus simple de l'Equation de Schrödinger (lorsque le coefficient de diffusion est un imaginaire pur). A nouveau, nous avons appliqué notre formalisme de non-linéarisation contra-harmonique que nous a permis en particulier de considérer le cas de diffusion complexe le plus pertinente pour le filtrage d'image : la phase du coefficient de diffusion est proche de 0. Dans ce cas-là, l'image complexe obtenue à une partie réelle qui est la convolution par le kernel gaussien et la partie imaginaire la convolution par un kernel qui est asymptotiquement un filtre "laplacien of gaussian" (LoG) normalisé. Lorsqu'on introduit notre non-linéarisation, on obtient une image complexe où la partie réelle est la dilatation/érosion par une fonction structurante paraboloïdale et la partie imaginaire étant composée d'un opérateur composé qui peut être interprété comme une dérivée seconde morphologique régularisée.

Nous avons étudié très en détails ce nouvel opérateur morphologique, que nous avons appelé le laplacien parabolique non-linéaire, en le comparant avec son équivalant linéaire LoG, pour les tâches de rehaussement du contraste et de détection robuste de contours.

Principales publications

- J. Angulo. "**Pseudo-Morphological Image Diffusion using the Counter-Harmonic Paradigm**". In *Proc. of Acivs'2010 (2010 Advanced Concepts for Intelligent Vision Systems)*, LNCS 6474, Springer-Verlag Berlin Heidelberg, Part I, p. 426–437, Sydney, Australia, December 2010.
- J. Angulo. "**Non-Linearization of Free Schrodinger Equation and Pseudo-Morphological Complex Diffusion Operators**". In *IEEE ICIP'11 (2011 IEEE International Conference on Image Processing)*, Brussels, September 2011.
- J. Angulo. "**Parabolic Nonlinear Laplacian : Morphological Counterpart of Laplacian of Gaussian**". In *13th International Congress of Stereology (ICS-13)*, Beijing, China, October 2011.

9.3 Morphologie variable dans l'espace : Morphologie mathématique cyclique en coordonnées log-pol

Principe, mise en œuvre et propriétés d'invariance

Le principe de cette étude était très simple : on propose d'appliquer les opérateurs morphologiques après avoir fait une transformation géométrique d'une image, et ensuite d'obtenir la transformation inverse de l'image traitée. Grâce à cette procédure, le traitement des images dans le domaine transformé avec éléments structurants réguliers (carrés, disques, etc...) est équivalent à travailler avec les éléments structurants déformés dans la représentation originale. Plus précisément, la conversion de l'espace de pixels des coordonnées cartésiennes à coordonnées logarithmiques-polaires (log-pol) fournit des résultats satisfaisants dans le traitement des images qui ont un "centre" pertinent.

La mise en œuvre de la transformation log-pol directe et inverse doit se faire avec un schéma d'interpolation bilinéaire qui garantit la "régularité" des résultats. Par ailleurs, cette morphologique cyclique nécessite l'introduction de la périodicité de la variable angulaire : nous avons trouvé une solution très simple qui consiste à dupliquer l'image dans la dimension associée à l'angle.

La représentation log-pol présente des propriétés d'invariance intéressantes. Les rotations de l'image originale en cartésiennes deviennent des changements cycliques verticaux dans l'image log-pol par la nature périodique de la composante angulaire. De façon analogue, les changements de taille de l'image originale impliquent des déplacements horizontaux dans l'image transformée, conformément à la propriété d'autosimilarité de la fonction exponentielle. Ces propriétés sont extrêmement puissantes pour construire des images "normalisées" et donc des traitements morphologiques invariants aux rotations et à la taille.

Du point de vue de l'implémention d'éléments structurants, les avantages de l'approche sont aussi notables : les éléments structurants linéaires horizontaux et verticaux vont acquérir respectivement le sens radial et angulaire sur l'image d'origine lors du traitement dans le domaine transformé. Par exemple, une dilatation par élément structurant vertical correspond à une dilatation par arc de cercle dans l'image originale, avec une largeur variable dans l'espace, selon la distance à l'origine ; une dilatation avec un carré correspond à la dilatation par un secteur circulaire variable.

Application en microscopie biomédicale : l'analyse de la forme des globules rouges

La première application que nous a permis d'illustrer l'intérêt de la morphologie cyclique était l'analyse de la forme des érythrocytes (les globules rouges sanguins). En particulier, nous avons montré,

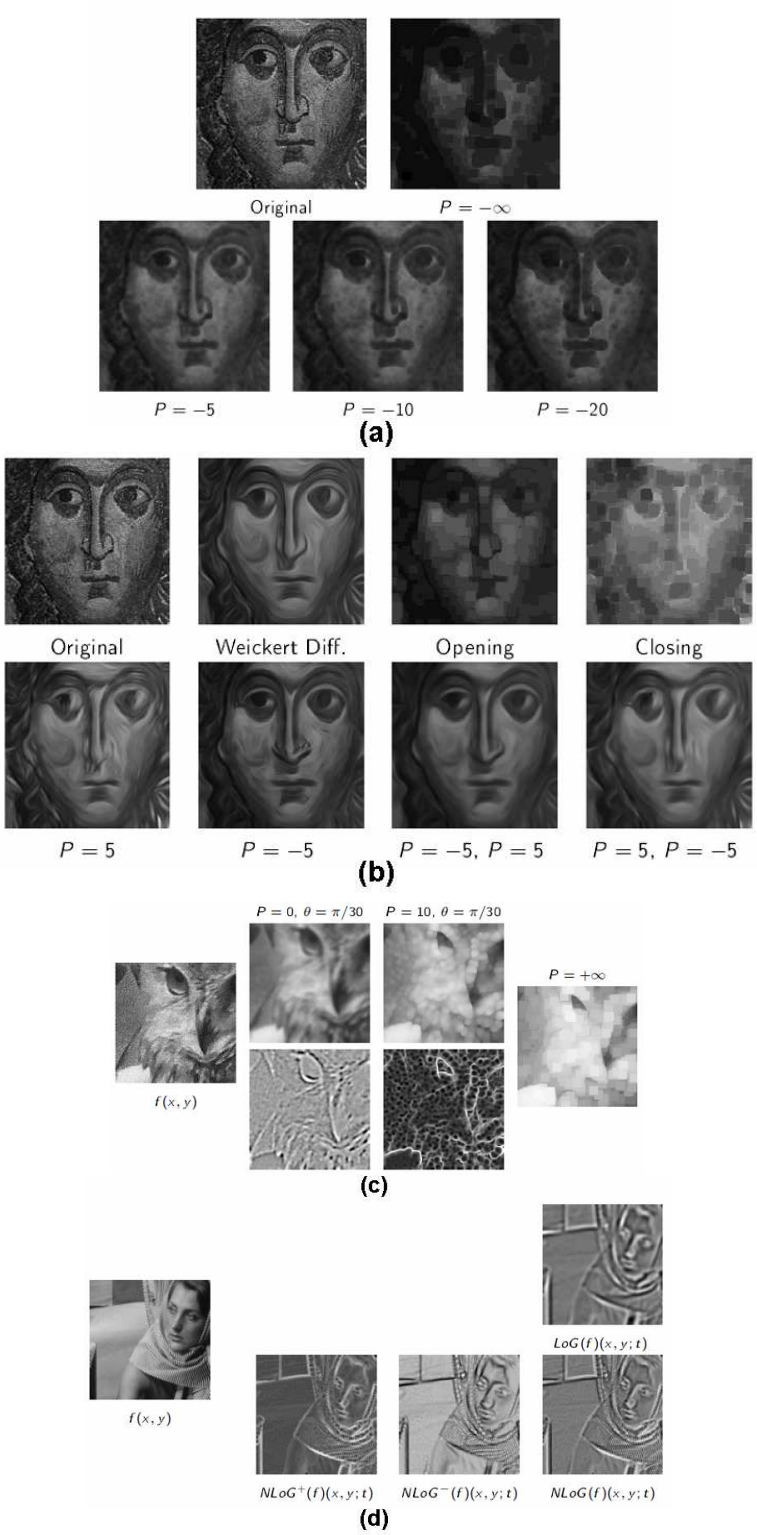

FIG. 9.2 – Non-linéarisation de la diffusion réelle et complexe et filtrage asymptotiquement morphologique : a) espace-échelle contra-harmonique gaussien ; b) non-linéarisation du modèle de diffusion anisotrope de Weickert ; c) non-linéarisation de la diffusion complexe ; d) Laplacien parabolique non-linéaire.

d'une part, comme les ouvertures/fermetures circulaires en log-pol obtenues à partir d'éléments structurants linéaires permettent l'extraction très précise des zones d'extrusions/intrusions dans le contour des érythrocytes et qui sont liées à des anomalies particulières des globules rouges. D'autre part, nous avons aussi montré que le squelette binaire calculé en coordonnées log-pol donne lieu à un squelette radial partant du centre de la forme et qui constitue un descripteur très pertinent de ce type d'objets.

Application en microscopie biomédicale : segmentation des spots de microarrays

L'analyse robuste (contrôle de qualité, segmentation et quantification) des spots des images de puces à ADN est une exigence pour les logiciels de lecture automatique des puces, ce qui est d'une importance fondamentale pour une analyse génomique à haut débit basée sur ce type de technologie.

Nous avons développé une approche avancée pour la qualification, segmentation et quantification adaptative de chaque spot en fonction d'un modèle de sa morphologie (avec différentes typologies de spots). L'extraction de caractéristiques et de classification du spot est basée sur des opérateurs de la morphologie cyclique en coordonnées polaires. La segmentation du contour du spot peut aussi être obtenue en travaillant en coordonnées polaires par le calcul du plus court chemin circulaire, qui est facilement obtenu avec la fonction de distance généralisée. Selon la typologie du spot, plusieurs chemins minimaux peuvent être calculés pour obtenir une segmentation multi-région.

Application en biométrie : segmentation de l'iris

Nous avons aussi utilisé ces travaux pour développer une nouvelle approche de segmentation rapide de l'iris sur des images tout venant de l'œil, qui s'appuie sur l'anatomie de l'iris en structures fermées imbriquées (la sclère est plus brillante que l'iris, et l'iris est plus lumineux que la pupille) et sur sa symétrie polaire. La méthode utilise des algorithmes de morphologie mathématique cyclique en coordonnées log-pol pour le filtrage circulaire/angulaire et pour la segmentation circulaire en utilisant les plus courts chemins à partir de la fonction distance généralisée aux images à niveaux de gris.

Cet algorithme avait obtenu de bons résultats dans la compétition internationale NICE-I (finaliste en huitième position) et montré un comportement très robuste, surtout lorsqu'il s'agit des yeux mi-clos, différentes couleurs de peau/variations d'éclairage et sur des sujets portant des lunettes.

Principales publications

- M. Luengo-Oroz and J. Angulo. "**Cyclic Mathematical Morphology in Polar-logarithmic Representation**". *IEEE Transactions on Image Processing*, Vol. 18, No. 5, 1090–1096, 2009.
- M.A. Luengo-Oroz, J. Angulo, G. Flandrin and J. Klossa. "**Mathematical morphology in polar-logarithmic coordinates. Application to erythrocyte shape analysis**". In *Proc. of the 2nd Iberian Conference on Pattern Recognition and Image Analysis (IbPRIA'2005)*, Estoril, Portugal, June 2005. Vol. LNCS 3523, p. 199–205, Springer, 2005.
- J. Angulo. "**Polar modelling and segmentation of genomic microarray spots using mathematical morphology**". *Image Analysis and Stereology*, Vol. 27, 107–124, 2008.
- M. Luengo-Oroz, E. Faure and J. Angulo. "**Robust iris segmentation on uncalibrated noisy images using mathematical morphology**". *Image Vision and Computing*, Vol. 28, 278–284, 2009.

9.4 Morphologie variable dans l'espace : Morphologie mathématique anisotrope

Formulation et implémentation des opérateurs variables spatialement

Le plus souvent, la morphologie mathématique est utilisée dans une approche invariante par translation, où le fonctionnement de base d'une dilatation (érosion) consiste à placer un ensemble fixe,

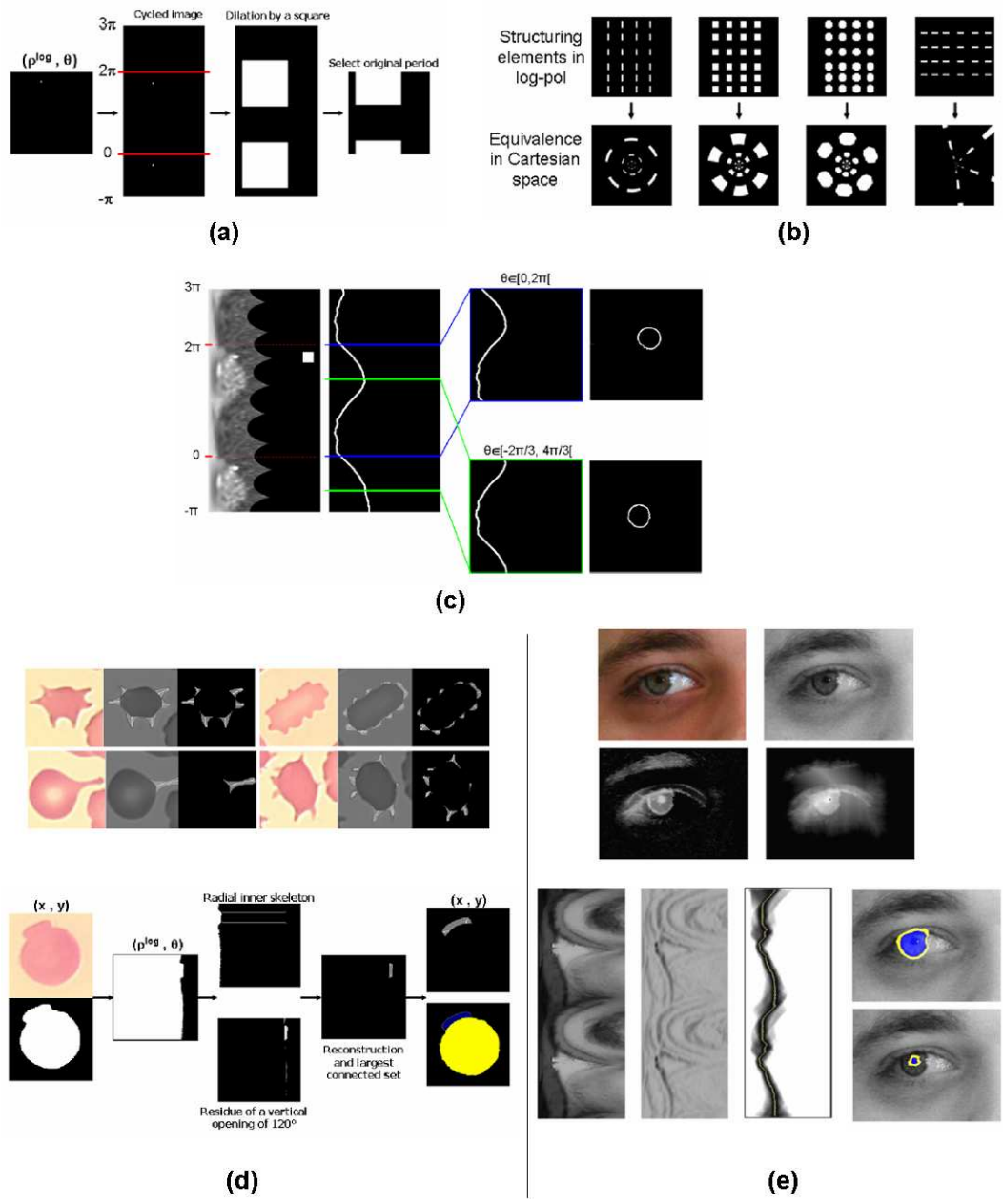

FIG. 9.3 – Morphologie mathématique cyclique en coordonnées log-pol : a) principe de la dilatation log-pol sur une image cyclique ; b) éléments structurants en log-pol ; c) segmentation par plus court chemin circulaire ; d) application à l'analyse de la forme de globules rouges ; e) application à la segmentation de l'iris.

appelé élément structurant, sur chaque pixel de l'image pour calculer le supremum (l'infimum) des valeurs tombant sous l'ensemble. Or, la morphologie mathématique discrète variable spatialement est très intéressante aussi bien d'un point de vue théorique que pour les applications : un traitement adaptatif avec un élément structurant qui adapte sa taille, forme, orientation, etc... à chaque pixel.

La théorie existe depuis des années, mais la formulation standard de la dilatation/érosion adjointes dans le cas variable implique une mise en œuvre assez complexe des opérateurs ouverture/fermeture. En effet, pour avoir une ouverture (opérateur croissant, idempotent et anti-extensif), il faut commencer par une érosion variable qui sera suivie d'une dilatation variable avec un élément structurant réciproque à celui de l'érosion. Le calcul de l'élément structurant peut être très compliqué à obtenir.

Ainsi, nous avons revu cette théorie pour formaliser les définitions de la dilatation, l'érosion l'ouverture et la fermeture variables spatialement en utilisant exclusivement l'élément structurant, sans recourir à son réciproque. Le cas binaire donne lieu à des définitions géométriques simples à mettre en œuvre ; pour le cas des niveaux de gris, nous utilisons les fonctions pulse pour construire des cylindres dont la base pour chaque pixel est lié à la forme de l'élément structurant.

Champ dense et régularisé d'orientation locale

Nous nous intéressions dans ce travail principalement à l'adaptabilité de l'orientation de l'élément structurant selon l'information directionnelle calculée à partir de l'image à traiter, soit binaire ou à niveaux de gris.

La méthode que nous avons proposée pour estimer l'orientation locale des structures commence par calculer le gradient au carré moyenné. Il y a donc par le carré une élimination de l'information de direction, en nous limitant à l'orientation ; et d'autre part, il y a aussi une première régularisation par moyenne dans une fenêtre. Cependant ce processus de régularisation est insuffisant pour avoir une information pertinente de l'orientation pour tout pixel de l'image : nous n'avons pas de gradient dans les zones homogènes de l'image et par ailleurs l'estimation locale n'est pas très robuste (augmenter la taille de la fenêtre de moyenne ne permet pas d'avoir un résultat spatialement régulier). Nous avons donc introduit une méthode de régularisation variationnelle de l'image d'orientations locale.

Elle consiste à combiner un terme de diffusion de l'information d'orientation vers les endroits où elle n'existe pas, tout en gardant la fidélité sur les pixels où l'orientation est bonne (zones où le module du gradient est élevé). La particularité de notre approche est le fait de re-formuler la solution de l'équation de minimisation dans le domaine de la fréquence. Ce qui fait que la régularisation est calculée itérativement comme un filtre par FFT.

Plus récemment, nous avons généralisé ce type d'estimation et de régularisation de la cartographie d'orientation locale à des images à d dimensions.

Filtrage morphologique anisotrope

Une fois l'orientation régularisée et étendue à toute l'image, cette information est utilisée pour adapter l'orientation de l'élément structurant sur chaque pixel de l'image. Par conséquent, nous pouvons calculer des ouvertures/fermetures localement orientées ainsi que d'autres filtres plus sophistiqués, par combinaison de ces deux-là. Nous avons aussi utilisé l'information d'orientation plus celle de la distance aux bords des structures (calculée par seuillage du gradient), pour construire des éléments structurants anisotropes type rectangle orienté (la forme dépendant de la distance aux bords).

Nous avons montré leur capacité de débruitage et de rehaussement des caractéristiques anisotropes telles que la cohérence et le flot directionnel de structures semblables, cela aussi bien pour les images binaires qu'à niveaux de gris.

Il faut noter que la régularité du champ des orientations est fondamentale pour avoir des opérateurs morphologiques satisfaisants : cela assure que dans une certaine zone structurellement similaire, les éléments structurants des différents pixels doivent être aussi similaires.

Principales publications

- R. Verdú-Monedero, J. Angulo and J. Serra. "**Spatially-Variant Anisotropic Morphological Filters Driven by Gradient Fields**". *Proc. of ISMM'09 (2009 International Symposium on Mathematical Morphology)*, LNCS 5720, Springer-Verlag Berlin Heidelberg, p. 115–125, Groningen, The Netherlands, August 2009.
- R. Verdú, J. Angulo, J. Serra. "**Anisotropic morphological filters with spatially-variant structuring elements based on image-dependent gradient fields**". *IEEE Trans. on Image Processing*, Vol. 20, No. 1, 200–212, 2011.
- J. Larrey-Ruiz, R. Verdu-Monedero, J. Morales-Sanchez, J. Angulo. "**Frequency domain regularization of d-dimensional structure tensor-based directional fields**". *Image Vision and Computing*, Vol. 29, 620–630, 2011.

9.5 Morphologie variable dans l'espace : Morphologie mathématique bilatérale

Des noyaux bilatéraux de convolution aux fonctions structurantes bilatérales

Le développement de filtrage localement adaptatif est bien établi dans la théorie et la pratique du filtrage gaussien. En particulier, le filtrage bilatéral est une convolution gaussienne localement adaptative pour débruiter/lisser les images tout en préservant les contours : pour chaque pixel, les coefficients de noyau gaussien (liés à la distance spatiale) sont pondérés par la distance d'intensité avec ses voisins. Ses résultats sont généralement très acceptables, sa formulation est assez simple et ne nécessite que deux paramètres faciles à choisir : l'un pour la taille spatiale et l'autre pour le contraste afin de préserver les caractéristiques. Par ailleurs le filtrage bilatéral est fortement lié à la théorie du filtrage robuste (pondération par moindres carrés) et au filtrage par solution de l'EDP de diffusion de Perona et Malik.

Poursuivant notre intérêt pour les opérateurs morphologiques variables dans l'espace, nous avons étudié comment généraliser ces approches de convolution gaussienne dans le but d'introduire des filtres adaptatifs non linéaires, qui correspondent asymptotiquement à des dilatations/érosions bilatérales.

En particulier, à partir du filtrage bilatéral et en utilisant le formalisme de la moyenne contre-harmonique, nous avons obtenu la notion de fonctions structurantes bilatérales : l'équivalent morphologique du produit de deux termes gaussiens, l'un pour la distance spatiale et l'autre pour la distance en intensité et une fonction structurante somme d'un terme quadratique de distance spatiale et d'un terme aussi de distance en intensité au carré. Il s'agit donc à nouveau d'une connexion logarithmique entre les noyaux de convolution et les fonctions structurantes. Par ailleurs, nous avons considéré aussi d'autres noyaux que le gaussien : ceux de Laplace et de Cauchy-Lorentz et les homologues logarithmiques. Ces fonctions structurantes bilatérales peuvent être utilisées pour construire des dilatations/érosion bilatérales non-plates ; or, nous avons aussi voulu introduire la notion de morphologie bilatérale plate avec des éléments structurants.

Eléments structurants bilatéraux par seuillage de fonctions structurantes bilatérales

Après seuillage des fonctions structurantes bilatérales, il devient possible d'obtenir des éléments structurants isotropes adaptatifs pour les utiliser avec des opérateurs variables dans l'espace, type dilatation/érosion ou ouverture/fermeture et utilisant les mêmes algorithmes que nous avions mis au point pour la morphologie anisotrope.

Nous avons formalisé une paramétrisation très simple dans la construction de ces éléments structurants bilatéraux : un paramètre du rayon du disque et un paramètre de contraste pour supprimer certaines parties du disque (dans les zones proches des contours des structures). Bien évidemment, le

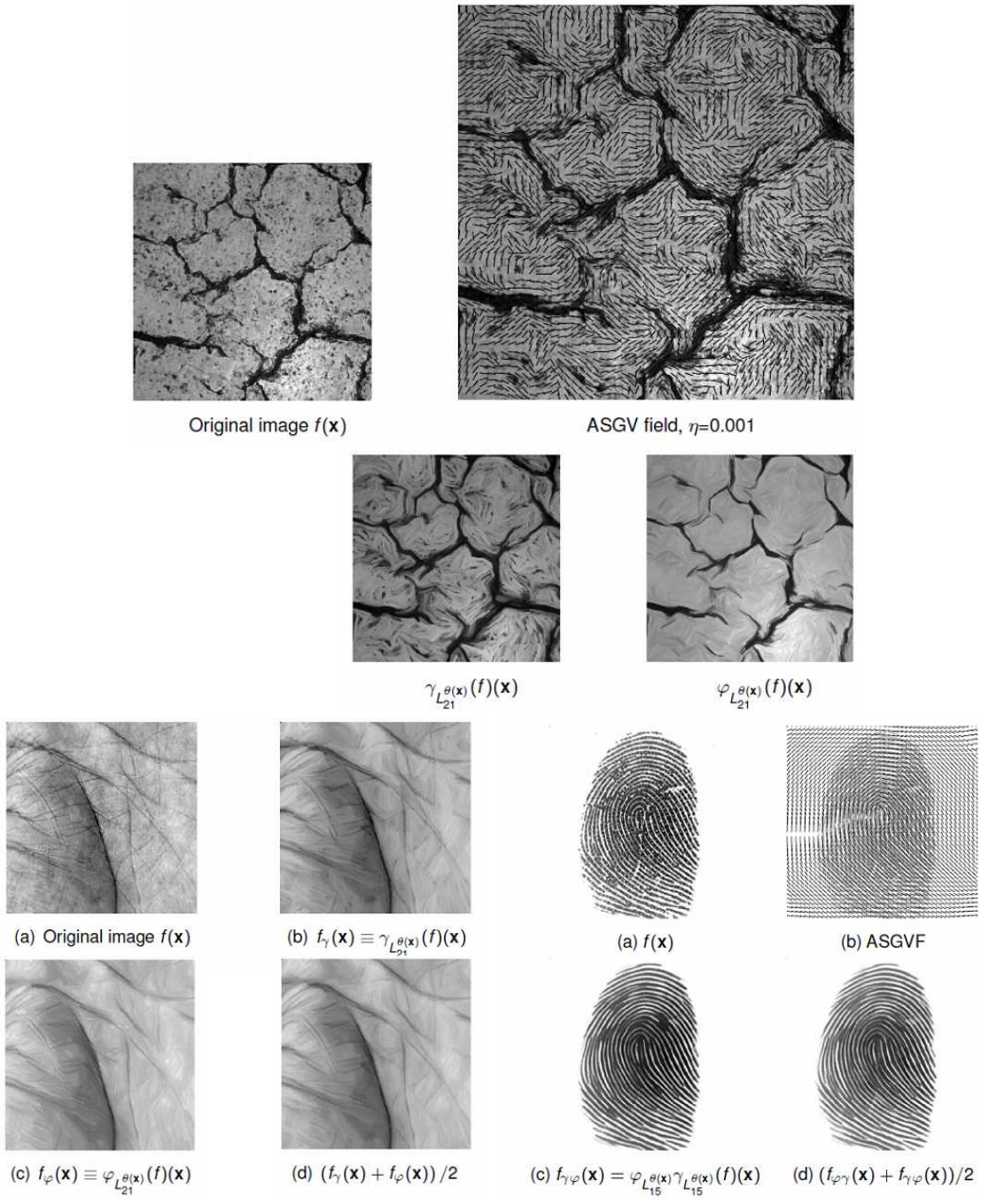

FIG. 9.4 – Morphologie mathématique anisotrope variable dans l'espace : haut, obtention du champ dense et régularisé d'orientation locale et ouverture/fermeture anisotrope associée ; bas, filtrage morphologique anisotrope des images.

calcul de ces disques tronqués dépend de la forme de la fonction structurante de départ (gaussienne, laplacienne, ou type Cauchy-Lorentz).

Il est important à remarquer que par rapport à d'autres approches d'obtention d'éléments structurants adaptatifs qui généralement utilisent des distances géodésiques entre le pixel central et ses voisins (comme les voisinages géodésiques ou les amibes morphologiques), la complexité dans le calcul des éléments structurants bilatéraux est plus faible car ils utilisent des distances euclidiennes.

Les résultats que nous avons obtenus dans nos différents tests montrent une très bonne capacité de filtrage adaptatif, en produisant par exemple des dilatations/érosions qui ne modifient pas les structures principales de l'image. Nous travaillons actuellement à l'étude de l'EDP qui est liée à ce type de filtre discret.

Principales publications

- J. Angulo. "**Morphological bilateral filtering and spatially-variant adaptive structuring functions**". In *Proc. of ISMM'11 (2011 International Symposium on Mathematical Morphology)*, LNCS 6671, Springer-Verlag Berlin Heidelberg, p. 212–223, Intra (Lake Maggiore), Italy, July 2011.
- J. Angulo. "**Morphological Bilateral Filtering**". 25p., Submitted, 2011.

9.6 Morphologie variable dans l'espace : Morphologie structurellement adaptative

Modèle structurel d'image et décomposition par pyramide de nivellements

Nous avons proposé un modèle additif d'image associé à une décomposition non-linéaire multi-échelle de l'image. Cette décomposition est fondée sur une famille de nivellements visqueux, où les marqueurs sont des filtres alternés séquentiels. Les paramètres fondamentaux du modèle sont au nombre de deux : la taille maximale dans la décomposition et l'incrément de taille entre échelles de la décomposition. L'image du nivellement à la taille maximale est considérée comme la composante de structure de l'image ; l'image différence (avec des valeurs positives/négatives donc) entre deux échelles successives de nivellement correspond à la composante de texture pour l'échelle en question. Ainsi l'image initiale peut être parfaitement reconstruite comme la somme de la composante de structure plus la somme de toutes les composantes de texture. Chaque pixel a donc une valeur dans chacune de ces composantes de structure, plus de texture multi-échelle.

Opérateurs structurellement adaptatifs et leurs propriétés

En travaillant maintenant sur cette décomposition, nous pouvons introduire les opérateurs morphologiques structurellement adaptatifs. Le principe consiste à considérer que chaque structure de l'image est traitée avec une fonction structurante dont la taille est adaptée intrinsèquement à l'échelle locale correspondant à cette structure. En pratique, l'idée pour faire une dilatation consiste donc à dilater chaque échelle par une fonction structurante de taille l'index de l'échelle et ensuite, par somme des images de toutes les échelles, obtenir l'image de la dilatation structurellement adaptive. Chaque pixel aura donc été dilaté dans les différents niveaux de la décomposition à condition qu'il soit associé à l'une des échelles correspondantes.

Nous avons montré que, dans des applications pratiques, les opérateurs proposés donnent de meilleurs résultats que ceux habituels pour l'extraction d'objets par résidu d'ouvertures/fermetures, pour le débruitage par centre morphologique, pour le rehaussement de contraste par soustraction de laplacien, etc... Ce comportement positif est justifié par le fait que, en utilisant des opérateurs géodésiques de décomposition de l'image, les différents objets sont traitées pratiquement de façon individuelle et les "interférences" entre objets adjacents sont notablement réduites. De plus, nous

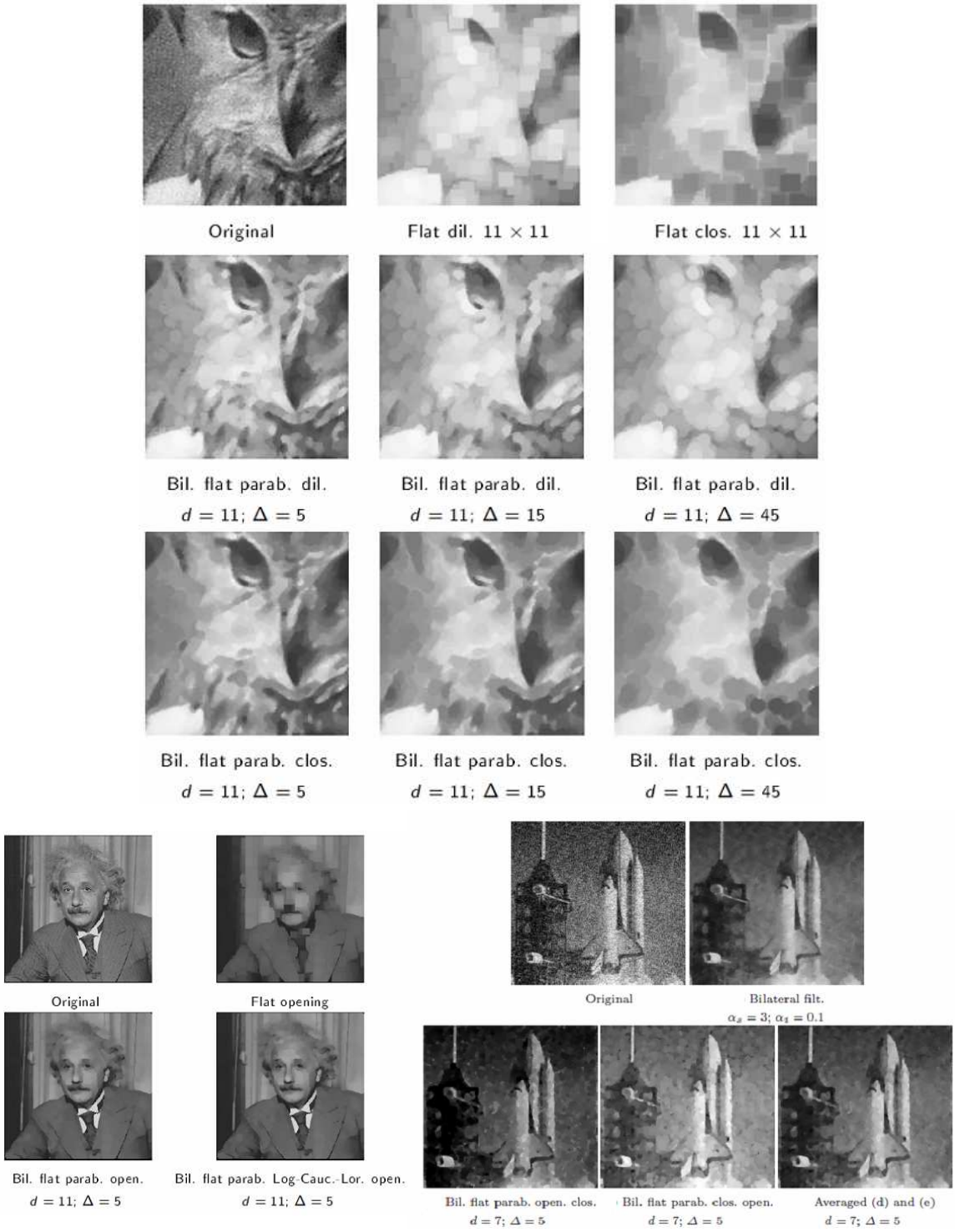

FIG. 9.5 – Morphologie mathématique bilatérale : haut, opérateurs variable dans l'espace par des éléments structurant bilatéreaux par seuillage de fonctions structurantes bilatérales ; bas, filtrage bilatérale pour la simplification d'images et le debruitage.

avons prouvé qu'un autre avantage de l'adaptabilité est le fait que le choix de la "taille" pour les érosions/dilatations et les ouvertures/fermetures est beaucoup moins critique. Cependant, nous avons également démontré que le cadre algébrique sous-jacent à ces opérateurs adaptatifs est moins riche que le cadre des opérateurs standard (un certain nombre de propriétés importantes ne sont plus vérifiés).

Principales publications

- J. Angulo and S. Velasco-Forero. "**Structurally Adaptive Mathematical Morphology on Nonlinear Scale-Space Representations**". In *IEEE ICIP'10 (2010 IEEE International Conference on Image Processing)*, p. 121-124, Hong Kong, September 2010.
- J. Angulo and S. Velasco-Forero. "**Structurally Adaptive Mathematical Morphology Based on Nonlinear Scale-Space Decompositions**". *Image Analysis and Stereology*, Vol. 30, 111–122, 2011.

9.7 Morphologie robuste : Symétrie hexagonale, micro-viscosité et flocons de neige

Les nouvelles adjonctions de Meyer pour les éléments de la grille hexagonale

Dans certaines situations, il est utile d'introduire une certaine forme de viscosité dans les opérateurs morphologiques géodésiques, tels que les ouvertures par reconstruction et les nivellements. En l'absence d'une telle "viscosité", l'opérateur géodésique reconstruit trop de détails et peut produire des "fuites". L'opérateur le plus petit de viscosité qu'on peut introduire dans les nivellements est basé sur un cas particulier de la transformée en tout-ou-rien. F. Meyer a montré que cet opérateur peut aussi être analysé comme une séquence d'adjonctions non classiques, où source et destination ne sont pas les mêmes.

En particulier, en travaillant sur la grille hexagonale, en plus des pixels de la grille, on considère également les centres d'arêtes reliant les pixels voisins ou les centres des faces formées par triplets de pixels. La combinaison des opérateurs de dilatation et érosion dans ces différentes adjonctions donne lieu, non seulement à des nivellements visqueux, mais aussi à toute une famille de filtres morphologiques particulièrement robustes pour le traitement des images bruitées.

Micro-opérations et opérateurs avec des effets visqueux

En utilisant les adjonctions entre les nœuds et les arêtes de la grille hexagonale, nous avons montré qu'il est possible de mixer des relations de voisinage pour construire des opérateurs nouveaux, intéressants par leurs propriétés de régularisation des effets des pseudo-dilatations/érosions.

L'approche consiste par exemple à combiner une micro-opération sup/inf entre paires de nœuds voisins qui donne des valeurs sur les arêtes, suivie d'une opération qui prend les valeurs des arêtes pour calculer par inf/sup la valeur à mettre sur le pixel en question. A partir de toutes les adjonctions possibles sur l'hexagone unitaire, il est possible de construire plusieurs familles de ces opérateurs micro-visqueux.

Les flocons de neige morphologiques pour le filtrage robuste

Dans la suite de l'étude précédente, nous avons introduit une autre famille d'opérateurs non-linéaires qui sont robustes au bruit, en combinant le calcul de la valeur sup/inf pour la dilatation/érosion avec une étape de débruitage intégrée à l'opérateur principal.

Plus précisément, les filtres robustes unitaires sont calculés en utilisant un nouvel ensemble d'éléments structurants (plus grands que l'hexagone unitaire) basés dans la symétrie hexagonale, et que nous avons appelés flocons de neige. Leur configuration est directement inspirée de la morphologie réelle

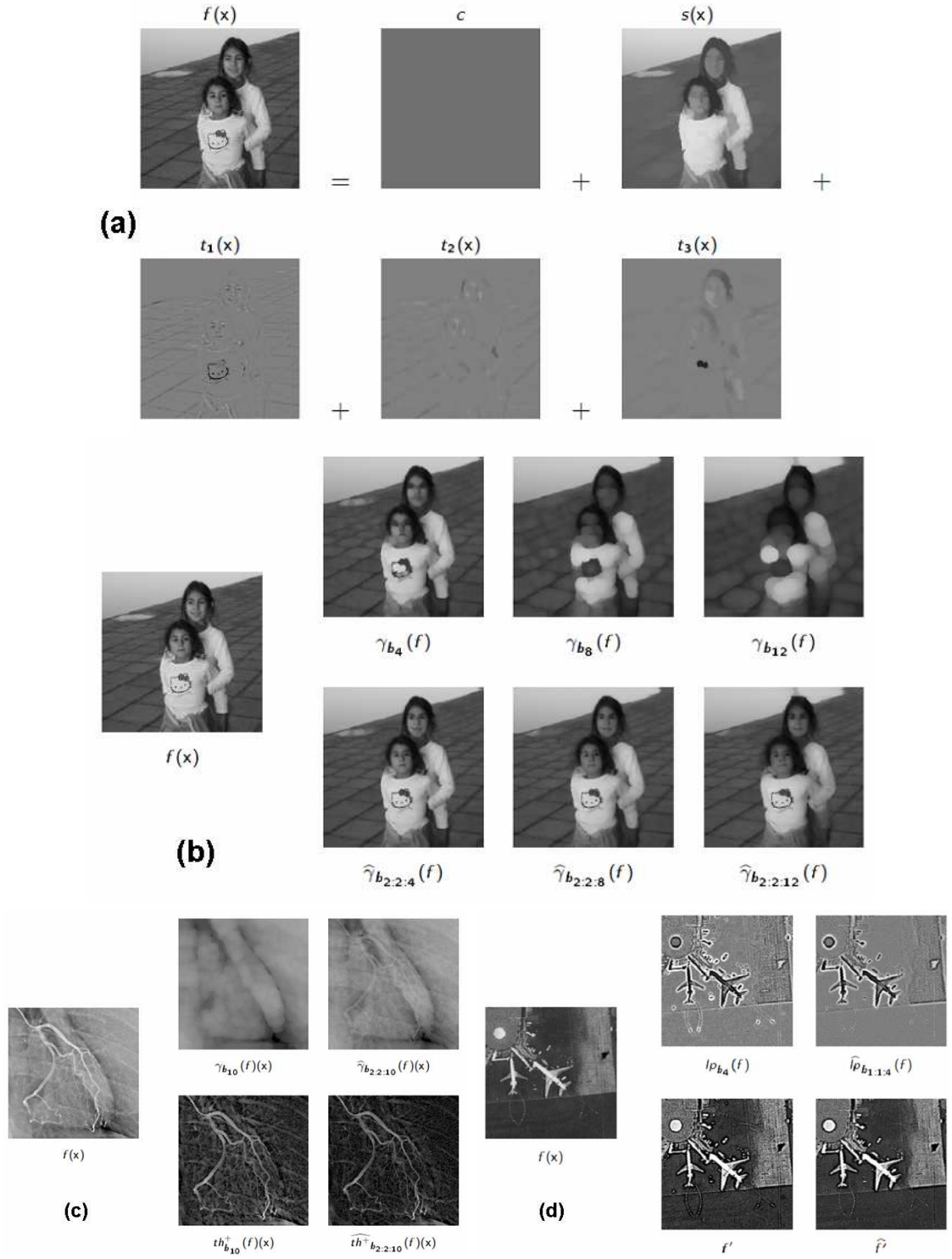

FIG. 9.6 – Morphologie structurellement adaptative : a) modèle structurel et décomposition par nivellement ; b) comparaison des ouvertures classiques vs. des ouvertures structurelles ; c) application à l'extraction de background inhomogène par résidu d'ouvertures ; d) rehaussement du contraste par soustraction du laplacien morphologique.

des flocons de neige. Dans ce cadre, il y a deux familles différentes de filtres qui peuvent être définies : les opérateurs de second ordre (typiquement on calcule une médiane dans chaque micro-voisinage avant de calculer le sup/inf des différentes valeurs de médiane) et les opérateurs localement sélectifs (on calcule la variance dans chaque micro-voisinage et on n'utilise pour le sup/inf que les valeurs des micro-voisinages à faible variance). Outre la comparaison de l'intérêt pratique des différentes familles de filtres, nous avons commencé à étudier leurs propriétés algébriques et surtout leurs propriétés statistiques de robustesse face au bruit. Cette dernière partie de notre travail fait l'objet d'une étude en cours sur l'optimalité statistique des différents flocons de neige selon le type de bruit considéré.

Principales publications

- F. Meyer, J. Angulo. "**Micro-viscous morphological operators**", In *Proc. of the 8th International Symposium on Mathematical Morphology (ISMM'2007)*, Rio de Janeiro, Brazil, October 2007. p. 165–176, MCT/INPE, 2007.
- S. Koudoro, S. Velasco-Forero, J. Angulo. "**Morphological Snowflakes for Robust Nonlinear Filtering**". In *Proc. of 13th International Congress of Stereology (ICS-13)*, Beijing, China, October 2011.

9.8 Vers une morphologie mathématique parcimonieuse

Représentations positives des images : Factorisation non-négative parcimonieuse de matrices

Comme nous l'avons déjà mentionné à plusieurs reprises dans ce mémoire, la représentation de signaux dans des sous-espaces (avec réduction de la dimensionnalité) implique l'obtention d'un ensemble de composantes qui forment la base de projection et des coefficients de projection sur cette base. On peut aussi voir cette base comme un dictionnaire composée d'atomes, plus un codage qui permet d'approximer chaque signal avec une combinaison pondérée des atomes. Lorsqu'on utilise des techniques linéaires comme l'ACP ou l'ICA, les coefficients de projection pour les combinaisons linéaires peuvent être positifs ou négatifs, et ces combinaisons linéaires impliquent généralement des annulations complexes entre les nombres positifs et négatifs. Par conséquent, ces représentations n'ont pas la signification intuitive de décomposition des signaux en morceaux ou parties. Cette propriété est particulièrement problématique dans le cas de la morphologie mathématique puisque l'opérateur binaire de base, la dilatation d'un ensemble, est définie comme l'opérateur qui commute avec l'union des parties de l'ensemble.

La factorisation non-négative de matrices (NMF) impose des contraintes de non-négativité pour les images d'apprentissage de la base mais aussi sur la représentation obtenue : la valeur des pixels de l'image qui en résulte ainsi que les coefficients pour la reconstruction sont tous non-négatifs. Cela garantit que NMF est une procédure de décomposition d'une image en morceaux. Nous avons comparé la pertinence des différentes variantes d'algorithme NMF pour représenter des familles des images binaires. Ainsi nous avons constaté que la NMF avec des contraintes de parcimonie (dans la construction du dictionnaire, chaque image est représentée par un nombre minimal d'atomes) produit les meilleures approximations des images.

Pseudo-dilatation/érosion binaire parcimonieuse

Nous avons commencé par nous intéresser aux images binaires et l'approximation des opérateurs de dilatation et érosion. Nous partons donc d'un ensemble de M images binaires que nous allons représenter par une base de K composantes non-négatives (image numériques) : chaque image binaire sera approximée par une combinaison linéaire positive des K images, suivie d'un seuillage pour binariser.

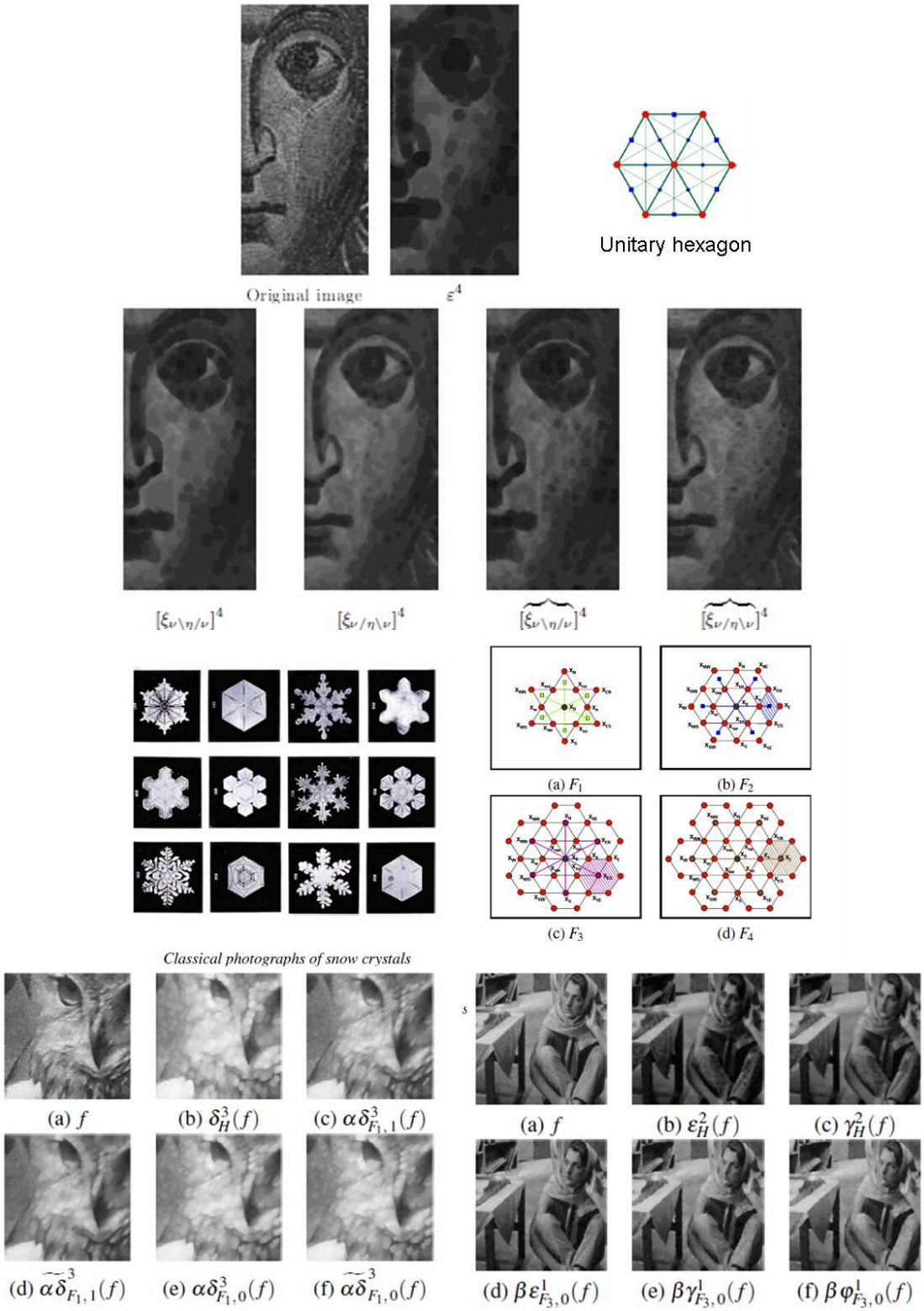

FIG. 9.7 – Morphologie robuste et symétrie hexagonale : haut, micro-opérateurs avec des effets visqueux ; bas, flocons de neige morphologiques pour le filtrage robuste (gauche, opérateurs de second ordre avec médiane ; droite, opérateurs localement sélectifs).

En utilisant, pour la dilatation, la propriété fondamentale de commutation avec l'union des parties et en la réécrivant en termes de dilation numérique plus binarisation, nous avons montré que les représentations non-négatives issues de la NMF parcimonieuse s'ajustent parfaitement à l'approximation des dilatations binaires. En fait cela consiste à dilater chaque composante de la base et à utiliser les coefficients de chaque image pour obtenir sa dilatation (suivie à nouveau d'un seuillage). Le cas des érosions binaires à été considéré par dualité : cela revient à calculer le négatif de la base, la dilater et puis calculer à nouveau le négatif.

Etant donné que ces approximations ne produisisent pas des opérateurs vérifiant les propriétés fondamentales de la dilatation/érosion, nous utilisons la terminologie "pseudo-".

Morphologie parcimonieuse pour des images scalaires

Nous avons aussi proposé une première extension de la morphologie parcimonieuse pour des images scalaires. Pour ce faire, nous nous sommes appuyés sur la représentation des images numériques par des ensembles de niveaux, c'est-à-dire par une pile d'image binaire. On peut ensuite considérer le résultat fondamental qui nous permet d'obtenir l'application d'un opérateur morphologique sur une image à niveaux de gris par application du même opérateur à chacune des images binaires des ensembles de niveaux. Ainsi, nous utilisons le même formalisme présenté ci-dessus pour approximer les ensembles de niveaux sous forme d'une représentation parcimonieuse, qui est ensuite traitée pour approximer les ensembles de niveaux traités.

Nous travaillons à présent sur d'autres alternatives pour construire des opérateurs non-linéaires parcimonieux pour des images scalaires.

Principales publications

– J. Angulo and S. Velasco-Forero. "**Sparse Mathematical Morphology using Non-Negative Matrix Factorization**". In *Proc. of ISMM'11 (2011 International Symposium on Mathematical Morphology)*, LNCS 6671, Springer-Verlag Berlin Heidelberg, p. 1–12, Intra (Lake Maggiore), Italy, July 2011.

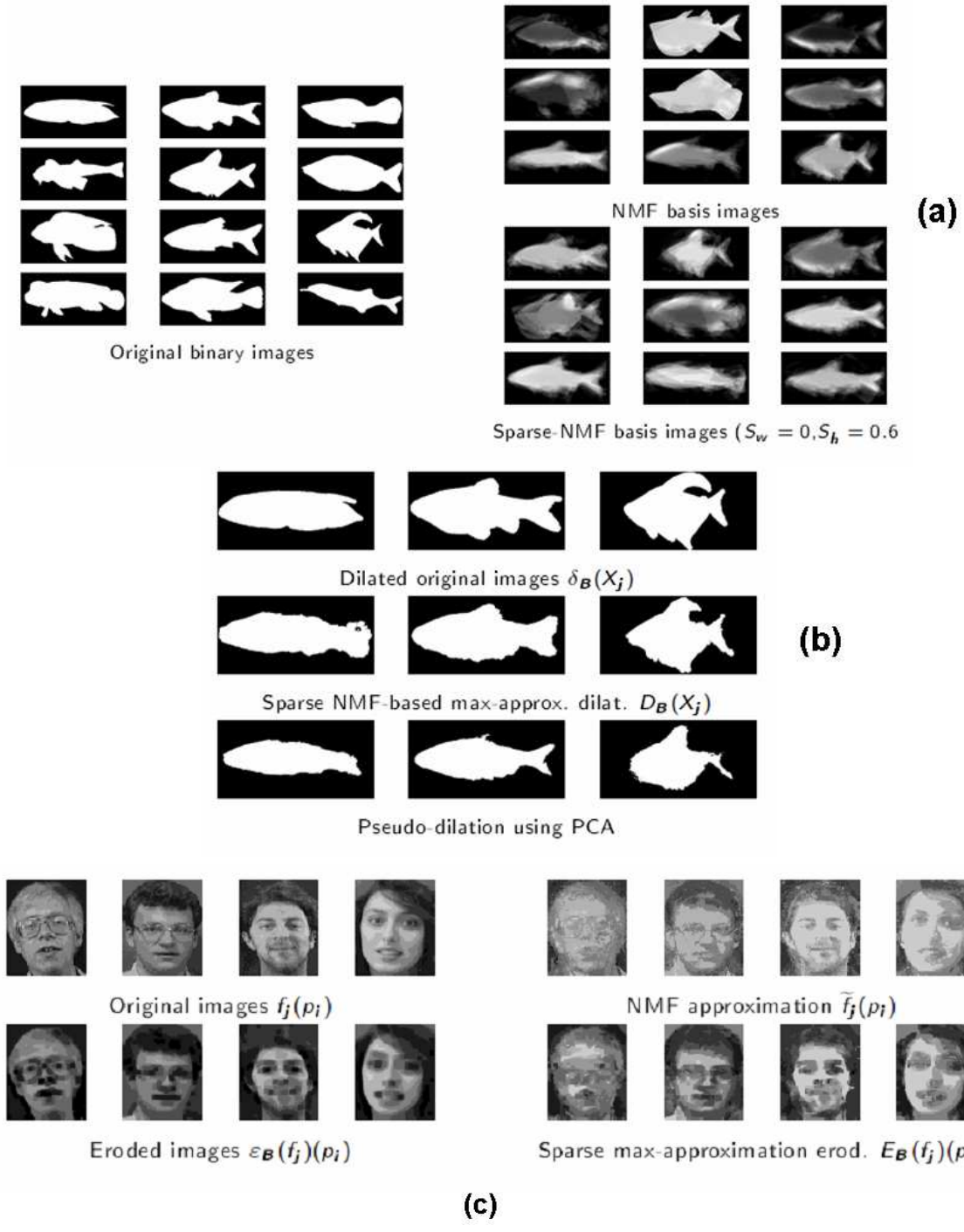

FIG. 9.8 – Morphologie mathématique parcimonieuse : a) représentations positives d'images par factorisation non-négative de matrices ; b) pseudo-dilatation/érosion binaire parcimonieuse ; c) morphologie parcimonieuse pour images à niveaux de gris.

Troisième partie

Travaux applicatifs et activités de valorisation industrielle

Chapitre 10

Applications en microscopie biomédicale

Dans le domaine de l'image numérique en microscopie biomédicale, l'information spectrale, dont la couleur, constitue une source importante d'information laquelle, combinée avec la géométrie et la morphologie des structures, permet le développement de techniques quantitatives plus performantes et robustes. En effet, depuis plus d'un siècle, les préparations biologiques sont fixées et colorées avec des protocoles standards, avant d'être étudiées sous le microscope. Ainsi, malgré d'importantes avancées en biologie moléculaire, génomique, etc., le recours à l'analyse et à la quantification microscopique occupe encore une place importante dans l'anatomopathologie, la cytologie et l'hématologie cellulaire.

Par ailleurs, l'imagerie par fluorescence est une technique sensible et largement utilisée pour la détection de composants particuliers d'entités biomoléculaires : un fluorophore (colorant fluorescent) peut être lié chimiquement aux structures cellulaires, aux acides nucléiques ou aux anticorps, entre autres molécules biologiques. Ces fluorophores sont conçus pour localiser un spécimen biologique, ou pour la quantification de la distribution de fluorescence. Une fois excité par une longueur d'onde donnée à partir d'une source externe, le fluorophore émettra de la lumière selon une longueur d'onde plus grande que celle de l'excitation. Un filtre situé devant le détecteur laisse passer la lumière émise mais bloque la lumière d'excitation, permettant ainsi de ne surveiller et ne détecter que la fluorescence émise par le fluorophore particulier. De cette manière, il est possible de produire une image pour chaque fluorophore incorporé à l'échantillon biologique ; et par conséquent, produire une image multi-variée (en général, pour des questions de sélectivité des filtres, le nombre de marqueurs est de l'ordre de quatre). L'imagerie en fluorescence est le principe de quelques technologies modernes d'analyse biologique haut débit/haut contenu telles que les puces à ADN et les puces à cellules (phénotypage cellulaire).

Dans ce contexte, je présente dans ce chapitre un rappel très bref des applications que j'ai développées en traitement des images couleur/multi-spectrales et des images de fluorescence issues du domaine de la microscopie biomédicale (puces à ADN, modélisation de l'organisation cellulaire, cytologie hématologie et phénotypage cellulaire).

10.1 Analyse des images de puces à ADN

Les puces à ADN ou biopuces sont à la base d'une technologie expérimentale répandue pour explorer le génome. Même si en général nous n'avons que deux couleurs, l'analyse d'image est un aspect important dans l'interprétation du résultat d'une expérience de biopuces.

J'ai beaucoup travaillé dans la mise au point d'algorithmes performants pour la lecture de puces à ADN de différentes technologies. En particulier, j'ai considéré les aspects suivants :

- **Segmentation et quantification des puces à ADN marquées à la fluorescence.** Avec J. Serra, nous avons développé une chaîne logicielle complète de lecture des images de puces à ADN classiques. Il s'agissait d'une approche totalement automatique qui utilisait des outils avancées de la morphologie. La publication de la méthode avait eu un succès important à l'époque car les logiciels disponibles étaient assez "rudimentaires". Ce travail a eu des retombés par la suite car notre participation à plusieurs projets a été possible grâce à l'expertise et la reconnaissance acquises par ce travail. Par ailleurs, une partie de nos algorithmes ont même été intégrés dans les logiciels d'une société du domaine des biopuces.
- **Détection and quantification des puces à ADN marquées à la radioactivité.** Même si la technologie des puces à ADN marquées à la radioactivité a été complètement abandonnée par la suite, j'ai aussi développé un algorithme morphologique pour l'analyse de ces images. D'ailleurs, du point de vue morphologique, la problématique de ce type d'image était plus intéressante que celle des puces à la fluorescence.
- **Modélisation des spots et segmentation adaptée en coordonnées polaires.** En valorisant mes travaux sur la morphologie en coordonnées (log-)pol, j'ai proposé des algorithmes plus avancés de quantification des spots qui constituent les images des puces à ADN. En particulier, il s'agissait d'avoir des segmentations adaptées à la qualité et à la morphologie de chaque spot et surtout en utilisant des segmentations par plus courts chemins qui pouvaient être plus précises que celles obtenues par la LPE.
- **Filtrage et rehaussement des images de biopuces intégrées.** Nous avons participé dans un projet de biopuces intégrées, où la lame avec l'ADN marqué à la fluorescence était directement posée sur un capteur CCD sans aucune optique. Les images produites présentaient un certain nombre de problèmes : dynamique très variable des signaux, manque d'uniformité, structures floues, etc... Nous avons développé des techniques d'acquisition multiple et de filtrage morphologique pour améliorer les images et permettre leur quantification.

Principales publications

- J. Angulo and J. Serra. "**Automatic analysis of DNA microarray images using mathematical morphology**". *Bioinformatics*, Vol. 19, No. 5, pp. 553–562, 2003.
- J. Angulo. "**Mathematical morphology operators for reading radioactivity DNA array images**". In *Proc. of the IASTED International Conference on Visualization, Imaging, and Image Processing (VIIP'2004)*, p. 802–807, Marbella, Spain, September 2004.
- J. Angulo. "**Polar modelling and segmentation of genomic microarray spots using mathematical morphology**". *Image Analysis and Stereology*, Vol. 27, 107–124, 2008.
- J. Angulo, C. Lajaunie, M. Bilodeau, L. Martinelli, F. Le Boulaire and F. Meyer. "**Preprocessing and analysis of microarray images from integrated lensless bio-photonic sensors**". In *Proc. of SPIE Photonics Europe 2008 : Optical and Digital Image Processing*, SPIE Vol. 7000, 12 p., Strasbourg, France, April 2008.

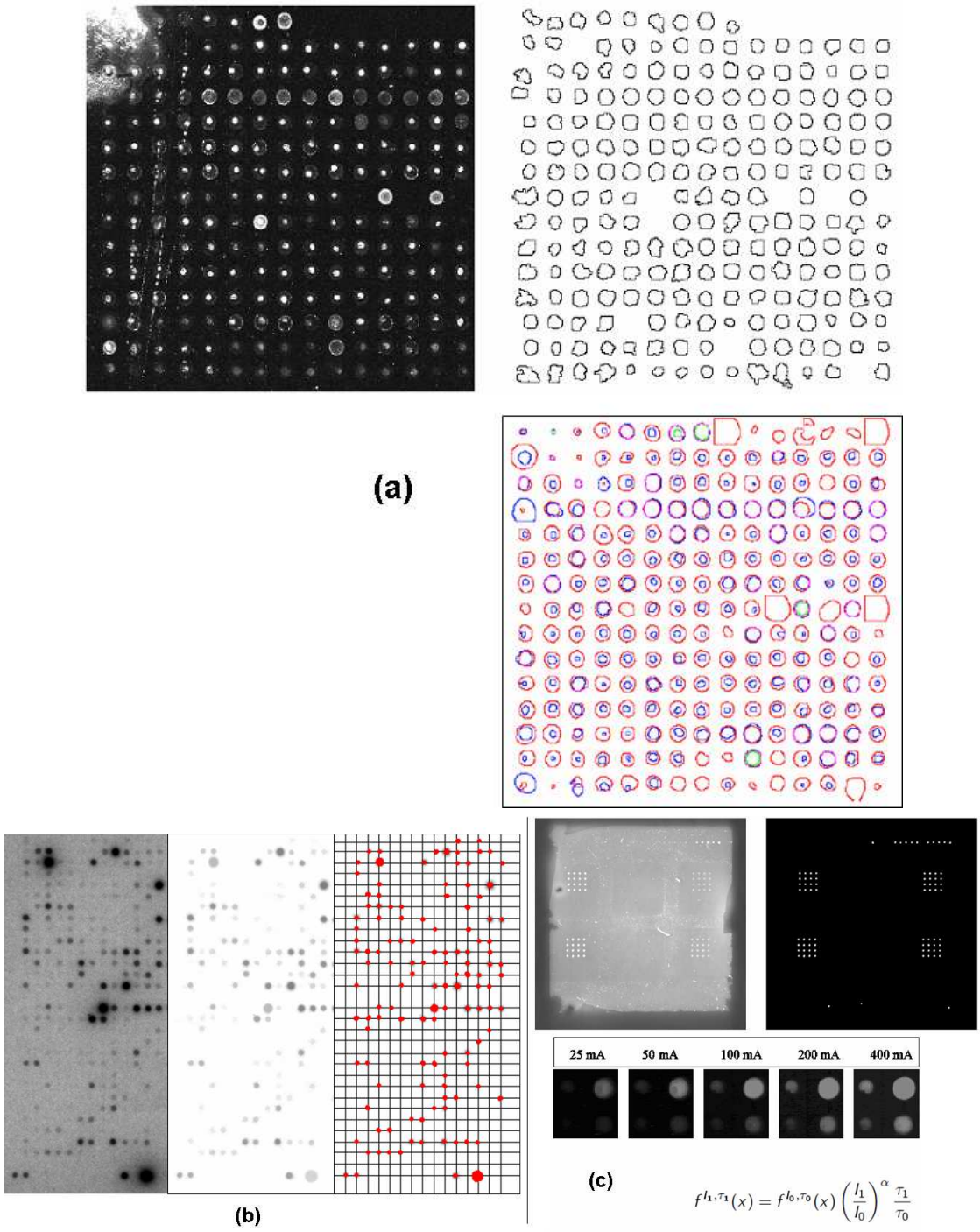

FIG. 10.1 – Analyse des images de puces à ADN : a) modélisation des spots et segmentation adaptée en coordonnées polaires des puces à ADN marquées à la fluorescence ; b) détection and quantification des puces à ADN marquées à la radioactivité ; c) filtrage et rehaussement des images de biopuces intégrées.

10.2 Quantification morphologique de l'angiogenèse au niveau cellulaire : modèle des cellules endothéliales cultivées *in vitro*

J'ai travaillé à la quantification morphologique de l'angiogenèse au niveau cellulaire, un sujet très important pour la recherche en pharmacologie de molécules actives pro-angiogéniques (réparation des tissus) ou anti-angiogéniques (bloquer la croissance de tumeurs cancéreux. En particulier, j'ai proposé en collaboration avec S. Matou, à l'époque chercheuse associée à la Fac. de Pharmacie de Paris et à l'IFREMER, des méthodes avancées pour décrire les images issues d'un modèle d'organisation des cellules endothéliales, très répandu pour l'étude de l'angiogenèse *in vitro*. J'ai considéré deux aspects particuliers de la problématique.

- **Segmentation et reconstruction du réseau tubulaire.**
- **Mesure des caractéristiques morphologiques et topologiques des structures tubulaires et arborescentes.**

Principales publications

- J. Angulo, S. Matou. "**Automatic quantification of *in vitro* endothelial cell networks using mathematical morphology**". In *Proc. of the IASTED International Conference on Visualization, Imaging, and Image Processing (VIIP'2005)*, p. 51–56, Benidorm, Spain, September 2005.
- J. Angulo and S. Matou. "**Application of mathematical morphology to the quantification of *in vitro* endothelial cell organization into tubular-like structures**". *Cellular and Molecular Biology*, Vol. 53, No. 2, 22–35, April 2007.

10.3 Cytologie hématologique : analyse de populations de lymphocytes basée sur des ontologies cellulaires

J'avais commencé à travailler au cours de ma thèse dans le domaine de l'hématologie cellulaire, plus précisément dans l'analyse de populations de lymphocytes. En étroite collaboration avec le Prof. G. Flandrin et la société TRIBVN, j'ai développé une chaîne logicielle complète avec une série d'étapes :

- **Détection de la zone de bonne lecture sur des frottis sanguins.** Cela consiste à déterminer sur les images la densité des cellules et le dégré d'étalement
- **Classification des leucocytes et segmentation des lymphocytes.** L'usage combiné de l'information de la couleur et de la texture était très utile pour cette tâche.
- **Description morphologique de lymphocytes, projections sur une ontologie ad-hoc et analyse de population sous forme d'histogrammes des caractéristiques.** La partie la plus originale de l'approche consiste à décrire les caractéristiques morphologiques de chaque lymphocyte sous forme d'une ontologie cellulaire *ad-hoc*, résultat d'un processus de consensus entre des experts dans le domaine. Ensuite, une population de lymphocytes est représentée comme la projection de chaque cellule dans l'ontologie ce qui donne lieu à une représentation très compacte sous forme d'histogrammes des caractéristiques de l'ontologie.

Ces travaux se sont poursuivis en 2005, dans le cadre du stage de fin d'étude de M.A. Luengo-Oroz, en travaillant sur le même type d'images et d'approche, en se focalisant cette fois-ci sur les érythrocytes (globules rouges), avec deux tâches principales :

- **Classification des anomalies des globules rouges.**
- **Détection et classification des inclusions dans les globules rouges.**

Motivés par nos recherches en traitement des images multi-spectrales, nous avons poursuivi ces travaux en hématologie cellulaire en travaillant, dans une partie de la thèse de S. Velasco-Forero sur

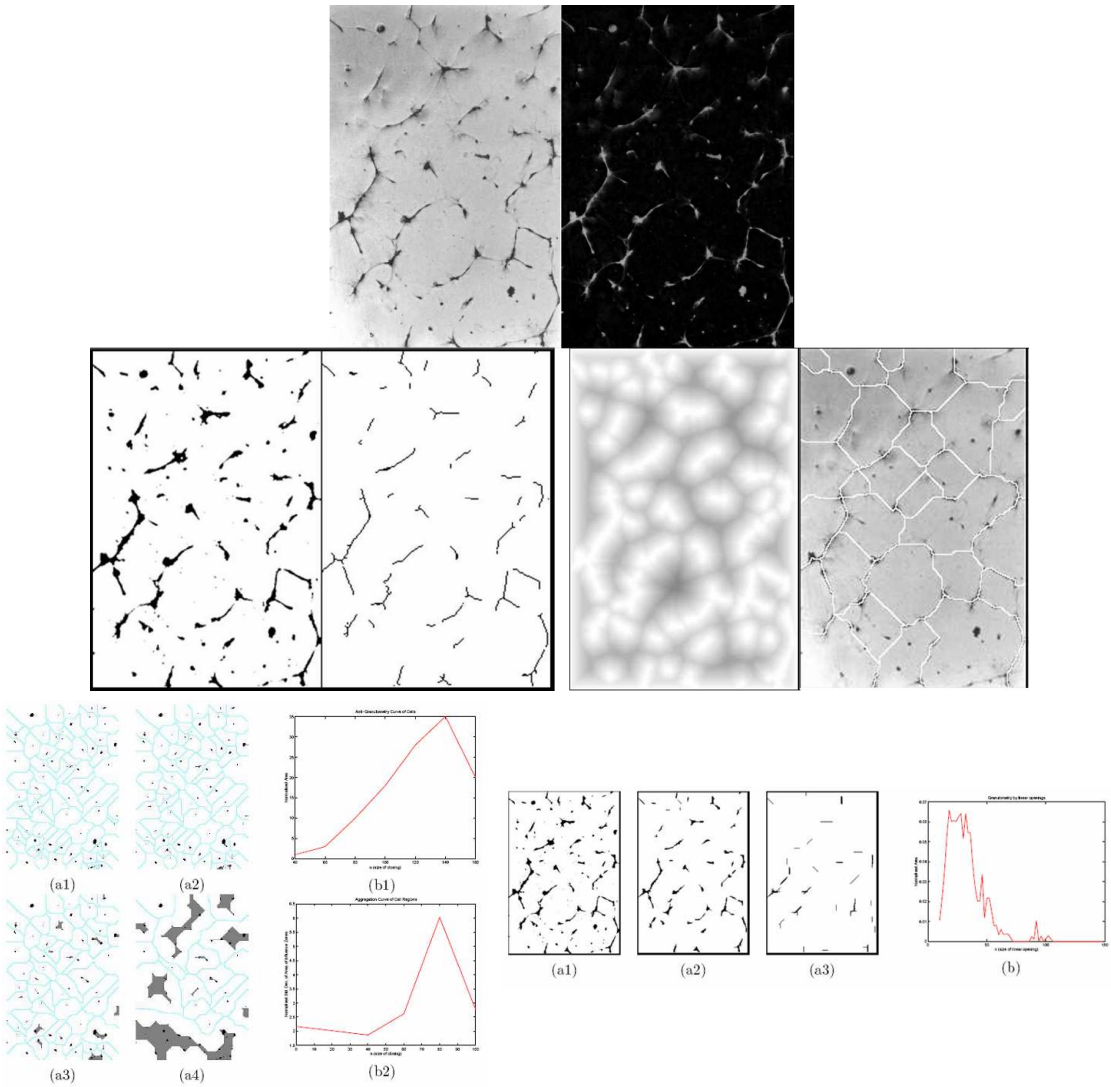

FIG. 10.2 – Quantification et modélisation morphologique de cellules endothéliales cultivées *in vitro* : haut, segmentation, et reconstruction du réseau tubulaire ; bas, quantification de l'agrégation cellulaire et de la distribution des longueurs.

des lymphocytes acquis avec une dizaine de bandes spectrales dans le visible et avec plusieurs images de focalisation par bande. Nous avons considéré les aspects suivants :

- **Prétraitement des images.** Définition d'une stratégie d'acquisition en multi-z et combinaison des images pour obtenir une image de profondeur de champ étendue ; obtention d'une image RVB optimisée à partir de la dizaine des bandes spectrales disponibles.
- **Développement des algorithmes d'imagerie multispectrale pour la segmentation des entités cellulaires et l'extraction des caractéristiques morphologiques.** Segmentation du noyau/cytoplasme de chaque lymphocyte ; décomposition morphologique de chaque bande spectrale ; calcul de la matrice de corrélation des images morpho-spectrales de chaque cellule
- **Classification supervisée des cellules normales/pathologiques grâces aux caractéristiques spectrales et morphologiques.** Nous avons exploré deux approches différentes de classification supervisée des lymphocytes normaux vs. cellules lymphoïdes LLC : texture spectrale par histogramme de classes discrètes et texture spectrale par matrice de corrélation.

Principales publications

- J. Angulo and G. Flandrin. "**Automated detection of working area of peripheral blood smears using mathematical morphology**". *Analytical Cellular Pathology*, Vol. 25, No. 1, pp. 37–49, 2003.
- J. Angulo and G. Flandrin. "**Microscopic image analysis using mathematical morphology : Application to haematological cytology**". In *Edited by A. Mendez-Vilas*, "*Science, Technology and Education of Microscopy : An overview*" (ISBN 84-607-6679-7), Vol. 1, pp. 304–312, FORMATEX Eds., Badajoz, Spain, 2003.
- J. Angulo, J. Klossa and G. Flandrin. "**Ontology-based lymphocyte population description using mathematical morphology on colour blood images**". *Cellular and Molecular Biology*, Vol. 52, No. 6, 2–15, May 2006.

10.4 Traitement morphologique d'image pour le phénotypage cellulaire haut-contenu

Observer le phénotype d'une population cellulaire après lui avoir appliqué une perturbation est en effet devenu un outil majeur d'investigation en biologie. Par exemple, bloquer un gène par un SiRNA peut mettre en évidence l'effet de ce gène sur le fonctionnement normal de la cellule. Observer l'effet d'une molécule toxique peut révéler de nouveaux modes d'action et mettre sur la piste de nouveaux médicaments. Les modifications de phénotypes pouvant être très subtiles, il faut des techniques de marquage et de microscopie en fluorescence très évoluées pour les observer et des méthodes de traitement d'images et d'analyse des données très raffinées pour les quantifier.

Depuis quelques années, je travaille dans le domaine du phénotypage cellulaire dans le cadre de plusieurs projets de recherche, en collaboration avec plusieurs partenaires académiques et industriels, avec des applications en cancérologie, pharmacologie et toxicologie. J'ai par exemple développé des méthodes avancées très performantes pour extraire et segmenter noyaux, cellules et organites cellulaires en s'appuyant sur l'information disponible dans les images de fluorescence associées aux différents marqueurs. D'autres aspects nécessaires à l'analyse de ce type d'images, sur lesquels j'ai participé au développement d'algorithmes performants sont

- **Projection des piles d'images en z et profondeur étendue du champ.**
- **Normalisation des images de fluorescence.**
- **Modélisation et individualisation des amas cellulaires, segmentation automatique des cellules.**
- **Description fine et classification des structures cellulaires : réseau microtubulaire, chromatine et ADN.**

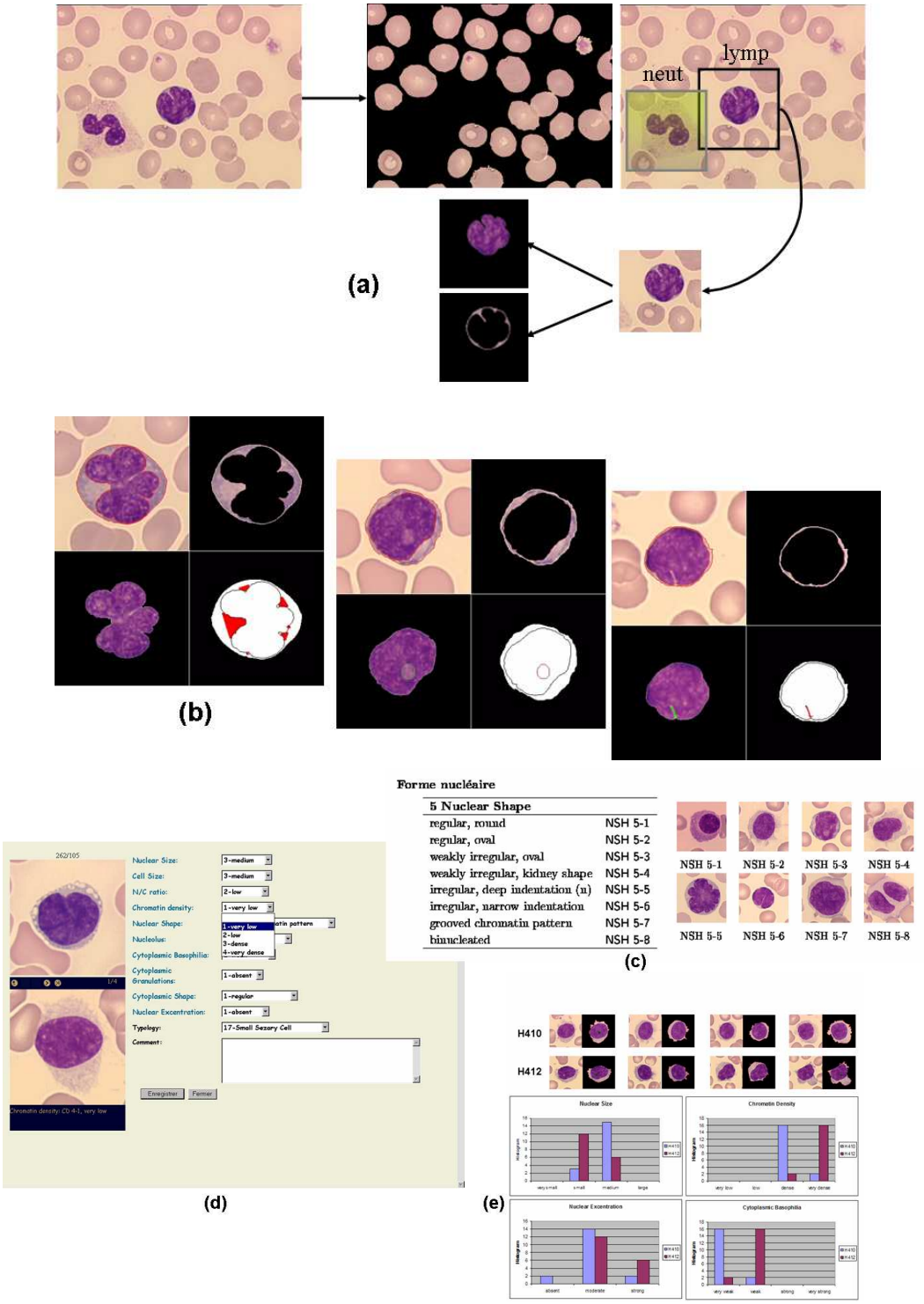

FIG. 10.3 – Analyse de populations de lymphocytes basée sur des ontologies cellulaires : a) classification des leucocytes et segmentation des lymphocytes ; b) description morphologiques de lymphocytes ; c) ontologie morphologique ; d) outil d'annotation pour construire les bases d'apprentissage ; e) projections sur l'ontologie et analyse de populations sous forme d'histogrammes des caractéristiques.

Principales publications

- F. Lemaire, C. Mandon, J. Reboud, A. Papine, J. Angulo, H. Pointu, C. Diaz-Latoud, C. Lajaunie, F. Chatelain, A.-P. Arrigo and B. Schaack. "**Toxicity Assays in Nanodrops Combining Bioassay and Morphometric Endpoints**" *PLOS One*, 2(1) : e163, 2007.
- J. Angulo and B. Schaack. "**Morphological-based adaptive segmentation and quantification of cell assays in high content screening**". In *Proc. of the 5th IEEE International Symposium on Biomedical Imaging (ISBI'2008)*, p. 360–363, Paris, France, May 2008.
- J. Angulo. " **Nucleus modelling and segmentation in cell clusters**," In *Proc. of the 15th ECMI (European Conference on Mathematics for Industry) 2008*, p. XX, London, UK, July 2008.

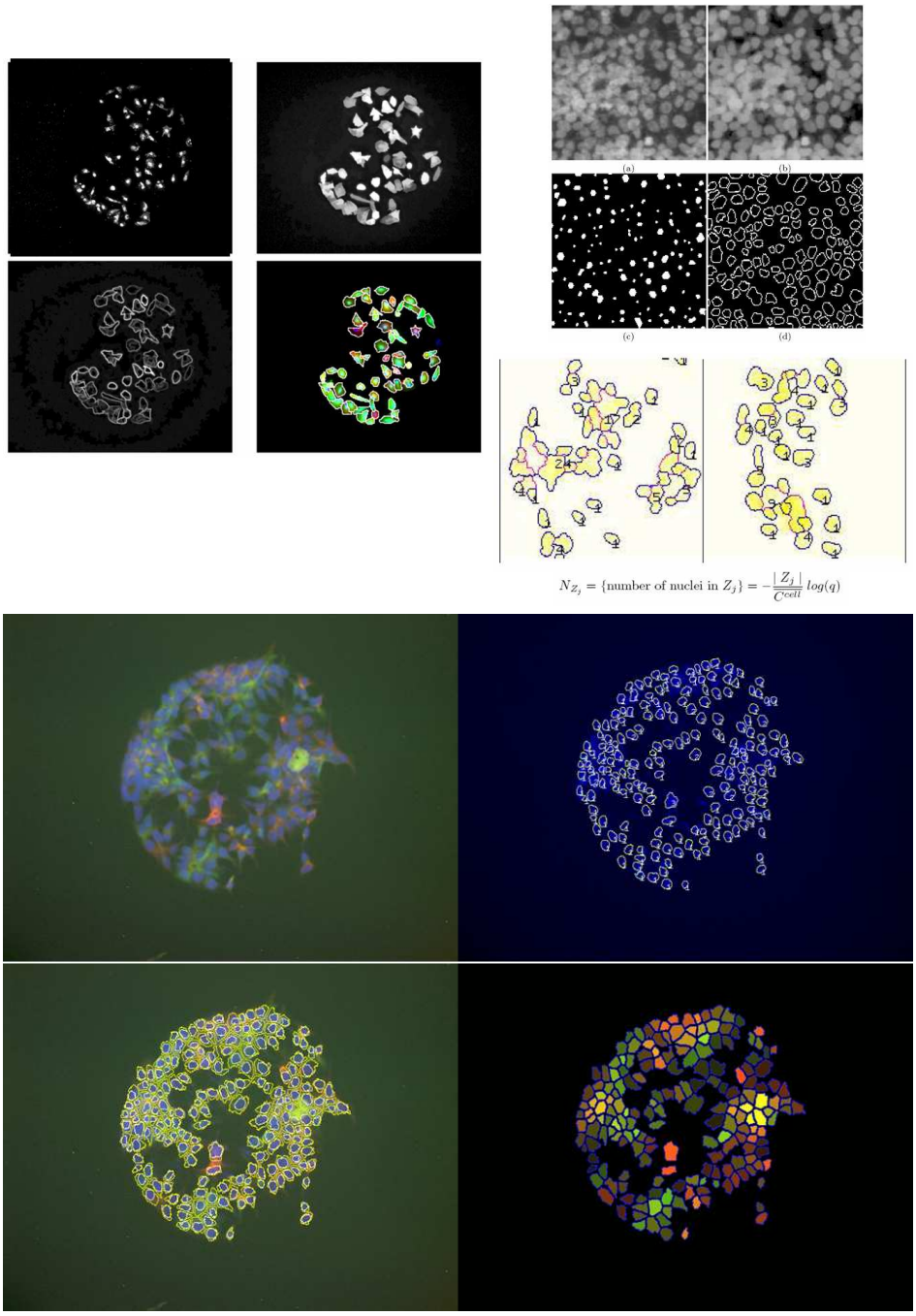

FIG. 10.4 – Modélisation et individualisation des amas cellulaires et segmentation automatique des cellules.

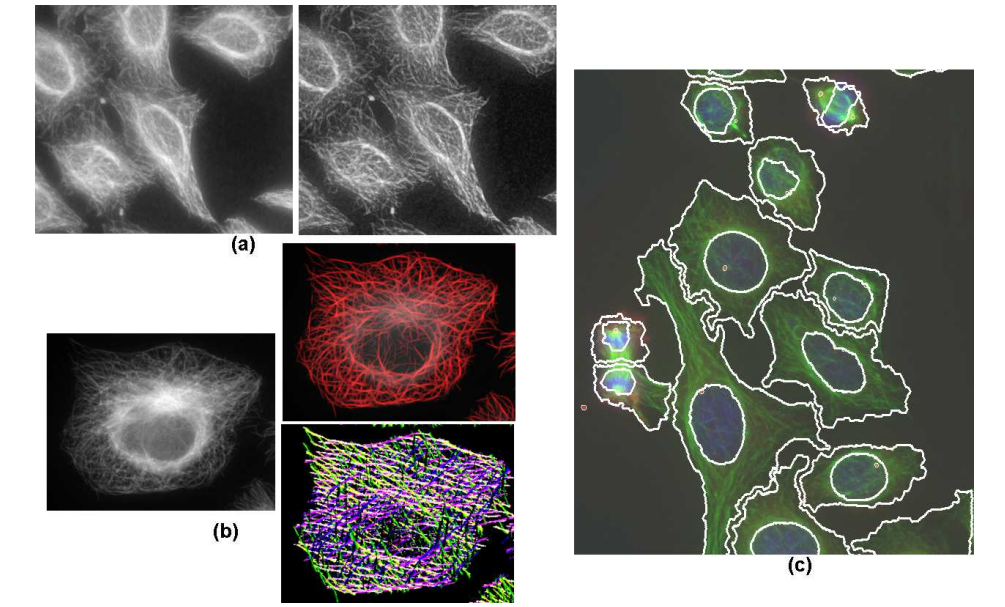

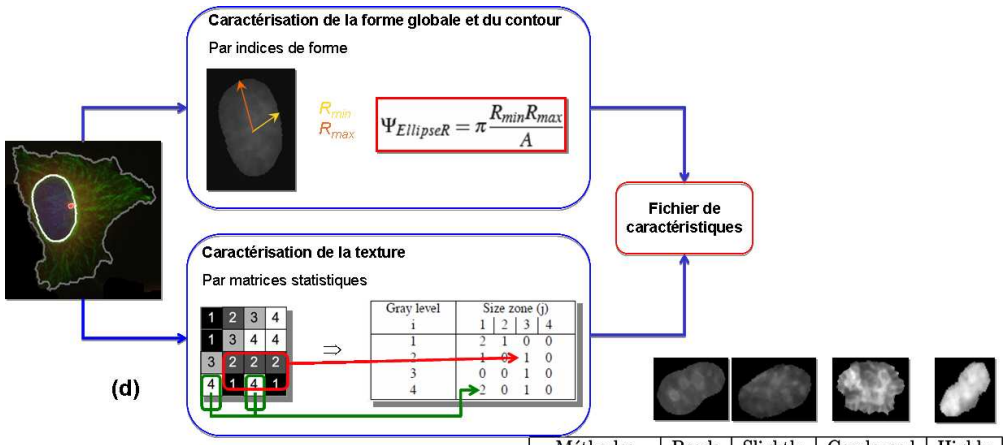

Méthodes	Beads	Slightly	Condensed	Highly
$\mathcal{GD}_f^8(d_n, g_m)$	85,7	85,8	86,1	89,1
$\mathcal{GD}_f^{16}(d_n, g_m)$	88,1	87,6	90,75	95,3
$\mathcal{GD}_f^{32}(d_n, g_m)$	86,1	89	92	93
$\widetilde{\mathcal{GD}}_f(d_n, g_m)$	89,75	89	91,9	95,05
$\widetilde{\mathcal{GS}}_f(s_n, g_m)$	91,3	88,1	89,75	92,2

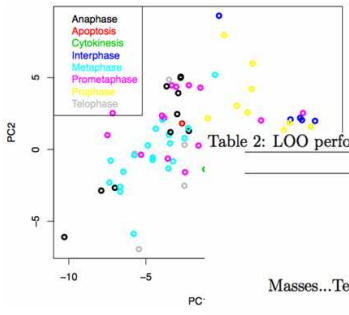

(e)

Table 2: LOO performance of automatic annotation by a nonlinear SVM.

	N classes	LOO accuracy
Phase	8	76.07
Masses...Number	3	83.76
Masses...Size	4	71.79
Masses...Intensity	6	87.18
Masses...Texture	7	59.83
Masses...Texture.homogeneity	2	84.62
Masses...Shape	8	56.41
Masses...Contour	4	80.34
Nucleoli.Number	6	65.81
Micronuclei	2	91.45
Lagging.chromosomes...Number	5	81.20

FIG. 10.5 – Analyse morphologique pour le phénotypage cellulaire haute-résolution de la mitose : a) projection des piles d'images en z et profondeur étendue du champ ; b) analyse du réseau microtubulaire ; c) segmentation de structures cellulaires ; d) description fine et classification des structures cellulaires ; e) classification d'une population cellulaire et construction de phénotypes.

Chapitre 11

Activité contractuelle et de valorisation

J'ai travaillé 12 ans au Centre de Morphologie Mathématique (CMM), en commençant avec ma thèse de doctorat et ensuite avec différents postes. Le CMM est l'un des centres de recherche commun à MINES ParisTech et à ARMINES ; ARMINES étant l'association qui gère l'activité contractuelle des centres communs. En plus de faire une recherche académique de haut niveau, la vocation des laboratoires de MINES ParisTech est le développement en parallèle d'une recherche appliquée avec un transfert vers l'industrie via des projets collaboratifs ou bien des contrats directs.

Par rapport aux chercheurs d'autres écoles d'ingénieurs ou d'autres institutions académiques (universités, CNRS, etc...) qui ont une charge d'enseignement importante, les chercheurs de MINES ParisTech consacrent une partie considérable de leur temps aux activités liées aux projets ARMINES.

Je voudrais préciser que, en gardant un équilibre raisonnable entre la partie plus académique et la partie plus de valorisation, ceci ne doit pas se considérer comme une pénalisation pour la qualité scientifique de nos travaux. Le contact soutenu avec nos partenaires industriels nous permet d'identifier de nouveaux problèmes pratiques qui, une fois résolus de manière innovante, conduisent dans beaucoup de situations à une généralisation des méthodes utilisées et en conséquence font avancer notre savoir-faire. Les grandes avancées méthodologiques de la morphologie mathématique ont été motivées par des challenges issus de collaborations multidisciplinaires avec des partenaires industriels.

Dans ce contexte, depuis ma thèse de doctorat, j'ai participé activement aux travaux contractuels du CMM. Evidemment mon rôle a évolué avec le temps et les compétences acquises. Aujourd'hui j'assure le montage, suivi, et coordination de contrats de recherche ; mais je continue aussi à réaliser des travaux techniques de programmation dans ces projets.

Comme j'ai déjà montré dans le chapitre précédent, jusqu'à présent j'ai presque exclusivement travaillé sur des projets dans le domaine de la microscopie biomédicale. Avec cette spécialisation, j'au pu développer des partenariats solides dans le temps. J'ai toutefois commencé à élargir les domaines applicatifs dans lesquels je mène mes travaux, en particulier en vision industrielle et télédétection.

Je présente dans ce chapitre mon rôle dans chacun des projets, certains d'eux encore en cours.

11.1 Projet ArcelorMittal/IDSIA/CMM- Financement ArcelorMittal (Sept 10/Sept 13)

New Framework for 2D-Mapping Sensors Data Processing - Contribution of hyperspectral imaging

Sans entrer dans les détails couverts par la confidentialité, l'objectif de ce projet est le développement de techniques morphologiques pour la détection de défauts dans des données spatiales multi-variées de différentes natures (images à niveaux de gris acquises sous plusieurs conditions d'illumination, cartographies obtenues par des capteurs magnétiques, images hyperspectrales, etc...).

Dans ce projet en cours, je suis co-responsable avec Dominique Jeulin des travaux réalisés au CMM et du co-encadrement d'un doctorant avec l'IDSIA (Université de Lugano). Dans une première phase j'ai aussi pris en charge la réalisation des travaux techniques.

11.2 Projet IMHO - Financement ANR-TecSan'07 (Dec 07/Mai 11)

Imagerie Hybride en Microscopie Oncologique

L'objectif de ce projet était l'étude de l'apport conjoint de la spectroscopie en lumière visible et de la spectroscopie Raman pour un meilleur diagnostic des leucémies. CMM/ARMINES a été le responsable de la tâche 2 du projet IHMO et prenait en charge l'exploration, la mise au point et les développements algorithmiques visant à l'usage de l'imagerie multispectrale combinée avec la morphologie mathématique pour le diagnostic des LLC. En particulier nous avons exploré deux approches différentes de classification supervisée des lymphocytes normaux vs. cellules lymphoïdes LLC : une première approche basée sur la notion de texture spectrale par histogrammes de classes discrètes et une deuxième approche fondée sur une représentation de la texture spectrale par des matrices de corrélation selon une décomposition échelle morphologique/bande spectrale.

J'avais participé activement à la conception et au montage de ce projet car il s'agissait de la suite naturelle des projets MATCHCELL et MATCHCELL2. J'étais le responsable au CMM du projet qui a permis de financer en partie la thèse de Santiago Velasco-Forero. Les travaux techniques du projet ont été réalisés par Santiago Velasco-Forero et par moi-même.

11.3 Projet RAMIS - Pôle de compétitivité Cancer-Bio-Santé, Toulouse (Jan 08/Dec 10)

Innovative image-based high content screening strategy for the discovery of new molecules and/or targets and the proposal of new anti-cancer therapies

L'objectif du projet RAMIS était le développement d'une stratégie innovante de criblage basée sur l'imagerie multi-paramétrique haute résolution pour la caractérisation phénotypique de nouvelles molécules et de nouvelles cibles interférant avec la division cellulaire de cellules cancéreuses humaines, en particulier avec la mitose. Le rôle de CMM/ARMINES était donc de réaliser une plate-forme complète de traitement, de caractérisation et d'analyse d'une population de cellules acquise par microscope à fluorescence. Pour chacune de ces étapes, l'élaboration de nouveaux algorithmes robustes, performants et innovants a été nécessaire. La phase de prétraitement des images RAMIS consiste à

prendre en entrée les données brutes d'une expérience, c'est-à-dire les séries des quatre z-stacks (ADN, Microtubules, Gamma-tubuline, Centromères) et produire en sortie, la collection des cellules individualisées, avec leurs structures cellulaires segmentées. Pour arriver à ce but, nous avons mis au point des algorithmes pour : la projection des z-stacks, la normalisation des images projetées, l'extraction du réseau de microtubules, la segmentation des structures cellulaires (noyaux, cytoplasmes, centrosomes). Ensuite, l'extraction des caractéristiques consiste à décrire numériquement les cellules afin de pouvoir prédire statistiquement la phase de la mitose dans laquelle chaque cellule se trouve. Les descripteurs principaux que nous avons développés sont basés sur des paramètres de forme et des distributions bi-variées pour caractériser la texture de l'ADN ou du réseau microtubulaire. La mise au point et la validation des différents développements ont été faites sur un volume de données d'environ 3000 séries d'images qui ont été analysées (projetées, normalisées, améliorées, segmentées, analysées, caractérisées et classées) et qui ont montré de manière quantitative la pertinence des algorithmes élaborés.

J'étais avec F. Meyer co-responsable technique au CMM du projet. En plus de réaliser une partie des travaux techniques, j'ai notamment encadré dans le projet les travaux des post-docs Dalila Benboudjema (12 mois), Erik Urbach (4 mois) et Guillaume Thibault (16 mois). J'étais aussi responsable du transfert technologique des modules logiciels de la plate-forme à la société ADCIS et qui sont désormais intégrés dans le logiciel RAMIS qui sera valorisé par ADCIS.

11.4 Projet PARTOX - Financement ANR-SEST'07 (Jan 08/Dec 08)

Tests parallélisés sur puces à cellules de cytotoxicité aigüe de nanoparticules à morphologie contrôlée

PARTOX était un projet court ayant deux volets : i) approfondir la toxicologie des nanoparticules les plus répandues sur le marché : les silices ultrafines, le dioxyde de titane et l'oxyde de zinc ultrafins. Leur effet toxique sera mis en lien avec leurs caractéristiques géométriques, structurales, physiques et chimiques ; ii) explorer une technologie permettant de caractériser la cytotoxicité des nanoparticules par l'analyse du phénotype de cellules cultivées sur une lame de verre (Cell on Chip ou puces à cellules). L'exploitation des données issues des puces à cellules nécessite, dans une première étape, l'utilisation d'algorithmes de traitement d'image pour extraire les intensités des signaux de fluorescence. Comme résultat du projet, CMM/ARMINES avait mis au point une plateforme logicielle (sous forme du code Python), qui permet l'analyse des 800 images d'une puce ; ceci inclut la segmentation des cellules de chaque goutte, suivie de la quantification des paramètres de fluorescence de chaque cellule. La sortie de l'analyse d'une puce est un fichier de résultats avec tous les paramètres-mesures ainsi que les images intermédiaires pour valider si nécessaire la qualité de la segmentation.

J'ai monté et je coordonne le projet impliquant, outre le CMM, trois laboratoires de recherche de MINES ParisTech : le CBIO, le CEP et le CMAT, ainsi que le CEA. J'ai réalisé tous les travaux techniques de mise au point et de programmation des algorithmes.

11.5 Projet BIOTYPE - Financement pôle de compétitivité "Medicen", Ile de France (Oct 06/Mars 09)

Biotypage moléculaire et cellulaire multidimensionnel

Le projet BIOTYPE impliquait le CMM, le CBIO, Sanofi Aventis, 6 PME Franciliennes actives dans le domaine de la médecine moléculaire (Imstar, PartnerChip, Serial Genetics, Genomic Vision,

Genewave et SIBIO), ainsi que le CEA, l'Institut Pasteur, CeRePP et le CEDIB. Ce projet vise à créer une plate-forme unique permettant le biotypage d'échantillons biologiques à l'aide de multiples technologies de génotypage et phénotypage.

Une grosse partie des aspects d'analyse d'image de ces différentes technologies (puces à ADN, puces à cellules et peignage de l'ADN) avaient été confiés au CMM. Il s'agissait d'un projet assez complexe dont la partie la plus importante des travaux techniques avait été à ma charge (soutenu en fin de projet par quelques mois de post-doc de Jean Stawiaski).

11.6 Projet INDIGO - European STREP in the FP6 (Août 05/Jan 09)

Integrated Highly Sensitivity Fluorescence-based Biosensor for Diagnostic Applications

Le projet européen INDIGO avait comme objectif la mise au point d'un système miniaturisé d'hybridation et de lecture de puces à ADN. L'originalité de l'approche vient du fait que le capteur est placé directement en contact avec une puce amplificatrice de lumière, évitant l'usage de tout autre système optique. Comme pour le cas d'autres systèmes de puces à ADN, il faut analyser les images pour extraire automatiquement les mesures de fluorescence associées à des mesures génomiques. Le fait de ne pas avoir d'optique implique que dans le cas des puces INDIGO les images produites ont des problèmes particuliers (focalisation, cross-talk, etc...). Par ailleurs, l'amplification de la fluorescence suppose une amplification du bruit et des artefacts ainsi que des problèmes de saturation pour les signaux forts. Il avait donc fallu mettre au point une chaîne complète de restauration des images pour corriger les différents problèmes.

Dans le cadre du projet INDIGO, j'avais réalisé la plus grosse partie des travaux techniques (développements des algorithmes, transfert du code aux autres partenaires) ; j'étais aussi co-responsable avec Michel Bilodeau de l'un des workpackages du projet.

11.7 Projet GEMBIO - Financement Conseil Général des Mines (Jan 04/Dec 06)

Développement de méthodes mathématiques pour l'analyse des données de puces à ADN pour l'aide au diagnostic et pronostic médicale et thérapeutique

En collaboration avec le CBIO de MINES ParisTech et l'Ecole des Mines d'Alès, le projet GEMBIO (2004-2006) était un financement du Conseil General des Mines (Comité d'Orientation Stratégique) qui visait à favoriser l'émergence d'une compétence forte en bioinformatique au sein des Ecole des Mines, en se concentrant notamment sur l'analyse de données de biopuces, et par la mise en place de partenariats avec des laboratoires et des entreprises impliqués dans l'utilisation de biopuces à des fins biomédicales.

Ce projet avait financé mon post-doc au CMM et nous avait permis le montage d'autres coopérations industrielles ou académiques dans le domaine : projets INDIGO, BIOTYPE et PARTOX. Au cours de cette période, j'avais transféré à une société biotech les algorithmes de traitement des images de puces à ADN, développés dans ma thèse, pour intégration dans ses logiciels d'analyse.

11.8 Projet MATCHCELL2 - Financement BIO CRITT (Jan 04/Sept 04)

Automatisation dans la caractérisation des globules rouges à partir d'images couleur de frottis de sang périphérique

Ce projet était la suite du projet MATCHCELL, aussi cyto-hématologie quantitative. Ce prolongement visait à transposer le travail réalisé sur les lymphocytes à la caractérisation et à la classification des globules rouges.

Les travaux techniques du projet avaient été réalisés par Miguel A. Luengo-Oroz dans le cadre de son projet fin d'études que j'avais dirigé.

11.9 Projet MATCHCELL - Financement BIO CRITT (Jan 01/Sept 01)

Développement d'outils de traitement d'image pour des assistants numériques d'aide au diagnostic en hématologie cellulaire (caractérisation de lymphocytes)

L'objectif du projet MATCHELL, en collaboration avec la société de microscopie TRIBVN et le Prof. G. Flandrin, était la mise au point d'une plate-forme de téléconsensus et d'un logiciel automatisé d'analyse de populations de lymphocytes à partir d'images couleur de frottis sanguins. Nous avions voulu réviser la morphologie des syndromes lymphorolifératifs (leucémies et autres) pour montrer comment les nouveaux outils de télémédecine (standardisation des préparations, échange des images, etc...) permettaient aussi un développement d'outils d'analyse d'image et la classification de cellules efficaces pour l'aide au diagnostic en cyto-hématologie.

Ce projet relativement modeste avait financé une partie de ma thèse doctorale.

Quatrième partie

Perspectives

Chapitre 12

Projet de Recherche

"Prudens futuri temporis exitum Caliginosa nocte premit deus". Horace.

Après avoir fait le point sur mes activités de recherche passées, nous arrivons au chapitre de l'avenir. Un avenir où le développement de la morphologie mathématique reste au cœur de mes motivations.

Bien évidemment, mon projet de recherche se situe dans la continuité de mes travaux précédents, dont j'estime certains très prometteurs et méritant l'approfondissement dans le cadre de collaborations avec d'autres chercheurs ; typiquement dans le cadre de thèses de doctorat ou des post-docs. Par ailleurs, il existe aussi de nouvelles pistes de recherche vers des thématiques plus ouvertes que je désire poursuivre, en souhaitant de nouveau des collaborations avec d'autres chercheurs, seniors cette fois-ci. Le challenge de ces travaux plus théoriques, que j'espère aussi plus féconds à long terme, nécessitera que je puisse leur consacrer des périodes importantes de mon temps. Finalement, je voudrais continuer à appliquer mes travaux à la résolution de problèmes réels qui présentent un intérêt pour l'industrie. Par conséquent, la valorisation et le transfert technologique, via des contrats et des projets de recherche multidisciplinaire, continuera à représenter une partie importante de mes activités. Mon objectif est bien de maintenir un équilibre d'environ 60% de temps consacré à la recherche théorique et méthodologique et 40% à la recherche appliquée dans des contrats et projets.

Plus particulièrement, au cours des cinq prochaines années, j'envisage d'approfondir la série de sujets qui sont évoqués de manière sommaire dans ce chapitre.

Bibliographie

[1] L. Alvarez, F. Guichard, P-L. Lions, J-M. Morel. "Axioms and fundamental equations of image processing." *Arch. for Rational Mechanics,* 123(3) : 199–257, 1993.

[2] H. Attouch, D. Aze. "Approximation and regularization of arbitrary functions in Hilbert spaces by the Lasry-Lions method." *Ann. Inst. Henri Poincaré,* 10 : 289–312, 1993.

[3] N. Azzabou, N. Paragios, F. Guichard. "Random Walks, Constrained Multiple Hypotheses Testing and Image Enhancement." In *Proc. of 9th European Conference in Computer Vision (ECCV'06),* 2006.

[4] I. Bengtsson, K. Zyczkowski. *Geometry of quantum states : an introduction to quantum entanglement.* Chapter 2 "Geometry of probability distributions", University Press, 2006.

[5] S. Beucher, C. Lantuéjoul. "Use of watersheds in contour detection." In *Proc. Int. Workshop on image processing, real-time edge and motion detection-estimation,* 17–21, 1979.

[6] S. Beucher, F. Meyer. "The Morphological Approach to Segmentation : The Watershed Transformation." In (E. Dougherty Ed.) *Mathematical Morphology in Image Processing,* Marcel-Dekker, New York, 433–481, 1992.

[7] I. Bloch. "Lattices of fuzzy sets and bipolar fuzzy sets, and mathematical morphology." *Information Sciences,* 181(10) : 2002–2015, 2011.

[8] T. Bülow. "Spherical Diffusion." *Technical Report MS-CIS-01-38,* University of Pennsylvania, 2001.

[9] B. Burgeth, A. Bruhn, S. Didas, J. Weickert, M. Welk. "Morphology for tensor data : Ordering versus PDE-based approach." *Image and Vision Computing,* 25(4) : 496–511, 2007.

[10] B. Burgeth, N. Papenberg, A. Bruhn, M. Welk, J. Weickert. "Mathematical morphology for matrix fields induced by the Loewner ordering in higher dimensions." *Signal Processing,* 87(2) : 277–290, 2007.

[11] G. Birkhoff. *Lattice theory.* American Mathematical Society, Providence, 1984.

[12] L. Corrias. "Fast Legendre-Fenchel Transform and Applications to Hamilton-Jacobi Equations and Conservation Laws." *SIAM Journal on Numerical Analysis,* 33(4) : 1534–1558, 1996.

[13] L. Dorst, R. van den Boomgaard. "Morphological Signal Processing and the Slope Transform." *Signal Processing,* 38 :79–98, 1994.

[14] L. Florack, B. ter Haar Romeny, M. Viergever, J. Koenderink. "The Gaussian Scale-Space Paradigm and the Multiscale Local Jet." *International Journal of Computer Vision,* 18 :61–75, 1996.

[15] M. Gondran. "Analyse MINPLUS". *C.R. Acad. Sci. Paris,* 323(série 1) : 371–375, 1996.

[16] M. Gondran, M. Minoux. *Graphes, dioïdes et semi-anneaux - noveaux modèles et algorithmes*, Chapitre 7 "Dioïdes et analyses non linéaires", Editions Tec&Doc, 2001.

[17] H. Hadwiger. *Vorlesungen über Inhalt, Oberfläche und Isoperimetrie.* Springer, 1957.

[18] H. Hadwiger. "Normale körper im euclidischen raum und ihre topologishen und metrischen eigenschaften." *Math. Zeitschr.* 71 : 124–149, 1959.

[19] A. Hanbury, J. Serra. "Morphological Operators on the Unit Circle." *IEEE Transactions on Image Processing,* 10(12) :1842–1850, 2001.

[20] H.J.A.M. Heijmans, C. Ronse. "The algebraic basis of mathematical morphology - part I : Dilations and erosions." *Computer Vision, Graphics and Image Processing,* 50 : 245–295, 1990.

[21] H.J.A.M. Heijmans. *Morphological Image Operators,* Academic Press, Boston, 1994.

[22] H.J.A.M. Heijmans, J. Goutsias. "Multiresolution Signal Decomposition Schemes : Part 2 : Morphological Wavelets." *IEEE Trans. Image Processing,* 9(11) :1897–1913, 2000.

[23] C.J. Isham. *Lectures on Quantum Theory : Mathematical and Structural Foundations.* Imperial College Press, 1995.

[24] R. Kimmel. "Demosaicing : Image reconstruction from color CCD samples." *IEEE Trans. on Image Processing,* 8(9) :1221-8, 1999.

[25] R. Kimmel, R. Malladi, and N. Sochen. "Images as embedded maps and minimal surfaces : Movies, color, texture, and volumetric medical images." *Int. J. Computer Vision,* 39 :111–129, 2000.

[26] J.M. Lasry, P.L. Lions. "A remark on regularization in Hilbert spaces." *Israel J. Math.* 55 :257–266, 1986.

[27] P.L. Lions, P.E. Souganidis, J.L. Vázquez. "The Relation Between the Porous Medium and the Eikonal Equations in Several Space Dimensions." *Revista Matemática Iberoamericana,* 3(3-4) : 275–310, 1987.

[28] G.L. Litvinov, V.P. Maslov, G. B. Shpiz. "Idempotent functionals analysis : an algebraic approach." *Mathematical Notes,* 69(5) : 696–729, 2001.

[29] Y. Liu, H. Hel-Or, C.S. Kaplan, L. Van Gool. "Computational Symmetry in Computer Vision and Computer Graphics." Foundations and Trends in Computer Graphics and Vision, 5(1–2) : 199 pages, 2010.

[30] Y. Lucet. "Faster than the Fast Legendre Transform, the Linear-time Legendre Transform." *Numerical Algorithms,* 16(2) : 171–185, 1997.

[31] P. Maragos. "Slope Transforms : Theory and Application to Nonlinear Signal Processing." *IEEE Trans. on Signal Processing,* 43(4) : 864–877, 1995.

[32] P. Maragos. "Differential morphology and image processing." *IEEE Trans. on Image Processing,* 5(1) : 922-937, 1996.

[33] V.P. Maslov. "On a new superposition principle for optimization problems." *Russian Math. Surveys,* 42(3) : 43–54, 1987.

[34] G. Matheron. *Elements pour une théorie des milieux poreux.* Masson, Paris, 1967.

[35] G. Matheron. *Random Sets and Integral Integral Geometry.* Wiley, New York, 1975.

[36] G. Matheron, J. Serra. "The Birth of Mathematical Morphology." In *(H. Talbot and R. Beare, Eds) Proc. of ISMM'02,* pp. 1–16, CSIRO Publishing, 2002.

[37] H. Minkowski. Allgemeine lehrs atze uber konvexe polyeder. *Nachr. Ges. Wiss. Gottingen,* 198–219, 1897.

[38] H. Minkowski. uber die begriffe l ange, oberfl ache und volumen. *Jahresbericht der Deutschen Mathematiker Vereinigung,* 9 : 115–121, 1901.

[39] F. Meyer. *Cytologie quantitative et morphologie mathématique.* Thèse doctorale, Centre de Morphologie Mathématique, Ecole des Mines, Paris, 1979.

[40] F. Meyer. “Un algorithme optimal de ligne de partage des eaux.” In *Proceedings 8ème Congrès AFCET,* 447–457, Lyon-Villeurbanne, France, 1991.

[41] F. Meyer. “Color image segmentation.” In *Proc. of 4th Conf. Image Processing and Applications,* 53–56, Maastrich, The Netherlands, 1992.

[42] F. Meyer. “Minimum spanning forests for morphological segmentation.” In (Serra and Soille Eds.) *Mathematical Morphology and its Applications to Image and Signal Processing,* Kluwer, 77–84, 1994.

[43] F. Meyer. “An Overview of Morphological Segmentation.” *International Journal of Pattern Recognition and Artificial Intelligence,* 15 :1089–1118, 2001.

[44] F. Meyer, J. Stawiaski. “Morphology on Graphs and Minimum Spanning Trees.” In *Proc. of ISMM'09 (2009 International Symposium on Mathematical Morphology),* LNCS 5720, Springer-Verlag Berlin Heidelberg, 2009.

[45] F. Meyer, J. Stawiaski. “A stochastic evaluation of the contour strength.” In *Proc. of 32nd Annual Symposium of the German Association for Pattern Recognition (DAGM 2010),* Springer-Verlag, 513–522, 2010.

[46] Y. Meyer. *Oscillating Patterns in Image Processing and Nonlinear Evolution Equations,* University Lecture Series Vol. 22, AMS 2002.

[47] I.S. Molchanov, P. Teran. “Distance transforms for real-valued functions.” *J. Math. Anal. Appl.*, 278 : 472–484, 2003.

[48] N. Ovcharova. “Second-order analysis of the Moreau-Yosida and the Lasry-Lions regularizations.” *Optimization Methods & Software,* Vol. 25, 109–116, 2010.

[49] C. Ronse, H.J.A.M. Heijmans. “The algebraic basis of mathematical morphology - part I : Openings and closings.” *Computer Vision, Graphics and Image Processing : Image Understanding,* 54 : 74–97, 1991.

[50] P. Salembier. “Study on nonlocal morphological operators.” In *Proc. of 6th IEEE International Conference on Image Processing (ICIP'09),* pp. 2269–2272, 2009.

[51] A. Sofou, G. Evangelopoulos, and P. Maragos. “Coupled geometric and texture PDE-based segmentation.” In *Proc. of IEEE International Conference on Image Processing (ICIP'2005),* Vol. II, 650–653, 2005.

[52] J. Serra. *Image Analysis and Mathematical Morphology,* Vol. I. Academic Press, London, 1982.

[53] J. Serra. “Morphological optics.” *J. of Microscopy,* Vol. 145, pt 1, 1–22, 1987.

[54] J. Serra. *Image Analysis and Mathematical Morphology : Theoretical Advances,* Vol II. Academic Press, London, 1988.

[55] J. Serra. “Anamorphoses and Function Lattices (Multivalued Morphology).” In (E. Dougherty Ed.) *Mathematical Morphology in Image Processing,* Marcel-Dekker, 483–523, 1992.

[56] J. Serra, P. Soille. “The Centre de Morphologie Mathématique : An overview.” In *Mathematical Morphology and Its Applications to Image Processing (Proc. of ISMM'93),* Kluwer, 1993.

[57] J. Serra. “A lattice approach to image segmentation.” *Journal of Mathematical Imaging and Vision,* 24 : 83-–130, 2006.

[58] N. Sochen, R. Kimmel, and R. Malladi. “A general framework for low level vision.” *IEEE Trans. on Image Processing,* 7 : 310–318, 1998.

[59] N. Sochen. “Stochastic Processes in Vision : From Langevin to Beltrami.” In Proc. of *International Conference on Computer Vision (ICCV'01),* 2001.

[60] N. Sochen, R. Deriche, L. Lopez-Perez. “The Beltrami Flow over Manifolds.” *Technical report TR-4897, INRIA Sophia-Antipolis,* France, 2003.

[61] S.R. Sternberg. “Grayscale morphology.” *Comput. Vision Graphics Image Process.,* 35(3) : 333–355, 1986.

[62] C. Vachier, F. Meyer. “News from viscous Land.” In *Proc. of International Symposium on Mathematical Morphology (ISMM'07),* pp. 189–200, Oct. 2007.

[63] S. Velasco-Forero, J. Angulo, P. Soille. “Conditional mathematical morphology for edge enhancement and salt-and-pepper noise reduction”. Submitted to *IEEE Transactions on Image Processing*, 2011.

[64] T. Vinh-Thong, A. Elmoataz, O. Lezoray. “Nonlocal PDEs-Based Morphology on Weighted Graphs for Image and Data Processing.” *IEEE Trans. on Image Processing,* 20(6) : 1504–1516, 2011.

[65] M. Welk, M. Breuß, O. Vogel. “Morphological Amoebas Are Self-snakes.” *Journal of Mathematical Imaging and Vision,* 39(2) : 87–99, 2011.

[66] Y. Yang, Z. Jiang, B. Xu, D.W. Repperger. “An investigation of two-dimensional parameter-induced stochastic resonance and applications in nonlinear image processing.” *Journal of Physics A : Mathematical and Theoretical,* 42 : 145207, 2009.

[67] Y. You, M. Kaveh. “Fourth-order partial differential equations for noise removal.” IEEE Transactions on Image Processing, 9 : 1723–1730, 2000.

Cinquième partie

Publications jointes

Chapitre 13

Publications jointes

13.1 Publication I : J. Angulo, J. Serra. "Modelling and Segmentation of Colour Images in Polar Representations.". *Image Vision and Computing*, Vol. 25, No. 4, 475–495, 2007

Available online at www.sciencedirect.com
ScienceDirect
Image and Vision Computing 25 (2007) 475–495
www.elsevier.com/locate/imavis

Modelling and segmentation of colour images in polar representations

Jesús Angulo [a,*], Jean Serra [b]

[a] Centre de Morphologie Mathématique – Ecole des Mines de Paris, 35 rue Saint Honoré, 77300 Fontainebleau, France
[b] Laboratoire A2SI – ESIEE, B.P. 99 93162, Noisy-le-Grand, France

Received 20 September 2005; received in revised form 14 June 2006; accepted 31 July 2006

Abstract

The suitability of polar representation for quantitative image processing tasks is investigated. The classical colour polar-based representations (HLS, HSV, etc.) lead to brightness and saturation with nonconsistent properties. After a short critical analysis of the gamma correction, a new polar representation using the L_1 norm is proposed. It satisfies several quantitative requirements.

The relevance of this representation is demonstrated by means of luminance/saturation histograms, which exhibit typical alignments. Their physical interpretation leads to a model for light reception in terms of linearly regionalized spectra. A full example illustrates the application of the histogram approach.

Colour images are multivariable functions, and for segmenting them one must go through a reducing step. It is classically obtained by calculating a gradient module, which is then segmented as a grey tone image. An alternative solution is proposed. It is based on separated segmentations, followed by a final merging into a unique partition. The generalisation of the top-hat transformation for extracting colour details is also considered. These new marginal colour operators take advantage of an adaptive combination of the chromatic and the achromatic (or the spectral and the spatio-geometric) colour components.

Keywords: Colour mathematical morphology; Colour segmentation; Saturation; Norms; Bi-variate histograms; Jump connection

1. Introduction

In quantitative colour imaging, the first question which arises is that of the a convenient representation for the colour variables. The RGB colour representation has some drawbacks: strongly correlated components, poor human interpretation, nonuniformity, etc. Polar representation, with one variable for light intensity and with two variables defined on the chromatic circle, may allow us a better handling of the colour parameters for quantitative purposes. Starting from the classical work by Kender [26], many research studies took interest in the polar space colour representations, see for instance Smith [48], Levkowitz and Herman [29], Shih [47], Carron [10] or Gevers and Smeulders [19].

The aim of this study is to evaluate the suitability of this representation for quantitative image processing tasks. Such a goal supposes that we define some processing tasks, and that we compare the relevance of various polar representations with respect to these tasks.

A critical discussion on the classical polar representation has been developed by Hanbury and Serra in [23], and completed in [44], by taking the gamma correction into account. The ISMM'05 presentation [44] is summarized below in Sections 2 and 3. But firstly, a brief reminder on the gamma correction is necessary (Section 2.1), as we have to justify the creation of new parameters, of saturation in particular (Section 3). An excellent presentation of the theme may be found in Ch. Poynton's book [38], see also [54].

The analysis of Section 3 results in several norm based polar representations. They are compared in Section 4 in

* Corresponding author. Tel.: +33 1 64 69 47 75; fax: +33 1 64 69 47 07.
E-mail addresses: jesus.angulo@ensmp.fr (J. Angulo), jean.serra@ensmp.fr (J. Serra).
URLs: http://cmm.ensmp.fr/~angulo (J. Angulo), http://cmm.ensmp.fr/~serra (J. Serra).

0262-8856/$ - see front matter © 2006 Elsevier B.V. All rights reserved.
doi:10.1016/j.imavis.2006.07.018

the light of the bi-dimensional they lead to. Some results of Angulo and Serra [3,4], who showed that the L_1 norm histograms exhibit typical alignments, are recalled in this section, and extended in Section 6 to nongamma corrected data, within the framework of a comprehensive example. In parallel, the alignments which appear in the 2-D histograms are the matter of a physical model in Section 5. The idea here is that each region of the space, which generates an alignment, is composed of pixels where the light spectrum consists in the sum of two fixed spectra, with variable weights from point to point.

The suitability of the L_1 norm representation for image processing is then examined via one filtering and two segmentation tasks. In the filtering question (Section 8) we seek a generalization to colour case of the notion of a residual. The paradigm used to define colour top-hat operators allows us an interesting *colour separation* of details according their multi-dimensional nature.

There exists an abundant recent literature on colour image segmentation, which still constitutes an active challenging field, see the detailed state-of-the-art by Cheng et al. [11]. Examples of classical methods are: colour clustering [13], colour region growing [53], colour gradients [19], etc. A classical way to define morphological colour operators is based on defining conditional ordering (C-ordering) by means of lexicographical cascades [51] [5]. Other interesting orderings have been studied, for instance the application of matrix Wilson theory [56,21]. An inconvenient of these C-orderings (vectorial approach) is the computational complexity of the algorithms which leads to slow implementations. However, we do not follow this sort of approach below.

Concerning segmentation, the problem is the following: sooner or later, the processing of such multi-dimensional data goes through a *scalar reduction*, which in turn yields the final partition [5]. Usually, the scalar reduction arises rapidly, since in the most popular procedures it consists in replacing, from the beginning, the bunch of images by a sole gradient module on which the various minimizations hold. Sections 7 and 9 illustrate such an approach. However, when the scalar reduction occurs too soon, it risks to ignore specific features of each band, and to destroy them in the melting pot that generates the 1-D variable. The alternative approach we propose in Section 10 works in the exactly opposite way. We will try and obtain first various intermediary partitions, and then make the final segmentation hold on them.

The present approach relies on the assumption that the hue is more significant for segmenting the highly saturated regions, and the luminance for the weakly saturated ones. This way of thinking already appears in literature with Demarty and Beucher [15], and with Lambert and Carron [28]. But it is developed here differently, as we seek for an optimal partition by combining the three segmentations of the polar coordinates [1]. The obtained results are compared with the more classical approach by watershed of gradient (Section 9). Although an original gradient is specifically designed for the purpose, the results are not better than by partition mixing (Section 10). In Section 11, both new segmentation algorithms are extensively compared by using images from a reference database (Berkeley).

1.1. Notation

For the notation of the colour variables, we follow Ch. Poynton, who differentiates by apostrophes the electronic (or gamma-corrected) colours (e.g., r') from the light intensities (e.g., r). Below, the rule is extended to the operations themselves; for example the arithmetic mean is written m for intensities and m' for video variables. Also, we adopt the convention of the CIE, which designates the absolute quantities by upper letters (e.g., X, Z) and the relative ones by lower case letters (e.g., x, z).

Let $E, \mathcal{T}$ be nonempty sets. We denote by $\mathcal{F}(E,\mathcal{T})$ the power set $\mathcal{T}^E$, i.e., the set of functions from E onto $\mathcal{T}$. Typically for the digital 2-D images $E \subset \mathbb{Z}^2$. If $\mathcal{T}$ is a complete lattice, then $\mathcal{F}(E,\mathcal{T})$ is a complete lattice too. Let f be a grey level image, $f : E \to \mathcal{T}$, in the case of discrete image values $\mathcal{T} = \{t_{\min}, t_{\min}+1, \ldots, t_{\max}\}$ (in general $\mathcal{T} \subset \mathbb{Z}$ or $\mathbb{R}$, or any compact subset of $\mathbb{Z}$ or $\mathbb{R}$) is an ordered set of grey-levels. Given the three sets $\mathcal{T}^h, \mathcal{T}^c, \mathcal{T}^s$, we denote by $\mathcal{F}(E, [\mathcal{T}^h \otimes \mathcal{T}^c \otimes \mathcal{T}^s])$ or $\mathcal{F}(E, \mathcal{T}^{hcs})$ all colour images in a "hue/clearness/saturation" representation ($\mathcal{T}^{hcs}$ is the product of $\mathcal{T}^h, \mathcal{T}^c, \mathcal{T}^s$, i.e., $\mathbf{p}_i \in \mathcal{T}^{hcs} \Longleftrightarrow \mathbf{p}_i = \{(h_i, c_i, s_i); h_i \in \mathcal{T}^h, c_i \in \mathcal{T}^c,\ s_i \in \mathcal{T}^s\}$). See in Section 3.1 the mathematical definitions of these colour components. We denote the elements of $\mathcal{F}(E, \mathcal{T}^{hcs})$ by $\mathbf{f}$, where $\mathbf{f} = (f_H, f_C, f_S)$ are the colour component functions. Using this representation, the value of $\mathbf{f}$ at a point $x \in E$, which lies in $\mathcal{T}^{hcs}$, is denoted by $\mathbf{f}(x) = (f_H(x), f_C(x), f_S(x))$. Note that the sets $\mathcal{T}^c, \mathcal{T}^s$ corresponding to the clearness and the saturation are complete totally ordered lattices. The hue component is an angular function defined on the unit circle, $\mathcal{T}^h = \mathcal{C}$, which has no partial ordering. Hence the hue needs to be processed in a special way.

2. The 3-D representations of the colour

Colour image processing rests on a few basic operations (addition, comparison, etc.) and properties (increasingness, distances, etc.). Have these tools a physical meaning? Indeed, the only additive notion is the spectral power distribution (SPD) of the light radiating from or incident on a surface. This intensity has the dimension of an energy per unit area, such as watt per m^2. When the light arrives at a photo-receiver, this sensor filters the intensities of each frequency by weighting them according to fixed values. The sum of the resulting intensities generates a signal that exhibits a certain "colour". The CIE (Commission Internationale de l'Eclairage), in its *Rec 709*, has standardized the weights which yield the triplet R_{709}, G_{709}, B_{709} [14]. As energies, the intensities are additive, so that all colours accessible from an RGB basis are obtain by sums of the primary colours R, G, and B and by multiplications by nonnegative constants.

The exploration of the spectrum is lower bounded by $R = G = B = 0$ (zero energy) higher bounded by a maximum red R_0, green G_0 and blue B_0 that are given by the context (illumination, technological limits of the sensors, or of the eye, etc.) in which we work. Generally, each technology fixes the three bounds, which therefore define the reference white, and then introduces the *reduced variables*

$$r = \frac{R}{R_0}, \quad g = \frac{G}{G_0}, \quad b = \frac{B}{B_0}. \tag{1}$$

The digital sensitive layers of cameras transform the light intensities into voltages; conversely, the cathodic tubes (CRT) and the flat screens that display images return photons from the electrical current. Now, their response is not linear, but a power function of the input voltage whose exponent γ, (gamma), varies around 2.5 according to the technologies. If we want the light intensities of the CRT to be proportional to those of the scene itself, the gamma effect has to be compensated. In video systems, this *gamma correction* is universally at the camera. The *Rec. 709* of CIE proposes the following correction function

$$r' = \begin{cases} 4.5r & \text{if } r \leqslant 0.018 \\ 1.099r^{0.45} - 0.099 & \text{if } r > 0.018 \end{cases} \tag{2}$$

that we write here for the reduced red intensity r, and where $1/\gamma = 0.45$. The same transfer function is applied to both green and blue bands. In fact, the values 0.45 and 2.5 are not inverse of each other, because a contrast enhancement is applied on the TV screens, which are not really black.

In image processing, the algorithms for colour are practically always based on *corrected* variables. They can be the intensities (r', g', b'), or some derived systems, such as HLS, YUV, etc. The reason is clear: these data come from cameras, or TV cameras, or from data bases, which all are intended to be displayed on monitors requiring the gamma correction. Now this correction is obviously incompatible with the arithmetic operations. However, as a matter of fact, Rel. (2) defines an extremely regular function. It is very well approximated by limited expansions for fluctuations which do not exceed 25% of the whole range of variation of the intensities [44].

Therefore, the quality of these approximation justifies that we develops the vector formalism below for both reduced intensities (r, g, b) and (r', g', b'), nevertheless it is physically sound for the first triplet only. Although it is not usual in the image processing community, it would be also wise to go back from the video bands (r', g', b') to the reduced intensities (r, g, b) by means of the inverse transform of Rel. (2). When starting from the usual 3×8 bits (r', g', b') images, the best should probably be to code in 3×16 bits for computation (or in floating variables), and to work with these variables. This alternative is developed in Section 6, in connection with colour histograms. In practice people keeps the (r', g', b') video space, which is implicitly modelled as a part of a vector space, from which arithmetic means, projections, histograms, Fourier transforms, etc. are build, and often seem to be significant.

2.1. Colour vector spaces

The physical meaning of the reduced intensities suggests to model them by a 3-D vector space, and to restrict it to the unit cube $[0,1] \times [0,1] \times [0,1]$, say E, of $\mathbb{R}^3$. Formally speaking, one can always do the same for the corrected variables, and consider the unit video cube (r', g', b') as a part, E' say, of a three-dimensional vector space.

Fig. 1 depicts, for example, the unit cube E'. The vector $\vec{x}'$, of coordinates (r', g', b') can also be decomposed into two orthogonal vectors $\vec{c}'$ and $\vec{l}'$ of the chromatic plane and the a-chromatic (or grey) axis, respectively. The latter is the main diagonal of the cube going through the origin O and the chromatic plane is perpendicular to the grey axis in O. The two vectors $\vec{c}'$ and $\vec{l}'$ have the following coordinates:

$$\begin{aligned} 3\vec{c}' &= (2r' - g' - b', 2g' - b' - r', 2b' - r' - g') \\ 3\vec{l}' &= (r' + g' + b', r' + g' + b', r' + g' + b') \end{aligned} \tag{3}$$

2.2. Clearness and saturation

The word *luminance* is quantified by the CIE *Rec. 709*. It defines a white point and three weighting functions of the

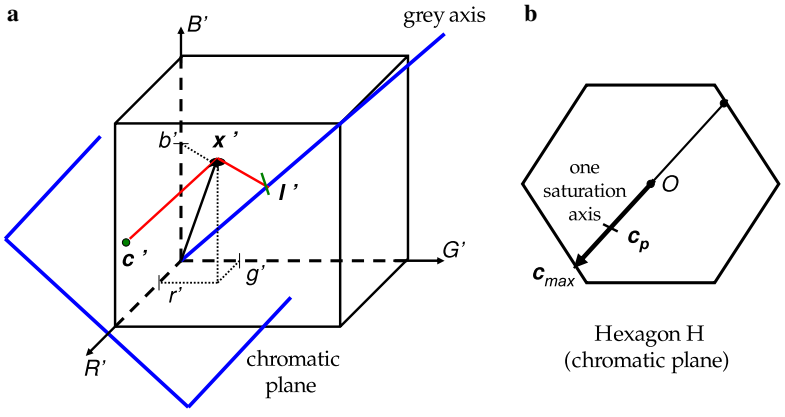

Fig. 1. (a) The unit r', g', b' cube in the video vector space. The same drawing stands for the intensities vector space as well, by suppressing the sign "prime" on the symbols. (b) The chromatic plane in the intensities vector space.

spectrum which lead to the variables R_{709}, G_{709}, and B_{709}, then to the *luminance*

$$Y_{709} = 0.212R_{709} + 0.715G_{709} + 0.072B_{709} \quad (4)$$

and to the luminance Y_W of the associated white point.

When dealing with gamma corrected variables, many authors consider the transforms

$$r' = r^{1/\gamma}, \quad g' = g^{1/\gamma}, \quad b' = b^{1/\gamma} \quad (5)$$

for $\gamma \simeq 2.2$ as generating *perceptual intensities*. For example, the *Rec. BT 601-E* proposes the *luma* y'_{601} as a perceptual brightness measurement

$$y'_{601} = 0.299r' + 0.587g' + 0.144b'. \quad (6)$$

However, this luma, as established from video values has not an energy dimension, and not any more the deriving additivity properties. The CIE follows the same direction, but defines the *lightness* l^* by taking a slightly different exponent

$$l^* = 116\left(\frac{Y_{709}}{Y_W}\right)^{1/3} - 16, \quad Y_{709} \geqslant 0.0089Y_W.$$

Besides, in HSL, the last letter stands for *lightness*, and in related systems HSI and HSB, it means *intensity* and *brightness*. It seems that the word *clearness* escaped for the moment to all these "copyright" on the dictionary.

The CIE is more interested in various formulations of the brightness–luminance–lightness of the light than in its saturation, which is defined, without formal expression, as "*the colourfulness of an area judged in proportion to its brightness*". In other words, it is the concern of the part of uniform spectrum (i.e., of grey) in a colour spectrum, so that any maximal monochromatic colour has a unit saturation and so that any triplet $r = g = b$ has a zero saturation.

The previous terms are either vague (the saturation) or excessively narrow to be used in a formal developments. Therefore we prefer to adopt the generic term of *clearness* and to make more precise the saturation by introducing the following two definitions.

Definition 1. Let $\mathbf{x}(r,g,b)$ be a variable point on the unit cube E of the reduced intensities, of projection $\mathbf{c}_p$ on the orthogonal chromatic plane. Any scalar function of $\mathbf{x}$ which increases with r, g, and b and ranges from 0 for $(0,0,0)$ to a maximum for $(1,1,1)$ is a *clearness*.

Similarly, any scalar function s of the projection $\mathbf{c}_p$ on the chromatic hexagon, such that $s(\lambda\mathbf{c}_p)$ increases with λ, and ranges from 0 for the centre of the hexagon (see Fig. 1), to a maximum for all points of its border, is a *saturation*.

Both notions are similarly defined in the cube E' of the gamma corrected reduced intensities.

With regard to clearness, the physical meaning of the increasingness is clear: clearness varies in the same sense as the *energy* of the light. The above luminance, luma, lightness, intensity, and brightness are all clearnesses.

3. Quantitative requirements

Quantitative image processing demands three basic requirements [23]:

(1) one must be able to sum up colour images and to multiply them by constants,
(2) one must be able to express that an image is more or less similar to another,
(3) two colour points which have the same projection on the chromatic plane must have the same saturation.

The list is not exhaustive, and perhaps too comprehensive for some applications, but it summarizes the essentials of the quantitative needs. Besides, one easily translate it into mathematical terms:

(1) $\Rightarrow$ vector space,
(2) $\Rightarrow$ norm and distance,
(3) $\Rightarrow$ invariance of the saturation under addition of grey vector (i.e., three equal values).

By a norm on a vector space V is meant a mapping n such that

(1) $n(x) \geqslant 0$ for every $x \in V$,
(2) $n(x) \neq 0$ for every x different from the origin,
(3) $n(x+y) \leqslant n(x) + n(y)$ for all $x, y \in V$,
(4) $n(\mu x) = |\mu| n(x)$ for every $x \in V$ and every $\mu \in R$ (homogeneity).

The first three axioms suggest some relation with the notion of a distance. Indeed, the norm $n(x)$ is also a distance $d(x,0)$ between point x and the origin. More generally, the quantity

$$d(x,y) = n(x-y) \quad x, y \in V$$

turns out to be a distance on the vector space V ([12], section VII-1-4). But in addition the fourth axiom, of homogeneity, provides this distance with a physical meaning which fits exactly with our goal, as it implies that all clearnesses and saturations deriving from norms fulfill the conditions of Definition 1.

Point (1) was just treated, we now consider the two other ones, by focusing on the case of the E' unit cube.

3.1. L_1 norm

3.1.1. Clearness

As regards the needs for quantitative image processing, the weights that appear in Rel. (4) or (6) loose any reason of being. Indeed, the processed operations never hold on *perceived* images, but on *objects under study*. In microscopy, the histological stainings usually range from blue to violet; the spectrum of a sunset, or that of a human face do not correspond to the weights

given to r, g, and b in Rel. (4) or (6). For a specific database (e.g., some histological staining) one can always try and built *specific weights* for r', g', and b' in a specific clearness, but in the absence of a priori information on the spectra of the objects under study, the purpose of segmentation or filtering leads us to take as clearness a *symmetrical function* of primary colours.

Then the simplest clearness function is the arithmetic mean m' (respectively, m).

$$m' = \tfrac{1}{3}(r' + g' + b'). \tag{7}$$

When applied to the r, g, b triplet, it preserve the energy dimension of the variables.

Now, the mean (7) is nothing but the restriction to the cube E' of the L_1 norm, which is defined in the whole space $\mathbb{R}^3$ by the relation:

$$L_1(x') = |r'(x)| + |g'(x)| + |b'(x)| = 3m'(x'). \tag{8}$$

3.1.2. Saturation

The sake of consistency suggests us to keep the same L_1 norm for the hexagon H' of the chromatic plane for defining the saturation s'. By using Rel. (3) we find

$$s'(x') = L_1(c'_p) = \tfrac{1}{4}[|2r' - g' - b'| + |2g' - b' - r'| + |2b' - r' - g'|]. \tag{9}$$

By symmetry, $s'(x')$ depends on the three functions $\max' = \max(r', g', b')$, $\min' = \min(r', g', b')$, and $\mathrm{med}' = \mathrm{median}(r', g', b')$ only, which gives

$$s' = \begin{cases} \tfrac{3}{2}(\max' - m') & \text{if } m' \geqslant \mathrm{med}' \\ \tfrac{3}{2}(m' - \min') & \text{if } m' \leqslant \mathrm{med}' \end{cases} \tag{10}$$

3.1.3. Hue

In the L_1 norm, the hue is given by the following expression, which avoids to bring trigonometric terms into play,

$$h' = \frac{\pi}{3}\left[\lambda + \frac{1}{2} - (-1)^{\lambda}\frac{\max' + \min' - 2\mathrm{med}'}{2s'}\right] \tag{11}$$

with λ equals

$$\begin{array}{lll} 0 \text{ if } r' > g' \geqslant b' & 1 \text{ if } g' \geqslant r' > b' & 2 \text{ if } g' > b' \geqslant r' \\ 3 \text{ if } b' \geqslant g' > r' & 4 \text{ if } b' > r' \geqslant g' & 5 \text{ if } r' \geqslant b' > g'. \end{array}$$

The hue h', as a coordinate on the unit circle, is defined modulo 2π. The value $h' = 0$ in Eq. (11) corresponds to the red. For $s' = 0$, colour point lies on the grey axis, so that its hue is meaningless. The inverse formulae are given in [23] and in [3], and the detailed proofs may be found in [42].

In all processings that follows, from Section 4 to the end of the paper, the f_C, f_S, and f_H components of the colour image $\mathbf{f}$ are always those of Rel. (7), (10), and (11) of the L_1 norm. We call 1-HCS this representation. Fig. 2 depicts the colour image "parrots" and its corresponding components in the 1-HCS representation.

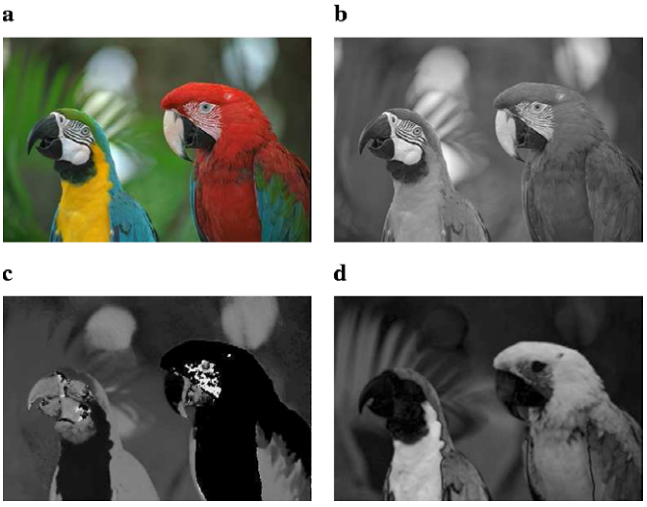

Fig. 2. Initial "parrots" image $\mathbf{f}$ (a), and decomposition of the color image according to the representation in norm L_1: (b) clearness f_C, (c) hue f_H (d) saturation f_S.

3.2. Properties and physical meaning of the norms

In the Euclidean space $\mathbb{R}^3$ the relation:

$$n(x') = (|r'(x)|^{\alpha} + |g'(x)|^{\alpha} + |b'(x)|^{\alpha})^{1/\alpha}, \quad \alpha \geqslant 1 \tag{12}$$

generates a family of the so-called *Minkowski norms* as soon as $\alpha \geqslant 1$. All these norms are symmetrical and. For $\alpha = 1$, it yields the above L_1 norm. For $\alpha = 2$, we obtain the usual Euclidean norm L_2, and for $\alpha = \infty$, the "max" norm. We have a few nice properties.

- As any norm, L_1 generates a distance in $\mathbb{R}^3$ as well, of course, as its restrictions to the unit cube E', and to hexagon H' (or E and H), by the relation

  $$L_1(x'_1, x'_2) = L_1(x'_1 - x'_2) \tag{13}$$

  Thus, for $\alpha = 1$, both clearness $m'(x')$ and distance $d(x'_1, x'_2) = m'(|x'_1 - x'_2|)$ in E' derive from a unique concept. This latter relation is important, as in segmentation a number of algorithms which were established for numerical functions extend to vector functions when a distance is provided (e.g., watershed). In addition, the L_1 norm satisfies the *equality* $L_1(x'_1, x'_2) = L_1(x'_1) + L_1(x'_2)$ (and $L_1(x_1,\ x_2) = L_1(x_1) + L_1(x_2)$), and not only the inequality $\leqslant$, such as the other Minkowski norms do.
- The norm homogeneity provides clearness and saturation with the same physical dimension as the coordinates of the space, so that in the r, g, and b case they preserve the energy dimension of the intensities.
- This homogeneity leads to another consequence. In the unit cube E (or E') as well as on the chromatic hexagon H (or H'), the following triangular inequality holds (axiom 3)

  $$n(x_1 + x_2) \leqslant n(x_1) + n(x_2).$$

  By combining it with homogeneity axiom, we obtain the *barycentric relation*

$$n\left(\frac{\mu_1 x_1 + \mu_2 x_2}{\mu_1 + \mu_2}\right) \leqslant \frac{\mu_1 n(x_1) + \mu_2 n(x_2)}{\mu_1 + \mu_2}. \quad (14)$$

In the chromatic hexagon H the symbols x_1 and x_2 indicate two saturations c_{p1} and c_{p2}, and Rel. (14) is the exact transcription of Newton disc experiment: the saturation of the weighted average is less than the weighted sum of the individual saturations.

- Finally, the Minkowski norms present the significant advantage to *separate the variables*: two points x_1 and $x_2 \in E$ (or x'_1 and $x'_2 \in E'$) which have the same projection on the chromatic plane (respectively on the grey axis) have the same saturation (respectively the same clearness). However, the last property, about clearness, vanishes when the three bands are given different weights in the mean m (or m'), though the third requirement, about saturation, remains satisfied.

In the L_1 norm, the saturation algorithm Eq. (9) is equivalent to the expression

$$s(x) = L_1(c_p) = \tfrac{3}{4}(|r - m| + |g - m| + |b - m|), \quad (15)$$

written here for the intensities, and where the clearness m is the arithmetic average of r, g, and b. This presentation enlightens us about the spectral meaning of the L_1 norm. Partition the intensity spectrum sp(v) into K bands of the same with Δv, where K may be very large, and denote by i_k the mean intensity in the band k, $k \in [1, K]$. One proves by induction that both clearness and saturation extend to this K-dimensional case, and that

$$m(x) = \frac{1}{K} \sum_{1 \leqslant k \leqslant K} i_k(x),$$

and

$$s(x) = \Delta v \sum_{1 \leqslant k \leqslant K} |i_k(x) - m|.$$

Clearness is nothing but the average of the spectrum, and saturation the sum of the absolute deviations to the average m.

If in a multivariate analysis with K components, we reduce all variables in order to make them vary in [0,1], then, the "grey axis" is that where all components are equal, and the "chromatic variety" is the subspace orthogonal to the grey axis.

How to choose between the two norms L_1 and L_2, which exhibit the same theoretical advantages? We shall ask the clearness/saturation histograms to answer the question: the better norm will be that which better reflects the colour features of the images under study. But before these experiments, we would like to show, as a counter example, what happens when the quantitative requirements are neglected.

3.3. HLS polar representation

Most of the polar representation of colour date from the end of the seventies [48], and were conceived neither for processing purposes, nor for the current computing facilities (e.g., HSI, HSB, HSV, HLS, etc.). This results in a confusing choice between models which essentially all offer the same representation. The most popular one is the HLS triplet of System (16), which appears in many software packages. The comments which follow hold on this particular model, but they apply to the other ones. The HLS triplet derives from RGB by the following system

$$\begin{cases} l'_{\mathrm{HLS}} = \frac{\max(r',g',b') + \min(r',g',b')}{2} \\ s'_{\mathrm{HLS}} = \begin{cases} \frac{\max(r',g',b') - \min(r',g',b')}{\max(r',g',b') + \min(r',g',b')} & \text{if } l'_{\mathrm{HLS}} \leqslant 0.5 \\ \frac{\max(r',g',b') - \min(r',g',b')}{2 - \max(r',g',b') - \min(r',g',b')} & \text{if } l'_{\mathrm{HLS}} \geqslant 0.5 \end{cases} \end{cases} \quad (16)$$

One easily checks that the HLS expressions do not preserve the above requirements of linearity (for the clearness), of increasingness (for the saturation) and of variables separation.

Fig. 3 depicts a situation when the HLS luminance of both RGB triplets $(1/2, 1/2, 0)$ and $(0, 1/2, 1/2)$ equals 1/4, whereas that of their mean equals 3/8, i.e., it is lighter than both terms of the mean. Similarly, in Fig. 4, the HLS saturations of the RGB triplets $(4/6, 1/6, 1/6)$ and $(2/6, 3/6, 3/6)$ equals 3/5 and 1/5, respectively, whereas that of their sum is 1: it is just Newton's experiment denial! [35].

Finally the independence property is no more satisfied. Take the two RGB triplets (1/2,1/2,0) and (3/4,3/4,1/4). One passes from the first to the second by adding the grey $r' = g' = b' = 1/4$. Hence both triplets have the same projection on the chromatic plane. However, the HLS saturation of the first one equals 1 and that of the second 1/2.

The HLS system can satisfy the above quantitative requirements when it is improved as follows [23]:

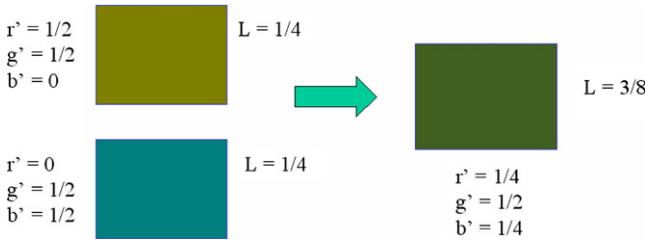

Fig. 3. For HLS luminance, where $l = (\max + \min)/2$, the mean of two colours on the left is more luminous than each of them.

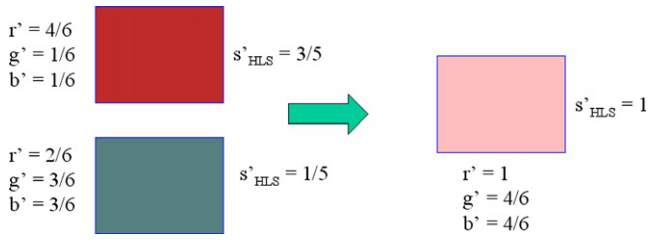

Fig. 4. The two colours of the left have HLS saturations 3/5 and 1/5. Their sum has a saturation 1, which completely contradicts Newton's theory of synthesis of colours (Newton's disk).

(1) replace the HLS luminance l'_{HLS} by any norm (a weighted average for example),
(2) replace the HLS saturation s'_{HLS} by the quantity

$$s'_{improved} = \max(r', g', b') - \min(r', g', b') = s'_{HLS}(1 - 2|0.5 - l'_{HLS}|)$$

which is a norm in the chromatic plane.

We just showed the lack of consistency HLS representation. Similar doltishnesses may be found as well in the HSV mode. For quantitative image processing, both turn out to be simply catastrophic.

4. 2-D Histograms and linearly regionalized spectra

In practice, is it really worth deviating from beaten tracks, and lengthening the polar triplets list? What for? We may answer the question by comparing the *clearness/saturation* bi-dimensional histograms for HLS system and for various norms. The reader may find a few dozens of example images which are treated this way in Refs. [3,4]. Two of them are depicted below, in Fig. 5, and studied step by step below.

4.1. Bi-dimensional histograms

In the first image, we observe strong reflections on the rubber ring, and various types of shadows. The corresponding L_1, L_2, and HLS histograms are reported in Fig. 6, with clearness on the x axis and saturation on y axis. No information can be drawn from HLS histogram. On the L_2 histogram some features appear, but not clearly. Finally, well-drawn alignments turn out to be visible on L_1 histogram.

By coming back to the images, we can localize the pixels which give alignments, as depicted in Fig. 7. They correspond to three types of areas:

- shadows with steady hue,
- graduated shading on a plane,
- reflections with a partial saturation.

Consider now the more complex image of "Ana Blanco", in Fig. 5(b). It includes various light sources (television monitor, alpha-numerical incrustations, etc.), and the light diffused by the background is piecewise uniform over the space. However, there are still alignments, which do not always go through points (0,0), or (1,0), and are sometimes parallel. In the *clear/hue* plane of the L_1 norm representation, several horizontal lines (constant hue) are located at different hue levels, and alternate with elongated clouds of points (Fig. 8(b)). Again, the image regions associated to the alignments can be extracted, see Fig. 9.

All in all, we draw from the above histograms four main informations.

(1) In the *clear/sat* histogram, there is no accumulation of pixels at point (1,0). It means that the sensors we

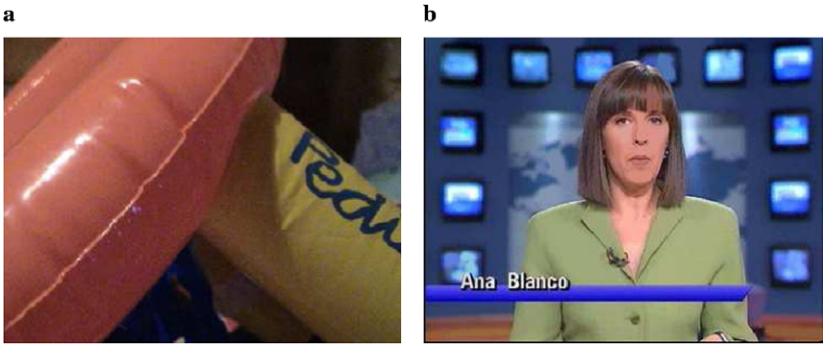

Fig. 5. Two test images: (a) rubber ring, (b) Ana Blanco.

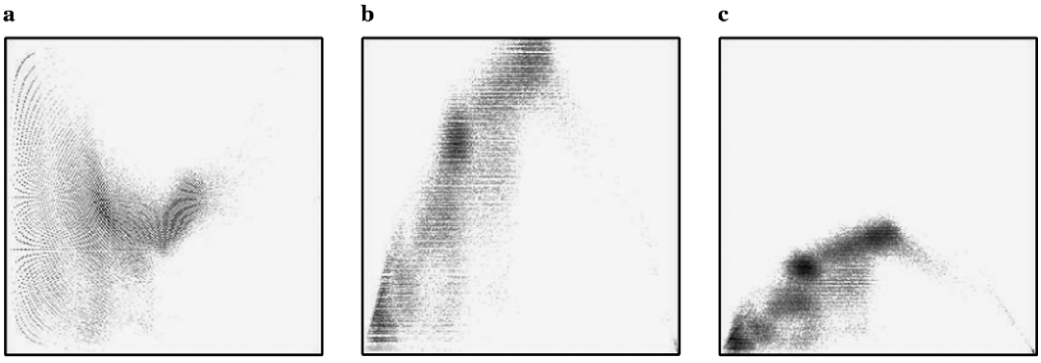

Fig. 6. Bi-dimensional histograms of the "rubber ring" image. The x-axis corresponds the clearness and the y-axis to the saturation. (a) HLS representation, (b) L_2 norm, (c) L_1 norm.

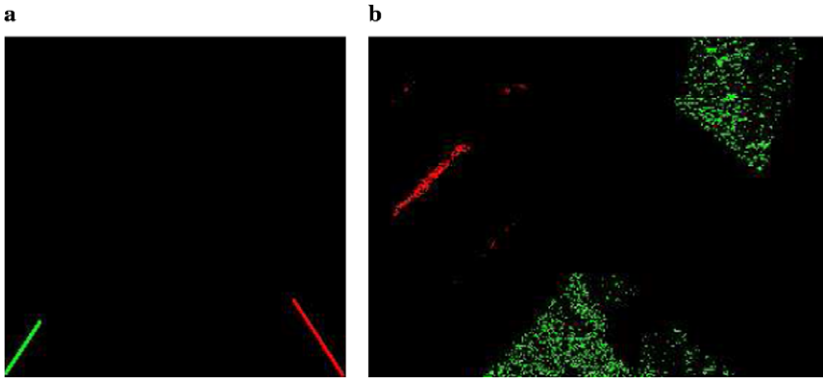

Fig. 7. Zones of "rubber ring" associated with alignments. The left image (a) shows the supports of the alignments in Fig. 6 (in L_1 norm), and the right image (b) indicate the locations of the aligned pixels in the space of the initial picture. The red (respectively green) alignments of (a) correspond to the red (respectively green) pixels of (b).

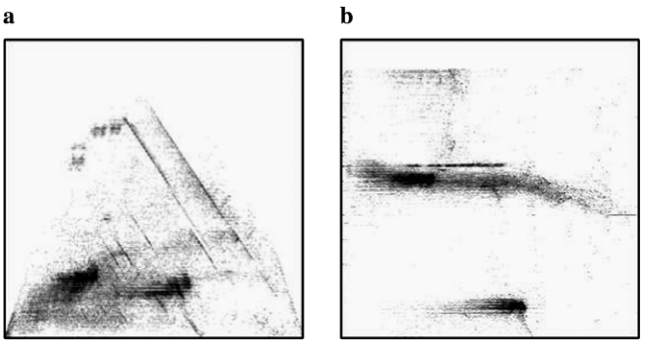

Fig. 8. (a and b) The two histograms of "Ana Blanco", in the *clearness/saturation* and the *clearness/hue* plane, respectively, both in L_1 norm.

use are not physically saturated, which make realistic the proposed linear approach;

(2) Still in the *clear/sat* histogram, some well drawn alignments can be extrapolated to point $(0,0)$ or point $(1,0)$. The others are parallels to the first ones;

(3) However, most of the pixels form clouds in both *clear/sat* and *clear/hue* histograms are not aligned at all, whether the model does not apply, or the homogeneous zones are too small;

(4) In the *clear/hue* histogram, most often the aligned pixels exhibit a (quasi) constant hue, i.e., draw horizontal lines. But sometimes, these "lines" turn out to be a narrow horizontal stripe.

Such characteristic structures, such distinct lines suggest we seek a physical explanation of the phenomenon. This is what we will do now. But besides any physical model, a first point is worth to be noticed: the only norm that enables us the extraction of reflection areas, of shadows and gradations is L_1. No other polar model results in such an achievement.

5. Linearly regionalized spectra (LR model)

If we assume that the alignments are a property of the spectrum, and not an artefact due to some particular repre-

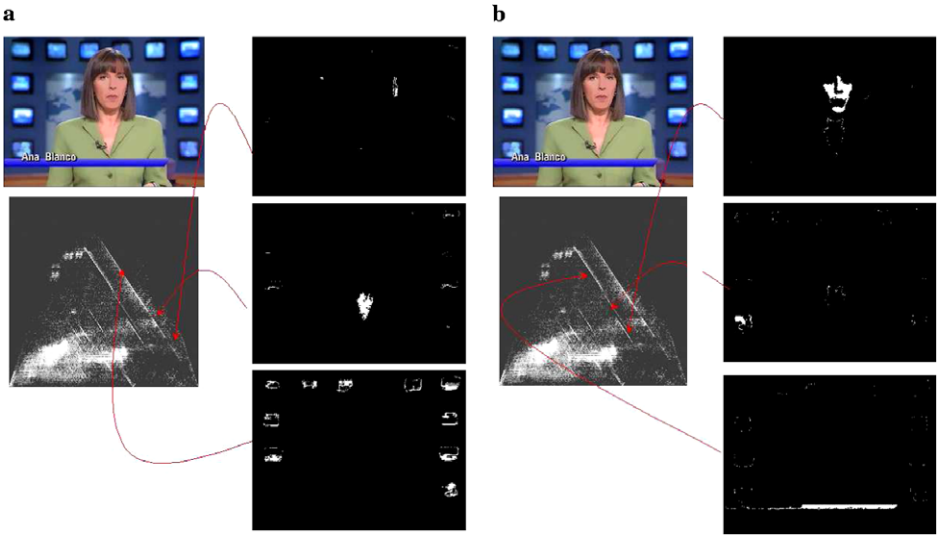

Fig. 9. (a) "Ana Blanco" zones associated to main alignments. (b) Other areas from alignments, parallel to the previous ones.

sentation, we have to express the spectrum in such a way that the sequence

$$(\text{spectrum}) \to (r', g', b') \to (m', s', h') \to (m' = \alpha s' + \beta)$$

be true (in the alignments) whatever the weights generating r, g, and b are, and also whatever the spectrum itself is. Consider a zone Z of the space whose all pixels yield an alignment in the L_1 histogram. Denote by $\mathrm{sp}(v;z)$ the spectrum of the light intensity at point $z \in Z$. We will say that this spectrum is *linearly regionalized* in Z when for each point $z \in Z$ one can decompose $\mathrm{sp}(v;z)$ into the sum of a first spectrum $\mathrm{sp}_0(v)$, independent of point z, and of a second one, $\overline{\omega}(z)\mathrm{sp}_1(v)$, which proportionally varies in Z from one point to another. For all $z \in Z$, we have

$$\mathrm{sp}(v;z) = \mathrm{sp}_0(v) + \overline{\omega}(z)\mathrm{sp}_1(v) \tag{17}$$

where $\overline{\omega}(z)$ is a numerical function which depends on z only, and where sp_0 and sp_1 are two fixed spectra.

In the spectrum $\mathrm{sp}(v;z)$, though sp_0 usually corresponds to diffuse light and sp_1 to specular one, we do not need to distinguish between the emitted and reflected components of the light. It can be the concern of the light transmitted through a net curtain, for example, or of that of a TV monitor; but it can also come from passive reflectance, such as those described by Shafer's dichromatic model [46], or by Obein et al.'s model of glossiness [36]. But unlike these two models, the term $\overline{\omega}(z)\mathrm{sp}_1$ may also represent an absorption, when it is negative. Similarly, we do not need to distinguish between diffuse and specular lights. The term sp_0 may describe a diffuse source over the zone Z, as well as a constant specular reflection stemming from the same zone. But above all, the emphasis is put here on the *space variation* of the spectrum. It is introduced by the weight $\overline{\omega}(z)$, that depends on point z, but not on spectrum sp_1. This weight may bring into play cosines, when the angle of the incident beam varies, or the normal to a glossy surface, etc.

The three spectra sp, sp_0, and sp_1 are known only through the weighting functions that generate a (R, G, B) triplet. We use here the notation (R, G, B) in a canonical manner, i.e., it may designate the (X, Y, Z) coordinates of the CIE, or the perceptual system (L, M, S) [54], as well as the (Y, U, V) and (Y, I, Q) TV standards. In all cases it is a matter of *scalar products* of the spectra by such or such frequency weight. In particular, the white colour given by $r = g = b = 1$ can be obtained from a spectrum which is far from being uniform. We write

$$r(z) = \int sp(v;z)\xi(v)\,\mathrm{d}v = \int [sp_0(v) + \overline{\omega}(z)sp_1(v)]\xi(v)\,\mathrm{d}v = r_0 + r_1\overline{\omega}(z), \tag{18}$$

$$g(z) = \int sp(v;z)\chi(v)\,\mathrm{d}v = g_0 + g_1\overline{\omega}(z), \tag{19}$$

and

$$b(z) = \int s(v;z)\psi(v)\,\mathrm{d}v = b_0 + b_1\overline{\omega}(z), \tag{20}$$

where ξ, χ, and ψ are the three weighting functions that generate the primary colours r, g, and b.

As sp_0 and sp_1 are power spectra, they induce *intensities* r, g, and b. Now, in the above histograms, the L_1 norm applies to the *video variables* $r' = r^{1/\gamma}$, $g' = g^{1/\gamma}$, and $b' = b^{1/\gamma}$ (if we neglect the behaviour near the origin). Then we draw from Rel. (18)

$$r'(z) = [r(z)]^{1/\gamma} = [r_0 + \overline{\omega}(z)r_1]^{1/\gamma}, \tag{21}$$

with similar derivations for the video green and blue bands.

Is the linearly regionalized model able to explain the alignments in video histograms, despite the gamma correction? For the sake of simplicity, we will tackle this question by fixing the order of the video bands as $r' \geqslant g' \geqslant b'$, and $m' \geqslant g'$. Then we have

$$3m'(z) = r'(z) + g'(z) + b'(z),$$
$$2s'(z) = 2r'(z) - g'(z) - b'(z).$$

5.1. Alignments with the dark point

In the *clearness/saturation* histograms in L_1 norm, several alignments are in the prolongation of the point $(0,0)$, of zero clearness and saturation. The shadow regions of the "rubber ring" image illustrate this situation.

Suppose that, in the relation Eq. (17) which defines the LR spectrum, the term $\mathrm{sp}_0(v;z)$ is identically zero. Then $r(z)$ reduces to $\overline{\omega}(z)r_1$, which gives

$$r'(z) = r^{1/\gamma} = \overline{\omega}^{1/\gamma} r_1^{1/\gamma} = \overline{\omega}^{1/\gamma}(z) r_1',$$

with similar derivations for two other bands. Therefore, we have

$$3m'(z) = \overline{\omega}^{1/\gamma}(z)\left[r_1^{1/\gamma} + g_1^{1/\gamma} + b_1^{1/\gamma}\right] = 3\overline{\omega}^{1/\gamma}(z)m_1'$$

and

$$2s'(z) = 2r'(z) - g'(z) - b'(z) = \overline{\omega}^{1/\gamma}(z)\left[2r_1' - g_1' - b_1'\right],$$

hence $m'(z)s_1' = m_1's'(z)$. In the space E of the intensities, we find in the same way that $m(z)s_1 = m_1 s(z)$. Therefore the nullity of the constant spectrum $\mathrm{sp}_0(v)$ entails that both m' and s' on the one hand, and m and s on the other one, are proportional. Each *video alignment* indicates a zone where the *intensities spectrum* varies proportionally from one point to another.

5.2. Alignments with the white point

The "rubber ring" image generates also an alignment along a line going through the point $(1,0)$, i.e., the point with maximum clearness and zero saturation. That suggests to suppose the spectrum $\mathrm{sp}_0(v;z)$ constant and equal to 1, and in addition that the three colors r_1, g_1, b_1 are not identical (if not, the saturation s' should be zero). We have

$$r(z) = 1 + \overline{\omega}(z)r_1 \tag{22}$$

and the two sister relations for $g(z)$ and $b(z)$. Under gamma correction, $r(z)$ becomes

$$r'(z) = (1 + \overline{\omega}(z) r_1)^{1/\gamma}.$$

Now, to say that the alignment is close to a point of maximum clearness comes down to saying that r_1, g_1, and b_1 are small with respect to 1, or, using the limited expansion, that

$$r'(z) = 1 + \frac{\overline{\omega}(z)}{\gamma} r_1 + \varepsilon(r_1), \tag{23}$$

hence $m'(z) \simeq 1 + \frac{\overline{\omega}(z)}{\gamma} m_1$ and $s'(z) \simeq \frac{\overline{\omega}(z)}{\gamma}[2r_1 - g_1 - b_1]$. We observe that the two conditions $r_1 \geqslant 0$ and $r'(z) \leqslant 1$, jointly with Rel. (23) imply that the coefficient $\overline{\omega}(z)$ is negative. Moreover, as the three colours r_1, g_1, and b_1 are distinct, the condition $s'(z) \geqslant 0$ implies in turn that the quantity $2r_1 - g_1 - b_1$ is strictly negative. By putting $\sigma_1 = -(2r_1 - g_1 - b_1) > 0$ (σ_1 is not the saturation at point z_1), we obtain the following linear relation with positive coefficients

$$m'(z) \simeq 1 - \frac{m_1}{\sigma_1} s'(z). \tag{24}$$

As in the previous case, but without approximations, the mean $m(z)$ and the saturation $s(z)$ of the intensities are linked by the same Eq. (24): it is a direct consequence of Eq. (22). Again, both video and intensity histograms carry the same information, and indicate the zones of almost white reflections.

5.3. Alignments with a grey point

There appears in some images, as "Ana Blanco", series of parallel alignments. Their supports go through points of (quasi) zero saturation but their clearness is strictly comprised between 0 and 1. The interpretation we just gave for the case of reflections extends to such a situation. It is still assumed that $r_0 = g_0 = b_0$, but with $0 < r_0 \leqslant 1$, and that the terms $\overline{\omega}(z) r_1$, $\overline{\omega}(z) g_1$, and $\overline{\omega}(z) b_1$ are small with respect to r_0. Then we have,

$$r'(z) = (r_0 + \overline{\omega}(z) r_1)^{1/\gamma} \simeq r_0^{1/\gamma} + r_0^{1/\gamma - 1} \frac{\overline{\omega}(z)}{\gamma} r_1,$$

and the two sister relations for g' and b'. Hence

$$m'(z) \simeq r_0^{1/\gamma} + r_0^{1/\gamma - 1} \frac{\overline{\omega}(z)}{\gamma} m_1,$$

$$s'(z) \simeq -r_0^{1/\gamma - 1} \frac{\overline{\omega}(z)}{\gamma} \sigma_1,$$

so that, finally

$$m'(z) \simeq r_0^{1/\gamma} - \frac{m_1}{\sigma_1} s'(z). \tag{25}$$

When the colour component (r_1, g_1, b_1) remains unchanged, but that the grey component (r_0, g_0, b_0) takes successively various values, then each of them induces an alignment of the same slope $\frac{m_1}{s_1}$. Rel. (25) extends, without approximation, to the histograms of the intensities themselves.

Finally, we derive from Eq. (11) that, in the three cases, the hue remains *constant* in each alignment zone.

6. Application of LR model for a full example

We present in this section a final example which illustrates the possibilities of the LR model for image interpretation and segmentation.

On the top of Fig. 10 are given three colour images from the same scene, acquired under three different illumination conditions: (a) daylight, (b) fluorescent light, and (c) tungsten light bulb. The images have been obtained using a standard high quality digital camera. Starting from these images, the aim is to study the variation of the clearness/saturation distributions according to the different illuminations. In previous sections, we have studied the alignments from the video variables C'/S', but in this example we would like to compare with the physical variables C/S, after removing the gamma correction (Fig. 10 depicts these histograms).

We can observe, on the one hand, that the zones corresponding to the relative achromatic objects (low saturations, e.g., the wall paper) appear closer to the vertical axis for "white" illuminants than for the tungsten light (which enhances pinkish objects). On the other hand, the distribution of the chromatic objects and especially, the presence of alignments in both kind of histograms, is very instructive.

Two alignments with the dark point, and different slope, appear in the histogram C/S for the images (a) and (b), which verify the LR model. We designate by *Slope 1* the alignment of highest inclination and by *Slope 2* the other one. In the video histograms C'/S' the alignments are less marked than in the intensities histogram C/S, even if the proportionality of the clearness and the saturation is partially verified. They appear more as "wide stripes" or "rounded clouds". In the case of the image (c), presenting shadows and graduated shadings, the module of the two alignments is low in C/S, and only one appears clearly for the video histogram. More precisely, the image zones corresponding to the alignments have been segmented to interpret better the meaning for the images.

Let us to start by the image (a). In fact, both alignments do not follow an exact straight line. Each alignment is composed of two linear segments: one starting from the dark point, named *Slope 1l* and *Slope 2l*, and a second prolongation of the first one (*Slope 1h* and *Slope 2h*). In Fig. 11 are given the segmentations for the four pieces of alignment. Note that the alignment *Slope 1h* is relatively wide and for *Slope 2h* the points follow a "curved line". We remark that both segments of *Slope 1* correspond to the same objects: blue box and red elements (in order to separate them, the histogram clearness/hue can be used), but *Slope 1l* marks the dark zones and *Slope 1h* the bright ones. A similar analysis of *Slope 2l* and *Slope 2h* yields the dark yellow (shadow of yellow cylinder) and bright yellow (shading

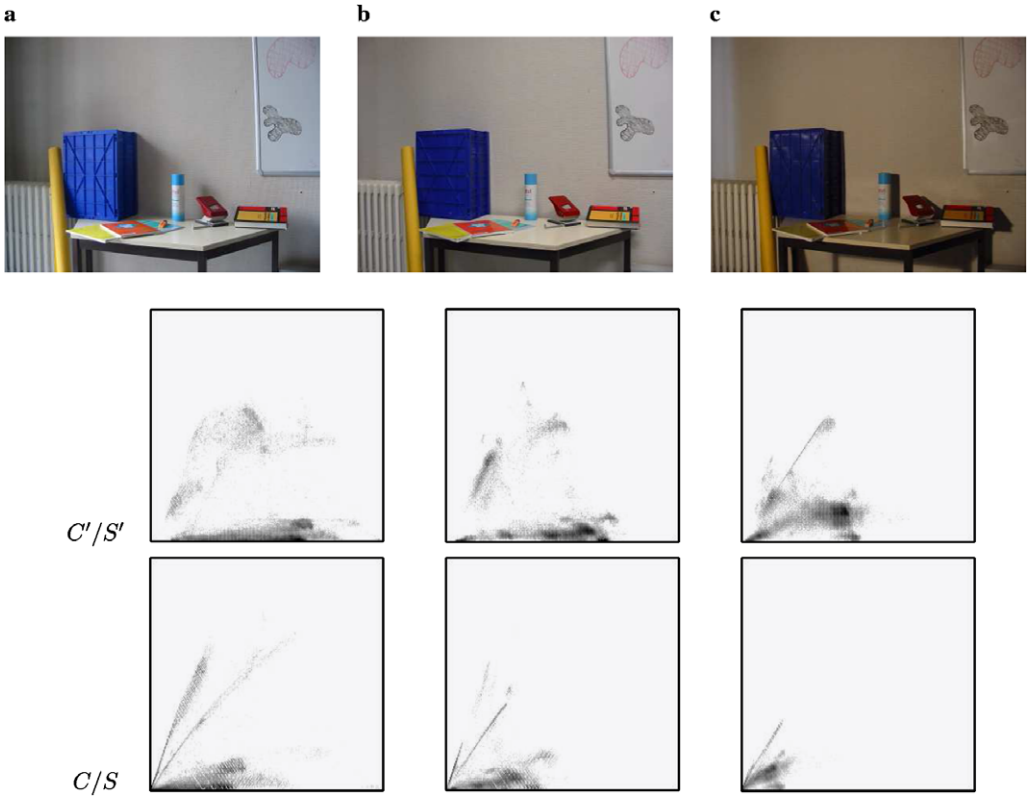

Fig. 10. Three colour images from the same scene, acquired under three different illumination conditions: (a) daylight, (b) fluorescent light, and (c) tungsten light bulb. For each image are given the clearness/saturation histograms for the video variables C'/S' and, after removing the gamma correction, for the physical variables C/S.

of yellow cylinder and of yellow book) objects, respectively. From the video histograms C'/S', only two partial linear segments are visible. The *Slope 1* (respectively *Slope 2*) here corresponds partially to *Slope 1l* (respectively *Slope 2l*) of C/S. That is, only the lines of intensity which go through point $(0,0)$ have equivalent video lines, which is coherent with the analytical analysis of previous section.

In the case of the image (b), the alignment of highest slope is composed of two noncontinuous segments (*Slope 1l* and *Slope 1h*) which extract correctly the blue box and the red/orange objects (more homogenous in terms of light intensity). The yellow objects are also more homogeneous in this image, and the associated alignment only comprises a long segment (*Slope 2*). This time, the equivalent structures in video histograms are wide stripes, more difficult to analyse. Again, the need to remove the effect of the gamma correction is here justified in order to use the LR model of light (Fig. 12).

Finally, for the image (c), the alignment of *Slope 2* extracts the yellow cylinder, and has a corresponding linear structure in the video histogram. The *Slope 1* of C/S allows to extract the chromatic blue/red objects as well as image regions of shadow on the wall (its hue is close to magenta); however the associated region in the gamma corrected histogram is merged with other cluster and very difficult to separate (Fig. 13).

7. Circular centered operators on the unit circle for the hue

The unit circle has no order of importance, and no dominant position. In mathematical terms, this signifies that we cannot construct a lattice on the unit circle, unless assigning it an arbitrary origin. This is a severe verdict against morphological treatments (i.e., operators relying on lattices) when we use them on the unit circle. However, is it really impossible to bypass this interdiction? If we consider the standard morphological operators, three paths at least seem possible, that Hanbury and Serra investigated in [22]. Only the first path is recalled here, which is based on increments. This approach is interesting to transfer to the circular case the class of operators which bring into play only increments, such as gradients, top-hats, medians, etc. It is possible also to make a lattice of labels by adding a bottom element (meaning no hue) and a top element (meaning hue conflict). If one considers the hue circle and the "no hue" bottom element, one has a complete inf-semi-lattice [25]. See details in the work of Ronse and Agnus on morphology for label images [39].

Let $a : E \rightarrow \mathcal{C}$ be an angular function, we fix an origin a_0 on the unit circle $\mathcal{C}$ with centre o by, for example, choosing the topmost point, and indicate the points a_i on the circle by their curvilinear coordinate in the trigonometric sense between 0 and 2π from a_0. Given two points a and a', we

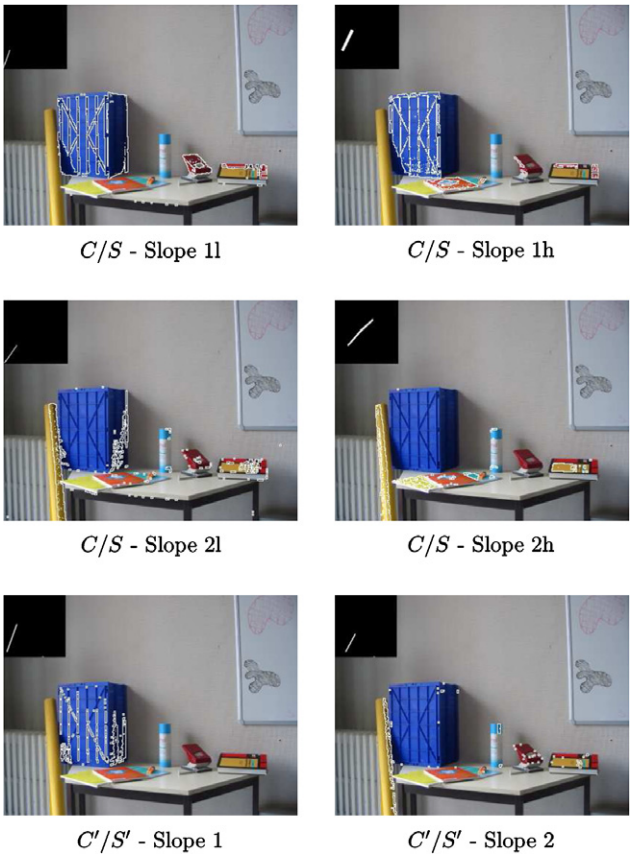

Fig. 11. Segmentation of alignments of image Fig. 10(a). The corresponding alignment is shown in the upper left corner of the colour image.

use the notation $a \div a'$ to indicate the absolute value of the acute angle aoa', i.e.,

$$a \div a' = \begin{cases} |a - a'| & \text{if } |a - a'| \leqslant \pi \\ 2\pi - |a - a'| & \text{if } |a - a'| \geqslant \pi \end{cases} \quad (26)$$

If the a_i are digital values between 0 and 255 (for example), the expression "$\leqslant\pi$" becomes "$\leqslant$127", and "2π" becomes "255". Rel. (26) appears in [37] applied also to the treatment of the hue band of colour images.

Therefore it is possible to fix an origin on the hues denoted by h_0, associated to a "colour of reference". We can now define a h_0-centered hue function by computing $f_H(x) \div h_0$. The function $(f_H \div h_0)(x)$ is a partially ordered set (i.e., two hue values can have the same angular distance

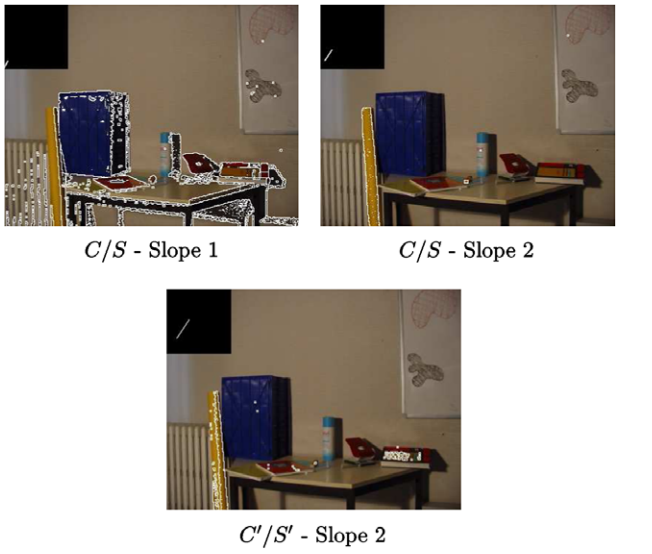

Fig. 13. Segmentation of alignments of image Fig. 10(c). The corresponding alignment is shown in the upper left corner of the colour image.

to the origin). In order to have a total order we need to impose an additional priority (absolute distance to the origin h_0 in the sense of the unit circle), see [3]. This totally ordered complete lattice is denoted by $\mathcal{T}^{h \div h_0}$.

7.1. Circular hue gradient

We know that in the Euclidean space $\mathbb{R}^n$, to determine the modulus of the gradient, at point x, of a numerical differentiable function f, one considers a small sphere $S(x,r)$ centered on x with radius r. Then one takes the supremum of the increments $|f(x) - f(y)|$, where y describes the small sphere S, i.e., $g(x,\ r) = [\sup\{|f(x) - f(y)|,\ y \in S(x,\ r)\}]/r$. Finally, one determines the limit of the function $g(x,\ r)$ as r tends to zero. This limit exists as the function f is differentiable in x. In the two-dimensional digital case, it is sufficient to apply the previous relation, taking for $S(x,\ r)$ the unit ball centered on x (square or hexagon). This is the classic Beucher algorithm for the gradient [7].

Consider now an image h of hues or of directions, $h : E \to \mathcal{C}$. As the previous development only involves increments, we can transpose the previous gradient to the circular function h by replacing all the $|h(x) - h(y)|$ by $|h(x) \div h(y)|$. This transposition then defines the modulus

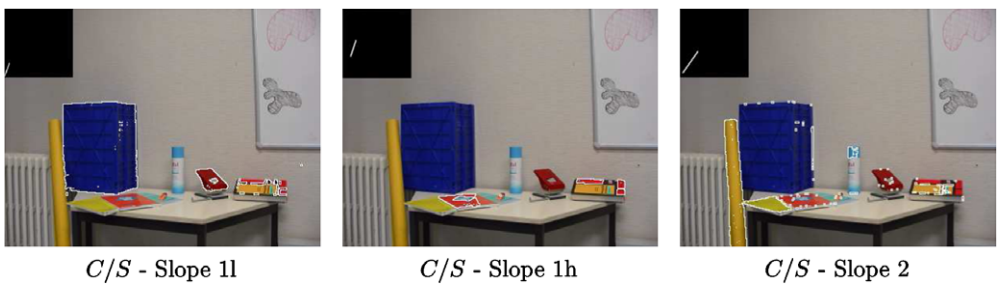

Fig. 12. Segmentation of alignments of image Fig. 10(b). The corresponding alignment is shown in the upper left corner of the colour image.

of the gradient of the circular distribution. For example, in $\mathbb{Z}^n$, $K(x)$ indicates the set of neighbours at distance one from point x, hence

$$\varrho^{\circ}(h)(x) = [\sup\{|h(x) \div h(y)|, y \in K(x)\}] \quad (27)$$

The angular gradient is invariant to rotations of the pixel values.

7.2. Circular hue top-hat

In the sense of Meyer [32], there are two versions of the top-hat for numerical functions ($f : E \to \mathcal{T}$). The *white top-hat* is the residue of the initial image f and an opening $\gamma_B(f)$, i.e., $\rho_B^+(f) = f - \gamma_B(f)$ (extracting bright structures) and the *black top-hat* is the residue of a closing $\varphi_B(f)$ and f, i.e., $\rho_B^-(f) = \varphi_B(f) - f$ (extracting dark structures).

This numerical residue involves increments and hence can be defined to circular functions as the hue component. The circular centered top-hat of an angular function is defined by (see [22] for full details):

$$\rho_B^{\circ}(h(x)) = \sup\{\varepsilon^{\circ}(z), z \in B(x)\}, \quad (28)$$

with $\varepsilon^{\circ}(h(x)) = \{\inf[h(y) \div h(x), \ y \in B(x)]\}$, $B(x)$ is the structuring element centered at x. This top-hat extracts fast angular variations of the function h.

8. Colour top-hats for feature extraction

Starting from these grey-level transformations, let us propose a series of definitions for the top-hat of a colour image $\mathbf{f}$ from a 1-HCS representation.

- The *chromatic top-hat* is given by

  $$\rho_B^C(\mathbf{f}) = [f_S \times \rho_B^{\circ}(f_H)] \vee \rho_B^+(f_S), \quad (29)$$

  where the product sign "×" means a pointwise multiplication of function values. This operator extracts the fast variations of colour regions on a saturated colour background (i.e., saturated colour peaks on uniform colour regions) and the fast variations of saturated colour regions on an achromatic (unsaturated) background (i.e., saturated colour peaks on achromatic regions).
- The *white-achromatic top-hat* is the absolute value difference between the chromatic top-hat and the global bright top-hat,

  $$\rho_B^{A+} = |\rho_B^C - \rho_B^{\uparrow}|, \quad (30)$$

  where the *global bright top-hat* is calculated by

  $$\rho_B^{\uparrow}(\mathbf{f}) = \rho_B^+(f_L) \vee \rho_B^-(f_S). \quad (31)$$

  It characterizes the fast variations of bright regions (i.e., positive peaks of clearness) and the fast variations of achromatic regions on a saturated background (i.e., unsaturated peaks: black, white and grey on colour regions).
- The *black-achromatic top-hat* is the difference $\rho_B^{A-} = |\rho_B^C - \rho_B^{\downarrow}|$, where the *global dark top-hat* is obtained by $\rho_B^{\downarrow}(\mathbf{f}) = \rho_B^-(f_L) \vee \rho_B^-(f_S)$. Dually, it tackles the fast variations of dark regions (i.e., negative peaks of clearness) and the fast variations of achromatic regions on a saturated background. The term $\rho_B^-(f_S)$ appears in both $\rho_B^{\uparrow}$ and $\rho_B^{\downarrow}$ to achieve symmetrical definitions.

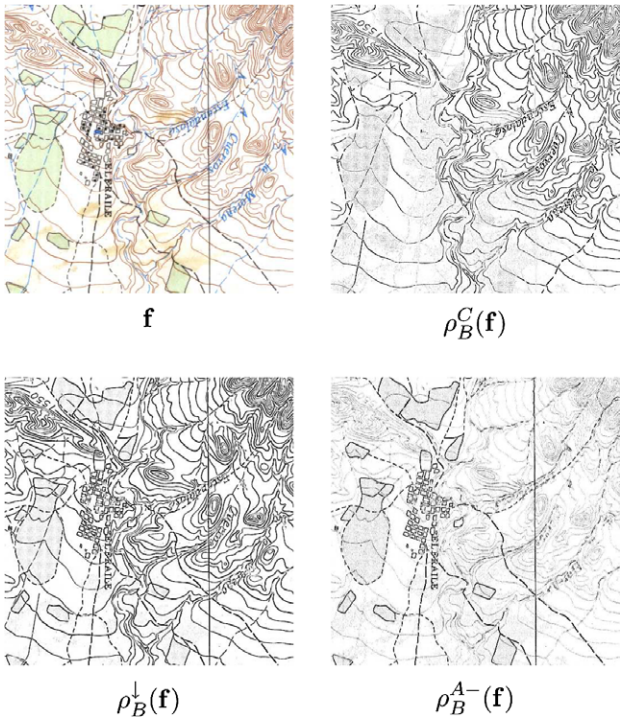

Fig. 14. Colour top-hat's for detail extraction in a cartographic image.

Fig. 14 shows the colour top-hats of a cartographic image [2]. The extracted objects are different and certain kinds of details are better defined on one top-hat than on the other. Their contributions are consequently complementary. This preliminary classification of image structures can make easier the subsequent post-processing of extracted details. Usually, the top-hat transformation is accompanied by a thresholding operation, in order to binarize these details. Besides the problem for finding the optimal threshold value, if we apply a thresholding transformation directly on the top-hat image, it is probably that the results will be very noisy. We have developed an algorithm based on the area opening to simplify and make more robust the binarization of these colour top-hats. In Fig. 15 is given an example.

9. Segmentation by weighting saturation I: colour gradient

Consider a colour function $\mathbf{f}$, and its 1-HCS representation in L_1 norm. The circular gradient of the hue of $\mathbf{f}$ can be inserted into a global gradient $\varrho(\mathbf{f})$ which takes the three components of $\mathbf{f}$ into account. There are number of such gradients [1,3], but the above comments on the saturation in L_1 norm representation suggests us to construct a *barycentric* gradient, where the L_1 saturation balances the effects of clearness and hue gradients, i.e.,

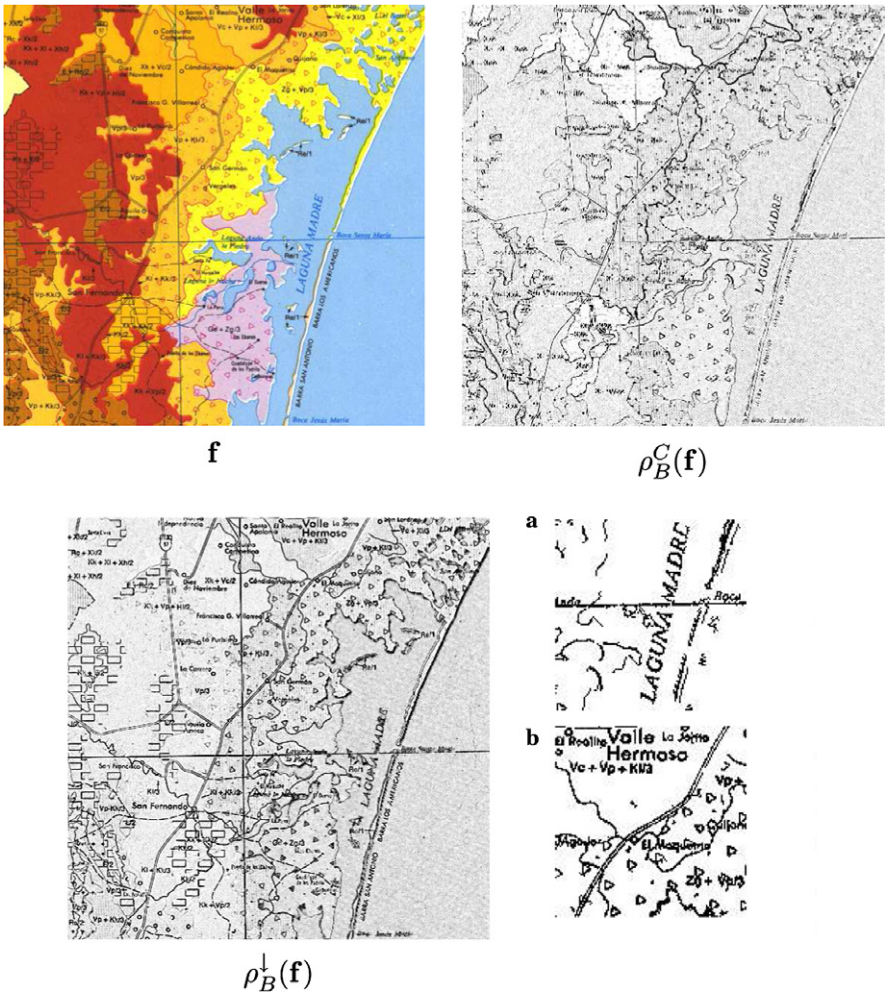

Fig. 15. Cartographic image, and colour top-hat's. The binary images (a) and (b) show details extracted from $\rho_B^C(\mathbf{f})$ and $\rho_B^{A+}(\mathbf{f})$, respectively, after area opening-based thresholding.

$$\varrho(\mathbf{f}) = f_S \times \varrho^{\circ}(f_H)(x) + (1 - f_S) \times \varrho(f_C). \tag{32}$$

It is well known that the watershed of the gradient $\varrho(f)$ of a numerical function f provides us with the contours of f [33,7]. This property extends to the vector functions of the space, because then the term $\varrho(\mathbf{f})$ is still a numerical function ($\varrho(\mathbf{f}) : E \to \mathcal{T}$), which is sufficient for the theory. Other similar more complex saturation-based colour gradients have been proposed in the literature [9].

We can then apply to the function $\mathbf{f}$ and his gradient according to Rel. (32) the Beucher's *segmentation* method of known as "*waterfalls*" (hierarchical nonparametric generalization of the watershed [8]), which proceeds as follows:

(1) to calculate the colour gradient $g = \varrho(\mathbf{f})$ (g is a positive and bounded function, i.e., $0 \leqslant g(x) \leqslant t_{\mathrm{Max}}$);
(2) to compute its watershed transformation $W(g)$, which yields a first segmentation of the image;
(3) to assign to each segmented class the median (or the mean) of the red, green and blue components of function $\mathbf{f}$ inside the corresponding class in question, obtaining a new colour image;
(4) to build a new function h: $h(x) = g(x)$ iff $x \in W(g)$ and $h(x) = M$ iff $x \in W^c(g)$ (h is obviously greater than g) and then, g is reconstructed by geodesic erosions from h, i.e., $\widehat{g} = \gamma^{\mathrm{rec}}(g, h)$. The minima of the resulting function $\widehat{g}$ correspond to the significant markers of the original g, moreover, the watershed transform of $\widehat{g}$ produces the catchment basins associated with these significant markers;
(5) by iterating the procedure described above, a hierarchy of segmentations is obtained.

We take the standard "parrots" image, Fig. 2, to illustrate this approach by applying several iterations of waterfalls operator. For this image, the best fit occurs at the fourth level of the hierarchy. That led to the mosaics of Fig. 16. At first sight the major forms seem preserved. However a real loss of information appears when one superimposes the partitions on the initial image. The first three levels contain too many insignificant zones, and we must await the fourth level for a better partition, but not really satisfactory. Small structures as the eyes have

Fig. 16. On the left side, four iterations of the "waterfalls" hierarchy involving the mosaic images. On the right, partitions associated to the hierarchy, superimposed on the initial image.

disappeared, some unrealistic borders have appeared on the feathers, etc.

10. Segmentation by weighting saturation II: merging of partitions

In fact, the previous approach suffers of a too early reduction of the information, which becomes scalar from the beginning, when one calculates the first $\varrho(\mathbf{f})$. We will better preserve the relevant information using the following two steps segmentation procedure:

(1) to *separately* segment the clearness, the saturation and the hue in a correct quantitative colour representation;
(2) to combine the obtained partitions of the clearness and of the hue by means of that of the saturation: the latter is taken as a *criterion* for choosing at each place either the clearness class, or the hue one.

The three bands of the "parrots" image of Fig. 2(a), in L_1 representation, are depicted in Fig. 2(b–d). Each band is segmented by the *jump connection* algorithm [43].

Consider a function $f : E \to \mathcal{T}$ (the arrival space $\mathcal{T}$ is metric and totally ordered). In this segmentation algorithm, one groups into common classes all points x where $f(x)$ differs by less than k from an extremum in the same connected component, these classes are then withdrawn from the image, and one iterates the region partition until the space is filled. A detailed algorithm of this segmentation method can be found in [45]: basically, we need to accumulate the nested connected components obtained by taking successive one-jump images; and the elementary one-jump connection is achieved by means of the reconstruction of the image using as marker its shifted (down or up) version by constant k (which varies geometrically, i.e., $k = 1, 2, 4, 8, \ldots$). The method depends only on the jump positive value k, called the range or the jump. This allows to build up multiscale segmentation schemes. This segmentation algorithm has already shown its performance to segment textures (e.g., chromatin of lymphocytes [3]).

As the parameter k increases, the over-segmentations reduce, but in compensation heterogeneous regions appear. A satisfactory balance seems to be reached for k between 10 and 20 (for 8-bits images). However, some small areas to be removed still remain. One can filter out the classes of surface area smaller than 50, and reconstitute the partition using the skeleton by influence zones or as well by an algorithm of fusion of regions [18]; the two methods lead to more or less identical results, and we have applied the fusion of regions.

The proposed approach for the clearness is applied also for the hue. The only difference comes from the fact that we must choose an origin (necessarily arbitrary) of the hues. We obtain the segmentation results depicted in Fig. 17, giving the examples for $k = 10$ and $k = 20$, and area merging for regions of 50 pixels. The contours superimposed on the original image are also shown.

10.1. Synthetic partition

How to combine the two partitions of images A_c and A_h from Fig. 17? The idea consists in splitting the saturation image into two sets X_s and X_s^c of high and low saturations, respectively, and in assigning the hue partition to the first set, and the clearness one to the second. A class of the synthetic partition is either the intersection of a clearness class with the low saturation zone X_s^c, or the intersection of a hue class with the high saturation zone X_s. If the classes of the clearness, the hue, and the synthetic partition at point x are denoted by $A_c(x)$, $A_h(x)$, and $A(x)$, respectively, we have

$$A(x) = A_c(x) \cap X_s^c \quad \text{when } x \in X_s^c$$
$$A(x) = A_h(x) \cap X_s \quad \text{when } x \in X_s.$$

The simplest way to generate the set X_s consists, of course, in thresholding the saturation image at value u_S. But this risks to result in an irregular set X_s, with holes, small particles, etc. Preferably, one can start from the mosaic image of the saturation provided by the same segmentation algorithm as for the the hue and the clearness (Fig. 18(a)). An

Fig. 17. Grey segmentations using the jump connection algorithm with modules of jump $k = 10$ and $k = 20$, and area merging for regions of 50 pixels: partition of clearness A_c, and partition of hue, A_h. On the left, the partitions are depicted in false colours, and on the right, the corresponding contours are superimposed on the original colour image.

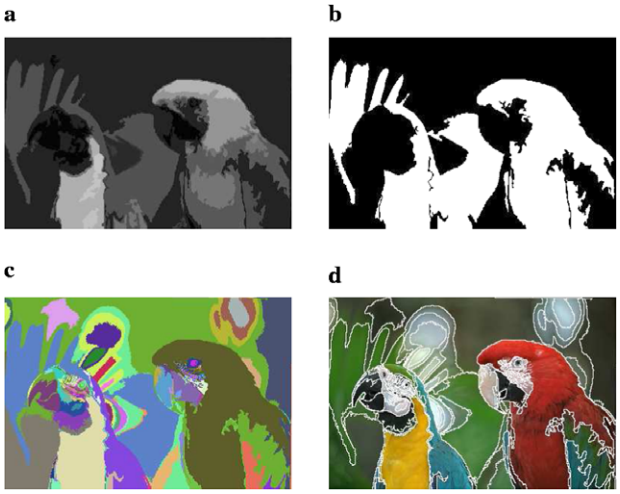

Fig. 18. (a) Segmentation of the saturation of "parrots" (presented in grey tones) obtained by means of the jump connection algorithm $k = 20$ as for Fig. 17, (b) optimal threshold of image (a) at values $\geqslant 45$, (c) final synthetic partition from $A_c(x)$ and $A_h(x)$ of Fig. 17, (d) contours of synthetic partition superimposed to the initial image.

optimal threshold on the saturation histogram determines the value for the a-chromatic/chromatic separation (Fig. 18(b)). We finally obtain the composite partition depicted in Fig. 18(c), which is excellent.

10.2. A few remarks on the method

Here are a few remarks to complete the discussion on the limitations and advantages of the saturation-based merging of partitions.

- Several alternatives for colour segmentation based on physical models, e.g., Shafer's dichromatic reflection model [46,27,31] which has widely been used by various authors [16,17,52]. Other physical models have also been proposed such as the unichromatic reflection model by Healey [24] or the difference scaling of gloss model by Obein et al. [36].
  Using these image physical models Gevers, Smeulders, and Stokman can distinguish the shadow, highlight and material edges or boundaries for the objects of a colour image [19,20]. See also [55,49]. Moreover, one is able to define image descriptors invariant to illumination colour [19,40] and [6].
- The jump connection works on scalar functions. Therefore, it is needed to fix an origin on the hue before applying this segmentation method. As rough approximation, it can be taken the red according to the usual practice (i.e., red is 0°). However, in order to minimise the effect of this choice we propose to study the hue histogram (of significant colours) and compute the anti-dominant hue value as adapted origin. After clustering, the anti-dominant hue is defined as the central angle of the less significant class of circular histogram [3].
  Other methods of partition of the hue which do not need an origin could be employed.
- Fig. 19 gives an example of variation in the number of regions and in the total perimeter of regions according to the value of k, for the images of clearness and hue of "parrots". Obviously these two parameters decrease when the value of k increases, moreover the curves of variation are very similar for different images. These curves associated to a hierarchy can be used to choose the level k if the input value is for instance the number of regions.
  The critical parameter u_S of the method, for the achromatic/chromatic separation, is automatically calculated for each colour image. Typically, the histogram of the saturation (or of its mosaic after jump connection partition) is multi-modal. It is however possible to define an optimal threshold value u_S between the two main modes of the histogram. The algorithm is divided into three steps (details in [3]): (1) smooth histogram, (2) selection of the two most relevant peaks using the dynamics of the maxima (or the two highest contrast extinction values), and (3) obtain the best histogram partition u_S with respect to a criterion of variance.

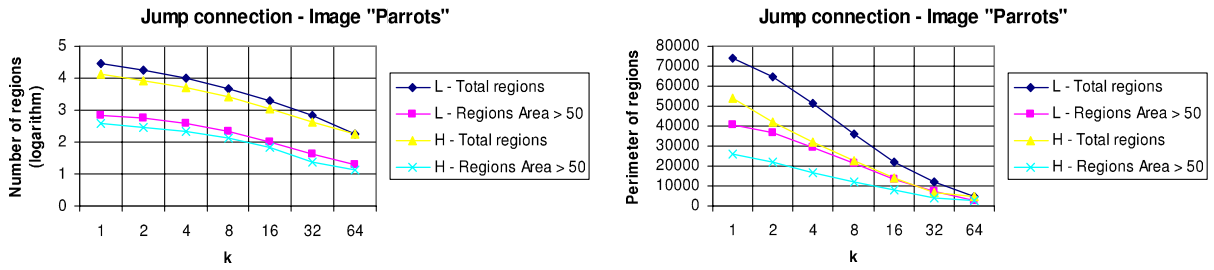

Fig. 19. Variation of two parameters in a hierarchy by jump connection (according to the value of k) for image "parrots": number of regions (in logarithmic scale) and total perimeter of regions, comparing also with the partitions after removing the regions of surface area <50 pixels.

- Similarly to the watershed-based methods of segmentation, the behaviour of the jump connection in presence of noise becomes irregular. In this case, the image must be filtered using typically connected filters, like the levellings [34], which suppress details/textures/noises (associated to irrelevant extrema) but preserve the contours of the remaining structures.
- The L*a*b* colour system has been especially constructed to yield a colour representation whose principal advantage is the perceptual uniformity. This colour representation is widely applied in segmentation, by using the Euclidean distance for clustering, gradients, etc. We have already compared the results of waterfalls-based segmentation using the derived L*a*b* gradient [1]. However, the transformation from RGB to L*a*b* space is done by first transforming to the XYZ space, and then to the L*a*b* space [57]. The XYZ coordinates are depending on the device-specific RGB primaries and on the white point of illuminant. In most situations, the illumination conditions are unknown and therefore a hypothesis must be made (i.e., the most common option is the CIE D_{65} daylight illuminant). Besides this incertitude, our method of merging of partitions can not be applied in the L*a*b* space: how to combine the three partitions (two chromatic for *a and b* and an achromatic for L*)? The same remark is valid for RGB and other colour representation such as YUV. Here lies the main advantage of the saturation variable, which allows combining the chromatic/achromatic components.

11. Experimental segmentation results: berkeley segmentation dataset and benchmark (BSDB)

To complement the experimental part of this article, we have applied both colour segmentation algorithms, presented in previous sections, on a selection of images from a reference database of colour images, the "Berkeley segmentation dataset and benchmark" (BSDB) [30], available on line. The BSDB includes 12000 hand-labeled segmentations of natural greyscale/colour images (300 available publicly for tests). The fact of evaluating our results on the BSDB allows us to compare the performance of the approach developed with a reference human-based segmentation and in addition, a later comparison among the various techniques of segmentation suggested by the scientific community.

The results are shown in Figs. 20–22 (the image number corresponds to that assigned in the BSDB). For both methods, all the images were segmented using the same typical parameters: (1) iteration 4 of the waterfalls and (2) jump connection with $k = 20$ and a surface area >50 (obviously, the saturation was optimally thresholded for each case).

As we can observe, for most of the shown images, the results obtained with both morphological methods are satisfactory compared to the manual reference: the most important chromatic/achromatic regions are well detected (i.e., the associated mosaics give us an acceptable minimal colour representation of image contents). In general, the iteration of the watershed on the colour gradient gives quite large regions but which can cut homogeneous areas or which can lose small details. The merging of jump connections provides results with a reasonable trade-off between the great homogeneous areas and the small significant details. As it was expected, the poorest performances always correspond to the most textured images (it should be reminded that the images are treated without any pre-filtering, which could reduce textures notably). On the other hand, we can remark also that the hand segmented images integrate a huge amount of semantic knowledge of the objects by the human subjects who drew the contours, and therefore it is difficult to be absolutely compared with automatic methods based only on spatial/colorimetric features.

12. Conclusions

We shall conclude, first, that the use of polar colour spaces, when clearness and saturation are defined by norms, ensure an appropriate representation for quantitative processing tasks, working directly on gamma-corrected digital colour images. These representations are well adapted to segmentation or to filtering algorithms, for averaging colours, computing distances, etc. On the other hand, we conclude that for studies aiming at modelling or exploiting the physical properties of colours and

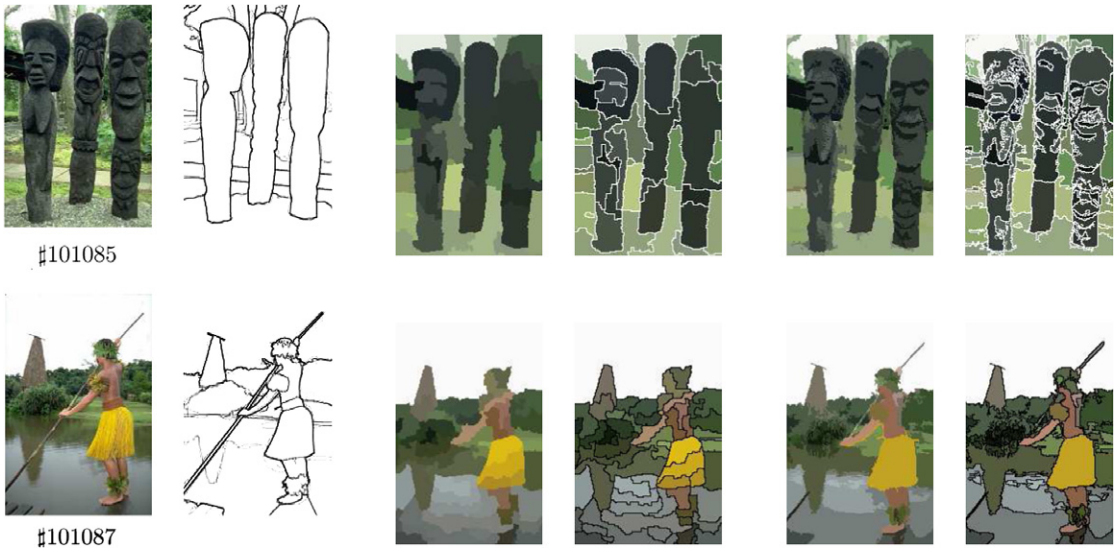

Fig. 20. Results of segmentation for both present segmentation algorithms on image of the BSDB. From left to right: original colour images, hand reference segmentations, segmentations by waterfalls (mosaic images and associated contours), segmentations by jump connection (mosaic images and associated contours).

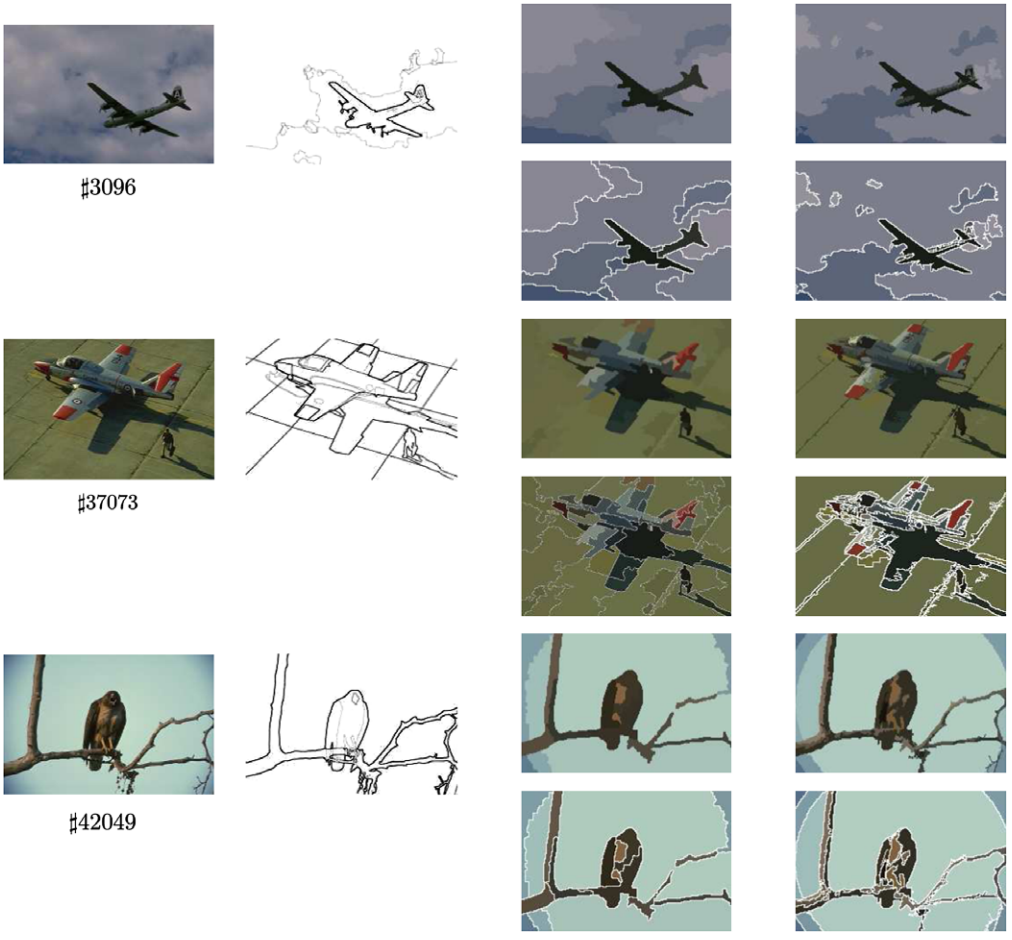

Fig. 21. Results of segmentation for both present segmentation algorithms on image of the BSDB. Idem. Fig. 20.

light, the effect of the gamma correction must be removed for a better consistency with the physical structure of light.

In the second part, we have introduced new marginal colour operators which take advantage of an adaptive combination of the chromatic and the achromatic (or the

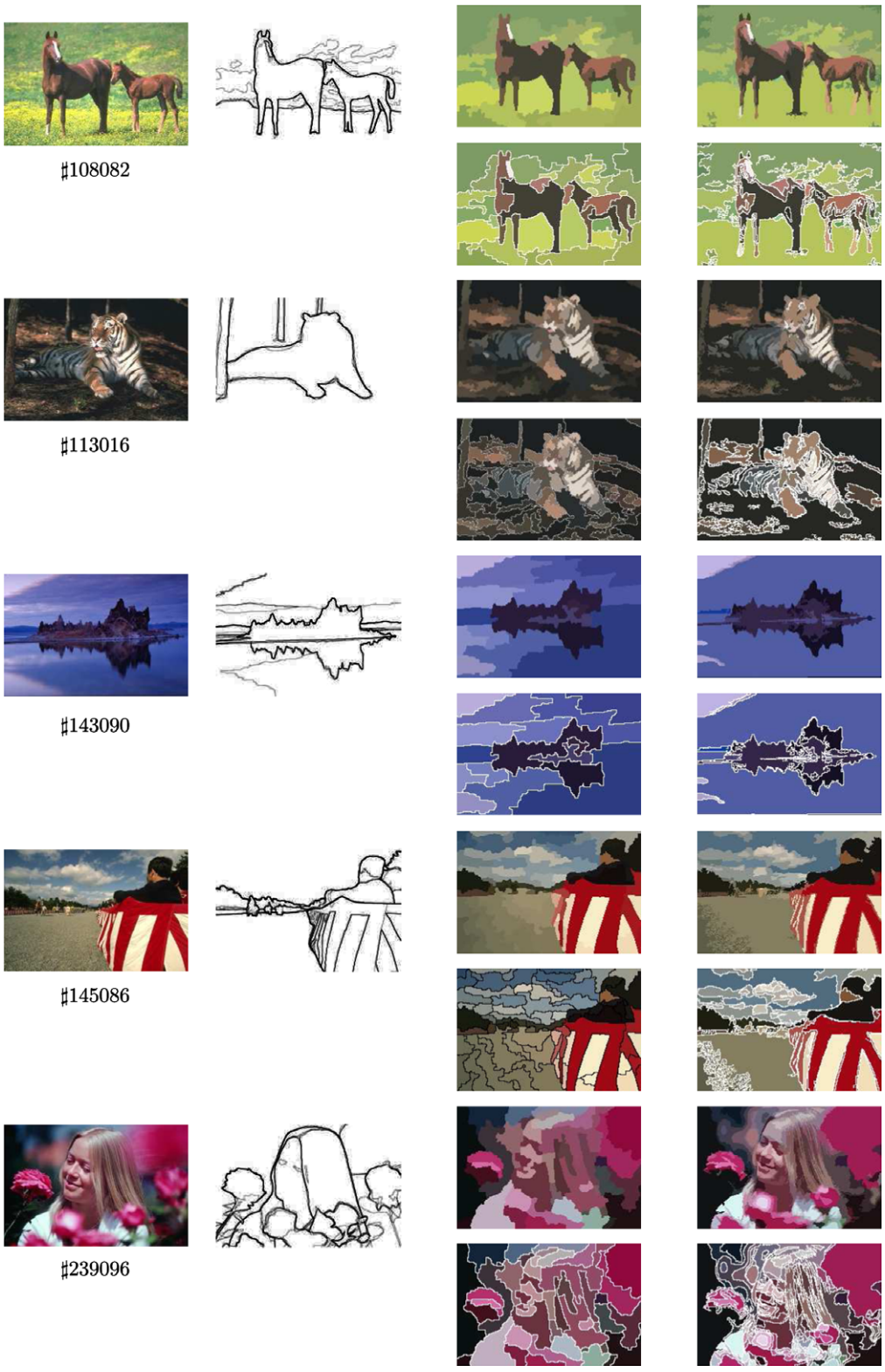

Fig. 22. Results of segmentation for both present segmentation algorithms on image of the BSDB. Idem. Fig. 20.

spectral and the spatial-geometrical) components. Moreover, these separable mechanisms allow the application of classical grey level implementations with simple complexity elements to be added.

The studies which compose this paper require imperatively a correct quantitative definition of the polar representation and in particular of the saturation. In addition, such colour representation allows us an intuitive

interpretation of the effects of the operators (as usual in mathematical morphology).

The above studies illustrate also a certain approach to segmentation. We have attempted to show that maximum partitions can be "added", conditioned by one another, can form hierarchies, etc. in order to express segmentations in the sense of [45], whose main theorems underlay all the above examples.

Acknowledgements

The authors gratefully thank the reviewers and Prof Ch. Ronse for the valuable comments and the improvements they suggested.

References

[1] J. Angulo, J. Serra, Color segmentation by ordered mergings, in: Proceedings of IEEE International Conference on Image Processing (ICIP'03), IEEE, vol. 2, Barcelona, Spain, September 2003, pp. 125–128.

[2] J. Angulo, J. Serra, Mathematical morphology in color spaces applied to the analysis of cartographic images, in: Proceedings of International Workshop Semantic Processing of Spatial Data (GEOPRO'03), IPN-Mexico Ed, 2003, pp. 59–66.

[3] J. Angulo, Morphologie mathématique et indexation d'images couleur. Application à la microscopie en biomédecine. Thèse de Doctorat, Centre de Morphologie Mathématique, Ecole des Mines, Paris, Décembre 2003.

[4] J. Angulo, J. Serra, "Traitements des images de couleur en représentation luminance/saturation/teinte par norme L_1", Traitement du Signal 21 (6) (2004) 583–604.

[5] J. Angulo, Unified morphological color processing framework in a lum/sat/hue representation, in: C. Ronse, L. Najman, E. Decencière (Eds.), Mathematical Morphology: 40 Years On (Proceedings of the 7th International Symposium on Mathematical Morphology – ISMM'2005), Kluwer, 2005, pp. 387–396.

[6] D. Berwick, S.W. Lee, Spectral gradients for color-based object recognition and indexing, Computer Vision and Image Understanding 99 (2004) 28–43.

[7] S. Beucher, F. Meyer, The morphological approach to segmentation: the watershed transformation, in: Dougherty (Ed.), Mathematical Morphology in Image Processing, Marcel-Dekker, New York, 1992, pp. 433–481.

[8] S. Beucher, Watershed, hierarchical segmentation and waterfall algorithm, in: Mathematical Morphology and its Applications to Image and Signal Processing, Proceedings of ISMM'94, Kluwer, 1994, pp. 69–76.

[9] T. Carron, P. Lambert, Color edege detector using jointly Hue, Saturation and Intensity, in: Proceedings of IEEE International Conference on Image Processing (ICIP'94), IEEE, 1994, pp. 977–981.

[10] T. Carron, Segmentations d'images couleur dans la base Teinte-Luminance-Saturation: approche numérique et symbolique, Thèse de Doctorat, Université de Savoie, 1995.

[11] H.D. Cheng, X.H. Jiang, Y. Sun, J. Wang, Color image segmentation: advances and prospects, Pattern Recognition 34 (2001) 2259–2281.

[12] G. Choquet, Topology, Academic Press, New York, 1966.

[13] M. Celnek, A color clustering technique for image segmentation, Computer Vision, Graphics and Image Processing 52 (1990) 145–170.

[14] Commission Internationale de l'Eclairage (CIE), Colorimetry, second ed. CIE Publication No. 15.2, Vienna, 1986.

[15] C.-H. Demarty, S. Beucher, Color segmentation algorithm using an HLS transformation, in: Proceedings of the International Symposium on Mathematical Morphology (ISMM '98), Kluwer, 1998, pp. 231–238.

[16] G.D. Finlayson, G. Schaefer, Solving for colour constancy using a constrained dichromatic reflection model, International Journal of Computer Vision 42 (2001) 127–144.

[17] G.D. Finlayson, R. Xu, Illuminant and gamma comprehensive normalisation in log rgb space, Pattern Recognition Letters 24 (2003) 1679–1690.

[18] L. Garrido, P. Salembier, D. Garcia, Extensive operators in partition lattices for image sequence analysis, Signal Processing 66 (2) (1998) 157–180.

[19] Th. Gevers, A.W.M. Smeulders, Color based object recognition, Pattern Recognition 32 (1999) 53–464.

[20] Th. Gevers, H. Stokman, Classifying color edges in video into shadow-geometry, highlight, or material transitions, IEEE Transactions on Multimedia 5 (2003) 237–243.

[21] J. Goutsias, H.J.A.M. Heijmans, K. Sivakumar, Morphological operators for image sequences, Computer Vision and Image Understanding 62 (1995) 326–346.

[22] A. Hanbury, J. Serra, Morphological operators on the unit circle, IEEE Transactions on Image Processing 10 (12) (2001) 1842–1850.

[23] A. Hanbury, J. Serra, Colour image analysis in 3D-polar coordinates, in: Proceedings of DAGM symposium, Vienna, April 2003.

[24] G. Healey, Using color for geometry-insensitive segmentation, Journal of the Optical Society of America A 6 (6) (1989) 920–937.

[25] H.J.A.M. Heijmans, R. Keshet, Inf-semilattice approach to self-dual morphology, Journal of Mathematical Imaging and Vision 17 (2002) 55–80.

[26] J. Kender, Saturation, hue and normalized color: calculation, digitization effects, and use, Master's Thesis, Dept. of Computer Science, Carnegie-Mellon University, 1976.

[27] G.J. Klinker, S.A. Shafer, T. Kanade, The measurement of highlights in color images, International Journal of Computer Vision 2 (1988) 7–32.

[28] P. Lambert, T. Carron, Symbolic fusion of luminance-hue-chroma features for region segmentation, Pattern Recognition 32 (1999) 1857–1872.

[29] H. Levkowitz, G.T. Herman, GLHS: a generalized lightness, hue and saturation color model, Graphical Models and Image Processing 55 (4) (1993) 271–285.

[30] D. Martin, C. Fowlkes, D. Tal, J. Malik, A database of human segmented natural images and its application to evaluating segmentation algorithms and measuring ecological statistics, in: Proceedings of the 8th International Conference Computer Vision (ICCV'01), vol. 2, Vancouver, Canada, 2001, pp. 416–423. <http://www.cs.berkeley.edu/projects/vision/grouping/segbench//>.

[31] B.A. Maxwell, S.A. Shafer, Physics-based segmentation of complex objects using multiple hypotheses of image formation, Computer Vision and Image Understanding 65 (1997) 269–295.

[32] F. Meyer, Constrast features extraction, in: Chermant (Ed.), Quantitative Analysis of Microstructures in Materials Science, Biology and Medecine, Riederer Verlag, 1977, pp. 374–380.

[33] F. Meyer, S. Beucher, Morphological segmentation, Journal of Visual Communication and Image Representation 1 (1) (1990) 21–46.

[34] F. Meyer, Levelings, Image simplification filters for segmentation, Journal of Mathematical Imaging and Vision 20 (2004) 59–72.

[35] I. Newton, A theory concerning light and colors, Philosophical Transactions of the Royal Society, No. 80, 1671/71, 3075–3087.

[36] G. Obein, K. Knoblauch, F. Viénot, Perceptual scaling of the gloss of a one-dimensional series of painted black samples, Perception 31 (Suppl.) (2002) 65.

[37] R.A. Peters II. Mathematical morphology for angle-valued images, in: Non-Linear Image Processing VIII, vol. SPIE 3026, 1997, pp. 84–94.

[38] Ch. Poynton, Digital video and HDTV – algorithms and interfaces, Morgan Kaufmann, Elsevier Science, San Francisco, 2003.

[39] Ch. Ronse, V. Agnus, Morphology on label images: flat-type operators and connections, Journal of Mathematical Imaging and Vision 22 (2005) 283–307.

[40] V. Risson, Application de la Morphologie Mathématique à l'analyse des conditions d'éclairage des images couleur, Thèse de Doctorat, Centre de Morphologie Mathématique, Ecole des Mines, Paris, Décembre 2001.
[42] J. Serra, Espaces couleur et traitement d'images, Rapport Technique CMM-Ecole des Mines de Paris, N-34/02/MM, Octobre 2002.
[43] J. Serra, Connectivity for sets and functions, Fundamenta Informaticae 41 (2000) 147–186.
[44] J. Serra, Morphological segmentations of colour images, in: C. Ronse, L. Najman, E. Decencière (Eds.), Mathematical Morphology: 40 Years On (Proceedings of the 7th International Symposium on Mathematical Morphology – ISMM'2005), Kluwer, 2005, pp. 151–176.
[45] J. Serra, A lattice approach to image segmentation, Journal of Mathematical Imaging and Vision 24 (2006) 83–130.
[46] S.A. Shafer, Using color to separate reflection components from a color image, Color Research and Applications 10 (4) (1985) 210–218.
[47] T.Y. Shih, The reversibility of six geometric color spaces, Photogrammetric Engineering and Remote Sensing 61 (10) (1995) 1223–1232.
[48] A.R. Smith, Color gammet transform pairs, Computer Graphics 12 (3) (1978) 12–19.
[49] J. Stander, R. Mech, J. Ostermann, Moving cast shadows detection for object segmentation, IEEE Transactions on Multimedia 1 (1999) 65–76.
[51] H. Talbot, C. Evans, R. Jones, Complete ordering and multivariate mathematical morphology: algorithms and applications, in: Proceedings of the International Symposium on Mathematical Morphology (ISMM'98), Kluwer, Dordrecht, 1998, pp. 27–34.
[52] S. Tominaga, Surface identification using the dichromatic reflection model, IEEE Transactions on Pattern Analysis and Machine Intelligence 13 (7) (1991) 658–670.
[53] A. Tremeau, N. Borel, A region growing and merging algorithm to color segmentation, Pattern Recognition 30 (7) (1997) 1191–1203.
[54] A. Tremeau, Ch. Fernandez-Maloigne, P. Bonton, Image numérique couleur, Ed. Dunod, Paris, 2004.
[55] W.T. Tsang, P.W.H. Tsang, Suppression of false edge detection due to specular reflection in color images, Pattern Recognition Letters 18 (1997) 165–171.
[56] S.S. Wilson, Theory of matrix morphology, IEEE Transaction on Pattern Analysis and Machine Intelligence 14 (1992) 636–652.
[57] G. Wysecki, W.S. Stiles, Color Science: Concepts and Methods, Quantitative Data and Formulae, second ed., John Wiley, New York, 1982.

13.2 Publication II : J. Angulo. "Morphological colour operators in totally ordered lattices based on distances. Application to image filtering, enhancement and analysis". *Computer Vision and Image Understanding*, Vol. 107, No. 2–3, 56–73, 2007.

Available online at www.sciencedirect.com
ScienceDirect
Computer Vision and Image Understanding 107 (2007) 56–73
Computer Vision and Image Understanding
www.elsevier.com/locate/cviu

Morphological colour operators in totally ordered lattices based on distances: Application to image filtering, enhancement and analysis

Jesús Angulo *

Centre de Morphologie Mathématique—Ecole des Mines de Paris, 35, rue Saint-Honor, 77305 Fontainebleau, France

Received 14 April 2006; accepted 13 November 2006
Available online 12 January 2007
Communicated by Rastislav Lukac

Abstract

The extension of mathematical morphology operators to multi-valued functions, and in particular to colour images, is neither direct nor general. In this paper, a generalisation of distance-based and lexicographical-based approaches is proposed, allowing the extension of morphological operators to colour images for any colour representation (e.g., RGB, LSH and L*a*b*) and for any metric distance to a reference colour. The performance of the introduced operators is illustrated by means of different applications: colour feature extraction using openings (closings) by reconstruction, colour gradients for segmenting, colour denoising by the centre operator and colour enhancement by the contrast mapping. Examples from natural colour images and biomedical microscopic colour images are given.

Keywords: Colour mathematical morphology; Colour distance; Multivariate ordering; Colour feature extraction; Colour noise removal; Colour contrast enhancement; LSH; L*a*b*

1. Introduction

Mathematical morphology is the application of lattice theory to spatial structures. This means that the definition of morphological operators needs a totally ordered complete lattice structure, i.e., the possibility of defining an ordering relationship between the points to be processed. Therefore, the application of mathematical morphology to colour images is difficult due to the vectorial nature of the colour data. For a general account on mathematical morphology the interested reader should refer to [44,21], whereas vector morphology is extensively discussed in [46,17,50].

Multivariate data ordering is not straightforward, because there is no notion of natural ordering in a vector field, as opposed to one-dimensional (scalar) case [8]. To overcome the problem, the following four approaches to ordering multichannel samples, such as colour data, have been identified [8,40,31]. In *marginal ordering* (M-ordering) the components of the colour vectors are ordered independently (pointwise ordering). However, this approach produces new colour vectors which were not originally present in the input image, thus often introducing colour artifacts into the output image [46]. To preserve the input colour vectors, the *conditional ordering* (C-ordering) approach, also known as lexicographic ordering, is frequently used. The C-ordering produces the ordered set of the colour vectors according to the ordering of one component or more generally, some marginal components selected sequentially according to different conditions. When all the components are used, the C-ordering is a total ordering. Note that this approach does not use the full vectorial nature of the input. The *partial ordering* or P-ordering is based on the partition of the vectors into groups, such that the groups can be distinguished with respect to rank or extremeness. This is computed by using convex-hull like

* Fax: +33 1 64 69 47 07.
E-mail address: jesus.angulo@ensmp.fr
URL: http://cmm.ensmp.fr/~angulo

1077-3142/$ - see front matter © 2007 Elsevier Inc. All rights reserved.
doi:10.1016/j.cviu.2006.11.008

sets. The *reduced ordering* or R-ordering which performs the ordering of vectors according to some scalars, computed from the components of each vector with respect to different measure criteria, typically distances or projections onto a reduced space (using for instance the principal component analysis). The application of P- or R-orderings also preserves the input colour vectors.

As discussed in the sequel, the above ordering approaches have been used to support morphological operations on colour data. For example, in [46], Serra suggested an intermediate ordering between an M-ordering and a C-ordering. Weber and Acton [54] introduced an M-ordering in HSV colour space by using a rotation in the hue band (shifting the H discontinuity by k-means clustering).

The C-ordering has been also widely studied in the framework of colour morphology, especially in a luminance/saturation/hue representation, by Peters [39], by Talbot et al. [50], by Hanbury and Serra [18], by Ortiz et al. [37], by Louverdis et al. [28], and by Angulo [5]. The C-ordering has been also applied in the RGB representation by Iwanowski and Serra [23], and by Angulo and Serra [4]; or in the Lab representation by Hanbury and Serra [20]. Vardavoulia et al. [52] defined also vectorial median filters with C-orderings.

A P-ordering is the starting point, in a fuzzy logic paradigm, for a method proposed by Köppen et al. [25] to implement Pareto fuzzy colour morphology. Another P-ordering has been introduced by Mojsilovic and Soljanin [35], using a sampling based on the Fibonacci succession. Gibson et al. [16] used a local convex hull to define the pixels of a region as extreme/non-extreme, which is necessary to build morphological connected operators.

The R-ordering has been widely used in colour denoising applications (i.e., vector median filters and other statistical filters) by Astola et al. [7], by Pitas and Tsakalides [40], by Trahanias et al. [51], and more recently by Lukac et al. [31,32]. The R-ordering has been also used to build morphological operators by means of Euclidean distances by Comer and Delp [15] and by Ortiz et al. [36]; or using Mahalanobis distances by Goutsias et al. [17], and by Al-Otum [1]. Sartor and Weeks [55,43] proposed a combination of an R-ordering and a C-ordering; in fact, our present approach can be considered as a generalisation of this interesting study. In [27], J. Li and Y. Li proposed an R-ordering based on fuzzy first principal component in RGB colour space, and in [56], Wheeler and Zmuda a R-ordering with vector projections in RGB. And in [59], Zaharescu et al. explored R-orderings based on a geometrical interpretation of a triangle representation of colours.

Other alternative total orderings have been studied. Goutsias et al. [17] used the matrix Wilson theory [57]. Chanussot and Lambert [14] suggested an approach based on space-filling curves. In [12], Busch and Eberle proposed a pseudo-morphology for colour-coded (or labeled) images by introducing the ordering according semantic rules (a C-ordering). It is also possible to define an ordering on labels, such as the hue component image, by adding a bottom element (meaning no hue) and a top element (meaning hue conflict), see details in the work of Ronse and Agnus [42].

The aim of this paper is to generalise the distance-based approaches and the lexicographical approaches, in order to propose a generic framework allowing the extension of morphological operators to colour images for any colour representation and metric distance. The proposed approach is a combination of R-ordering and C-ordering, the R-ordering being based on the distance to a reference colour and a subsequent lexicographical ordering used to resolve any ambiguities. In fact, we introduce a generalisation of mathematical morphology to multivariate functions, according to a distance-to-origin-based interpretation of the notion of total ordering between the points of a complete lattice. Whilst the use of a combination of sub-orderings to produce a total ordering is not new, the approach presented here does have some distinctive features, in particular its applicability to different colour spaces/distances and the use of any reference colour (including colours other than black and white).

The rest of the paper is organised as follows. In Section 2 we give a reminder on some notions of colour representation and colour distances. In Section 3, a discussion of our framework of total orderings using distances completed with lexicographical cascades is given. Then, in Section 4, we introduce the definition on the derived main morphological colour operators. The performances of these transformations for filtering, noise reduction, enhancement and feature extraction are illustrated in Section 5. Finally, the conclusions and perspectives are discussed in Section 6.

2. Colour representations and colour distances

The most direct way to manipulate digital colour images is to work on the RGB colour space. However, the RGB colour representation has some drawbacks: strongly correlated components, lack of human interpretation, non-uniformity, etc. A polar representation with the variables luminance, saturation and hue (lum/sat/hue) allows us to solve these problems. The HLS system is the most popular lum/sat/hue triplet. In spite of its popularity, the HLS representation (and another classical one like HSV) often yields unsatisfactory results, for quantitative processing at least, because its luminance and saturation expressions are not norms, so average values or distances, are falsified. The drawbacks of the HLS system can be overcome by various alternative representations, according to different norms used to define the luminance and the saturation. The reader can find a comprehensive analysis of this question by Angulo and Serra [6]. In particular, we have used in this paper the lum/sat/hue in norm L_1 [47,48,6]. In the present study, we have also worked with the $L^*a^*b^*$ colour space, the classical representation in colorimetry, which presents a perceptual uniformity (useful for segmentation). The transformations between RGB and $L^*a^*b^*$ are well-known [24,58].

Let f be a grey-level image, $f : E \to \mathscr{T}$, in that case $\mathscr{T} = \{t_{\min}, t_{\min}+1, \cdots, t_{\max}\}$ (in general $\mathscr{T} \subset \mathbb{Z}$ or $\mathbb{R}$) is

an ordered set of grey-levels and typically for the digital 2D images $E \subset \mathbb{Z}^2$ is the support of the image. We denote by $\mathscr{F}(E,\mathscr{T})$ the functions from E onto $\mathscr{T}$. If $\mathscr{T}$ is a complete lattice, then $\mathscr{F}(E,\mathscr{T})$ is a complete lattice too. The theoretical framework of mathematical morphology is nowadays phrased in terms of complete lattices and operators defined on them. Given the three sets of scalar values $\mathscr{T}^l,\mathscr{T}^s,\mathscr{T}^h$, we denote by $\mathscr{F}(E,[\mathscr{T}^l\otimes\mathscr{T}^s\otimes\mathscr{T}^h])$ or $\mathscr{F}(E,\mathscr{T}^{\mathrm{lsh}})$ all colour images in a luminance/saturation/hue representation ($\mathscr{T}^{\mathrm{lsh}}$ is the product of $\mathscr{T}^l,\mathscr{T}^s,\mathscr{T}^h$, i.e., $\mathbf{c}_i\in\mathscr{T}^{\mathrm{lsh}}\Longleftrightarrow\mathbf{c}_i=\{(l_i,s_i,h_i);l_i\in\mathscr{T}^l,s_i\in\mathscr{T}^s,h_i\in\mathscr{T}^h\}$). We denote the elements of $\mathscr{F}(E,\mathscr{T}^{\mathrm{lsh}})$ by $\mathbf{f}$, where $\mathbf{f}=(f_L,f_S,f_H)$ are the colour component functions. Using this representation, the value of $\mathbf{f}$ at a point $x\in E$, which lies in $\mathscr{T}^{\mathrm{lsh}}$, is denoted by $\mathbf{f}(x)=(f_L(x),f_S(x),f_H(x))$. In a similar way, the colour images in a RGB representation or in a L*a*b representation are respectively elements of the product sets $\mathscr{F}(E,\mathscr{T}^{\mathrm{rgb}})$ and $\mathscr{F}(E,\mathscr{T}^{L^*a^*b^*})$. Note that the sets $\mathscr{T}^r$, $\mathscr{T}^g$, $\mathscr{T}^b$ are complete totally ordered lattices. The sets $\mathscr{T}^l,\mathscr{T}^s$ corresponding to the luminance and the saturation are also totally ordered lattices (likewise the components of L*a*b* $\mathscr{T}^{L^*}$, $\mathscr{T}^{a^*}$ and $\mathscr{T}^{b^*}$). The hue component is an angular function defined on the unit circle, $\mathscr{T}^h=\mathscr{C}$, which has no partial ordering. Hence, the hue needs to be processed in a special way. Let $h:E\to\mathscr{C}$ be an angular function, the angular difference [39,19] is defined as

$$h_i \div h_j = \begin{cases} |h_i-h_j| & \text{if} \quad |h_i-h_j|\leqslant 180^\circ \\ 360^\circ-|h_i-h_j| & \text{if} \quad |h_i-h_j|>180^\circ \end{cases} \tag{1}$$

Therefore, it is possible to fix an origin on the hues denoted by h_0, associated to a "colour of reference". We can now define a h_0-centered hue function by computing $f_H(x)\div h_0$. The function $(f_H\div h_0)(x)$ is a partially ordered set (i.e., two hue values can have the same angular distance to the origin). In order to have a total order we need to impose an additional priority (absolute distance to the origin h_0 in the sense of the unit circle), see [2]. This totally ordered complete lattice is denoted by $\mathscr{T}^{h\div h_0}$.

Let $\mathbf{c}_k=(c_k^U,c_k^V,c_k^W)$ be the colour point k in any generic colour space UVW (e.g., in LSH $\mathbf{c}_k=(c_k^L,c_k^S,c_k^H)$). We can now define the colour distance between two colour vectors i and j as $||\mathbf{c}_i-\mathbf{c}_j||_{\Delta}^{\mathrm{UVW}}$ where Δ is a particular metric.

The family of Minkowski metric distances $d_L(\mathbf{c}_i,\mathbf{c}_j)=(\sum_{n=1}^{3}|c_i^n-c_j^n|^L)^{1/L}=||\mathbf{c}_i-\mathbf{c}_j||_L$, is the most commonly used measure to quantify colour distances. The most popular members of this class of metrics are obtained when $L=1$ (city-block distance), $L=2$ (Euclidean distance) and $L=\infty$ (chessboard distance). The Mahalanobis distance is a special case of the quadratic-form generalised distance metric in which the transform matrix is given by the covariance matrix $\mathbf{\Gamma}$ obtained from a training set of data that represents the reliability or scale of the measurement in each direction. The Mahalanobis distance between two vectors is given by $\|\mathbf{c}_i-\mathbf{c}_j\|_M=(\mathbf{c}_i-\mathbf{c}_j)^T\mathbf{\Gamma}^{-1}(\mathbf{c}_i-\mathbf{c}_j)$.

Any of the above recalled metrics can be applied to colour vectors according to the different colour space representations, e.g., in RGB using L_2 we have $||\mathbf{c}_i-\mathbf{c}_j||_2^{\mathrm{RGB}}=\sqrt{(c_i^R-c_j^R)^2+(c_i^G-c_j^G)^2+(c_i^B-c_j^B)^2}$. The L_2 distance in L*a*b* is particularly used in image processing, indeed the perceptual difference between two colours in L*a*b* is given by their Euclidean distance. Other more sophisticated colour distances have been proposed in the literature [31]. From the mathematical morphology point of view, some issues must be taken into account. As pointed out above, the functions associated with the RGB components, with the L*a*b* components (although the ordering for chromatic components a* and b* is hardly meaningful), and with the luminance and saturation components of the LSH representation are complete totally ordered lattices, but not the hue. Therefore, for all the colour metric distances in LSH, the term associ-ated to the hue must use the angular difference, e.g., $||\mathbf{c}_i-\mathbf{c}_j||_1^{\mathrm{LSH}}=|c_i^L-c_j^L|+|c_i^S-c_j^S|+|c_i^H\div c_j^H|$.

Nevertheless, due to the instability of the hue component for the low saturation points (which is an important issue to build hue-based distances, gradients, ordering, etc.) this last distance is useless. In order to cope with this drawback, the different solutions are generally based on a weighting of the hue by the saturation [13,18,5]. We propose to use the simplest technique, multiplying the angular difference by the average saturation, i.e., $\frac{(c_i^S+c_j^S)}{2}|c_i^H\div c_j^H|$. As suggested in [13], other more sophisticated saturation-based weighing functions can be applied (e.g., sigmoid). Another more interesting way to compute colour distances in LSH representation involves working in polar coordinates, i.e., $||\mathbf{c}_i-\mathbf{c}_j||_2^{\mathrm{LSH}}=\sqrt{(c_i^L-c_j^L)^2+(c_i^S)^2+(c_j^S)^2-2c_i^Sc_j^S\cos(c_i^H\div c_j^H)}$. We suggest to use this last colour distance.

Before applying these colour distances to define morphological operators, a relevant analysis of the alternative distances shall be made. Firstly, the L_∞ norm distances could cause serious artefacts in the filtered colour images, since colour vectors will be ordered according to only one of the components, which can change for a set of points. We can suppose that the results according to L_1 or L_2 will be relatively similar. In fact, the Mahalanobis distance can be interpreted as their generalisation with the advantage of setting different weights for the components. Moreover, for the sake of simplicity of this paper, we consider that in the three colour representations the components are statistically independent and we can rewrite the Mahalanobis distance as a weighting distance, i.e., $||\mathbf{c}_i-\mathbf{c}_j||_{M(\omega_1,\omega_2,\omega_3)}^{\mathrm{UVW}}=\omega_1(c_i^U-c_j^U)^2+\omega_2(c_i^V-c_j^V)^2+\omega_3(c_i^W-c_j^W)^2$.

3. Colour total orderings using distances completed with lexicographical cascades

We have previously studied in depth the extension of morphological operators to colour images based on lexicographical cascades from a LSH representation [2,5]. Fig. 1

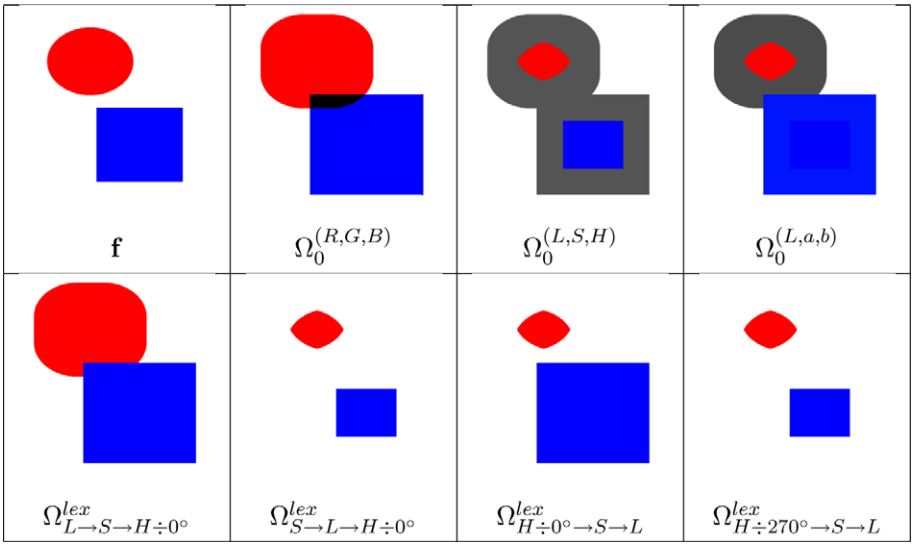

Fig. 1. Comparison of colour erosion for the image **f** (the structuring element B is a square of size $n = 35$), $\varepsilon_{\Omega,nB}(f)$, using different orderings Ω: three examples of marginal orderings Ω_0 in the RGB, LSH and L*a*b* colour spaces and four examples of total lexicographic-based orderings Ω^{lex} in LSH giving the priority to the luminance, or to the saturation, or to the h_0-centred hue (origins in the red 0° and in the purple 270°). (For interpretation of the references to color in this figure legend, the reader is referred to the Web version of this article.)

shows a comparison of colour erosion for the image **f**, using different orderings Ω. Namely, three examples of marginal orderings Ω_0 in the RGB, LSH and L*a*b* colour spaces and four examples of total lexicographic-based orderings Ω^{lex}. We observe the appearance of false colours when the marginal processing is applied, i.e., starting from two colours, the erosion gives another one; moreover the interpretation of results in LSH or L*a*b* becomes tricky. The original colours are preserved when the lexicographical cascades in LSH are used. In addition, giving the priority to the luminance (the background—brightest colour—is eroded), or to the saturation (the most saturated colours are eroded), or to the h_0-centred hue (origins in the red 0° and in the purple 270°), we can act on the structures mainly by the first component chosen in the cascade. The rationale behind the approach developed in this paper is more ambitious, proposing a generic framework valid for any colour representation and adding the flexibility of a "reference colour"-based morphology.

3.1. Distance-based grey-level morphology

The effect of morphological operators is determined by the specification of a partial ordering on the underlying image space, or from an image processing viewpoint, by the choice of what is foreground and what is background [22]. Usually, in grey-level images, the foreground corresponds to the bright levels (close to $t_{\max}$) and the background to the dark ones (close to $t_{\min}$). The associated partial ordering is the usual ordering $\leqslant$, which can be used to compute the infimun $\wedge$ and the supremum $\vee$ between a set of pixels B (structuring element). Then, the two basic morphological operators erosion and dilation applied to a grey-level image $f(x)$ are given by: $\varepsilon_B(f(x)) = \{f(y): f(y) = \wedge[f(z)],\ z \in B_x\}$ and $\delta_B(f(x)) = \{f(y): f(y) = \vee[f(z)],\ z \in B_x\}$, respectively.

After defining as reference the maximum grey value $g_0 = t_{\max}$, the classical greyscale morphology can be also interpreted in terms of distance to this reference:

- the dilation δ tends to move toward this reference, i.e., δ at point x is the grey value which has minimal distance to the reference g_0 within the structuring element B centered at x:

$$\delta_B(f(x)) = \{f(y) : y = \arg_z \inf(|f(z) - t_{\max}|), z \in B_x\}, \quad (2)$$

- the erosion ε tends to move away from g_0; i.e., ε is the value with maximal distance to g_0,

$$\varepsilon_B(f(x)) = \{f(y) : y = \arg_z \sup(|f(z) - t_{\max}|), z \in B_x\}. \quad (3)$$

In fact, this is only the convention that we have adopted. It is also possible to define the dilation (erosion) as the operation which tends to move away from (toward) the reference g_0, but the reference being the minimum grey value $g_0 = t_{\min}$. In this case, the dilation is given by

$$\delta_B(f(x)) = \{f(y) : y = \arg_z \sup(|f(z) - t_{\min}|), z \in B_x\},$$

and the dual expression defines the erosion.

Fig. 2 depicts an example of grey-level dilation and erosion in terms of distance to a reference value (R-ordering), when this reference is $t_{\max}$. We note the need of a reference value to fix a partial ordering. Actually, we can define two operators based on the distance between the grey-levels but which are independent from the reference. To do that, the cumulative distance of each point to the other points within the structuring element, i.e., $D(f(x)) = \sum_k d_E(f(x), f(k))$, $k \in B_x$, is firstly calculated. Then, the *distance-based median*

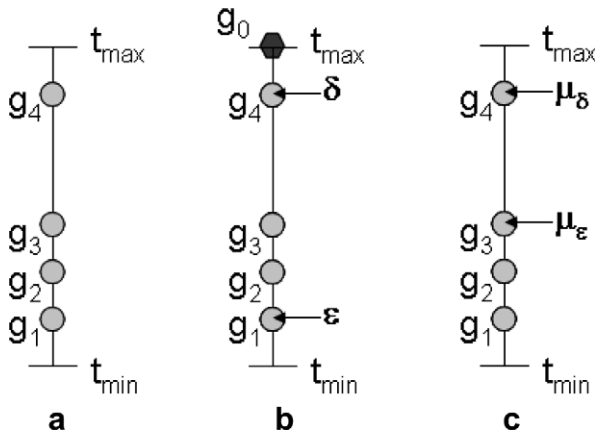

Fig. 2. Example of grey-level dilation and erosion in terms of distance to the reference value (R-ordering): (a) four original scalar points, $g_i \in \mathscr{T}$, to be processed, (b) corresponding values of dilation δ and erosion ε when the reference is $g_0 = t_{\max}$. In (c) are given the values of the median μ_ε and the anti-median μ_δ defined in terms of the cumulative distance.

is defined as $\mu_\varepsilon(f(x)) = \{f(y): y = \arg_z\inf(D(f(z)),\ z \in B_x\}$; and by duality, the *distance-based anti-median* is defined as $\mu_\delta(f(x)) = \{f(y): y = \arg_z\sup(D(f(z)), z \in B_x\}$. Fig. 2 gives also the corresponding example of this "eccentricity"-based operators. A classical generalisation of these definitions to multi-channel images leads to the vector median filters [7,40]. Several works, see for instance Plaza et al. [41], propose to use these two filters to define multispectral morphological operators, however, it is easy to see that the obtained operators are not an adjunction erosion/dilation. In particular, μ_ε and μ_δ do not commute with the infimum and supremum, respectively, a property underlying the definition of erosion and dilation. At the most, we can consider μ_ε and μ_δ as pseudo-morphological operators. We believe that any generalisation of morphological operators to multivariate functions (e.g., colour images) must be compatible with the definitions of these operators for univariate functions (grey-level images).

3.2. Total orderings associated with a reference colour

The paradigm of distance-to-reference-based grey morphology is directly applicable to colour images, after fixing the colour representation UVW, the reference colour $\mathbf{c}_0$ and the colour distance Δ, by defining the following ordering for two colour points:

$$\mathbf{c}_i <_{\mathbf{c}_0} \mathbf{c}_j \iff \|\mathbf{c}_i - \mathbf{c}_0\|_\Delta^{\mathrm{UVW}} > \|\mathbf{c}_j - \mathbf{c}_0\|_\Delta^{\mathrm{UVW}}. \tag{4}$$

But this is only a partial ordering or pre-ordering, i.e., two or more distinct colour vectors within the structuring element can be equidistant from the reference. This problem also arises in the grey-level case if the erosion and dilation are defined by the distance to a reference g_0 which is different from the bounds $t_{\max}$ or $t_{\min}$. For example, fixing $t_{\max} = 255$, $t_{\min} = 0$ and $g_0 = 100$, given two grey pixels $g_1 = 50$ and $g_2 = 150$, one has $|g_1 - g_0| = |g_2 - g_0|$ with $g_1 \neq g_2$ and consequently, the supremum/infimum between both pixels are not defined. An additional condition is needed to complete the ordering; for instance, fixing the following ordering: $g_i <_{g_0} g_j \iff (|g_i - g_0| > |g_j - g_0|)$ or $(|g_i - g_0| = |g_j - g_0|$ and $g_i > g_j)$. For the previous example, it is obtained that $g_1 = 50 >_{g_0} g_2 = 150$. More specifically, in order to have a total ordering for colour images we propose to complete the primary R-ordering of relation (4) with a lexicographical cascade.

The total Ω-ordering or $<_\Omega$ is defined as:

$$\mathbf{c}_i <_\Omega \mathbf{c}_j \iff \begin{cases} \|\mathbf{c}_i - \mathbf{c}_0\|_\Delta^{\mathrm{UVW}} > \|\mathbf{c}_j - \mathbf{c}_0\|_\Delta^{\mathrm{UVW}} & \text{or} \\ \|\mathbf{c}_i - \mathbf{c}_0\|_\Delta^{\mathrm{UVW}} = \|\mathbf{c}_j - \mathbf{c}_0\|_\Delta^{\mathrm{UVW}} & \text{and} \\ \quad \begin{cases} c_i^U < c_j^U & \text{or} \\ c_i^U = c_j^U \quad \text{and} \quad c_i^V < c_j^V & \text{or} \\ c_i^U = c_j^U \quad \text{and} \quad c_i^V = c_j^V \quad \text{and} \quad c_i^W < c_j^W \end{cases} \end{cases} \tag{5}$$

We denote, compactly, this lexicographical cascade by $\Omega \equiv \{\|\cdot\|_\Delta^{\mathrm{UVW}}, \mathbf{c}_0 = (c_0^U, c_0^V, c_0^W) \vdash (U \to V \to W)\}$. Moreover, in the examples given below, when the Mahalanobis distance $\|\cdot\|_{M(\omega_1,\omega_2,\omega_3)}^{\mathrm{UVW}}$ is applied, the component k of the reference colour $\mathbf{c}_0$ can be undefined (or unsignificant), which is denoted by "–", if the weight k is zero $\omega_k = 0$; e.g., $\|\cdot\|_{M(0,1,2)}^{\mathrm{UVW}}$, $\mathbf{c}_0 = (-,255,128)$.

In the ordering (5), after a comparison based on the Δ distance to c_0, the priority is given to the component U, then to V and finally to W. Obviously, it is possible to define other orders for imposing a dominant role to any other of the vector components. To simplify the number of alternatives, and based on the best results obtained from our previous works on lexicographical cascades, we propose to fix the ordering of the components for the three colour spaces representations as follows,

(1) in RGB: $\vdash(G \to R \to B)$,
(2) in LSH: $\vdash(L \to S \to -(H \div h_0))$, where the origin of the hues h_0 corresponds to the same as for $\mathbf{c}_0^{\mathrm{LSH}} = (l_0, s_0, h_0)$; and $h_i \div h_0$ is obtained by means of Eq. (1),
(3) in L*a*b*: $\vdash(L \to a \to b)$.

Note that one easily verifies that the family of colour orderings given by the expression (5) generalises the lexicographical orderings, i.e., using the weighing distance $\|\cdot\|_M^{\mathrm{UVW}}$ with the weights $M(\omega_1, \omega_2, \omega_3) = M(1,0,0)$ and the reference equals to the upper bound of axis U, $\mathbf{c}_0 = (c_{\max}^U, -, -)$, the relation (5) is equivalent to the ordering $\Omega_{U\to V\to W}^{\mathrm{lex}}$:

$$\mathbf{c}_i <_{\Omega^{\mathrm{lex}}} \mathbf{c}_j \iff \begin{cases} c_i^U < c_j^U & \text{or} \\ c_i^U = c_j^U \quad \text{and} \quad c_i^V < c_j^V & \text{or} \\ c_i^U = c_j^U \quad \text{and} \quad c_i^V = c_j^V \quad \text{and} \quad c_i^W < c_j^W \end{cases}$$

3.3. Erosion and dilation on complete lattice $\mathscr{T}^{\mathrm{uvw}}$

Using the total Ω-ordering $<_\Omega$ we have $\mathbf{c}_i = \mathbf{c}_j$ or $\mathbf{c}_i <_\Omega \mathbf{c}_j$ or $\mathbf{c}_j <_\Omega \mathbf{c}_i$ for every pair $(\mathbf{c}_i, \mathbf{c}_j)$. Therefore, it is defined for any family of colour points $(\mathbf{c}_k)_{k\in I} \in \mathscr{T}^{\mathrm{uvw}}$ the colour supremum $\sup_\Omega[\mathbf{c}_k] = \bigvee_{k\in I}^{\mathbf{c}_0}\mathbf{c}_k$ and the colour infimum $\inf_\Omega[\mathbf{c}_k] = \bigwedge_{k\in I}^{\mathbf{c}_0}\mathbf{c}_k$. Furthermore, the following extremes exist for the complete lattice $\mathscr{T}^{\mathrm{uvw}}$: the upper bound ("greatest colour") is $\mathbf{c}_0$ itself, i.e., $\top^{\mathbf{c}_0} = \mathbf{c}_0$; the lower bound ("smallest colour"), $\perp_{\mathbf{c}_0}$, is the most distant colour point of $\mathbf{c}_0$. In fact, $\perp_{\mathbf{c}_0}$ corresponds to one of the extremal points of bounded space $\mathscr{T}^u \times \mathscr{T}^v \times \mathscr{T}^w$; e.g., in RGB (each grey-level component $\in[0,255]$) with $\mathbf{c}_0 = (10,10,200)$ the lower bound is the corner of the RGB cube $\perp = (255,255,0)$.

The theory of adjunctions on complete lattices has played an important role in mathematical morphology [44,21]. In particular, using the major results, the most general definition of erosion and dilation is as follows. The operator ε between the complete lattice $\mathscr{T}^{\mathrm{uvw}}$ and itself is an erosion if $\varepsilon(\bigwedge_{k\in I}^{\mathbf{c}_0}\mathbf{c}_k) = \bigwedge_{k\in I}^{\mathbf{c}_0}\varepsilon(\mathbf{c}_k)$ for every family $(\mathbf{c}_k)_{k\in I}$. A similar dual definition holds for dilation δ (i.e., commutation with the supremum). The pair (ε, δ) is called an adjunction between $\mathscr{T}^{\mathrm{uvw}} \to \mathscr{T}^{\mathrm{uvw}}$ if $\delta(\mathbf{c}_y) \leqslant_\Omega \mathbf{c}_x \iff \mathbf{c}_y \leqslant_\Omega \varepsilon(\mathbf{c}_x)$. Moreover, to every erosion ε corresponds a unique dilation δ given by $\delta(\mathbf{c}_y) = \bigwedge^{\mathbf{c}_0}\{\mathbf{c}_x \in \mathscr{T}^{\mathrm{uvw}} : \mathbf{c}_y \leqslant_\Omega \varepsilon(\mathbf{c}_x)\}$ such that (ε,δ) is an adjunction. These theoretical definitions are interesting to consider if the proposed colour ordering verifies the basic properties of erosion/dilation, however, they do not allow computing erosion/dilation in practice. We recall the algorithmic definition of colour erosion and dilation, and derived operators, in the next section.

3.4. Complementary colours and quasi-duality

One of the most interesting properties of (binary and grey-level) morphological operators is the duality by the complementation. Let $f(x) \in \mathscr{F}(E,\mathscr{T})$ be a grey-level image, where $\mathscr{T}$ is bounded by $[t_{\min}, t_{\max}]$. The complement image (or negative image) $\overline{f}(x)$ is defined as the reflection of $f(x)$ with respect to $(t_{\min} + t_{\max})/2$; i.e., $\overline{f}(x) = t_{\max} - f(x) + t_{\min}$, $\forall x \in E$. Let the pair $(\varepsilon, \delta) : \mathscr{F}(E,\mathscr{T}) \to \mathscr{F}(E,\mathscr{T})$ be an adjunction, that is let $\varepsilon(f)$ and $\delta(f)$ be respectively an erosion and its associated dilation in $\mathscr{F}(E,\mathscr{T})$. The property of duality holds:

$$\varepsilon(\overline{f}) = \overline{\delta(f)} \Rightarrow \varepsilon(f) = \overline{\delta(\overline{f})},$$

and this is verified for any other pair of dual operators, such as the opening/closing. In practice, this property allows us to implement exclusively the dilation, and using the complement, to be able to obtain the corresponding erosion.

The complement of a colour image, $\mathbf{f} \in \mathscr{F}(E, \mathscr{T}^{\mathrm{uvw}})$, is defined as the complement of each colour component; i.e., $\overline{\mathbf{f}} = (\overline{f}_U, \overline{f}_V, \overline{f}_W)$. Moreover for each colour pixel i the complementary colour is given by $\overline{\mathbf{c}}_i = (c^U_{\max} - c^U_i + c^U_{\min}, c^V_{\max} - c^V_i + c^V_{\min}, c^W_{\max} - c^W_i + c^W_{\min})$, where $c^U_{\max}$ and $c^U_{\min}$ are, respectively, the upper and lower bounds of $\mathscr{T}^u$ (idem. for V and W components). We need to study if there exists an equivalent property of duality for colour operators according to the family of orderings given by (5). Let us use for our discussion the example of Fig. 3. For the sake of simplicity, it deals with a two dimensional case: the bounded vector space $[x_{\min}, x_{\max}] \times [y_{\min}, y_{\max}]$. The simplified total ordering is

$$\mathbf{v}_i <_{\mathbf{v}_0} \mathbf{v}_j \iff \begin{cases} \|\mathbf{v}_i - \mathbf{v}_0\|_2 > \|\mathbf{v}_j - \mathbf{v}_0\|_2 & \text{or} \\ \|\mathbf{v}_i - \mathbf{v}_0\|_2 = \|\mathbf{v}_j - \mathbf{v}_0\|_2 & \text{and} \begin{cases} x_i < x_j & \text{or} \\ x_i = x_j & \text{and} \quad y_i < y_j \end{cases} \end{cases}$$

Let $(\mathbf{v}_i)_{i\in I}$ be a family of nine points and $\mathbf{v}_0$, $\mathbf{v}'_0$, $\mathbf{v}''_0$ and $\mathbf{v}'''_0$ be four reference points. Choosing the reference $\mathbf{v}_0$ in Fig. 3(a), we obtain the supremum $\bigvee_{i\in I}^{\mathbf{v}_0}\mathbf{v}_i = \mathbf{v}_3$ and the infimum $\bigwedge_{i\in I}^{\mathbf{v}_0}\mathbf{v}_i = \mathbf{v}_8$. Working with the complemented points given in Fig. 3(b), the supremum is $\bigvee_{i\in I}^{\mathbf{v}_0}\overline{\mathbf{v}}_i = \overline{\mathbf{v}}_9$ and the infimum is $\bigwedge_{i\in I}^{\mathbf{v}_0}\overline{\mathbf{v}}_i = \overline{\mathbf{v}}_3$, and consequently, $\bigvee_{i\in I}^{\mathbf{v}_0}\mathbf{v}_i = \overline{\bigwedge_{i\in I}^{\mathbf{v}_0}\overline{\mathbf{v}}_i}$, but nevertheless $\bigwedge_{i\in I}^{\mathbf{v}_0}\mathbf{v}_i \neq \overline{\bigvee_{i\in I}^{\mathbf{v}_0}\overline{\mathbf{v}}_i}$. If the reference is now $\mathbf{v}'_0$, we obtain for $(\mathbf{v}_i)_{i\in I}$ the supremum $\mathbf{v}_1$ and the infimum $\mathbf{v}_5$ and for $(\overline{\mathbf{v}}_i)_{i\in I}$, $\overline{\mathbf{v}}_5$ and $\overline{\mathbf{v}}_1$ respectively. Hence, the property

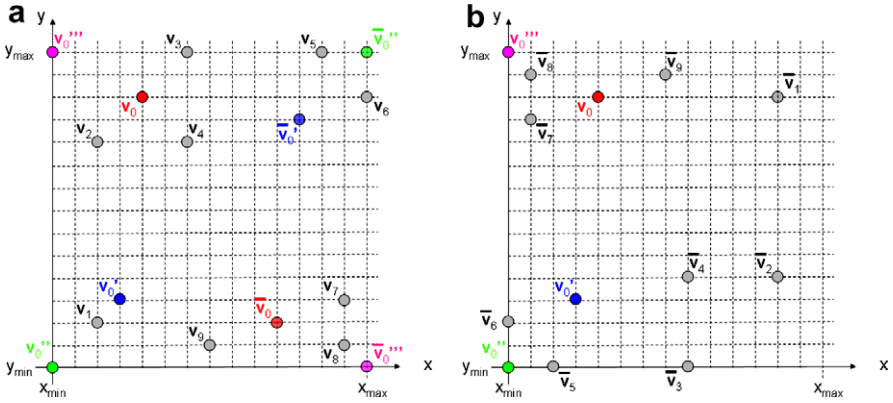

Fig. 3. Bounded vector space $[x_{\min}, x_{\max}] \times [y_{\min}, y_{\max}]$: (a) family of nine points $(\mathbf{v}_i)_{i\in I}$ and four references $\mathbf{v}_0$, $\mathbf{v}'_0$, $\mathbf{v}''_0$, $\mathbf{v}'''_0$ (and corresponding complemented references), (b) complemented points $(\overline{\mathbf{v}}_i)_{i\in I}$ and same references.

of duality is preserved. The same result is obtained for $\mathbf{v}_0'' = (x_{\min}, y_{\min})$. We can suppose based on these examples that the duality is verified when the reference is one of the extremal points or a point on the main diagonals of the space. Unfortunately this is not true in general: a counterexample is obtained by choosing as reference $\mathbf{v}_0''' = (x_{\min}, y_{\max})$ (the sup and the inf are, respectively, $\mathbf{v}_2$ and $\mathbf{v}_8$ whereas in the complemented space, the sup is $\overline{\mathbf{v}}_8$ and the inf$\overline{\mathbf{v}}_3$).

Note that one easily verifies that the duality is always valid for the orderings grounded exclusively in lexicographical cascades, without including the pre-ordering based on the distance to a reference. Incidentally, we can observe that the duality is verified for the total orderings including the reference $\mathbf{v}_0 = (x_0,y_0)$ if and only if the supremum and the infimum associated to the total distance to $\mathbf{v}_0$ are the same as the supremum and the infimum associated to the separate distances to x_0 and to y_0. In other words, a property of *separability* of both axis x and y in the computation of the distance to $\mathbf{v}_0$ is required to guarantee the duality.

In conclusion, we have the following property for colour images. If the reference colour $\mathbf{c}_0$ verifies the above property of separability for any pair of distinct points $c_i, c_j \in \mathscr{T}^{\text{uvw}}$, it holds that $(c_i <_{\Omega_{c_0}} c_j) \Longleftrightarrow (\overline{c}_i >_{\Omega_{c_0}} \overline{c}_j)$. Consequently, for an erosion/dilation adjunction defined in $\mathscr{F}(E, \mathscr{T}^{\text{uvw}})$ it follows then that $\varepsilon_{\Omega_{c_0}}(\mathbf{f}) = \overline{\delta_{\Omega_{c_0}}(\overline{\mathbf{f}})}$. This property is named *quasi-duality* of the family of orderings given by (5).

We can also investigate the effect of computing the complement of the reference colour, or in other words, under which conditions the property $(c_i <_{\Omega_{c_0}} c_j) \Longleftrightarrow^{?} (c_i >_{\Omega_{\overline{c}_0}} c_j)$ is verified. From the example of Fig. 3(a), for $\overline{\mathbf{v}}_0$ we have that the supremum $\bigvee_{i\in I}^{\overline{\mathbf{v}}_0}\mathbf{v}_i = \mathbf{v}_7$ and the infimum $\bigwedge_{i\in I}^{\overline{\mathbf{v}}_0}\mathbf{v}_i = \mathbf{v}_3$ implies that $\bigwedge_{i\in I}^{\mathbf{v}_0}\mathbf{v}_i \neq \bigvee_{i\in I}^{\overline{\mathbf{v}}_0}\mathbf{v}_i$. Moreover, in the case $\overline{\mathbf{v}}_0'$ (or $\overline{\mathbf{v}}_0''$), the supremum is $\mathbf{v}_7$ and the infimum $\mathbf{v}_1$, and consequently the duality is not verified either. In conclusion, no property of duality seems to be associated to the complement of the reference colour.

4. Morphological colour operators

Once the family of total orderings (5) have been established, the morphological colour operators are defined in the standard way. We limit here our developments to the flat operators, i.e., the structuring elements are planar. The non-planar structuring functions are defined by weighting values on their support [44]. The implementation and the use of colour structuring functions will be the object of future research.

We need to recall a few notions which characterise the properties of morphological operators. Let ψ be an operator on a complete lattice $\mathscr{F}(E, \mathscr{T}^{\text{uvw}})$. ψ is increasing if $\forall \mathbf{f}, \mathbf{g} \in \mathscr{F}(E, \mathscr{T}^{\text{uvw}})$, $\mathbf{f} \leqslant_\Omega \mathbf{g} \Rightarrow \psi(\mathbf{f}) \leqslant_\Omega \psi(\mathbf{f})$. It is anti-extensive if $\psi_\Omega(\mathbf{f}) \leqslant_\Omega \mathbf{f}$ and it is extensive if $\mathbf{f} \leqslant_\Omega \psi_\Omega(\mathbf{f})$. An operator is idempotent if it is verified that $\psi(\psi(\mathbf{f})) = \psi(\mathbf{f})$.

4.1. Erosion and dilation

The *colour erosion* of an image $\mathbf{f} \in \mathscr{F}(E, \mathscr{T}^{\text{uvw}})$ at pixel $x \in E$ by the structuring element $B \subset E$ of size n is given by

$$\varepsilon_{\Omega,nB}(\mathbf{f})(x) = \{\mathbf{f}(y) : \mathbf{f}(y) = \wedge_\Omega[\mathbf{f}(z)], z \in n(B_x)\}, \tag{6}$$

where $\inf_\Omega$ is the infimum according to the total ordering Ω. The corresponding *colour dilation* $\delta_{\Omega,nB}$ is obtained by replacing the $\inf_\Omega$ by the $\sup_\Omega$, i.e.,

$$\delta_{\Omega,nB}(\mathbf{f})(x) = \{\mathbf{f}(y) : \mathbf{f}(y) = \vee_\Omega[\mathbf{f}(z)], z \in n(B_x)\}. \tag{7}$$

The erosion and the dilation are increasing operators. Moreover, the erosion is anti-extensive and the dilation is extensive. In practice, the colour erosion shrinks the structures which have a colour close to the reference; "peaks of colour" thinner than the structuring element disappear by taking the colour of neighboring structures with a colour away from the reference. As well, it expands the structures which have a colour far from the reference. Dilation produces the dual effects, enlarging the regions having a colour close to the reference and contracting the others.

4.2. Morphological filters

In general, a morphological filter is an increasing operator that is also idempotent (the erosion/dilation are not idempotent).

4.2.1. Opening and closing

A *colour opening* is an erosion followed by a dilation, i.e.,

$$\gamma_{\Omega,nB}(\mathbf{f}) = \delta_{\Omega,nB}(\varepsilon_{\Omega,nB}(\mathbf{f})), \tag{8}$$

and a *colour closing* is a dilation followed by an erosion, i.e.,

$$\varphi_{\Omega,nB}(\mathbf{f}) = \varepsilon_{\Omega,nB}(\delta_{\Omega,nB}(\mathbf{f})). \tag{9}$$

The opening (closing) is an anti-extensive (extensive) operator. More precisely, the opening removes colour peaks that are thinner than the structuring element, having a colour close to the reference; the closing remove colour peaks that are thinner than the structuring element, having a colour far from the reference.

4.2.2. Alternate sequential filters

Once the colour opening and closing are defined it is indubitable how to extend other classical operators such as the *colour alternate sequential filters* (or ASF), obtained by concatenation of openings and closings, i.e.,

$$ASF(\mathbf{f})_{\Omega,nB} = \varphi_{\Omega,nB}\gamma_{\Omega,nB} \cdots \varphi_{\Omega,2B}\gamma_{\Omega,2B}\varphi_{\Omega,B}\gamma_{\Omega,B}(\mathbf{f}). \tag{10}$$

A dual family of ASF operators is obtained by changing the order of the openings/closings. The ASF act simultaneously on the peaks and the valleys, simplifying (smoothing) them. They are useful when dealing with noisy signals.

4.2.3. Contrast mappings

The contrast mapping is a particular operator from a more general class of transformations called toggle

mappings [45]. A contrast mapping is defined, on the one hand, by two primitives ϕ_1 and ϕ_2 applied to the initial function, and on the other hand, by a decision rule which makes, at each point x the output of this mapping toggles between the value of ϕ_1 at x and the value of ϕ_2, according to which is closer to the input value of the function at x. If the primitives are an erosion $\varepsilon_{\Omega,nB}(\mathbf{f})$ and the adjunction dilation $\delta_{\Omega,nB}(\mathbf{f})$, the *colour contrast mapping* for an image $\mathbf{f}$ is given by [26]:

$$\kappa^{\varepsilon\delta}_{\Omega,nB}(\mathbf{f})(x)=\begin{cases}\delta_{\Omega,nB}(\mathbf{f})(x) & \text{if } \|\mathbf{f}(x)-\delta(\mathbf{f})(x)\|\leqslant\|\mathbf{f}(x)-\varepsilon(\mathbf{f})(x)\|\\ \varepsilon_{\Omega,nB}(\mathbf{f})(x) & \text{if } \|\mathbf{f}(x)-\delta(\mathbf{f})(x)\|>\|\mathbf{f}(x)-\varepsilon(\mathbf{f})(x)\|\end{cases} \tag{11}$$

where $\delta(\mathbf{f})$ and $\varepsilon(\mathbf{f})$ of the norms correspond to $\delta_{\Omega,nB}(\mathbf{f})$ and $\varepsilon_{\Omega,nB}(\mathbf{f})$ respectively. Usually, the norm used to compute the distance in the contrast mappings is the same as the norm applied in the Ω-ordering associated to the colour erosion/dilation. This morphological transformation enhances the local contrast of $\mathbf{f}$ by sharpening its colour edges. It is usually applied more than once, being iterated, and the iterations converge to a limit reached after a finite number of iterations. Another interesting colour contrast mapping $\kappa^{\gamma\varphi}_{\Omega,nB}(\mathbf{f})$ is defined by changing in the previous expression the pair of colour erosion/dilation by a colour opening $\gamma_{\Omega,nB}(\mathbf{f})$ and the dual closing $\varphi_{\Omega,nB}(\mathbf{f})$ [33]. This second contrast operator is idempotent but a decreasing transformation (it cannot be considered strictly as a morphological filter). More recently, these sharpening methods are called shock filters [38].

4.2.4. Morphological centre

The opening/closing are non-linear smoothing filters, and classically an opening followed by a closing (or a closing followed by an opening) can be used to suppress impulse noise, i.e., suppressing positive spikes via the opening and negative spikes via the closing and without blurring the contours. However, the results are usually not satisfactory. A more interesting operator to suppress colour noise is the morphological centre, also known as automedian filter [44,45]. Given an opening $\gamma_\Omega(\mathbf{f})$ and the dual closing $\varphi_\Omega(\mathbf{f})$ with a small structuring element (typically square of size equal to the "noise size"), the *colour morphological centre* associated to these primitives for an image $\mathbf{f}$ is given by the algorithm:

$$\zeta_\Omega(\mathbf{f})=[f\vee_\Omega(\gamma\varphi\gamma(\mathbf{f})\wedge_\Omega\varphi\gamma\varphi(\mathbf{f}))]\wedge_\Omega(\gamma\varphi\gamma(\mathbf{f})\vee_\Omega\varphi\gamma\varphi(\mathbf{f})). \tag{12}$$

This is an increasing and autodual operator, not idempotent, but the iteration of ζ presents a point monotonicity and converges to the idempotence, i.e., $\widehat{\zeta}_\Omega(\mathbf{f})=[\zeta_\Omega(\mathbf{f})]^i$, such that $[\zeta]^i=[\zeta]^{i+1}$.

4.2.5. Residue-based operators

Moreover, using a colour distance to calculate the image distance d, $d\in\mathscr{F}(E,\mathscr{T})$ (a scalar function), given by the difference point-by-point of two colour images $d(x)=\|\mathbf{f}(x)\text{-}\mathbf{g}(x)\|$, we can easily define the *morphological colour gradient*, i.e.,

$$\varrho_\Omega(\mathbf{f})=\|\delta_{\Omega,B}(\mathbf{f})-\varepsilon_{\Omega,B}(\mathbf{f})\|. \tag{13}$$

This function gives the contours of the image, attributing more importance to the transitions between regions close/far to the colour reference. For the sake of coherence, the norm used for the distance d is the same as the norm applied in the ordering Ω associated with the corresponding colour operator. However, another different colour norm can also be considered.

The *positive colour top-hat transformation* is the residue of a colour opening, i.e.,

$$\rho^+_{\Omega,nB}(\mathbf{f})=\|\mathbf{f}-\gamma_{\Omega,nB}(\mathbf{f})\|. \tag{14}$$

Dually, the *negative colour top-hat transformation* is given by

$$\rho^-_{\Omega,nB}(\mathbf{f})=\|\varphi_{\Omega,nB}(\mathbf{f})-\mathbf{f}\|. \tag{15}$$

The top-hat transformation yields grey-level images and is used to extract contrasted components with respect to the background, where the background corresponds to the structures far from the reference. Moreover, top-hats remove the slow trends, and thus enhancing the contrast of objects smaller than the structuring element used for the opening/closing.

4.3. Geodesic reconstruction, derived operators, leveling

In addition, we also propose the extension of operators "by reconstruction", implemented using the geodesic dilation. The *colour geodesic dilation* is based on restricting the iterative dilation of a function marker $\mathbf{m}$ by B to a function reference $\mathbf{f}$ [53], i.e.,

$$\delta^n_\Omega(\mathbf{m},\mathbf{f})=\delta^1_\Omega\delta^{n-1}_\Omega(\mathbf{m},\mathbf{f}), \tag{16}$$

where the unitary conditional dilation is given by $\delta^1_\Omega(\mathbf{m},\mathbf{f})=\delta_{\Omega,B}(\mathbf{m})\wedge_\Omega\mathbf{f}$. Typically, B is an isotropic structuring element of size *1*.

The *colour reconstruction* by dilation is then defined by

$$\gamma^{\mathrm{rec}}_\Omega(\mathbf{m},\mathbf{f})=\delta^i_\Omega(\mathbf{m},\mathbf{f}), \tag{17}$$

such that $\delta^i_\Omega(\mathbf{m},\mathbf{f})=\delta^{i+1}_\Omega(\mathbf{m},\mathbf{f})$ (idempotence). Whereas the adjunction opening $\gamma_{\Omega,nB}(\mathbf{f})$ (from an erosion/dilation) modifies the colour contours, the associated opening by reconstruction $\gamma^{\mathrm{rec}}_\Omega(\mathbf{m},\mathbf{f})$ (where the marker $\mathbf{m}=\varepsilon_{\Omega,nB}(\mathbf{f})$ or $\mathbf{m}=\gamma_{\Omega,nB}(\mathbf{f})$) is aimed at efficiently and precisely reconstructing the contours of the colour objects having a colour close to the reference and which have not been totally removed by the marker filtering process.

In a similar way, the *colour leveling* $\lambda_\Omega(\mathbf{m},\mathbf{f})$ of a reference function $\mathbf{f}$ and a marker function $\mathbf{m}$ is a symmetric geodesic operator computed by means of an iterative algorithm with geodesic dilations and geodesic erosions until idempotence [34], i.e.,

$$\lambda_\Omega(\mathbf{m},\mathbf{f})^i=\left[\mathbf{f}\wedge_\Omega\delta^i_\Omega(\mathbf{m})\right]\vee_\Omega\varepsilon^i_\Omega(\mathbf{m}), \tag{18}$$

until $\lambda_\Omega(\mathbf{m},\mathbf{f})^i=\lambda_\Omega(\mathbf{m},\mathbf{f})^{i+1}$. The leveling simplifies the colour image, removing the objects and textures smaller than the

structuring element and preserving the contours of the remaining objects. Moreover, it acts simultaneity on the "positive objects" (i.e., having a colour close to the reference) and "negative objects" (i.e., colour far from the reference).

5. Results and discussion

We explore in this section the effects of these morphological operators when they are applied to colour images according to the family of orderings introduced in this paper. We try to illustrate a wide variety of morphological colour operators with different colour spaces, distances and colour references. As mentioned, the present approach generalises other orderings proposed in the literature. Even if we are conscious of the fact that a further study would need more extensive comparisons, we consider that the following comparative examples allow us to draw some interesting conclusions.

Fig. 4 gives a first comparison of the results obtained for the image "Baboon", when the same operator, a colour opening by reconstruction $\gamma_{\Omega}(\mathbf{f})$, is applied using different orderings. It is observed that the results are absolutely

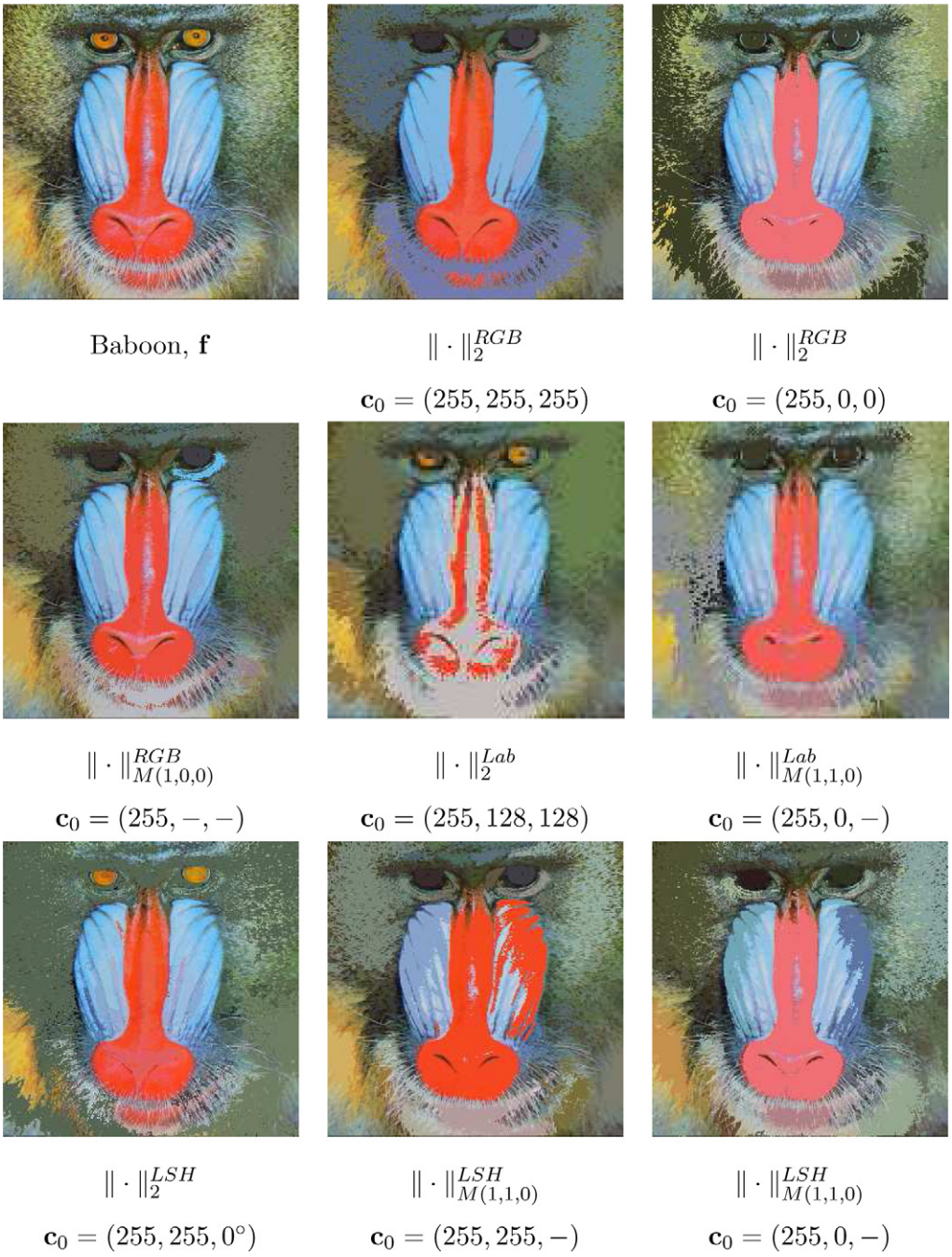

Fig. 4. Comparison of colour opening by reconstruction $\gamma_{\Omega}^{\text{rec}}(\mathbf{f})$ for the image $\mathbf{f}$ "Baboon" (the marker is an erosion $\varepsilon_{\Omega,\, nB}(\mathbf{f})$ where the structuring element B is a square of size $n = 20$) according to different distance-based total orderings.

different according to the distance-based total ordering chosen. We show only examples for the L_2 and the Mahalanobis distance. As expected, the orderings based on L_∞ produce very unsatisfactory visual results and the results for L_1 norm distances are almost equal to the results achieved using L_2. Note also the flexibility of the approach: for instance, in RGB the result of the opening for L_2 distance to the origin (255,0,0) (pure red), which suppresses all the small red objects, is very different from the Mahalonobis distance with weights (1,0,0) (the R component is exclusively considered) to the same origin, which suppresses the bright objects according only the red component. On the other hand, we observe that the orderings with distances including chromatic components (i.e., h, a^* and b^*) produce poor results. Moreover the choice of the origin is not easily understandable for the a^* and b^* components (chromatic axis of opposite colours). Even if the Euclidean distance in the $L^*a^*b^*$ colour space has interesting perceptual properties, we remark that for the implementation of morphological operators the most important issue is in fact the choice of the origin. Hence, the use of the L_2 distance in LSH or $L^*a^*b^*$ should be considered for feature extraction operators according to a specific reference colour. We remark also that in order to remove all the bright structures of a natural colour image by means of an opening, the results are more satisfactory from a visual point of view for $\|\cdot\|_2^{\mathrm{RGB}}$, $\mathbf{c}_0 =$ (255,255,255) than for $\|\cdot\|_{M(1,1,0)}^{\mathrm{LSH}}$, $\mathbf{c}_0 = (255,255,\text{–})$.

In order to illustrate the effect of geodesic operators, Fig. 5 gives an example of colour "swamping" or reconstruction of a function by imposing markers for the maxima (to remove the useless maxima). In this case, the one-point marker is a pixel on the big bear ("mrk 1" touches the dark part of the fur), which value in RGB is approximately (140,120,100). Working in RGB and using L_2 distance, we observe that, if the reference colour is (255,255,255), the propagation from the marker imposes that any other pixel must have a colour whose distance to the reference (maximal luminance) is longer than the distance of the marker to the reference. Consequently, there is not any pixel upper intensities RGB other than the marker. When the reference colour matches with the marker, $\mathbf{c}_0 = (140,120,100)$, the marked object is preserved and moreover, the other regions with the same colour are removed (only one maxima after this swamping transformation remains). In this case, the dark part of the fur is again preserved and the objects which have a colour very distant from the marker are also preserved (bright part of the image).

Fig. 6 shows the comparison of different colour levelings for the simplification of image "Lenna", where the markers are ASF. We observe that the degree of simplification (i.e., which structures are preserved and which structures are removed) is relatively equivalent for the different orderings; and the differences between the orderings are associated to the final colours of simplified structures. We again remark that the visual results for $\|\cdot\|_2^{\mathrm{RGB}}$, $\mathbf{c}_0 = (255,255,255)$ are slightly better than for $\|\cdot\|_{M(1,1,0)}^{\mathrm{LSH}}$, $\mathbf{c}_0 = (255,255,\text{–})$. It is also shown how a part of the image structures can be harshly leveled (the violet part of the hat) by imposing their colour as reference, i.e., (100,50,100).

In Fig. 7 the use of colour residue-based operators is compared for detail extraction. In RGB, a closing is given for L_2 distance and $\mathbf{c}_0 = (255,255,255)$, and the corresponding residue (i.e., black top-hat) with the same distance, which extracts the dark details (the letters of panels and a part of the texture). We observe that, if we fix $\mathbf{c}_0 = (0,0,0)$, we obtain by black top-hat the bright details (the interstices between the letters and the "positive" parts of textures). Here, we found the usefulness of quasi-duality property since the residue of a closing with $\mathbf{c}_0 = (0,0,0)$ is approximately equivalent to the residue of an opening with $\mathbf{c}_0 = (255,255,255)$. Once again, the result for RGB is compared with $\|\cdot\|_{M(1,1,0)}^{\mathrm{LSH}}$, $\mathbf{c}_0 = (255,255,\text{–})$, without observing substantial differences.

Fig. 8 depicts an example of colour segmentation by inner/outer markers-driven watershed transformation [9]. In this example the aim is to define the contour of the horse, and hence the inner marker is a segment going through the horse and the outer marker is the image border. The different colour gradients are then used with the watershed transformation. This example is particularly interesting to show the importance of the choice of the gradient for colour segmentation. The colour of the horse is variable with approximately RGB value of (250,110,90)

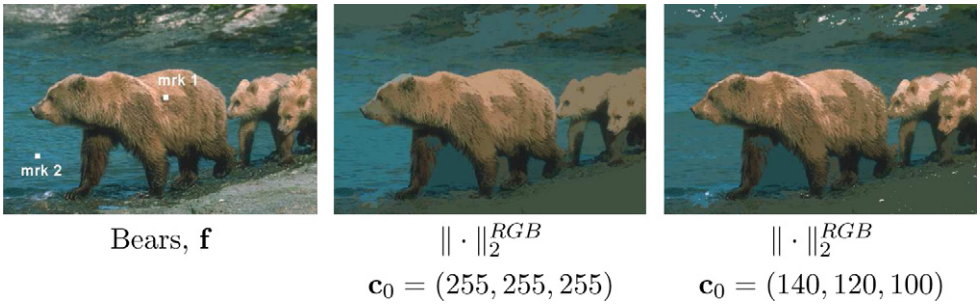

Fig. 5. Example of colour swamping for the image "Bears", where the one-point marker is a pixel on the fur ("mrk 1"), which value in RGB is approximately (140,120,100).

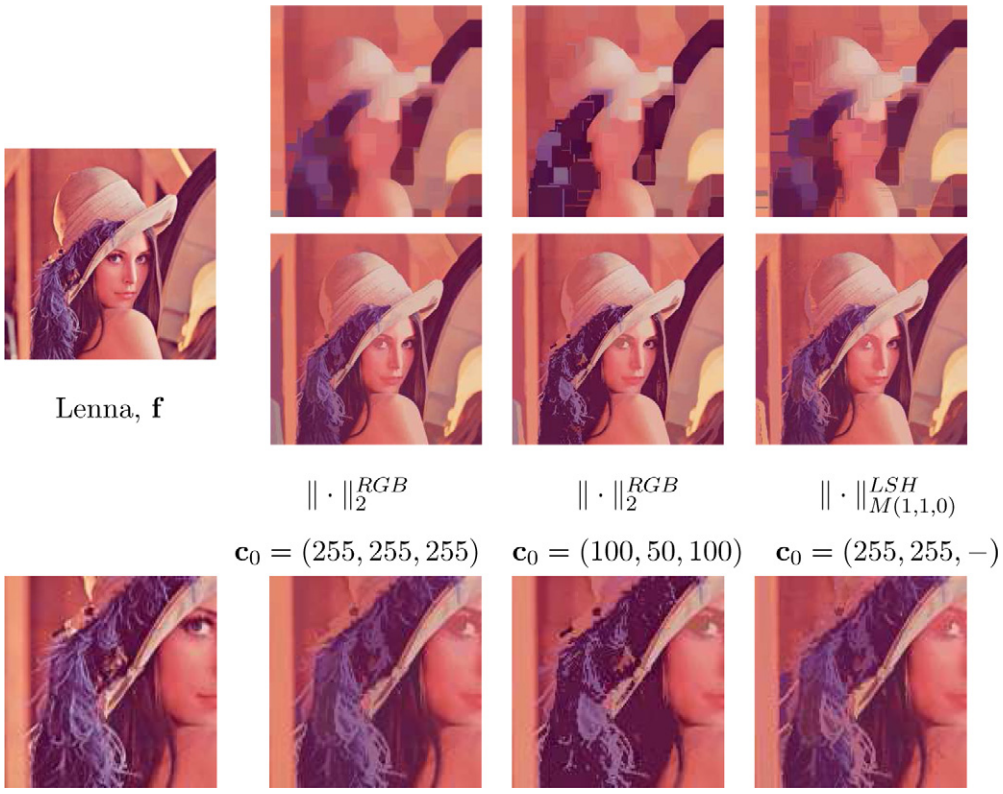

Fig. 6. Comparison of colour leveling $\lambda_{\Omega}(\mathbf{f})$ for the image $\mathbf{f}$ "Lenna" according to different distance-based total orderings. Upper row, the marker is an ASF, $ASF_{\Omega,nB}(\mathbf{f})$, where the structuring element B is a square of size $n = 15$; lower row, the corresponding levelings. At the bottom are zoom-in frames of a square section cropped from the initial (left) leveled images.

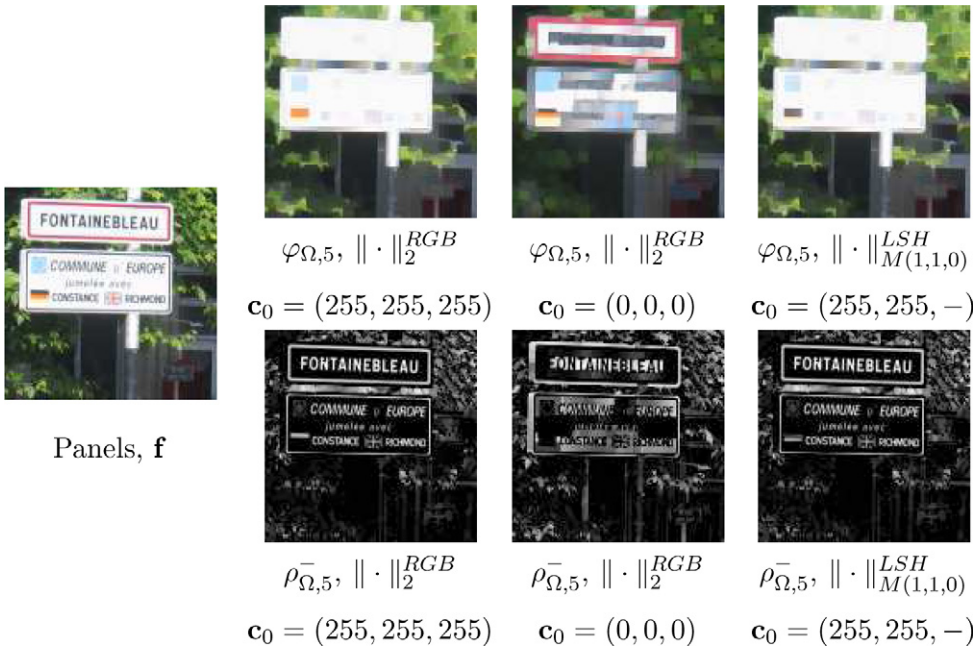

Fig. 7. Colour details extraction of image "Panels". Upper row, square closing of size 5×5 pixels; lower row, the associated negative top-hats.

or LSH value of (180,128,0°). We observe that, even if the results in RGB or LSH are better when the reference $\mathbf{c}_0$ equals the horse colour than the maximal value, the obtained segmentation is not satisfactory. In fact, the horse has an homogenous hue (around 10°) but a variable luminance and saturation (similar to the values of luminance

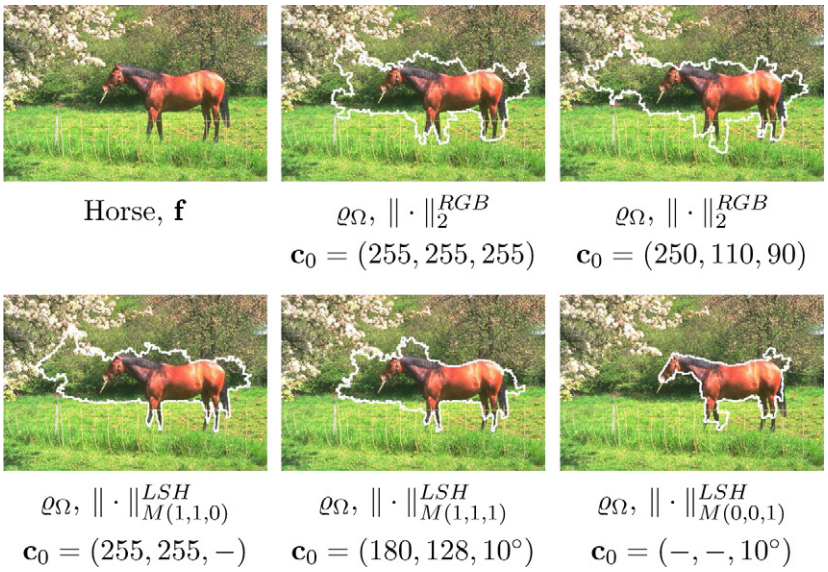

Fig. 8. Application of colour gradients for watershed-based segmentation of image "Horse". The white contour corresponds to the region obtained using an inner marker for the horse region (the outer marker is the image border).

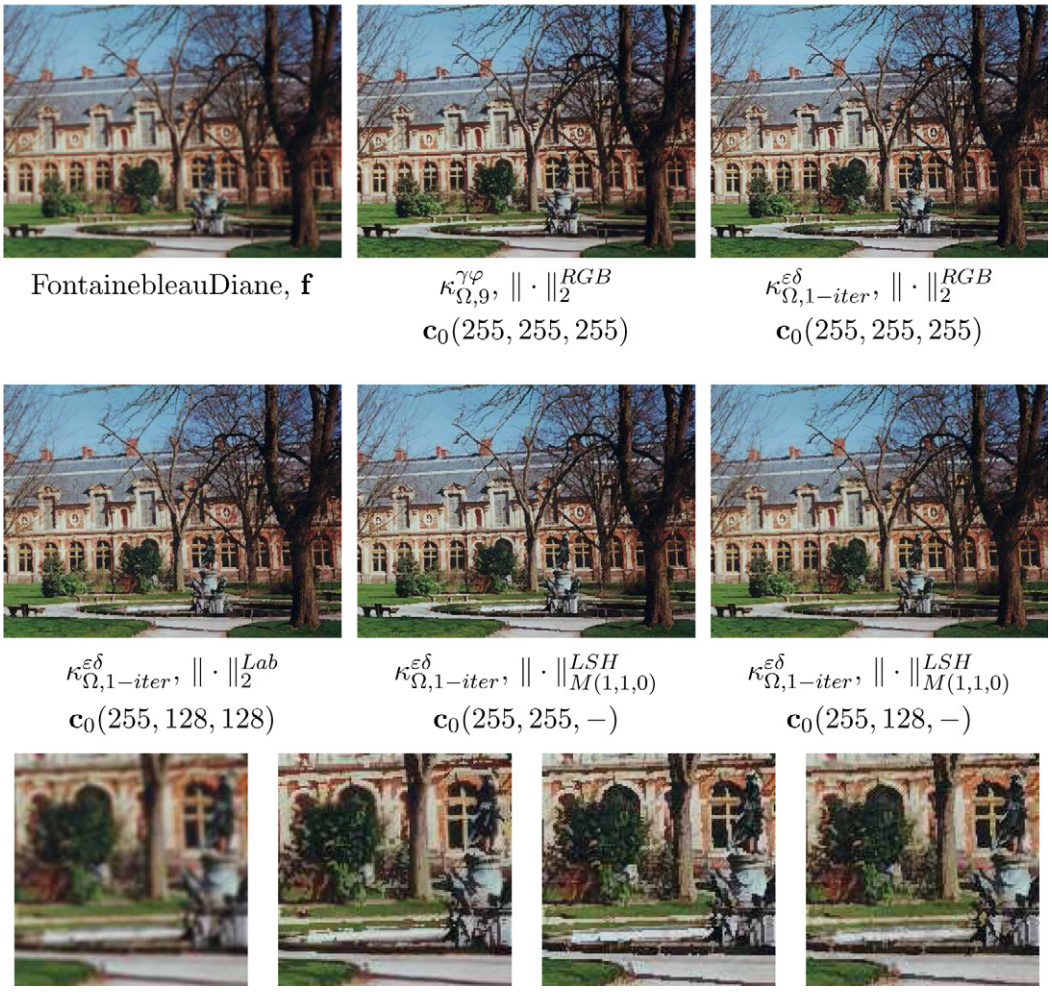

Fig. 9. Contrast enhancement of colour image "FontainebleauDiane" using the contrast mapping κ. At the bottom are zoom-in frames of a square section cropped from the initial (left) and three of enhanced images (using $\kappa_{\Omega,9}^{\gamma\varphi}$ in RGB, $\kappa_{\Omega,1-iter}^{\varepsilon\delta}$ in RGB and $\kappa_{\Omega,1-iter}^{\varepsilon\delta}$ in LSH with $\mathbf{c}_0$(255,128,–), respectively).

and saturation of background). Therefore, a gradient exclusively using the hue component (distance $\|\cdot\|^{\mathrm{LSH}}_{M(0,0,1)}$ and reference $\mathbf{c}_0(-,-,10°)$) yields the best result.

Fig. 9 shows a comparative example of contrast enhancement of the blurred image "FontainebleauDiane". The blur involves a Gaussian filter with $\sigma = 5$. It is well known that, in order to have significant enhancement, the size of contrast mapping based on opening/closing $\kappa^{\gamma\varphi}$ must be considerable and that it can involve visual artefacts. For this example, the size $n = 9$ seems to be a trade-off to obtain a perceptible enhancement. In fact, the effects obtained are in general better for the iteration of $\kappa^{\varepsilon\delta}$. Concerning the distance-based total ordering, it seems that for this example the best visual result is associated with the choice $\|\cdot\|^{\mathrm{LSH}}_{M(1,1,0)}$, $\mathbf{c}_0(255,128,-)$, which enhances the bright/dark structures, with an intermediate saturation (chromatic and achromatic simultaneously) and independently from the hue.

In Fig. 10 is given an example of morphological centre to filter colour noise. The image "CarmenBianca" has been corrupted by adding salt-and-pepper noise on the hue component (occurring with probability 0.05) and where the luminance for noise pixels is maximal and the saturation is half. As we can observe, for this noise distribution, the results are better using only the luminance component ($\|\cdot\|^{\mathrm{LSH}}_{M(1,0,0)}$, $\mathbf{c}_0(255,-,-)$) than the RGB components ($\|\cdot\|^{\mathrm{RGB}}_{2}$, $\mathbf{c}_0(255,255,255)$). Note also that the result associated with the opening-closing operator for a size equal to the centre is worse in terms of noise suppression. We show in the zoom-in images the results of an equivalent marginal RGB median which suppresses the noise but rounds off the colour contours. The result for $\|\cdot\|^{\mathrm{LSH}}_{M(1,1,0)}$, $\mathbf{c}_0(255,128,-)$, which corresponds to the noise distribution properties, is relatively satisfactory. In fact, it seems that the flexible choice of a particular distance and a colour reference can be interesting in order to obtain optimal filters for a particular distribution of noise. The challenge lies in estimating the statistical colour noise properties, so that the Mahalanobis distance is naturally well adapted to this problem (applying an estimated covariance matrix $\mathbf{\Gamma}$).

As a matter of fact, we cannot conclude from the qualitative analysis of these examples that a specific ordering is more suitable for one operator or another. In fact, we believe that it is not possible to assert which ordering is more appropriate for a given morphological operator.

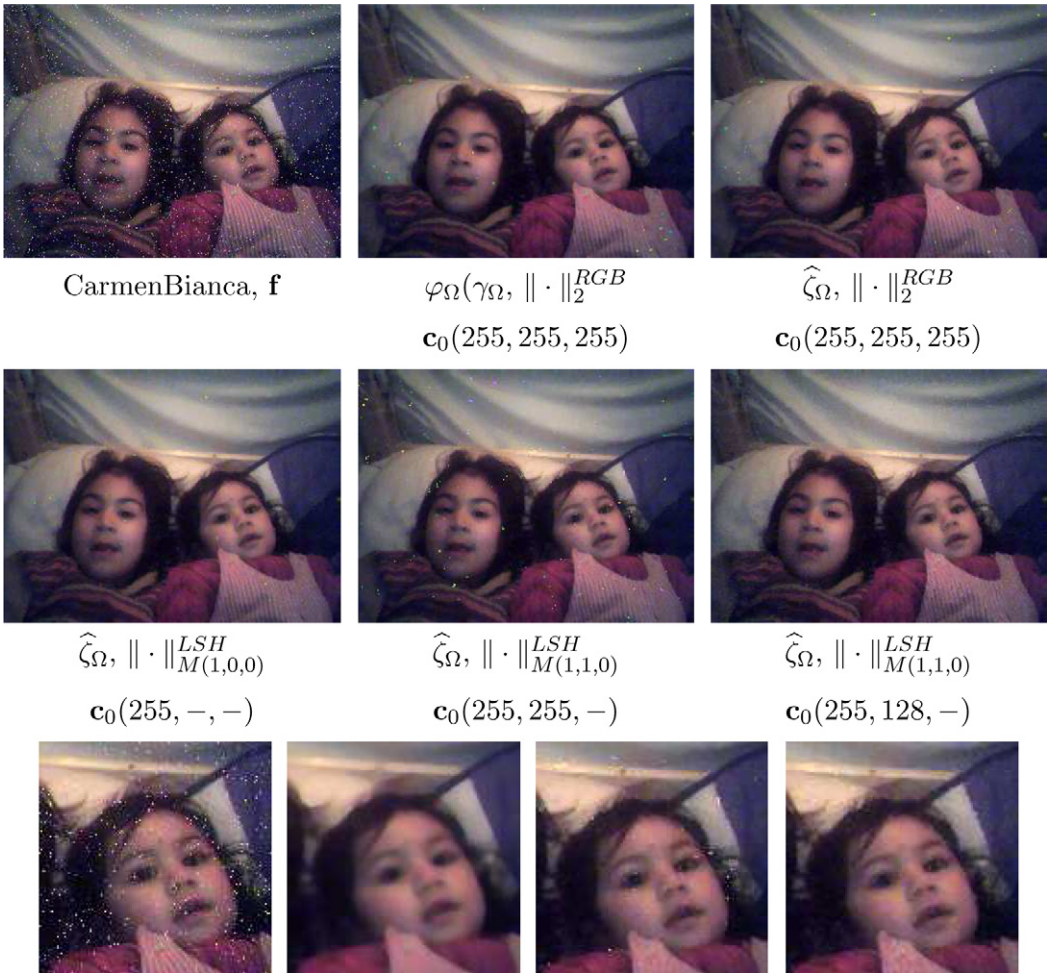

Fig. 10. Denoising of colour image "CarmenBianca" using the morphological centre $\widehat{\zeta}$. At the bottom are zoom-in frames of a square section cropped from the initial (left), a marginal median (in RGB of equivalent size) and two of centered images (using $\widehat{\zeta}_\Omega$ in LSH with $\mathbf{c}_0(255,255,-)$ and $\mathbf{c}_0(255,128,-)$ respectively).

The right choice of a colour distance and a colour reference depends on the nature of the image, the features of the target structures, as well as the properties of the operation applied, and others. For instance, using only one image we cannot determine the best gradient for colour segmentation. However, using a database of manually segmented images we can evaluate the segmentation obtained with the different gradients and determine the best gradient for the type of images. In addition, machine learning techniques can be applied to automatically adapt the best parameters for a specific problem.

5.1. Application to biomedical microscopic colour images

To complement the experimental part of this article, we propose to illustrate the application of morphological colour operators to biomedical microscopic colour images. In biomedicine, the microscopic samples (tissues, cells, proteins, etc.) are classically fixed and stained by different chemical components, in order to enhance the interesting structures with a particular colour [10]. In addition, recent advances in molecular biology allow to mark specific targets with fluorochrome probes [49]. The application of colour processing to these images is an active field.

Fig. 11 gives the example of colour analysis of an image with cells marked with dark violet, located on a heterogeneous tissue (marked bright yellow and pink). The aim of this processing is to separate the cells and the tissue to make easier the later quantification of both elements (count cells, evaluate cell aggregation, study the distribution of colour pink/yellow on the tissue, etc.). The dichotomy dark/bright implies the use of luminance information; moreover the different colour elements present a similar saturation. Hence, the two "colour phases" are extracted by closing/opening by reconstruction using the ordering based on $\|\cdot\|^{\mathrm{LSH}}_{M(1,0.2,0)}$, $\mathbf{c}_0(255,128,-)$. Even if the saturation has a low contribution, we have observed that the result is better where the luminance information also includes the saturation information. For the tissue, the marker is a dilation of 25, which removes the dark structures and by dual reconstruction recovers the tissue contours. In the case of cells, the marker is an erosion of size 75 which propagates the cell colour followed by the reconstruction that fills up the background.

Fig. 12 shows the successive steps of an example of analysis for a Cy3/Cy5 cDNA microarray images [11,3]. From the viewpoint of this paper, a cDNA microarray image is a two-channel Red–Green image (it can be seen as an RGB image with zero blue component) consisting of green, red and yellow spots. The goal of microarray image analysis is to locate and segment the spots and to quantify the intensity for each spot. Since microarray images are usually very noisy, image filtering and enhancement [29,30] are required in order to increase the accuracy of the subsequent analysis processes. Our aim in the particular example of Fig. 12 is to extract the spots marked with red fluorescence (pure red and yellow spots). Firstly, the image f is pre-filtered by means of the contrast and centre operators (to remove the noise and to enhance the spot contours), followed by an opening by reconstruction of size 3 (to regularise the spots, by removing the intensity structures of size lower that 3×3 pixels). Both transformations are based on the luminance/saturation processing ($\|\cdot\|^{\mathrm{LSH}}_{M(1,1,0)}$, $\mathbf{c}_0(255,128,-)$). Then, the reconstruction using as marker an erosion of size 15 (rough estimate of spot diameter) removes the spots which has a pure green colour

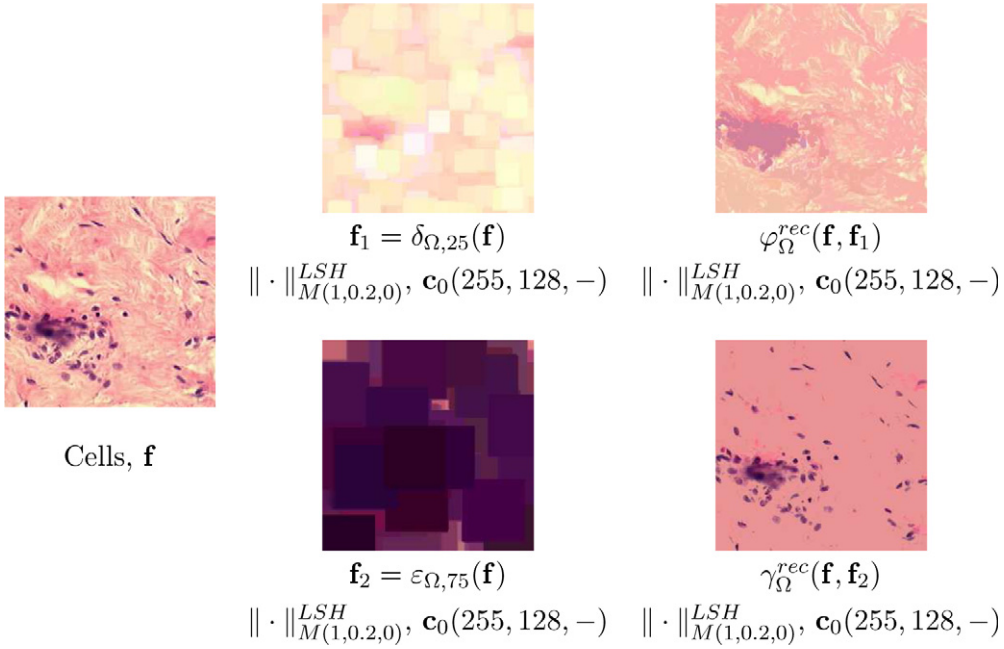

Fig. 11. Analysis of the colour image "Cells". See the text for details.

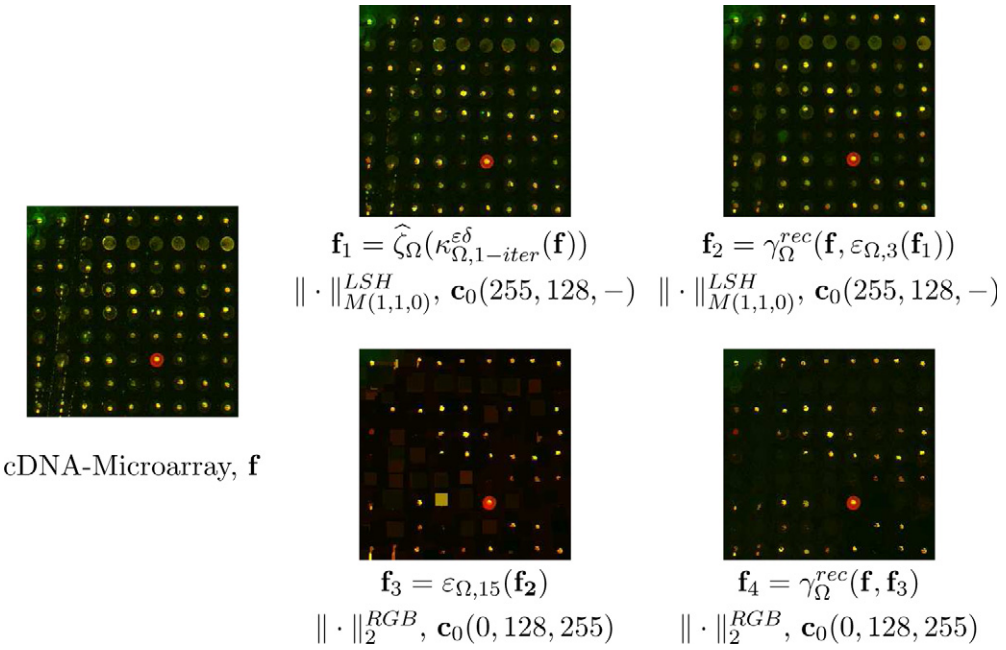

Fig. 12. Successive steps of the analysis of the colour image "cDNA-Microarray". See the text for details.

($\|\cdot\|_2^{\mathrm{RGB}}$, $\mathbf{c}_0$(0,128,255)). The output image $\mathbf{f}_4$ can be used to specifically segment the red/yellow spots.

Fig. 13 illustrates an example of fluorescence-marked cell segmentation in high content screening. For this kind of applications, the touching cells must be separated in order to be able to individually analyse each cell. To apply the watershed segmentation a colour gradient is needed as well as the markers for each cell. A gradient f_g calculated using the red and green component, $\|\cdot\|_{M(2,1,0)}^{\mathrm{RGB}}$, $\mathbf{c}_0$(255,255,–), allows defining the main contours of cells (the blue component introduces an additional contour for the cell nuclei). An opening by reconstruction of size 20 is then applied on the colour image $\mathbf{f}$ to remove the structures associated to the nuclei. The colour difference in RGB between the filtered image $\mathbf{f}_2$ and the original one $\mathbf{f}$ yields a grey-level image with the nuclei. The markers for each cell f_{mrks} are then obtained by computing the maxima of structures having a minimal diameter of 10 (using an isotropic opening). The watershed transformation of f_g and f_{mrks} provides the cell contours.

The last study-case of Fig. 14 gives another example of colour cell segmentation using the watershed transformation. Two classes of cells are presented in the image (colours brown and blue). In addition, the image $\mathbf{f}$ is very

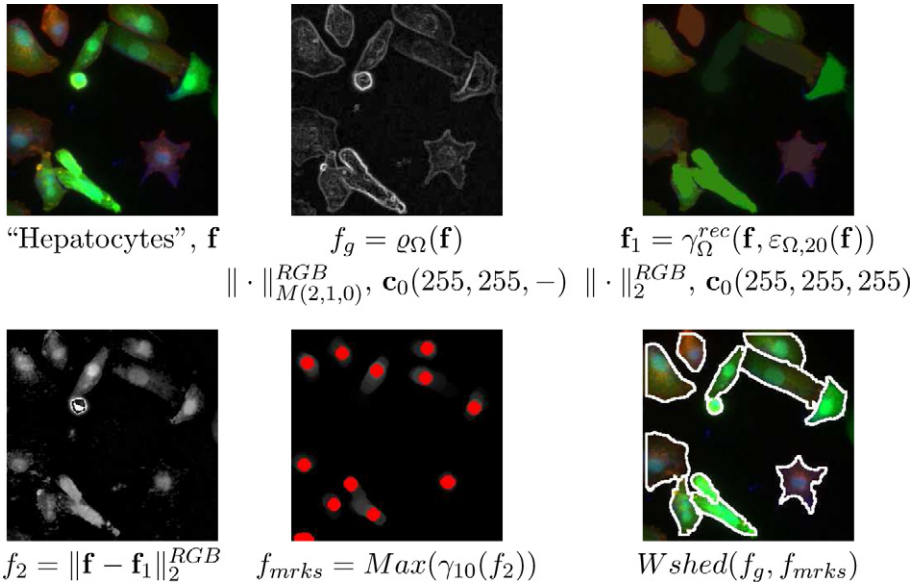

Fig. 13. Successive steps of the analysis of the colour image "Cells2". See the text for details.

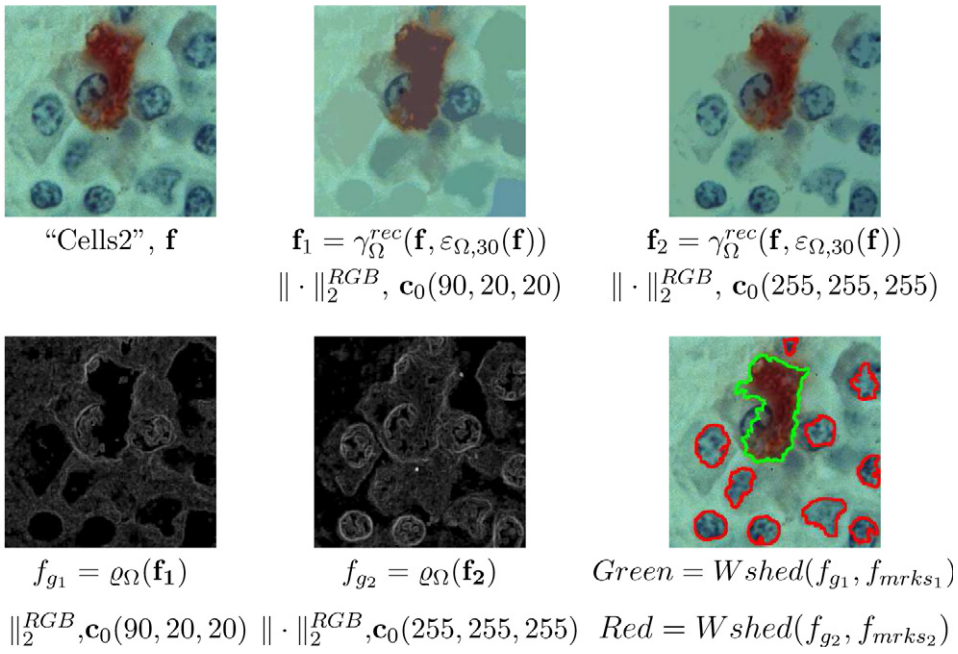

Fig. 14. Successive steps of the analysis of the colour image "Cells2". See the text for details.

textured and it is suggested to simplify the structure before computing the gradients. In this case, a first simplification $\mathbf{f}_1$ is obtained from an opening by reconstruction working on the brown structures ($\|\cdot\|_2^{\mathrm{RGB}}$, $\mathbf{c}_0$(90,20,20)) and a second simplified image $\mathbf{f}_2$ removing the bright structures ($\|\cdot\|_2^{\mathrm{RGB}}$, $\mathbf{c}_0$(255,255,255)). With the same orderings, a morphological gradient is calculated for each image. The gradient $\mathbf{f}_1$ is used to obtain the contours of brown cells and the gradient of $\mathbf{f}_2$ the contours of blue cells. Here, the markers for each cell are obtained using a similar approach to the previous example.

6. Conclusions and perspectives

In this study, we have introduced an algorithmic framework to apply, in a reliable and generic way, mathematical morphology operators to colour images. The methodology is based on an R-ordering (using the distance to a reference colour) completed by a C-ordering (using a lexicographical cascade). This framework could also be valid to develop other rank-based operators such as colour median filters.

The effects of these operators have been illustrated by means of different examples: colour image simplification using levelings, colour feature extraction using openings (closings) by reconstruction, colour gradients for segmenting, colour denoising by the centre operator, colour enhancement by the contrast mapping, etc. We have shown the suitability of the approach with examples from natural colour images and biomedical microscopic colour images. Exhaustive tests to evaluate quantitatively the performance of different orderings for the corresponding image processing tasks can be the object of future studies. Nevertheless, we hope that we have succeeded in giving the reader an impression of the potential of this approach.

The results of this paper have to be considered as a first step towards a general methodology of multivariate morphology using total ordering based on distance to references completed with a cascade of conditions. In future work we want to address various other important issues such as: the study of theoretical properties of operators derived from these orderings; the investigation of alternatives orderings based on other measures (correlations, projections, etc.) between the points and the reference, or based on a kind of fuzzification; the definition of particular orderings for other multivariate data such as hyper-spectral images, images of temporal series, etc.

Acknowledgments

The author gratefully thanks the reviewers for the valuable comments and improvements they suggested. Thanks are also addressed to Raffi Enficiaud for some stimulating discussions on adjunctions and semilattices.

References

[1] H. Al-Otum, Morphological operators for color image processing based on Mahalanobis distance measure, SPIE Optical Engineering Journal 42 (9) (2003) 2595–2606.
[2] J. Angulo, Morphologie mathématique et indexation d'images couleur. Application à la microscopie en biomédecine. Ph.D. Thesis, Ecole des Mines, Paris, December 2003.
[3] J. Angulo, J. Serra, Automatic analysis of DNA microarray images using mathematical morphology, Bioinformatics 19 (5) (2003) 553–562.
[4] J. Angulo, J. Serra, Morphological coding of color images by vector connected filters, in: Proceedings of IEEE 7th International Symposium on Signal Processing and Its Applications (ISSPA'03), Paris, July 2003, vol. I, pp. 69–72.

[5] J. Angulo, Unified morphological color processing framework in a lum/sat/hue representation, in: Proceedings of International Symposium on Mathematical Morphology (ISMM'05), Kluwer, 2005, pp. 387–396.
[6] J. Angulo, J. Serra, Modelling and segmentation of colour images in polar representations, Image and Vision Computing 25 (4) (2007) 475–495.
[7] J. Astola, P. Haavisto, Y. Nuevo, Vector median filters, Proceedings of the IEEE 78 (4) (1990) 678–689.
[8] V. Barnett, The ordering of multivariate data, Journal Of The Royal Statistical Society A 139 (3) (1976) 318–354.
[9] S. Beucher, F. Meyer, The morphological approach to segmentation: the watershed transformation, in: E. Dougherty (Ed.), Mathematical Morphology in Image Processing, Marcel-Dekker, New York, 1992, pp. 433–481.
[10] T. Boenisch (Ed.), Immunochemical Staining Methods Handbook, third ed., DakoCytomation, Carpinteria, CA, USA, 2001.
[11] P.O. Brown, D. Botstein, Exploring the NewWorld of the genome with DNA microarrays, Nature Genetics 21 (Suppl.) (1999) 33–37.
[12] C. Busch, M. Eberle, Morphological operations for color-coded images, in: EUROGRAPHICS '95, Computer Graphics Forum, vol. 14 (3), 1995, pp. C193–C204.
[13] T. Carron, P. Lambert, Color edege detector using jointly Hue, Saturation and Intensity, in: Proceedings of IEEE International Conference on Image Processing (ICIP'94), 1994, pp. 977–981.
[14] J. Chanussot, P. Lambert, Total ordering based on space filling curves for multivalued morphology, in: H.J.A.M. Heijmans, J.B.T.M. Roerdink (Eds.), Mathematical Morphology and its Applications to Image and Signal Processing (Proceedings of ISMM'98), Kluwer, 1998, pp. 51–58.
[15] M.L. Comer, E.J. Delp, Morphological operations for colour image processing, Journal of Electronic Imaging 8 (3) (1999) 279–289.
[16] S. Gibson, J.A. Bangham, R. Harvey, Evaluating a colour morphological scale-space, in: Proceedings of British Machine Vision Conference (BMVC'03), Norwich UK, July 2003.
[17] J. Goutsias, H.J.A.M. Heijmans, K. Sivakumar, Morphological operators for image sequences, Computer Vision and Image Understanding 62 (3) (1995) 326–346.
[18] A. Hanbury, J. Serra, Mathematical morphology in the HLS colour space, in: Proceedings 12th British Machine Vision Conference (BMV'01), Manchester, 2001, pp. II-451–460.
[19] A. Hanbury, J. Serra, Morphological operators on the unit circle, IEEE Transactions on Image Processing 10 (12) (2001) 1842–1850.
[20] A. Hanbury, J. Serra, Mathematical morphology in the CIELAB space, Image Analysis and Stereology 21 (3) (2002) 201–206.
[21] H.J.A.M. Heijmans, Morphological Image Operators, Academic Press, Boston, 1994.
[22] H.J.A.M. Heijmans, R. Keshet, Inf-semilattice approach to self-dual morphology, Journal of Mathematical Imaging and Vision 17 (1) (2002) 55–80.
[23] M. Iwanowski, J. Serra, Morphological interpolation and color images, in: Proceedings of ICIAP'99, Venice, Italy, 1999.
[24] G.M. Johnson, M.D. Fairchild, Visual Psychophysics and Color Appearance, in: CRC Digital Color Imaging Handbook, 2003.
[25] M. Köppen, Ch. Nowack, G. Rösel, Fuzzy-subsethood based color image processing, in: Proceedings of the 11th Scandinavian Conference on Image Analysis (SCIA'99), Kangerlussnaq, Greenland, vol. 1, 1999, pp. 195–202.
[26] H. Kramer, J. Bruckner, Iterations of non-linear transformations for enhancement on digital images, Pattern Recognition 7 (1975) 53–58.
[27] J. Li, Y. Li, Multivariate mathematical morphology based on principal component analysis: initial results in building extraction, in: Proceedings of the 20th ISPRS Congress, Instanbul, Turkey, vol. 35(B7), 2004, pp. 1168–1173.
[28] G. Louverdis, M.I. Vardavoulia, I. Andradis, Ph. Tsalides, A new approach to morphological color image processing, Pattern Recognition 35 (2002) 1733–1741.
[29] R. Lukac, K.N. Plataniotis, B. Smolka, A.N. Venetsanopoulos, A multichannel order-statistic technique for cDNA microarray image processing, IEEE Transactions on Nanobioscience 3 (4) (2004) 272–285.
[30] R. Lukac, K.N. Plataniotis, B. Smolka, A.N. Venetsanopoulos, cDNA microarray image processing using fuzzy vector filtering framework, Journal of Fuzzy Sets and Systems 152 (1) (2005) 17–35.
[31] R. Lukac, B. Smolka, K. Martin, K.N. Plataniotis, A.N. Venetsanopoulos, Vector filtering for color imaging, IEEE Signal Processing Magazine 22 (1) (2005) 74–86.
[32] R. Lukac, K.N. Plataniotis, A taxonomy of color image filtering and enhancement solutions, in: P.W. Hawkes (Ed.), Advances in Imaging and Electron Physics, vol. 140, Elsevier, 2006, pp. 187–264.
[33] F. Meyer, J. Serra, Contrasts and activity lattice, Signal Processing 16 (1989) 303–317.
[34] F. Meyer, The levelings, in: H.J.A.M. Heijmans, J.B.T.M. Roerdink (Eds.), Mathematical Morphology and its Applications to Image and Signal Processing (Proceedings of ISMM'98), Kluwer, 1998, pp. 199–206.
[35] A. Mojsilovic, E. Soljanin, Quantization of color spaces and processing of color images by fibonacci lattices, in: Proceedings of Human Vision and Electronic Imaging V, vol. SPIE 3959, 2000, pp. 345–355.
[36] F. Ortiz, F. Torres, P. Gil, J. Pomares, S. Puente, F. Candelas, Vectorial ordering by distance for HSI mathematical morphology, in: Proceedings of the IX Spanish Symposium on Pattern Recognition and Image Analysis, Castellón, Spain, vol II, 2001, pp. 379–384.
[37] F. Ortiz, F. Torres, J. Angulo, S. Puente, Comparative study of vectorial morphological operations in different color spaces, in: Proceedings of the SPIE Conference on Intelligent Robots and Computer Vision XX, Boston, MA, SPIE vol. 4572, November 2001, pp. 259–268.
[38] S. Osher, L.I. Rudin, Feature-oriented image enhancement using shock filters, SIAM Journal of Numerical Analysis 27 (1990) 919–940.
[39] R.A. Petters II, Mathematical morphology for angle-valued images, in: Proceedings of Non-Linear Image Processing VIII, vol. SPIE 3026, 1997, pp. 84–94.
[40] I. Pitas, P. Tsakalides, Multivariate ordering in color image processing, IEEE Transactions on Circuits Systems Video Technology 1 (3) (1991) 247–256.
[41] A. Plaza, P. Martinez, R. Perez, J. Plaza, Spatial/spectral endmember extraction by multidimensional morphological operations, IEEE Transactions on Geoscience and Remote Sensing 40 (9) (2002) 2025–2041.
[42] Ch. Ronse, V. Agnus, Morphology on label images: flat-type operators and connections, Journal of Mathematical Imaging and Vision 22 (2005) 283–307.
[43] L.J. Sartor, A.R. Weeks, Morphological operations on color images, Electronic imaging 10 (2) (2001) 548–559.
[44] J. Serra, Image analysis and mathematical morphology. Vol I, and Image Analysis and Mathematical Morphology. Vol II: Theoretical Advances, Academic Press, London, 1982, 1988.
[45] J. Serra, Toggle mappings, in: J.C. Simon (Ed.), From Pixels to Features, Amsterdam, North Holland, 1989, pp. 61–72.
[46] J. Serra, Anamorphoses and function lattices (multivalued morphology), in: E.R. Dougherty (Ed.), Mathematical Morphology in Image Processing, Marcel-Dekker, 1992, pp. 483–523.
[47] J. Serra, Espaces couleur et traitement d'images, CMM-Ecole des Mines de Paris, Internal Note N-34/02/MM, October 2002, 13 p.
[48] J. Serra, Morphological segmentation of colour images by merging of partitions, in: Proceedings of International Symposium on Mathematical Morphology (ISMM '05), Kluwer, 2005, pp. 151–176.
[49] J. Slavik (Ed.), Fluorescence Microscopy and Fluorescent Probes, vol. 2, Plenum Press, New York, USA, 1998, 423 p.
[50] H. Talbot, C. Evans, R. Jones, Complete ordering and multivariate mathematical morphology: algorithms and applications, in: Proceed-

ings of the International Symposium on Mathematical Morphology (ISMM'98), Kluwer, pp. 27–34.
[51] P.E. Trahanias, D. Karakos, A.N. Venetsanopoulos, Directional processing of color images: theory and experimental results, IEEE Transactions on Image Processing 5 (6) (1996) 868–880.
[52] M.I. Vardavoulia, I. Andreadis, Ph. Tsalides, A new vector median filter for colour image processing, Pattern Recognition Letters 22 (6–7) (2001) 675–689.
[53] L. Vincent, Morphological grayscale reconstruction in image analysis: applications and efficient algorithms, IEEE Transactions on Image Processing 2 (2) (1993) 176–201.
[54] K.R. Weber, S.T. Acton, On connected filters in color image processing, Journal of Electronic Imaging 13 (3) (2004) 619–629.
[55] A.R. Weeks, L.J. Sartor, Color morphological operators using conditional and reduced ordering, in: Proceedings of the SPIE Conference on Applications of Digital Image Processing XXII, vol. SPIE 3808, 1999, pp. 358–366.
[56] M. Wheeler, Z.A. Zmuda, Processing color and complex data using mathematical morphology, in: Proceedings of the IEEE National Aerospace and Electronics Conference (NAECON 2000), 2000, pp. 618–624.
[57] S.S. Wilson, Theory of matrix morphology, IEEE Transaction on Pattern Analysis and Machine Intelligence 14 (1992) 636–652.
[58] G. Wyszecki, W.S. Stiles, Color Science: Concepts and Methods, Quantitative Data and Formulae, second ed., John Wiley & Sons, New-York, 1982.
[59] E. Zaharescu, M. Zamfir, C. Vertan, Color morphology-like operators based on color geometric shape characteristics, in: Proceedings of International Symposium on Signals, Circuits and Systems (SCS'03), vol. 1, 2003, pp. 145–148.

13.3 Publication III : G. Noyel, J. Angulo and D. Jeulin. "A new spatio-spectral morphological segmentation for multispectral remote sensing images". *International Journal of Remote Sensing*, Vol. 31, No. 22, 5895-–5920, 2010.

International Journal of Remote Sensing
Vol. 31, No. 22, 20 November 2010, 5895–5920

Taylor & Francis
Taylor & Francis Group

A new spatio-spectral morphological segmentation for multi-spectral remote-sensing images

G. NOYEL*, J. ANGULO and D. JEULIN
MINES ParisTech, CMM - Centre de Morphologie Mathématique, Mathématiques et Systèmes, 35 rue Saint Honoré - 77305 Fontainebleau cedex, France

A general framework of spatio-spectral segmentation for multi-spectral images is introduced in this paper. The method is based on classification-driven stochastic watershed (WS) by Monte Carlo simulations, and it gives more regular and reliable contours than standard WS. The present approach is decomposed into several sequential steps. First, a dimensionality-reduction stage is performed using the factor-correspondence analysis method. In this context, a new way to select the factor axes (eigenvectors) according to their spatial information is introduced. Then, a spectral classification produces a spectral pre-segmentation of the image. Subsequently, a probability density function (pdf) of contours containing spatial and spectral information is estimated by simulation using a stochastic WS approach driven by the spectral classification. The pdf of the contours is finally segmented by a WS controlled by markers from a regularization of the initial classification.

1. Introduction

Multi-spectral (or hyper-spectral) images that are composed of several tens or hundreds of spectral bands are currently used in remote sensing. These spectral bands bring a lot of information concerning the structure of the ground, the vegetation, buildings, etc. However, in order to efficiently process these large amount of data, one has to develop new methods to analyse these images, and, especially, to segment them (i.e. to group similar pixels into connected classes). Standard methods of segmentation need to be extended to this type of rich images.

Two types of information are carried out by multi-/hyper-spectral images:

(i) spatial information contained in the position of each pixel and in the geometry of neighbourhood pixels according to the location on the bitmap grid and
(ii) spectral information contained in the spectral bands, in such a way that a spectrum is associated to each pixel.

Simultaneously using both kinds of information is a crucial point to get a robust and accurate method of segmentation. More precisely, one can compare the spectral information of each pixel and group them into classes. This comparison is global on the image, since each pixel is compared to all the others. However, in this point-wise comparison, the spatial relationship is usually not taken into account. Another method consists of comparing the pixels in a neighbourhood leading to an approach based on a spatial comparison, but usually this spatial processing is achieved

*Corresponding author. Email: noyel@cmm.ensmp.fr

International Journal of Remote Sensing
ISSN 0143-1161 print/ISSN 1366-5901 online © 2010 Taylor & Francis
http://www.tandf.co.uk/journals
DOI: 10.1080/01431161.2010.512314

impenitently for each spectral band. With these remarks, we understand the necessity of combining both kinds of information.

1.1 *State-of-the-art on segmentation of multi-spectral images*

In the literature, there are several other methods of segmentation that can be used for segmentation of multi-spectral images.

Watershed (WS)-based segmentation was used by Soille (1996) to separate the histogram of the multi-spectral image into classes. The mean-shift algorithm was used by Genova *et al.* (2006) to segment hyper-spectral data cubes. Moreover, various classification methods were considered to group pixels into non-connected classes. Support vector machines (SVMs) were applied, for instance, to remote sensing by Gualtieri and Cromp (1999), Lennon *et al.* (2002), and Archibald and Fann (2007). One of the advantages of this method is that it is not sensitive to the dimensionality problem, which is also called the 'Hughes phenomenon' (Hughes 1968, Landgrebe 2002). '*K*-nearest neighbours' was used as a spatio-spectral classification method by Polder (2004) and Marcal and Castro (2005). In Schmidt *et al.* (2007), a classification method based on wavelets was introduced.

In order to analyse the structures in an image, Pesaresi and Benediktsson (2001) developed a morphological profile based on the granulometry principle (Serra 1982). The morphological profile (MP) is composed of a series of openings by reconstruction of increasing sizes and of a series of closings by reconstruction (obtained by the dual operation) (Soille 2003). With these operations, the size and the shape of the objects contained in the image are determined. Therefore, the MP contains only spatial information. A straightforward method to extend the MP to hyper-spectral images is to build the MP for each channel. This approach is called the extended morphological profile (EMP). In fact, Benediktsson *et al.* (2005) use first principal components obtained by a principal component analysis (PCA) of the hyper-spectral image. Consequently, the EMP contains spatial and spectral information. Finally, a classifier, such as a SVM or a neural network (Fauvel *et al.* 2007), is applied to the EMP to obtain a classification in which the classes are not necessarily connected. In the present paper, we consider a segmentation as a partition of connected classes of an image following the definition given in Serra (2006) in the framework of lattice theory.

Gradient-based approaches, such as the WS segmentation, cannot detect thin objects in remote-sensing images. Indeed, thin objects have no interior on the image of the gradient. Consequently, the flooding procedure, which defines a region starting from markers on the gradient, does not take into account the thin objects. These thin objects and other 'small' structures can be obtained, on the one hand, using segmentation techniques based on connective criteria for pixel aggregation Noyel *et al.* 2007b, Soille (2008), or, on the other hand, using the residue of an opening (known as the top-hat operator) that has been extended to multi-variate images in Angulo and Serra (2007). As discussed in Soille (2008), this is a limitation for some applications, e.g. extraction of road networks in aerial images.

The WS transformation is one of the most powerful tools for segmenting images, and was introduced by Beucher and Lantuéjoul (1979). According to the flooding paradigm, the WS lines associate a catchment basin to each minimum of the relief to flood (i.e. a grey-scale image) (Beucher and Meyer 1992). Typically, the relief to flood is a gradient function that defines the transitions between the regions. Using the WS

on a scalar image without any preparation leads to a strong over-segmentation (due to a large number of minima). There are two alternatives in order to eliminate the over-segmentation. The first one consists of initially determining markers for each region of interest. Then, using the homotopy modification, the only local minima of the gradient function are imposed by the region markers. The extraction of the markers, especially for generic images, is a difficult task. The second alternative involves hierarchical approaches based on non-parametric merging of catchment basins (waterfall algorithm) or based on the selection of the most significant minima according to different criteria (dynamics, area or volume extinction values) using extinction functions (Meyer 2001).

We have introduced a general method to segment hyper-spectral images by WS (Noyel *et al.* 2007a). Several multi-variate gradients were studied. The markers are obtained from a previous spectral classification.

Although this approach is powerful, it is a deterministic process that tends to build irregulars contours and can produce an over-segmentation. The stochastic WS was proposed in order to regularize and to produce more significant contours (Angulo and Jeulin 2007). The initial framework was then extended to multi-spectral images (Noyel *et al.* 2007c, Noyel *et al.* 2008a, Noyel 2008).

1.2 *Aim of the paper*

Based on the experience of our previous work on multi-variate image segmentation, the aim of this study is to present a complete chain for an automatic spatio-spectral segmentation of multi-spectral images, and to illustrate the method with some examples of remote-sensing images.

Let us start by presenting a general paradigm of WS-based segmentation of multi-spectral images (figure 1). This segmentation requires two basic ingredients:

(i) some markers for the regions of interest 'mrk' and
(ii) a relief to flood that describes the 'energy' of the frontiers between the regions g.

The markers can be chosen interactively by a user or automatically by means of a morphological criteria ξ_N, or with the classes of a previous spectral classification. The relief to flood is a scalar function (i.e. a grey-scale image). For the deterministic WS, it is usually a gradient (in fact its norm), or a distance function. For the stochastic WS, the function to flood is a probability density function (pdf) of the contours appearing

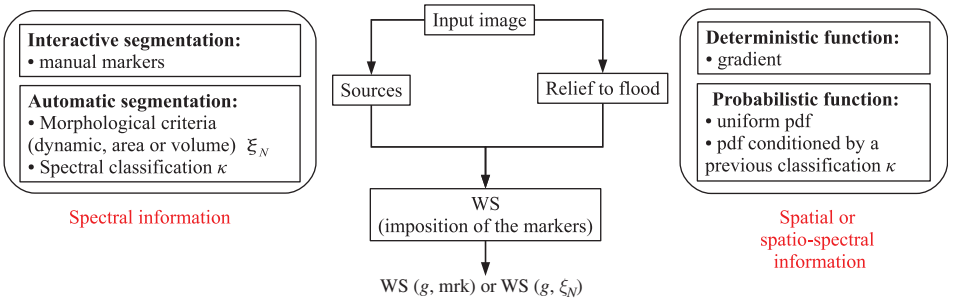

Figure 1. General framework of multi-spectral image segmentation.

in the image. After extracting the markers, they are imposed as sources of the relief to flood, and the WS is computed. The results are noted WS(g,mrk) or WS(g, ξ_N).

The segmentation framework for remote-sensing images introduced in this paper is coherent with the general paradigm of WS-based segmentation. More precisely, the method is based on classification-driven stochastic WS by Monte Carlo simulations, and, as we will show, it gives more regular and reliable contours than standard WS.

The approach is decomposed into several sequential steps. Each step was partially considered in our previous work, where our methods were compared with more standard ones. However, the main objective of this paper is to introduce the global pipeline, presenting, exclusively for each step, the algorithm leading to the best performance.

Firstly, §2 presents the notation used in this paper and the image data considered in the experiments. In §3, a dimensionality reduction stage is performed using factor-correspondence analysis (FCA) (Benzécri 1973). In this context, a new way to select the factor axes (i.e. the eigenvectors) according to their spatial information is introduced. Then, in §4, the reader is reminded of the standard stochastic WS. The spectral classification on the factor space that produces a spectral pre-segmentation of the image is described in §5. Subsequently, a pdf of contours containing spatial and spectral information is estimated by simulation using a stochastic WS approach driven by the spectral classification. In §6, the algorithm for the construction of the classification-driven stochastic WS is discussed. It also includes the way to segment the pdf of contours by a WS controlled by markers from a regularization of the initial classification. Finally, in §7, the conclusions and perspectives of the paper are discussed.

2. Notation

In a formal way, each pixel of a multi-spectral image is a vector with values in wavelength. To each wavelength corresponds an image in two dimensions called a channel. The number of channels depends on the nature of the specific problem under study (satellite imaging, spectroscopic images, temporal series, etc.). Let us denote a hyper-spectral image as

$$\mathbf{f}_\lambda : \begin{cases} E & \rightarrow & \mathcal{T}^L, \\ x & \rightarrow & \mathbf{f}_\lambda(x) = (f_{\lambda_1}(x), f_{\lambda_2}(x), \ldots, f_{\lambda_L}(x)) \end{cases} \tag{1}$$

where:

- $E \subset \mathbb{R}^2$, $\mathcal{T} \subset \mathbb{R}$ and $\mathcal{T}^L = \mathcal{T} \times \mathcal{T} \times \ldots \mathcal{T}$,
- $x = x_i \ / \ i \in \{1, 2, \ldots, P\}$ is the spatial coordinate of a vector pixel $\mathbf{f}_\lambda(x_i)$ (P is the number of pixels of E),
- $f_{\lambda_j} \ / \ j \in \{1, 2, \ldots, L\}$ is a channel (L is the number of channels) and
- $f_{\lambda_j}(x_i)$ is the value of vector pixel $\mathbf{f}_\lambda(x_i)$ on channel f_{λ_j}.

Figure 2 gives an example of a five-band satellite simulated image PLEIADES, acquired by the Centre National d'Etudes Spatiales (CNES), the French space agency and provided by Flouzat *et al.* (1998). Its channels are the following: f_{λ_1}, blue; f_{λ_2}, green; f_{λ_3}, red; f_{λ_4}, near-infrared; and f_{λ_5}, panchromatic. The panchromatic channel, initially 1460×1460 pixels with a resolution of 0.70 m, was resized to 365×365 pixels. Therefore, the resolution is 2.80 m in an image of $365 \times 365 \times 5$ pixels. In order to represent a multi-spectral image in a synthetic way, we created a synthetic red, green, blue (RGB) image using channels f_{λ_3} red, f_{λ_2} green and f_{λ_1} blue.

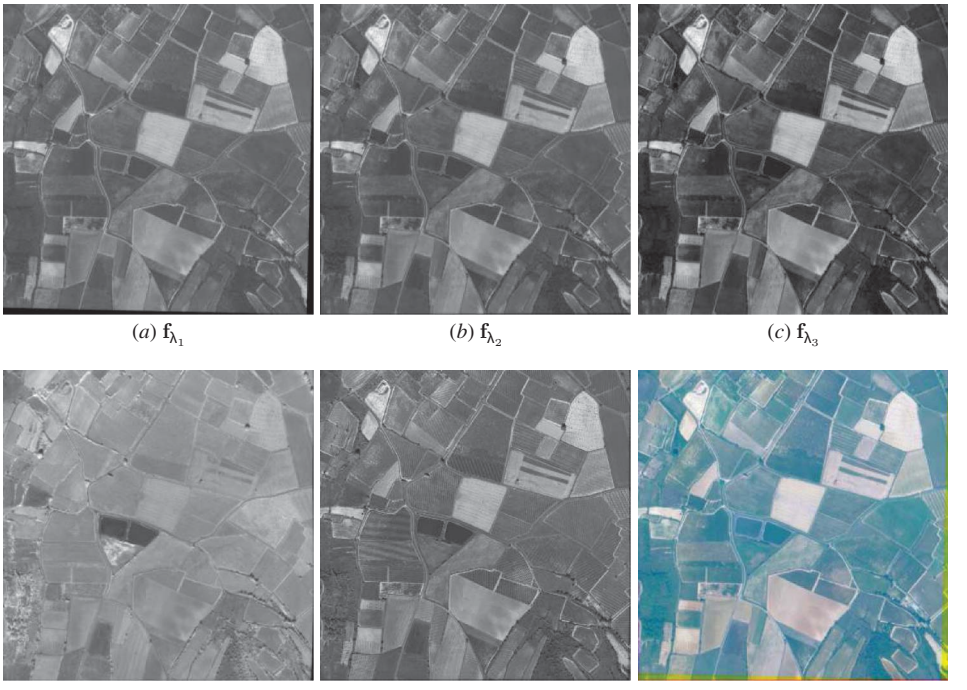

Figure 2. Channels of multi-spectral image $\mathbf{f}_\lambda$ 'Roujan' (©CNES): (*a*) $\mathbf{f}_{\lambda_1}$ blue, (*b*) $\mathbf{f}_{\lambda_2}$ green, (*c*) $\mathbf{f}_{\lambda_3}$ red, (*d*) $\mathbf{f}_{\lambda_4}$ near-infrared, (*e*) $\mathbf{f}_{\lambda_5}$ panchromatic and (*f*) synthetic RGB representation.

The downsampling method consists of, by averaging, keeping only one pixel on four pixels in both directions of the plane. The coordinates (i,j) of the pixels are ordered as the standard ordering used for matrices. Moreover, we also notice that even if the downsampled panchromatic image has values strongly correlated to average intensity of the red, blue and green channels, the spatial resolution of the panchromatic is better than the chromatic bands, and consequently there is a better resolution of the contours, which is important for the aim of image segmentation. Indeed, to deal with the redundancy, the FCA transforms the original channels into uncorrelated factor channels (according to the chi-squared metric).

3. Dimensionality reduction

As the number of channels in a multi-spectral image is usually important, the spectrum information contained in these channels is redundant. Therefore, in order to avoid the Hughes phenomenon (Hughes 1968, Landgrebe 2002) associated with the spectral dimensionality problem, as well as to reduce the computational time, it is necessary to reduce the number of channels.

Consequently, a data reduction is performed using FCA (Benzécri 1973). We prefer using an FCA instead of a PCA or a maximum noise fraction (MNF) (Green *et al.* 1988) because image values are positive and the spectral channels can be considered as probability distributions.

Green *et al.* (1988) have demonstrated that PCA and MNF are equivalent in the case of an uncorrelated noise with equal variance in all channels. This explains why PCA is often used to remove noise on hyper-spectral images in which the noise is almost uncorrelated with the same variance on all channels.

As for PCA, from selected factorial FCA axes, the image can be partially reconstructed. The metric used in FCA is the chi-squared, which is adapted to probability laws and normalized by channels weights. FCA can be seen as a transformation going from image space to a factorial space. In the factorial space, the coordinates of the pixel vector, on each factorial axis, are called pixel factors. The pixel factors can be considered as another multi-spectral image whose channels correspond to the factorial axes:

$$\zeta : \begin{cases} \mathcal{T}^L & \rightarrow \quad \mathcal{T}^K / K < L, \\ \mathbf{f}_\lambda(x) & \rightarrow \quad \mathbf{c}^{\mathbf{f}}_\alpha(x) = \left(c^{\mathbf{f}}_{\alpha_1}(x), \ldots, c^{\mathbf{f}}_{\alpha_K}(x) \right). \end{cases} \tag{2}$$

A limited number K, with $K < L$, of factorial axes is usually chosen. Therefore, FCA can be seen as a projection of the initial vector pixels in a factor space with a lower dimension. Moreover, as for PCA, FCA reduces the spectral noise on multi-spectral images (Green *et al.* 1988, Noyel *et al.* 2007a, Noyel 2008). Figure 3 shows FCA factor pixels $\mathbf{c}^{\mathbf{f}}_\alpha$ of image 'Roujan'. Consequently, we have two spaces for multi-variate segmentation: the multi-spectral image space (MIS) and the factor image space (FIS).

A common problem in remote-sensing applications is the registering of the various spectral images. If the registering step is not perfect, the spatial shifts introduces into the dimensionality reduction an FCA factor containing this information; see for instance, in figure 3, the FCA factor image $c^{\mathbf{f}}_{\alpha_2}$. This image looks like a Laplacian image, but for the purpose of segmentation, it should be considered as a factor image containing spatial noise. We only show below how to detect and remove these 'noisy' factor images.

Another approach to reduce the number of channels consists of modelling the spectrum of each vector pixel $\mathbf{f}_\lambda(x_i)$ and creating a new multi-spectral image composed of the parameters of the model (Noyel *et al.* 2007a); however, for generic multi-spectral remote-sensing images, this kind of modelling is quite difficult.

As shown by Benzécri (1973) and Green *et al.* (1988), some factor pixels on factor axes contain mainly noise, and others contain signal information. In order to select relevant axes containing information (i.e. signal against noise), we introduce a new method based on a measurement of the signal to noise ratio (SNR) of every factor image. For each factorial axis α_k, the centred spatial covariance is computed by a two-dimensional (2D) fast Fourier transform (FFT) on the pixel factors:

$$\overline{g}_{\alpha_k}(h) = E[\overline{c}^{\mathbf{f}}_{\alpha_k}(x)\overline{c}^{\mathbf{f}}_{\alpha_k}(x+h)],$$

with $\overline{c}^{\mathbf{f}}_{\alpha_k}(x) = c^{\mathbf{f}}_{\alpha_k}(x) - E[c^{\mathbf{f}}_{\alpha_k}(x)]$, where E is the mathematical expectation (here the statistical expectation).

The covariance peak, at the origin, contains the sum of the signal variance and the noise variance of the image. Then, the signal variance is estimated by the maximum (i.e. value at the origin) of the covariance $\overline{g}$. Based on the property of the morphological opening, which removes intensity peaks smaller than the structuring element (SE) used, we apply a morphological opening γ on the covariance image with a unitary centred SE (square of 3×3 pixels) in order to remove the peak of signal associated with the noise variance: $\mathrm{Var(signal)} = \gamma\overline{g}_{\alpha_k}(0)$. The noise variance is

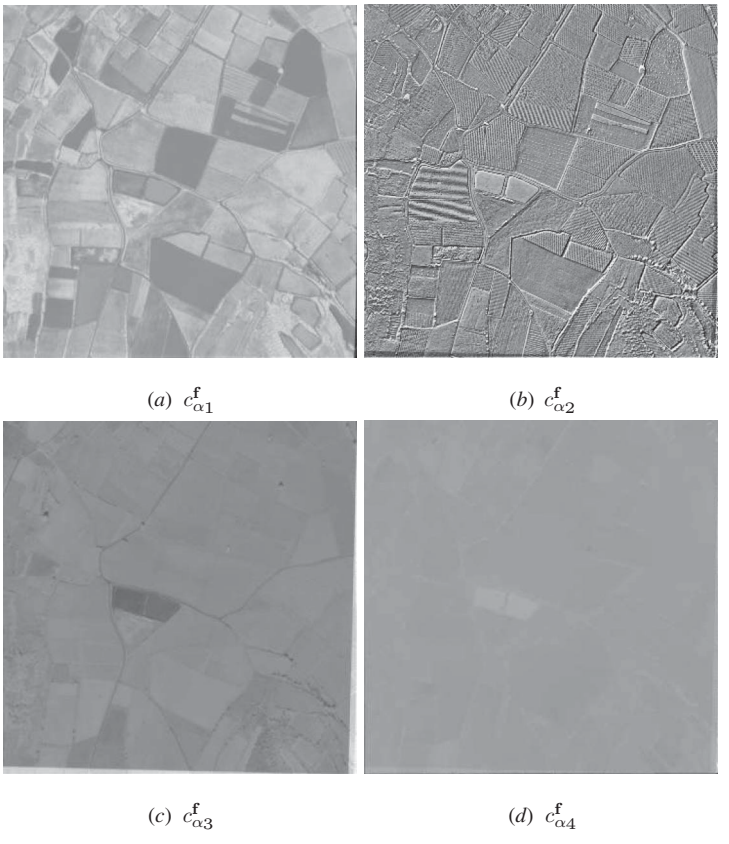

(*a*) $c^{\mathbf{f}}_{\alpha 1}$ (*b*) $c^{\mathbf{f}}_{\alpha 2}$

(*c*) $c^{\mathbf{f}}_{\alpha 3}$ (*d*) $c^{\mathbf{f}}_{\alpha 4}$

Figure 3. FCA factors pixels $\mathbf{c}^{\mathbf{f}}_{\alpha}$ of image 'Roujan' on axes: (*a*) 1, (*b*) 2, (*c*) 3 and (*d*) 4, with respective inertias 84.1%, 8.7%, 6.2% and 1%.

therefore given by the residue of the opening of the covariance at the origin: $\mathrm{Var(noise)} = \overline{g}_{\alpha_k}(0) - \gamma\overline{g}_{\alpha_k}(0)$ (figure 4). Hence, the SNR is defined for a factor axis α_k as:

$$\mathrm{SNR}_{\alpha_k} = \frac{\mathrm{Var(signal)}}{\mathrm{Var(noise)}} = \frac{\gamma\overline{g}_{\alpha_k}(0)}{\overline{g}_{\alpha_k}(0) - \gamma\overline{g}_{\alpha_k}(0)}. \tag{3}$$

In the current example, by analysis of the factor pixels and their SNRs, we observe that they are higher for axes 1, $c^{\mathbf{f}}_{\alpha_1}$, and 3, $c^{\mathbf{f}}_{\alpha_3}$, than for axes 2, $c^{\mathbf{f}}_{\alpha_2}$, and 4, $c^{\mathbf{f}}_{\alpha_4}$. Therefore, the axes 1 and 3 are retained. For an automatic selection of factor axes, the axes with a SNR lower than 1 are rejected.

In figure 5, we notice that axis 3, which is selected, has a lower inertia than axis 2, which is rejected. Therefore, SNR analysis makes it possible to describe the relevant signal in dimensionality reduction, more than the inertia-like criterion.

4. Introduction to stochastic WS

Angulo and Jeulin (2007) defined a new method of stochastic WS for grey-scale and colour images. This method was extended to hyper-spectral images by Noyel *et al.*

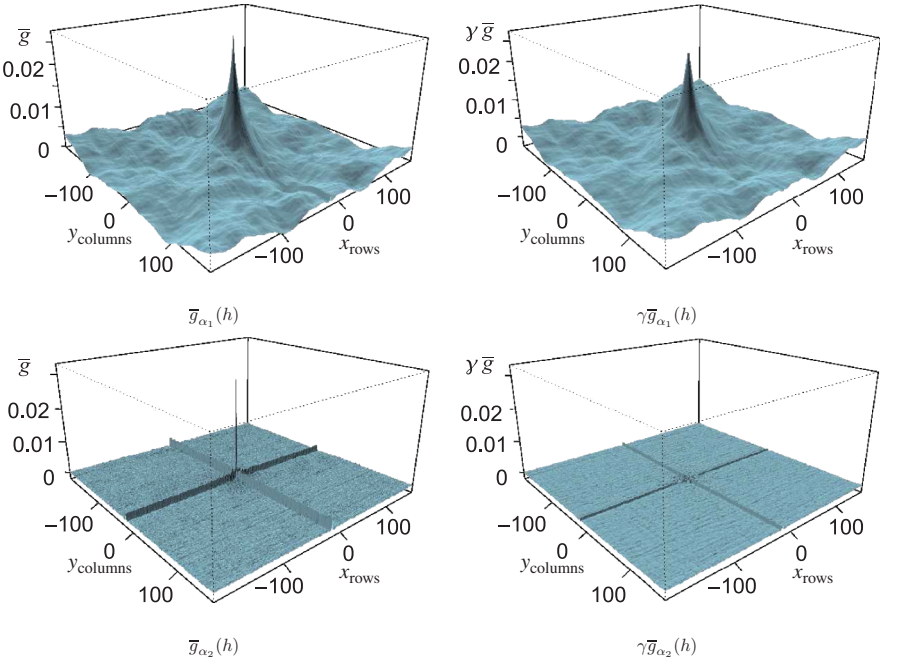

Figure 4. Two-dimensional covariances for factor pixels $c^{\mathbf{f}}_{\alpha_1}$ and $c^{\mathbf{f}}_{\alpha_2}$ of image 'Roujan' before (left) and after opening (right).

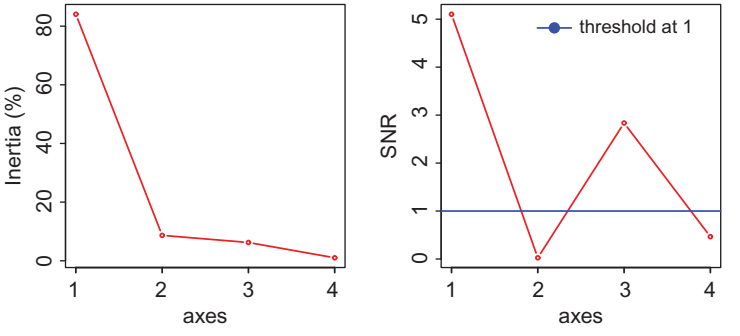

Figure 5. Inertia (%) and SNR for factor pixels of image 'Roujan'.

(2007c). In addition, the segmentation of multi-spectral images by classical (deterministic) WS was presented in Noyel *et al.* (2007a). Several improvements were made by Noyel (2008) and Noyel *et al.* (2008a).

4.1 *Principle of the stochastic WS*

One of the main artefacts of the classical WS is that small regions strongly depend on the position of the markers, or on the volume (i.e. the integral of the grey levels) of the catchment basin, associated with their minima. In fact, there are two kinds of contours associated with the WS of a gradient: first-order contours, which correspond

to significant regions and which are relatively independent from markers; second-order contours, associated with 'small', 'low' contrasted and textured regions, which depend strongly on the location of markers. Stochastic WS aims at enhancing the first order contours from a sampling effect, to improve the result of the WS segmentation.

Let us consider $\{\mathrm{mrk}_i(x)\}_{i=1}^{M}$ a series of M realizations of N uniform or regionalized random germs. Each of these binary images is considered as the marker for a WS segmentation of a scalar gradient or a vector gradient. Therefore, a series of segmentations is obtained, i.e. $\{\mathrm{sg}_i^{\mathrm{mrk}}(x)\}_{i=1}^{M}$. Starting from M realizations of the contours, the pdf(x) of contours is computed using the Parzen window method. The kernel density estimation using the Parzen window (Duda and Hart 1973) is a way to estimate the pdf of a random variable. Let $\mathbf{x}_1, \mathbf{x}_2, \ldots, \mathbf{x}_M \in \mathbb{R}^n$ be M samples of a random variable, the kernel-density approximation of its pdf is: $\widehat{f}_h(\mathbf{x}) = \frac{1}{Nh}\sum_{i=1}^{N} K\left(\frac{\mathbf{x}-\mathbf{x}_i}{h}\right)$, where $K(\mathbf{x})$ is some kernel and the bandwidth h is a smoothing parameter. Usually, $K(\mathbf{x})$ is taken to be a Gaussian function, G_σ, with mean zero and variance σ^2. The smoothing effect of the Gaussian convolution kernel (typically $\sigma = 3$ working on contours of one pixel width) is important to obtain a function where near contours, such as textured regions or associated with small regions, are added together. In other words, the WS lines with a very low probability, which correspond to non-significant boundaries, are filtered out.

The pdf of contours could be thresholded to obtain the most prominent contours. However, to obtain closed contours, the pdf image can also be segmented, as we consider here, using a WS segmentation.

4.2 *Influence of parameters*

The stochastic WS needs two parameters:

(i) M realizations of germs. The method is almost independent on M if it is large enough. Practically, the convergence is ensured for M in the range 20–50. We propose to use M equal to 100.

(ii) N germs (or markers). In WS, the number of regions obtained is equal to the number of markers. In the case of the stochastic WS, if N is small, a segmentation in large regions is privileged; if N is too large, the over-segmentation of $\mathrm{sg}_i^{\mathrm{mrk}}$ leads to a very smooth pdf, which loses its properties to select the R regions. Therefore, the stochastic WS mainly depends on N, but is linked to the number of regions R that should be finally selected. As was shown in Angulo and Jeulin (2007), it is straightforward to use $N > R$.

As described below, in this study, the number of markers of each realization used in the conditioned stochastic WS will be equal to the number of connected classes of the classification $\widehat{\kappa}$ different of the void class.

5. Generation of markers from a classification

To segment the pdf of contours by WS, it is necessary to have markers for the spectral objects of interests. The latter are obtained by a spectral classification. This classification step groups the pixels into classes with similar spectra. In fact, each pixel is compared to all the others, leading to a global comparison of the image spectra. We have tested two kinds of methods for spectral classification on multi-spectral images: unsupervised methods and supervised methods.

In the case of remote sensing, we show results obtained using an unsupervised method such as 'clara' (Kaufman and Rousseeuw 1990). Unsupervised and supervised methods in remote sensing using mathematical morphology, as well as the 'clara' method, are also investigated in Epifanio and Soille (2007). For other contexts different from remote sensing, we tested other unsupervised methods, such as k-means, and supervised methods, such as linear-discriminant analysis (Noyel 2008, Noyel *et al.* 2008b). One of the strong points of supervised approaches is to integrate prior information about spectrum classes into the classification. However, in generic remote-sensing segmentation problems, we are not looking for a special kind of spectrum. Therefore, we prefer, in the presentation of the current paper, to use an unsupervised classification with a unique parameter, namely the number of classes.

Hence, after data reduction and the spectral filtering stage by FCA, a spectral classification by 'clara' is performed on the factor space. We have to stress that a correct classification, used later for constructing the pdf, requires factor pixels without noise. The classification algorithm uses an Euclidean distance that is coherent with the metric of the factor space (Noyel *et al.* 2007a). The unique parameter is the number of classes, which is chosen in order to get a good separation of the classes. Here, for this example, three classes are retained (figure 6).

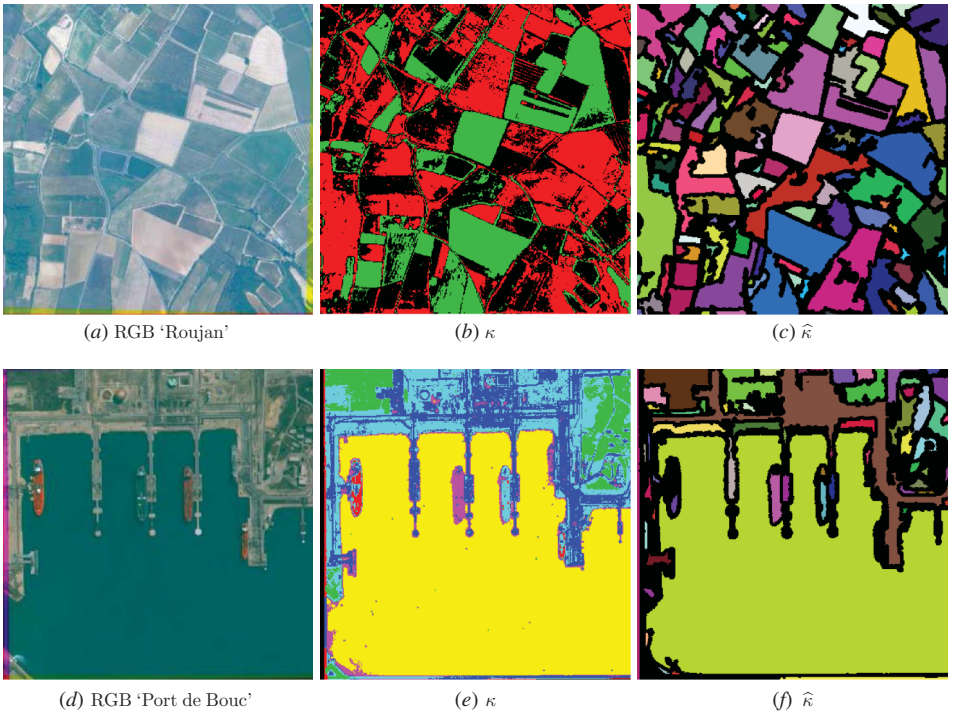

(*a*) RGB 'Roujan' (*b*) κ (*c*) $\widehat{\kappa}$

(*d*) RGB 'Port de Bouc' (*e*) κ (*f*) $\widehat{\kappa}$

Figure 6. First line: (*a*) synthetic RGB image 'Roujan', (*b*) classification κ in three classes in factor space formed by $c^{\mathbf{f}}_{\alpha_1}$ and $c^{\mathbf{f}}_{\alpha_3}$ and (*c*) transformed classification $\widehat{\kappa} = \Upsilon(\kappa)$. Second line: (*d*) synthetic RGB image 'Port de Bouc', (*e*) classification κ in seven classes in factor space formed by $c^{\mathbf{f}}_{\alpha_1}$ and $c^{\mathbf{f}}_{\alpha_2}$ and (*f*) transformed classification $\widehat{\kappa} = \Upsilon(\kappa)$. The void class is in black on the images $\widehat{\kappa}$. The way to compute the transformed classification is explained in §6.1. The colours correspond to the labels of the transformed classification obtained after new labelling.

6. Multi-spectral segmentation by stochastic WS

The previously obtained spectral classification of pixels leads to a spatial partition of the image on regions that are spectrally homogeneous. This initial partition is denoted κ. However, they do not define a partition into spatial connected classes: various connected components belong to the same spectral class. In order to address this issue, a segmentation stage is needed that introduces spatial information (i.e. regional information). In this section, after presenting an algorithm to pre-process the previous classification κ, the extension of stochastic WS to multi-spectral images is explained; then we show a way to constrain the pdf by the previous spectral classification.

6.1 *Pre-processing of markers from the classification*

Pre-processing of the connected classes of the classification is necessary for two reasons:

(i) To give necessary degrees of freedom to the final WS of the pdf. Actually, if we use the connected classes of the classification κ as markers of the flooding process, then the WS is completely defined by the limit of the classes after labelling them into connected classes. Therefore, we propose to process the initial partition using an anti-extensive transformation such as an erosion (Serra 1982, Soille 2003). For instance, using an SE of size 5×5 pixels each spatial class is reduced, and the smallest classes disappear. We consider that classes corresponding to 'noise' are totally removed. The smallest classes could also be removed by means of an area opening (Soille 2003). Therefore, after processing the initial partition, a partial partition is obtained. There are several alternatives to deal with the problem that the partial partition is not a partition of the support space; for instance, adding the singletons outside its support to the partial partition. We prefer, however, the following solution. We introduce a particular label, the 'void class', in such a way that after processing the initial partition, covering the whole space, a new partition is also obtained. In the new partition, the existing classes are modified (reduced) and, in addition, a new class is introduced, the void class. If we want to keep all the classes, for instance, if the aim is to segment thin objects as a network of roads, we could use a homotopic thinning instead of an erosion.

(ii) To fill the holes inside the largest classes with an extensive transformation such as a closing by reconstruction with an SE of size, for instance, 3×3 pixels (Serra 1982, Soille 2003).

The transformations are applied to each class of the initial spectral classification. More precisely, an index function (i.e. a binary image)

$$h_{\kappa(n)}(x) = \begin{cases} 1, & \text{if } x \in \kappa(n); \\ 0, & \text{otherwise.} \end{cases} \tag{4}$$

is associated with each spectral class, $\kappa(n)$ with $n = 1, \ldots, N$, of the previous classification $\kappa = \cup_n \kappa(n)$. Then, the sequence of the anti-extensive and extensive transformations are applied to each index function, $h_{\kappa(n)}$ for all $n = 1, \ldots, N$, in order to obtain the transformed index function $h'_{\kappa(n)}$. Then, the supremum (union) of the index functions is computed, followed by a standard labelling to obtain the connected components that correspond to markers for the segmentation, except for the void

class that is not a marker. The complete transform is noted Υ, and it results in a new partition $\widehat{\kappa} = \Upsilon(\kappa)$ (figure 6). The partition $\widehat{\kappa}$ will then be strongly used for the spatial segmentation by stochastic WS.

6.2 *Extension of the stochastic WS to multi-variate or hyper-spectral images*

The extension of the stochastic WS was first presented in Noyel *et al.* (2007c). The key points are recalled in the current paper.

6.2.1 Spectral distances and gradient. In order to segment images according to WS-based paradigms, a gradient is needed. A gradient image, in fact, its norm, is a scalar function with values in the reduced interval [0, 1] (after normalization), i.e. $\varrho(x) : E \rightarrow [0, 1]$. In order to define a gradient, two approaches are considered: the standard symmetric morphological gradient on each marginal channel and a metric-based vectorial gradient on all channels.

The morphological gradient is defined for scalar images f as the difference between dilation and erosion by a unit SE B, i.e.

$$\begin{aligned}\varrho(f_{\lambda_j}(x)) &= \delta_B(f_{\lambda_j}(x)) - \varepsilon_B(f_{\lambda_j}(x)) \\ &= \vee[f_{\lambda_j}(y), y \in B(x)] - \wedge[f_{\lambda_j}(y), y \in B(x)].\end{aligned}$$

As was shown in Hanbury and Serra (2001), the morphological gradient can be generalized to a vectorial image by using the following relation:

$$\{f(x) - \vee[f(y), y \in B(x), y \neq x]\} = \wedge\{f(x) - f(y), y \in B(x), y \neq x\},$$

and the relation obtained by the inversion of the suprema and infima. The morphological gradient can be written in a form that is only composed of increments computed in the neighbourhood B centred at point x:

$$\varrho(f)(x) = \vee[f(x) - f(y), y \in B(x), y \neq x] - \wedge[f(x) - f(y), y \in B(x), y \neq x].$$

To extend this relation to multi-variate functions, it is sufficient to replace the increment $[f(x) - f(y)]$ by a distance between vector pixels $d(\mathbf{f}_\lambda(x), \mathbf{f}_\lambda(y))$ to obtain the following metric-based gradient:

$$\varrho_d \mathbf{f}_\lambda(x) = \vee[d(\mathbf{f}_\lambda(x), \mathbf{f}_\lambda(y)), y \in B(x), y \neq x] - \wedge[d(\mathbf{f}_\lambda(x), \mathbf{f}_\lambda(y)), y \in B(x), y \neq x].$$

Various metric distances, useful for multi-spectral images, are available for this gradient:

- the Euclidean distance

$$d_{\mathrm{E}}(\mathbf{f}_\lambda(x), \mathbf{f}_\lambda(y)) = \sqrt{\sum_{j=1}^{L} (f_{\lambda_j}(x) - f_{\lambda_j}(y))^2}$$

  and
- the chi-squared distance

$$d_{\chi^2}(\mathbf{f}_\lambda(x_i), \mathbf{f}_\lambda(x_{i'})) = \sqrt{\sum_{j=1}^{L} \frac{S}{f_{\cdot\lambda_j}} \left(\frac{f_{\lambda_j}(x_i)}{f_{x_i\cdot}} - \frac{f_{\lambda_j}(x_{i'})}{f_{x_{i'}\cdot}} \right)^2},$$

with $f_{\cdot\lambda_j} = \sum_{i=1}^{P} f_{\lambda_j}(x_i)$, $f_{x_i\cdot} = \sum_{j=1}^{L} f_{\lambda_j}(x_i)$ and $S = \sum_{j=1}^{L} \sum_{i=1}^{P} f_{\lambda_j}(x_i)$.

An important point is to choose an appropriate distance depending on the space used for image representation: the chi-squared distance is adapted to the MIS and the Euclidean distance to the FIS. More details on multi-variate gradients are given by Noyel *et al.* (2007a). Another example of a multi-variate gradient is given by Scheunders (2002).

6.2.2 Probability density function for multi-spectral images. We studied two ways to extend the pdf gradient to multi-spectral images:

(i) the first one is a marginal approach (i.e. channel by channel) called the marginal pdf (mpdf) (algorithm *1* and figure 7) and
(ii) the second one is a vectorial approach (i.e. vector pixel by vector pixel) called the vectorial pdf (vpdf) (algorithm *2* and figure 8).

Algorithm *1* mpdf

1: For the morphological gradient of each channel $\varrho(f_{\lambda_j})$, $j \in [1,\ldots,L]$, throw M realizations of N uniform random germs, i.e. the markers $\{\mathrm{mrk}_i^j\}_{i=1\ldots M}^{j=1\ldots L}$, generating $M \times L$ realizations. Get the series of segmentations, $\{\mathrm{sg}_i^j(x)\}_{i=1\ldots M}^{j=1\ldots L}$, by WS associated to morphological gradients of each channel $\varrho(f_{\lambda_j})$.
2: Get the mpdfs on each channel by the Parzen method: $\mathrm{pdf}_j(x) = \frac{1}{M}\sum_{i=1}^{M} \mathrm{sg}_i^j(x) * G_\sigma$.
3: Obtain the weighted mpdf:

$$\mathrm{mpdf}(x) = \sum_{j=1}^{L} w_j \mathrm{pdf}_j(x), \tag{5}$$

with $w_j = 1/L, j \in [1,\ldots,L]$ in the MIS and w_j equal to the inertia axes in the FIS.

Algorithm *2* vpdf

1: For the vectorial gradient $\varrho^d(\mathbf{f}_\lambda)$, throw $M \times L$ realizations of N uniform random germs, i.e. the markers $\{\mathrm{mrk}_i\}_{i=1\ldots M\times L}$, with L being the channels number. Get the segmentation, $\{\mathrm{sg}_i(x)\}_{i=1\ldots M\times L}$, by WS associated with the vectorial gradient $\varrho^d(\mathbf{f}_\lambda)$, with $d = d_{\chi^2}$ in the MIS or $d = d_{\mathrm{E}}$ in the FIS.
2: Obtain the pdf:

$$\mathrm{vpdf}(x) = \frac{1}{M \times L} \sum_{i=1}^{M\times L} \mathrm{sg}_i(x) * G_\sigma. \tag{6}$$

The probabilistic gradient was also defined in Angulo and Jeulin (2007) to ponder the enhancement of the largest regions by the introduction of smallest regions. It is defined as $\varrho_{\mathrm{prob}} = \mathrm{mpdf} + \varrho^d$: after normalization in [0,1] of the weighted mpdf and the metric-based gradient ϱ^d.

In order to obtain a partition from the mpdf, vpdf or the gradient ϱ_{prob}, these probabilistic functions can be segmented for instance by a hierarchical WS with a volume criterion (see the examples of figure 9), as studied in Noyel *et al.* (2007c). In such a case, the goal is not to find all the regions. In fact, the stochastic WS addresses the problem of segmentation of an image in few pertinent regions, according to a combined criterion of contrast and size. In the present study, as we discuss below, the

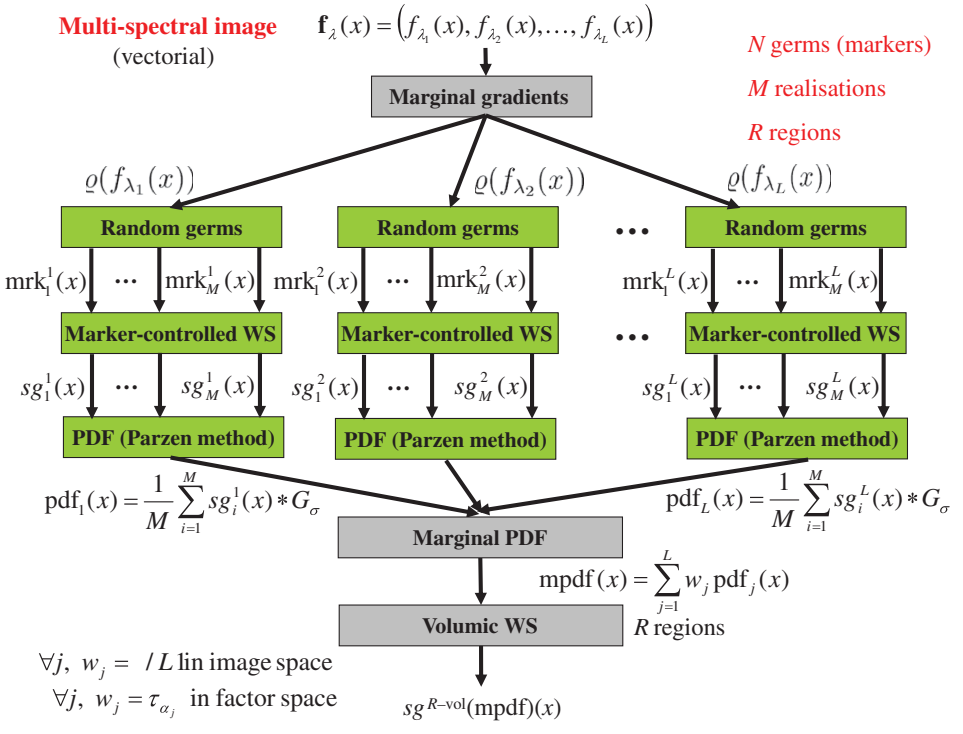

Figure 7. General framework stochastic WS on the mpdf for multi-spectral images.

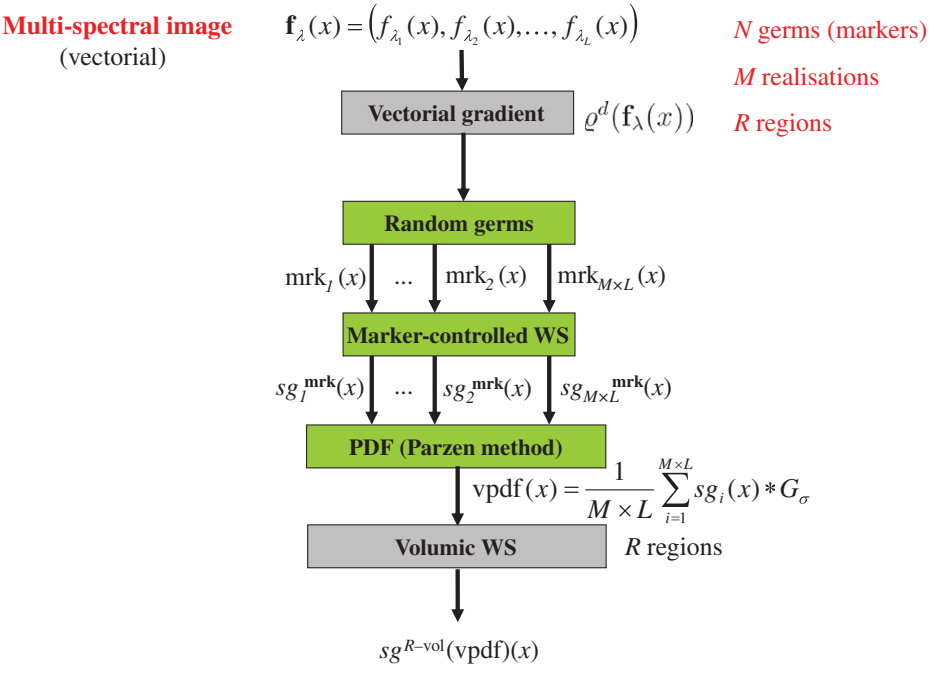

Figure 8. General framework stochastic WS on the vpdf for multi-spectral images.

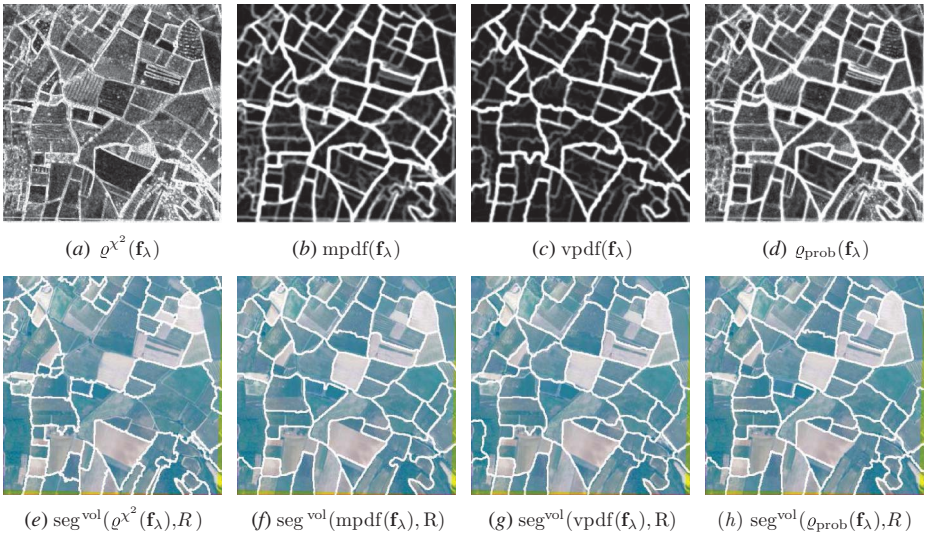

Figure 9. Top: (*a*) gradients and (*b,c,d*) pdfs. Bottom: (*e,f,g,h*) associated WS segmentations, with a volume criterion, on image 'Roujan', in the MIS, with $N = 50$ points, $M = 100$ realizations, $R = 50$ regions with the largest volume.

segmentation of the pdf is obtained from markers of the processed classification. In Noyel *et al.* (2007c), it was also shown that the mpdf and vpdf give similar results in the MIS and the FIS, as we can also observe in the comparisons of figure 9. Consequently, in what follows, we choose to work on the MIS to show that our method is not limited by the number of channels.

6.3 *Conditioning the germs of the pdf by a previous classification*

The pdf of contours with uniform random germs is constructed without any prior information about the spatial/spectral distribution of the image. In this part, we introduce spectral information by conditioning the germs by the previous transformed classification $\widehat{\kappa}$. Therefore, the pdf obtained contains spatio-spectral information. It is possible to use point germs or random-ball germs whose location is conditioned by the classification. An exhaustive study was presented by Noyel (2008) and Noyel *et al.* (2008c). In the sequel, we present random-ball germs regionalized by a classification where each connected class may be hit one time, $\mathrm{mrk}_i^{\kappa-b}(x)$.

Let us explain the procedure. The transformed classification $\widehat{\kappa}$ is composed of connected classes, $\widehat{\kappa} = \cup_k C_k$ with $C_k \cap C_{k'} = \emptyset$, for $k \neq k'$. The void class is written C_0. Then, the random germs are drawn conditionally to the connected components C_k of the filtered classification $\widehat{\kappa}$. To do this, the following rejection method is used: the random point germs are uniformly distributed. If a point germ m falls inside a connected component C_k of minimal area S and not yet marked, then it is kept, otherwise it is rejected. Therefore, not all the germs are kept. These point germs are called random point germs regionalized by the classification κ. However, the regionalized point germs sample all the classes independently of their prior estimate of class size/shape, given by the classification. In order to tackle this limitation, we propose to use random balls as germs.

The centres of the balls are the random point germs, and the radii r are uniformly distributed between 0 and a maximum radius, Rmax: $\mathcal{U}[1, \text{Rmax}]$. Only the intersection between the ball $B(m, r)$ and the connected component C_p is kept as a germ. These balls are called random-ball germs regionalized by the classification κ and noted $\text{mrk}_i^{\kappa-b}(x)$.

Algorithm 3 sketches the process. We notice that N is the number of random germs to be generated. The effective number of implanted germs is less than N.

Algorithm *3* Random-ball germs regionalized by a classification (each connected class may be hit one time) $\text{mrk}_i^{\kappa-b}(x)$.

1: Given N the number of drawn germs m.
2: Set the background class and the void class C_0 to *marked*.
3: **for all** drawn germs m from 1 to N do
4: **if** C_k, such as $m \in C_k$, is *not marked* **then**
5: $r = \mathcal{U}[1, \text{Rmax}]$
6: Keep as a germ $\text{B}(m, r) \cap C_k$
7: Set the class C_k to *marked*
8 : **end if**
9: **end for**

We use the mpdf to show our results. Some random-ball germs regionalized by a classification, $\{\text{mrk}_i^{\kappa-b^j}(x)\}_{i=1\ldots5}^{j=1}$, their associated realizations of contours, $\{\text{sg}_i^j(x)\}_{i=1\ldots5}^{j=1}$, and the mpdf computed in the MIS, $\text{mpdf}^{\kappa-b}(\mathbf{f}_\lambda)$, are presented in figure 10.

A comparison between the mpdf with uniform random point germs, $\text{mpdf}^{\text{pt}}(\mathbf{f}_\lambda)$ (noted $\text{mpdf}(\mathbf{f}_\lambda)$) and the mpdf with random-ball germs $\text{mpdf}^{\kappa-b}(\mathbf{f}_\lambda)$ is shown in figure 11. These pdf are segmented by hierarchical WS with a volume criterion, $\text{sg}^{R-\text{vol}}(\text{mpdf}^{\text{pt}}(\mathbf{f}_\lambda))$ and $\text{sg}^{R-\text{vol}}(\text{mpdf}^{\kappa-b}(\mathbf{f}_\lambda))$. In this particular example, the advantage of the pdf obtained with the conditioned random balls is obvious with respect to the pdf from uniform random point germs. Moreover, in order to compare the results of segmentation of the example of figure 11, we must notice that, in both images, only the eight most important regions have been segmented. If the purpose is to segment all the objects, including the smallest ones, we only need to increase the number of desired volumic regions.

6.4 *Segmentation of the pdf*

After having built the pdf, a segmentation stage is required to obtain the contours of the image. Two possibilities were tested:

(i) a marker-controlled WS using as markers the transformed classification $\text{sg}^{\text{mrk}}(\text{mpdf}^{\kappa-b}(\mathbf{f}_\lambda), \widehat{\kappa})$ (Noyel *et al.* 2008a); in this case, no more parameters are required and
(ii) a hierarchical WS with a volume criterion $\text{sg}^{R-\text{vol}}(\text{mpdf}^{\kappa-b}(\mathbf{f}_\lambda))$ (Noyel *et al.* 2007c); therefore, it is necessary to define an additional parameter: the number of regions with the largest volume.

In order to show the robustness of our approach, we used the same method to build the pdf conditioned by the classification on similar images 'Roujan', 'Roujan 0 2' and 'Roujan 0 9'. As for image 'Roujan', factor axes $c_{\alpha_1}^{\mathbf{f}}$ and $c_{\alpha_3}^{\mathbf{f}}$ are kept because the SNR

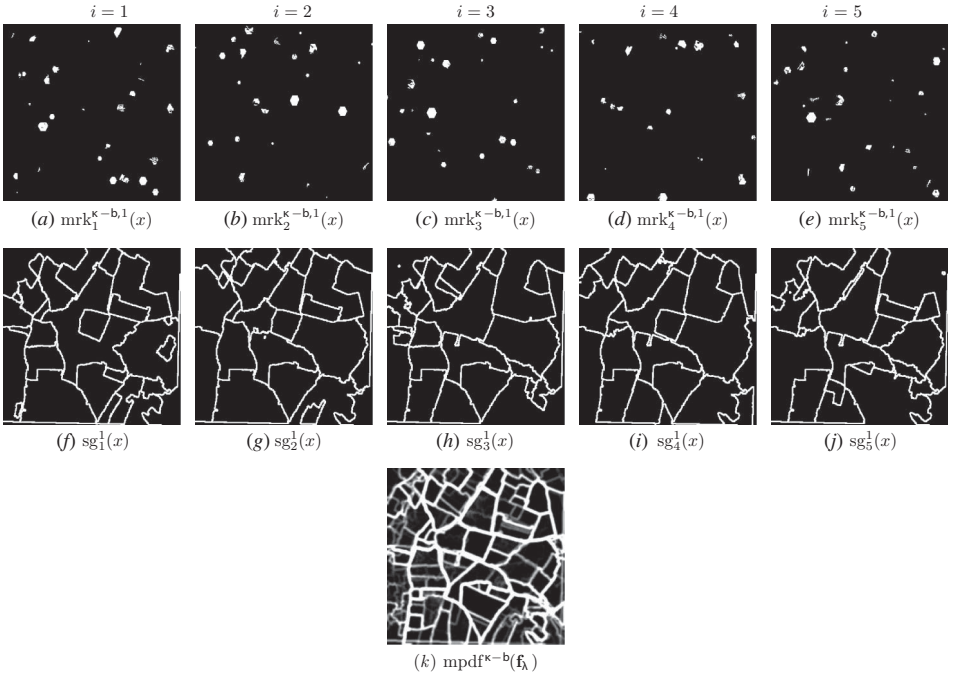

Figure 10. (*a–e*) A few realizations of regionalized random-ball germs $\{\mathrm{mrk}_i^{\kappa-bj}(x)\}_{i=1\ldots5}^{j=1}$ (top) by the classification κ and (*f–j*) associated contours of WS $\{\mathrm{sg}_i^j(x)\}_{i=1\ldots5}^{j=1}$ (bottom). i is the index of realizations and j the number of the considered channel. The parameters are the maximum radius Rmax = 30 pixels and the maximum number of germs $N = 50$. (*k*) The mpdf with regionalized random-ball germs $\mathrm{mpdf}^{\kappa-b}(\mathbf{f}_\lambda)$ is computed with $M = 100$ realizations.

is less than the thresholded value (1). Inertias and SNRs for factor axes of images 'Roujan X X' are presented in tables 1 and 2.

A classification 'clara' is made on the factor pixels of these two axes. The mpdf, $\mathrm{mpdf}^{\kappa-b}(\mathbf{f}_\lambda)$, is produced as explained for image 'Roujan'.

The parameters for the stochastic WS controlled by markers $\mathrm{sg}^{\mathrm{mrk}}(\mathrm{mpdf}^{\kappa-b}(\mathbf{f}_\lambda), \widehat{\kappa})$ are:

- the number of classes for the classification κ: $Q = 3$, which is the only important parameter;
- the maximum number of random-ball germs: $N = 50$, which must be high enough and which must be of the the same order as the number of regions in the image;
- the number of realizations for each channel: $M = 100$, which always has the same value;
- the minimum area $S = 10$ pixels for the connected classes of the classification, generally the same;
- the parameters for pre-processing the initial spectral classification are an erosion using a 5×5 square and a closing by reconstruction using as marker a dilation using a 3×3 square, generally the same; and
- the maximum radius of the random ball Rmax = 30, generally the same.

The final segmentations with marker-controlled WS, $\mathrm{sg}^{\mathrm{mrk}}(\mathrm{mpdf}^{\kappa-b}(\mathbf{f}_\lambda), \widehat{\kappa})$, and hierarchical WS with a volume criterion, $\mathrm{sg}^{R-\mathrm{vol}}(\mathrm{mpdf}^{\kappa-b}(\mathbf{f}_\lambda))$, are shown in figure 12. We notice that the number of regions, resulting from the segmentation, strongly

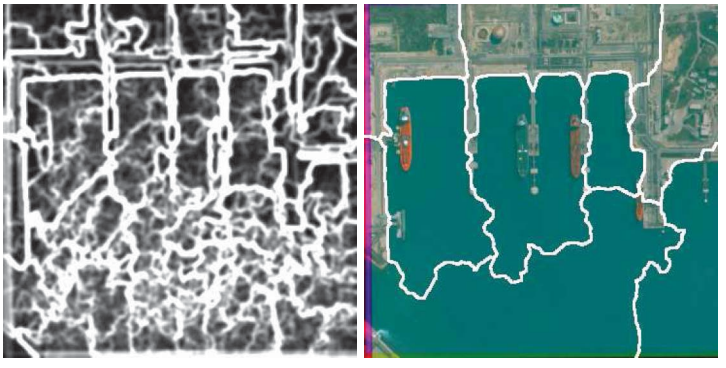

(a) $\mathrm{mpdf}^{\mathrm{pt}}(\mathbf{f}_\lambda)$ (b) $\mathrm{sg}^{\mathsf{R}-\mathrm{vol}}(\mathrm{mpdf}^{\mathrm{pt}}(\mathbf{f}_\lambda))$

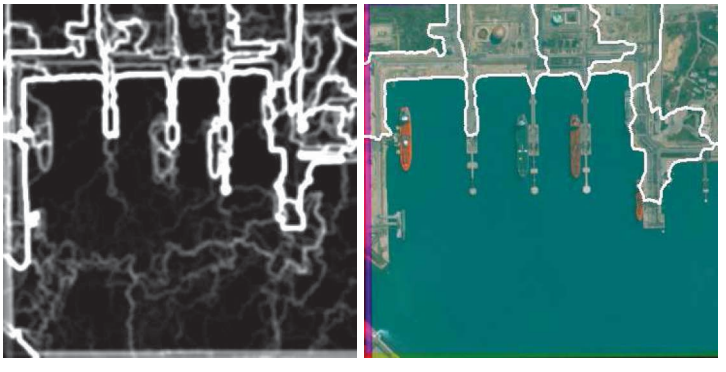

(c) $\mathrm{mpdf}^{\kappa-\mathsf{b}}(\mathbf{f}_\lambda)$ (d) $\mathrm{sg}^{\mathsf{R}-\mathrm{vol}}(\mathrm{mpdf}^{\kappa-\mathsf{b}}(\mathbf{f}_\lambda))$

Figure 11. Comparison between (*a*) the pdf $\mathrm{mpdf}^{\mathrm{pt}}(\mathbf{f}_\lambda)$ and (*b*) the associated stochastic WS with uniform random point germs with a volume criterion $\mathrm{sg}^{R-\mathrm{vol}}(\mathrm{mpdf}^{\mathrm{pt}}(\mathbf{f}_\lambda))$ to (*c*) the pdf $\mathrm{mpdf}^{\kappa-b}(\mathbf{f}_\lambda)$ and (*d*) the associated stochastic WS with regionalized random-ball germs with a volume criterion $\mathrm{sg}^{R-\mathrm{vol}}(\mathrm{mpdf}^{\kappa-b}(\mathbf{f}_\lambda))$. Only $R = 8$ regions with the largest volume are retained. For visualization, the contours of the segmentations are dilated by an SE of size 3×3 pixels.

Table 1. Parts of inertia for factor axes of images 'Roujan X X'.

Image	$c^{\mathbf{f}}_{\alpha_1}$	$c^{\mathbf{f}}_{\alpha_2}$	$c^{\mathbf{f}}_{\alpha_3}$	$c^{\mathbf{f}}_{\alpha_4}$
'Roujan'	84.1%	8.7%	6.2%	1%
'Roujan 0 2'	75.6%	13.7%	9.2%	1.5%
'Roujan 1 9'	77.5%	12.1%	9%	1.4%

Table 2. SNRs for factor axes of images 'Roujan X X'.

Image	$c^{\mathbf{f}}_{\alpha_1}$	$c^{\mathbf{f}}_{\alpha_2}$	$c^{\mathbf{f}}_{\alpha_3}$	$c^{\mathbf{f}}_{\alpha_4}$
'Roujan'	5.10	0.03	2.84	0.47
'Roujan 0 2'	2.66	0.01	2.53	0.32
'Roujan 1 9'	3.15	0	2.90	0.51

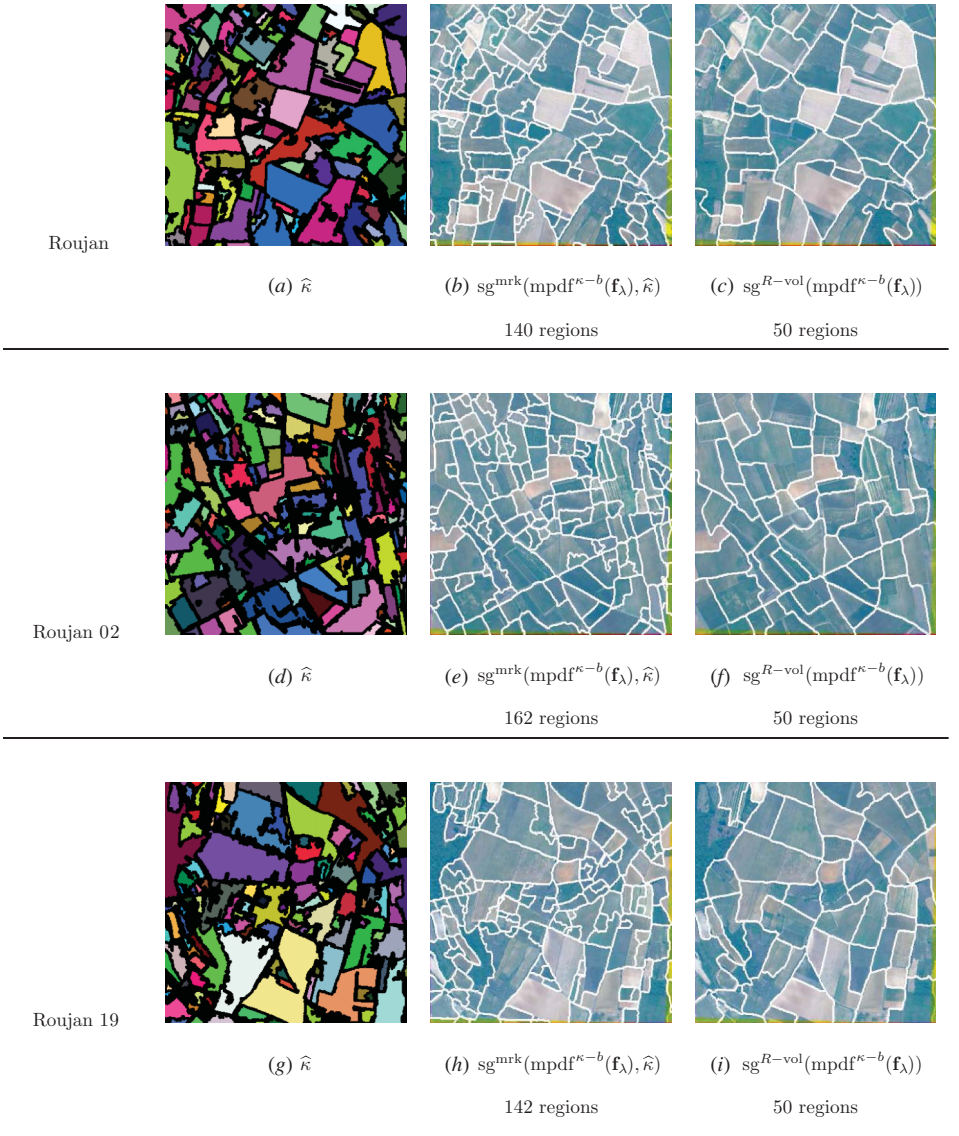

Figure 12. Comparison between segmentations $\mathrm{sg}^{\mathrm{mrk}}(\mathrm{mpdf}^{\kappa-b}(\mathbf{f}_\lambda), \widehat{\kappa})$ (*b,e,h*) with markers from the filtered classification $\widehat{\kappa}$ (*a,d,g*) and segmentations $\mathrm{sg}^{R-\mathrm{vol}}(\mathrm{mpdf}^{\kappa-b}(\mathbf{f}_\lambda))$ (*c,f,i*) by stochastic WS with a prior given number of regions $R = 50$. The results are given for images: 'Roujan', 'Roujan 0 2' and 'Roujan 1 9'.

depends on the image, whereas the number of spectral classes is the same for similar images. In fact, the number of regions for volumic WS, $\mathrm{sg}^{\mathrm{vol}}$, must be chosen according to the spatial diversity of the considered image, and cannot be easily fixed *a priori* (50 here). The number of regions depends on the size and the complexity of the image, while the number of spectral classes depends on the spectral content, which for a specific domain can be relatively constant. Consequently, it is more relevant to segment the pdf with markers that are also from the classification $\mathrm{sg}^{\mathrm{mrk}}$. Indeed, only one parameter is needed for the marker-controlled WS $\mathrm{sg}^{\mathrm{mrk}}(\mathrm{mpdf}^{\kappa-b}(\mathbf{f}_\lambda), \widehat{\kappa})$:

the number of classes Q in the classification κ. Moreover, in that sense, the approach based on the number of classes Q produces a more robust segmentation than the approach based on the number of regions R.

In order to show that the stochastic WS, conditioned by a previous classification, produces contours that are more regular and robust than deterministic (standard) WS, we compare the results of a deterministic approach to a stochastic one:

(i) for both cases, an unsupervised classification κ ('clara') is processed in factor space FIS and transformed $\widehat{\kappa} = \Upsilon(\kappa)$;

(ii)
- for the deterministic approach, a chi-squared metric based gradient $\varrho^{\chi^2}(\mathbf{f}_\lambda)$ is computed in image space MIS, as a function to flood;
- for the stochastic approach, an mpdf, $\text{mpdf}^{\kappa-b}(\mathbf{f}_\lambda)$, with regionalized random-ball germs conditioned by the classification κ, is processed, in image space MIS, as a function to flood; and

(iii) in both cases, the flooding function is segmented by a WS using as sources of flooding the markers from the transformed classification $\widehat{\kappa}$.

The parameters for the stochastic WS controlled by markers are the same as at the beginning of the current paragraph (§6.4). In figure 13, the results of segmentation by deterministic and stochastic WS for image 'Roujan' with markers from the transformed classification $\widehat{\kappa}$ are given. We observe that the contours are smoother and follow more precisely the main limits of the regions for the stochastic approach than for the deterministic one. The same observation is made on the image 'Port de Bouc' classified in $Q = 7$ classes (figure 14).

6.5 *General method of multi-spectral segmentation by stochastic WS*

After all these observations and analysis, we can now summarize the algorithmic pipeline of the general method of segmentation of multi-spectral image by stochastic WS. The framework is presented in figure 15. The different steps are as follows:

- an FCA to reduce the spectral dimension of the image $\mathbf{f}_\lambda$ and eventually to filter the noise, this transformation creates a factor image $\mathbf{c}^{\mathbf{f}}_\alpha$;
- the previous step requires the selection of factorial axes by the SNR of the factor pixels;
- a spectral classification to group pixels into homogeneous classes (global pointwise comparison);
- a morphological transform Υ of each class, the image transformed is noted $\widehat{\kappa} = \Upsilon(\kappa)$;
- the building of a pdf of contours that can be marginal (mpdf) or vectorial (vpdf) starting from a gradient on the image space $\mathbf{f}_\lambda$ (MIS) or factor space $\mathbf{c}^{\mathbf{f}}_\alpha$ (FIS) with random-balls germs regionalized by the spectral classification; and
- a segmentation of the pdf by a WS controlled by markers from the classes of the transformed classification $\widehat{\kappa}$

Some of the steps presented in the flowchart of figure 15 have not been discussed in this paper. These steps are very useful for other applications of multi-variate image segmentation; the interested reader can find more details in Noyel *et al.* (2008b).

7. Conclusion

A novel method to segment multi-spectral images is presented in this paper. First, a dimensionality reduction by FCA is performed. It reduces the spectral noise and

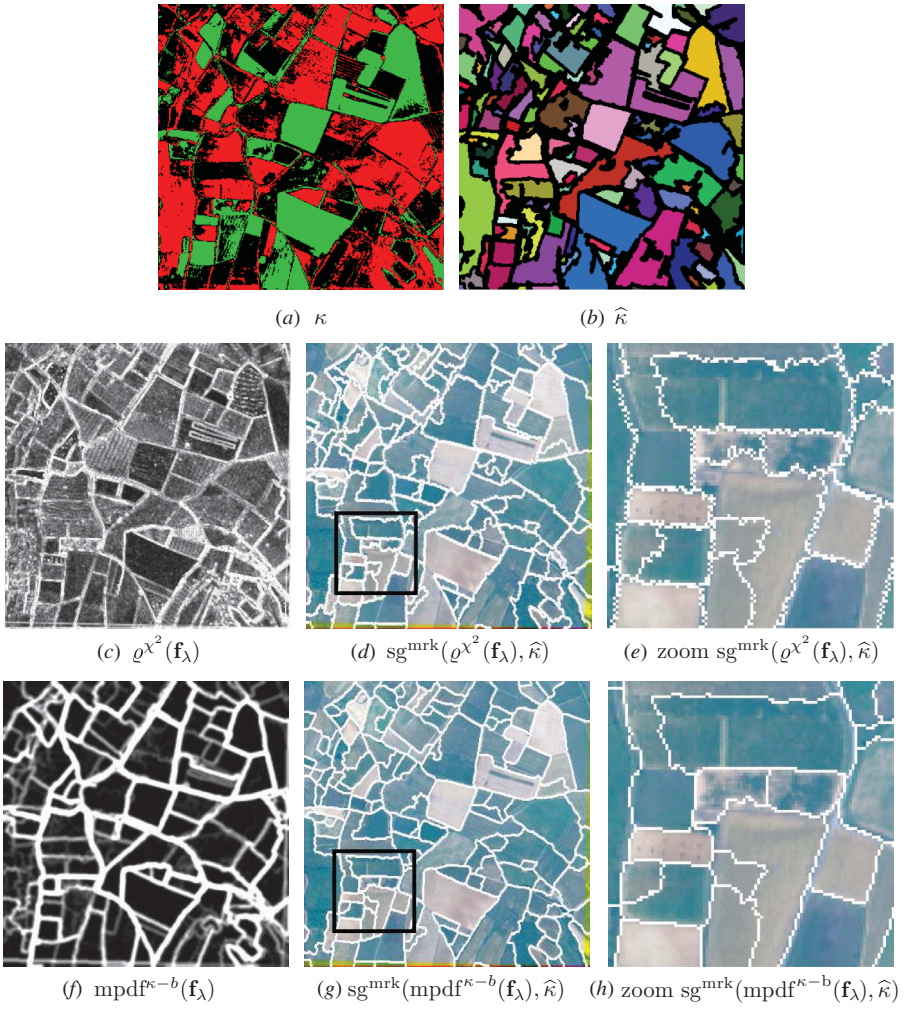

Figure 13. First line: (*a*) classification in three classes κ and (*b*) markers from the classification $\widehat{\kappa}$ on image 'Roujan'. Second line: (*d*),(*e*) deterministic approach $\mathrm{sg}^{\mathrm{mrk}}(\varrho^{\chi^2}(\mathbf{f}_\lambda), \widehat{\kappa})$ on (*c*) the chi-squared metric based gradient $\varrho^{\chi^2}(\mathbf{f}_\lambda)$. Third line: (*g*),(*h*) stochastic approach $\mathrm{sg}^{\mathrm{mrk}}(\mathrm{mpdf}^{\kappa-b}(\mathbf{f}_\lambda), \widehat{\kappa})$ on (*f*) the mpdf $\mathrm{mpdf}^{\kappa-b}(\mathbf{f}_\lambda)$. The parameters are $Q = 3$ classes, $N = 50$ germs, $M = 100$ realizations, minimal area $S = 10$ pixels, maximum radius $\mathrm{Rmax} = 30$ pixels). For presentation of images without zoom, the contours are dilated by an SE of size 3×3 pixels.

preserves the spatial information. A new way to select factor axes is presented. It uses the spatial information carried by the factor pixels (i.e. SNR) and not on only the statistical information (i.e. inertia). Then, a classification stage ensures a global pixel-wise comparison and groups pixels into classes with similar spectra. A morphological transformation is subsequently applied to obtain markers for the final segmentation. Then, a pdf of contours conditioned by the previous classification is built with random-ball germs. This pdf contains spatial and spectral information and is estimated by Monte-Carlo simulations. During the pdf estimation process, regional

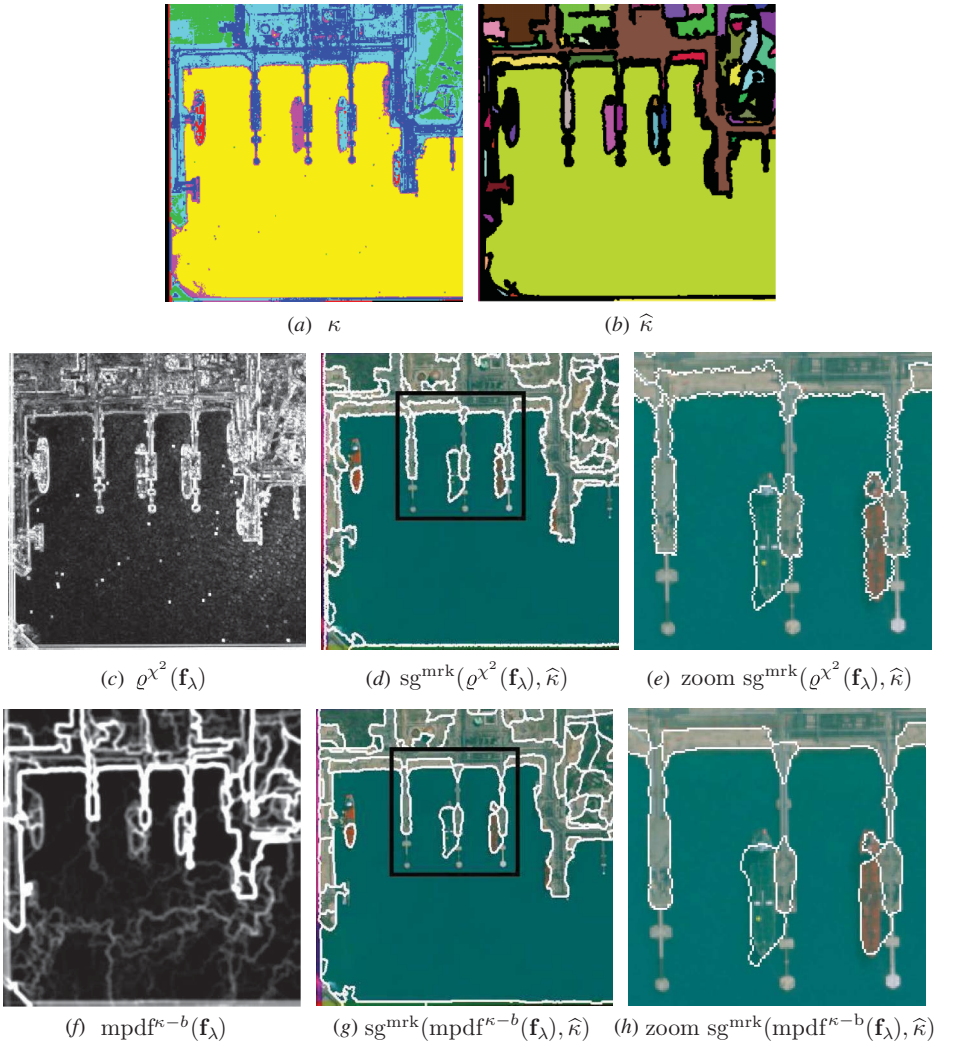

Figure 14. First line: (*a*) classification in three classes κ and (*b*) markers from the classification $\widehat{\kappa}$ on image 'Port de Bouc'. Second line: (*d*), (*e*) deterministic approach $\mathrm{sg}^{\mathrm{mrk}}(\varrho^{\chi^2}(\mathbf{f}_\lambda), \widehat{\kappa})$ on (*c*) the chi-squared metric based gradient $\varrho^{\chi^2}(\mathbf{f}_\lambda)$. Third line: (*g*),(*h*) stochastic approach $\mathrm{sg}^{\mathrm{mrk}}(\mathrm{mpdf}^{\kappa-b}(\mathbf{f}_\lambda), \widehat{\kappa})$ on (*f*) the mpdf $\mathrm{mpdf}^{\kappa-b}(\mathbf{f}_\lambda)$. The parameters are $Q = 7$ classes, $N = 50$ germs, $M = 100$ realizations, minimal area $S = 10$ pixels, maximum radius Rmax $= 30$ pixels). For presentation of images without zoom, the contours are dilated by an SE of size 3×3 pixels.

information between pixels is compared. Finally, the pdf is segmented by a WS controlled by markers from the transformed classification.

Moreover, this spatio-spectral method of segmentation needs few and well-controlled parameters:

- the threshold of the SNR for the FCA (dimensionality reduction stage); this can be selected according to the knowledge of the amount of noise in the images:
- the number of classes of the classification that corresponds to the number of different kinds of spectra in the image: this parameter is more robust than the

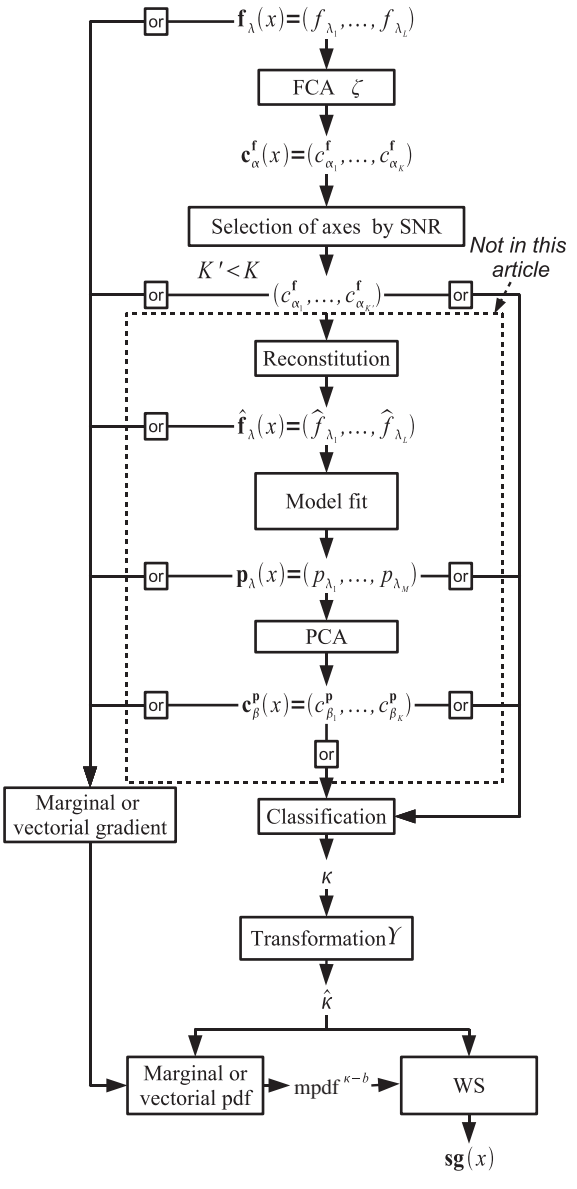

Figure 15. General framework of WS controlled by a classification, with regionalized random-balls germs. The part outlined with a dotted line is not presented in this paper.

number of regions with the largest volume in the standard hierarchical WS segmentation;

- eventually, a size criterion to remove small regions that must be excluded of the segmentation;
- the number of random germs (linked to the number of regions) N;
- the number of realizations (fixed) $M = 100$; and
- the maximum radius of the ball (related to the surface area of the zones of interest) Rmax.

It is shown that, in the case of segmentation of similar images these parameters can be easily fixed.

The approach is perfectly valid for very-high-resolution images: the only requirement is to start from an initial classification representing all the most significant regions, and of course, the regions must have a minimal thickness to define the notion of the inner maker for the WS segmentation.

This general method of segmentation is not limited to the field of remote sensing but can also be applied to medical images (Noyel *et al.* 2008b), microscopy images, thermal images (Noyel *et al.* 2007a), time series, multi-variate series, and so on.

We are now thinking about two interesting perspectives: to introduce more prior information on the construction of the pdf of contours and to use a more advanced multi-variate kernel during the estimation process of the pdf.

Acknowledgements

The authors are grateful to Prof. Guy Flouzat (Laboratoire de Télédétection à Haute Résolution, LTHR/ ERT 43 / UPS, Université Paul Sabatier, Toulouse 3, France) for providing the PLEIADES satellite simulated images, obtained in the framework of the ORFEO program (Centre National d'Etudes Spatiales, the French space agency).

We would like to dedicate this paper to the memory of Prof. Guy Flouzat.

References

Angulo, J. and Jeulin, D., 2007, Stochastic watershed segmentation. In *Proceedings of the Mathematical Morphology and its Applications to Signal and Image Processing, 8th International Symposium on Mathematical Morphology*, **1**, pp. 265–276.

Angulo, J. and Serra, J., 2007, Modelling and segmentation of colour images in polar representations. *Image Vision Computing*, **25**, pp. 475–495.

Archibald, R. and Fann, G., 2007, Feature selection and classification of hyperspectral images with support vector machines. *IEEE Geoscience and Remote Sensing Letters*, **4**, pp. 674–677.

Benediktsson, J., Palmason, J. and Sveinsson, J., 2005, Classification of hyperspectral data from urban areas based on extended morphological profiles. *IEEE Transactions on Geoscience and Remote Sensing*, **42**, pp. 480–491.

Benzécri, J., 1973, *L'Analyse Des Données, L'Analyse des Correspondances*, Vol. 2 (Paris, France: Dunod).

Beucher, S. and Lantuéjoul, C., 1979, Use of watersheds in contour detection. In *Proceedings of the International Workshop on Image Processing, Real-time Edge and Motion Detection-Estimation*, September 1979, Rennes, France, pp. 17–21. Available online at http://cmm.ensmp.fr/~beucher/publi/watershed.pdf.

Beucher, S. and Meyer, F., 1992, The morphological approach to segmentation: the watershed transformation. In *Mathematical Morphology in Image Processing*, pp. 433–481 (New York, NY: Marcel-Dekker).

Duda, R. and Hart, P., 1973, *Pattern Classification and Scene Analysis* (New York, NY: Wiley).

Epifanio, I. and Soille, P., 2007, Morphological texture features for unsupervised and supervised segmentations of natural landscapes. *IEEE Transactions on Geoscience and Remote Sensing*, **45**, pp. 1074–1083.

Fauvel, M., Chanussot, J., Benediktsson, J. and Sveinsson, J., 2007, Spectral and spatial classification of hyperspectral data using SVMs and morphological profiles. In *Proceedings of the IEEE International Geoscience and Remote Sensing Symposium, IGARSS 2007*, 23–28 July 2007, Barcelona, Spain, pp. 4834–4837.

FLOUZAT, G., AMRAM, O. and CHERCHALI, S., 1998, Spatial and spectral segmentation of satellite remote sensing imagery using processing graphs by mathematical morphology. In *Proceedings of the IEEE Geoscience and Remote Sensing Symposium, IGARSS '98*, 6–10 July 1998, Seattle, WA, USA, pp. 1769–1771.

GENOVA, F., PETREMAND, M., BONNAREL, F., LOUYS, M. and COLLET, C., 2006, Reduction and segmentation of hyperspectral data cubes. In *Proceedings of the Astronomical Data Analysis Software & Systems XVI*, October 2006, Tucson, Arizona, USA.

GREEN, A., BERMAN, M., SWITZER, P. and CRAIG, M., 1988, A transformation for ordering multispectral data in terms of image quality with implications for noise removal. *IEEE Transactions on Geoscience and Remote Sensing*, **26**, pp. 65–74.

GUALTIERI, J. and CROMP, R., 1999, Support vector machines for hyperspectral remote sensing classification. In *27th AIPR Workshop, Advances in Computer Assisted Recognition*, 14–16 October 1998, Washington, D.C., USA, pp. 221–232.

HANBURY, A. and SERRA, J., 2001, Morphological operators on the unit circle. *IEEE Transactions on Image Processing*, **10**, pp. 1842–1850.

HUGHES, G., 1968, On the mean accuracy of statistical pattern recognizers. *IEEE Transactions on Information Theory*, **14**, pp. 55–63.

KAUFMAN, L. and ROUSSEEUW, P., 1990, *Finding Groups in Data. An Introduction to Cluster Analysis* (Chichester, UK: John Wiley and Sons).

LANDGREBE, D., 2002, Hyperspectral image data analysis. *IEEE Signal Processing Magazine*, **19**, pp. 17–28.

LENNON, M., MERCIER, G. and HUBERT-MOY, L., 2002, Classification of hyperspectral images with nonlinear filtering and support vector machines. In *Proceedings of the IEEE International Geoscience and Remote Sensing Symposium, IGARSS '02*, 24–28 June 2002, pp. 1670–1672.

MARCAL, A. and CASTRO, L., 2005, Hierarchical clustering of multispectral images using combined spectral and spatial criteria. *IEEE Geoscience and Remote Sensing Letters*, **2**, pp. 59–63.

MEYER, F., 2001, An overview of morphological segmentation. *International Journal of Pattern Recognition and Artificial Intelligence*, **15**, pp. 1089–1118.

NOYEL, G., 2008, Filtrage, réduction de dimension, classification et segmentation morphologique hyperspectrale. PhD thesis, Ecole des Mines de Paris, France.

NOYEL, G., ANGULO, J. and JEULIN, D., 2007a, Morphological segmentation of hyperspectral images. *Image Analysis and Stereology*, **26**, pp. 101–109.

NOYEL, G., ANGULO, J. and JEULIN, D., 2007b, On distances, paths and connections for hyperspectral image segmentation. In *Proceedings of the 8th International Symposium on Mathematical Morphology, Mathematical Morphology and its Applications to Signal and Image Processing*, 10–13 October 2007, Rio de Janeiro, Brazil, pp. 399–410. Available online at: http://urlib.net/dpi.inpe.br/ismm@80/2007/03.05.11.23.

NOYEL, G., ANGULO, J. and JEULIN, D., 2007c, Random germs and stochastic watershed for unsupervised multispectral image segmentation. In *Proceedings of the KES 2007/WIRN 2007*, III of *LNAI 4694*, 12–14 September 2007, Vietri sul Mare, Italy, pp. 17–24 (Berlin, Germany: Springer-Verlag).

NOYEL, G., ANGULO, J. and JEULIN, D., 2008a, Classification-driven stochastic watershed. Application to multispectral segmentation. In *Proceedings of the IS&T's Fourth European Conference on Color in Graphics Imaging and Vision CGIV 2008*, 9–13 June, Terrassa - Barcelona, Spain, pp. 471–476.

NOYEL, G., ANGULO, J. and JEULIN, D., 2008b, Filtering, segmentation and region classification by hyperspectral mathematical morphology of DCE-MRI series for angiogenesis imaging. In *Proceedings of the IEEE International Symposium on Biomedical Imaging ISBI 2008*, 14–17 May 2008, Paris, France, pp. 1517–1520.

NOYEL, G., ANGULO, J. and JEULIN, D., 2008c, Regionalized random germs by a classification for probabilistic watershed. Application: angiogenesis imaging segmentation. In

Proceedings of the European Consortium For Mathematics in Industry, ECMI 2008, 30 June-4 July, University College London, UK.

Pesaresi, M. and Benediktsson, J., 2001, A new approach for the morphological segmentation of high resolution satellite imagery. *IEEE Transactions on Geoscience and Remote Sensing*, **39**, pp. 309–320.

Polder, G., 2004, Spectral imaging for measuring biochemicals in plant material. PhD thesis, Technische Universiteit Delft.

Scheunders, P., 2002, A multivalued image wavelet representation based on multiscale fundamental forms. *IEEE Transactions on Image Processing*, **11**, pp. 568–575.

Schmidt, F., Douté, S. and Schmitt, B., 2007, Wavanglet: an efficient supervised classifier for hyperspectral images. *IEEE Transactions on Geoscience and Remote Sensing*, **45**, pp. 1374–1385.

Serra, J., 1982, *Image Analysis and Mathematical Morphology*, Vol. I (London, UK: Academic Press).

Serra, J., 2006, A lattice approach to image segmentation. *Journal of Mathematical Imaging and Vision*, **24**, pp. 83–130.

Soille, P., 1996, Morphological partitioning of multispectral images. *Journal of Electronic Imaging*, **5**, pp. 252–263.

Soille, P., 2003, *Morphological Image Analysis*, 2nd edn (Berlin, Germany: Springer-Verlag).

Soille, P., 2008, Constrained connectivity for hierarchical image partitioning and simplification. *IEEE Transactions on Pattern Analysis and Machine Intelligence*, **30**, pp. 1132–1145.

13.4 Publication IV : S. Velasco-Forero and J. Angulo. "Supervised ordering in R^n : Application to morphological processing of hyperspectral images". *IEEE Transactions on Image Processing*, Vol. 20, No. 11, 3301–3308, 2011.

is proven based on the direct comparisons between our proposed approach with other methods such as Bertalmio's, "f-Inpaint," and median-background-estimation methods.

REFERENCES

[1] Anonymous, GenePix 4000 A User's Guide 1999.

[2] P. Arena, L. Fortuna, and L. Occhipinti, "A CNN algorithm for real time analysis of DNA microarrays," *IEEE Trans. Circuits Syst. I, Fundam. Theory Appl.*, vol. 49, no. 3, pp. 335–340, Mar. 2002.

[3] D. Bassett, M. Eisen, and M. Boguski, "Gene expression informatics—It's all in your mine," *Nat. Genetics*, vol. 21, no. 1 Suppl, pp. 51–55, Jan. 1999.

[4] M. Bertalmio, G. Sapiro, V. Caselles, and C. Ballester, "Image inpainting," in *Proc. 27th Annu. Conf. Comput. Graph. Interactive Tech.*, New York, 2000, pp. 417–424.

[5] A. Bertozzi and M. Bertalmio, "Navier–Stokes fluid dynamics and image and video inpainting," in *Proc. IEEE Comput. Soc. Conf. CVPR*, 2001, vol. 1, pp. 355–362.

[6] J. Canny, "A computational approach to edge detection," *IEEE Trans. Pattern Anal. Mach. Intell.*, vol. 8, no. 6, pp. 679–698, Nov. 1986.

[7] Y. Chen, E. Dougherty, and M. Bittner, "Ratio-based decisions and the quantitative analysis of cDNA microarray images," *J. Biomed. Opt.*, vol. 2, no. 4, pp. 364–374, Oct. 1997.

[8] L. O. Chua and T. Roska, *Cellular Neural Networks and Visual Computing: Foundation and Applications*. Cambridge, U.K.: Cambridge Univ. Press, 2002.

[9] L. O. Chua and L. Yang, "Cellular neural networks: Theory and applications," *IEEE Trans. Circuits Syst.*, vol. 35, no. 10, pp. 1273–1290, Oct. 1988.

[10] M. B. Eisen, ScanAlayse Mar. 2010 [Online]. Available: http://rana.lbl.gov/eisensoftware.htm

[11] K. Fraser, Z. Wang, and X. Liu, *Microarray Image Analysis*. New York: Taylor & Francis, Feb. 2010.

[12] E. L. Korn, J. K. Habermann, M. B. Upender, T. Ried, and L. M. McShane, "Objective method of comparing DNA microarray image analysis systems," *Biotechniques*, vol. 36, no. 6, pp. 960–967, Jun. 2004.

[13] T. Kozek and T. Roska, "A double time-scale CNN for solving two-dimensional navier—Stokes equation," *Int. J. Circuit Theory Appl.*, vol. 24, no. 1, pp. 49–55, 1996.

[14] A. Lehmussola, P. Ruusuvuori, and O. Yli-Harja, "Evaluating the performance of microarray segmentation algorithms," *Bioinformatics*, vol. 22, no. 23, pp. 2910–2917, Dec. 2006.

[15] P. Luchini, "Two-dimensional numerical integration using a square mesh," *Comput. Phys. Commun.*, vol. 31, no. 4, pp. 303–310, Mar. 1984.

[16] M. M. Oliveira, R. McKenna, B. Bowen, and Y.-S. Chang, "Fast digital image inpainting," in *Proc. Int. Conf. VIIP*, Marbella, Spain, 2001, pp. 261–266.

[17] P. O'Neill, G. Magoulas, and X. Liu, "Improved processing of microarray data using image reconstruction techniques," *IEEE Trans. Nanobiosci.*, vol. 2, no. 4, pp. 176–183, 2003.

[18] P. Perona and J. Malik, "Scale-space and edge detection using anisotropic diffusion," *IEEE Trans. Pattern Anal. Mach. Intell.*, vol. 12, no. 7, pp. 629–639, Jul. 1990.

[19] C. Rekeczky, T. Roska, and A. Ushida, "CNN-based difference-controlled adaptive non-linear image filters," *Int. J. Circuit Theory Appl.*, vol. 26, no. 4, pp. 375–423, 1998.

[20] T. Roska and L. O. Chua, "The CNN universal machine: An analogic array computer," *IEEE Trans. Circuits Syst. II, Analog Digit. Signal Process.*, vol. 40, no. 3, pp. 163–173, Mar. 1993.

[21] H. Samartzidou, L. Turner, T. Houts, M. Frorne, J. Worley, and H. Albertsen, "Lucidea microarray ScoreCard: An integrated analysis tool for microarray experiments," *Life Sci. News*, vol. 7, no. 13, pp. 1–10, 2001.

[22] S. Samavi, S. Shirani, N. Karimi, and M. Deen, "A pipeline architecture for processing of DNA microarrays images," *J. VLSI Signal Process.*, vol. 38, no. 3, pp. 287–297, Nov. 2004.

[23] M. Schena, D. Shalon, R. W. Davis, and P. O. Brown, "Quantitative monitoring of gene expression patterns with a complementary DNA microarray," *Science*, vol. 270, no. 5235, pp. 467–470, Oct. 1995.

[24] Y. H. Yang, M. J. Buckley, S. Dudoit, and T. P. Speed, "Comparison of methods for image analysis on cDNA microarray data," *J. Comput. Graph. Statist.*, vol. 11, no. 1, pp. 108–136, 2002.

[25] B. Zineddin, Z. Wang, and X. Liu, "A cellular neural network for microarray image reconstruction," in *Proc. 16th Int. Conf. Autom. Comput.*, Birmingham, U.K., 2010, pp. 106–111.

Supervised Ordering in $\mathbb{R}^p$: Application to Morphological Processing of Hyperspectral Images

Santiago Velasco-Forero, *Student Member, IEEE*, and Jesus Angulo

***Abstract*—A novel approach for vector ordering is introduced in this paper. The generic framework is based on a supervised learning formulation which leads to reduced orderings. A training set for the background and another training set for the foreground are needed as well as a supervised method to construct the ordering mapping. Two particular cases of learning techniques are considered in detail: 1) kriging-based vector ordering and 2) support vector machines-based vector ordering. These supervised orderings may then be used for the extension of mathematical morphology to vector images. In particular, in this paper, we focus on the application of morphological processing to hyperspectral images, illustrating the performance with practical examples.**

***Index Terms*—Hyperspectral imagery, learning an ordering, mathematical morphology, supervised learning.**

I. INTRODUCTION

Mathematical morphology is a nonlinear image processing methodology based on the application of lattice theory to spatial structures [1], [2]. This means that the definition of morphological operators needs a complete lattice structure, i.e., the possibility of defining an ordering relationship between the points to be processed. From a theoretical viewpoint, a partial ordering is sufficient to construct complete lattices; however, as discussed below, in practical algorithms, we should require a total ordering (i.e., any pair of unequal points must be ordered). Extending ordering to multivariate data is not straightforward, because there is no notion of natural ordering in a vector space, as opposed to 1-D (scalar) case [3]. Therefore, the extension of mathematical morphology to vector spaces, for instance to hyperspectral images, is neither direct nor trivial due to the high-dimensional nature of the data. For a general account on mathematical morphology, the interested reader should refer to [4]–[7], whereas the theoretical formulation of vector morphology is extensively discussed in [8]–[10]. To overcome the lack of natural ordering, the following four families of ordering for multichannel samples have been identified in the literature [3], [11]. In *marginal ordering* (M-ordering), components of vectors are ordered independently (pointwise ordering). This approach produces new vectors which were not originally present in the input image thus, in the case for instance of color images, introducing color artifacts into the output image [8]; this is known in the literature as the *false color problem*. However, by an appropriate color representation, typically a hue/saturation/luminance, marginal ordering can lead to good results [12]. To strictly preserve input vectors, the *conditional ordering* (C-ordering) approach, also known as lexicographic ordering, is frequently used. The C-ordering is based on the ordering of the components selected sequentially according to different conditions or priorities. When all the components are used, the C-ordering is a total ordering. Note that this approach does not use simultaneously the full vector nature of the input. The *P-ordering* is based on the partition of the vectors into groups,

Manuscript received December 08, 2010; revised March 25, 2011; accepted April 07, 2011. Date of publication April 21, 2011; date of current version October 19, 2011. The associate editor coordinating the review of this manuscript and approving it for publication was Dr. Maya Gupta.

The authors are with the Centre de Morphologie Mathematique de l'Ecole des Mines de Paris, France.

Color versions of one or more of the figures in this paper are available online at http://ieeexplore.ieee.org.

Digital Object Identifier 10.1109/TIP.2011.2144611

such that the groups can be distinguished with respect to rank or extremeness. The *reduced ordering* or R-ordering which performs the ordering of vectors according to some scalars, computed from a mapping of the vector onto a different representation where the ordering is naturally defined, typically distances or projections onto a dimensionality reduced space (using for instance the principal component analysis).

A. Previous Works on Vector Morphology

During the last 15 years, the extension of mathematical morphology to color and vector images has been an active field and therefore many different approaches have been proposed. For a detailed state of the art on color mathematical morphology, the reader is referred to [13] and [14]. Let us focus on those works which are more related with our approach, that is, those based on R-ordering. A quite useful idea is to introduce a reference color together with a distance metric and then define the ordering between two points by their distances to the [14]. This concept of reference was previously used also to define a partial ordering on the unit circle [15], recently generalized to the case of multireference for the construction of partial ordering for the hue [16]. In particular, the Mahalanobis distance has been employed in several works on multivariate morphology [9], [17], [18]. Obviously, the main interest of the Mahalanobis distance is its ability to deal with a distribution of probability for the notion value of "reference," i.e., for instance, in [18], it is shown how to use a manually selected region (defined by a mean and a covariance matrix) as the reference to construct the ordering. Another way to consider R-ordering with the notion of reference color is to use vector projections. This idea has been exploited, for instance, in [19], where, working on color quaternion representations, several orderings were introduced by considering the decomposition of each color according to the parallel part to the reference color and the corresponding perpendicular part. However, in all of these cases, the R-ordering is only a partial ordering and to avoid the ambiguity of ordering for two different points which have the same distance to the reference, a lexicographic cascade of the vector components is required to complete the ordering schema; this issue was deeply studied for instance in [14]. We must remark also that these methodologies have in common the fact that the reference color, or the distribution of reference, are associated to the "image foreground." This means that dilation tends to approach the colors towards the reference, and, by duality, the erosion tends to move further away the reference, but without defining to which "image background" the colors must be addressed. This *asymmetric* situation is one the problems that are considered in this paper. Strategies based on P-ordering have been also considered for practical applications; however, from a theoretical viewpoint, the obtained operators presents fundamental limitations. For instance, in the specific field of hyperspectral image processing, some works [20] have introduced vector nonlinear filtering preprocessing which the authors considered as the extension of morphological operators to vector images. However, as was already pointed out in [14], these operators based on min/max cumulated distances are in fact vector median [21] and anti-median filters and cannot be referred as the multivariate extension of dilations and erosions in the mathematical morphology framework, i.e., the pair of vector median and vector anti-median are not adjunct operators and consequently they cannot be used to defined morphological filters as the openings/closings. In the field of color image processing, combinatorial techniques have been also used to construct ordering. More precisely, in [22], the color vectors belonging to the processing window (i.e., the structuring element) are represented by a graph and then, by computing the Hamiltonian path bounds, it produces an ordering of the colors. There is however a problem of this approach: the ordering is locally depending on the values of the window, consequently it is not a partial ordering for the set of color values of the image, i.e., for instance the dilation (erosion) obtained does not commute with the supremum (infimum). More recently, very powerful manifold learning techniques have been used to construct total lattices [23], and hence this yields the possibility to apply mathematical morphology to quite general spaces, including vector images. The basic idea is to reduce the dimension of the initial values by projecting them on a lower dimensionality space, using for instance diffusion maps or Laplacian eigenmaps. In practice, the algorithms typically consist of defining the ordering according to the first eigenvector and, hence, it is only a partial ordering (with respect to the studied taxonomy, these works are also R-orderings). The learning techniques considered are unsupervised, i.e., the ordering is reflecting the intrinsic statistical distribution of the values.

B. Aim of the Paper and Organization

This paper introduces a supervised learning formulation which leads to reduced orderings for vector spaces. This work is an extended and improved version of a conference contribution [24]. We start in Section II by considering the theoretical framework of h-orderings, as introduced in [9], and then the various families of h-mappings associated with R-orderings are studied, to finally arrive to the notion of h-supervised ordering. In our model, a training set for the background and another training set for the foreground as well as a supervised method, are needed to construct the h-ordering mapping. According to the learning technique considered, two particular cases are studied in detail in Section III. On the one hand, the kriging-based vector ordering and on the other hand, the support vector machines-based vector ordering. Some analytical results and pedagogical examples allow us to understand how the corresponding orderings are constructed. These supervised orderings may then be used for the extension of mathematical morphology to vector images. In Section IV, the general definitions of morphological operators in vector spaces are briefly revised. Then, we focus, in Section V, on their application to hyperspectral image processing. The performance of the morphological operators is illustrated with some examples. Conclusions close the paper in Section VI.

II. Complete Lattices in $\mathbb{R}^p$

Here, fundamentals of complete lattices for $\mathbb{R}^p$ is reviewed, and a new supervised ordering is introduced. For a detailed exposition on complete lattice theory, refer to [1], [25], and [26].

A. Basic Definitions

A space $\mathcal{L}$ endowed with a partial order $\leq$ is called a *complete lattice*, denoted $(\mathcal{L}, \leq)$ if every subset $\mathcal{H} \subseteq \mathcal{L}$ has both supremum (join) $\bigvee \mathcal{H}$ and infimum (meet) $\bigwedge \mathcal{H}$. The *smallest* $n \in \mathcal{H}$ is an element contained in all other elements of $\mathcal{H}$, that is, $l \in \mathcal{H} \Rightarrow n \leq l$. We denote the smallest element (bottom) of $\mathcal{L}$ by $\bot$. Equivalently, the *largest* n in $\mathcal{H}$ is an element that contains every element of $\mathcal{H}$, that is, $l \in \mathcal{H} \Rightarrow l \leq n$. We denote the largest element (top) of $\mathcal{L}$ by $\top$. Let R be a nonempty set and $\mathcal{L}$ a complete lattice. Furthermore, let $h : R \rightarrow \mathcal{L}$ be a surjective mapping. As it was defined in [9], we refer by $\leq_h$ as the h-ordering given by

$$r \leq_h r' \Leftrightarrow h(r) \leq h(r'), \quad \forall r, r' \in R.$$

Note that $\leq_h$ preserves reflexivity ($r \leq_h r$) and transitivity ($r_1 \leq_h r_2$ and $r_2 \leq_h r_3 \Rightarrow r_1 \leq_h r_3$) but is not a total ordering. Additionally, an equivalence class is defined by $\mathcal{L}[z] = \{r \in R \mid h(r) = z\}$. We remark that in practical application, the h-ordering has to be completed in each equivalence class to lead to a h-injective, furthermore, a complete total ordering.

B. Reduced Ordering

For multiband imagery, as color or hyperspectral images, pixel values are vectors defined in $\mathbb{R}^p$. Consequently, the main challenge to build complete lattice structures is to define a mapping $h : \mathbb{R}^p \rightarrow \mathcal{L}$,

where $\mathcal{L}$ can be the lattice of the extended real line $(\overline{\mathbb{R}}, \leq)$ using $\overline{\mathbb{R}} = \mathbb{R} \bigcup \{-\infty, +\infty\}$ and $\leq$ as the "less than or equal to" operation (the natural partial ordering). Once an ordering is defined for a set, the application of mathematical morphology operators is direct, and these operators are useful for denoising, object extraction and other tasks. Many authors have already worked in this idea. As was noted in [3], two main families of mappings h for a given $\mathbf{x} = (x_1, x_2, \ldots, x_p) \in \mathbb{R}^p$ can be defined as follows.

- Based on projections (unsupervised), i.e.:

$$h(\mathbf{x}) = \sum_{i=1}^{p} \lambda^i x_i. \tag{1}$$

  That can be obtained by using the more representative projection in a statistical dimensional reduction technique, for example, a linear approach as PCA [27].
- Based on distances (supervised): Given a subset $T \subset R, T = \{\mathbf{t}_1, \ldots, \mathbf{t}_{|T|}\}$, with $\mathbf{t}_i \in \mathbb{R}^p, \forall i$; the mapping $h(\mathbf{x})$ can be written as

$$h(\mathbf{x}) = \sum_{i=1}^{|T|} \lambda^i \phi(\mathbf{t}_i, \mathbf{x}) \tag{2}$$

  where $\phi : \mathbb{R}^p \times \mathbb{R}^p \rightarrow \mathbb{R}^+$ is a kernel-induced distance. Different authors have utilized this approach using mainly the Mahalanobis distance, as in [9], [17], and [18]. Nonlinear approaches as Kernel PCA [28] or ISOMAP [29] are also examples of this category. An interesting example had been introduced in [23] using Laplacian eigenmaps [30].

Additionally, projections can take in consideration local structures in $\mathbb{R}^p$, mainly under so-called "cluster assumption" (the data is "structured" into groups of points, in such a way that a local coordinate system for each group is more efficient than a global one), namely, (1) and (2) can be generalized to the following.

- Based on local projections: the different projections are obtained per cluster, i.e.,

$$h(\mathbf{x}) = \sum_{i=1}^{p} \lambda^i_{\mathbf{x}} x_i. \tag{3}$$

  Examples of techniques useful for that are Local-PCA [31] and mixtures of factor analysis as in [32]. The clusters are usually determined using unsupervised algorithms such as Expectation-Maximization (EM) algorithm or k-means, which usually require at least the number of clusters.
- Based on local adaptive distances: given on a reference set $T \subset R$, as in (2), but including a contribution which depends on $\mathbf{x}$. Thus, $h(\mathbf{x})$ can be written as

$$h(\mathbf{x}) = \sum_{i=1}^{|T|} \lambda^i_{\mathbf{x}} \phi(\mathbf{t}_i, \mathbf{x}) \tag{4}$$

  where ϕ is a kernel-induced distance and weights $\lambda^i_{\mathbf{x}}$ are fitted for each vector $\mathbf{x}$ in $\mathbb{R}^n$. As will be presented in Section III–A, if $\phi(\mathbf{t}_i, \mathbf{x}) = \phi(\mathbf{t}_i, \mathbf{t}_i)$, we obtain the local linear combination based on kriging [33].

C. h-Supervised Ordering

Let us focus on the case of h-ordering based on distances. We define a *h-supervised ordering* for a nonempty set R based on the subsets $B, F \subset R$, such that $B \bigcap F = \emptyset$, as an h-ordering that satisfies the conditions $h(\mathbf{b}) = \bot$, if $\mathbf{b} \in B$, and $h(\mathbf{f}) = \top$ if $\mathbf{f} \in F$. Note that $\bot, \top$ are the smallest and largest elements in the lattice $\mathcal{L}$. Such an *h-supervised ordering* is denoted by $h_{\{B,F\}}$. Fig. 1 illustrates the main idea for a h-supervised ordering function. Note the important conditions $B \subseteq \mathcal{L}(\bot)$ and $F \subseteq \mathcal{L}(\top)$.

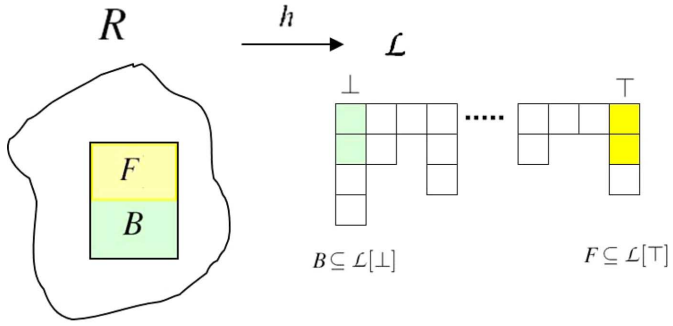

Fig. 1. Scheme of h-supervised function producing a partial ordering on the original set R based on the subsets B and F. The h-supervised function requires that $h(\mathbf{b})$ belong to the equivalence class $\mathcal{L}[\bot]$, for all $\mathbf{b} \in B$ and equivalently $h(\mathbf{f})$ belong to $\mathcal{L}[\top]$. $\mathcal{L}$ is the lattice $(\overline{\mathbb{R}}, \leq)$ using $\leq$ as the "less than or equal to" operation.

Once this additional supervised restriction is imposed, an adequate vector ranking scheme can be formulated based on $T = B \cup F$. The main motivation of defining this new supervised ordering schema is to obtain maximum and minimum in the lattice $\mathcal{L}$ interpretable with respect to sets B and F. It is important to remember that $\mathbf{max}$ and $\mathbf{min}$ are the basic words in the construction of all mathematical morphology operators. At this point, the problem is how to define an adequate supervised ordering for a given vector space and two pixel subsets B, F. Our approach takes advantage of algorithms to solve a supervised classification problem to define the function $h(\mathbf{x})$ as in (4), but based on B, F as follows:

$$\begin{aligned} h(\mathbf{x}) &= \sum_{i=1}^{|T|} \lambda^i_{\mathbf{x}} \phi(\mathbf{t}_i, \mathbf{x}) \\ &= \sum_{k=1}^{|B|} \lambda^k_{\mathbf{x}} \phi(\mathbf{b}_k, \mathbf{x}) + \sum_{j=1}^{|F|} \lambda^j_{\mathbf{x}} \phi(\mathbf{f}_j, \mathbf{x}). \end{aligned} \tag{5}$$

Different h-mappings and induced ordering $\leq_h$ are illustrated in Fig. 2 for some vectors in $\mathbb{R}^2$.

III. Learning the h-Supervised Ordering

Here, we introduce how to calculate h-supervised ordering using well-known supervised learning algorithms. The two approaches presented in this paper are selected to illustrate the design of h-supervised ordering, but other supervised or semi-supervised approaches can be also explored. However, due to $h(\cdot)$ is not necessary injective, the complete ordering has to be completed in practical examples.

A. Kriging

A kriging model gives an interpolating predictor, which can be used to approximate a function based on a finite number of evaluations. Kriging was originated in geostatistics by Matheron [33]. Kriging is also referred to as the Gaussian process predictor in the machine learning domain [34]. The kriging model postulates estimate an unknown function of interest in the value $\mathbf{x}$ as a linear combination of known realizations of the form $\hat{h}(\mathbf{x}) = \sum \lambda^i_{\mathbf{x}} h(\mathbf{t}_i)$. The most commonly used variant is called *ordinary kriging*, which is often referred to as a best linear unbiased estimator (BLUE) [35]. It is considered to be best because it minimizes the variance of the estimation error. It is "linear" because estimates are a weighted linear combination of available data, and is "unbiased" since it aims to have the mean error equal to zero. A more complete introduction to kriging can be found

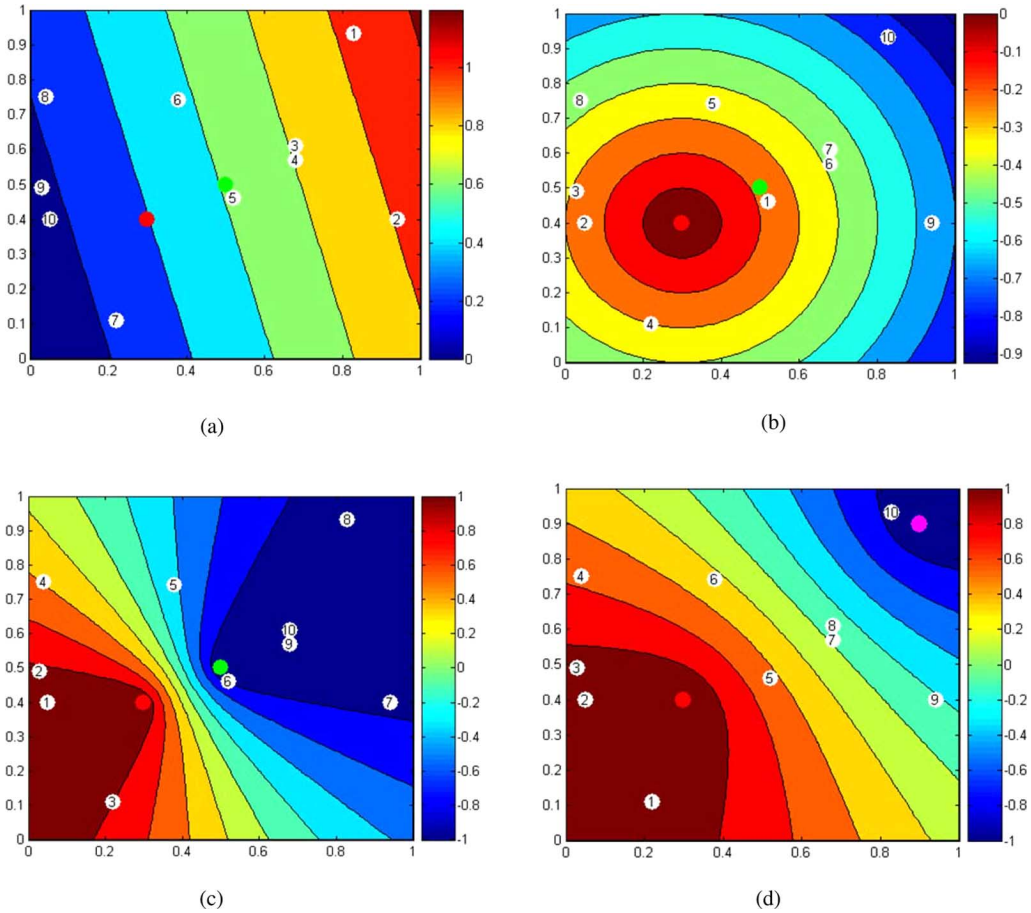

Fig. 2. Comparison of h-mappings and their corresponding h-ordering $\leq_h$ in $\mathbb{R}^2$. (a) Unsupervised ordering using first principal component. $h(\mathbf{x}) = h(x_1, x_2) = \sum_{i=1}^{2} \lambda^i x_i$. (b) Supervised ordering using a single reference vector $\mathbf{t}$ (red circle). $h_{\{\mathbf{t}\}}(\mathbf{x}) = (\mathbf{K}(\mathbf{x}, \mathbf{t}))$. (c) Supervised ordering $h_{\{\mathbf{b},\mathbf{t}\}}$ based on $B = \mathbf{b_1}$ (green circle) and $F = \mathbf{f}$ (red circle). (d) Supervised ordering $h_{\{\mathbf{b},\mathbf{t}\}}$ based on $B = \mathbf{b_2}$ (purple circle) and $F = \mathbf{f}$ (red circle).

in [35]. Formalizing this objective function with its constraint results in the following system [35]:

$$\varphi\left(\lambda_x^1, \ldots, \lambda_x^{|T|}, \mu\right) = \mathrm{Var}(e) - 2\mu\left(\sum_i^{|T|} \lambda_{\mathbf{x}}^i - 1\right) \tag{6}$$

where μ is a Lagrangian multiplier. Setting the partial first derivatives of (6) to zero with respect to μ and λ's. After $|T| + 1$ differentiations, the set of weight that minimize the error variance can be expressed in matrix form as:

$$\begin{pmatrix} \mathbf{K} & 1 \\ 1^t & 0 \end{pmatrix} \begin{pmatrix} \lambda_{\mathbf{x}} \\ \mu \end{pmatrix} = \begin{pmatrix} \mathbf{K_x} \\ 1 \end{pmatrix} \tag{7}$$

where $\mathbf{K}$ is the matrix $|T| \times |T|$ of points' pairwise covariances. Pairwise covariances are often modeled as a function of points separation. The flexibility in kriging is achieved through a variety of spatial correlation functions [35]. Finally, to obtain an h-supervised ordering based on B, F, we set $h(\mathbf{b}) = \perp = -1$ and $h(\mathbf{f}) = \top = 1$ to interpret $\hat{h}(\mathbf{x})$ as a kriging interpolation using $\mathbf{K}$. Thus, the h-supervised ordering using ordinary kriging is given by

$$\begin{aligned} \hat{h}(\mathbf{x}) &= \sum_i^{|T|} \lambda_{\mathbf{x}}^i h(\mathbf{t_i}) \\ &= \sum_i^{|F|} \lambda_{\mathbf{x}}^i h(\mathbf{f}) - \sum_j^{|B|} \lambda_{\mathbf{x}}^j h(\mathbf{b}) \\ &= \sum_i^{|F|} \lambda_{\mathbf{x}}^i - \sum_j^{|B|} \lambda_{\mathbf{x}}^j \end{aligned} \tag{8}$$

where the $\lambda_{\mathbf{x}}$'s are found using (7), that is, by solving the corresponding linear system (7). Note that (8) is defined in the sense of (5), and it can be used to obtain a supervised ordering. As an illustrative example, we propose to solve (7) when both background and foreground sets are unitary, that is to say, $B = \{\mathbf{b}\}$ and $F = \{\mathbf{f}\}$. In this case, we use the notation $u = \mathbf{K}(\mathbf{x}, \mathbf{x}), v = \mathbf{K}(\mathbf{f}, \mathbf{b}), c = \mathbf{K}(\mathbf{b}, \mathbf{x})$ and $d = \mathbf{K}(\mathbf{f}, \mathbf{x})$. From (7), we obtain

$$\lambda_x^1 = \frac{u - v + (c - d)}{2(u - v)}, \quad \lambda_x^2 = \frac{u - v - (c - d)}{2(u - v)}.$$

Clearly, $\lambda_{\mathbf{x}}^i$ depend on $\mathbf{x}$ because of values $c = \mathbf{K}(\mathbf{b}, \mathbf{x})$ and $d = \mathbf{K}(\mathbf{f}, \mathbf{x})$. Finally, we obtain the following h-supervised ordering using (8):

$$\hat{h}(\mathbf{x}) = \lambda_{\mathbf{x}}^1 - \lambda_{\mathbf{x}}^2 = \frac{d - c}{u - v} = \frac{\mathbf{K}(\mathbf{f}, \mathbf{x}) - \mathbf{K}(\mathbf{b}, \mathbf{x})}{\mathbf{K}(\mathbf{x}, \mathbf{x}) - \mathbf{K}(\mathbf{f}, \mathbf{b})}. \tag{9}$$

Thus, the supervised reduced ordering is basically the difference between kernelized distances. Note that, as $u > v$, then, if $\mathbf{x} \to \mathbf{f} \Rightarrow h(\mathbf{x}) \to 1$ and if $\mathbf{x} \to \mathbf{b} \Rightarrow h(\mathbf{x}) \to -1$, where "$\to$" means "tends to."

B. Support Vector Machines (SVMs)

Let us focus now on linearly separable problems, because they are the simplest for SVMs [36]. Given a labeled training set

$\{(\mathbf{t}_1, y_1), (\mathbf{t}_2, y_2), \ldots, (\mathbf{t}_i, y_i), \ldots, (\mathbf{t}_{|T|}, y_{|T|})\}$, where $\mathbf{t} \in \mathbb{R}^p$ and a class label $y_i = \pm 1$, it is said to be linearly separable if there exists a linear discriminant function whose sign matches the class of all training examples. In this case, the discrimination function is modeled by $\hat{y}(\mathbf{x}) = \beta^T \mathbf{x} + \beta_0$, and it is used to separate the two classes. However, there usually exist infinite separating hyperplanes which can separate the training set perfectly. Vapnik [37] proposes to choose the separating hyperplane that maximizes the margin. This new additional requirement, at the basis of the SVM framework, is the main difference, with respect to classical classifiers as Fisher's linear discriminant or logistic regression. As has been pointed out by several authors [36], the signed distance from a point $\mathbf{x}$ to a given hyperplane is $(1)/(\|\beta\|)(\beta^T \mathbf{x} + \beta_0)$. Hence, the aim is to obtain the biggest positive C, which makes all examples satisfy $(1)/(\|\beta\|)(\beta^T \mathbf{t_i} + \beta_0) \geq C, \forall i$. Since the length of β is insignificant, SVM assumes $(1)/(\|\beta\|) = C$. Thus, the constrained optimization problem can be written as

$$\begin{cases} \max_{\beta, \beta_0}, & \frac{1}{2}\|\beta\|^2 \\ \text{subject to}, & \frac{1}{\|\beta\|} y_i(\beta^T \mathbf{t}_i + \beta_0) \geq 1, \forall i. \end{cases} \tag{10}$$

Due to dual formulation of the primal problem and the equation involved in this formulation [36]–[38], we can express the original linear model as:

$$\hat{y}(\mathbf{x}) = \beta^T \mathbf{x} + \beta_0 = \sum_{i=1}^{|T|} \lambda_i y_i \mathbf{t}_i^T \mathbf{x} + \beta_0 \tag{11}$$

where λ's are the Lagrangian coefficients. Additionally, this formulation can be extended to construct nonlinear classifiers in the original space. Notice that in (11) the training points are included only via their inner products. Thus, we obtain using nonlinear functions a "kernel trick" [36], $\hat{y}(\mathbf{x}) = \sum_{i=1}^{|T|} \lambda_i y_i \mathbf{K}(\mathbf{x}, \mathbf{t}_i) + \beta_0$. The evaluation function is discriminating between labels as background and foreground, then to obtain an h-supervised ordering, we set $y_i = h(\mathbf{b}) = \perp = -1$ and $y_i = h(\mathbf{f}) = \top = 1$. Thus, omitting B_0 because it is constant for all $\mathbf{x}$, our h-ordering based on SVM is obtained by

$$\hat{h}(\mathbf{x}) = \sum_{i=1}^{|F|} \lambda_i \mathbf{K}(\mathbf{x}, \mathbf{f}_i) - \sum_{j=1}^{|B|} \lambda_j \mathbf{K}(\mathbf{x}, \mathbf{b}_j) \tag{12}$$

where λ's are the Lagrangian solution in (10). Note that (12) can be used to obtain a supervised ordering because it is defined in the sense of (5). For the example presented in Section III.A, the corresponding function of h-ordering based on SVM can be calculated. Thus, we obtain $\lambda_1 = \lambda_2$, substituting this into a kernelized dual formulation, and finding the value where the derivative is equal to zero, we can say that $\phi_D = 2\lambda_1 - \lambda_1^2(u - v) \Rightarrow \lambda_1 = \lambda_2 = (1)/(u - v)$. Thus, from (12), the h-ordering using SVM in the unitary background and foreground example is

$$\begin{aligned} \hat{h}(\mathbf{x}) &= \lambda_1 \mathbf{K}(\mathbf{x}, \mathbf{f}_i) - \lambda_2 \mathbf{K}(\mathbf{x}, \mathbf{b}_j) \\ &= \frac{d - c}{u - v} \\ &= \frac{\mathbf{K}(\mathbf{f}, \mathbf{x}) - \mathbf{K}(\mathbf{b}, \mathbf{x})}{\mathbf{K}(\mathbf{x}, \mathbf{x}) - \mathbf{K}(\mathbf{f}, \mathbf{b})}. \end{aligned}$$

We must remark that this is the same h-ordering found in (9) using ordinary kriging. In Fig. 2, we provide a comparison among different ordering schemes in $\mathbb{R}^2$. Fig. 2(a) shows nonsupervised ordering using the first principal component, Fig. 2(b) shows an ordering based on a unique reference vector [14], and Fig. 2(c) and (d) shows two examples of h-ordering using the proposed supervised ordering.

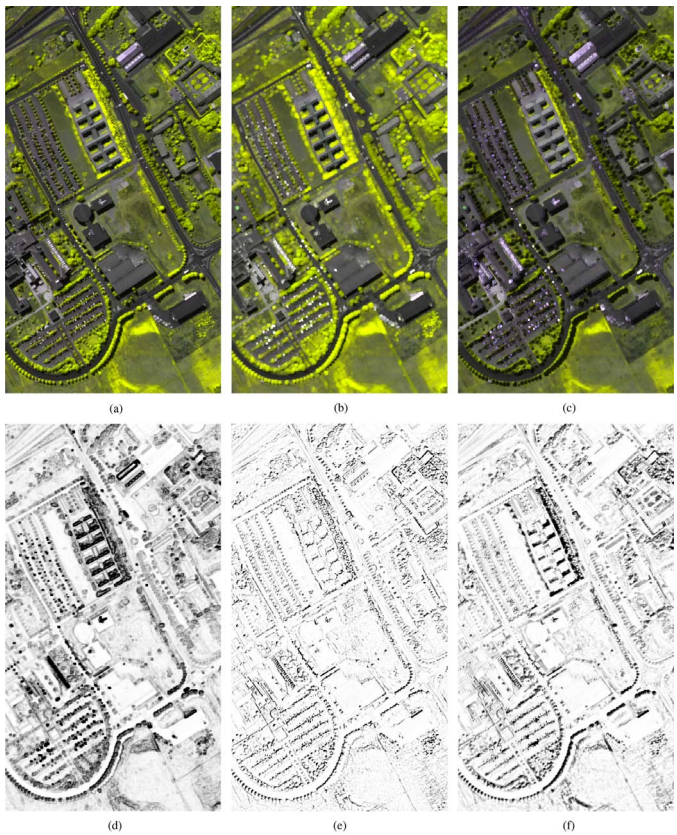

Fig. 3. *Pavia University* with 340×610 pixels in 103 bands. Supervised dilation, erosion, gradient, and positive top-hats for a set of background/foreground pixels $\{\mathbf{b}_0, \mathbf{f}_0\}$ illustrated in Fig. 4. Unitary structured element S is a square. Spectra are shown using bands $\{80, 90, 70\}$. h-ordering is calculated using (9) with a polynomial kernel of order 2. (This figure should be viewed in color and by zooming on a computer screen.) (a) $\mathbf{I}$. (b) $\delta_{\{\mathbf{b}_0, \mathbf{f}_0\}, S}(\mathbf{I})$. (c) $\varepsilon_{\{\mathbf{b}_0, \mathbf{f}_0\}, S}(\mathbf{I})$. (d) $\rho_{\{\mathbf{b}_0, \mathbf{f}_0\}, S}(\mathbf{I})$. (e) $\rho^+_{\{\mathbf{b}_0, \mathbf{f}_0\}, 2S}(\mathbf{I})$. (f) $\rho^+_{\{\mathbf{b}_0, \mathbf{f}_0\}, 5S}(\mathbf{I})$.

C. Kriging Versus SVM

As we have shown, the same function $h(\mathbf{x})$ is obtained for both methods in the simplest case, when the training set is composed of a vector for the background set and a vector for the foreground. However, in general, the results are different. Let us compare in detail kriging and SVM ordering approaches. First of all, we notice that the ordering in kriging is formulated as an interpolation problem, whereas in SVM as an optimization one. In both cases, the choice of the kernelized distance introduces a great flexibility and the possibility to extend the approach to non vector spaces. From a computational viewpoint, kriging requires a global computation of the Gram matrix for the training set and the vector of distances for each vector: the value is obtained by the product of the inverse matrix and the vector. Hence, it is a linear algorithm, without any parameter, and quite efficient for a low number of training vectors. The optimization algorithms used for SVM requires basically a few penalization parameters. After the learning procedure, only a subset of the training vectors (the support vectors) are used to compute the value of the ordering function at each vector. It has been proven that SVM are particularly robust in the case of high-dimensional spaces and SVM are also very efficient in large training sets.

IV. Morphological Operators in Vector Spaces

Once the family of orderings has been established, the morphological vector operators are defined in the standard way. All morphological operators based on the h-supervised ordering will be referred to as supervised. We limit here our developments to the flat operators, i.e.,

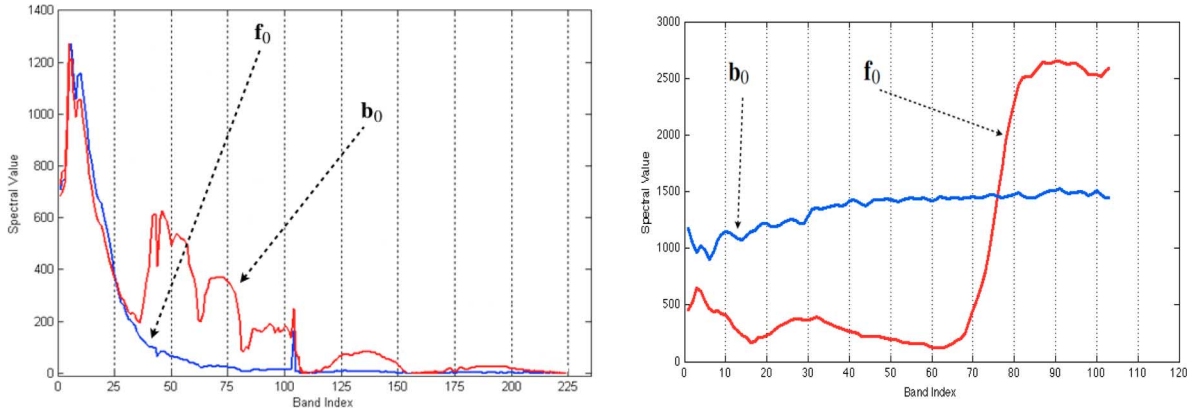

(a) (b)

Fig. 4. (a) Training spectra for Yellowstone Scene: $\mathbf{b}_0$ (land) and $\mathbf{f}_0$ (water). (b) Training spectra for Pavia University: $\mathbf{b}_0$ (tree) and $\mathbf{f}_0$ (gravel). Morphological operators are calculated using the h-supervised ordering induced by $B = \{\mathbf{b}_0\}$ and $F = \{\mathbf{f}_0\}$.

the structuring elements are planar shapes. The *supervised erosion* of an image $\mathbf{I} \in \mathcal{F}(E, \mathcal{L})$ at pixel $\mathbf{x} \in \mathbb{R}^p$ by the structuring element $S \subset E$ based on the set of pixels B, F is given by

$$\varepsilon_{\{B,F\},S}(\mathbf{I})(\mathbf{x}) = \{\mathbf{I}(\mathbf{y}) : \mathbf{I}(\mathbf{y}) = \wedge_{h_{\{B,F\}}}[\mathbf{I}(\mathbf{z})], \mathbf{z} \in S_{\mathbf{x}}\} \tag{13}$$

where $\wedge_{h_{\{B,F\}}}$ is the infimum according to the total ordering $h_{\{B,F\}}$ and $S_{\mathbf{x}}$ is the neighborhood region centered on the considered pixel $\mathbf{x}$. The corresponding adjunct *supervised dilation* $\delta_{\{B,F\}}$ is obtained by replacing $\wedge_{h_{\{B,F\}}}$ by $\vee_{h_{\{B,F\}}}$, i.e., $\delta_{\{B,F\},S}(\mathbf{I})(\mathbf{x}) = \{\mathbf{I}(\mathbf{y}) : \mathbf{I}(\mathbf{y}) = \vee_{h_{\{B,F\}}}[\mathbf{I}(\mathbf{z})], \mathbf{z} \in (\hat{S})_{\mathbf{x}}\}$, where $\hat{S}$ is the reflected structuring element [5]. The erosion and the dilation are increasing operators. Moreover, the erosion is anti-extensive and the dilation is extensive. In practice, the supervised erosion shrinks the structures which have a spectrum close to the foreground; "peaks of spectra" thinner than the structuring element disappear by taking the spectrum of neighboring structures with a spectrum values close to the background. As well, it expands the structures which have a vector value close to background. Dilation produces the dual effects, enlarging the regions having a spectrum close to the foreground and contracting the background. One of the most interesting properties of gray-level morphological operators is the duality by the complementation. The *complement image* f^c is defined as the negative of f $(f(\mathbf{x}))^c = -f(\mathbf{x}) = f^c(\mathbf{x})$. Letting the pair of erosion/dilation (ε, δ) be an adjunction, the property of *duality* holds that $\varepsilon(f^c) = (\delta(f))^c \Rightarrow \varepsilon(f) = (\delta(f^c))^c$, and this is verified for any other pair of dual operators, such as the opening/closing. In practice, this property allows us to implement exclusively the dilation and, using the complement, to be able to obtain the corresponding erosion. In our case, it is easy to see that we have the following equivalent properties of duality $\varepsilon_{h_{\{B,F\}},S}(\mathbf{I}) = \delta_{h_{\{F,B\}},S}(\mathbf{I})$ and $\varepsilon_{h_{\{B,F\}},S}(\mathbf{I}) = \delta_{-h_{\{B,F\}},S}(\mathbf{I})$. Dilation and erosion allow us to define morphological filters [4], [5]. In general, a morphological filter is an increasing operator that is also idempotent (the erosion/dilation are not idempotent). A *supervised opening* is an erosion followed by a dilation, i.e., $\gamma_{\{B,F\},S}(\mathbf{I}) = \delta_{\{B,F\},S}(\varepsilon_{\{B,F\},S}(\mathbf{I}))$, and a *supervised closing* is a dilation followed by an erosion. The opening (closing) is an anti-extensive (extensive) morphological filter. More precisely, the opening removes spectra peaks that are thinner than the structuring element, having a vector value close to the foreground; the closing remove vector values peaks that are thinner than the structuring element, having a spectrum close to background. The *positive supervised top-hat transformation* is the residue of a supervised opening, i.e., $\rho^{+}_{\{B,F\},S}(\mathbf{I}) = h_{\{B,F\}}(\mathbf{I}) - h_{\{B,F\}}(\gamma_{\{B,F\},S}(\mathbf{I}))$. The positive top-hat transformation yields gray level images and it is used to extract contrasted components with respect to the background.

V. Applications to Hyperspectral Imagery

In practice, the construction of a total order is required to avoid random decisions in lattice operations. In sequel, the total ordering is induced including a lexicographic order in $\mathcal{L}[z]$, for all z, in cases with equal value in the induced ordering h and hence a complete totally ordered lattice $\tilde{\mathcal{L}}$ is obtained for the hyperspectral images. We must notice however that using h-mapping for $\mathbb{R}^p$ $(p \gg 2)$ the possibility of having two different spectra with equal value in h is quite rare. We present our examples over two images, given here.

- *Pavia University hyperspectral image* is an urban area that was recorded by the ROSIS-03 optical sensor with spatial resolution of 1.3 m per pixel. The number of bands is 115 with a spectral coverage ranging from 0.43 to 0.86 μm. The 12 noisiest channels have been removed, and the experiments are conducted on the 103-band image. Fig. 3(a) shows the false-color preview for the 340 columns, with 610 rows in 103 bands. Fig. 4(b) shows the two pixels selected as background and foreground for the experiments.
- *Yellowstone calibrated scene 3* is an AVIRIS image which has been provided in [39]. The spatial resolution is 20 m per pixel. Fig. 5(a) shows the false-color preview for the 512 columns, with 677 rows in 224 bands. In the experiments, only two pixels for foreground and background had been selected, as is shown in Fig. 4(a).

Erosion and dilation operators [Figs. 5(c) and 3(c) and Figs. 5(b), and 3(b)] do not introduce false spectra. By computing the morphological gradient in Figs. 5(d) and 3(d), as the difference in h between the erosion and the dilation, we obtain contours which correspond here to the spatial transition, but it gives priority to changes according with the training set, i.e., water–land or trees–gravel. Obviously, the results obtained can be improved including a higher number of training pixels in F and B. Examples illustrate that even using a limited number of training set size, our approach produces operators that can be interpreted as gray-scale mathematical morphological operators according with the spatial size of the structuring element S, but it takes into consideration the inherent dependence of our approach to the sets B and F. Therefore, the selection of reference spectra have to be done according to practical needs.

Morphological opening and closing are appropriate operators for structure extraction according to their spatial/spectral properties. More

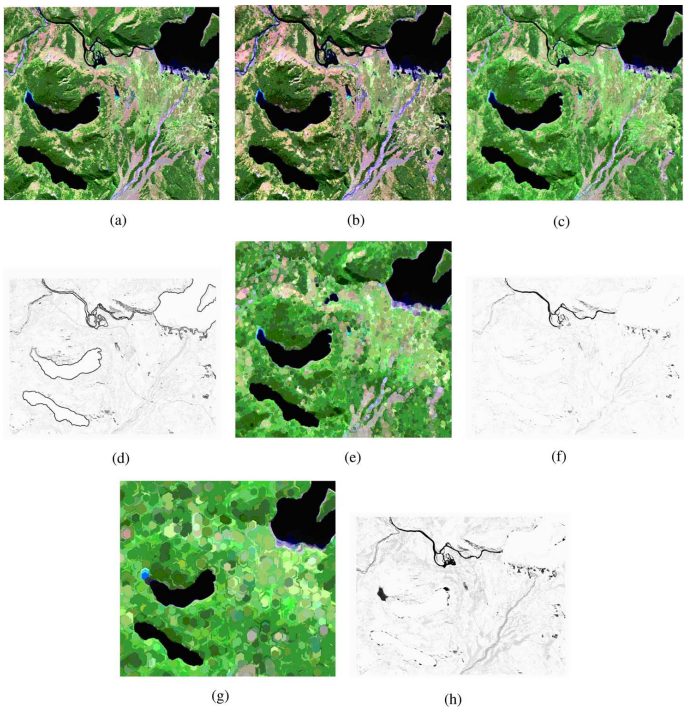

Fig. 5. *Yellowstone scene* with 512×677 pixels in 224 bands. Supervised dilation, erosion, opening, and their positive top-hats for a set of background/foreground pixels $\{\mathbf{b}_0, \mathbf{f}_0\}$ illustrated in Fig. 4. Unitary structured element S is an hexagon. Spectra are shown using bands $\{125, 70, 30\}$. The h-ordering is calculated using (9) with a polynomial kernel of order 2. (This figure should be viewed in color and by zooming on a computer screen.) (a) $\mathbf{I}$. (b) $\delta_{\{\mathbf{b}_0,\mathbf{f}_0\},S}(\mathbf{I})$. (c) $\varepsilon_{\{\mathbf{b}_0,\mathbf{f}_0\},S}(\mathbf{I})$. (d) $\rho_{\{\mathbf{b}_0,\mathbf{f}_0\},S}(\mathbf{I})$. (e) $\gamma_{\{\mathbf{b}_0,\mathbf{f}_0\},4S}(\mathbf{I})$. (f) $\rho^{+}_{\{\mathbf{b}_0,\mathbf{f}_0\},4S}$. (g) $\gamma_{\{\mathbf{b}_0,\mathbf{f}_0\},10S}(\mathbf{I})$. (h) $\rho^{+}_{\{\mathbf{b}_0,\mathbf{f}_0\},10S}(\mathbf{I})$.

precisely, the top-hats or residues between the original image and the opened/closed image give the structures selectively removed by the opening/closing. Examples of positive supervised top-hat are shown in Figs. 5(f), 3(e), and 3(f), which allow us to extract regions with a size smaller than the corresponding structuring element and whose spectra are close to the F. By modifying the size of the structuring element, a scale-space spectral extraction is obtained.

VI. Conclusion

Hyperspectral imaging is an active field of image analysis which is usually considered under the supervised paradigm [40]: both the complexity of the data and the typical real-life applications require the construction of training sets of spectra which drive the algorithms of classification, feature extraction, and segmentation, among others. Hence, from our viewpoint, the construction of hyperspectral mathematical morphology operators should be also coherent with this idea of supervised processing. In previous works, some of the introduced ideas were useful but their formulation was not correct in the theoretical framework of mathematical morphology. Other works, following direct extensions of the works on color morphology, were basically based on the notion of color of reference (for the supervised ones) or on the projection on main directions (for the unsupervised ones). We consider that the present methodology generalizes most of the precedent works on vector mathematical morphology. In particular, we have shown how mathematically sound machine learning techniques can be also used to define supervised partial orderings in vector spaces. In fact, using for instance the kernel-trick and SVM algorithms, the framework is valid to define supervised ordering in any space providing that a kernel between the points is defined. Additionally, this formulation based on both a background and a foreground training set allows an adequate interpretation of dual morphological operations. The examples given in the paper illustrate the potential interest of the algorithms; however, more advanced applications are currently under study.

References

[1] G. Birkhoff, "Lattice theory," *Amer. Math. Soc.*, vol. 25, no. 3, p. 420, 1967.
[2] C. Ronse, "Why mathematical morphology needs complete lattices," *Signal Process.*, vol. 21, no. 2, pp. 129–154, 1990.
[3] V. Barnett, "The ordering of multivariate data (with discussion)," *J. Royal Stat. Soc. A*, vol. 139, no. 3, pp. 318–354, 1976.
[4] J. Serra, *Image Analysis and Mathematical Morphology*. Orlando, FL: Academic, 1983.
[5] P. Soille, *Morphological Image Analysis*. Berlin, Germany: Springer-Verlag, 1999.
[6] J. Goutsias and H. Heijmans, *Mathematical Morphology*. Amsterdam, The Netherlands: IOS, 2000.
[7] R. Haralick, S. Sternberg, and X. Zhuang, "Image analysis using mathematical morphology," *IEEE Trans. Pattern Anal. Mach. Intell.*, vol. 9, no. 4, pp. 532–550, Jul. 1987.
[8] J. Serra, "Anamorphoses and function lattices (multivalued morphology)," *Math. Morphol. Image Process.*, pp. 483–523, 1993.
[9] J. Goutsias, H. Heijmans, and K. Sivakumar, "Morphological operators for image sequences," *Comp. Vis. Image Understandin*, vol. 62, no. 3, pp. 326–346, 1995.
[10] H. Talbot, C. Evans, and R. Jones, "Complete ordering and multivariate mathematical morphology," in *Proc. ISMM*, Norwell, MA, 1998, pp. 27–34.
[11] I. Pitas and P. Tsakalides, "Multivariate ordering in color image processing," *IEEE Trans. Circuits Syst. Video Technol.*, vol. 1, no. 3, pp. 247–256, 1991.
[12] J. Serra, "The "false colour" problem," in *Proc. ISMM*, 2009, pp. 13–23.
[13] E. Aptoula and S. Lefèvre, "A comparative study on multivariate mathematical morphology," *Pattern Recognit.*, vol. 40, no. 11, pp. 2914–2929, 2007.
[14] J. Angulo, "Morphological colour operators in totally ordered lattices based on distances: Application to image filtering, enhancement and analysis," *Comp. Vis. Image Understanding*, vol. 107, no. 1–2, pp. 56–73, 2007.
[15] A. Hanbury and J. Serra, "Morphological operators on the unit circle," *IEEE Trans. Image Process.*, vol. 10, no. 12, pp. 1842–1850, Dec. 2001.
[16] E. Aptoula and S. Lefèvre, "On the morphological processing of hue," *Image Vision Comput.*, vol. 27, no. 9, pp. 1394–1401, 2009.
[17] H. M. Al-Otum, "Morphological operators for color image processing based on mahalanobis distance," *Opt. Eng.*, vol. 42, no. 9, pp. 2595–2606, 2003.
[18] A. Garcia, C. Vachier, and J. Vallée, J. T. Astola, K. O. Egiazarian, and E. R. Dougherty, Eds., "Multivariate mathematical morphology and Bayesian classifier application to colour and medical images," *Proc. SPIE: Image Process.: Algorithms Syst. VI*, vol. 6812, no. 1, p. 681203, 2008.
[19] J. Angulo, "Geometric algebra colour image representations and derived total orderings for morphological operators—Part I: Colour quaternions," *J. Vis. Comun. Image Represent.*, vol. 21, no. 1, pp. 33–48, 2010.
[20] A. Plaza, P. Martinez, R. Perez, and J. Plaza, "A new approach to mixed pixel classification of hyperspectral imagery based on extended morphological profiles," *Pattern Recognit.*, vol. 37, no. 6, pp. 1097–1116, 2004.
[21] J. Astola, P. Haavisto, and Y. Neuvo, "Vector median filters," *Proc. IEEE*, vol. 78, no. 4, pp. 678–689, Apr. 1990.
[22] O. Lezoray, A. Elmoataz, and C. Meurie, "Mathematical morphology in any color space," in *Proc. ICIAPW*, 2007, pp. 183–187.
[23] O. Lezoray, C. Charrier, and A. Elmoataz, "Learning complete lattices for manifold mathematical morphology," in *Proc. ISMM*, 2009, pp. 1–4.

[24] S. Velasco and J. Angulo, "Morphological processing of hyperspectral images using kriging-based supervised ordering," in *Proc. 17th IEEE Int. Conf. Image Process.*, 2010, pp. 1409–1412.
[25] S. Roman, *Lattices and Ordered Sets*. Berlin, Germany: Springer-Verlag, 2008.
[26] H. Heijmans, "Theoretical aspects of gray-level morphology," *IEEE Trans. Pattern Anal. Mach. Intell.*, vol. 13, no. 6, pp. 568–582, Jun. 1991.
[27] I. T. Jolliffe, *Principal Component Analysis*. Berlin, Germany: Springer-Verlag, 1986.
[28] B. Scholkopf, A. Smola, and K. Muller, "Nonlinear component analysis as a kernel eigenvalue problem," *Neural Comp.*, vol. 10, no. 5, pp. 1299–1319, 1998.
[29] J. Tenenbaum, V. Silva, and J. Langford, "A global geometric framework for nonlinear dimensionality reduction," *Science*, vol. 290, no. 5500, pp. 2319–2323, Dec. 2000.
[30] M. Belkin and P. Niyogi, "Laplacian eigenmaps for dimensionality reduction and data representation," *Neural Comp.*, vol. 15, pp. 1373–1396, 2002.
[31] N. Kambhatla and T. Leen, "Dimension reduction by local principal component analysis," *Neural Comp.*, vol. 9, no. 7, pp. 1493–1516, 1997.
[32] Z. Ghahramani and G. E. Hinton, "The EM algorithm for mixtures of factor analyzers," Dept. of Comput. Sci., Univ. of Toronto, Tech. Rep., 1997.
[33] G. Matheron, "Le Krigeage Universel," Ecole des Mines de Paris, 1969.
[34] C. E. Rasmussen and C. K. I. Williams, *Gaussian Processes for Machine Learning*. Cambridge, MA: MIT Press, 2006.
[35] E. H. Isaaks and R. M. Srivastava, *An Introduction to Applied Geostatistics*. Oxford, U.K.: Oxford Univ. Press, 1989.
[36] N. Cristianini and J. Shawe-Taylor, *An Introduction to Support Vector Machines and Other Kernel Based Learning Methods*. Cambridge, U.K.: Cambridge Univ. Press, 2000.
[37] V. Vapnik and A. Lerner, "Pattern recognition using generalized portrait method," *Autom. Remote Control*, vol. 24, pp. 774–780, 1963.
[38] S. Boyd and L. Vandenberghe, *Convex Optimization*. Cambridge, U.K.: Cambridge Univ. Press, 2004.
[39] A. Kiely and M. Klimesh, "Exploiting calibration-induced artifacts in lossless compression of hyperspectral imagery," *IEEE Trans. Geosci. Remote Sens.*, vol. 47, no. 8, pp. 2672–2678, Aug. 2009.
[40] F. Melgani and L. Bruzzone, "Classification of hyperspectral remote sensing images with support vector machines," *IEEE Trans. Geosci. Remote Sens.*, vol. 42, no. 8, pp. 1778–1790, Aug. 2004.

Segmentation and Tracking Multiple Objects Under Occlusion From Multiview Video

Qian Zhang, *Student Member, IEEE*, and King Ngi Ngan, *Fellow, IEEE*

***Abstract*—In this paper, we present a multiview approach to segment the foreground objects consisting of a group of people into individual human objects and track them across the video sequence. Depth and occlusion information recovered from multiple views of the scene is integrated into the object detection, segmentation, and tracking processes. *Adaptive background penalty with occlusion reasoning* is proposed to separate the foreground regions from the background in the initial frame. Multiple cues are employed to segment individual human objects from the group. To propagate the segmentation through video, each object region is independently tracked by motion compensation and uncertainty refinement, and the motion occlusion is tackled as layer transition. The experimental results implemented on both our sequences and other's sequence have demonstrated the algorithm's efficiency in terms of subjective performance. Objective comparison with a state-of-the-art algorithm validates the superior performance of our method quantitatively.**

***Index Terms*—Graph cut, layer transition, multiview video, object segmentation, object tracking.**

I. Introduction

Object detection, segmentation, and tracking are the key topics in computer vision and have facilitated many important applications, such as visual surveillance, human behavior analysis, and object recognition. Segmenting and tracking multiple human objects correctly and consistently when overlapping with each other under occlusion in a complex scene is a more challenging task than when the targets are separated due to the nonrigid motion of deformable objects and the dynamic change of object attributes, such as color distribution, shape, and visibility.

Recently, segmenting and tracking multiple simultaneous objects under occlusion have been addressed in the literature [1]–[9]. A number of video segmentation and tracking approaches and systems have been proposed [1]–[3] for handling objects occlusion in a single view. However, in the cluttered scene and wide-range surveillance, segmenting and tracking crowded people scene with high density using monocular camera is insufficient due to the limited visibility and substantial occlusion. To solve this challenging problem, stereo/multiple cameras are reasonable alternatives to collect more information from different perspectives of the same scene to improve the segmentation and tracking efficiency. This improvement can be achieved by gathering evidence from multiple views [4], combining probabilistic occupancy map [5] or camera collaboration [6]. A relatively new area uses the ground plane homography [7]–[9], which projects feature in each view onto the common view for data fusion.

Manuscript received July 16, 2010; revised November 30, 2010 and March 28, 2011; accepted May 25, 2011. Date of publication June 09, 2011; date of current version October 19, 2011. The work described in this paper was supported by the Research Grants Council of Hong Kong Special Administrative Region, China, under Project CUHK415707. The associate editor coordinating the review of this manuscript and approving it for publication was Dr. A. G. Bors.

The authors are with the Department of Electrical Engineering, The Chinese University of Hong Kong, Shatin, Hong Kong (e-mail: qzhang@ee.cuhk.edu.hk; knngan@ee.cuhk.edu.hk).

Color versions of one or more of the figures in this paper are available online at http://ieeexplore.ieee.org.

Digital Object Identifier 10.1109/TIP.2011.2159228

13.5 Publication V : J. Angulo. "Hypercomplex mathematical morphology". *Journal of Mathematical Imaging and Vision*, Volume 41, No. 1–2, 86–108, 2011.

J Math Imaging Vis (2011) 41:86–108
DOI 10.1007/s10851-011-0266-2

Hypercomplex Mathematical Morphology

Jesús Angulo

Published online: 23 February 2011

Abstract The natural ordering of grey levels is used in classical mathematical morphology for scalar images to define the erosion/dilation and the evolved operators. Various operators can be sequentially applied to the resulting images always using the same ordering. In this paper we propose to consider the result of a prior transformation to define the imaginary part of a complex image, where the real part is the initial image. Then, total orderings between complex numbers allow defining subsequent morphological operations between complex pixels. More precisely, the total orderings are lexicographic cascades with the local modulus and phase values of these complex images. In this case, the operators take into account simultaneously the information of the initial image and the processed image. In addition, the approach can be generalized to the hypercomplex representation (i.e., real quaternion) by associating to each image three different operations, for instance directional filters. Total orderings initially introduced for colour quaternions are used to define the evolved morphological transformations. Effects of these new operators are illustrated with different examples of filtering.

Keywords Nonlinear image filtering · Mathematical morphology · Adjunction · Complex images · Complex ordering · Hypercomplex ordering · Quaternion

J. Angulo (✉)
CMM-Centre de Morphologie Mathématique, Mathématiques et Systèmes, MINES ParisTech, 35, rue Saint-Honoré, 77305 Fontainebleau cedex, France
e-mail: jesus.angulo@mines-paristech.fr

1 Introduction

Let $f(\mathbf{x}) = t$ be a scalar image, $f : E \to \mathcal{T}$. In general $t \in \mathcal{T} \subset \mathbb{Z}$ or $\mathbb{R}$, but for the sake of simplicity of our study, we consider that $\mathcal{T} = \{1, 2, \ldots, t_{\max}\}$ (e.g., $t_{\max} = 255$ for 8 bits images) is an ordered set of positive grey-levels. Typically, for digital 2D images $\mathbf{x} = (x, y) \in E$ where $E \subset \mathbb{Z}^2$ is the support of the image. For 3D images $\mathbf{x} = (x, y, z) \in E \subset \mathbb{Z}^3$. According to the natural scalar partial ordering $\leq$, $\mathcal{T}$ is a complete lattice, and then $\mathcal{F}(E, \mathcal{T})$ is a complete lattice too.

Mathematical morphology is a nonlinear image processing approach based on the application of lattice theory to spatial structures [20, 42]. In particular, morphological operators are naturally defined in the framework of functions $\mathcal{F}(E, \mathcal{T})$. Various operators can be sequentially applied to the resulting images always using the same ordering $\leq$.

The methodological corpus of mathematical morphology is composed of several families of operators which address many applications, including denoising, multi-scale image decomposition, feature extraction, segmentation, etc. [50]. Furthermore, besides the algebraic definitions, most of morphological operators have associated a geometric interpretation.

Aim of the Paper. The objective of this study is to construct (hyper)-complex image representations which will be endowed with total orderings and consequently, which will lead to complete lattices. More precisely, it is proposed to use the result of a prior morphological transformation to define the imaginary part of a complex image, where the real part is the initial scalar image. Then, total orderings between complex numbers allow defining subsequent morphological operations between complex pixels. In this case, the operators take into account simultaneously the scalar intensities of both the initial and the transformed images. The complex

scalar value brings information about the invariance of intensities with respect to a particular size and shape structure (i.e., using openings, closings or alternate filters) as well as information about the local contrast of intensities in the image structures (i.e., by means of top-hat transformations). Hence, the interpretation of the local amplitude and phase in the proposed complex representations is basically a geometrical one, useful for image processing, but without a physical counterpart. More precisely, the choice of the imaginary part is determined by the required properties of the morphological complex operator (dilation or erosion) as well as the mathematical rationale of defining morphological adjunctions. In addition, the approach is also generalized to the hypercomplex representation (i.e., real quaternion) by associating to each image three different operations, for instance a series of directional filters.

The motivation of these methodological developments is to obtain "regularized" morphological operators. That is, dilations and erosions whose result depends not only on the supremum and infimum of the grey values, locally computed in the structuring element, but also on differential information or on more regional information.

The theoretical results of the paper are illustrated with various comparative examples based on the application of well-known morphological operators, defined in their (hyper)-complex versions, such as top-hat, morphological center, morphological laplacian, opening by reconstruction, leveling, etc. In particular, the potential interest of the proposed operators for real applications in medical imaging is also considered.

Previous Works on Regularized Mathematical Morphology. The objective of *regularized* erosion/dilation has been previously considered, under different viewpoints, in the state-of-the art of mathematical morphology.

Taking into account the historical formulation of mathematical morphology from Boolean algebra, the framework of fuzzy logic is an appropriate alternative, with several approaches of fuzzy morphology [6, 7, 10] as well as soft morphology [25]. Physics-based statistical morphology has been also explored in [56] within a formulation using thermodynamics concepts. The approach is based on constructing a Gibbs probability distribution where the energy state depends on the intensity values of the neighborhood and a temperature parameter. Morphological operations are interpreted as the minimal variance estimators of this probabilistic model, using the notion of mean field approximation for the computation of the estimated values. More precisely, erosion and dilation are limit cases when the temperature of the system tends to zero, with respectively positive and negative sign of the energy.

More recently, two other families of approaches have to be cited. On the one hand, adaptive operators based on local size density estimation have been used for robust filtering of binary and grey level images [58]. On the other hand, several works have studied the way to introduce a kind of viscosity on morphological operators. The morphological viscosity involves typically an unit dilation obtained after an opening of the space, leading to the viscous lattice [45], which is neither distributive, nor complemented, but is interesting for defining viscous geodesic propagations. In fact, the unitary step of the geodesic viscous dilation (erosion), which includes a prior unit opening (closing), has been also considered on the construction of viscous levellings [32, 33]. The idea of using a prior operator, a closing whose size depends on the intensity, to filter out the gradient before computing the watershed, leads to the notion of viscous watershed [51]. This kind of viscous closing, an adaptive operator where its size depends at each point on the value of intensity has been also used for reconnecting several edge portions [52]. In addition, another approach to the viscosity in morphology has been addressed under the notion of microviscous effect by second-order operators [34, 35]. The rationale is to include a nonlinear micro-operation embedded in the main nonlinear operation; this framework has shown a good performance for regularized filtering.

More generally, the theory and algorithms of self-dual morphology, by defining activity-decreasing modifications of the median filter [21] as well as by considering an adaptive reference image [22, 24], leads to robust operators appropriate to deal with noisy and strong structured images.

Previous Works on the Application of Geometric Algebra to Image Processing. Geometric algebraic representations have been previously used for image modelling and processing. Classically, in one-dimensional (1D) signal processing, the analytic signal is a powerful complex-model which provides access to local amplitude and phase. The complex signal is built from a real signal by adding its Hilbert transform—which is a phase-shifted version of the signal—as an imaginary part to the signal. The approach was extended to 2D signals and images in [8] by means of the quaternionic Fourier transform. In parallel, another theory introduced in [17] to extend the analytic model in 2D is based on the application of the Riesz transform as generalized Hilbert transform, leading to the notion of monogenic signal which delivers an orthogonal decomposition into amplitude, phase and orientation. Later, the monogenic signal was studied in the framework of scale-spaces [18]. More recently, in [57], the 2D scalar-valued images are embedded into the geometric algebra of the Euclidean 4D space and then the image structures are decomposed using monogenic curvature tensor.

We are dealing here with grey-level images, however, the geometric algebra representations have been mainly used for modelling colour images. Therefore, let us consider the

particular state-of-the art of colour geometric algebra. Di Zenzo [12] proposed in his pioneer work a tensor representation of colour derivatives in order to compute the colour gradient by considering the colour image as a surface in $\mathbb{R}^3$. Later, Sochen and Zeevi [47] and Sochen et al. [48] considered a colour image as a two-dimensional manifold embedded in the five-dimensional non-Euclidean space, whose coordinates are $(x, y, R, G, B) \in \mathbb{R}^5$, which is described by Beltrami colour metric tensor. But all these studies consider only the differential representation of the colour triplet, which is useful for differential geometric colour processing, e.g., colour image enhancement and smoothing using PDE. Another algebraic tool used to represent and to perform colour transformations by taking into account the 3D vector nature of colour triplets is the quaternion. The first application of quaternion colour processing was reported by Sangwine [39] for computing a Fourier colour transform. Other quaternionic colour transformations were then explored by Sangwine and Ell such as colour image correlation [15], colour convolution for linear filtering [41] and for vector edge-detecting [40] as well as new results on quaternion Fourier transforms of colour images [16]. Ell [13] introduced recently the application of quaternion linear transformations of colour images (e.g., rotation and reflections of colours). Other works by Denis et al. [11] and Carré and Denis [9] have also explored new approaches for colour spectral analysis, edge detection and colour wavelet transform. Quaternion representations have been also used to define colour statistical moments and derived applications by Pei and Cheng [36] and to build colour Principal Component Analysis [29, 37, 46]. Quaternion algebra can be generalized in terms of Clifford algebra. In this last framework, Labunets *et al.* have studied Fourier colour transform [28], including colour wavelets for compression and edge detection, as well as computation of invariants of nD colour images [26, 27]. Ell [14] has also started to study this representations for colour convolution and Fourier transform. More recently, Batard et al. [4, 5] have also studied the application of Clifford algebras to analyse (edge detection and Fourier Transform) colour images.

Finally, we have recently explored also the interest of colour quaternions for extending mathematical morphology to colour images [3], with two main contributions. On the one hand, we have studied different alternatives to introduce the scalar part in order to obtain full colour quaternions. On the other hand, several lexicographic total orderings for quaternions based on their various decompositions have been defined.

Paper Organization. The paper's body is organized into four major sections. Section 2 introduces the notion of morphological complex image and two total orderings for complex images. Once a total ordering is defined, a pair of dilation/erosion can be defined; the fundamental properties that any complex dilation/erosion should verify are also considered in this section. The next step, in Sect. 3, is to study the most useful complex dilations and erosions, according to the operator chosen to define the complex part of the image. The geometric interpretation of the corresponding operators as well as their mathematical properties are considered in detail. Section 4 deals with the multi-operator case by means of real quaternions. The proposed hypercomplex mathematical morphology framework is a generalization of the complex formulation; but the specificity of quaternion representations allows us to introduce other useful total orderings. The examples and applications discussed in Sect. 5 will justify the interest of the present operators and their performance in comparison with the standard ones. Finally, the conclusion and perspectives of Sect. 6 close the paper.

A short version of this paper has been published in [2].

2 Complex Representation and Associated Total Orderings

The aim of this section is to introduce the notion of morphological complex image as well as two total orderings for complex spaces. The properties of the general complex dilation/erosion using these total orderings are also discussed.

2.1 Morphological Complex Image

Let $\psi : \mathcal{T} \to \mathcal{T}$ be a morphological operator for scalar images. We need to recall a few notions which characterize the properties of morphological operators. ψ is increasing if $\forall f, g \in \mathcal{F}(E, \mathcal{T})$, $f \leq g \Rightarrow \psi(f) \leq \psi(g)$. It is anti-extensive if $\psi(f) \leq f$ and it is extensive if $f \leq \psi(f)$. An operator is idempotent if $\psi(\psi(f)) = \psi(f)$.

The transformation ψ is applied to $f(\mathbf{x}) \in \mathcal{F}(E, \mathcal{T})$ according to the shape and size associated to the structuring element B and it is denoted as $\psi_B(f)(\mathbf{x})$. We may now define the following mapping from the scalar image to the ψ-complex image:

$$f(\mathbf{x}) \mapsto \mathbf{f}_C(\mathbf{x}) = f(\mathbf{x}) + i\psi_B(f)(\mathbf{x}), \tag{1}$$

with $\mathbf{f}_C \in \mathcal{F}(E, \mathcal{T} \times i\mathcal{T})$. The data of the bivalued image are discrete complex numbers: $\mathbf{f}_C(\mathbf{x}) = \mathbf{c}_n = a_n + b_n i$, where a_n and b_n are respectively the real and the imaginary part of the complex of index n in the finite space $\mathcal{T} \times i\mathcal{T} \subset \mathbb{C}$. Let us consider the polar representation, i.e., $\mathbf{c}_n = \rho_n \exp(i\theta_n)$, where the modulus is given by

$$\rho_n = |\mathbf{c}_n| = \sqrt{a_n^2 + b_n^2}$$

and the phase is computed as

$$\theta_n = \arg(\mathbf{c}_n) = \operatorname{atan2}(b_n, a_n) = \operatorname{sign}(b_n) \operatorname{atan}(|b_n|/a_n),$$

with $\operatorname{atan2}(\cdot) \in (-\pi, \pi]$. The phase can be mapped to $[0, 2\pi)$ by adding 2π to negative values. We notice that $\operatorname{atan2}(a, a) = \pi/4$ for $a \neq 0$ but $\operatorname{atan2}(0, 0) = 0$. To avoid this discontinuity, we have excluded the grey-level $t = 0$.

2.2 Total Orderings for Complex Images

Working in the polar representation, two alternative total orderings based on lexicographic cascades can be defined for complex numbers:

$$\mathbf{c}_n \leq_{\Omega_1^{\theta_0}} \mathbf{c}_m \quad \Leftrightarrow \quad \begin{cases} \rho_n < \rho_m \text{ or} \\ \rho_n = \rho_m \text{ and } \theta_n \preceq_{\theta_0} \theta_m \end{cases} \tag{2}$$

and

$$\mathbf{c}_n \leq_{\Omega_2^{\theta_0}} \mathbf{c}_m \quad \Leftrightarrow \quad \begin{cases} \theta_n \prec_{\theta_0} \theta_m \text{ or} \\ \theta_n =_{\theta_0} \theta_m \text{ and } \rho_n \leq \rho_m \end{cases} \tag{3}$$

where $\preceq_{\theta_0}$ depends on the angular difference to a reference angle θ_0 on the unit circle, i.e.,

$$\theta_n \preceq_{\theta_0} \theta_m \quad \Leftrightarrow \quad \begin{cases} (\theta_n \div \theta_0) > (\theta_m \div \theta_0) \text{ or} \\ (\theta_n \div \theta_0) = (\theta_m \div \theta_0) \text{ and } \theta_n \leq \theta_m \end{cases} \tag{4}$$

such that

$$\theta_p \div \theta_q = \begin{cases} |\theta_p - \theta_q| & \text{if } |\theta_p - \theta_q| \leq \pi \\ 2\pi - |\theta_p - \theta_q| & \text{if } |\theta_p - \theta_q| > \pi. \end{cases} \tag{5}$$

These total orderings can be easily interpreted. In $\leq_{\Omega_1^{\theta_0}}$, priority is given to the modulus, in the sense that a complex is greater than another if its modulus is greater, and if both have the same modulus the greater value is the one whose phase is closer to the reference θ_0. In case of equal phase angular distances, the last condition for a total ordering is based on the absolute distance to the phase origin θ_0. The ordering $\leq_{\Omega_2^{\theta_0}}$ uses the same priority conditions, but they are reversed. Furthermore, by the equivalence of norms, we can state that $\rho_n \leq \rho_m \Leftrightarrow |a_n| + |b_n| \leq |a_m| + |b_m|$.

Given now a set $Z \subset E$ of pixels of the initial image $[f(\mathbf{z})]_{\mathbf{z}\in Z}$, the basic idea behind our approach is to use, for instance $\leq_{\Omega_1^{\theta_0}}$, for ordering the set Z of initial pixels. Formally, we have

$$\mathbf{f}_C(\mathbf{y}) \leq_{\Omega_1^{\theta_0}} \mathbf{f}_C(\mathbf{z}) \quad \Longrightarrow \quad f(\mathbf{y}) \preccurlyeq_{\Omega_1^{\theta_0}} f(\mathbf{z}),$$

where the *indirect total ordering* $\preccurlyeq_{\Omega_1^{\theta_0}}$ allows to compute the supremum $\widetilde{\bigvee}_{\Omega_1^{\theta_0}}$ and the infimum $\widetilde{\bigwedge}_{\Omega_1^{\theta_0}}$ in the original scalar-valued image, i.e.,

$$\mathbf{f}_C(\mathbf{y}) = \bigvee_{\Omega_1^{\theta_0}, \mathbf{z}\in Z} [\mathbf{f}_C(\mathbf{z})] \quad \Longrightarrow \quad f(\mathbf{y}) = \widetilde{\bigvee_{\Omega_1^{\theta_0}, \mathbf{z}\in Z}} [f(\mathbf{z})].$$

We notice that the complex total orderings are only defined once the transformation ψ_B is totally defined. In addition, we remark that if $\psi_B \equiv \mathrm{Id}$, both total orderings $\leq_{\Omega_1^{\theta_0}}$ and $\leq_{\Omega_2^{\theta_0}}$ bring on the standard grey level morphology, where Id denoted the identity operator mapping and image f onto itself.

The next question to be studied is what kind of morphological operators are useful to build basic operators such as dilations and erosions. But before that, let us study the basic properties of the complex orderings.

2.3 Properties

Adjunction and Duality by Complementation. The theory of adjunctions on complete lattices has played an important role in mathematical morphology [20, 43]. More precisely, the notion of adjunction links two operators (ε, δ), in such a way that for any given dilation δ, there is a unique erosion ε such that (ε, δ) is an adjunction [23]. Moreover, the two products of the dilation and its adjunct erosion leads to a pair of morphological closing and opening [38]. The notion of adjunction will be enlightened below, by its use for the complex operators introduced in this paper.

Given the total ordering $\leq_\Omega$, the operator ε between the complete lattice $\mathcal{T}$ and itself is an *erosion* if

$$\varepsilon\Big(\bigwedge_{\Omega, k\in I} [f(\mathbf{x}_k)]\Big) = \bigwedge_{\Omega, k\in I} \varepsilon\big([f(\mathbf{x}_k)]\big), \quad \forall f \in \mathcal{F}(E, \mathcal{T}).$$

A similar dual definition holds for *dilation* δ (i.e., commutation with the supremum):

$$\delta\Big(\bigvee_{\Omega, k\in I} [f(\mathbf{x}_k)]\Big) = \bigvee_{\Omega, k\in I} \delta\big([f(\mathbf{x}_k)]\big), \quad \forall f \in \mathcal{F}(E, \mathcal{T}).$$

The pair (ε, δ) is called an *adjunction* between $\mathcal{T} \to \mathcal{T}$ iff

$$\delta(f)(\mathbf{x}) \leq_\Omega g(\mathbf{x}) \quad \Leftrightarrow \quad f(\mathbf{x}) \leq_\Omega \varepsilon(g)(\mathbf{x}).$$

Refer to [43] or [23] for general proofs. If we have an adjunction for the ordering $\leq_\Omega$, the products of (ε, δ) such as the opening $\gamma = \delta\varepsilon$ and the closing $\varphi = \varepsilon\delta$ can be defined in a standard way. Hence, it is important from a theoretical viewpoint that the proposed complex erosions/dilations verifies the property of adjunction.

One of the most interesting properties of standard grey-level morphological operators is the duality by the complementation $\complement$. The *complement image* (or negative image) $\complement f$ is defined as the reflection of f with respect to $(t_{\min} + t_{\max})/2$ (in our case $t_{\min} = 1$); i.e.,

$$\complement f(\mathbf{x}) = t_{\max} - f(\mathbf{x}) + 1 = f^c(\mathbf{x}), \quad \forall \mathbf{x} \in E.$$

Let the pair (ε, δ) be an adjunction, the property of *duality* holds that [42]:

$$\varepsilon\big(f^c\big) = \big(\delta(f)\big)^c \quad \Longrightarrow \quad \varepsilon(f) = \big(\delta\big(f^c\big)\big)^c,$$

and this is verified for any other pair of dual operators, such as the opening/closing. In practice, this property allows us to implement exclusively the dilation, and using the complement, to be able to obtain the corresponding erosion. In our case, we have the following mapping:

$$f \mapsto \complement f \quad \Longrightarrow \quad \mathbf{f}_C \mapsto \tilde{\mathbf{f}}_C = \complement f + i\psi_B(\complement f) = \complement f + i\complement\xi_B(f)$$

where $\xi_B(f) = \complement\psi_B(\complement f)$ is the *dual operator* of ψ_B. Note that this result is different from the complement of the ψ-complex image, i.e., $\complement\mathbf{f}_C = \complement f + i\complement\psi_B(f)$.

Ordering Invariance and Commutation Under Anamorphosis. The concepts of ordering invariance and commutation of sup and inf operators under intensity image transformations is also important in the theory of complete lattices [30, 44]. More precisely, in mathematical morphology a mapping $A : \mathcal{T} \to \mathcal{T}$ which satisfies the criterion

$$t \leq_\Omega s \quad \Leftrightarrow \quad A(t) \leq_\Omega A(s), \quad \forall t, s \in \mathcal{T},$$

is called an *anamorphosis* for $\leq_\Omega$. Then, we say that the total ordering $\leq_\Omega$ is invariant under A. Any increasing morphological operator ψ commutes with any anamorphosis, i.e., $\psi(A(f)) = A(\psi(f))$. It is well known for the grey-tone case that any strictly increasing mapping A is an anamorphosis.

A typical example is the following truncated linear transformation:

$$A(t) = \begin{cases} K(t) & \text{if } 1 \leq K(t) \leq t_{\max} \\ 1 & \text{if } K(t) < 1 \\ t_{\max} & \text{if } K(t) > t_{\max} \end{cases}$$

where $K(t) = \alpha t + \beta$, with $\alpha \geq 0$. We notice that the interval of variation of intensities should be preserved in order to remain in the corresponding complex plane quadrant.

In our case, we have for the ψ-complex image:

$$f \mapsto f' = A(f) \quad \Longrightarrow \quad \mathbf{f}_C \mapsto \mathbf{f}'_C = A(f) + i\psi_B\big(A(f)\big) = A(f) + iA\big(\psi_B(f)\big),$$

i.e., both axes of complex plane are equivariant modified according to the same mapping (scaled and shifted for the example of the linear transformation). Obviously, the partial ordering according to the modulus is invariant under A. The partial ordering with respect to the phase is also invariant if θ is defined in the first quadrant. Hence, the orderings $\leq_{\Omega_1^{\theta_0}}$ and $\leq_{\Omega_2^{\theta_0}}$ commutes with anamorphosis applied on the scalar function f.

3 Complex Dilations and Erosions

We study in this section the operators ψ_B which are useful to define the complex part of morphological representations and the corresponding complex operators.

3.1 γ-Complex Dilations and φ-Complex Erosions

Opening and Closing. A morphological filter is an increasing operator that is also idempotent (i.e., erosion and dilation are not idempotent). The two basic morphological filters, as products of erosions/dilations, are the opening $\gamma_B(f) = \delta_B(\varepsilon_B(f))$ and the closing $\varphi_B(f) = \varepsilon_B(\delta_B(f))$. Besides the idempotence, the opening (closing) is an anti-extensive (extensive) operator; i.e., $f \geq \gamma_B(f)$ and $f \leq \varphi_B(f)$.

In order to grasp the nature of opening/closing-complex operators, and to make preparations for later arguments as well, let us review some fundamental expressions concerning the opening/closing. Let $B(\mathbf{x})$ represent the structuring element centered at point $\mathbf{x}$, the opening and the closing for binary (or set) images, i.e., $f_b : E \to \mathcal{P}(E)$ such that $f_b(\mathbf{x}) = \bigcup\{\{\mathbf{x}\} | \{\mathbf{x}\} \subseteq f_b\}$, can be analytically formulated as [43]:

$$\gamma_B(f_b) = \bigcup\big\{B(\mathbf{x}) \mid B(\mathbf{x}) \subseteq f_b\big\},$$

$$\varphi_B(f_b) = \bigcup\Big\{\mathbf{x} \mid B(\mathbf{x}) \subseteq \bigcup\big[B(\mathbf{x}) \mid \mathbf{x} \in f_b\big]\Big\}.$$

The geometrical meaning of the binary opening is clear: $\gamma_B(f_b)$ is the region of the space swept by all structuring sets $B(\mathbf{x})$ that are included in f_b. Or in other words, the union of the points of f_b which are invariant to the structuring element B. The dual interpretation for the complement of f_b is valid for the closing $\varphi_B(f_b)$.

To extend this interpretation to grey-level images, let us introduce the following pulse function $i_{\mathbf{x},t}$ of level t at point $\mathbf{x}$ [23]:

$$i_{\mathbf{x},t}(\mathbf{x}) = t \quad \text{when } \mathbf{y} = \mathbf{x};$$

$$i_{\mathbf{x},t}(\mathbf{y}) = 0 \quad \text{when } \mathbf{y} \neq \mathbf{x}.$$

Image f can be decomposed into the supremum of its pulses, i.e., $f = \bigvee\{i_{\mathbf{x},f(\mathbf{x})},\ \mathbf{x} \in E\}$. Dilating $i_{t,\mathbf{x}}$ by the structuring element B results in the cylinder $C_{B(\mathbf{x}),t}$ of base $B(\mathbf{x})$ and height t. Now, it is possible to write the opening for a grey-level image as follows [54]:

$$\gamma_B(f) = \bigvee\{C_{B(\mathbf{x}),t} \leq f,\ \mathbf{x} \in E\}.$$

In the product space $E \times \mathcal{T}$ the subgraph of the opening $\gamma_B(f)$ is generated by the zone swept by all cylinders $C_{B(\mathbf{x}),t}$ smaller than f. Since, the opening is an operator which removes bright structures and peaks of intensity that are thinner than the structuring element B, the structures

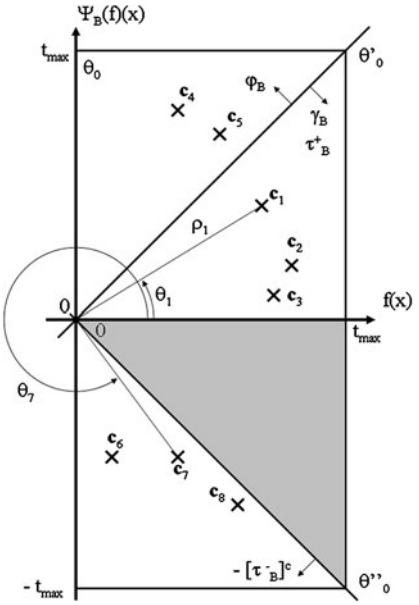

Fig. 1 Complex plane for points $\in f(\mathbf{x}) + i\psi_B(f)(\mathbf{x})$ (see the text for the various cases)

larger than B preserve their intensity values. In the standard case of translation invariance, the closing is obtained as $\varphi_B(f) = (\gamma_B(f^c))^c$, and a dual analysis is valid, i.e., the closing removes the dark structures and valleys of intensity.

Preliminary Geometrical Analysis. Therefore, by their simplicity and easy interpretation, the opening and closing seem particularly appropriate to build the ψ-complex image.

Let us use the diagram depicted in Fig. 1 for illustrating how the complex values are ordered. If we consider for instance $\psi_B \equiv \gamma_B$ and $\Omega_1^{\theta_0}$, the pixels in structures invariant according to B have module values which are greater than pixels having the same initial grey value but belonging to structures that do not match B. In the diagram, $\mathbf{c}_1$ is greater than $\mathbf{c}_3$, but for $\mathbf{c}_1$ and $\mathbf{c}_2$ which have the same modulus, a reference θ_0 is needed. By the anti-extensivity, we have $f(\mathbf{x}) \geq \gamma_B(f)(\mathbf{x})$ and hence $0 \leq \theta \leq \pi/4$. By taking $\theta_0 = \pi/2$, we consider that, with equal modulus, a point is greater than another if the intensities before and after the opening are more similar (i.e., more invariant). In other words, when the ratio $\gamma_B(f)(\mathbf{x})/f(\mathbf{x})$ is closer to 1 or θ is closer to $\pi/4$, and consequently to $\pi/2$ (the last choice is justified by the needed symmetry with the closing, see below). This implies that the opening is an appropriate transformation to define a dilation which propagate the bright intensities associated in priority to B-invariant structures. If we choose $\Omega_2^{\theta_0}$, with $\theta_0 = \pi/2$, the same conditions of ordering are used, but starting with the pre-order associated to the angular distance to $\pi/2$, and considering the value of intensity represented by the modulus only where the angular distances are equal.

The same analysis leads to justify the choice of $\psi_B \equiv \varphi_B$ and $\Omega_{1,2}^{\pi/2}$ for the complex erosion. Note that now $\varphi_B(f)(\mathbf{x})/f(\mathbf{x}) \geq 1 \Rightarrow \pi/4 \leq \theta \leq \pi/2$. A pixel is lesser than another is its modulus is lesser; by taking the reference $\theta_0 = \pi/2$, the idea of intensities invariance before and after the closing is again used, in the ordering by θ, for considering now that a point is lesser than another if both have the same modulus and the first is farther from $\theta_0 = \pi/2$ (closer to $\pi/4$) than the second (in the example of Fig. 1, $\mathbf{c}_5$ is lesser than $\mathbf{c}_4$). Figure 2 depicts a full example of γ, φ-complex representation of a noisy grey-scale image.

Formal Definitions. The previous analysis motivates us to define mathematically the basic complex operators as follows.

Definition 1 The $(\Omega_1^{\pi/2}, \gamma)$-complex dilation is defined by

$$\begin{cases} \mathbf{f}_C(\mathbf{x}) = f(\mathbf{x}) + i\gamma_{B_C}(f)(\mathbf{x}), \\ \delta_{\langle 1,\gamma_{B_C},B\rangle}(f)(\mathbf{x}) \\ \quad = \{f(\mathbf{y}) : \mathbf{f}_C(\mathbf{y}) = \bigvee_{\Omega_1^{\pi/2}}[\mathbf{f}_C(\mathbf{z})],\ \mathbf{z} \in B(\mathbf{x}))\} \end{cases} \tag{6}$$

and the dual $(\Omega_1^{\pi/2}, \varphi)$-complex erosion is formulated as follows:

$$\begin{cases} \mathbf{f}_C(\mathbf{x}) = f(\mathbf{x}) + i\varphi_{B_C}(f)(\mathbf{x}), \\ \varepsilon_{\langle 1,\varphi_{B_C},B\rangle}(f)(\mathbf{x}) \\ \quad = \{f(\mathbf{y}) : \mathbf{f}_C(\mathbf{y}) = \bigwedge_{\Omega_1^{\pi/2}}[\mathbf{f}_C(\mathbf{z})],\ \mathbf{z} \in B(\mathbf{x}))\}. \end{cases} \tag{7}$$

Definition 2 The equivalent $(\Omega_2^{\pi/2}, \gamma)$-complex dilation and $(\Omega_2^{\pi/2}, \varphi)$-complex erosion are respectively

$$\delta_{\langle 2,\gamma_{B_C},B\rangle}(f)(\mathbf{x}) = \left\{ f(\mathbf{y}) : \mathbf{f}_C(\mathbf{y}) = \bigvee_{\Omega_2^{\pi/2}} \left[\mathbf{f}_C(\mathbf{z})\right],\ \mathbf{z} \in B(\mathbf{x}) \right\}, \tag{8}$$

and

$$\varepsilon_{\langle 2,\varphi_{B_C},B\rangle}(f)(\mathbf{x}) = \left\{ f(\mathbf{y}) : \mathbf{f}_C(\mathbf{y}) = \bigwedge_{\Omega_2^{\pi/2}} \left[\mathbf{f}_C(\mathbf{z})\right],\ \mathbf{z} \in B(\mathbf{x}) \right\}, \tag{9}$$

where the complex part of the image $\mathbf{f}_C(\mathbf{x})$ is again an opening for the dilation and a closing for the erosion.

Hence, complex operators requires two independent structuring elements:

- B_C associated to the transformation of the imaginary part;
- B which is properly the structuring element of the complex transformation.

Obviously, B_C and B can have different size and shape.

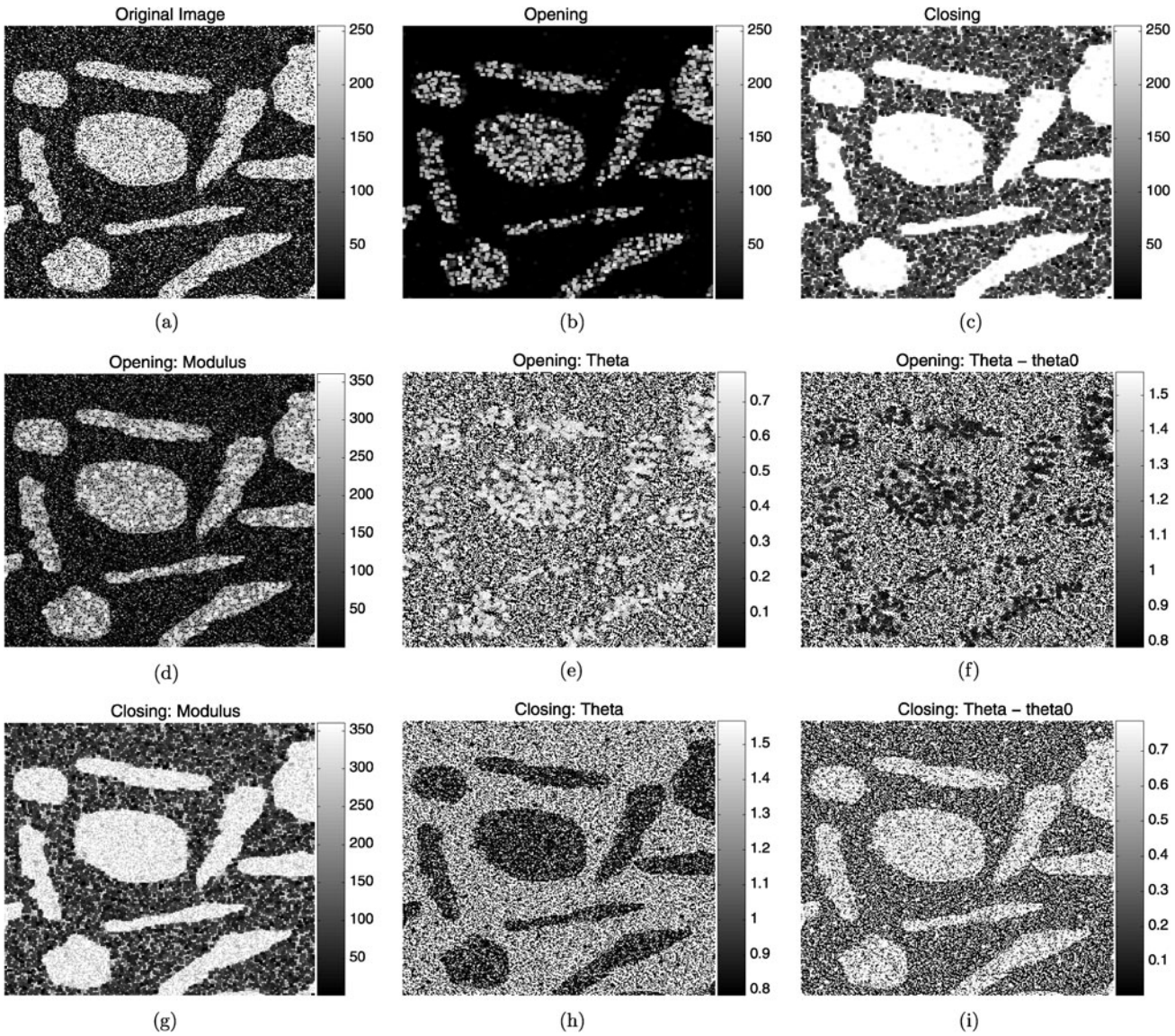

Fig. 2 γ, φ-complex representation of a noisy grey-scale image: (**a**) original image $f(\mathbf{x})$, (**b**) opening $\gamma_B(f)(\mathbf{x})$, (**c**) closing $\varphi_B(f)(\mathbf{x})$, (**d**) modulus image $\rho(\mathbf{x})$ from complex image $f(\mathbf{x}) + i\gamma_B(f)(\mathbf{x})$, (**e**) phase image $\theta(\mathbf{x})$ from complex image $f(\mathbf{x}) + i\gamma_B(f)(\mathbf{x})$, (**f**) angular distance image $\theta(\mathbf{x}) \div \pi/2$ from complex image $f(\mathbf{x}) + i\gamma_B(f)(\mathbf{x})$, (**g**) modulus image $\rho(\mathbf{x})$ from complex image $f(\mathbf{x}) + i\varphi_B(f)(\mathbf{x})$, (**h**) phase image $\theta(\mathbf{x})$ from complex image $f(\mathbf{x}) + i\varphi_B(f)(\mathbf{x})$, (**i**) angular distance image $\theta(\mathbf{x}) \div \pi/2$ from complex image $f(\mathbf{x}) + i\varphi_B(f)(\mathbf{x})$. For the opening and closing B is a square of size 3 pixels

Properties We can now study the properties of these operators.

Proposition 3 *The pair* $(\delta_{\langle 1,\gamma_{B_C},B\rangle}, \varepsilon_{\langle 1,\varphi_{B_C},B\rangle})$ *is an adjunction, i.e.,*

$$\delta_{\langle 1,\gamma_{B_C},B\rangle}(f)(\mathbf{x}) \preccurlyeq_{\Omega_1^{\pi/2}} g(\mathbf{x}) \quad \Leftrightarrow \quad f(\mathbf{x}) \preccurlyeq_{\Omega_1^{\pi/2}} \varepsilon_{\langle 1,\varphi_{B_C},B\rangle}(g)(\mathbf{x}),$$

$\forall f, g \in \mathcal{F}(E,\mathcal{T})$. *Similarly, the pair* $(\delta_{\langle 2,\gamma_{B_C},B\rangle}, \varepsilon_{\langle 2,\varphi_{B_C},B\rangle})$ *is also an adjunction.*

Proof We consider the values of points $\mathbf{z} \in B(\mathbf{x})$, and we have $\bigvee_{\Omega_1^{\pi/2}}[\mathbf{f}_C(\mathbf{z})] \leq_{\Omega_1^{\pi/2}} \mathbf{g}_C(\mathbf{x}) \Leftrightarrow \bigvee_{\Omega_1^{\pi/2}}[f(\mathbf{z}) + i\gamma_{B_C}(f)(\mathbf{z})] \leq_{\Omega_1^{\pi/2}} g(\mathbf{x}) + i\gamma_{B_C}(g)(\mathbf{x}) \Leftrightarrow f(\mathbf{x}) + i\gamma_{B_C}(f)(\mathbf{x}) \leq_{\Omega_1^{\pi/2}} g(\mathbf{x}) + i\gamma_{B_C}(g)(\mathbf{x})$. This is true because if the inequality is true for the biggest point, it is also true for any point $\mathbf{z}$, including the center $\mathbf{x}$. In addition, due to the fact that $\varphi_{B_C}(f)(\mathbf{x}) \geq f(\mathbf{x}) \geq \gamma_{B_C}(f)(\mathbf{x})$, we have $g(\mathbf{x}) + i\gamma_{B_C}(g)(\mathbf{x}) \leq_{\Omega_1^{\pi/2}} g(\mathbf{x}) + i\varphi_{B_C}(g)(\mathbf{x})$, and hence, $f(\mathbf{x}) + i\gamma_{B_C}(f)(\mathbf{x}) \leq_{\Omega_1^{\pi/2}} g(\mathbf{x}) + i\varphi_{B_C}(g)(\mathbf{x})$.

Note that when the equality holds, $\varphi_{B_C}(f)(\mathbf{x}) = f(\mathbf{x}) = \gamma_{B_C}(f)(\mathbf{x})$, the complex values are in the main diagonal,

and consequently the phase θ is equal to $\pi/4$ for $f(\mathbf{x}) + i\gamma_{B_C}(f)(\mathbf{x})$ and $f(\mathbf{x}) + i\varphi_{B_C}(f)(\mathbf{x})$, having also the same distance to $\pi/2$ and hence we obtain

$$g(\mathbf{x}) + i\gamma_{B_C}(g)(\mathbf{x}) = g(\mathbf{x}) + i\varphi_{B_C}(g)(\mathbf{x}).$$

On the other hand, we have $f(\mathbf{x}) + i\varphi_{B_C}(f)(\mathbf{x}) \leq_{\Omega_1^{\pi/2}} \bigwedge_{\Omega_1^{\pi/2}}[g(\mathbf{z}) + i\varphi_{B_C}(g)(\mathbf{z})] \Leftrightarrow f(\mathbf{x}) + i\gamma_{B_C}(f)(\mathbf{x}) \leq_{\Omega_1^{\pi/2}} f(\mathbf{x}) + i\varphi_{B_C}(f)(\mathbf{x}) \leq_{\Omega_1^{\pi/2}} g(\mathbf{x}) + i\varphi_{B_C}(g)(\mathbf{x})$. So the two inequalities are equivalent and consequently, we establish that

$$\bigvee_{\Omega_1^{\pi/2}} \big[\mathbf{f}_C(\mathbf{z})\big] \leq_{\Omega_1^{\pi/2}} \mathbf{g}_C(\mathbf{x}) \quad \Leftrightarrow \quad \mathbf{f}_C(\mathbf{x}) \leq_{\Omega_1^{\pi/2}} \bigwedge_{\Omega_1^{\pi/2}} \big[\mathbf{g}_C(\mathbf{z})\big].$$

Because

$$\frac{\varphi_{B_C}(f)(\mathbf{x})}{f(\mathbf{x})} \geq 1 \geq \frac{\gamma_{B_C}(f)(\mathbf{x})}{f(\mathbf{x})},$$

we have

$$\begin{aligned}\operatorname{atan2}\big(\varphi_{B_C}(f)(\mathbf{x}), f(\mathbf{x})\big) &\geq \pi/4 \\ &\geq \operatorname{atan2}\big(\gamma_{B_C}(f)(\mathbf{x}), f(\mathbf{x})\big)\end{aligned}$$

and as we fixed $\theta_0 = \pi/2$, the angular distance for the closing is always closer to $\pi/2$ than for the opening, hence is also verified that $f(\mathbf{x}) + i\gamma_{B_C}(f)(\mathbf{x}) <_{\Omega_2^{\pi/2}} f(\mathbf{x}) + i\varphi_{B_C}(g)(\mathbf{x})$.

Consequently, as well as for the previous case of $\Omega_1^{\pi/2}$, we establish that

$$\bigvee_{\Omega_2^{\pi/2}} \big[\mathbf{f}_C(\mathbf{z})\big] \leq_{\Omega_2^{\pi/2}} \mathbf{g}_C(\mathbf{x}) \quad \Leftrightarrow \quad \mathbf{f}_C(\mathbf{x}) \leq_{\Omega_2^{\pi/2}} \bigwedge_{\Omega_2^{\pi/2}} \big[\mathbf{g}_C(\mathbf{z})\big].$$

□

Proposition 4 *The two pairs of γ-complex dilation and φ-complex erosion are dual operators, i.e.,*

$$\delta_{\langle 1,\gamma_{B_C},B\rangle}(f) = \big[\varepsilon_{\langle 1,\varphi_{B_C},B\rangle}\big(f^c\big)\big]^c;$$
$$\delta_{\langle 2,\gamma_{B_C},B\rangle}(f) = \big[\varepsilon_{\langle 2,\varphi_{B_C},B\rangle}\big(f^c\big)\big]^c.$$

Proof If we apply the dilation to the complemented original image, we have

$$\begin{aligned}&\bigvee_{\Omega_1^{\pi/2}} \big[f^c(\mathbf{z}) + i\gamma_{B_C}\big(f^c\big)(\mathbf{z})\big] \\ &= \bigvee_{\Omega_1^{\pi/2}} \big[f^c(\mathbf{z}) + i\varphi^c_{B_C}(f)(\mathbf{z})\big] \\ &= \Big[\bigwedge_{\Omega_1^{\pi/2}} \big[f^c(\mathbf{z}) + i\varphi^c_{B_C}(f)(\mathbf{z})\big]^c\Big]^c \\ &= \Big[\bigwedge_{\Omega_1^{\pi/2}} \big[f(\mathbf{z}) + i\varphi_{B_C}(f)(\mathbf{z})\big]\Big]^c, \quad \mathbf{z} \in B(\mathbf{x}).\end{aligned}$$

The proof is also valid for $\Omega_2^{\pi/2}$. □

It should be remarked that the dilation is extensive according to the orderings $\Omega_{1:2}^{\pi/2}$:

$$f(\mathbf{x}) \preccurlyeq_{\Omega_{1:2}^{\pi/2}} \delta_{\langle 1:2,\gamma_{B_C},B\rangle}(f)(\mathbf{x}),$$

but not necessarily according to the standard ordering: $f(\mathbf{x}) \not\leq \delta_{\langle\gamma_{1:2,B_C},B\rangle}(f)(\mathbf{x})$. If this last property is required for any reason, we can define the *γ-complex upper dilation* as:

$$\widehat{\delta}_{\langle 1:2,\gamma_{B_C},B\rangle}(f)(\mathbf{x}) = \delta_{\langle 1:2,\gamma_{B_C},B\rangle}(f)(\mathbf{x}) \vee f(\mathbf{x}).$$

Using the standard infimum $\wedge$, the dual definition leads to the *φ-complex lower erosion* $\widehat{\varepsilon}_{\langle\phi_{B_C},B\rangle}(f)(\mathbf{x})$, which is anti-extensive according to the grey level ordering.

Products of Complex Dilation and Erosion. Because they constitute an adjunction, the pairs of γ-complex dilation and the φ-complex erosion can be combined to construct evolved complex operators such as the *γ, φ-complex openings*

$$\gamma_{\langle 1:2,\{\varphi_{B_C},\gamma_{B_C}\},B\rangle}(f) = \delta_{\langle 1:2,\gamma_{B_C},B\rangle}\big(\varepsilon_{\langle 1:2,\varphi_{B_C},B\rangle}(f)\big); \quad (10)$$

and the *γ, φ-complex closings*

$$\varphi_{\langle 1:2,\{\gamma_{B_C},\varphi_{B_C}\},B\rangle}(f) = \varepsilon_{\langle 1:2,\varphi_{B_C},B\rangle}\big(\delta_{\langle 1:2,\gamma_{B_C},B\rangle}(f)\big); \quad (11)$$

as well as complex gradients and even complex geodesic operators (e.g., opening by reconstruction, leveling, etc.) by replacing the standard dilation/erosion by the complex counterparts. Figure 3 gives a comparative example of the $(\Omega_{1:2}^{\pi/2}, \gamma)$, $(\Omega_{1:2}^{\pi/2}, \varphi)$-complex dilation, erosion, opening and closing with respect to the standard operators. More advanced examples and applications are given in Sect. 5.

Instead of a morphological opening/closing for the γ-complex dilation and the φ-complex erosion, any other pair of anti-extensive/extensive dual transformations can play a similar role, as it is illustrated just below. In ongoing research it should be also studied the interest of self-dual operators, as the Gaussian filters, for defining Gaussian-complex dilation/erosion. We can also suppose that the $\gamma\phi\gamma$-complex dilation and $\phi\gamma\phi$-complex erosion can have interesting regularization properties (note that these operators are ordered between then, i.e., $\phi\gamma\phi(f) \geq \gamma\phi\gamma(f)$, but not with respect to the scalar part f and in addition there are not dual).

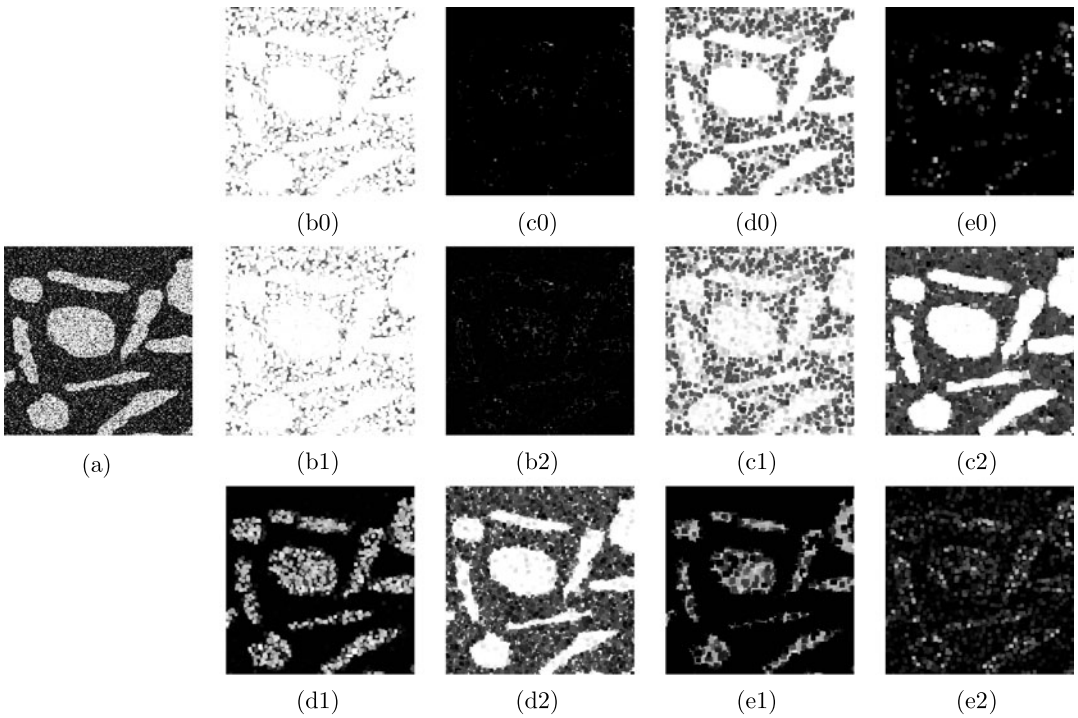

Fig. 3 Comparison of γ, φ-complex basic morphological operators: (**a**) original image $f(\mathbf{x})$, (**b0**) standard dilation $\delta_B(f)$, (**c0**) standard erosion $\varepsilon_B(f)$, (**d0**) standard closing $\varphi_B(f)$, (**e0**) standard opening $\gamma_B(f)$, (**b1**) $\Omega_1^{\pi/2}$-complex dilation $\delta_{\langle 1,\gamma_{B_C},B\rangle}(f)$, (**c1**) $\Omega_1^{\pi/2}$-complex erosion $\varepsilon_{\langle 1,\gamma_{B_C},B\rangle}(f)$, (**d1**) $\Omega_1^{\pi/2}$-complex closing $\varphi_{\langle 1,\{\gamma_{B_C},\varphi_{B_C}\},B\rangle}(f)$, (**e1**) $\Omega_1^{\pi/2}$-complex opening $\gamma_{\langle 1,\{\varphi_{B_C},\gamma_{B_C}\},B\rangle}(f)$, (**b2**) $\delta_{\langle 2,\gamma_{B_C},B\rangle}(f)$, (**c2**) $\varepsilon_{\langle 2,\gamma_{B_C},B\rangle}(f)$, (**d2**) $\varphi_{\langle 2,\{\gamma_{B_C},\varphi_{B_C}\},B\rangle}(f)$, (**e2**) $\gamma_{\langle 2,\{\varphi_{B_C},\gamma_{B_C}\},B\rangle}(f)$. The structuring element of the main operation B is a square of size 5 whereas the structuring element of the complex part operation B_C is a square of size 3

3.2 τ^+-Complex Dilations and $[\tau^-]^c$-Complex Erosions

Let us consider another family of complex dilation/erosion using now the residues of the opening/closing. We remind that the white top-hat τ^+ and the black top-hat τ^- are respectively the residue of the opening and the closing [31], i.e.,

$$\tau_B^+(f)(\mathbf{x}) = f(\mathbf{x}) - \gamma_B(f)(\mathbf{x}) \quad \text{and}$$
$$\tau_B^-(f)(\mathbf{x}) = \varphi_B(f)(\mathbf{x}) - f(\mathbf{x}).$$

The top-hat transformations yield positive grey-level images and are used to extract contrasted components (i.e., structures smaller than the structuring element used for the opening/closing) with respect to the background and removing the slow trends. The top-hat is an idempotent transformation and if $f(\mathbf{x}) \geq 0$ then $\tau^+(f)(\mathbf{x})$ is anti-extensive and $[\tau^-(f)(\mathbf{x})]^c = (t_{\max}+1) - \varphi_B(f)(\mathbf{x}) + f(\mathbf{x})$ is extensive, and in addition $(\tau^+(f), [\tau^-(f)]^c)$ are dual operators, i.e., $[\tau^-(f)]^c = [\tau^+(f^c)]^c$.

This last property of anti-extensivity of top-hat and extensivity of complemented dual top-hat motivates us to propose the following two alternative complex dilations and erosions.

Definition 5 The $(\Omega_{1:2}^{\pi/2}, \tau^+)$-complex dilations (of type 1 and type 2) are defined as

$$\begin{cases} \mathbf{f}_C(\mathbf{x}) = f(\mathbf{x}) + i\tau_{B_C}^+(f)(\mathbf{x}), \\ \delta_{\langle 1:2,\tau_{B_C}^+,B\rangle}(f)(\mathbf{x}) \\ \quad = \{f(\mathbf{y}) : \mathbf{f}_C(\mathbf{y}) = \bigvee_{\Omega_{1:2}^{\pi/2}}[\mathbf{f}_C(\mathbf{z})], \mathbf{z} \in B(\mathbf{x})\} \end{cases} \tag{12}$$

and the associated $(\Omega_{1:2}^{-\pi/2}, [\tau^-]^c)$-complex erosion are given by

$$\begin{cases} \mathbf{f}_C(\mathbf{x}) = f(\mathbf{x}) - i[\tau_{B_C}^-(f)(\mathbf{x})]^c, \\ \varepsilon_{\langle 1:2,[\tau_{B_C}^-]^c,B\rangle}(f)(\mathbf{x}) \\ \quad = \{f(\mathbf{y}) : \mathbf{f}_C(\mathbf{y}) = \bigwedge_{\Omega_{1:2}^{-\pi/2}}[\mathbf{f}_C(\mathbf{z})], \mathbf{z} \in B(\mathbf{x})\}. \end{cases} \tag{13}$$

We must remark that for the $[\tau^-]^c$-erosion $\mathbf{f}_C \in \mathcal{F}(E, \mathcal{T} \times -i\mathcal{T})$. We can use again the diagram of Fig. 1 to interpret these operators.

By using the ordering $\Omega_2^{\theta_0}$, the supremum in the $\tau_{B_C}^+$-dilation favours the complex points closer to $\pi/2$ (in fact, to $\pi/4$, and by the extensivity, also to $\pi/2$) which correspond to those where the initial intensity is more similar to the intensity of the top-hat (the point $\mathbf{c}_1$ is greater than the points $\mathbf{c}_2$ and $\mathbf{c}_3$); or in other words,

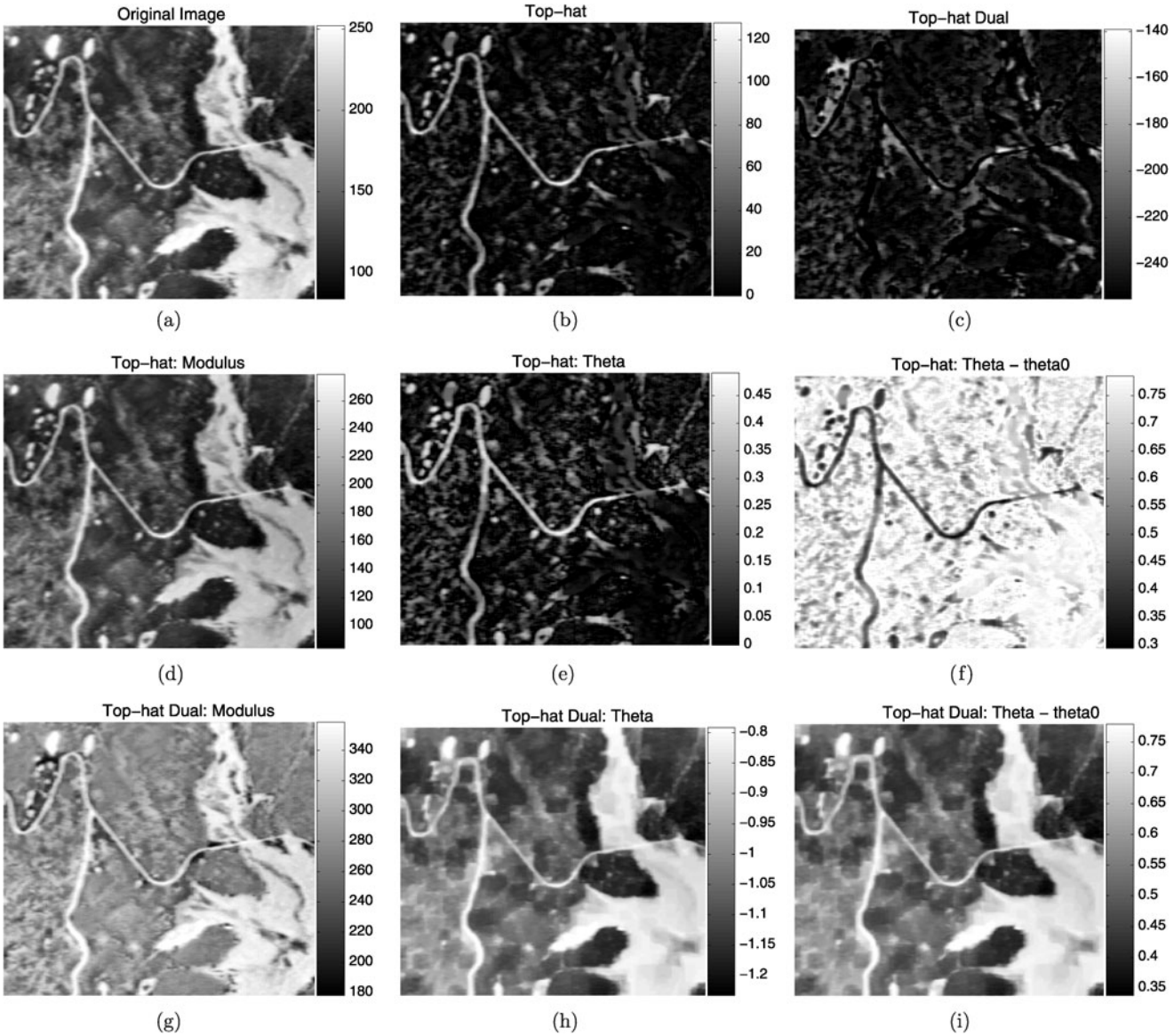

Fig. 4 $\tau^+, [\tau^-]^c$-complex representation of a grey-scale image: (**a**) original image $f(\mathbf{x})$, (**b**) white top-hat $\tau_B^+(f)(\mathbf{x})$, (**c**) black top-hat $\tau_B^-(f)(\mathbf{x})$, (**d**) modulus image $\rho(\mathbf{x})$ from complex image $f(\mathbf{x}) + i\tau_B^+(f)(\mathbf{x})$, (**e**) phase image $\theta(\mathbf{x})$ from complex image $f(\mathbf{x}) + i\tau_B^+(f)(\mathbf{x})$, (**f**) angular distance image $\theta(\mathbf{x}) \div \pi/2$ from complex image $f(\mathbf{x}) + i\tau_B^+(f)(\mathbf{x})$, (**g**) modulus image $\rho(\mathbf{x})$ from complex image $f(\mathbf{x}) - i[\tau^-]^c(f)(\mathbf{x})$, (**h**) phase image $\theta(\mathbf{x})$ from complex image $f(\mathbf{x}) - i[\tau^-]_B^c(f)(\mathbf{x})$, (**i**) angular distance image $\theta(\mathbf{x}) \div -\pi/2$ from complex image $f(\mathbf{x}) + i[\tau^-]_B^c(f)(\mathbf{x})$. For the white top-hat and black top-hat B is a square of size 3 pixels

the points belonging to structures well contrasted with respect to B_C. The interpretation of the modulus is similar, and consequently $\Omega_1^{\theta_0}$ involves that in the supremum the contrasted structured are reinforced. In the case of the erosion, a point is lesser than another if the θ of the first is farthest from $-\pi/2$ (closer to $-\pi/4$) than the θ of the second. Using $\Omega_2^{\theta_0}$, in the diagram, $\mathbf{c}_7$ is lesser than $\mathbf{c}_6$, and $\mathbf{c}_8$ is the lowest between the three (even if $\mathbf{c}_8$ presents the biggest initial intensity). In summary, by means of the τ^+-complex dilation and $[\tau^-]^c$-complex erosion, a mechanism of filtering based on the local contrast of structures is obtained. The complete example given in Fig. 4, which corresponds to an aerial image with well contrasted bright/dark structures, allows to easily interpret the modulus and phase of the complex dilation and erosion.

In fact, it is obvious to see that the proposed $\Omega_{1:2}^{-\pi/2}$ erosions with $\mathbf{f}_C(\mathbf{x}) = f(\mathbf{x}) - i[\tau_{B_C}^-(f)(\mathbf{x})]^c$ is equivalent to an erosion with $\mathbf{f}_C(\mathbf{x}) = f(\mathbf{x}) + i[\tau_{B_C}^-(f)(\mathbf{x})]^c$ but changing the complex orderings to $\Omega_{1:2}^{+\pi/2}$. As a result, the following properties holds (their proofs are similar to the those of the γ, φ-complex operators).

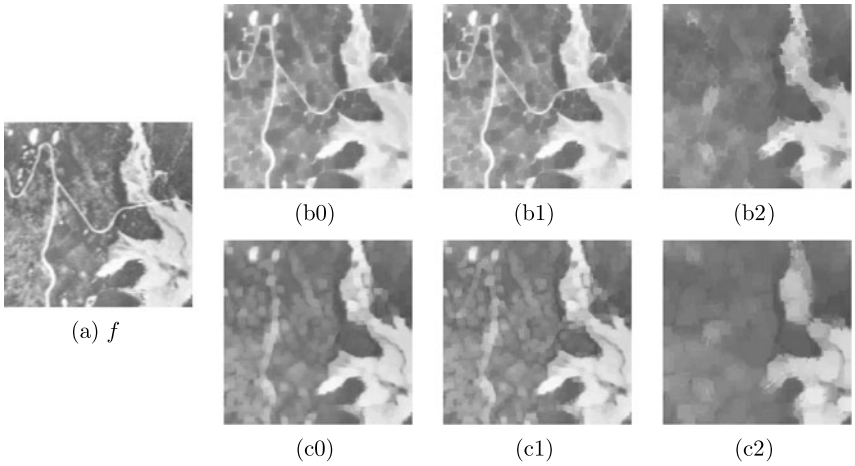

Fig. 5 Comparison of $\tau^+, [\tau^-]^c$-complex openings and closings: (**a**) original image $f(\mathbf{x})$, (**b0**) standard closing $\varphi_B(f)$, (**c0**) standard opening $\gamma_B(f)$, (**b1**) $\Omega_1^{\pi/2,-\pi/2}$-complex closing $\varphi_{\langle 1,\{\tau^+_{B_C},[\tau^-]^c_{B_C}\},B\rangle}(f)$, (**c1**) $\Omega_1^{\pi/2,-\pi/2}$-complex opening $\gamma_{\langle 1,\{[\tau^-]^c_{B_C},\tau^+_{B_C}\},B\rangle}(f)$, (**b2**) $\varphi_{\langle 2,\{\tau^+_{B_C},[\tau^-]^c_{B_C}\},B\rangle}(f)$, (**c2**) $\gamma_{\langle 2,\{[\tau^-]^c_{B_C},\tau^+_{B_C}\},B\rangle}(f)$. The structuring element of the main operation B is a square of size 7 whereas the structuring element of the complex part operation B_C is a square of size 10

Proposition 6 *The pair of* $(\delta_{\langle 1,\tau^+_{B_C},B\rangle}, \varepsilon_{\langle 1,[\tau^-_{B_C}]^c,B\rangle})$ *is an adjunction, i.e.,*

$$\delta_{\langle 1,\tau^+_{B_C},B\rangle}(f)(\mathbf{x}) \preccurlyeq_{\Omega_1^{\pi/2}} g(\mathbf{x})$$
$$\Leftrightarrow \quad f(\mathbf{x}) \preccurlyeq_{\Omega_1^{-\pi/2}} \varepsilon_{\langle 1,[\tau^-_{B_C}]^c,B\rangle}(g)(\mathbf{x}),$$

$\forall f, g \in \mathcal{F}(E,\mathcal{T})$. *Similarly, the pair* $(\delta_{\langle 2,\tau^+_{B_C},B\rangle}, \varepsilon_{\langle 2,[\tau^-_{B_C}]^c,B\rangle})$ *is also an adjunction.*

Proposition 7 *The two pairs of* τ^+*-complex dilation and* $[\tau^-]^c$*-complex erosion are dual operators, i.e.,*

$$\delta_{\langle 1,\tau^+_{B_C},B\rangle}(f) = \left[\varepsilon_{\langle 1,[\tau^-_{B_C}]^c,B\rangle}\left(f^c\right)\right]^c;$$
$$\delta_{\langle 2,\tau^+_{B_C},B\rangle}(f) = \left[\varepsilon_{\langle 2,[\tau^-_{B_C}]^c,B\rangle}\left(f^c\right)\right]^c.$$

Figure 5 provides a comparative example on the aerial image of the complex openings and closings associated to these top-hat-based dilations/erosions.

4 Generalization to Multi-operator Cases Using Real Quaternions

We generalize in this section the ideas introduced above by the extension to image representations based on hypercomplex numbers or real quaternions [19]. Before that, let us remind the foundations of quaternions.

4.1 Remind on Quaternionic Representations

Hypercomplex Representation. A quaternion $\mathbf{q}_n \in \mathbb{H}$ may be represented in hypercomplex form as

$$\mathbf{q}_n = a_n + b_n i + c_n j + d_n k, \tag{14}$$

where a_n, b_n, c_n and d_n are real. A quaternion has a *real part or scalar part*, $S(\mathbf{q}_n) = a_n$, and an *imaginary part or vector part*, $V(\mathbf{q}_n) = b_n i + c_n j + d_n k$, such that the whole quaternion may be represented by the sum of its scalar and vector parts as $\mathbf{q}_n = S(\mathbf{q}_n) + V(\mathbf{q}_n)$. A quaternion with a zero real/scalar part is called a *pure quaternion*.

The addition of two quaternions, $\mathbf{q}_n, \mathbf{q}_m \in \mathbb{H}$, is defined as follows $\mathbf{q}_n + \mathbf{q}_m = (a_n + a_m) + (b_n + b_m)i + (c_n + c_m)j + (d_n + d_m)j$. The addition is commutative and associative. The quaternion result of the *product of two quaternions*, $\mathbf{q}_l = \mathbf{q}_n\mathbf{q}_m = S(\mathbf{q}_l) + V(\mathbf{q}_l)$, can be written in terms of dot product $\cdot$ and cross product $\times$ of vectors as $S(\mathbf{q}_l) = S(\mathbf{q}_n)S(\mathbf{q}_m) - V(\mathbf{q}_n)\cdot V(\mathbf{q}_m)$ and $V(\mathbf{q}_l) = S(\mathbf{q}_n)V(\mathbf{q}_m) + S(\mathbf{q}_m)V(\mathbf{q}_n) + V(\mathbf{q}_n)\times V(\mathbf{q}_m)$. The multiplication of quaternions is not commutative, i.e., $\mathbf{q}_n\mathbf{q}_m \neq \mathbf{q}_m\mathbf{q}_n$; but it is associative.

Polar Representation. Any quaternion may be represented in polar form as

$$\mathbf{q}_n = \rho e^{\xi_n \theta_n}, \tag{15}$$

with

$$\rho_n = \sqrt{a_n^2 + b_n^2 + c_n^2 + d_n^2}, \tag{16}$$

$$\xi_n = \frac{b_n i + c_n j + d_n k}{\sqrt{b_n^2 + c_n^2 + d_n^2}} = \overline{b}_n i + \overline{c}_n j + \overline{d}_n k, \tag{17}$$

$$\theta_n = \arctan\left(\frac{\sqrt{b_n^2 + c_n^2 + d_n^2}}{a_n}\right). \tag{18}$$

A quaternion can be then rewritten in a trigonometric version as $\mathbf{q}_n = \rho_n(\cos\theta_n + \xi_n \sin\theta_n)$. In the polar formulation,

$\rho_n = |\mathbf{q}_n|$ is the modulus of $\mathbf{q}_n$; ξ_n is the pure unitary quaternion associated to $\mathbf{q}_n$ (by the normalization, the pure unitary quaternion discards "intensity" information, but retains orientation information), sometimes called *eigenaxis*; and θ_n is the angle or argument, sometimes called *eigenangle*, between the real part and the 3D imaginary part.

Parallel/Perpendicular Decomposition. It is possible to describe vector decompositions using the product of quaternions. A full quaternion $\mathbf{q}_n$ may be decomposed about a pure unit quaternion, named here "reference" quaternion, $\widehat{\mathbf{p}}_0$ [15, 16]:

$$\mathbf{q}_n = \mathbf{q}_{\perp n} + \mathbf{q}_{\parallel n},$$

the *parallel part* of $\mathbf{q}_n$ according to $\widehat{\mathbf{p}}_0$, also called the *projection part*, is given by $\mathbf{q}_{\parallel n} = S(\mathbf{q}_n) + V_{\parallel}(\mathbf{q}_n)$, and the *perpendicular part*, also named the *rejection part*, is obtained as $\mathbf{q}_{\perp n} = V_{\perp}(\mathbf{q}_n)$ where

$$V_{\parallel}(\mathbf{q}_n) = \frac{1}{2}\big(V(\mathbf{q}_n) - \widehat{\mathbf{p}}_0 V(\mathbf{q}_n)\widehat{\mathbf{p}}_0\big) \tag{19}$$

and

$$V_{\perp}(\mathbf{q}_n) = \frac{1}{2}\big(V(\mathbf{q}_n) + \widehat{\mathbf{p}}_0 V(\mathbf{q}_n)\widehat{\mathbf{p}}_0\big). \tag{20}$$

It should be remarked that the rejection part is a pure quaternion, independent from the scalar part of $\mathbf{q}_n$, but of course, it depends on the reference quaternion $\widehat{\mathbf{p}}_0$ used for the decomposition. Hence, the moduli of two terms of a decomposed quaternion are given by

$$|\mathbf{q}_{\parallel n}| = \sqrt{a_n^2 + \big|V_{\parallel}(\mathbf{q}_n)\big|^2}; \qquad |\mathbf{q}_{\perp n}| = \big|V_{\perp}(\mathbf{q}_n)\big|.$$

Let us precise the main term of the decomposition according to a pure reference quaternion $\mathbf{p}_0 = x_0 i + y_0 j + z_0 k$, with the unitary counterpart $\widehat{\mathbf{p}}_0 = \widehat{x}_0 i + \widehat{y}_0 j + \widehat{z}_0 k$ such that $(\widehat{x}_0^2 + \widehat{y}_0^2 + \widehat{z}_0^2) = 1$. By developing the triple product for quaternions, it is obtained

$$\begin{aligned}\widehat{\mathbf{p}}_0 V(\mathbf{q}_n)\widehat{\mathbf{p}}_0 = {} & \big(b_n - 2b_n\widehat{x}_0^2 - 2c_n\widehat{x}_0\widehat{y}_0 - 2d_n\widehat{x}_0\widehat{z}_0\big)i \\ & + \big(c_n - 2c_n\widehat{y}_0^2 - 2b_n\widehat{x}_0\widehat{y}_0 - 2d_n\widehat{y}_0\widehat{z}_0\big)j \\ & + \big(d_n - 2d_n\widehat{z}_0^2 - 2b_n\widehat{x}_0\widehat{z}_0 - 2c_n\widehat{y}_0\widehat{z}_0\big)k.\end{aligned} \tag{21}$$

4.2 Total Orderings for Quaternions

Total orderings introduced initially for colour quaternions in [3] can be used also to define the derived morphological transformations in quaternionic image representations.

Hence, we can generalize the polar-based total orderings, proposed above for complex, to hypercomplex numbers. The ordering $\leq_{\Omega_1^{\mathbf{q}_0}}$ imposes the priority to the modulus, i.e.,

$$\mathbf{q}_n \leq_{\Omega_1^{\mathbf{q}_0}} \mathbf{q}_m \quad \Leftrightarrow \quad \begin{cases} \rho_n < \rho_m \text{ or} \\ \rho_n = \rho_m \text{ and } \theta_n \prec_{\theta_0} \theta_m \text{ or} \\ \rho_n = \rho_m \text{ and } \theta_n =_{\theta_0} \theta_m \text{ and } \|\xi_n - \xi_0\| \geq \|\xi_m - \xi_0\| \end{cases} \tag{22}$$

where θ_0 is the phase of reference quaternion $\mathbf{q}_0$, the angular ordering $\preceq_{\theta_0}$ is given in expression 4 and

$$\|\xi_k - \xi_0\| = \sqrt{\left(\frac{\widehat{b}_k}{\sqrt{\mu_k}} - \frac{\widehat{b}_0}{\sqrt{\mu_0}}\right)^2 + \left(\frac{\widehat{c}_k}{\sqrt{\mu_k}} - \frac{\widehat{c}_0}{\sqrt{\mu_0}}\right)^2 + \left(\frac{\widehat{d}_k}{\sqrt{\mu_k}} - \frac{\widehat{d}_0}{\sqrt{\mu_0}}\right)^2}$$

with $\mu_k = \widehat{b}_k^2 + \widehat{c}_k^2 + \widehat{d}_k^2$. In this ordering, for two quaternions having the same module, the quaternion with lower angular distance between its phase and the phase of reference quaternion is greater or, if phases distances are equal, with the lower eigenaxis distance to the reference quaternion. Two other orderings can be defined, giving respectively the priority to the distance of phases or to the distance between the eigenaxis, i.e.,

$$\mathbf{q}_n \leq_{\Omega_2^{\mathbf{q}_0}} \mathbf{q}_m \quad \Leftrightarrow \quad \begin{cases} \theta_n \prec_{\theta_0} \theta_m \text{ or} \\ \theta_n =_{\theta_0} \theta_m \text{ and } \rho_n < \rho_m \text{ or} \\ \theta_n =_{\theta_0} \theta_m \text{ and } \rho_n = \rho_m \text{ and } \|\xi_n - \xi_0\| \geq \|\xi_m - \xi_0\| \end{cases} \tag{23}$$

and

$$\mathbf{q}_n \leq_{\Omega_3^{\mathbf{q}_0}} \mathbf{q}_m \quad \Leftrightarrow \quad \begin{cases} \|\xi_n - \xi_0\| > \|\xi_m - \xi_0\| \text{ or} \\ \|\xi_n - \xi_0\| = \|\xi_m - \xi_0\| \text{ and } \rho_n < \rho_m \text{ or} \\ \|\xi_n - \xi_0\| = \|\xi_m - \xi_0\| \text{ and } \rho_n = \rho_m \text{ and } \theta_n \prec_{\theta_0} \theta_m. \end{cases} \tag{24}$$

However these ones are only partial orderings or pre-orderings, i.e., two distinct quaternions, $\mathbf{q}_n \neq \mathbf{q}_m$, can verify the equality of the ordering because even if $\xi_n \neq \xi_m$ their corresponding distances to the reference can be equal, $\|\xi_n - \xi_0\| = \|\xi_m - \xi_0\|$. In order to have total orderings we propose to complete the proposed cascades with an additional lexicographical cascade of the hypercomplex values; see below how is completed a pre-ordering for the case of parallel/perpendicular ordering.

But we can also introduce another family of total orderings based on the $\parallel$ / $\perp$ decomposition. We consider in par-

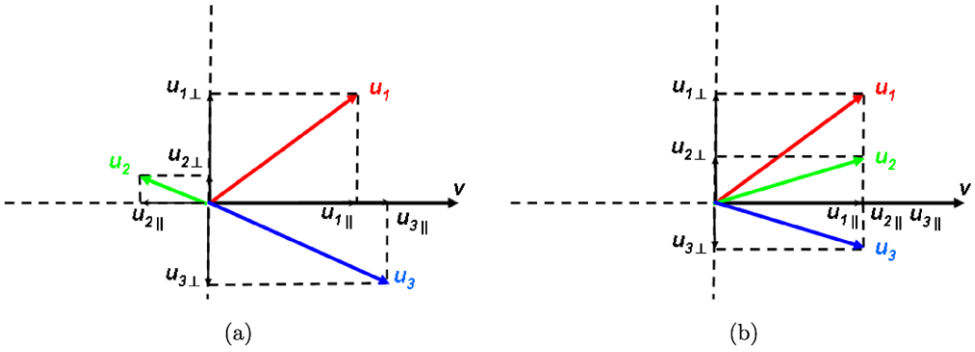

Fig. 6 Ordering of quaternions $\mathbf{u}_i$ according to their decomposition $\mathbf{u}_{i\parallel} + \mathbf{u}_{i\perp}$ about the pure quaternion $\mathbf{v}$: (**a**) $|\mathbf{u}_{3\parallel}| > |\mathbf{u}_{1\parallel}| > |\mathbf{u}_{2\parallel}| \Rightarrow \mathbf{u}_3 > \mathbf{u}_1 > \mathbf{u}_2$, (**b**) $|\mathbf{u}_{1\parallel}| = |\mathbf{u}_{2\parallel}|$ and $|\mathbf{u}_{1\perp}| > |\mathbf{u}_{2\perp}| \Rightarrow \mathbf{u}_1 < \mathbf{u}_2$. But quaternions $\mathbf{u}_2$ and $\mathbf{u}_3$ which have equal modulus of both parallel and perpendicular parts cannot be ordered without an additional condition

ticular the two following cases:

$$\mathbf{q}_n \leq_{\Omega_4^{\mathbf{q}_0}} \mathbf{q}_m \quad \Leftrightarrow$$

$$\begin{cases} |\mathbf{q}_{\parallel n}| < |\mathbf{q}_{\parallel m}| \text{ or} \\ |\mathbf{q}_{\parallel n}| = |\mathbf{q}_{\parallel m}| \text{ and } |\mathbf{q}_{\perp n}| > |\mathbf{q}_{\perp m}| \text{ or} \\ |\mathbf{q}_{\parallel n}| = |\mathbf{q}_{\parallel m}| \text{ and } |\mathbf{q}_{\perp n}| = |\mathbf{q}_{\perp m}| \text{ and} \\ \quad \begin{cases} b_n < b_m \text{ or} \\ b_n = b_m \text{ and } c_n < c_m \text{ or} \\ b_n = b_m \text{ and } c_n = c_m \text{ and } d_n \leq d_m \end{cases} \end{cases} \tag{25}$$

and

$$\mathbf{q}_n \leq_{\Omega_5^{\mathbf{q}_0}} \mathbf{q}_m \quad \Leftrightarrow$$

$$\begin{cases} |\mathbf{q}_{\parallel n}| < |\mathbf{q}_{\parallel m}| \text{ or} \\ |\mathbf{q}_{\parallel n}| = |\mathbf{q}_{\parallel m}| \text{ and} \\ \quad \begin{cases} b_n < b_m \text{ or} \\ b_n = b_m \text{ and } c_n < c_m \text{ or} \\ b_n = b_m \text{ and } c_n = c_m \text{ and } d_n \leq d_m. \end{cases} \end{cases} \tag{26}$$

The pure unitary quaternion required for the $\parallel$ / $\perp$ decomposition is just the corresponding to the reference quaternion $\mathbf{q}_0$. The ordering $\leq_{\Omega_4^{\mathbf{q}_0}}$ is achieved by considering that a quaternion is greater than another one with respect to $\mathbf{q}_0$ if the modulus of the parallel part is greater or if the length of parallel parts are equal and the modulus of the perpendicular part is lesser, see the examples depicted in Fig. 6. The interest of the simplified version $\leq_{\Omega_5^{\mathbf{q}_0}}$ is considered below. We do not consider in the last ordering the fact that the perpendicular parts follows the same ordering as the parallel parts because that will be equivalent to an ordering starting from the modulus.

Obviously, other orderings are possible by considering a different priority in the choice of the polar and parallel/perpendicular component or even taking the same components but selecting a different sense in the inequalities. For the sake of coherence we limit here our discussion to the above introduced orderings.

4.3 $(\vec{\Psi}^+, \Omega_+^{\mathbf{q}_0})$-Hypercomplex Dilation and $(\vec{\Psi}^-, \Omega_-^{\mathbf{q}_0})$-Hypercomplex Erosion

We generalize the construction of morphological complex image representations to the hypercomplex ones as follows.

Definition 8 Given the four-variate transformation

$$\vec{\Psi} = \left(\psi_{B_0}^0, \psi_{B_I}^I, \psi_{B_J}^J, \psi_{B_K}^K\right)$$

applied to the scalar image $f(\mathbf{x}) \in \mathcal{F}(E, \mathcal{T})$, the $\vec{\Psi}$-hypercomplex image is defined by the mapping

$$\begin{aligned} f(\mathbf{x}) \mapsto \mathbf{f}_H(\mathbf{x}) &= \psi_{B_0}^0(f)(\mathbf{x}) + i\psi_{B_I}^I(f)(\mathbf{x}) \\ &\quad + j\psi_{B_J}^J(f)(\mathbf{x}) + k\psi_{B_K}^K(f)(\mathbf{x}), \end{aligned} \tag{27}$$

where $\mathbf{f}_H(\mathbf{x}) : E \to \mathbb{H}$ and the four transformations are scalar operators, i.e., $\psi_B : \mathcal{T} \to \mathcal{T}$.

We notice that in this definition the scalar part of the $\vec{\Psi}$-hypercomplex image is also the result of a morphological transformation of the original grey-scale image.

After choosing a particular $\vec{\Psi}$-hypercomplex representation as well as a particular quaternionic total ordering $\Omega_*^{\mathbf{q}_0}$, we have the following operators.

Definition 9 A generic pair of $(\vec{\Psi}^+, \Omega_+^{\mathbf{q}_0})$-hypercomplex dilation and $(\vec{\Psi}^-, \Omega_-^{\mathbf{q}_0})$-hypercomplex erosion is given respectively by the expressions

$$\begin{cases} \vec{\Psi}^+ = (\psi_{B_0}^{0+}, \psi_{B_I}^{I+}, \psi_{B_J}^{J+}, \psi_{B_K}^{K+}) : f(\mathbf{x}) \mapsto \mathbf{f}_H(\mathbf{x}), \\ \delta_{\langle \Psi^+, \Omega_+^{\mathbf{q}_0}, B \rangle}(f)(\mathbf{x}) \\ \quad = \{f(\mathbf{y}) : \mathbf{f}_H(\mathbf{y}) = \bigvee_{\Omega_+^{\mathbf{q}_0}} [\mathbf{f}_H(\mathbf{z})], \mathbf{z} \in B(\mathbf{x}))\} \end{cases} \tag{28}$$

and

$$\begin{cases} \vec{\Psi}^- = (\psi_{B_0}^{0-}, \psi_{B_I}^{I-}, \psi_{B_J}^{J-}, \psi_{B_K}^{K-}) : f(\mathbf{x}) \mapsto \mathbf{f}_H(\mathbf{x}), \\ \varepsilon_{\langle \Psi^-, \Omega_-^{\mathbf{q}_0}, B \rangle}(f)(\mathbf{x}) \\ \quad = \{f(\mathbf{y}) : \mathbf{f}_H(\mathbf{y}) = \bigwedge_{\Omega_-^{\mathbf{q}_0}} [\mathbf{f}_H(\mathbf{z})], \mathbf{z} \in B(\mathbf{x}))\}. \end{cases} \tag{29}$$

Therefore two kinds of degrees of freedom must be set up to have totally stated the operator:

- the hypercomplex transformation, which includes the set of structuring elements

$$\{B_0, B_I, B_J, B_K\},$$

- the quaternionic ordering, which includes the choice of the reference quaternion $\mathbf{q}_0$.

We should notice that this framework generalize the complex operators introduced in previous section; e.g., the dilation $\delta_{\langle \Psi^+, \Omega_+^{\mathbf{q}_0}, B\rangle}$, with $\vec{\Psi}^+ = (\mathrm{Id}, \gamma_{B_C}, 0, 0)$, $\Omega_+^{\mathbf{q}_0} \equiv \Omega_1^{\mathbf{q}_0}$ and with $\mathbf{q}_0 = 1 + i$ is equivalent to the γ-complex dilation $\delta_{\langle 1, \gamma_{B_C}, B\rangle}$.

As discussed in previous section, openings/closings and white/black top-hats are useful for the transformations ψ_B^*, but also the gradients, which favour the dilation/erosion of points close to the object contours, can be considered. In addition, the four-variate hypercomplex transformation can be used for instance to introduce directional effects according to the main grid directions in 3D images:

$$\begin{aligned}\mathbf{f}_H(\mathbf{x}) &= \psi^0_{B_0}(f)(\mathbf{x}) + i\psi^I_{L_x}(f)(\mathbf{x})\\ &\quad + j\psi^J_{L_y}(f)(\mathbf{x}) + k\psi^K_{L_z}(f)(\mathbf{x})\end{aligned}$$

where B_0 is an isotropic (disk) structuring element of size s (which can be $s = 0$ so the transformation is the identity) and where L_x is an linear structuring element of size x according the direction x. This particular case will be considered in the examples of next section.

Any of the quaternionic orderings could be applied; but as we have studied in detail for the complex case, the choice of the pair of transformations $(\vec{\Psi}^+, \vec{\Psi}^-)$ as well as the reference quaternion in the orderings $\Omega_+^{\mathbf{q}_0}$ and $\Omega_-^{\mathbf{q}_0}$ should be coherent in order to have, if possible, a pair of hypercomplex dilation and erosion which are an adjunction.

Instead of developing an analysis for the adjunctions associated to polar orderings, let us focus now specifically on an example of orderings $\Omega_4^{\mathbf{q}_0}$ and $\Omega_5^{\mathbf{q}_0}$, associated to the $\| \,/\, \perp$ decomposition according to a reference quaternion.

Proposition 10 *Given* $\vec{\gamma} = (\gamma^0_{B_0}, \gamma^I_{B_I}, \gamma^J_{B_J}, \gamma^K_{B_K})$ *and* $\vec{\varphi} = (\varphi^0_{B_0}, \varphi^I_{B_I}, \varphi^J_{B_J}, \varphi^K_{B_K})$, *and the reference quaternion* $\mathbf{q}_0 = x_0 i + y_0 j + z_0 k$ *with* $x_0, y_0, z_0 \geq 0$, *the pair*

$$(\delta_{\langle \vec{\gamma}, \Omega_5^{\mathbf{q}_0}, B\rangle}, \varepsilon_{\langle \vec{\varphi}, \Omega_5^{\mathbf{q}_0}, B\rangle})$$

is an adjunction; *however, the pair* $(\delta_{\langle \vec{\gamma}, \Omega_4^{\mathbf{q}_0}, B\rangle}, \varepsilon_{\langle \vec{\varphi}, \Omega_4^{\mathbf{q}_0}, B\rangle})$ *is not an adjunction*.

Proof We must study under which conditions it is verified that:

$$\begin{aligned}&\left\{\bigvee_{\Omega_{4:5}^{\mathbf{q}_0}} \big[\mathbf{f}_H(\mathbf{z})\big],\ \mathbf{z} \in B(\mathbf{x})\right\} \leq_{\Omega_{4:5}^{\mathbf{q}_0}} \mathbf{g}_H(\mathbf{x})\\ &\quad\Leftrightarrow\quad \mathbf{f}_H(\mathbf{x}) \leq_{\Omega_{4:5}^{\mathbf{q}_0}} \left\{\bigwedge_{\Omega_{4:5}^{\mathbf{q}_0}} \big[\mathbf{g}_H(\mathbf{z})\big],\ \mathbf{z} \in B(\mathbf{x})\right\}.\end{aligned}$$

From proofs given in Sect. 3, we know that, after simple manipulations, we must check under which conditions we have

$$\begin{aligned}\vec{\gamma}(g)(\mathbf{x}) &= \gamma^0_{B_0}(f)(\mathbf{x}) + i\gamma^I_{B_I}(g)(\mathbf{x})\\ &\quad + j\gamma^J_{B_J}(g)(\mathbf{x}) + k\gamma^k_{B_K}(g)(\mathbf{x}) \leq_{\Omega_{4:5}^{\mathbf{q}_0}}\\ \vec{\varphi}(g)(\mathbf{x}) &= \varphi^0_{B_0}(g)(\mathbf{x}) + i\varphi^I_{B_I}(g)(\mathbf{x})\\ &\quad + j\varphi^J_{B_J}(g)(\mathbf{x}) + k\varphi^k_{B_K}(g)(\mathbf{x}).\end{aligned}$$

We notice that by definition we always have $\gamma^0_{B_0}(g) \leq \varphi^0_{B_0}(g)$, $\gamma^I_{B_I}(g) \leq \varphi^I_{B_I}(g), \ldots$. On the other hand, in the orderings $\leq_{\Omega_{4:5}^{\mathbf{q}_0}}$, we have to consider the following decomposition:

$$\begin{aligned}&\vec{\gamma}(g)(\mathbf{x}) = \vec{\gamma}(g)(\mathbf{x})_{\|} + \vec{\gamma}(g)(\mathbf{x})_{\perp} \quad \text{and}\\ &\vec{\varphi}(g)(\mathbf{x}) = \vec{\varphi}(g)(\mathbf{x})_{\|} + \vec{\varphi}(g)(\mathbf{x})_{\perp},\end{aligned}$$

according to reference quaternion $\mathbf{q}_0$. Then, for $\leq_{\Omega_4^{\mathbf{q}_0}}$ the two fundamental conditions of ordering are:

$$\begin{aligned}&\vec{\gamma}(g)(\mathbf{x}) \leq_{\Omega_4^{\mathbf{q}_0}} \vec{\varphi}(g)(\mathbf{x}) \quad \Leftrightarrow\\ &\quad\begin{cases}|\vec{\gamma}(g)(\mathbf{x})_{\|}| < |\vec{\varphi}(g)(\mathbf{x})_{\|}| \text{ or}\\ |\vec{\gamma}(g)(\mathbf{x})_{\|}| = |\vec{\varphi}(g)(\mathbf{x})_{\|}| \text{ and } |\vec{\gamma}(g)(\mathbf{x})_{\perp}| \geq |\vec{\varphi}(g)(\mathbf{x})_{\perp}|.\end{cases}\end{aligned}$$

To fix the ideas, we can for instance choose as reference quaternion $\mathbf{q}_0 = i + j$. A straightforward calculation from (21), applied on expressions (19) and (20) leads to

$$\begin{aligned}\vec{\gamma}(g)(\mathbf{x})_{\|} &= \gamma^0_{B_0}(f)(\mathbf{x}) + \frac{i}{2}\big[\gamma^I_{B_I}(f)(\mathbf{x}) + \gamma^J_{B_J}(f)(\mathbf{x})\big]\\ &\quad + \frac{j}{2}\big[\gamma^I_{B_I}(f)(\mathbf{x}) + \gamma^J_{B_J}(f)(\mathbf{x})\big],\\ \vec{\gamma}(g)(\mathbf{x})_{\perp} &= \frac{i}{2}\big[\gamma^I_{B_I}(f)(\mathbf{x}) - \gamma^J_{B_J}(f)(\mathbf{x})\big]\\ &\quad + \frac{j}{2}\big[\gamma^J_{B_J}(f)(\mathbf{x}) - \gamma^I_{B_I}(f)(\mathbf{x})\big] + k\gamma^K_{B_K}(f)(\mathbf{x}),\end{aligned}$$

and similar expressions for $\vec{\varphi}(g)(\mathbf{x})_{\|}$ and $\vec{\varphi}(g)(\mathbf{x})_{\perp}$ by putting, *mutatis mutandis*, φ instead of γ. In fact, by choosing another $\mathbf{q}_0 = x_0 i + y_0 j + z_0 k$ with $x_0, y_0, z_0 \geq 0$, the imaginary components of the $\|$ images are *positive* linear combinations of the imaginary components of the initial hy-

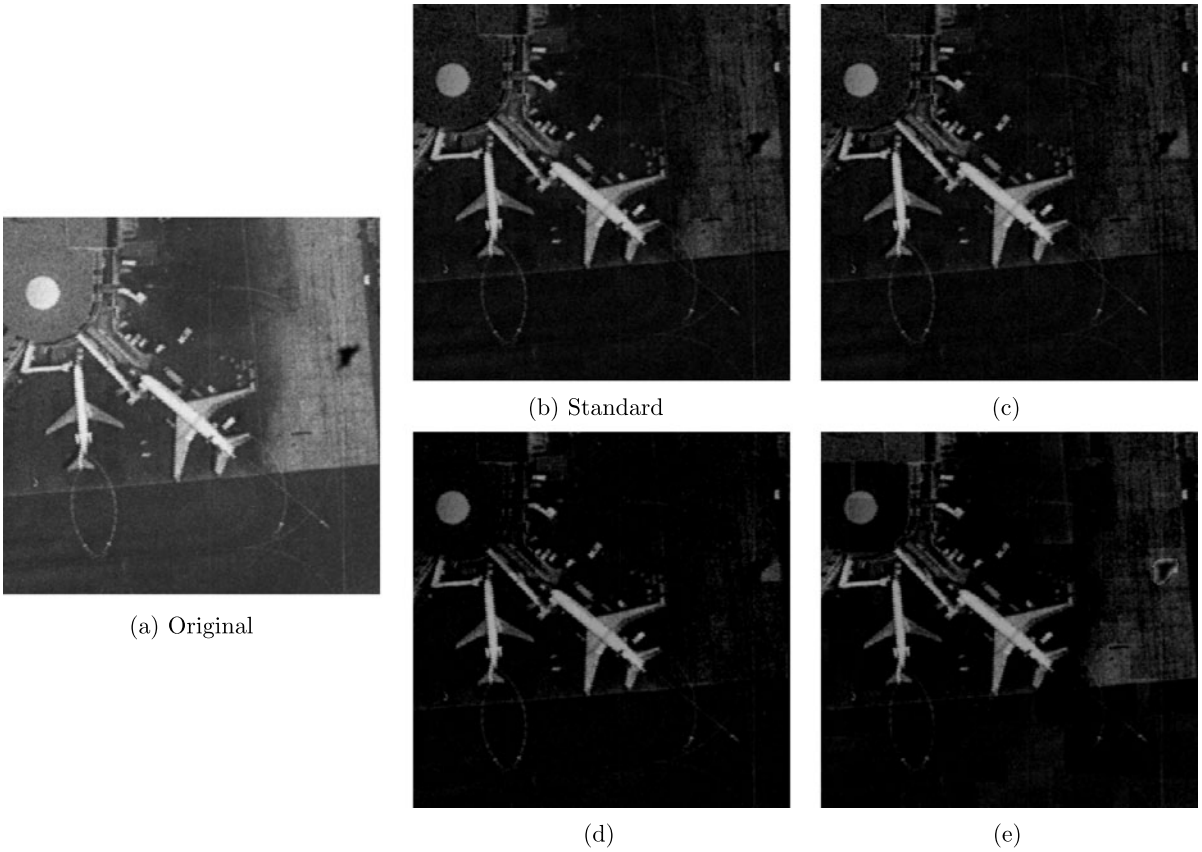

Fig. 7 Comparative example of structure extraction using bright top-hat τ_B^+ (for all the transformations B is a square of 25 pixels): (**a**) original image f, (**b**) standard transformation, (**c**) $(\Omega_1^{\pi/2}, \gamma_{B_C})$-complex dilation, $(\Omega_1^{\pi/2}, \varphi_{B_C})$-complex erosion, $B_C = D_{10}$, (**d**) $(\Omega_2^{\pi/2}, \gamma_{B_C})$-complex dilation, $(\Omega_2^{\pi/2}, \varphi_{B_C})$-complex erosion, $B_C = D_{10}$, (**e**) $\vec{\Psi}^{+/-} = (Id/Id, \varrho_{L_{10}^x}/-\varrho_{L_{10}^x}, \varrho_{L_{10}^y}/-\varrho_{L_{10}^y}, 0)$, $\Omega_4^{\mathbf{q}_0}$, $\mathbf{q}_0 = i + j$

percomplex image; and of course, the weights of the linear combination are the same for $\vec{\gamma}(g)(\mathbf{x})_{\|}$ and $\vec{\varphi}(g)(\mathbf{x})_{\|}$. Hence, $|\vec{\gamma}(g)(\mathbf{x})_{\|}|$ is always $\leq$ that $|\vec{\varphi}(g)(\mathbf{x})_{\|}|$. But, for the example $\mathbf{q}_0 = i + j$, we see that $|\vec{\gamma}(g)(\mathbf{x})_{\perp}|$ is not always $\geq$ that $|\vec{\varphi}(g)(\mathbf{x})_{\perp}|$, which is contradiction with for $\leq_{\Omega_4^{\mathbf{q}_0}}$. More generally, independently of the choice of $\mathbf{q}_0$, we cannot guarantee the second condition of the ordering cascade of $\leq_{\Omega_4^{\mathbf{q}_0}}$. Consequently, only if we skip the second condition the adjunction is verified, such as it is the case for $\leq_{\Omega_5^{\mathbf{q}_0}}$. □

However, independently of the previous result, in our experimental tests, we have observed for instance that the results obtained for dilations/erosions with the ordering $\leq_{\Omega_4^{\mathbf{q}_0}}$ are visually more reliable than those obtained for $\leq_{\Omega_5^{\mathbf{q}_0}}$. As a matter of fact, as we illustrate in the next Section, it is important to remark that even if a pair of dilation/erosion $(\delta_{\langle\vec{\gamma},\Omega_4^{\mathbf{q}_0},B\rangle}, \varepsilon_{\langle\vec{\varphi},\Omega_4^{\mathbf{q}_0},B\rangle})$ is not an adjunction, the practical behavior of evolved operators (openings/closings and other) can lead to interesting empirical filtering properties.

5 Examples and Applications

The (hyper-)complex dilations/erosions introduced in the paper can be used to build any of the advanced operators considered in the literature of mathematical morphology. The principle of generalization entails using always a homogeneous (hyper-)complex pair of dilation/erosion and then applying the standard definitions for construction the evolved (hyper-)complex operators. Our purpose in this section is to illustrate empirically the potential interest of the introduced (hyper-)complex filters, by comparing them with the standard scalar filters in typical tasks solved by mathematical morphology.

We start with the example given in Fig. 7. The aim is to extract the most bright contrasted structures from the uneven background this aerial image. This objective can be achieved by a white top-hat [42]

$$th_B^+(f)(\mathbf{x}) = f(\mathbf{x}) - \gamma_B(f)(\mathbf{x}),$$

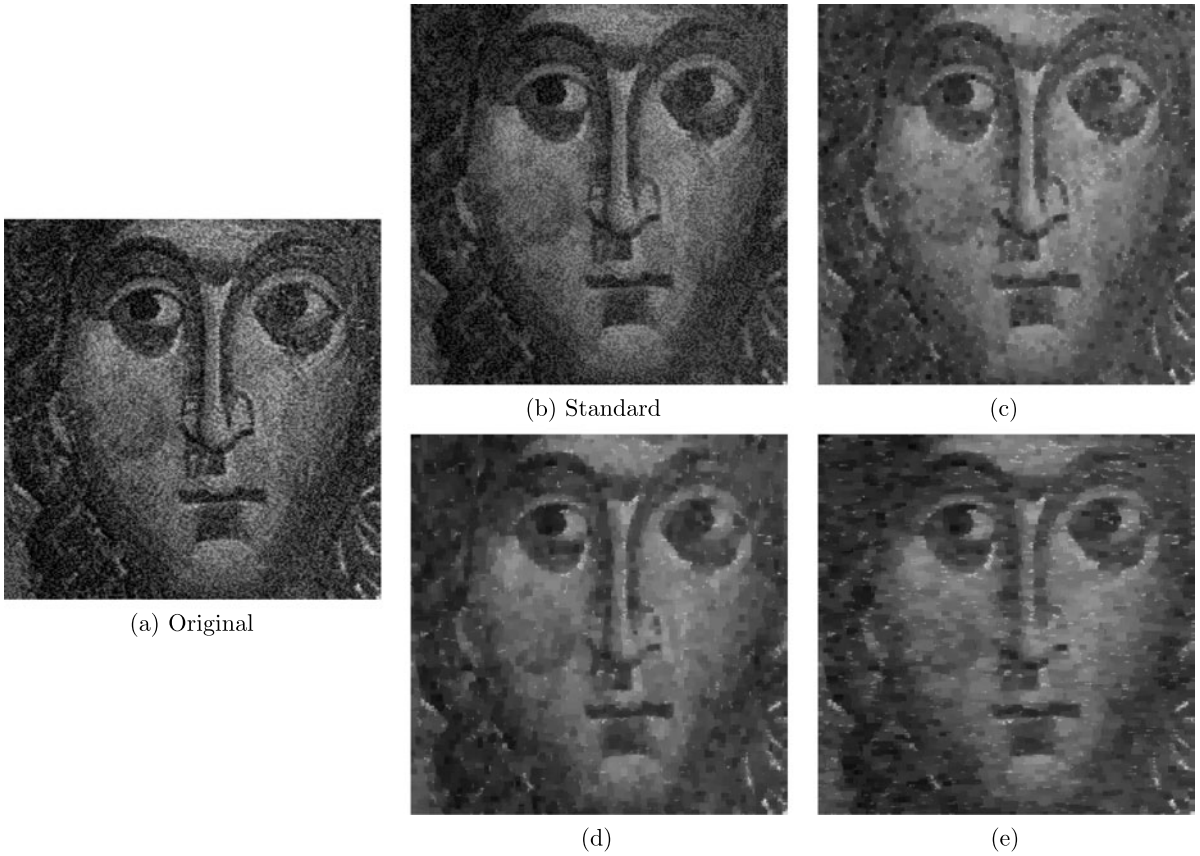

(a) Original (b) Standard (c) (d) (e)

Fig. 8 Comparative example of image filtering using morphological center ζ_B (for all the transformations B is a square of 3 pixels): (**a**) original image f, (**b**) standard transformation, (**c**) $(\Omega_1^{\pi/2}, \gamma_{B_C})$-complex dilation, $(\Omega_1^{\pi/2}, \varphi_{B_C})$-complex erosion, $B_C = D_5$, (**d**) $\vec{\Psi}^{+/-} = (\gamma_{D_5}/\varphi_{D_5}, \gamma_{L_5^x}/\varphi_{L_5^x}, \gamma_{L_5^y}/\varphi_{L_5^y}, 0)$, $\Omega_4^{\mathbf{q}_0}$, $\mathbf{q}_0 = i + j$, (**e**) $\vec{\Psi}^{+/-} = (\gamma_{D_5}/\varphi_{D_5}, \gamma_{L_5^x}/\varphi_{L_5^x}, \gamma_{L_5^y}/\varphi_{L_5^y}, 0)$, $\Omega_4^{\mathbf{q}_0}$, $\mathbf{q}_0 = i$

where the structuring element B determines the maximal size/shape of the structures to be extracted, here a square of 25×25 pixels. As it is observed in this example, the typical drawback of standard top-hat is that background irregularities lesser than B are also extracted independently of their relative contrast. It is shown here that the use of γ and ϕ-complex operators, with the ordering $(\Omega_2^{\pi/2}, \gamma_{B_C}/\varphi_{B_C})$ which gives the priority to the phase, allows to introduce a selection exclusively of most contrasted structures (according to an opening/closing by a square 10×10 pixels), compare Fig. 7(c) and (d). It is given also in Fig. 7(e) an example of hypercomplex operators using the x and y directional gradients for the imaginary component, i.e., $\varrho_{L_{10}^x}(f) = \delta_{L_{10}^x}(f) - \varepsilon_{L_{10}^x}(f)$, where L_{10}^x is an horizontal segment of 10 pixels; and the identity transformation for the scalar component. By choosing the reference quaternion $\mathbf{q}_0 = i + j$, and the positive sign of the gradient for the dilation and negative sign for the erosion, the corresponding hypercomplex top-hat favours the extraction of bright structures with strong gradients.

Figure 8 depicts an example of image filtering using the morphological center, an operator having more robust properties for denoising than the standard median. More precisely, the center can be defined as [43]

$$\zeta_B(f)(\mathbf{x}) = \big[f(\mathbf{x}) \vee \big(\gamma_B\varphi_B\gamma_B(f)(\mathbf{x}) \wedge \varphi_B\gamma_B\varphi_B(f)(\mathbf{x})\big)\big] \wedge \big(\gamma\varphi\gamma(f)(\mathbf{x}) \vee \varphi\gamma\varphi(f)(\mathbf{x})\big),$$

where the two operators $\gamma_B\varphi_B\gamma_B(f)$ $\varphi_B\gamma_B\varphi_B(f)$ pre-filter out in priority respectively the bright and dark noisy structures, with B an unit centered structuring element (square of 3×3 pixels). It is observed that the complex operators $(\Omega_1^{\pi/2}, \gamma_{B_C}/\varphi_{B_C})$, with B_C a square 5×5 pixels, see Fig. 8(c), lead to more strong simplification than the standard operator (b). Note that if we choose for B a square of 5×5 pixels the results obtained for the standard operator are almost the same than for 3×3 pixels. This example allows us to observe also how directional filtering effect can be introduced by the reference quaternion used in the hypercomplex $\parallel$ / $\perp$ ordering. We use directional x and y

Fig. 9 Comparative example of morphological edge detection ((∗-1) corresponds to the gradient and (∗-2) to the thresholded zero-crossing of laplacian, see the text for details): (**a**) original image f, (**b**-∗) standard transformation, (**c**-∗) $(\Omega_2^{\pi/2}, \tau_{B_C}^{+})$-complex dilation, $(\Omega_2^{-\pi/2}, -[\tau_{B_C}^{-}]^c)$-complex erosion, $B_C = D_5$, (**d**-∗) $\vec{\Psi}^{+/-} = (\gamma_{D_5}/\varphi_{D_5}, \gamma_{L_5^x}/\varphi_{L_5^x}, \gamma_{L_5^y}/\varphi_{L_5^y}, 0)$, $\Omega_4^{\mathbf{q}_0}$, $\mathbf{q}_0 = i + j$, (**e**-∗) $\vec{\Psi}^{+/-} = (Id/Id, \varrho_{L_5^x}/-\varrho_{L_5^x}, \varrho_{L_{10}^y}/-\varrho_{L_{10}^y}, 0)$, $\Omega_4^{\mathbf{q}_0}$, $\mathbf{q}_0 = i + j$

openings/closings for the imaginary part and isotropic opening/closing for the scalar part. By fixing $\mathbf{q}_0 = i + j$, similar importance is given to x and y directions, but by choosing $\mathbf{q}_0 = i$, it is focused on simplifying structures according to direction x.

A simple edge detector can be implemented using only morphological erosion and dilation. The idea was introduced in [53] and consists in defining the nonlinear laplace filter as

$$lp_B(f)(\mathbf{x}) = \big(\delta_B(f)(\mathbf{x}) - f(\mathbf{x})\big) - \big(f(\mathbf{x}) - \varepsilon_B(f)(\mathbf{x})\big),$$

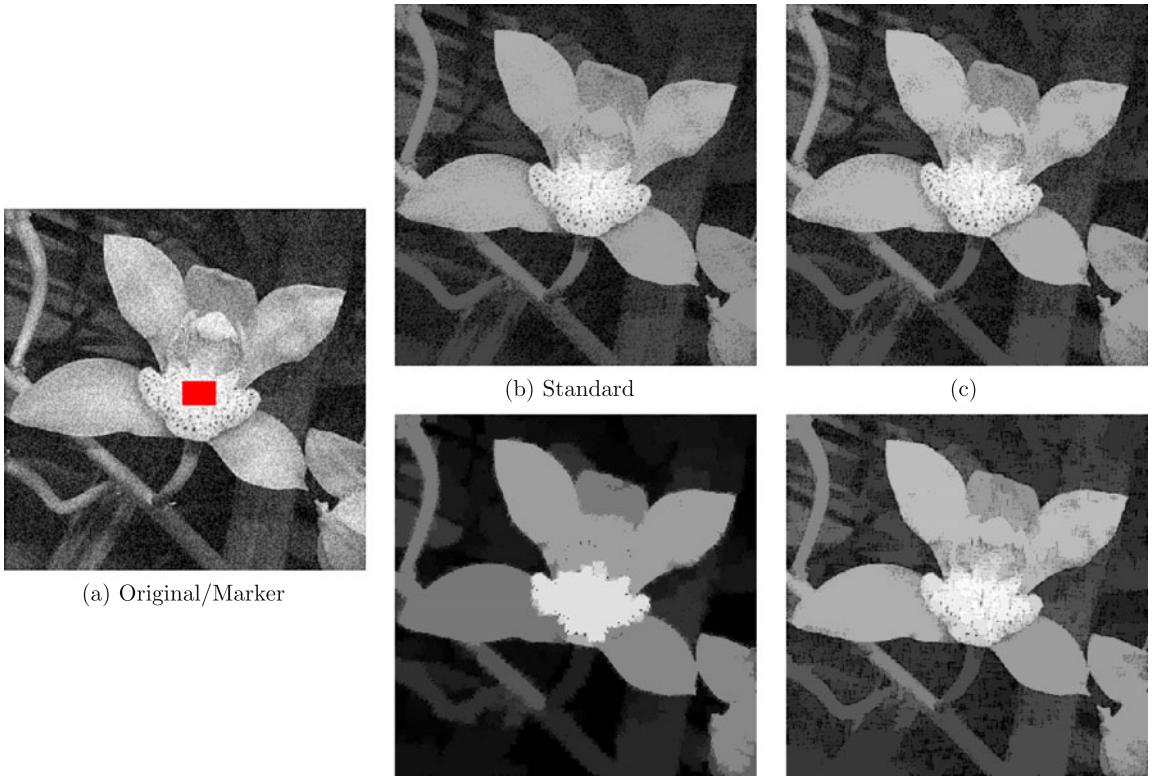

Fig. 10 (Color online) Comparative example of opening by reconstruction: (**a**) original image f and marker m (*red zone*), (**b**) standard transformation, (**c**) $(\Omega_1^{\pi/2}, \gamma_{B_C})$-complex dilation, $(\Omega_1^{\pi/2}, \varphi_{B_C})$-complex erosion, $B_C = D_5$, (**d**) $(\Omega_2^{\pi/2}, \tau_{B_C}^{+})$-complex dilation, $(\Omega_2^{-\pi/2}, -[\tau_{B_C}^{-}]^c)$-complex erosion, $B_C = D_5$, (**e**) $\vec{\Psi}^{+/-} = (\gamma_{D_5}/\varphi_{D_5}, \gamma_{L_5^x}/\varphi_{L_5^x}, \gamma_{L_5^y}/\varphi_{L_5^y}, 0)$, $\Omega_4^{\mathbf{q}_0}$, $\mathbf{q}_0 = i + j$

and the zero crossings of $lp_B(f)$, as in the classical Marr-Hildreth model, correspond to the edges of image f. In order to select only the most prominent edges, the zero crossing detector is "multiplied" with a threshold by hysteresis of the morphological gradient given by

$$\varrho_B(f)(\mathbf{x}) = \delta_B(f)(\mathbf{x}) - \varepsilon_B(f)(\mathbf{x}).$$

Hence, the single parameter of this edge detection model is the pair of threshold values for the gradient. In Fig. 9 is given a comparison of edge detection using various (hyper-) complex operators, using the same threshold values. For the four examples is shown the gradient $\varrho_B(f)$ and final detected edges. The original image is particulary textured and consequently the standard transformations produce many secondary contours. The visual comparison of the three illustrated alternatives yield to different degrees of selectivity of contours. In particular, the τ^+ and $[\tau^-]^c$ complex representation, with ordering by phase, is the most selective but presents some discontinuities.

Let us now consider an example of geodesic operators. We remind that the geodesic dilation is based on restricting the iterative dilation of an image marker $m(\mathbf{x})$ by B to a function reference $f(\mathbf{x})$ [55], i.e.,

$$\delta^n(m, f)(\mathbf{x}) = \delta^1 \delta^{n-1}(m, f)(\mathbf{x}),$$

where the unitary conditional dilation is given by $\delta^1(m, f)(\mathbf{x}) = \delta_B(m)(\mathbf{x}) \wedge f(\mathbf{x})$. Typically, B is an isotropic structuring element of size 1. The reconstruction by dilation, or opening by reconstruction, is then defined by

$$\gamma^{rec}(m, f)(\mathbf{x}) = \delta^i(m, f)(\mathbf{x}),$$

such that $\delta^i(m, f) = \delta^{i+1}(m, f)$ (idempotence). The opening by reconstruction $\gamma^{rec}(m, f)$ is aimed at efficiently and precisely reconstructing the contours of the objects of $f(\mathbf{x})$ which are marked by the image $m(\mathbf{x})$. In the example of Fig. 10, the marker m is a small rectangle in the center of the orchid and the opening by reconstruction should simplify strongly the image, preserving the main contours of the orchid. But usually, the standard operators reconstruct more texture and secondary contours than expected. It is observed that the three examples of (hyper-)complex operators involves stronger image simplifications. In particular, τ^+ and $[\tau^-]^c$ complex representation is especially strong; in addition, we see that the hypercomplex operators with the

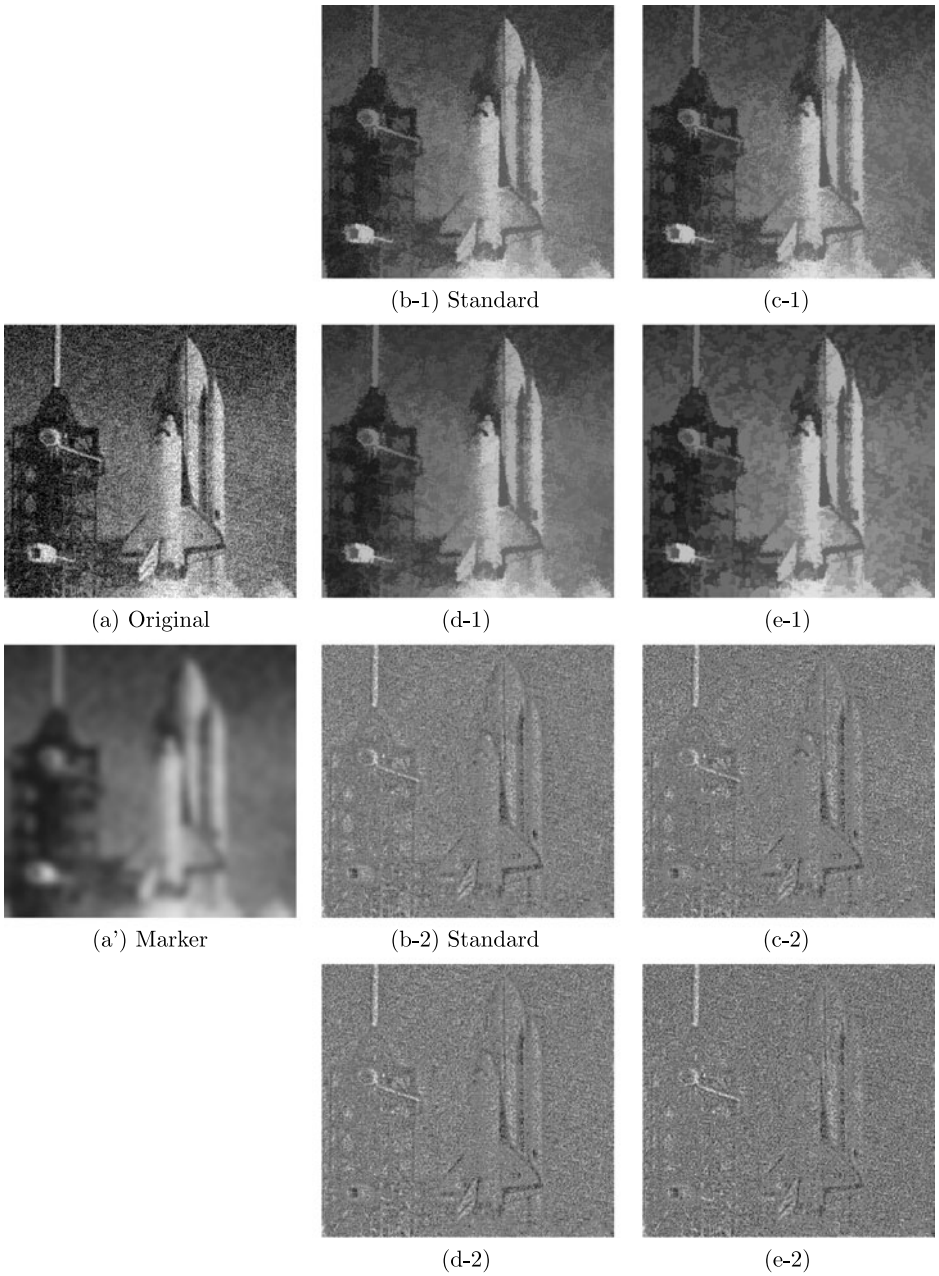

Fig. 11 Comparative example of morphological cartoon + texture/noise decomposition ((∗-1) corresponds to the levelling and (∗-2) to the pointwise difference between the original image and the levelling, see the text for details): (**a**) original image f, (**a'**) marker image $mrk = f * G_\sigma$, (**b**-∗) $(\Omega_1^{\pi/2}, \gamma_{B_C})$-complex dilation, $(\Omega_1^{\pi/2}, \varphi_{B_C})$-complex erosion, $B_C = D_5$, (**c**-∗) $\vec{\Psi}^{+/-} = (Id/Id, \gamma_{B_I}/\varphi_{B_I}, \gamma_{B_J}/\varphi_{B_J}, 0)$, $\Omega_4^{\mathbf{q}_0}$, $\mathbf{q}_0 = i + j$, $B_0 = D_5$, $B_I = L_5^x$, $B_J = L_5^y$, (**d**-∗) $\vec{\Psi}^{+/-} = (\gamma_{B_0}/\varphi_{B_0}, \gamma_{B_I}/\varphi_{B_I}, \gamma_{B_J}/\varphi_{B_J}, 0)$, $\Omega_4^{\mathbf{q}_0}$, $\mathbf{q}_0 = i + j$, $B_0 = D_5$, $B_I = L_5^x$, $B_J = L_5^y$

istropic/directional openings/closings and the $\parallel$ / $\perp$ decomposition leads to hard simplification than the γ and φ complex counterpart.

But the geodesic operators can be used to other applications than the supervised structure simplification. The levelling $\lambda(m, f)$ of a reference image f and a marker image m is a symmetric geodesic operator computed by means of an iterative algorithm with geodesic dilations and geodesic erosions until idempotence [32], i.e.,

$$\lambda(m, f)(\mathbf{x}) = \lambda^i(m, f)(\mathbf{x}) = \big[f(\mathbf{x}) \wedge \delta^i(m, f)(\mathbf{x})\big] \vee \varepsilon^i(m, f)(\mathbf{x}),$$

until $\lambda^i(m, f) = \lambda^{i+1}(m, f)$. The levelling simplifies the image f, removing the objects and textures which are not marked by m and preserving the contours of the remaining

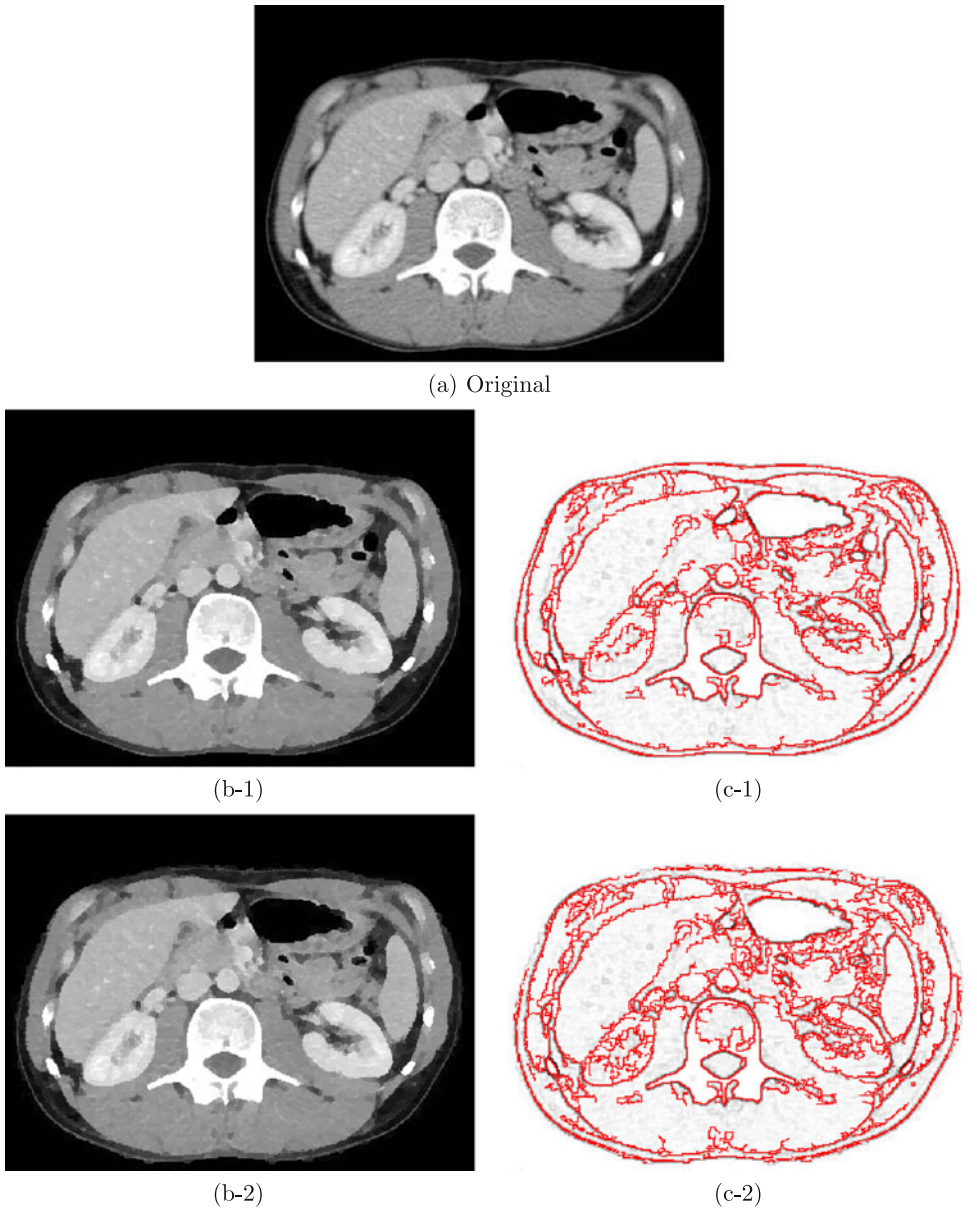

(a) Original

(b-1) (c-1)

(b-2) (c-2)

Fig. 12 (Color online) Edge detection in a single section of a CT scanner image: (**a**) original image, (**b**-$*$) filtered image by the morphological center, followed by a toggle mapping, (**c**-$*$) detected edges by thresholding zerocrossing of morphological laplacian (in *red*) superimposed on the gradient. ($*$-1) operators based on $(\Omega_1^{\pi/2}, \gamma_{B_C})$-complex dilation, $B_C = D_5$, ($*$-2) operators based on $(\Omega_2^{\pi/2}, \tau^+_{B_C})$-complex dilation, $(\Omega_2^{-\pi/2}, -[\tau^-_{B_C}]^c)$-complex erosion, $B_C = D_5$

objects. Moreover, it acts simultaneity on the bright and dark objects. By imposing as marker a rough simplification of the image, given for instance by a Gaussian filter, the corresponding levelling produces a Cartoon-like image; and the residue between the original and the levelled image is a representation of Texture/noise-like image [49], where the scale of texture is given by the σ^2 used in the Gaussian marker. Figure 11 depicts an example of a textured and noisy image and its Gaussian filtered version. We can compare the performances of the standard and (hyper-)complex levellings for this decomposition Cartoon + Texture/noise. In this case, it is compared particularly the hypercomplex operators, in $\| / \perp$ decomposition-based ordering, with directional openings/closings for the imaginary part and without vs. with an isotropic opening for the real part. The last case, as already remarked for other examples, is particularly appropriate in order to obtain good regularization effects.

5.1 Application to Medical Image Analysis

To conclude this section of results, we apply some of the (hyper)-complex operators illustrated above to the analysis of two concrete examples from medical imaging. The aim is not to solve a particular medical problem, but at least to give an overview of the potential interest of these operators for some typical images.

The first example given in Fig. 12 corresponds to a single section of a CT scanner acquisition. It is possible from these images to visualize the different organs and to detect anomalies, tumors, etc. In our case, we propose to detect

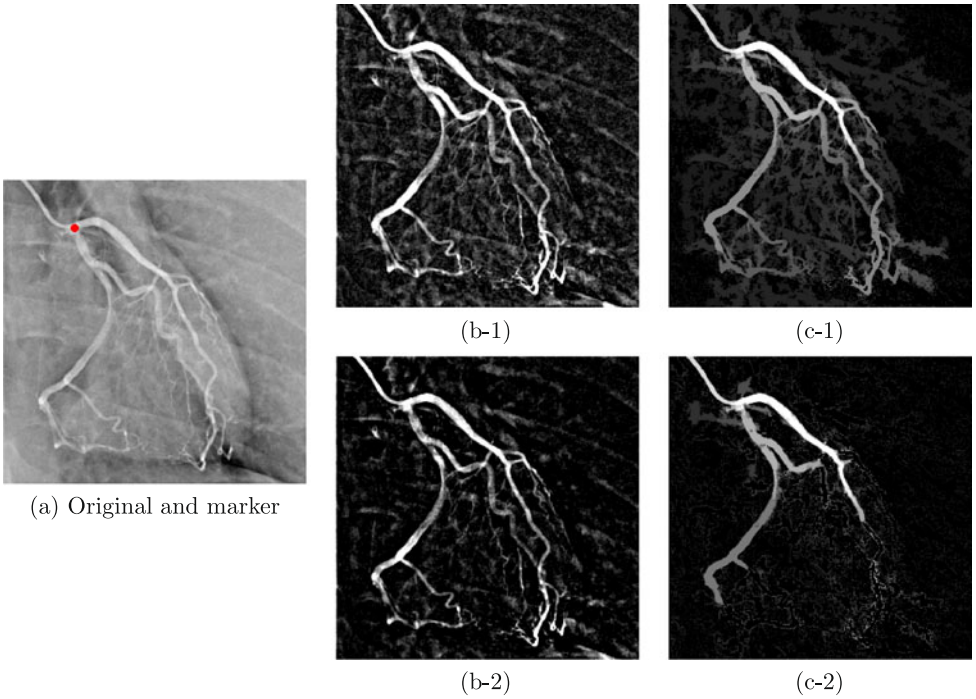

(a) Original and marker

Fig. 13 (Color online) Arteries extraction in a coronarography: (**a**) original image and marker (in *red*), (**b**-$*$) vessel enhancement by top-hat, (**c**-$*$) network extraction using marker-driven morphological opening. ($*$-1) $\vec{\Psi}^{+/-} = (Id/Id, \gamma_{B_I}/\varphi_{B_I}, \gamma_{B_J}/\varphi_{B_J}, 0)$, $\Omega_4^{\mathbf{q}_0}$, $\mathbf{q}_0 = i + j$, $B_0 = D_5$, $B_I = L_5^x$, $B_J = L_5^y$, ($*$-2) $\vec{\Psi}^{+/-} = (\gamma_{B_0}/\varphi_{B_0}, \gamma_{B_I}/\varphi_{B_I}, \gamma_{B_J}/\varphi_{B_J}, 0)$, $\Omega_4^{\mathbf{q}_0}$, $\mathbf{q}_0 = i + j$, $B_0 = D_5$, $B_I = L_5^x$, $B_J = L_5^y$

edges of the basic structures, which can be useful for subsequent measurements. The first step involves filtering out the image, in order to denoise it and to enhance the contrast of the structures. It is achieved by the application of a morphological center, followed by a toggle-mapping [42, 50]. The latter is a simple operator obtained by taking at each pixel the closer value to the original intensity between and erosion and a dilation. Then, after computing the morphological gradient, the edges are obtained by thresholding zerocrossing of morphological laplacian. In the example are compared two families of complex operators. We observe, for instance, that operators based on τ^+-complex dilations and $[\tau^-]^c$-complex erosions are more effective in the detection of small but contrasted objects than operators based on γ-complex dilations and φ-complex erosions.

In the second example of Fig. 13, we deal with an x-ray contrast image of the heart (coronarography) used for the examination of the coronary arteries. Our purpose is to clean the uneven background and then, using an interactive marker on the main artery, to extract the main vessels of the network. This problem is tackled by, first, using a top-hat and, second, by computing an opening by reconstruction with the interactive marker. Two hypercomplex families of operators are again compared. As we can observe, by considering alternatively the original image or an opening/closing one, it is possible to include in the operators an additional size constraint which allows being more selective in the extraction of the vessels of a minimal size (i.e., diameter).

6 Conclusions and Perspectives

We have introduced morphological operators for grey-level images based on indirect total orderings. The orderings are associated to hypercomplex image representations where the imaginary components of the hypercomplex function are obtained from a prior multi-valued transformation of the original image. The properties of the corresponding hypercomplex adjunctions have been studied.

The practical motivation was to introduce in the basic erosion/dilation operators some information on size invariance or on relative contrast of structures. The results obtained from some illustrative examples showed their potential applicative interest.

Other representations using upper dimensional Clifford Algebras [1] can be foreseen in order to have a more generic framework not limited to four-variables image representations. In addition, the approach can also be extended to already natural multivariate images (i.e., multispectral images) and, in this last case, it seems appropriate to envisage tensor representations and associated total orderings.

References

1. Ablamowicz, R., Sobczyk, G.: Lectures on Clifford (Geometric) Algebras and Applications. Birkhäuser, Basel (2004)
2. Angulo, J.: From scalar-valued images to hypercomplex representations and derived total orderings for morphological operators. In: Proc. of ISMM'09 (International Symposium on Mathematical Morphology), Groningen, The Netherlands, August 2009. LNCS, vol. 5720, pp. 238–249. Springer, Berlin (2009)
3. Angulo, J.: Geometric algebra colour image representations and derived total orderings for morphological operators—Part I: Colour quaternions. J. Vis. Commun. Image Represent. **21**, 33–48 (2010)
4. Batard, T., Berthier, M., Saint-Jean, C.: Clifford Fourier transform for color image processing. In: Proceedings of Applied Geometric Algebras in Computer Science and Engineering. LNCS. Springer, Berlin (2008)
5. Batard, T., Saint-Jean, C., Berthier, M.: A metric approach to nD images edge detection with Clifford algebras. J. Math. Imaging Vis. **33**(3), 296–312 (2009)
6. Bloch, I.: Duality vs. adjunction for fuzzy mathematical morphology and general form of fuzzy erosions and dilations. Fuzzy Sets Syst. **160**, 1858–1867 (2009)
7. Bloch, I., Maitre, H.: Fuzzy mathematical morphologies: a comparative study. Pattern Recognit. **28**(9) (1995)
8. Bülow, T., Sommer, G.: Hypercomplex signals—a novel extension of the analytic signal to the multidimensional case. IEEE Trans. Image Process. **49**(11), 2844–2852 (2001)
9. Carré, Ph., Denis, P.: Quaternionic wavelet transform for colour images. In: Wavelet Applications in Industrial Processing IV, vol. 6383, Boston, USA (2006)
10. Deng, T.Q., Heijmans, H.J.A.M.: Gray-scale morphology based on fuzzy logic. J. Math. Imaging Vis. **16**(2), 155–171 (2002)
11. Denis, P., Carré, Ph., Fernandez-Maloigne, Ch.: Spatial and spectral quaternionic approaches for colour images. Comput. Vis. Image Underst. **107**(2–3), 74–87 (2007)
12. Di Zenzo, S.: A note on the gradient of a multi-image. Comput. Vis. Graph. Image Process. **33**(1), 116–125 (1986)
13. Ell, T.A.: Hypercomplex color affine filters. In: Proc. of IEEE Conference on Image Processing (ICIP'07), vol. V, pp. 249–252 (2007)
14. Ell, T.A.: Multi-vectors color-image filters. In: Proc. of IEEE Conference on Image Processing (ICIP'07), vol. V, pp. 245–248 (2007)
15. Ell, T.A., Sangwine, S.J.: Hypercomplex Wiener-Khintchine theorem with application to color image correlation. In: IEEE ICIP'00, vol. II, pp. 792–795 (2000)
16. Ell, T.A., Sangwine, S.J.: Hypercomplex Fourier transform of color images. IEEE Trans. Image Process. **16**(1), 22–35 (2007)
17. Felsberg, M., Sommer, G.: The monogenic signal. IEEE Trans. Image Process. **49**(12), 3136–3144 (2001)
18. Felsberg, M., Sommer, G.: The monogenic scale-space: A unifying approach to phase-based image processing in scale-space. J. Math. Imaging Vis., **21**, 5–26 (2004)
19. Hamilton, W.R.: In: Ingram, R.E., Halberstam, N. (eds.) The Mathematical Papers of Sir William Rowan Hamilton, vol. III, Cambridge University Press, Cambridge (1967)
20. Heijmans, H.J.A.M.: Morphological Image Operators. Academic Press, Boston (1994)
21. Heijmans, H.J.A.M.: On the construction of morphological operators which are selfdual and activity-extensive. Signal Process. **38**, 13–19 (1994)
22. Heijmans, H.J.A.M., Keshet, R.: Inf-semilattice approach to self-dual morphology. J. Math. Imaging Vis. **17**(1), 55–80 (2002)
23. Heijmans, H.J.A.M., Ronse, C.: The algebraic basis of mathematical morphology—Part I: Dilations and erosions. Comput. Vis. Graph. Image Process. **50**, 245–295 (1990)
24. Kresch, R.: Extensions of morphological operations to complete semilattices and its applications to image and video processing. In: Mathematical Morphology and Its Application to Image and Signal Processing, Proc. of ISMM'98, pp. 35–42. Kluwer, Amsterdam (1998)
25. Kuosmanen, P., Astola, J.: Soft morphological filtering. J. Math. Imaging Vis. 231–262 (1995)
26. Labunets, V.: Clifford algebras as unified language for image processing and pattern recognition. In: Byrnes, J., Ostheimer, G. (eds.) Computational Noncommutative Algebra & Applications, NATO Sciences Series II Mathematics, Physics & Chemistry, vol. 136, Kluwer, Amsterdam (2003)
27. Labunets-Rundblad, E., Labunets, V.: Spatial-colour clifford algebras for invariant image recognition. In: Sommer, G. (ed.) Geometric Computing with Clifford Algebra, pp. 155–185. Springer, Berlin (2001)
28. Labunets-Rundblad, E., Maidan, A., Novak, P., Labunets, V.: Fast color wavelet transforms. In: Byrnes, J., Ostheimer, G. (eds.) Computational Noncommutative Algebra & Applications. NATO Sciences Series II Mathematics, Physics & Chemistry, vol. 136, pp. 401–412. Kluwer, Amsterdam (2003)
29. Le Bihan, N., Sangwine, S.J.: Quaternion principal component analysis of color images. In: Proc. of International Conference on Image Processing (ICIP'03), vol. 1, pp. 809–812 (2003)
30. Matheron, G.: Les treillis compacts. Technical Report—Paris School of Mines, N-23/90/G, November (1990)
31. Meyer, F.: Constrast features extraction. In: Chermant (ed.) Quantitative Analysis of Microstructures in Materials Science, Biology and Medecine, pp. 374–380. Riederer, Dordrecht (1977)
32. Meyer, F.: The levelings. In: Heijmans, Roerdink (eds.) Mathematical Morphology and Its Applications to Image and Signal Processing, Proc. of ISMM'98, pp. 199–206. Kluwer, Amsterdam (1998)
33. Meyer, F.: Alpha-beta flat zones, levelings and flattenings. In: Talbot, H., Beare, R. (eds.) Proceedings of ISMM'02, pp. 47–68, CSIRO Publishing (2002)
34. Meyer, F., Angulo, J.: Micro-viscous morphological operators. In: Mathematical Morphology and Its Applications to Signal and Image Processing (ISMM'07), pp. 165–176 (2007)
35. Meyer, F., Angulo, J.: Microviscosity micromorphology. To appear in Image Vis. Comput. (2010)
36. Pei, S.-C., Cheng, C.-M.: Color image processing by using binary quaternion-moment-preserving thresholding technique. IEEE Trans. Image Process., **8**(5), 614–628 (1999)
37. Pei, S.-C., Chang, J.-H., Ding, J.-J.: Quaternion matrix singular value decomposition and its applications for color image processing. In: Proc. of International Conference on Image Processing (ICIP'03), vol. 1, pp. 805–808 (2003)
38. Ronse, C., Heijmans, H.J.A.M.: The algebraic basis of mathematical morphology—Part II: Openings and closings. CVGIP, Image Underst. **54**, 74–97 (1991)
39. Sangwine, S.J.: Fourier transforms of colour images using quaternion, or hypercomplex, numbers. Electron. Lett. **32**(21), 1979–1980 (1996)
40. Sangwine, S.J.: Colour image edge detector based on quaternion convolution. Electron. Lett. **34**(10), 969–971 (1998)
41. Sangwine, S.J., Ell, T.A.: Mathematical approaches to linear vector filtering of colour images. In: Proc. of European Conference on Colour in Graphics, Imaging and Vision (CGIV'02), pp. 348–351 (2002)
42. Serra, J.: Image Analysis and Mathematical Morphology, vol I. Academic Press, London (1982)
43. Serra, J.: Image Analysis and Mathematical Morphology, vol II: Theoretical Advances. Academic Press, London (1988)
44. Serra, J.: Anamorphoses function lattices (multivalued morphology). In: Dougherty (ed.) Mathematical Morphology in Image Processing, pp. 483–523. Dekker, New York (1992)

45. Serra, J.: Viscous lattices. J. Math. Imaging Vis., **22**(2–3), 269–282 (2005)
46. Shi, L., Funt, B.: Quaternion color texture segmentation. Comput. Vis. Image Underst. **107**(1–2), 88–96 (2007)
47. Sochen, N., Zeevi, Y.Y.: Representation of colored images by manifolds embedded in higher dimensional non-Euclidean space. In: Proc. of International Conference on Image Processing (ICIP'98), vol. 1, pp. 166–170 (1998)
48. Sochen, N., Kimmel, R., Malladi, R.: A general framework for low level vision. IEEE Trans. Image Process. **7**(3), 310–318 (1998)
49. Sofou, A., Evangelopoulos, G., Maragos, P.: Coupled geometric and texture PDE-based segmentation. In: Proc. of IEEE International Conference on Image Processing (ICIP'05), vol. II, pp. 650–653 (2005)
50. Soille, P.: Morphological Image Analysis. Springer, Berlin (1999)
51. Vachier, C., Meyer, F.: The viscous watershed transform. J. Math. Imaging Vis. **22**(2–3), 251–267 (2005)
52. Vachier, C., Meyer, F.: News from viscousland. In: Proc. of International Symposium on Mathematical Morphology (ISMM'07), pp. 189–200 (2007)
53. van Vliet, L.J., Young, I.T., Beckers, G.L.: A nonlinear operator as edge detector in Noisy images. Comput. Vis. Graph. Image Process. **45**, 167–195 (1989)
54. Verdu, R., Angulo, J., Serra, J.: Anisotropic morphological filters with spatially-variant structuring elements based on image-dependent gradient fields. IEEE Trans. Image Process. **20**(1), 200–212 (2011)
55. Vincent, L.: Morphological grayscale reconstruction in image analysis: applications and efficient algorithms. IEEE Trans. Image Process. **2**(2), 176–201 (1993)
56. Yuille, A., Vincent, L., Geiger, D.: Statistical morphology. In: Proc. of SPIE Image Algebra and Morphological Image Processing II. SPIE, vol. 1568, pp. 271–282 (1991)
57. Zang, D., Sommer, G.: Signal modeling for two-dimensional image structures. J. Vis. Commun. Image Represent., **18**, 81–99 (2007)
58. Zingman, I., Meir, R., El-Yaniv, R.: Size-density spectra and their application to image classification. Pattern Recognit. **40**(12), 3336–3348 (2007)

Jesús Angulo received a degree in Telecommunications Engineering from Polytechnical University of Valencia, Spain, in 1999, with a Master Thesis on Image and Video Processing. He obtained his PhD in Mathematical Morphology and Image Processing, from the Ecole des Mines de Paris (France), in 2003, under the guidance of Prof. Jean Serra. He is currently a permanent researcher (ChargT de Recherche) in the Center of Mathematical Morphology (Department of Mathematics and Systems) at MINES ParisTech. His research interests are in the areas of multivariate image processing (colour, hyper/multi-spectral, temporal series, tensor imaging) and mathematical morphology (filtering, segmentation, shape and texture analysis, stochastic approaches, geometry), and their application to the development of theoretically-sound and high-performance algorithms and software in the Biomedicine/Biotechnology, Remote Sensing and Industrial Vision.

13.6 Publication VI : J. Angulo, D. Jeulin. "Stochastic watershed segmentation", In *Proc. of the 8th International Symposium on Mathematical Morphology (ISMM'2007)*, Rio de Janeiro, Brazil, October 2007. p. 265–276, MCT/INPE, 2007.

Stochastic watershed segmentation

Jesús Angulo and Dominique Jeulin

Centre de Morphologie Mathématique, Ecole des Mines de Paris, 35, rue Saint-Honoré, 77305 Fontainebleau, France
jesus.angulo,dominique.jeulin@ensmp.fr

Abstract This paper introduces a watershed-based stochastic segmentation methodology. The approach is based on using M realizations of N random markers to build a probability density function (pdf) of contours which is then segmented by volumic watershed for defining the R most significant regions. It over-performs the standard watershed algorithms when the aim is to segment complex images into a few regions. Three variants of the random germs framework are discussed, according to the algorithm used to build the pdf: 1) uniform random germs on the same gradient, 2) regionalised random germs on the same gradient, and 3) uniform random germs on levelled-based gradient. The last algorithm is more complex but it yields the best results.

Keywords: watershed transformation, leveling, Poisson points, density of contours, random germs segmentation.

1. Introduction

Watershed transformation is one of the most powerful tools for image segmentation. Starting from a gradient, the classical paradigm of watershed segmentation consists in determining markers for each region of interest. The markers avoid the over-segmentation (a region is associated to each minimum of the function) and moreover, the watershed is relatively robust to marker position [2]. The markers-based watershed is appropriate for interactive segmentation. Several watershed-based hierarchical approaches allow addressing fields where the markers cannot be easily defined (e.g. multimedia applications). Mainly, two hierarchical techniques can be distinguished: 1) non-parametric waterfalls algorithm [3] and 2) hierarchies based on extinction values, which allows to select the minima used in the watershed according to morphological criteria (dynamics, surface area and volume) [9, 15].

The volume-based hierarchical segmentation is particularly useful in many applications aiming at segmenting natural images since the volume, which combines the criteria of dynamics and area, selects the most significant regions from a visual viewpoint. However, the performance of the approach decreases drastically when the image is segmented in very few regions, which is just the goal of several applications (e.g., segmentation-based

image indexing). Figure 1 gives four colour images segmented by volumic watershed into $R = 10$, 20 and 50 regions and we can observe that many important regions are not well determined (even when $R = 50$). The classical solution involves to filter out the image in order to simplify the details and to enhance the main regions (typically using morphological filters such as levelings [10]).

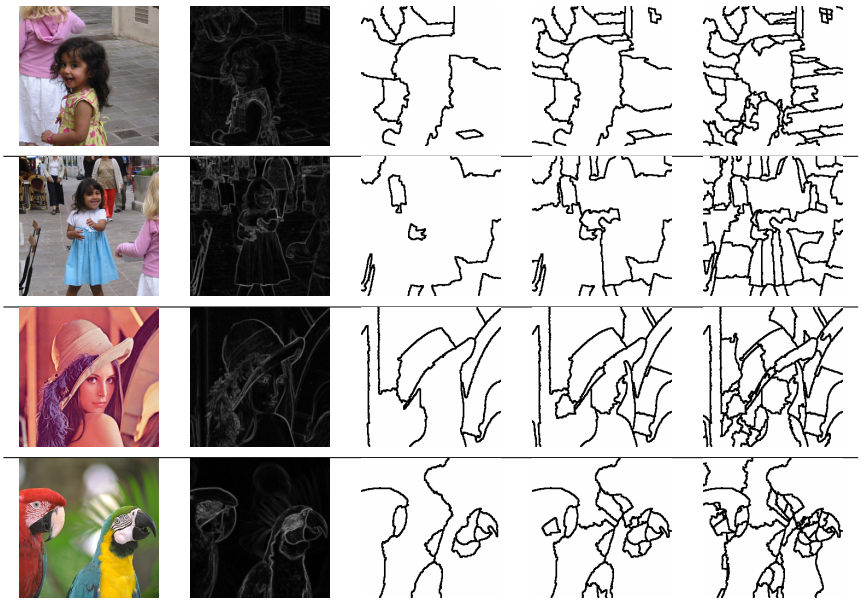

Figure 1. Examples of colour images segmented by means of volumic watershed into the R most significant regions. First column, original images $\mathbf{f}$; second column, colour gradient $\varrho^{LS+H}(\mathbf{f})$; third column, $sg^{R-vol}(\varrho^{LS+H}(\mathbf{f}), 10)$; fourth column $sg^{R-vol}(\varrho^{LS+H}(\mathbf{f}), 20)$, and last column $sg^{R-vol}(\varrho^{LS+H}(\mathbf{f}), 50)$.

In fact, the problem lies in the deterministic criterion of volume, computed for each minimum of the function to flood, which depends on the local image information; and nevertheless, the final flooding watershed is a competition between the different minima to determine the optimal partition (in fact, it is the solution of shortest path problem when the path cost is given by the maximum of the arc weights in the path [9]). The aim of this paper is to introduce a watershed-based probabilistic framework to detect the contours which are robust with respect to variations in the segmentation conditions. More precisely, we explore here a stochastic approach based on using random markers to build a probability density function of contours which is then segmented by volumic watershed for defining the most significant regions. Keeping in mind that the goal is the unsupervised segmentation of natural images in very few regions.

The probabilistic segmentation has been already studied in the literature, for instance using cooccurrence probability on graphs [5], Bayesian framework [16], Markov Random Fields [7] (combined with watershed segmentation [8]), Markov Chain Monte Carlo [14]. But to our knowledge, this is first study of probabilistic segmentation based on random markers simulations for watershed transformation. The closest previous work to our study is [13], where the sum of watersheds from a series of polarimetric images was used to define a final distribution of contours.

2. Basic notions and operators

Watershed segmentation. The function used in the watershed transformation is the image gradient. In this paper, the aim is to segment colour images and hence, according to our previous works [1], we propose to compute a colour gradient in a luminance/saturation/hue (LSH) representation, presenting better performances that other colour gradients. But any other colour gradient can be also used, including for instance marginal gradients in RGB. Let $\mathbf{f}(x) = (f_L(x), f_S(x), f_H(x))$ be a colour image in the LSH representation, the colour gradient is given by $\varrho^{LS+H}(\mathbf{f}(\mathbf{x})) = f_S(x) \times \varrho^{\circ}(f_H(x)) + (1 - f_S(x)) \times \varrho(f_L(x)) + \varrho(f_S(x))$, where $\varrho(g(x))$ is the morphological gradient of the scalar function $g(x)$ and $\varrho^{\circ}(a(x))$ is the circular centred gradient of the angular function $a(x)$.

Two watershed algorithms are used in this study. Let $mrk(x)$ be the image of markers, the binary image of segmentation contours associated to these markers, and according the colour gradient $\varrho^{LS+H}(\mathbf{f}(x))$, is denoted by $sg^{mrk}(\varrho^{LS+H}(x))$. Using the same gradient, the volumic-based segmentation into R regions is named $sg^{R-vol}(\varrho^{LS+H}(x))$.

Leveling. The leveling $\lambda(mrk, f)$ of a reference function f and a marker function mrk ($f(x)$ and $mrk(x)$ are two grey level images) can be computed by means of an iterative algorithm with geodesic dilations/erosions [10]. Several extensions to colour images have been proposed for levelings. We propose for this study to apply a marginal approach in RGB, which consists in computing a separated leveling for each red/green/blue colour component, i.e. the colour leveling of image $\mathbf{f}(x) = (f_R(x), f_G(x), f_B(x))$ according to the markers $mrk(x)$ is the colour image $\lambda(\mathbf{f}, mrk) = (\lambda(mrk, f_R), \lambda(mrk, f_G), \lambda(mrk, f_G))$. The marginal approach introduces false colour but this is not critical for segmentation purposes.

Generation of random germs. The paradigm of watershed segmentation lays on the appropriate choice of markers, which are the seeds to generate basins of attraction [2, 3]. It is claimed, and known from practice, that the most intelligent part of this technique of segmentation resides in the development of criteria used to select the required markers. In the present approach, we follow an opposite direction, by selecting random germs for markers. This arbitrary choice will be balanced by the use of a given number M of realizations, in order to filter out non significant fluctuations.

A rather natural way to introduce random germs [12] is to generate realizations of a Poisson point process with a constant intensity (namely average number of points per unit area) θ. It is well known that the random number of points N falling in a domain D with area $|D|$ follows a Poisson distribution with parameter $\theta\,|D|$. In addition, conditionally to the fact that $N = n$, the n points are independently and uniformly distributed over D. In what follows, we will fix the value N of the number of random germs (instead of using a random number as for the Poisson point process), and we will generate independent realizations of the location of the germs in D. In some cases, as will be illustrated below, it may be interesting to generate a non-uniform distribution of germs, with a regionalised intensity (or measure) $\theta(x)$. In the Poisson case, N follows a Poisson distribution with parameter $\theta(D)$, and conditionally to the fact that $N = n$, the n points are independently distributed over D with the probability density function $\theta(x)/\theta(D)$. In what follows, the intensity $\theta(x)$ will be generated from the image, and we will use a fixed number of germs N, as for the homogeneous case.

Parzen method to calculate a pdf. The kernel density estimation, or Parzen window method [6], is a way of estimating the probability density function (pdf) of a random variable. Let $\mathbf{x}_1$,$\mathbf{x}_2$, $\cdots$, $\mathbf{x}_M \in \mathbb{R}^n$ be M samples of a random variable, the kernel density approximation of its pdf is: $\hat{f}_h(\mathbf{x}) = \frac{1}{Nh}\sum_{i=1}^{N} K(\frac{\mathbf{x}-\mathbf{x}_i}{h})$, where $K(\mathbf{x})$ is some kernel and the bandwidth h a smoothing parameter. Usually, $K(x)$ is taken to be a Gaussian function with mean zero and variance σ^2, which determines the smoothing effect.

3. Uniform random germs segmentation

Let $\{mrk_i(x)\}_{i=1}^{M}$ be a series of M realizations of N uniform random markers. Each one of these binary images of points is considered as the markers for a watershed segmentation of colour gradient $sg^{mrk}(\varrho^{LS+H}(x))$ and consequently, a series of segmentations is obtained, i.e., $\{sg_i^{mrk}(x)\}_{i=1}^{M}$, see Figure 2. Note that the number of points determines the number of regions obtained (i.e., essential property of watershed transformation). As we can observe from the example, the main contours appear regardless of the position of germs.

Starting from the M realizations of contours, the probability density function of contours is computed by Parzen window method. The smoothing effect of the Gaussian kernel (typically $\sigma = 3$) is important to obtain a function where closed contours (e.g., in textured regions or associated to small regions) are added together. The $pdf(x)$ could be thresholded in order to obtain the most prominent contours, however the result are only pieces of contours (not enclosing regions). In addition, we have studied the histograms for several examples and there is not an optimal threshold to separate the classes of contours.

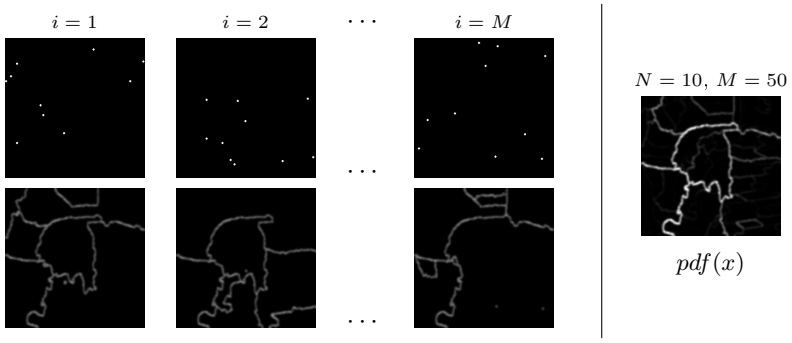

Figure 2. Left, M realizations of N uniform random germs, $mrk_i(x)$, and corresponding marker-based watershed contours, $sg_i^{mrk}(x)$. Right, probability density function of contours computed by Parzen window method for $N = 10$ and $M = 50$.

The main drawback of using a uniform distribution of the random markers is to induce an over-segmentation of the largest watersheds, since the average number of germs falling in a given region is proportional to its area. This is avoided by means of a volume-watershed segmentation, or by using a regionalised intensity of germs, as illustrated later. We propose to partition the $pdf(x)$ of contours with the volume-based watershed to obtain the R most significant regions, i.e., $sg^{R-vol}(pdf(x), R)$. Each catchment basin (each minima) of $pdf(x)$ corresponds to one the regions of the sum (or union) of the different $sg_i^{mrk}(x)$ and the integral of each catchment basin corresponds to the probability to be region of the segmentation. Consequently, the volumic watershed of $pdf(x)$ yields the regions according to their probabilities. In Figure 3 is given a comparison of segmentation into $R = 10$, 20 and 50 regions for two different $pdf(x)$. The results should be compared with those associated to $sg^{R-vol}(\varrho^{LS+H}(x), R)$ (see Figure 1). A property of the Gaussian filter, observed from the examples, is the regularisation of $pdf(x)$ which involves relatively rounded watershed contours.

3.1 Influence of parameters N and M

From the examples of Figure 1 and other similar results, we state that the method hardly depends on the number of realizations M, which is a good characteristic to guarantee its robustness. In practice, we have verified that the $pdf(x)$ converges to a stable distribution of contours even for low values of M (20 or 50). We propose in any case, to take a higher value, typically $M = 100$ or 200 in order to obtain more regular contours.

The random points explore uniformly the image space and the choice of N is important to fix the degree of stochastic sampling (note that the probability depends on the ratio between N and the image size or number of

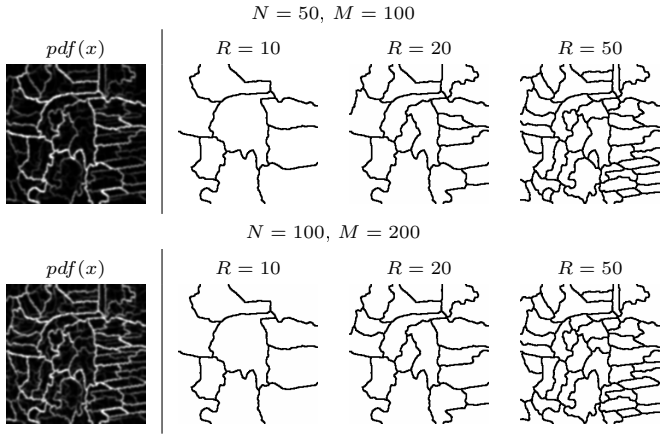

Figure 3. Left, probability density function of contours, $pdf(x)$ for N unifom germs and M realizations. Right, volumic watershed-based segmentation of $pdf(x)$ into the R most significant regions, $sg^{R-vol}(pdf), R)$.

pixels). Moreover, if the value of N is low, a segmentation into large regions is privileged; instead of a high value of N will produce smaller regions. If N is too high, the over-segmentation of sg_i^{mrk} leads to a very smooth $pdf(x)$, which loss its property for selecting the R contours. In fact, we can conclude that the uniform germs segmentation is mainly depending on parameter N which is related to R (number of regions to be determined) and it is logical to take $N > R$. But again, the method is quite robust to the choice of N: from the examples of images of size 256×256 to be segmented into $R = 10$, 20 or 50 the choice of $N = 50$ or 100 produces exactly the same results.

3.2 Probabilistic gradient

The function $pdf(x)$ can be combined with the initial gradient in order to reinforce the gradient contours which have a high probability: $\rho(x) = \omega_1 \varrho^{LS+H}(\mathbf{f}(x)) + \omega_2 pdf(x)$, considering a typical barycentric combination (both functions defined in $[0, 1]$), i.e., $\omega_1 = (1 - \lambda)$ and $\omega_2 = \lambda$.

We have studied the behaviour of $\rho(x)$ for volumic segmentation, i.e., $sg^{R-vol}(\rho(x))$, with respect to the value of control λ (note that for $\lambda = 0$ the gradient is obtained and for $\lambda = 1$, exclusively the probability density function of contours). In Figure 4 is shown an example of segmentation into 20 regions for different λ. It is observed that, even for low values of λ, the results of segmentation are notably improved. This is coherent with the fact that the $pdf(x)$, derived from the gradient, contains all the useful information for the segmentation. In any case, we have confirmed on the basis of many other examples that when $\lambda = 0,5$ (averaged combination)

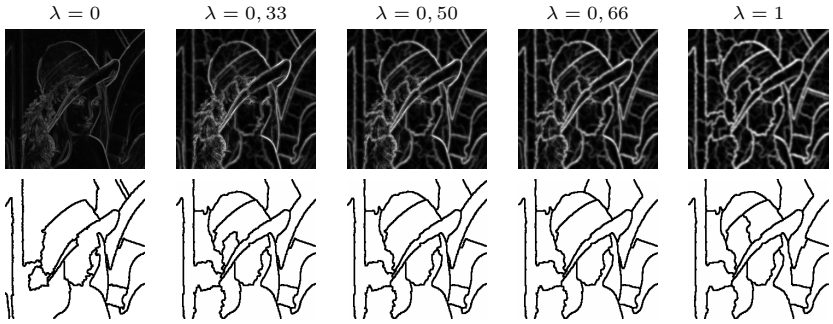

Figure 4. First row, probabilistic gradient $\rho(x)$ (i.e., linear combination of colour gradient and pdf) for different values of λ and second row, associated volumic watershed-based segmentation into $R = 20$ regions.

the results are in general more satisfactory.

4. Regionalised random germs segmentation

In the previous algorithm, the random germs are uniformly distributed in the image domain. We have also studied how a regionalised distribution of germs could be used to build the distribution of contours. The first question to deal with is the choice of the regionalisation function $\theta(x)$.

Several alternatives are possible. We can for instance use the component of luminance $\theta(x) = f_L(x)$ (respectively, the negative of luminance $\theta(x) = f_L^c(x)$), in such a way that the bright regions (respectively, the dark regions) will produce random germs. It is evident that this kind of regionalisation is not very useful for segmentation. It seems more natural to work on the colour gradient, $\theta(x) = \varrho^{LS+H}(x)$. In this case, the germs of $mrk_i^\theta(x)$ are located around the zones of high gradient value, that is the zones closed to the contours. Once the series of M contours $sg_i^{mrk^\theta}(x)$ is computed, the corresponding probability density of contours $pdf^\theta(x)$ is obtained by the Parzen window method. As previously, this function is finally segmented by volume-based watershed, see the example of Figure 5. The regionalised segmentation depends on the properties of dynamics of colour gradient. Moreover, the different random point realizations using the same $\theta(x)$ are quite similar and consequently, the realizations of contours too. By this regionalised sampling, another characteristic of the obtained $pdf^\theta(x)$ is that the distribution is very similar to the gradient, but where all the contours are enhanced. The final results of segmentation for $sg^{R-vol}(pdf^\theta, R)$ are in any case better than for $sg^{R-vol}(\varrho^{LS+H}, R)$. We have also evaluated the interest of $\theta(x)$ equal to the negative of the gradient (i.e., locating germs in low gradient zones); however in this case too many germs are introduced in

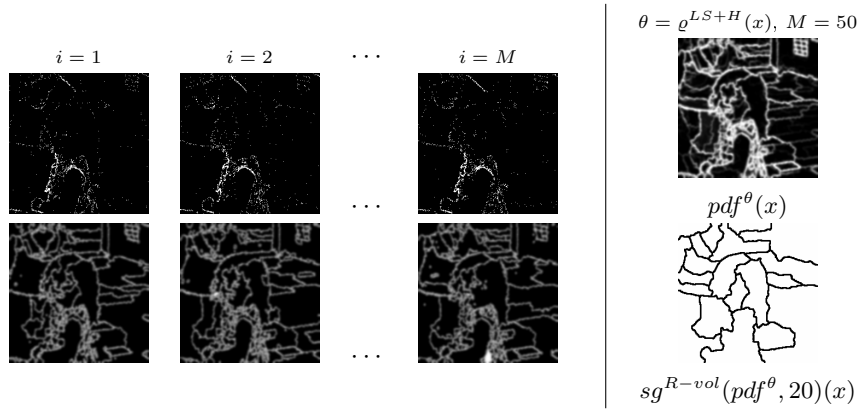

Figure 5. Left, M realizations of regionalised random germs (the function of regionalisation is the colour gradient $\theta = \varrho^{LS+H}$), $mrk_i(x)$, and corresponding marker-based watershed contours, $sg_i^{mrk^{\theta}}(x)$. Right, probability density function of contours computed by Parzen window method for $M = 50$, and segmentation of $pdf^{\theta}(x)$ into $R = 20$ volumic regions.

each realization and the over-segmentation involves useless pdf's.

5. Uniform random germs leveling and segmentation

The morphological connected filters suppress details but preserve the contours of the remaining objects. Levelings are a subclass of symmetric connected operators which are very useful to simplify an image before segmentation by watershed transformation [10]. In fact, the image marker for the leveling is a rough simplification of original image. Pushing our approach to the limit, the rationale behind the last variant of the proposed stochastic segmentation is based on using the random germs as markers before for the leveling, in order to obtain a very simplified gradient on which is computed the watershed with the same markers.

The steps of this algorithm are summarised as follows (see Figure 6),

- To throw the M realizations of N uniform random germs: $\{mrk_i(x)\}_{i=1}^{M}$.
- To compute the leveling for the colour image associated to each image of germs: $\mathbf{lev}_i(x) = \lambda(\mathbf{f}, mrk_i)$.
- To calculate the series of colour gradients associated to the leveled colour image: $\varrho_i(x) = \varrho_i^{LS+H}(\mathbf{lev}_i)$.
- Each colour gradient ϱ_i is segmented with the markers mrk_i: $sg_i^{lev-mrk}(x) = sg^{mrk_i}(\varrho_i)$.

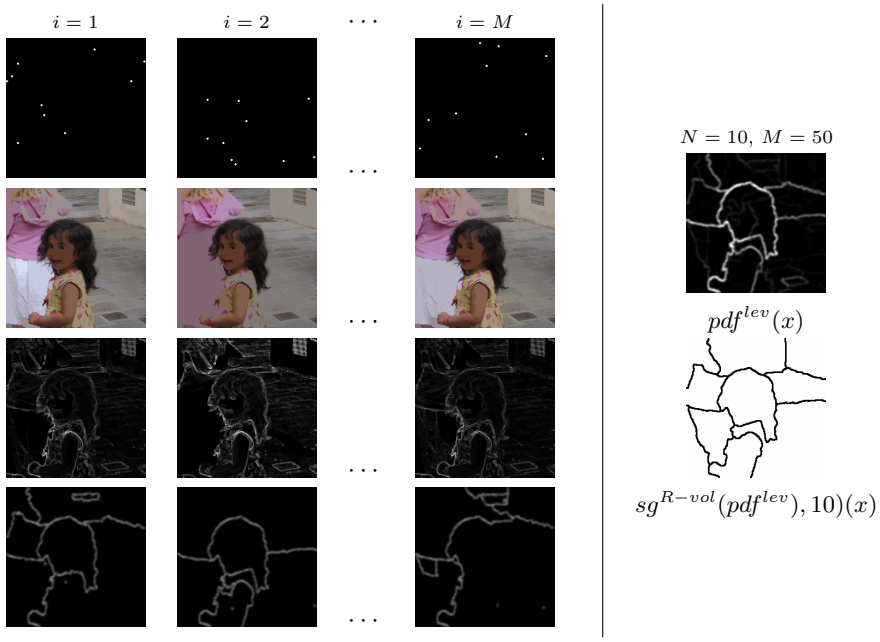

Figure 6. Left, M realizations of N uniform random germs, $mrk_i(x)$, marginal colour levelings using the random germs as markers, $lev_i(x)$, associated colour gradients, $\varrho_i(x)$ and corresponding marker-based watershed contours, $sg_i^{lev-mrk}(x)$. Right, probability density function of contours computed by Parzen window method for $N = 10$ and $M = 50$, and segmentation of $pdf^{lev}(x)$ into $R = 10$ volumic regions.

- To obtain the probability density function of contours: $pdf^{lev}(x) = \frac{1}{M}\sum_{i=1}^{M} sg_i^{lev-mrk} * G_\sigma$.

- Let $\widehat{\varrho}(x) = \frac{1}{M}\sum_{i=1}^{M} \varrho_i(x)$ be the averaged colour gradient for the M realizations, to compute the leveling-based probabilistic gradient which is defined as follows: $\rho^{lev}(x) = (1-\lambda)\widehat{\varrho}(x) + \lambda pdf^{lev}(x)$ (typ. $\lambda = 0.5$).

- To segment by volumic watershed into R regions the function of contours $sg^{R-vol}(pdf(x))$ (or the probabilistic gradient $sg^{R-vol}(\rho^{lev}(x))$).

Figure 7 shows a final comparison with examples of colour images segmented by volumic watershed ($R = 10$, 20 and 50) on probabilistic gradient $\rho(x)$ and on leveling-based probabilistic gradient $\rho^{lev}(x)$ (both with $\lambda = 0.5$). These results should be compared with those of Figure 1. It is evident that the stochastic algorithms proposed in this study yields to

better segmentations than the standard watershed. It is observed also that the last method including levelings results in very good image partitions.

6. Implementation issues

The M realizations of uniform/regionalised random germs contours are obtained from the same function (i.e., colour gradient) using different markers. Consequently, working on the neighbourhood graph of catchment basins and its minimum spanning tree (MST) [11], the N random markers can be considered as N random nodes of the MST instead of N image points. Two main advantages are associated to the graph implementation: firstly, a fast computation of M segmentations from different markers on the same MST; and secondly, the control of watershed bias which could be associated to the random positions of markers [4].

The algorithm using the uniform random germs as markers, first for the levelling and then for the watershed has an upper computational load (time of computation). Moreover, in each realization, the gradient is different (i.e., a different graph) and therefore the MST cannot be reused. In any case, nowadays using the fast implementations of watershed algorithms (100 ms for a 256×256 images running on a current standard Laptop), the time of execution to segment a colour image according our stochastic framework is around 10 s.

7. Discussion and conclusions

We have introduced in this paper a new morphological stochastic segmentation approach which improves the standard watershed algorithms when the aim is to segment complex images into a few regions. The improvement in the segmentation is less important for images presenting specific objects on a homogenous background. We have illustrated three variants of the random germs framework, according to the algorithm used to build the probability density of contours: uniform random germs on the same gradient, regionalised random germs on the same gradient and uniform random germs on levelled-based gradient. The last algorithm is more complex but it yields the best results.

In ongoing research, we consider to explore other variants using evolved random point simulations (structural grids, conditional models, etc.), working on a multi-scale framework (image pyramids and image decompositions). We are also working on probabilistic approaches combining colour gradients and texture information. In the last case, probabilistic rules of aggregation in the construction of the watersheds from the random seeds would introduce a second level of randomness in the segmentation process.

From a fundamental viewpoint, the idea behind our approach is that there are two types of contours associated to the watershed of a gradient:

1st order contours, which correspond to "significant" regions and which are relatively independent from markers; and *2nd order contours*, associated to "small", "low contrasted" or "textured" regions and which depend strongly on the place of markers. Our probabilistic framework aims at enhancing the 1st order contours from a sampling effect, to improve the result of watershed. It should be interesting to study if it is possible to determine by deterministic methods the type of each contour present in an image.

References

[1] J. Angulo and J. Serra, *Modelling and Segmentation of Colour Images in Polar Representations*, Image Vision and Computing **25** (2007), no. 4, 475–495.

[2] S. Beucher and F. Meyer, *The Morphological Approach to Segmentation: The Watershed Transformation*, New York (1992), Mathematical Morphology in Image Processing, (E. Dougherty Ed.), pp. 433–481.

[3] S. Beucher, *Watershed, hierarchical segmentation and waterfall algorithm*, ISMM'94 (1994), Mathematical Morphology and its Applications to Image and Signal Processing, pp. 69–76.

[4] S. Beucher, *Algorithmes sans biais de Ligne de Partage des Eaux*, Ecole des Mines de Paris, Internal Note CMM, 34 p., Februry 2002.

[5] K. Cho and P. Meer, *Image Segmentation from Consensus Information*, Computer Vision and Image Understanding **68** (1996), no. 1, 72–89.

[6] R.O. Duda and P.E. Hart, *Pattern Classification and Scene Analysis*, Wiley, New York, 1973.

[7] S. Geman and D. Geman, *Stochastic Relaxation, Gibbs Distributions, and the Bayesian Restoration of Images*, IEEE Trans. on Pattern Analysis and Machine Intelligence **6** (1984), 721–741.

[8] V. Grau, A.U.J. Mewes, M. Alcañiz, R. Kikinis, and S.K. Warfield, *Improved Watershed Transform for Medical Image Segmentation Using Prior Information*, IEEE Trans. on Medical Imaging **23** (2004), 447–458.

[9] F. Meyer, *An Overview of Morphological Segmentation*, International Journal of Pattern Recognition and Artificial Intelligence **15** (2001), no. 7, 1089–1118.

[10] F. Meyer, *Levelings, Image Simplification Filters for Segmentation*, Journal of Mathematical Imaging and Vision **20** (2004), 59–72.

[11] F. Meyer, *Grey-weighted, ultrametric and lexicographic distances*, ISMM'05 (2005), Mathematical Morphology and its Applications to Image and Signal Processing, pp. 289–298.

[12] D. Jeulin, *Modèles morphologiques de structures aléatoires et de changement d'échelle*, Université Caen, Thèse Doctorat ès Sciences Physiques, 1991.

[13] J. Serra and M. Mlynarczuk, *Morphological merging of multidimensional data*, STERMAT'00 (2000), 6th International Conference Stereology and Image Analysis in Materials Science, pp. 385–390.

[14] Z. Tu and S.-C. Zhu, *Image Segmentation by Data-Driven Markov Chain Monte Carlo*, IEEE Trans. on Pattern Analysis and Machine Intelligence **24** (2002), 657–673.

[15] C. Vachier and F. Meyer, *Extinction value: a new measurement of persistence*, (1995), IEEE Workshop on Nonlinear Signal and Image Processing, pp. 254–257.

[16] K.L. Vincken, A.S.E. Koster, and M.A. Viergever, *Probabilistic Multiscale Image Segmentation*, IEEE Trans. on Pattern Analysis and Machine Intelligence **19** (1997), 109–120.

Figure 7. Examples of colour images segmented by means of volumic watershed into the R most significant regions ($R = 10$, 20 and 50) on probabilistic gradients $\rho(x)$ and $\rho^{lev}(x)$ (both with $\lambda = 0.5$) and derived from $pdf(x)$ and $pdf^{lev}(x)$ respectively (both for $N = 100$ and $M = 200$).

13.7 Publication VII : J. Angulo. "Generalised Morphological Image Diffusion". Submitted to *Computer Vision and Image Understanding*, 2011.

Generalised Morphological Image Diffusion

Jesús Angulo

CMM-Centre de Morphologie Mathématique,

Mathématiques et Systèmes, MINES ParisTech;

35, rue Saint-Honoré, 77305 Fontainebleau cedex - France

jesus.angulo@mines-paristech.fr

June 2011 *

Abstract

Relationships between linear and morphological scale-spaces have been considered by various previous works. The aim of this paper is to study how to generalise the diffusion-based approaches in order to introduce nonlinear filters whose effects mimic morphological dilation and erosion. A methodology based on the counter-harmonic mean is adopted here. Details of numerical implementation are discussed and results are provided to illustrate the behaviour of various studied cases: isotropic, nonlinear and coherence-enhancing diffusion. We also rediscover the classical link between Gaussian scale-space and dilation/erosion scale-spaces based on quadratic structuring functions.

Keywords: counter-harmonic mean, mathematical morphology, quadratic structuring function, image diffusion, nonlinear scale-space theory

*Submitted to CVIU. The first draft of this study was started in June 2010.

1 Introduction

Two fundamental paradigms of image filtering appear distinguished nowadays in the state-of-the-art. On the one hand, differential methods inspired from the (parabolic) heat equation, including isotropic diffusion [22], nonlinear diffusion [27, 11], anisotropic diffusion [35], etc. The main properties of these techniques are the appropriateness to deal with the notion of scale-space of image structures and the ability to process symmetrically the bright/dark image structures. Practical algorithms involve (local-adaptive) kernel convolution as well as PDE-formulation and subsequent numerical solutions. The interested reader should refer to basic references [13] and [34]. On the other hand, mathematical morphology operators [30, 32] which are formulated in terms of geometric notions as well as in terms of complete lattice theory. Morphological filters entail mainly the computation of supremum and infimum values in neighbourhoods (or structuring elements) which correspond respectively to the dilation and the erosion, the two basic operators. Morphological operators present also good scale-space properties [19, 4] but, by the natural duality of complete lattices, most operators appear by pairs and one acts on bright structures and the other one on dark structures. This latter property of asymmetry is in fact an advantage which allows defining evolved operators by product of a pair of dual ones. For instance, the opening (resp. closing) is obtained by the product of an erosion (resp. dilation) followed by a dilation (resp. erosion), then the product of openings and closings leads to the alternate filters and other families of morphological filters [30, 32]. Diffusion involves blurring image structures whereas morphological dilation and erosion involve enhancement of image structure transitions. In fact, morphological operators are related to geometric optics models and in particular to the (hyperbolic) eikonal

equation. Hence, there exists also a well motivated formulation of morphological operators using PDEs [1, 3, 8, 24]. This differential or continuous-scale morphology can be solved using numerical algorithms for curve evolution [29]. Thus multiscale flat dilation/erosion by disks as structuring elements (resp. unflat dilation/erosion by parabolic structuring functions) can be modelled in a continuous framework. Morphological operators using geometric structuring elements are today one of the most successful areas in image processing. However, it is obvious that the soundness and maturity of numerical methods to implement the different versions of image diffusion constitute an advantage against continuous morphology implementation, which requires more specific numerical schemas to achieve robust results [5, 7].

The aim of this paper is to study how to generalise the diffusion-based approaches in order to introduce nonlinear filters whose effects mimic morphological dilation and erosion. Or using other words, our goal is to propose a new approach of generalised morphological image diffusion based on standard numerical implementations.

Related work. Theoretical investigation of the relation between the scale-space concepts of linear and morphological scale spaces has been carried out by various studies. A parallelism between the role which plays the Fourier transform in the convolution with Gaussian kernels and the dilation using quadratic structuring function has been established using the notion of slope transform. More generally, the slope transform and its applications to morphological systems was developed independently and simultaneously by [12] and [23]. In [10] it was shown that the slope transform in the $(\max, +)$-algebra corresponds to the logarithmic multivariate Laplace transform in the $(+, \cdot)$-algebra; and that the Cramer transform as the Legendre-Fenchel transform of the logarithmic Laplace transform. It was studied in [14]

the structural similarities between linear and morphological processes in order to construct a one-parameter semi-linear process that incorporates Gaussian scale-space, and both types of morphological scale-spaces by quadratic structuring elements as limiting processes of a one-parameter transformation of grey-level values. More recently, it was proposed in [37] a morphological scale-space by deforming the algebraic operations related to Minkowski (or L^p) norms and generalised means, where the Gaussian scale-space is a limit case. We adopted here a different methodology in order to link diffusion-based image filtering and morphological image filtering. The starting point of our approach is the notion of counter-harmonic mean [9]. In fact, the idea of using the counter-harmonic mean for constructing robust morphological-like operators, without the notions of supremum and imfimum, was proposed in [33]. Our purpose in this paper is to go further and to exploit the counter-harmonic mean to propose a more general framework which can be exploited for the various algorithms of image diffusion.

Paper organisation. This paper is an extended and improved version of a conference contribution [2]. In particular, in the present manuscript, a complete proof of the different results and properties is given, as well as a more illustrative examples are included.

The outline of the paper is as follows. In the next section we review the notion of counter-harmonic mean. The appropriateness of counter-harmonic mean to approximate flat dilation/erosion is considered in Section 3. Section 4 introduces the novel counter-harmonic Gaussian scale-space, or counter-harmonic isotropic diffusion. The limit relationships with parabolic dilation/erosion as well as other theoretical properties are also considered in Section 4. Section 5 extends these investigations to the nonlinear diffusion, in particular to the

Perona and Malik model and to the Weickert model of coherence-enhanced diffusion. The paper is concluded with a summary and perspectives in Section 6.

2 Counter-Harmonic Mean (CHM)

Let us start by presenting the basic notion of this paper.

Definition 1 *Let* $\mathbf{a} = (a_1, a_2, \cdots, a_n)$ *and* $\mathbf{w} = (w_1, w_2, \cdots, w_n)$ *be real* $n-$*tuples, i.e.,* $\mathbf{a}, \mathbf{w} \in \mathbb{R}^n$. *If* $r \in \overline{\mathbb{R}}$ *then the* $r-$th counter-harmonic mean *(CHM) of* $\mathbf{a}$ *with weight* $\mathbf{w}$ *is given by [9]*

$$\mathfrak{K}^{[r]}(\mathbf{a};\mathbf{w}) = \begin{cases} \frac{\sum_{i=1}^n w_i a_i^r}{\sum_{i=1}^n w_i a_i^{r-1}} & \text{if } r \in \mathbb{R} \\ \max(a_i) & \text{if } r = +\infty \\ \min(a_i) & \text{if } r = -\infty \end{cases} \tag{1}$$

It will be denoted $\mathfrak{K}^{[r]}(\mathbf{a})$ the equal weight case. We notice that $\mathfrak{K}^{[1]}(\mathbf{a};\mathbf{w})$ is the weighted arithmetic mean and $\mathfrak{K}^{[0]}(\mathbf{a};\mathbf{w})$ is the weighted harmonic mean.

The following two properties are useful for the rest of the paper.

Proposition 2 *If* $1 \leq r \leq +\infty$ *then* $\mathfrak{K}^{[r]}(\mathbf{a};\mathbf{w}) \geq \mathfrak{M}^{[r]}(\mathbf{a};\mathbf{w})$*; and if* $-\infty \leq r \leq 1$ *then the following stronger results holds:* $\mathfrak{K}^{[r]}(\mathbf{a};\mathbf{w}) \leq \mathfrak{M}^{[r-1]}(\mathbf{a};\mathbf{w})$*; where* $\mathfrak{M}^{[r]}(\mathbf{a};\mathbf{w}) = \left(\frac{1}{W}\sum_{i=1}^n w_i a_i^r\right)^{1/r}$ *is the* $r-$*th power-mean, or* Minkowski weighted mean of order r*, defined for* $r \in \mathbb{R}^*$. *Inequalities are strict unless* $r = 1, +\infty, -\infty$ *or* $\mathbf{a}$ *is constant.*

Proposition 3 *If* $\mathbf{a}$ *and* $\mathbf{w}$ *are* $n-$*tuples and if* $-\infty \leq r \leq s \leq +\infty$ *then* $\mathfrak{K}^{[r]}(\mathbf{a};\mathbf{w}) \leq \mathfrak{K}^{[s]}(\mathbf{a};\mathbf{w})$*, with equality if and only if* $\mathbf{a}$ *is constant.*

Proofs of the results given above as well as other properties can be found in [9].

3 Robust Pseudo-Morphological Operators using CHM

The CHM has been considered in the state-of-the-art of image processing as an appropriate filter to deal with salt and pepper noise [15]. More precisely, let $v = f(x, y)$ be a grey-level image: $f : \Omega \to \mathcal{V}$. Typically, for digital 2D images, $(x, y) \in \Omega$ where $\Omega \subset \mathbb{Z}^2$ is the discrete support of the image. The pixel values are $v \in \mathcal{V} \subset \mathbb{Z}$ or $\mathbb{R}$, but for the sake of simplicity of our study, we consider that $\mathcal{V} = [0, 1]$.

Definition 4 *The CHM filter is obtained as*

$$\kappa_B^P(f)(x,y) = \frac{\sum_{(s,t)\in B(x,y)} f(s,t)^{P+1}}{\sum_{(s,t)\in B(x,y)} f(s,t)^{P}} = \mathfrak{K}^{[P+1]}(\{f(s,t)\}_{(s,t)\in B(x,y)}) \tag{2}$$

where $B(x, y)$ is the window of the filter, centered at point (x, y), i.e., the structuring element in the case of morphological operators.

This filter is well suited for reducing the effect of pepper noise for $P > 0$ and of salt noise for $P < 0$. In the pioneering paper [33], starting from the natural observation that morphological dilation and erosion are the limit cases of the CHM, i.e.,

$$\lim_{P\to+\infty} \kappa_B^P(f)(x,y) = \max_{(s,t)\in B(x,y)} (f(s,t)) = \delta_B(f)(x,y) \tag{3}$$

and

$$\lim_{P\to-\infty} \kappa_B^P(f)(x,y) = \min_{(s,t)\in B(x,y)} (f(s,t)) = \varepsilon_B(f)(x,y); \tag{4}$$

it was proposed to use the CHM to calculate robust nonlinear operators which approach the morphological ones but without using max and min operators. In addition, these operators

are more robust to outliers (i.e., to noise) and consequently they can be considered as an alternative to rank-based filters in the implementation of pseudo-morphological operators.

3.1 Comparison with Minkowski Power Means

It is easy to see that for $P \gg 0$ ($P \ll 0$) the pixels with largest (smallest) values in the local neighbourhood B will dominate the result of the weighted sum. Of course, in practice, the range of P is limited due to the precision in the computation of the floating point operations. Proposition 2 of the previous Section justifies theoretically the suitability of CHM with respect to the alternative approach by high-order Minkowski mean, as considered by Welk [37]. Let us illustrate empirically how both means converge to the supremum (resp. infimum) when positive P increases (negative P decreases). Fig. 1 depicts convergence with respect to the value of P for the erosion (in blue) and dilation (in red), using Minkowski mean in (a) and using CHM in (b). The convergence is measured as the average difference value between the CHM for each P and the exact dilation/erosion obtained by max and min. The curves correspond to the image results provided on the website [1], which includes other comparative examples of the methods discussed in the present paper. The practical advantage of CHM to approach morphological operators is obvious: even for $P = 100$ (or $P = -100$) the dilation (resp. erosion) is not reached for Minkowski mean whereas the error in the results for CHM is already negligible for $P = 20$ (resp. $P = -20$). We notice also in the empirical curves, as expected from Proposition 2, that the convergence to the erosion with $P \ll 0$ is faster than

[1] http://cmm.ensmp.fr/∼angulo/research/examplesPseudoMorphoDiffusions/examplesPseudoMorphoDiffusions.html

to the dilation with equivalent $P \gg 0$, i.e., for $P > 0$

$$|\kappa_B^P(f)(x,y) - \delta_B(f)(x,y)| \geq |\kappa_B^{-P}(f)(x,y) - \varepsilon_B(f)(x,y)|, \quad \forall (x,y) \in \Omega$$

3.2 Properties

The asymmetry involves that $\kappa_B^P(f)$ and $\kappa_B^{-P}(f)$ are not dual operators with respect to the complement, i.e., for $P > 0$

$$\kappa_B^P(f) \neq \complement \kappa_B^{-P}(\complement f)$$

with $\complement f = 1 - f$. In Fig. 1(c) are also given rates of convergence of CHM to the opening and closing using the product of $\kappa_B^P(f)$ and $\kappa_B^{-P}(f)$: results are extremely good already for values $P = 10$. As it was already pointed out in [33], the fundamental drawback of $\kappa_B^P(f)$ (resp. $\kappa_B^{-P}(f)$) is the fact that $f(x,y) \not\leq \kappa_B^P(f)(x,y)$ with $P > 0$ (resp. $f(x,y) \not\geq \kappa_B^{-P}(f)(x,y)$ with $P < 0$). Or in other words, the extensitivity (resp. anti-extensitivity) for $P > 0$ (resp. $P < 0$) is not guaranteed. However, according to proposition 3, the following ordering relationship holds for $P > 0$:

$$\kappa_B^{-P}(f)(x,y) \leq \kappa_B^P(f)(x,y).$$

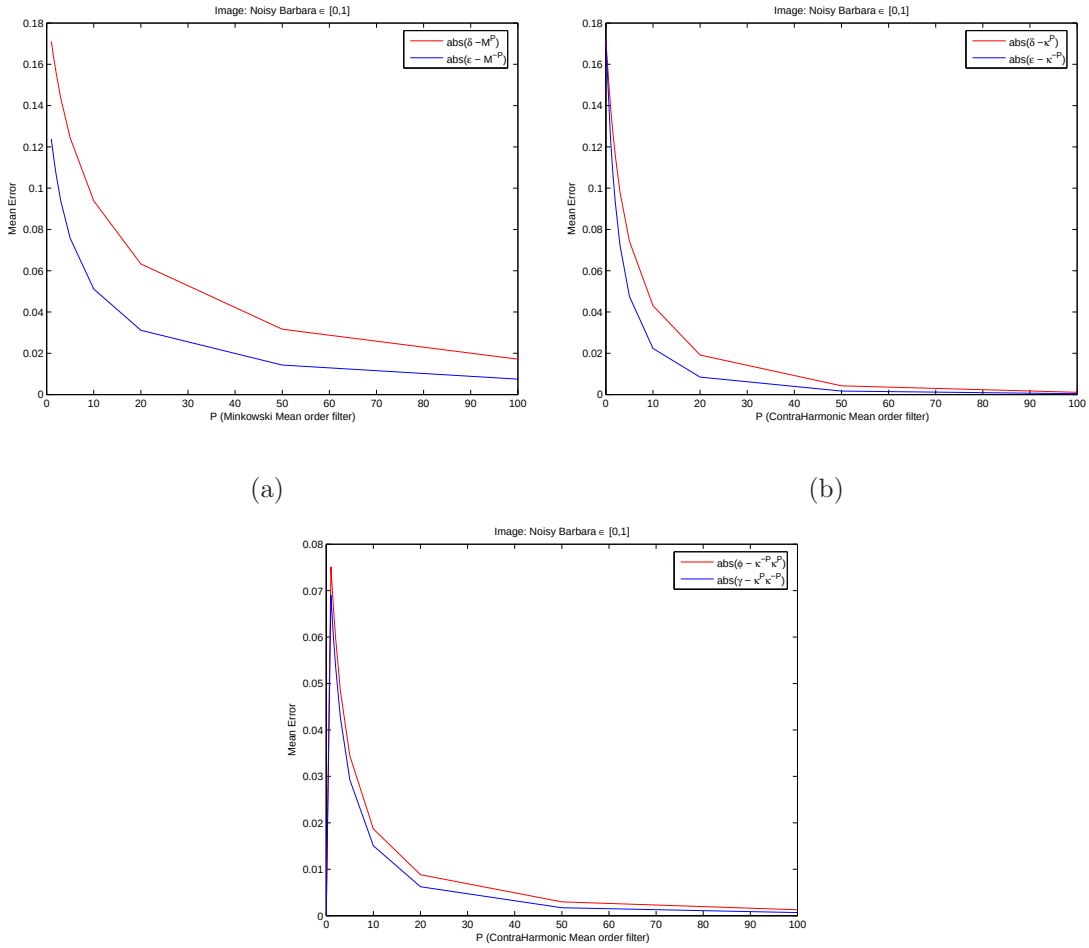

(a) (b)

(c)

Figure 1: Convergence with respect to P of nonlinear power means-based operators to morphological operators: (a) pseudo-dilation and pseudo-erosion using Minkowski mean, (b) pseudo-dilation and pseudo-erosion using Counter-Harmonic mean, (c) pseudo-opening and pseudo-closing using Counter-Harmonic mean.

4 Counter-Harmonic Gaussian Scale-Space

Canonic multiscale image analysis involves obtaining the multiscale linear convolutions of the original image:

$$\psi(f)(x,y;t) = (f * K_\sigma)(x,y) = \int_\Omega f(u,v)K_\sigma(x-u,y-v)dudv, \tag{5}$$

where K_σ is the two-dimensional Gaussian function $K_\sigma(x,y) = \frac{1}{2\pi\sigma^2}\exp\left(\frac{-(x^2+y^2)}{2\sigma^2}\right)$, whose variance (or width) σ^2 is proportional to the scale t; i.e., $\sigma^2 = 2t$. Larger values of t lead to simpler image representations.

We can define according to our paradigm the following generalised morphological scale-space.

Definition 5 *The counter-harmonic Gaussian scale-space of order P is defined as*

$$\eta(f)(x,y;t;P) = \frac{(f^{P+1} * K_{\sqrt{2t}})(x,y)}{(f^P * K_{\sqrt{2t}})(x,y)} = \frac{\int_E f(u,v)^{P+1}K_{\sqrt{2t}}(x-u,y-v)dudv}{\int_E f(u,v)^P K_{\sqrt{2t}}(x-u,y-v)dudv}. \tag{6}$$

By choosing $P > 0$ (resp. $P < 0$), $\eta(f)(x,y;t;P)$ leads to a scale-space of pseudo-dilations (resp. pseudo-erosions), whose filtering effects for a given scale t depend on the "nonlinearity order" of P, which skew the Gaussian weighted values towards the supremum or infimum value.

Fig. 2 depicts a comparative example of image filtering using the CHM Gaussian scale-space for a fixed t and variable P. The terminology of "pseudo-dilation", or more generally "pseudo-morphological operators" is probably inappropriate: so many operators have been published as pseudo-morphological ones, without relation with the present approach. However, due to the fact that the nonlinear filter $\eta(f)(x,y;t;P)$ for $P > 0$ (resp. $P < 0$) is not

extensive (resp. anti-extensive) and does not commute with the supremum (resp. with the infimum), it cannot be considered *stricto sensu* as a dilation (resp. erosion). We notice also that, for a fixed value of the nonlinear parameter P, the associated CHM Gaussian scale-space for a variable scale t leads to families of multi-scale pseudo-dilations/-erosions.

4.1 Limit statements

We know that $\eta(f)(x,y;t;P=+\infty) = \delta_B(f)(x,y)$ and $\eta(f)(x,y;t;P=-\infty) = \varepsilon_B(f)(x,y)$, i.e., flat dilation and flat erosion, where B is the square support of the kernel $\sigma = \sqrt{2t}$. Let us consider in detail the limit cases for $P \uparrow\uparrow$ and $P \downarrow\downarrow$.

Proposition 6 *For a given scale parameter t, the limits of $\eta(f)(x,y;t;P)$ with respect to P exist and are given by*

$$\lim_{P\to+\infty} \eta(f)(x,y;t;P) = \sup_{(u,v)\in\Omega} \left(f(x-u,y-v) - \frac{(u^2+v^2)}{2P(2t)} \right), \tag{7}$$

$$\lim_{P\to-\infty} \eta(f)(x,y;t;P) = \inf_{(u,v)\in\Omega} \left(f(x-u,y-v) + \frac{(u^2+v^2)}{2P(2t)} \right), \tag{8}$$

which can be interpreted respectively as the dilation and the erosion of $f(x,y)$ with a quadratic structuring function

$$b_{\sqrt{2t}}(x,y;P) = \frac{(x^2+y^2)}{2P(2t)},$$

i.e., the numerical dilation and erosion [30, 32] are defined by

$$(f \oplus b_{\sqrt{2t}})(x,y) = \sup_{(u,v)\in\Omega} \Big(f(x-u,y-v) - b_{\sqrt{2t}}(u,v) \Big),$$

$$(f \ominus b_{\sqrt{2t}})(x,y) = \inf_{(u,v)\in\Omega} \Big(f(x-u,y-v) + b_{\sqrt{2t}}(u,v) \Big).$$

Note that in these limiting cases the CHM framework involves a "normalization" by P of the original Gaussian kernel scale parameter during unlinearization, i.e., the nonlinear asymptotic scale parameter is $\widetilde{\sigma} = \sqrt{P}\sigma = \sqrt{P(2t)}$. This result is perfectly coherent with those obtained from totally different paradigms [37, 14]. Also, we notice again that for $P = +\infty$ the structuring function becomes flat and hence we obtain the flat dilation.

Proof. We only give the proof for the case $P \to +\infty$ since the case $P \to -\infty$ is exactly similar. By rewriting $f^P = \exp(P\log(f))$, taking first order Taylor expansion $\log(f) \approx f - 1$ and first order Taylor expansion of exponential function such that

$$\frac{N}{D} = \exp\left(\log\left(\frac{N}{D}\right)\right) \approx 1 + \log(N) - \log(D),$$

we have:

$$\begin{aligned}\lim_{P\to+\infty} \eta(f)(x,y;t;P) &= 1 + \log\int_\Omega \exp((P+1)[f(x-u,y-v) - \frac{(u^2+v^2)}{2(P+1)(2t)} - 1])dudv \\ &\quad - \log\int_\Omega \exp(P[f(x-u,y-v) - \frac{(u^2+v^2)}{2P(2t)} - 1])dudv,\end{aligned}$$

which can be rewritten as

$$\begin{aligned}&1 + (P+1)\log\left(\int_\Omega \left(\exp(f(x-u,y-v) - \frac{(u^2+v^2)}{2(P+1)(2t)} - 1)\right)^{(P+1)} dudv\right)^{\frac{1}{(P+1)}} \\ &-P\log\left(\int_\Omega \left(\exp(f(x-u,y-v) - \frac{(u^2+v^2)}{2P(2t)} - 1)\right)^{P} dudv\right)^{\frac{1}{P}},\end{aligned}$$

Using now the standard result

$$\lim_{P\to+\infty}\left\{\int_\Omega g^P(x)dx\right\}^{1/P} = \sup_{x\in\Omega} g(x),$$

which holds for positive and bounded function g with support space Ω, and and considering continuity and monotonicity of the logarithm, we obtain:

$$\begin{aligned}\lim_{P\to+\infty}\eta(f)(x,y;t;P) &= 1+(P+1)\sup_{(u,v)\in\Omega}(f(x-u,y-v)-\frac{(u^2+v^2)}{2(P+1)(2t)}-1)- \\ &\quad P\sup_{(u,v)\in\Omega}(f(x-u,y-v)-\frac{(u^2+v^2)}{2P(2t)}-1).\end{aligned}$$

By considering that both supremum operations gives closer values, i.e.,

$$\sup_{(u,v)\in\Omega}(f(x-u,y-v)-\frac{(u^2+v^2)}{2P(2t)}-1)\approx\sup_{(u,v)\in\Omega}(f(x-u,y-v)-\frac{(u^2+v^2)}{2(P+1)(2t)}-1),$$

we finally obtain the corresponding result. ■

4.2 Properties of CHM Gaussian Scale-Space

We discuss now in more detail several features of the double scale-space $\eta(f)(x,y;t;P)$.

4.2.1 Continuity

The generic kernel function $K_{\sqrt{2t}}(x,y)$ is a continuous function in $\mathbb{R}^2$.

Proposition 7 *The scale-space image $\eta(f)(x,y;t;P)$ is continuous for all $(x,y)\in\Omega$, for any $t\geq 0$ and for any $P\in\overline{\mathbb{R}}$.*

Proof. Consider $K_{\sqrt{2(t+\Delta t)}}(x+\Delta x,y+\Delta y)=K_{\sqrt{2t}}(x,y)+E(x,y)$ where assuming the continuity of $K(x,y)$, which implies the continuity of $K_{\sqrt{2t}}(x,y)$, we have

$$\lim_{\substack{|\Delta x|\to 0\\ |\Delta y|\to 0\\ \Delta t\to 0}} E(x,y)=0 \quad \text{for all } (x,y)\in\Omega \tag{9}$$

For $t > 0$, we have

$$\eta(f)(x+\Delta x, y+\Delta y; t+\Delta t; P) = \frac{\int_E f(x-u+\Delta x, y-v+\Delta y)^{P+1} K_{\sqrt{2(t+\Delta t)}}(u,v)dudv}{\int_E f(x-u+\Delta x, y-v+\Delta y)^{P} K_{\sqrt{2(t+\Delta t)}}(u,v)dudv}$$

Setting $w = u - \Delta x$ and $z = v - \Delta y$ we have

$$\begin{aligned}\eta(f)(x+\Delta x, y+\Delta y; t+\Delta t; P) &= \frac{\int_E f(x-w, y-z)^{P+1} K_{\sqrt{2(t+\Delta t)}}(w+\Delta x, z+\Delta y)dwdz}{\int_E f(x-w, y-z)^{P} K_{\sqrt{2(t+\Delta t)}}(w+\Delta x, z+\Delta y)dwdz} \\ &= \frac{\int_E f(x-w, y-z)^{P+1} \left(K_{\sqrt{2t}}(w,z) + E(w,z)\right) dwdz}{\int_E f(x-w, y-z)^{P} \left(K_{\sqrt{2t}}(w,z) + E(w,z)\right) dwdz}\end{aligned}$$

So, in the limit as $|\Delta x| \to 0$, $|\Delta y| \to 0$, $\Delta t \to 0$ and assuming that the expression (9) holds, hence

$$\eta(f)(x+\Delta x, y+\Delta y; t+\Delta t; P) \to \eta(f)(x, y; t; P)$$

establishing the continuity. ■

4.2.2 Ordering

We have the following property of ordering w.r.t. scale parameter t.

Proposition 8 *There exists a value of P such that for any $Q \geq P > 0$, we have that for any pair of ordered scales $0 < t_1 < t_2$ involves $\eta(f)(x, y; t_1; Q) \leq \eta(f)(x, y; t_2; Q)$. Similarly, there is a P such that for $R \leq P < 0$, if $0 < t_1 < t_2$ then $\eta(f)(x, y; t_1; R) \geq \eta(f)(x, y; t_2; R)$.*

Proof. If we consider that for a large enough $P > 0$, with $Q \geq P$ we have

$$\eta(f)(x, y; t_1; Q) = \sup_{(u,v)\in\Omega} \left(f(x-u, y-v) - \frac{(u^2+v^2)}{4Qt_1} \right)$$

and we have also for $0 < t_1 < t_2$: $\frac{(u^2+v^2)}{4Qt_2} < \frac{(u^2+v^2)}{4Qt_1}$, $\quad \forall (u,v) \in D$ where $D \subset \Omega$. Then we obtain

$$\sup_{(u,v)\in\Omega} \left(f(x-u, y-v) - \frac{(u^2+v^2)}{4Qt_1} \right) \leq \sup_{(u,v)\in\Omega} \left(f(x-u, y-v) - \frac{(u^2+v^2)}{4Qt_2} \right)$$

thus proving the proposition. Similarly, the proof can be obtained for $P < 0$ ■

Hence, the ordering properties associated to the spatial scale t appears only in the pseudo-morphological behaviour of the CHM for large enough $|P|$. The fundamental ordering relationship w.r.t. P is directly inherited from Proposition 3 of the CHM.

Proposition 9 *For any pair of nonlinearity orders $-\infty \leq R \leq S \leq +\infty$, we have*

$$\eta(f)(x, y; t; R) \leq \eta(f)(x, y; t; S)$$

for any $t \geq 0$, with equality for $t = 0$.

4.2.3 Dimensionality

Dimensionality is a fundamental concept in measurements. This principle was extended in [28] to image processing, in particular, in the framework of mathematical morphology, as a way to take into account the homogeneity of physical properties computed from images. Later, it was studied in [18] the case of nonflat scale-space mathematical morphology using elliptic poweroid structuring functions. Making a measurement on an image consists in applying a functional on the image, where a "functional" is a global parameter associated with a function. More precisely, a functional W on a function f is said to be dimensional if and only if exists constants k_1, k_2 such that for all λ_1, $\lambda_2 > 0$

$$W(f') = \lambda_1^{k_1} \lambda_2^{k_2} W(f)$$

where $f'(x,y) = \lambda_1 f(\lambda_2 x, \lambda_2 y)$ and where k_1 is the intensity dimension and k_2 the space dimension. Hence the parameter λ_1 accounts for the affinity along the gray tone axis and λ_2 for the homothety of the support space of image f. The relation $W(f')$ restricts the way in which affinities and homotheties of an image affect dimensional measurements on it and results in a decoupling between affinity and homothety measurements. We notice that if $k_1 = 0$ the functional W is invariant under intensity affinities and if $k_2 = 0$ involves invariance under homotheties. Let us consider under which conditions a dimensional functional of the CHM Gaussian scale-space is also a dimensional functional of the underlying image.

Let us define the transformed scale-space: $\lambda_1 \eta(f)(\lambda_2 x, \lambda_2 y; \lambda_3 t; \lambda_4 P)$, for any λ_1, λ_2, λ_3, $\lambda_4 > 0$.

Proposition 10 *A functional W of the nonlinear scale-space $\eta(f)(x,y;t;P)$ is dimensional if and only if $\lambda_2^2 = \lambda_3 \lambda_4$ and if $|P|$ is large enough or if $\lambda_2^2 = \lambda_3$ and $P = 0$. In such a case, there exist constants k_1 and k_2 and we have*

$$W\left(\eta(f')(x,y;t;P)\right) = \lambda_1^{k_1} \lambda_2^{k_2} W\left(\eta(f)(x,y;t;P)\right)$$

Proof. We start by writing

$$\lambda_1 \eta(f)(\lambda_2 x, \lambda_2 y; \lambda_3 t; \lambda_4 P) = \lambda_1 \frac{\int_E f(\lambda_2(x-u), \lambda_2(y-v))^{\lambda_4 P+1} K_{\sqrt{2\lambda_3 t}}(\lambda_2 u, \lambda_2 v) du dv}{\int_E f(\lambda_2(x-u), \lambda_2(y-v))^{\lambda_4 P} K_{\sqrt{2\lambda_3 t}}(\lambda_2 u, \lambda_2 v) du dv}.$$

On the one hand, we have $K_{\sqrt{2\lambda_3 t}}(\lambda_2 x, \lambda_2 y) = \frac{1}{4\pi\lambda_3 t} \exp\left(\frac{-(x^2+y^2)}{4t} \frac{\lambda_2^2}{\lambda_3}\right)$, on the other hand, we define $f'(x,y) = \lambda_1 f(\lambda_2(x,y))$. In addition, $\lambda_1^2 f^{\lambda_4 P+1}(\lambda_2(x,y)) = \lambda_1 f^{\lambda_4 P}(\lambda_2(x,y)) \lambda_1 f(\lambda_2(x,y)) = (f')^{\lambda_4 P}(x,y) f'(x,y) = (f')^{\lambda_4 P+1}(x,y)$. Thus

$$\lambda_1 \eta(f)(\lambda_2 x, \lambda_2 y; \lambda_3 t; \lambda_4 P) = \frac{\int_E f'(x-u, y-v)^{\lambda_4 P+1} e^{\frac{-(u^2+v^2)}{4t} \frac{\lambda_2^2}{\lambda_3}} du dv}{\int_E f'(x-u, y-v)^{\lambda_4 P} e^{\frac{-(u^2+v^2)}{4t} \frac{\lambda_2^2}{\lambda_3}} du dv}$$

Consequently if we fix $\lambda_2^2 = \lambda_3$, for the case $P = 0$ we have

$$\lambda_1 \eta(f)(\lambda_2 x, \lambda_2 y; \lambda_3 t; 0) = \eta(f')(x, y; t; 0)$$

and for the case $P \to +\infty$ and fixing $\lambda_2^2 = \lambda_3 \lambda_4$ we have

$$\lambda_1 \eta(f)(\lambda_2 x, \lambda_2 y; \lambda_3 t; \lambda_4 P) = \eta(f')(x, y; t; P)$$

■

In conclusion, a functional W will be dimensional only when a modification of homothety is compensated by an affinity on the spatial scale, which involves also to increase the non-linearity order. This point can be also studied under the viewpoint of the Heijmans theory of [16, 17].

4.2.4 Invariance

By its linearity, Gaussian scale-space is invariant under linear transformations $f \mapsto \hat{f} = \alpha f + \beta$ $\Rightarrow \left(\hat{f} * K_{\sqrt{2t}}\right)(x, y) = \alpha \left(f * K_{\sqrt{2t}}\right)(x, y) + \beta$. Morphological dilation/erosion are invariant only under grey-value shifts $f \mapsto \hat{f} = f + \beta \Rightarrow \left(\hat{f} \oplus b_{\sqrt{2t}}\right)(x, y) = \left(f \oplus b_{\sqrt{2t}}\right)(x, y) + \beta$. We notice that the flat dilation/erosion are invariant under anamorphosis [30, 25], i.e., any strictly increasing mapping is an anamorphosis. Let us look now at invariance properties of the CHM Gaussian scale-space.

Proposition 11 *The CHM Gaussian scale-space $\eta(f)(x, y; t; P)$ is invariant under scalar multiplication of grey-values for any P, $-\infty \leq P \leq +\infty$, i.e., $\eta(\alpha f)(x, y; t; P) = \alpha \eta(f)(x, y; t; P)$. In the limit cases $P = 0$ (equivalent to Gaussian scale-space) and $P \to \pm\infty$, the CHM*

Gaussian scale-space is invariant under linear transformations: $\eta(\alpha f+\beta)(x,y;t;P=0)=\alpha\eta(f)(x,y;t;P=0)+\beta$ *and* $\lim_{P\to\pm\infty}\eta(\alpha f+\beta)(x,y;t;P)=\alpha\lim_{P\to\pm\infty}\eta(f)(x,y;t;P)+\beta$.

Proof. The proofs are direct from the expressions of the limit cases. ■

Hence the most interesting cases of the CHM Gaussian scale-space are invariant to grey-level addition and multiplication.

4.2.5 Asymptotic separability and semi-group law

In the classical state-of-the-art on linear scale-spaces, the fundamental semi-group property [21], or recursivity principle [26], states as follows: $\forall t_1,t_2\geq 0$, $\left((f*K_{\sqrt{2t_1}})*K_{\sqrt{2t_2}}\right)=\left(f*K_{\sqrt{2(t_1+t_2)}}\right)$. This is due to the fact that the Gaussian convolution kernels are the only separable and rotationally invariant functions that preserve the shape under Fourier transform. That allows also a separability in the implementation of the 2D Gaussian kernel convolution at scale t, using two successive 1D Gaussian kernel convolutions (at directions x and y) at scale t. From the works by Van den Boomgaard [4], it is also well known that in mathematical morphology the parabolic structuring function (in fact, any quadratic structuring function) are the equivalent class of functions which are dimensionally separable and closed with respect to the dilation/erosion, i.e., $\forall t_1,t_2\geq 0$, $\left((f\oplus b_{\sqrt{2t_1}})\oplus b_{\sqrt{2t_2}}\right)=\left(f\oplus b_{\sqrt{2(t_1+t_2)}}\right)$, and similarly for the erosion. This result is usually proved in the slope transform domain [12, 23].

The filter family $\eta(f)(x,y;t;P)$ for a given $P\in\overline{\mathbb{R}}$ has no semi-group structure and is, therefore, not a scale-space in strict sense. However, using the limit expressions it is easy to

proof that for the asymptotic cases $P = 0$ and $P \to \pm\infty$, the following semi-group holds:

$$\eta\left(\eta(f)(x, y; t_1; P)\right)(x, y; t_2; P) = \eta(f)(x, y; t_1 + t_2; P);\ \ \forall t_1,\ t_2 \geq 0$$

This result constitutes an advantage for an efficient numerical computation of an acceptable approximation to the limit cases of 2D CHM Gaussian scale-space using 1D separable Gaussian kernel for the convolutions of f^{P+1} and of f^{P}. Nevertheless, since computational efficiency is often important, the result of the operator $\eta(f)(x, y; t; P)$ for any P can be computed using low-order recursive filters for the numerator and denominator 2D Gaussian convolutions of the CHM filter. For example, the approach introduced in [38] uses a third-order recursive filter with one real pole and a pair of complex poles, applied forward and backward to make a sixth-order symmetric approximation to the Gaussian with low computational complexity for any scale t.

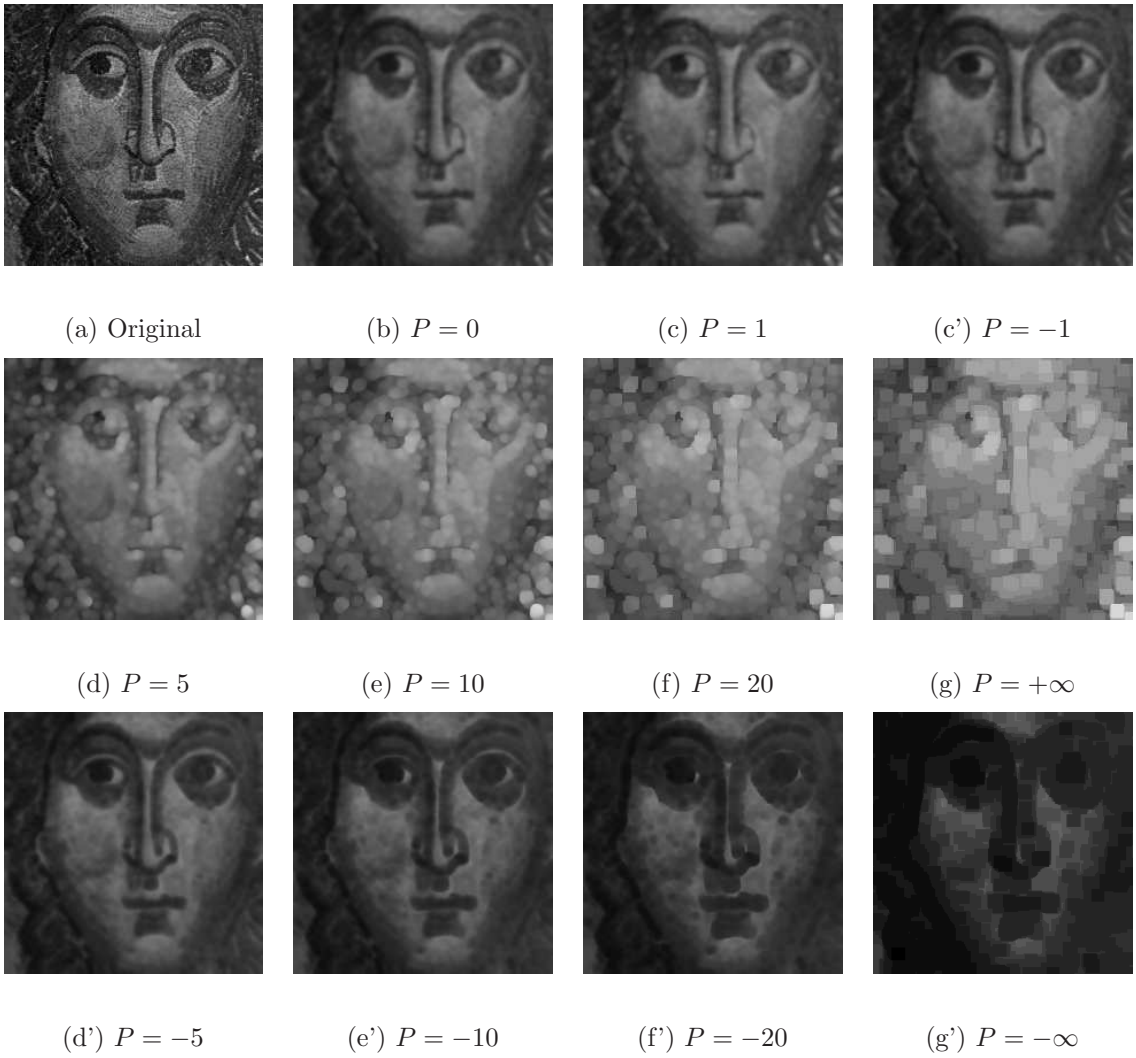

(a) Original (b) $P = 0$ (c) $P = 1$ (c') $P = -1$

(d) $P = 5$ (e) $P = 10$ (f) $P = 20$ (g) $P = +\infty$

(d') $P = -5$ (e') $P = -10$ (f') $P = -20$ (g') $P = -\infty$

Figure 2: Generalised morphological Gaussian convolution (isotropic linear diffusion) $\eta(f)(x, y; t; P)$ at scale $t = 5$: First row, original image, standard Gaussian filtered image ($P = 0$) and cases $P = 1$ and $P = -1$; middle row, counter-harmonic Gaussian pseudo-dilations ($P > 0$); bottom row, counter-harmonic Gaussian pseudo-erosions ($P < 0$).

4.3 Interpretation as CHM Linear Diffusion and iterative framework

A filtered image $u(x, y; t)$ of $f(x, y)$ is calculated by solving the diffusion equation with the original image as initial state, and reflecting boundary conditions:

$$\begin{aligned} \partial_t u = \operatorname{div}(c\nabla u) = c\Delta u = c\left(\frac{\partial^2 u}{\partial x^2} + \frac{\partial^2 u}{\partial y^2}\right) \\ u(x, y; 0) = f(x, y) \\ \partial_{\mathbf{n}} u|_{\partial\Omega} = 0 \end{aligned} \tag{10}$$

where c is the conductivity and $\mathbf{n}$ denotes the normal to the image boundary $\partial\Omega$. The popularity of the Gaussian scale-space is due to its linearity and the fact that the multiscale function $\psi(f)(x, y; t)$ can be generated from the isotropic heat diffusion, i.e.,

$$u(x, y; t) = (f * K_{\sqrt{2t}})(x, y) = \psi(x, y; t), \quad t > 0.$$

4.3.1 Numerical solution

The PDE can also be solved using finite differences in an explicit schema. Pixel i represents the location (x_i, y_i). Let h_l denote the grid size in the l direction (working on square grid, we assume 1 for horizonal and vertical directions and $\sqrt{2}$ for $45°$ and $-45°$ directions); and τ denote the time step size (to guarantee stability, the step size must satisfy [35]: $\tau = 1/(\sum_{l=1}^{m} 2/h_l^2)$), considering discrete times $t_k = k\tau$ (with k positive integer). By u_i^k we denote approximation to $u(x_i, y_i; t_k)$. The simplest discretization can be written in a compact way as [36]:

$$u_i^{k+1} = u_i^k + \tau\left(\sum_{l=1}^{m}\sum_{j\in\mathcal{N}_l(i)} \frac{c_j^k + c_i^k}{2h_l^2}(u_j^k - u_i^k)\right), \tag{11}$$

where $\mathcal{N}_l(i)$ consists of the two neighbours of pixel i along the l discretized direction. The conduction coefficients c_i^k are considered here constant in time and space.

Thus, the pseudo-morphological isotropic diffusion of order P can be rewritten as

$$\eta(f)(x,y;t;P) = \frac{[u(x,y;t)]^{P+1}}{[u(x,y;t)]^{P}}, \tag{12}$$

where $[u(x,y;t)]^P$ is the solution of diffusion equation 11 with the initial condition

$$u(x,y;0) = f(x,y)^P.$$

4.3.2 Coupled schema

Furthermore, starting from the PDE numerical solution, it is also possible to define an iterative CHM-based isotropic diffusion, $\widehat{\eta}(f)(x,y;t;P)$, by a coupled evolution of both power terms, according to the following discretization:

$$u_i^{k+1} = \frac{(u_i^k)^{P+1} + \tau\left(\sum_{l=1}^{m}\sum_{j\in\mathcal{N}_l(i)}\frac{c_j^k+c_i^k}{2h_l^2}((u_j^k)^{P+1} - (u_i^k)^{P+1})\right)}{(u_i^k)^{P} + \tau\left(\sum_{l=1}^{m}\sum_{j\in\mathcal{N}_l(i)}\frac{c_j^k+c_i^k}{2h_l^2}((u_j^k)^{P} - (u_i^k)^{P})\right)}. \tag{13}$$

As we can expect, the results of decoupled $\eta(f)(x,y;t;P)$ and coupled $\widehat{\eta}(f)(x,y;t;P)$ diffusions are different. In Fig. 3 is given a comparison of CHM linear diffusion using the decoupled iterative scheme (equivalent to the generalised Gaussian convolution) vs. the coupled iterative scheme, at spatial scale $t = 5$ and order $P = 10$. We observe from this experiment of pseudo-dilation, and other similar results provided in the above mentioned website, that the effects of $\widehat{\eta}(f)(x,y;t;P)$ are more "morphological" for equivalent order P, with sharper transitions between structures. We can conclude that the iteration n times of a unitary (i.e., $\sigma = \sqrt{2}$) generalised morphological Gaussian convolution introduces a nonlinearity degree superior than the corresponding generalised morphological Gaussian convolution at scale

$\sigma = \sqrt{2n}$. Another example is depicted in Fig. 6(e) and (f), which just corresponds to a comparison of the pseudo-opening obtained by product of pseudo-erosion and pseudo-dilation $\widehat{\eta}\left(\widehat{\eta}(f)(x,y;t;-P)\right)(x,y;t;P)$ and the counterpart decoupled diffusion operators.

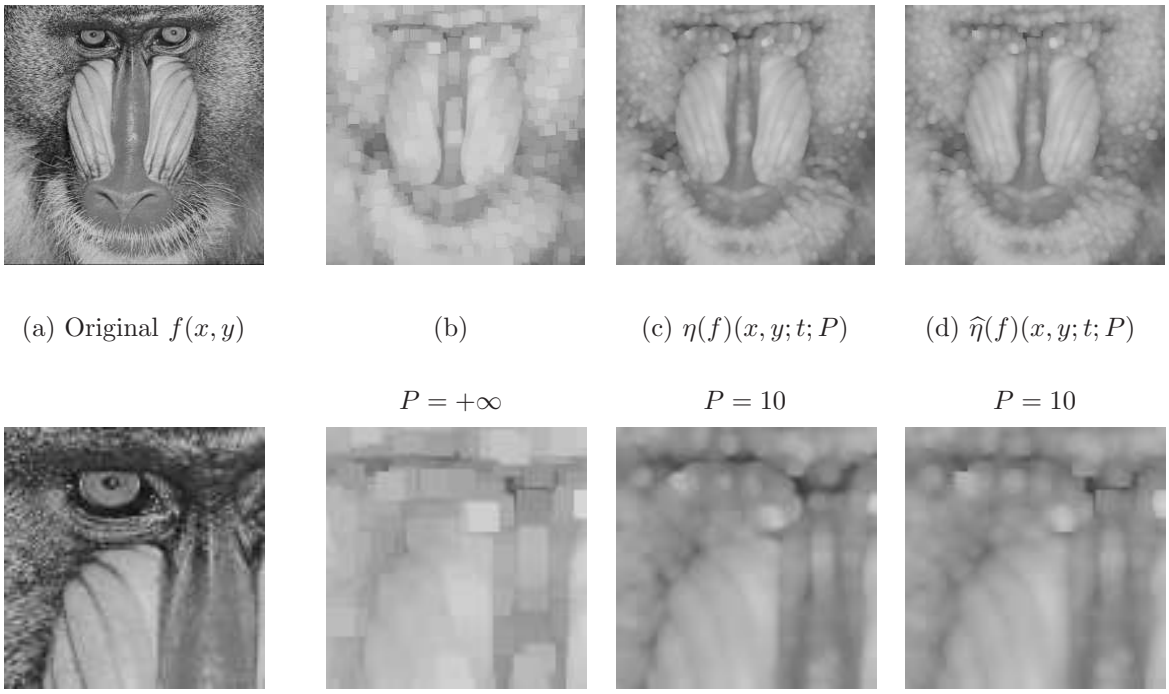

(a) Original $f(x,y)$ (b) (c) $\eta(f)(x,y;t;P)$ (d) $\widehat{\eta}(f)(x,y;t;P)$

$P = +\infty$ $P = 10$ $P = 10$

Figure 3: Comparison of CHM linear diffusion using the decoupled iterative scheme (equivalent to the generalised Gaussian convolution) vs. the coupled iterative scheme, at spatial scale $t = 5$ and order $P = 10$: (a) original image $f(x,y)$, (b) standard dilation, (c) decoupled $\eta(f)(x,y;t;P)$ and (d) coupled $\widehat{\eta}(f)(x,y;t;P)$. At the bottom are zoom-in frames of a square section cropped from the corresponding images.

5 Counter-Harmonic Nonlinear Diffusion

Ideas introduced above are extended in this section to two well-known cases of evolved image diffusion.

5.1 Nonlinear diffusion

The big disadvantage of isotropic diffusion is the fact that linear smoothers do not only smooth the noise but also blur and shift structure edges, which are important image features in some applications, i.e., segmentation and object recognition. The pioneering idea introduced by Perona and Malik [27] to reduce these problems is to locally adapt the diffusivity, i.e., the value of the conductivity c, to the gradient of the image at each iteration. More precisely, this nonlinear diffusion involves replacing the diffusion equation 10 by the following model:

$$\begin{aligned} \partial_t u &= \operatorname{div}\left(g\left(\|\nabla u\|^2\right)\nabla u\right) \\ u(x,y;0) &= f(x,y) \\ \partial_{\mathbf{n}} u|_{\partial\Omega} &= 0 \end{aligned} \tag{14}$$

In this model the diffusivity has to be such that $g\left(\|\nabla u\|^2\right) \to 0$ when $\|\nabla u\|^2 \to +\infty$ and $g\left(\|\nabla u\|^2\right) \to 1$ when $\|\nabla u\|^2 \to 0$. One of the diffusivities Perona and Malik proposed is the function

$$g(s^2) = 1/\left(1 + (s^2/\lambda^2)\right), \quad \lambda > 0,$$

where λ is a threshold parameter that separates forward and backward diffusion. This model accomplishes the aim of blurring small fluctuations (noise) while enhancing edges (by preventing excessive diffusion). To avoid some numerical and theoretical drawbacks of this model,

it was proposed in [11], a new version of Perona and Malik theory, based on replacing diffusivity $g\left(\|\nabla u\|^2\right)$ by a regularized version $g\left(\|\nabla u_\sigma\|^2\right)$ with $\nabla u_\sigma = \nabla\left(K_\sigma * u\right)$ where K_σ is a Gaussian kernel. This latter model is just used in our framework and the numerical solution can be obtained using the explicit scheme 11, where the local conductivity is here the approximation to the regularized term $g\left(\|\nabla u_\sigma\|^2\right)$, i.e.,

$$c_i^k = \frac{1}{1 + \frac{\|\nabla u_\sigma(x_i, y_i; t_k)\|^2}{\lambda^2}}, \tag{15}$$

with the gradient computed by central differences.

Similarly to the isotropic case, we can now define the pseudo-morphological counter-harmonic nonlinear diffusion of order P as

$$\xi(f)(x, y; t; P) = \frac{[u(x, y; t)]_{nl}^{P+1}}{[u(x, y; t)]_{nl}^{P}}, \tag{16}$$

where $[u(x, y; t)]_{nl}^{Q}$ is the solution of regularized Perona and Malik diffusion equation with the initial condition $u(x, y; 0) = f(x, y)^Q$. Fig. 4 provides the results of pseudo-dilation and pseudo-erosion ($P = 10$ and $P = -10$) using the regularized Perona and Malik model on a noisy image. Comparing with respect to the standard filtering ($P = 0$), the good properties of denoising without blurring are conserved but in addition, an effect of dilation/erosion is obtained. This kind of pseudo-morphology is useful for instance to compute morphological gradient, i.e.,

$$\xi(f)(x, y; t; P) - \xi(f)(x, y; t; -P),$$

of noisy images or to construct filters as morphological openings, i.e.,

$$\xi(\xi(f)(x, y; t; -P))(x, y; t; P).$$

See in Fig. 6(c) and (g) the comparison of the standard Perona and Malik diffusion and the corresponding pseudo-opening diffusion, which removes some small bright structures. It is also possible to define the coupled case by computing the counter-harmonic but this discussion is out of the paper scope.

A critical point here is the choice of parameter λ, which is an ill-posed problem. Sophisticated approaches in the state-of-the-art are based on noise estimation. We have determined empirically that the value

$$\lambda = \frac{1}{m}\left(\sum_{l=1}^{m} \text{Mean}(\nabla_l u(x,y;t))\right), \tag{17}$$

where m is the number of discretized directions, and which of course is different for P and $P+1$, leads to stable results.

5.2 Coherence-enhanced diffusion

Coherence-enhanced diffusion, or tensor-driven diffusion, was introduced by Weickert [35] in order to achieve an anisotropic diffusion filtering based on directionality information. The idea is to adapt the diffusion process to local image structure using the following nonlinear diffusion equation:

$$\partial_t u = \text{div}\left(\mathbf{D}\nabla u\right). \tag{18}$$

where the conductivity function becomes a symmetric positive definite diffusion tensor $\mathbf{D}$, which is a function adapted to the structure tensor

$$\mathbf{J}_\rho(\nabla u_\sigma) = K_\rho * (\nabla u_\sigma \otimes \nabla u_\sigma).$$

The eigenvectors of $\mathbf{J}_\rho$ are orthonormal and the eigenvalues are positive. The corresponding eigenvalues (let us call them $\mu_1 \geq \mu_2$) describe the local structure. Flat areas give $\mu_1 \approx \mu_2$, straight edges give $\mu_1 \gg \mu_2 = 0$ and corners give $\mu_1 \geq \mu_2 \gg 0$. In order to control the diffusion, $\mathbf{J}_\rho$ is not used directly, but tensor $\mathbf{D}$ has the same eigenvectors as $\mathbf{J}_\rho$, but different eigenvalues, thus controlling the diffusion in both directions. The eigenvalues are

$$\begin{cases} \lambda_1 &= \alpha \\ \lambda_2 &= \alpha + (1-\alpha)\exp(-C/\kappa) \end{cases}$$

where κ is the orientation coherence and $C > 0$ serves as a threshold parameter. Parameter $\alpha > 0$ is quite important and serves as a regularization parameter which keeps $\mathbf{D}$ uniformly positive definite. For this diffusion, we have used in our tests a numerical implementation using the additive operator splitting (AOS) scheme [35], which is particularly efficient and has the advantage of being rotationally invariant compared to their multiplicative counterparts.

As previously, the pseudo-morphological counter-harmonic coherence-enhanced diffusion of order P is defined as

$$\chi(f)(x,y;t;P) = \frac{[u(x,y;t)]_{ce}^{P+1}}{[u(x,y;t)]_{ce}^{P}}, \tag{19}$$

where $[u(x,y;t)]_{ce}^{Q}$ is the solution of Weickert diffusion equation 18 with the initial condition $u(x,y;0) = f(x,y)^Q$. As in the previous case, we have to adapt the regularization parameter α to the dynamics of the power images $f(x,y)^P$ in order to have numerical stable results. Empirically, we have observed that

$$\alpha = \begin{cases} 0.01|P| & \text{if} \quad P \neq 0 \\ 0.005 & \text{if} \quad P = 0 \end{cases} \tag{20}$$

lead to satisfactory results. Moreover, we have also observed in experimental tests that numerical solution of the CHM coherence diffusion given in expression (19) can introduce some instabilities and errors for $P > 0$, whereas for $P < 0$ the results are numerically regular. To avoid this drawback, we propose to compute, by duality, the coherence-enhanced pseudo-dilation $\chi(f)(x, y; t; P)$, with $P > 0$, by means of the operation $1 - \chi(1 - f)(x, y; t; -P)$. In any case, a deeper study on the numerical implementation of counter-harmonic Weickert diffusion, in particular in the case of coupled diffusion, is required.

Examples of pseudo-morphological anisotropic diffusion are given in Fig. 5 and Fig. 6(d)-(h). Dark regions are anisotropically pronounced in pseudo-erosion schemes ($P < 0$) whereas bright regions are anisotropically emphasized in pseudo-dilation as well as in their products, respectively the pseudo-openings and pseudo-closings.

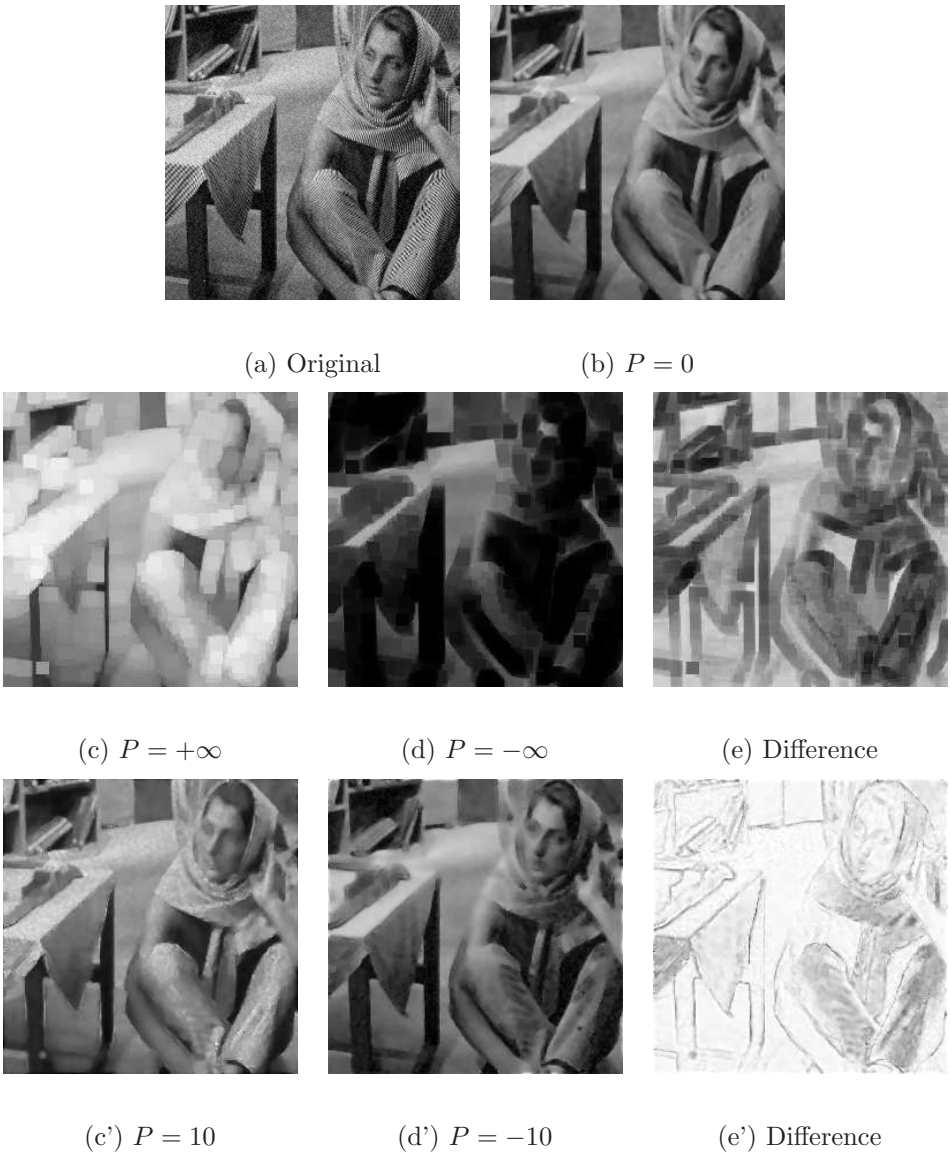

(a) Original (b) $P = 0$

(c) $P = +\infty$ (d) $P = -\infty$ (e) Difference

(c') $P = 10$ (d') $P = -10$ (e') Difference

Figure 4: Pseudo-morphological nonlinear diffusion $\xi(x, y; t)$ at scale $t = 5$ (regularization parameter $\sigma = 0.5$): (a) original image, (b) standard nonlinear diffusion, (c)/(d) standard dilation/(d) standard erosion, (e) image difference between dil./ero. (gradient), (c')/(d') pseudo-dilation/erosion by counter-harmonic nonlinear diffusion, (e') image difference between pseudo-dil./ero.

(a) Original (b) Weickert Diff. (c) Opening (d) Closing

(e) $P = 5$ (f) $P = -5$ (g) $P = -5$, $P = 5$ (h) $P = 5$, $P = -5$

Figure 5: Pseudo-morphological anisotropic diffusion $\chi(x, y; t; P)$ at scale $t = 10$ (with regularization parameters: local scale $\sigma = 1.5$, integration scale $\rho = 6$) : (a) original image, (b) standard anisotropic diffusion, (c)-(d) opening and closing of size equivalent to $t = 5$, (e)/(f) pseudo-dilation/erosion by counter-harmonic anisotropic diffusion, (g)/(h) pseudo-opening/closing by counter-harmonic anisotropic diffusion.

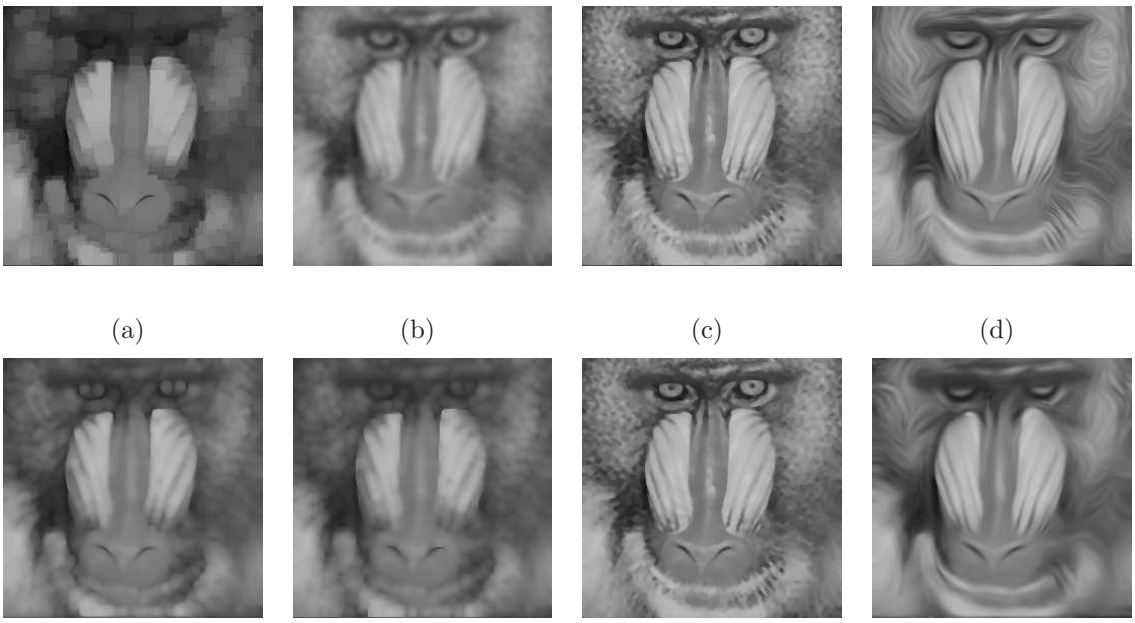

(a) (b) (c) (d)

(e) (f) (g) (h)

Figure 6: Comparison of standard diffusions and pseudo-morphological openings (the original image is given in Fig. 3: (a) standard opening using a square 11×11, (b) isotropic diffusion $t = 5$, (c) Perona and Malik diffusion $t = 5$, (d) Weickert diffusion $t = 10$, (e) pseudo-opening using isotropic diffusion $t = 5$, $P = 10, P = -10$, (f) pseudo-opening using coupled isotropic diffusion $t = 5$, $P = 10, P = -10$, (g) pseudo-opening using Perona and Malik diffusion $t = 5$, $P = 5, P = -5$, (h) pseudo-opening using Weickert diffusion $t = 10$, $P = 5, P = -5$.

6 Conclusions and perspectives

We have introduced a mathematical framework of pseudo-morphological image diffusion using the notion of counter-harmonic mean. In particular, we have proposed the counter-harmonic Gaussian scale-space, and we have studied in detail its properties. In the case of 2D images, the nonlinear smoothed signals $\eta(f)(x, y; t; P)$ taken as a whole can be considered as a continuous function on $\mathbb{R}^{2+2}$, that is, a double pseudo-scale-space with respect to t and with respect to P. This family of filters expands and includes the Gaussian scale-space and the morphological erosion/dilation scale-spaces. We have also proposed the corresponding generalization of Perona and Malik diffusion model as well as of Weickert model of coherence-enhanced diffusion.

As the dilation/erosion operators depend on the extreme values of the (additively weighted signal) in the neighbourhood of a point, impulse noise and other kind of high-frequency noise cause spurious results of the standard morphological processing of noisy image. Linear diffusion filtering is able to deal with the noise, however the averaging process blurs and limits also the effect of the filtering. The fundamental property of the present pseudo-morphological image diffusion is its ability to robustly filter out the noisy images in a nonlinear way, which can selectively bias the result toward high (low) values such as the dilation (erosion) filter.

We have given a first analysis about the limit statements, but a deeper study is still required about the behaviour of the counter-harmonic linear diffusion with respect to value of P. In particular, we believe that the relationship between our numerical framework and

an hybrid evolutionary PDE such as

$$\partial_t u = \alpha \Delta u \pm \beta \|\nabla u\|^2,$$

with variable coefficients α and β which determines the part of linear *versus* morphological smoothing w.r.t. P, should be explored. This hybrid equation was already mentioned in [8], considered in [14] and it is related also to Kuwahara-Nagao PDE introduced in [6] but, to our knowledge, it remains an open problem. Additionally, it should be considered how the present nonlinearization of image diffusion can be turned to the Laplace-Beltrami framework to describe diffusion process [31, 20].

A deeper study on the numerical implementation of counter-harmonic Perona-Malik and Weickert diffusions, and in particular in the case of coupled diffusion schemas, should be achieved. We have pointed out that, for data defined in the interval $[0, 1]$, the behaviour of filters with $P < 0$ is generally more stable than the case $P > 0$ and this is probably related with one of the properties of Proposition 2. However a better understating of these effects is still to be investigated.

References

[1] L. Alvarez, F. Guichard, P-L. Lions, J-M. Morel. Axioms and fundamental equations of image processing. *Arch. for Rational Mechanics,* 123(3): 199–257, 1993.

[2] J. Angulo. Pseudo-Morphological Image Diffusion using the Counter-Harmonic Paradigm. In *Proc.of Acivs'2010 (2010 Advanced Concepts for Intelligent Vision Systems),* LNCS Vol. 6474, Part I, 426–437, Springer, Sydney, Australia, December 2010.

[3] A.B. Arehart, L. Vincent, B.B. Kimia. Mathematical morphology: The Hamilton-Jacobi connection. In *Proc. of IEEE 4th Inter. Conf. on Computer Vision (ICCV'93),* 215–219, 1993.

[4] R. van den Boomgaard, L. Dorst. The morphological equivalent of Gaussian scale-space. In *Proc. of Gaussian Scale-Space Theory,* 203–220, Kluwer, 1997.

[5] R. van den Boomgaard. Numerical solution schemes for continuous-scale morphology. In *Proc. of Scale-Space Theories in Computer Vision,* LNCS Vol. 1682, 199–210, Springer, Berlin, 1999.

[6] R. van den Boomgaard. Decomposition of the Kuwahara-Nagao operator in terms of a linear smoothing and a morphological sharpening. In *Proc. of ISMM'2002,* 283–292, CSIRO Publishing, 2002.

[7] M. Breuß, J. Weickert. Highly accurate PDE-based morphology for general structuring elements. In *Proc. of Scale Space and Variational Methods in Computer Vision,* LNCS Vol. 5567, 758–769, Springer, Berlin, 2009.

[8] R.W. Brockett, P. Maragos. Evolution equations for continuous-scale morphology. *IEEE Trans. on Signal Processing,* 42(12):3377–3386, 1994.

[9] P.S. Bullen. *Handbook of Means and Their Inequalities,* 2nd edition, Springer, 1987.

[10] B. Burgeth, J. Weickert. An Explanation for the Logarithmic Connection between Linear and Morphological System Theory. *International Journal of Computer Vision,* 64(2–3):157–169, 2005.

[11] F. Catte, P.-L. Lions, J.-M. Morel, T. Coll. Image selective smoothing and edge detection by nonlinear diffusion. *SIAM Journal on Numerical Analysis,* 29(1):182–193: 1992.

[12] L. Dorst, R. van den Boomgaard. Morphological Signal Processing and the Slope Transform. *Signal Processing,* 38:79–98, 1994.

[13] L. Florack. *Image Structure,* Kluwer Academic Publishers, 1997.

[14] L. Florack, R. Maas, W. Niessen. Pseudo-Linear Scale-Space Theory, *International Journal of Computer Vision,* 31(2-3): 1–13, 1999.

[15] R.C.Gonzalez, R.E. Woods. *Digital Image Processing,* AAddison-Wesley, Boston, MA, USA, 1992.

[16] H.J.A.M. Heijmans, R. van den Boomgaard. Algebraic Framework for linear and morphological scale-spaces. *Journal of Visual Communication and Image Representation,* 13(1-2): 269–301, 2002.

[17] H.J.A.M. Heijmans. Morphological scale-spaces, scale invariance, and Lie groups. In *Proc. of International Symposium on Mathemtaical Morphology (ISMM 2002)*, CSIRO Ed., Sydney, 2002.

[18] P.T. Jackway. On Dimensionality in Multiscale Morphological Scale-Space with Elliptic Poweroid Structuring Functions. *Journal of Visual Communication and Image Representation,* 6(2), 189–195, 1995.

[19] P.T. Jackway, M. Deriche. Scale-Space Properties of the Multiscale Morphological Dilation-Erosion. *IEEE Trans. Pattern Anal. Mach. Intell.,* 18(1): 38–51, 1996.

[20] R. Kimmel, R. Malladi, N.A. Sochen. Image Processing via the Beltrami Operator. In *Proc. of Third Asian Conference on Computer Vision (ACCV'98),* LNCS Vol. 1351, Vol. I, 574–581, 1998.

[21] T. Lindeberg. Scale-Space for Discrete Signals. *IEEE Trans. Pattern Anal. Mach. Intell.,* 12(3):234–254, 1990.

[22] T. Lindeberg. *Scale-Space Theory in Computer Vision,* Kluwer Academic Publishers, 1994.

[23] P. Maragos. Slope Transforms: Theory and Application to Nonlinear Signal Processing. *IEEE Trans. on Signal Processing,* 43(4): 864–877, 1995.

[24] P. Maragos. Differential morphology and image processing. *IEEE Transactions on Image Processing,* 5(1): 922-937, 1996.

[25] G. Matheron. Les treillis compacts. *Technical Report - Paris School of Mines, N-23/90/G* (available online), November 1990.

[26] E.J. Pauwels, L.J. Van Gool, P. Fiddelaers, T. Moons. An Extended Class of Scale-Invariant and Recursive Scale Space Filters. *IEEE Trans. Pattern Anal. Mach. Intell.,* 17(7): 691–701, 1995.

[27] P. Perona, J. Malik. Scale-Space and Edge Detection Using Anisotropic Diffusion. *IEEE Trans. Pattern Anal. Mach. Intell.,* 12(7): 629–639, 1990.

[28] J.F. Rivest, J. Serra, P. Soille. Dimensionality in Image Analysis. *Journal of Visual Communication and Image Representation,* 3(2): 137–146, 1992.

[29] G. Sapiro, R. Kimmel, D. Shaked, B.B. Kimia, A.M. Bruckstein. Implementing continuous-scale morphology via curve evolution. *Pattern recognition,* 26(9): 1363–1372, 1993.

[30] J. Serra. *Image Analysis and Mathematical Morphology. Vol I, and Image Analysis and Mathematical Morphology. Vol II: Theoretical Advances,* London: Academic Press, 1982,1988.

[31] N.A. Sochen, R. Kimmel, R. Malladi. A general framework for low level vision. *IEEE Transactions on Image Processing,* 7(3): 310–318, 1998.

[32] P. Soille. *Morphological Image Analysis,* Springer-Verlag, Berlin, 1999.

[33] L.J. van Vliet. Robust Local Max-Min Filters by Normalized Power-Weighted Filtering. In *Proc. of IEEE 17th International Conference of the Pattern Recognition (ICPR'04),* Vol. 1, 696–699, 2004.

[34] J. Weickert. *Anisotropic Diffusion in Image Processing,* ECMI Series, Teubner-Verlag, Stuttgart, Germany, 1998.

[35] J. Weickert. Coherence-Enhancing Diffusion Filtering. *Int. J. Comput. Vision,* 31(2-3): 111–127, 1999.

[36] J. Weickert. Efficient image segmentation using partial differential equations and morphology. *Pattern Recognition,* 31(9): 1813–1824, 2001.

[37] M. Welk. Families of generalised morphological scale spaces. In *Proc. of 4th Inter. Conf. of Scale-Space Methods in Computer Vision,* LNCS Vol. 2695, 770–784, Springer, 2003.

[38] I.T. Young, L.J. van Vliet. Recursive implementation of the Gaussian filter. *Signal Processing,* 44: 139–151, 1995.

13.8 Publication VIII : M. Luengo-Oroz and J. Angulo. "Cyclic Mathematical Morphology in Polar-logarithmic Representation". *IEEE Transactions on Image Processing*, Vol. 18, No. 5, 1090–1096, 2009.

Cyclic Mathematical Morphology in Polar-Logarithmic Representation

Miguel Angel Luengo-Oroz and Jesús Angulo

***Abstract*—We propose in this paper to perform mathematical morphology operators in a geometric transformation of an image. As a result of this procedure, processing images with regular structuring elements in the transformed domain is equivalent to working with deformed structuring elements in the original representation. More specifically, the conversion into polar-logarithmic coordinates provides satisfying results in image analysis applied to round objects, if they are roughly origin-centered. We have illustrated the interest of the derived cyclic morphology with two pattern recognition examples: erythrocyte shape analysis and multiscale description of iris textures.**

***Index Terms*—Circular opening, granulometric iris code, polar-logarithmic coordinates, radial skeleton, red blood cell shape analysis, spatially variant mathematical morphology.**

I. Introduction

TRANSLATION, rotation, and scale invariant representations are very useful in shape analysis applications. Usually, these representations convert visual shape information into an abstract representation such as Fourier descriptors [1]. However, these spaces may not be suitable for the intuitive processing performed by mathematical morphological operators. One of the fundamental advantages of mathematical morphology [2] applied to image processing is that it is intuitive since it works directly on the spatial domain: the shape and the size of structuring elements considered as the *basic bricks*, play the same role as frequencies do in the analysis of sound. We try to maintain this intuitive advantage for morphological image analysis and find a representation system which presents more advantages than the traditional Cartesian representation when processing images which contain some kind of radial symmetry, or in general, which have a center. The selected transformation is the polar-logarithmic representation [3]. Morphological operators through this spatially variant support space have been previously studied from a theoretical point of view in [4], [5]. However, the direct implementation of polar operators proposed in these previous works implies very high computational cost. We propose here an alternative framework which consist in firstly doing the polar-logarithmic transformation of the image; secondly performing classic morphological operators in the transformed image and finally performing the inverse geometric transformation in order to restore the initial image modified by the operations with deformed structuring elements. We should point out the benefits of developments introduced in this paper are limited to transformations in which the object of interest remains (nearly) origin-centered.

A preliminary version of this work was presented in [6]. This paper is organized as follows. In Section II, we review the polar-logarithmic transform. In Section III, the theoretical support for cyclic morphology in the log-pol space is presented. Next, in Section IV, some morphological tools are proposed and their use is illustrated by two pattern recognition applications developed with the proposed methodology. Discussion concludes the paper.

Manuscript received June 19, 2007; revised December 02, 2008. First published March 24, 2009; current version published April 10, 2009. This work was supported in part by the Spanish grant FPI-CM(0362/2005). The associate editor coordinating the review of this manuscript and approving it for publication was Dr. Dimitri Van De Ville.

M. A. Luengo-Oroz is with the Biomedical Image Technologies Lab of ETSI Telecomunicación, Universidad Politécnica de Madrid, 28040, Madrid, Spain (e-mail: maluengo@die.upm.es).

J. Angulo is with the Center of Mathematical Morphology of Ecole des Mines de Paris, 77305 Fontainebleau, France (e-mail: angulo@cmm.ensmp.fr).

Digital Object Identifier 10.1109/TIP.2009.2013078

II. Polar-Logarithmic Representation

A. Geometric Transformations of Images

A geometric transformation of a digital image is an operation that converts the original image $f(\eta)$ into the transformed image $f(\hat{\eta})$ by applying a function $\xi : f(\eta) \rightarrow f(\hat{\eta})$ that maps each point in the source image to its corresponding point in the destination image. A simple solution to this problem is to perform an inverse-transformation ξ^{-1} from each pixel coordinate $\hat{\eta}$ in the destination image to a corresponding pixel location η in the source image. The calculated coordinates for the location of the pixel in the source image will only rarely be integers, so the calculated pixel location often lies in an area between multiple pixels in the original image. In order to solve this problem, we need to fit the discrete data to a continuous function and to calculate the corresponding interpolated value. Concerning this resampling step, the choice of the appropriate technique depends on the tradeoff between the demanded accuracy of the interpolation and the computational cost. The nearest-neighbor, bilinear, or bicubic interpolation provide enough quality in most cases; however, some applications may require more precise methods, such as spline-based models [7].

B. Polar-Logarithmic Coordinates

The polar-logarithmic representation, or log-pol coordinates, has already been used to map the visual cortex of primates [8]: the photoreceptors of the retina are placed according to the same organization. This model of log-pol fovea is applied mainly in artificial vision systems, for instance in robotics [9]. In addition, due to its scientific utility in describing fundamental aspects of human vision, the artificial fovea has also been applied in order to assess the optical flow [10] or to recognize and track objects [11]. The polar-logarithmic transformation converts the original image $\eta = (x, y)$ into another $\hat{\eta} = (\rho, \omega)$ in which the angular

Fig. 1. (a) → (b): Example of log-pol conversion $f(\eta) \rightarrow f(\hat{\eta})$, where η_c corresponds to the center of the image, near Lena's left eye.

coordinate is placed on the vertical axis and the logarithmic coordinate is placed on the horizontal one (see Fig. 1, notice that (x, y) and (ρ, ω) axis are placed as in Fig. 1 for all figures in the following sections). More precisely, with respect to a central point $\eta_c = (x_c, y_c)$: $\rho = \log(\sqrt{(x-x_c)^2 + (y-y_c)^2}$, $0 \leq \rho \leq \rho_{\max}$; $\omega = \arctan((y-y_c)/(x-x_c))$, $0 \leq \omega < 2\pi$.

PSEUDOCODE DIRECT TRANSFORMATION

Input: Cartesian $(x, y) \in N \times N$

→ Output: Log-polar $(r, \omega) \in M \times K$

$$\hat{x} = \frac{N/2-1}{M-1}(M-1)^{\frac{r}{M-1}}\cos\left(\frac{2\pi\omega}{K}\right) + \frac{N}{2}$$

$$\hat{y} = \frac{N/2-1}{M-1}(M-1)^{\frac{r}{M-1}}\sin\left(\frac{2\pi\omega}{K}\right) + \frac{N}{2}$$

PSEUDOCODE INVERSE TRANSFORMATION

Input: Log-polar $(r, \omega) \in N \times N$

→ Output: Cartesian $(x, y) \in X \times Y$

$$\hat{r} = N\frac{\log\left(\sqrt{\frac{(y-Y/2)^2}{Y^2/4} + \frac{(x-X/2)^2}{X^2/4}}\right)}{\log\left(\sqrt{(2)}\right)}$$

$$\hat{\omega} = \frac{N}{2} + \frac{N\arctan\left(\frac{y-Y/2}{Y/2}, \frac{x-X/2}{X/2}\right)}{2\pi}$$

Most of examples shown in this paper are images of size 256 × 256 pixels in (x, y) coordinates and a bilinear interpolation schema has been used for the image transformation. For the sake of coherence in the figures, the (ρ, ω) coordinates have been discretized in the same number of pixels than the Cartesian ones. However, as said above, the resolution can be increased by different interpolation schemes.

The log-pol representation presents some interesting properties. Rotations in the original Cartesian image become vertical cyclic shifts in the transformed log-pol image because of the periodic nature of the angular component. Analogously, the changes of size in the original image become horizontal shifts in the transformed image, according to the autosimilarity property of the exponential function. The choice of the center is crucial and all further treatments are sensitive to its choice (see Fig. 2). Ideally the center point should be previously defined by the nature of the object. If the center is not prefixed by any special feature, we may chose the center of gravity or the maximum of a certain distance function, for instance the geodesic center [12].

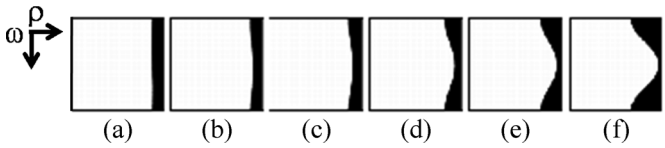

Fig. 2. Log-pol transformation centered in η_c of a circle whose central point is η_{circle} and radius r. The value of η_c is displaced from η_{circle} at different percentages of r: (a) 0%, (b) 8%, (c) 16%, (d) 32%, (e) 48%, and (f) 70%.

III. Cyclic Morphology

A. Definition

Let $f(x, y)$ be a 2-D image defined on the discrete space $E \subset Z^2$, $\eta = (x, y) \in (Z \times Z)$, with values of the complete lattice $\mathcal{T}$ (for simplicity the complete lattice is considered to be $\mathcal{T} = Z$ or a subset from Z corresponding to the grey levels $\mathcal{T} = \{0, 1, \cdots, 255\}$). The extension of the operators from classical mathematical morphology to the log-pol representation is achieved by changing the support of the image in order to introduce the principle of periodicity. The log-pol transformation of the function $f(x, y)$ generates a new function image $\hat{f}(\rho, \omega)$: $E_{\rho,\omega} \longrightarrow \mathcal{T}$, where the support of the image is the space $E_{\rho,\omega}$, $\hat{\eta} = (\rho, \omega) \in (Z \times Z_p)$ and where the angular variable $\omega \in Z_p$ is periodic with period p equivalent to 2π. A new relation of neighborhood is established between points at the top of the image $(\omega = 0)$ and the ones at the bottom of the image $(\omega = p - 1)$. Therefore, the image can be seen as a strip where the superior and the inferior borders are joined (see Fig. 3). The aim of this change is to preserve the invariance with respect to rotations in the Cartesian space, when morphological operations are done in the log-pol space.

Let $B_{S\omega,S\rho}(\hat{\eta}) = S\omega V(\hat{\eta}) \oplus S\rho H(\hat{\eta})$ be a rectangular structuring element (SE) centered at point $\hat{\eta}$, where $V(\hat{\eta})$ is the unit vertical SE and $H(\hat{\eta})$ the unit horizontal SE, and $S\omega$ and $S\rho$ their respective sizes (the symbol $\oplus$ is the Minkowski addition [2]). It is worth nothing the fact that horizontal and vertical neighborhoods respectively acquire radial and angular sense when processing in the original image representation. For instance, a vertical structuring element corresponds to an arc in the original image and a square corresponds to a circular sector. More precisely, working in the log-pol space with the SE $B_{S\omega,S\rho}(\hat{\eta})$ is completely equivalent to work in the cartesian space with the SE $\hat{B}_{S\omega,S\rho}(\eta, \eta_c)$ (see Fig. 3).

B. Implementation

The direct implementation of ω-periodicity needs the connectivity relationship to be modified by replacing the y coordinate by $y\, mod(y_{\max})$. As an alternative, we propose to extend the image along its angular direction by adding the top part of the image onto the bottom and the bottom part onto the top. The size of this duplicated part on each side should be bigger than the size of the vertical component of the structuring element in order to avoid a possible

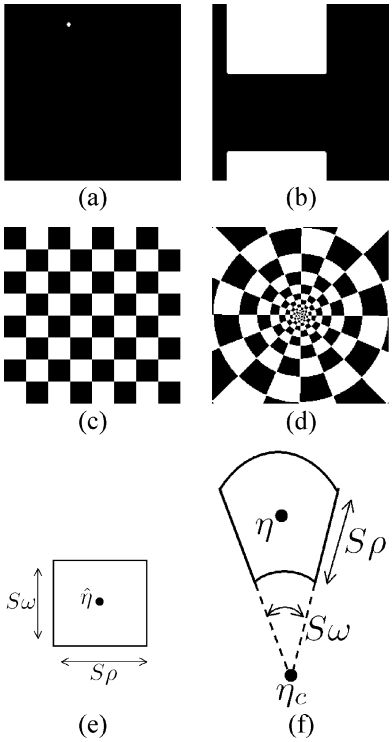

Fig. 3. (a) → (b): Dilation of one point by a square in log-pol coordinates. (c)↔ (d): Square structuring elements in log-pol space and their equivalence in cartesian space. (e) ↔ (f): $B_{S\omega,S\rho}(\hat{\eta})$ and its equivalence in cartesian space $\hat{B}_{S\omega,S\rho}(\eta,\eta_c)$.

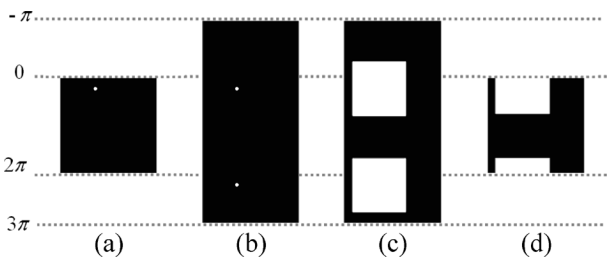

Fig. 4. Example of 2-D cyclic dilation (from left to right): (a) Original →; (b) cycled image →; (c) dilation by a square →; (d) original image mask: cyclic dilation.

edge effect. After having rendered the image cyclic, morphological operators should be applied as usual and only the image corresponding to the initial mask should be kept (see Fig. 4). After this preparation of the image, all the existing code of standard implementation of morphological operators in square neighborhoods may be used unchanged.

IV. Applications

In this section, we present two applications of cyclic mathematical morphology: one for shape analysis (binary images) and the other for texture description (grey-level images). Before describing these applications, we introduce the morphological operators which will be used in the sequel.

A. Morphological Tools

- *Circular filtering by openings/closings*.

The basic morphological operators are the *erosion*, i.e., $\varepsilon_{B_{S\omega,S\rho}}(\hat{f})(\hat{\eta})$ and the *dilation*, i.e., $\delta_{B_{S\omega,S\rho}}(\hat{f})(\hat{\eta})$. The two elementary operations of erosion and dilation can be composed together to yield a new set of operators having desirable filtering properties which are given by the *opening*, i.e., $\gamma_{B_{S\omega,S\rho}}(\hat{f})(\hat{\eta}) = \delta_{B_{S\omega,S\rho}}[\varepsilon_{B_{S\omega,S\rho}}(\hat{f})](\hat{\eta})$, and the *closing*, i.e., $\varphi_{B_{S\omega,S\rho}}(\hat{f})(\hat{\eta}) = \varepsilon_{B_{S\omega,S\rho}}[\delta_{B_{S\omega,S\rho}}(\hat{f})](\hat{\eta})$, The morphological *openings* (*closings*) filter out positive (negative) peaks from the structures according to the predefined size and shape of structuring element $B_{S\omega,S\rho}(\hat{\eta})$. Extracting inclusions or extrusions from the contour of a relatively rounded binary shape with simple log-pol openings $\gamma_{B_{S\omega,S\rho}}$ or closings $\varphi_{B_{S\omega,S\rho}}$ is the most direct application of cyclic morphology [see Fig. 5(a)].

A morphological tool that complements opening/closing operators for extraction of marked particles is the morphological reconstruction, implemented using the *geodesic dilation*, operator based on restricting the iterative dilation of a function marker $\hat{f}_m(\hat{\eta})$ by the unitary structuring element $B_{1,1}$ to a function reference $\hat{f}_r(\hat{\eta})$, i.e., $\delta^{(n)}_{\hat{f}_r}(\hat{f}_m) = \delta^{(1)}_{\hat{f}_r}\delta^{(n-1)}_{\hat{f}_r}(\hat{f}_m)$, where $\delta^{(1)}_{\hat{f}_r}(\hat{f}_m) = \delta_{B_{1,1}}(\hat{f}_m(\hat{\eta})) \wedge \hat{f}_r(\hat{\eta})$. The reconstruction by dilation or *opening by reconstruction* is then defined as $\gamma^{\mathrm{rec}}(\hat{f}_m,\hat{f}_r) = \delta^{(i)}_{\hat{f}_r}(\hat{f}_m)$ such that $\delta^{(i)}_{\hat{f}_r}(\hat{f}_m) = \delta^{(i+1)}_{\hat{f}_r}(\hat{f}_m)$ (idempotence). The definition of *closing by reconstruction* $\varphi^{\mathrm{rec}}(\hat{f}_m,\hat{f}_r)$ is obtained by duality. Whereas the adjunction opening $\gamma_{B_{S\omega,S\rho}}(\hat{f})$ (from an erosion/dilation) modifies the structures of the image, the associated opening by reconstruction $\gamma^{\mathrm{rec}}(\hat{f}_m,\hat{f})$ (where the marker $\hat{f}_m = \varepsilon_{B_{S\omega,S\rho}}(\hat{f})$ or $\hat{f}_m = \gamma_{B_{S\omega,S\rho}}(\hat{f})$) is aimed at efficiently and precisely reconstructing the "shape" of the structural peaks which are not totally removed by the marker filtering process (peaks of size $B_{S\omega,S\rho}$).

- *Radial skeletons*.

The concept of skeleton of a binary set X is very intuitive, however, its mathematical definition is not simple [13]. We propose to build the morphological skeletons using the thinning transformation. The *skeleton by thinning*, $Thin(X)$, is the application until stability of the hit-or-miss operator according to a predefined family of patterns. See in [2] details on the suitable series of patterns to be used to obtain homotopic skeletons. Using cyclic morphology, we define a *radial inner skeleton* $sk^{in}(f(\eta)) = Thin(\hat{f}(\hat{\eta}))$ as the skeleton obtained by homotopic thinning from the log-pol transformation of an objet $f(\eta)$. The invert transformation to Cartesian coordinates from the branches of the radial inner skeleton has radial sense and tends to converge on the center ($\rho = 0$). We also define the *radial outer skeleton* as the skeleton obtained by an homotopic thickening of the image, $\hat{f}^c(\hat{\eta})$ of the log-pol transformation of the object, $sk^{\mathrm{out}}(f(\eta)) = Thin(\hat{f}^c(\hat{\eta}))$. The inverse transformation to Cartesian coordinates from the branches of the radial outer skeleton has also radial sense and this time, they tend

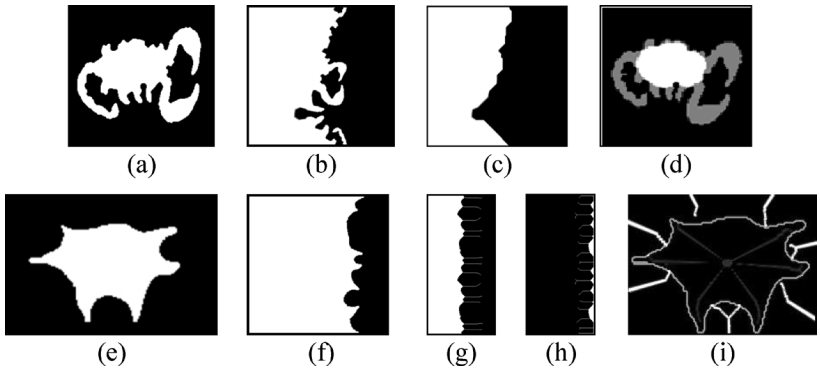

Fig. 5. Top row, extremities segmentation from "Leiurius quinquestriatus": (a) Original Cartesian image; (b) log-pol image (the center is the central image point); (c) opening in log-pol space with a vertical structuring element $S\omega = \pi/5$; (d) effect of filtering in Cartesian image. Bottom row, radial from an "Achantocyte" (red blood cell): (e) original Cartesian image; (f) log-pol image (the center is the central image point); (g)–(h) radial inner and radial outer skeletons respectively on cycled version of log-pol image; (i) effect of radial skeletons in Cartesian image.

to diverge to an hypothetical circumference in the infinity $(\rho \longrightarrow \infty)$ [see Fig. 5(b)].

- *Cyclic rectangular granulometry*.

A granulometry is the study of the size/shape structure distribution of an image. We focus here on rectangular granulometries, which uses rectangular SE and have been previously used to characterize document images [14]. Using horizontal/vertical operators in the log-pol representation, this shape and texture descriptor is specially adapted to analyze images with multiscale radial and angular patterns. Formally, a *granulometry* can be defined as an indexed family of transformations $\Gamma = (\gamma_{B_{S\omega,S\rho}})_{S\omega\geq 0, S\rho\geq 0}$, such that $\gamma_{B_{S\omega,S\rho}}$, or more generally Γ, verifies:

1) γ_0 is the identity mapping; i.e., $\gamma_0(f) = f$;
2) γ_λ is increasing; i.e., $f \leq g \Rightarrow \gamma_\lambda(f) \leq \gamma_\lambda(g), \forall \lambda \geq 0$, for every f and g;
3) γ_λ is anti-extensive; i.e., $\gamma_\lambda(f) \leq f, \forall \lambda \geq 0$, for every f;
4) γ_λ follows the absorption law; i.e., $\forall \lambda \geq 0, \forall \mu \geq 0$, $\gamma_\lambda \gamma_\mu = \gamma_\mu \gamma_\lambda = \gamma_{\max(\lambda,\mu)}$.

In particular, these axioms are valid for the adjunction opening $\gamma_{B_{S\omega,S\rho}}(f) = \delta_{B_{S\omega,S\rho}} \varepsilon_{B_{S\omega,S\rho}}(f)$ or for the opening by reconstruction $\gamma^{\gamma_{B_{S\omega,S\rho}}(f),f}$. Granulometries by *closings* (or *anti-granulometry*) can also be defined as families of increasing closings $\Phi = (\varphi_{B_{S\omega,S\rho}})_{S\omega\geq 0, S\rho\geq 0}$. Performing the granulometric analysis of an image in log-pol $\hat{f}(\hat{\eta})$ with Γ is equivalent to measuring the area of the opened image $\mathcal{M}(\gamma_{B_{S\omega,S\rho}}(\hat{f}))$ after each opening of sizes $S\omega$ (angular) $S\rho$ (radial), where $\mathcal{M}(\hat{f}(\hat{\eta}))$ is the Lebesgue measure of the image $\hat{f}(\hat{\eta})$ ($\mathcal{M}$ is the *area* in the binary case and the *volume* in the grey scale case). The *cyclic size distribution* of $\hat{f}(\hat{\eta})$ with respect to Γ, denoted $CSD^{\Gamma}_{\hat{f}}(S\omega, S\rho)$ is defined as the following (normalized) mapping $CSD^{\Gamma}_{\hat{f}}(S\omega, S\rho) = (\mathcal{M}(\hat{f}) - \mathcal{M}(\gamma_{B_{S\omega,S\rho}}(\hat{f})))/\mathcal{M}(\hat{f})$. The size distribution $CSD^{\Gamma}_{\hat{f}}(S\omega, S\rho)$ maps each angular/radial size $(S\omega, S\rho)$ to some measure of the positive structures with this size. The size distribution of dark structures is obtained from a family of closings, i.e., $CSD^{\Phi}_{\hat{f}}(S\omega, S\rho) = (\mathcal{M}(\gamma_{B_{S\omega,S\rho}}(\hat{f})) - \mathcal{M}(\hat{f}))/\mathcal{M}(\hat{f})$.

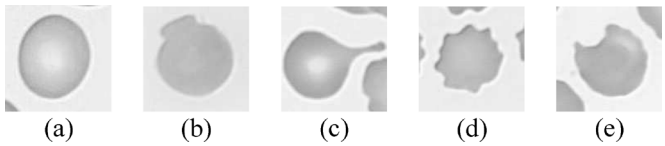

Fig. 6. Different typologies of red blood cells: (a) Normal erythrocyte;(b) "Mushroom" erythrocyte; (c) "Spicule" erythrocyte; (d) "Echinocyte" erythrocyte; (e) "Bitten" erythrocyte.

Another useful measure is the pattern spectrum [15], calculated as the derivative of size distribution $CSD^{\Gamma}_{\hat{f}}$ with respect to $S\omega$ or $S\rho$.

B. Application to the Erythrocyte Shape Analysis

In hematology, the visual analysis of the morphology of erythrocytes (size, shape, color, center,. . .) is of vital importance as it is well known that anomalies and variations from the typical red blood cell are associated with anemia or other illnesses [16]. In Fig. 6, a selection of abnormal erythrocytes is shown. We present hereafter one of the algorithms dedicated to the shape analysis developed in the MATCHCELL2 project [17], [18].

The aim of the proposed algorithm is to extract the inclusions from the erythrocyte shape, which is ideally round. This algorithm is used to identify the "bitten" class. It starts with the binary mask of the segmented erythrocyte, image (A), and its centroid η_c. The results correspond to image (E) (see Fig. 7); if $(\mathrm{E}) \neq \emptyset$ and the verifications are confirmed, it is classified as "bitten" erythrocyte (we have considered the gravity center as the center of the log-pol transformation).

1) Log-pol transformation $(A) \Rightarrow (B) = \xi_{\eta_c}(A)$.
2) Radial outer skeleton $(B) \Rightarrow (C) = sk^{\mathrm{out}}(B)$.
3) Circular filtering: Residue from a vertical closing of size $S\omega = \pi/3$ (maximal admissible angle for the inclusion) $(B) \Rightarrow (D) = \varphi_{\pi/3}(B) - (B)$ are the inclusion candidates.
4) Geodesic reconstruction of (D) using the marker $(C) \Rightarrow (E) = \gamma^{\mathrm{rec}}((C),(D))$.
5) We verify that $\forall\ E_i$ connected subset $\in$ (E), $[\mathrm{Surface}(E_i)/\mathrm{Sizeimage}] > \mu_1$.

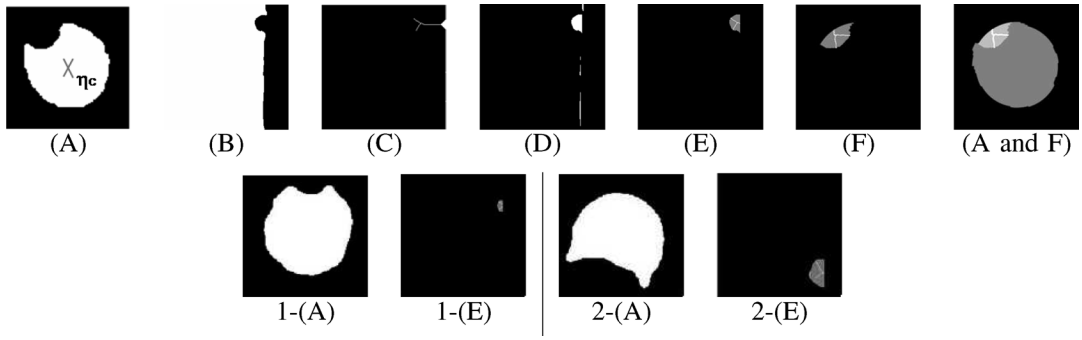

Fig. 7. Top row, extrusion extraction algorithm for "bitten" erythrocytes. Bottom row, other examples of "bitten" extraction (1,2).

6) Inverse transformation $(E) \Rightarrow (F) = \xi^{-1}(E)$.

The algorithm has an efficient and robust performance in the extraction of inclusions and extrusions. The use of the skeleton in order to sieve the candidates gives much greater robustness than would a mere opening or closing. This procedure removes small connected components preselected as deformations. Furthermore, the examples corresponding to "echinocytes," "spicules," and "mushroom" have been correctly classified (see more examples and details in [17]).

C. Application to Biometric Iris Identification

Iris texture patterns are considered to be different for each person and to remain stable over time. This interclass variability makes iris recognition one of the most interesting techniques for security applications, as very high recognition rates have been reported for iris identification systems [19]. However, only a few large-scale experiment evaluations have been reported, and there are insufficient publicly available databases. Further work in this field remains to be done, especially in validation and concerning with non ideal quality images. An iris recognition system can be divided into four parts: data acquisition, iris segmentation, iris feature extraction and classification. In this work, we just deal with the iris feature extraction. The goal is to produce a compact codification of the iris patterns from the segmented iris image which is made by a multiscale decomposition. The best known and proved system has been proposed by Daugman [20] and the encoding of the iris is done through the application of 2-D Gabor wavelet. Other methods use a Laplacian pyramid decomposition [21] or zero-crossing wavelet transform [22]. Regarding morphological approaches, a work based on skeletons representations of the iris patterns has been also proposed [23]. However, this method suffers from lack of robustness.

We propose to characterize the iris pattern by a grey-scale cyclic rectangular granulometry of openings by reconstruction and closings by reconstruction. Therefore, after eye's segmentation, each eye pattern in log-pol coordinates $\hat{f}_{\text{seg}}$ is characterized by the two bivariate histograms $CSD^{\Gamma^{\text{rec}}}_{\hat{f}_{\text{seg}}}(S\omega, S\rho)$ and $CSD^{\Phi^{\text{rec}}}_{\hat{f}_{\text{seg}}}(S\omega, S\rho)$ (see Fig. 8). Note that the use of openings and closings by reconstruction for the multiscale representation preserves contour information of the decomposed iris patterns (see Fig. 9). The measurements $CSD^{\Gamma^{\text{rec}}}_{\hat{f}}(S\omega, S\rho)$ and $CSD^{\Phi^{\text{rec}}}_{\hat{f}}(S\omega, S\rho)$ permit to describe the morphological size distribution of the different structures under a radial-angular metric. Tested images have shown interesting discriminative properties for the selected descriptors. This representation is invariant under size changes and rotations (which may be a problem due to the non perfect alignment of the user's head). Concerning the computational complexity, it is possible to perform a very efficient implementation by decomposing the rectangular SE in linear SE [24]. In relation to the next step in the biometric identification procedure, a codification of the CSD surfaces should be extracted to obtain the user's key. As it is desired to have a small key, the length $S\rho$ and $S\omega$ of the unit linear SE should be correlated to the quantity of information chosen for the codification (notice that the variation of the unit linear SE length provides a subsampling of the CSD surfaces).

The proposed methodology is currently being validated in larger databases. In first experiments, multivariate cyclic granulometries and its derived measurements show promising results as an alternative to wavelet analysis in iris biometric characterization.

V. Discussion

We have presented the general framework for cyclic morphology and some basic morphological tools adapted to this representation. Two pattern recognition examples developed with these operators have been presented.

The fundamental idea is that processing images in an intuitive geometric space can provide advantages over the traditional Cartesian representation. Regarding specifically mathematical morphology, the key issue is to obtain structuring elements that are adapted to the nature of the objects to be analyzed, not by deforming them (such as in morphological amoebas [25] or in viscous operators [26]), but by transforming the image itself. We consider that applying morphological operators with regular structuring elements in the transformed domain is equivalent to work with deformed structuring elements in the original image. Not only adapted metrics may be used, but also this kind of process provides benefits in terms of computational costs. More specifically, the conversion into polar-logarithmic coordinates as well as the derived cyclic morphology provides satisfying results in image analysis applied to round objects or spheroid-shaped 3-D-object models. The study of more complex morphological operators in the log-pol space still remains

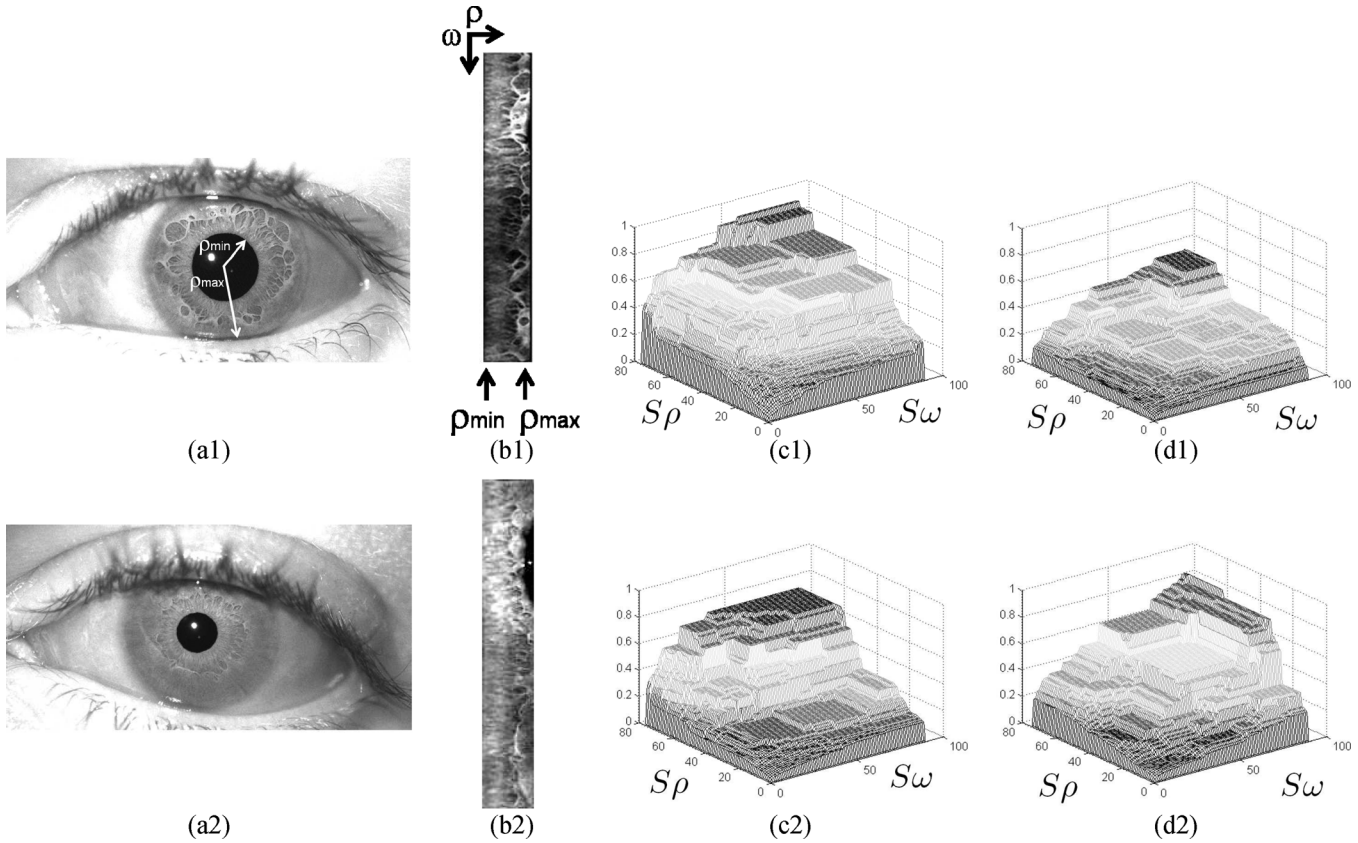

Fig. 8. Morphological description of two iris patterns: (a) Eye image (f); (b) segmented iris pattern in log-pol coordinates ($\hat{f}_{\text{seg}}$); (c) $CSD^{\Gamma\text{rec}}_{\hat{f}_{\text{seg}}}(S\omega, S\rho)$; (d) $CSD^{\Phi\text{rec}}_{\hat{f}_{\text{seg}}}(S\omega, S\rho)$.

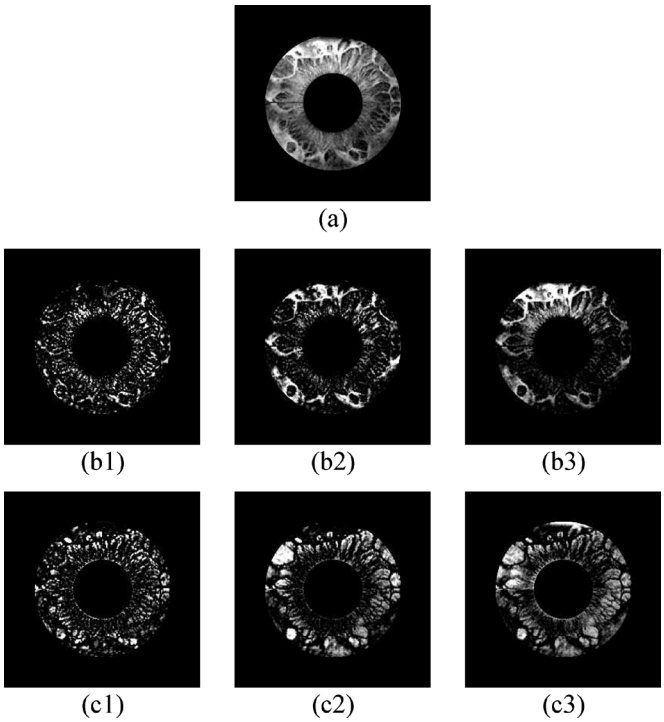

Fig. 9. Iris morphological decomposition: (a) Segmented iris pattern (f_{seg}); (b) cyclic opening-by-reconstruction top-hat ($f_{\text{seg}} - \gamma^{\text{rec}}_{B_{S\omega},S\rho}(f_{\text{seg}})$); (c) cyclic closing-by-reconstruction bottom-hat ($\varphi^{\text{rec}}_{B_{S\omega},S\rho}(f_{\text{seg}}) - f_{\text{seg}}$). The SE size $(S\omega, S\rho)$ used in the examples are: $b1(1/\pi, 20\%)$, $b2(\pi/6, 1\%)$, $b3(\pi/6, 20\%)$, $c1(1/\pi, 20\%)$, $c2(\pi/6, 1\%)$, $c3(\pi/6, 20\%)$.

an open topic, as well as the possibility to work under other geometric transformations.

ACKNOWLEDGMENT

The authors would like to thank F. Meyer, M. Huertas, G. Flandrin, J. Klossa, and C. Sanchez-Avila for fruitful discussions and their collaboration in the experimental sections.

REFERENCES

[1] C. Zahn and R. Roskies, "Fourier descriptors for plane closed curves," *IEEE Trans. Comput.*, vol. 21, pp. 269–281, Mar. 1972.
[2] J. Serra, *Image Analysis and Mathematical Morphology*. London, U.K.: Academic, 1982, 1988, vol. I,II.
[3] C. Weiman and G. Chaikin, "Logarithmic spiral grids for image processing and display," *Comput. Graph. Image Process.*, vol. 11, pp. 197–226, 1979.
[4] H. J. A. M. Heijmans and C. Ronse, "The algebraic basis of mathematical morphology. i dilations and erosions," *Comput. Vis., Graph., Image Process.*, vol. 50, no. 3, pp. 245–295, 1990.
[5] J. B. T. M. Roerdink, "Group morphology," *Pattern Recognit.*, vol. 33, no. 6, pp. 877–895, 2000.
[6] M. A. Luengo-Oroz, J. Angulo, G. Flandrin, and J. Klossa, "Mathematical morphology in polar-logarithmic coordinates. application to erythrocyte shape analysis," in *Proc. IbPRIA (2)*, 2005, pp. 199–206.
[7] M. Unser, "Splines: A perfect fit for signal and image processing," *IEEE Signal Process. Mag.*, vol. 16, no. 6, pp. 22–38, Jun. 1999.
[8] E. Schwartz, "Spatial mapping in the primate sensory projection: Analytic structure and relevance to perception," *Biol. Cybern.*, vol. 27, pp. 181–19 438, 1977.
[9] M. Bolduc and M. D. Levine, "A review of biologically motivated space-variant data reduction models for robotic vision," *Comput. Vis. Image Understand.*, vol. 69, no. 2, pp. 170–184, 1998.

[10] M. Tistarelli and G. Sandini, "On the advantages of polar and log-polar mapping for direct estimation of time-to-impact from optical flow," *IEEE Trans. Pattern Anal. Mach. Intell.*, vol. 15, no. 4, pp. 401–410, Apr. 1993.
[11] A. Bernardino and J. Santos-Victor, "A binocular stereo algorithm for log-polar foveated systems," in *Proc. Biologically Motivated Computer Vision*, 2002, pp. 127–136.
[12] C. Lantuejoul and F. Maisonneuve, "Geodesic methods in quantitative image analysis," *Pattern Recognit.*, vol. 17, no. 2, pp. 177–187, 1984.
[13] C. Lantuéjoul, "La squelettisation et son application aux mesures topologiques des mosaïques polycristallines," Ph.D. dissertation, School Mines of Paris, Paris, France, 1978.
[14] A. D. Bagdanov and M. Worring, "Multi-scale document description using rectangular granulometries," *Document Anal. Syst.*, pp. 445–456, 2002.
[15] P. Maragos, "Pattern spectrum and multiscale shape representation," *IEEE Trans. Pattern Anal. Mach. Intell.*, vol. 11, no. 7, pp. 701–716, Jul. 1989.
[16] P. J. H. Bronkorsta, M. J. T. Reinders, E. A. Hendriks, J. Grimbergen, R. M. Heethaar, and G. J. Brakenhoff, "On-line detection of red blood cell shape using deformable templates," *Pattern Recognit. Lett.*, vol. 21, no. 5, pp. 413–424, 2000.
[17] M. A. Luengo-Oroz, "Morphologie mathématique en coordonnées logarithmique-polaires et méthodes géométriques de classification. Application à l'étude des érythocytes," M.S. thesis, School Mines Paris, Paris, France, 2004.
[18] J. Angulo, "Morphologie mathématique et indexation d'images couleur. application à la microscopie en biomédecine," Ph.D. dissertation, School Mines Paris, Paris, France, 2003.
[19] J. Daugman, "Probing the uniqueness and randomness of iriscodes: Results from 200 billion iris pair comparisons," *Proc. IEEE*, vol. 11, pp. 1927–1935, 2006.
[20] J. Daugman, "High confidence visual recognition of persons by a test of statistical independence," *IEEE Trans. Pattern Anal. Mach. Intell.*, vol. 15, no. 11, pp. 1148–1161, Nov. 1993.
[21] R. P. Wildes, "Iris recognition: An emerging biometric technology," *Proc. IEEE*, vol. 85, pp. 1348–1363, 1997.
[22] C. Sanchez-Avila and R. Sánchez-Reillo, "Two different approaches for iris recognition using gabor filters and multiscale zero-crossing representation," *Pattern Recognit.*, vol. 38, no. 2, pp. 231–240, 2005.
[23] J. de Mira, Jr. and J. Mayer, "Identification of individuals through the morphological processing of the iris," in *Proc. Int. Conf. Image Processing*, 2003, pp. 341–344.
[24] L. Vincent, "Granulometries and opening trees," *Fundam. Inf.*, vol. 41, no. 1–2, pp. 57–90, 2000.
[25] R. Lerallut, E. Decencière, and F. Meyer, "Image filtering using morphological amoebas," *Image Vis. Comput.*, vol. 25, no. 4, pp. 395–404, 2007.
[26] C. Vachier and F. Meyer, "The viscous watershed transform," *J. Math. Imag. Vis.*, vol. 22, no. 2–3, pp. 251–267, 2005.

Miguel Angel Luengo-Oroz received the M.S. degree in telecommunications engineering from the Universidad Politécnica de Madrid (UPM), Spain, in 2004, with a M.S. thesis on mathematical morphology at the School of Mines, Paris, France. He received the M.S. degree in cognitive science from l'École Normale Supérieure and l'École des Hautes Etudes en Sciences Sociales, France, in 2005. He is currently pursuing the Ph.D. degree with a dissertation on biomedical engineering at the Biomedical Image Technologies Lab (UPM).

He is an associate researcher at the Complex Systems Institute, Paris. His main research interests are biomedical image processing, mathematical morphology, and biological complex systems.

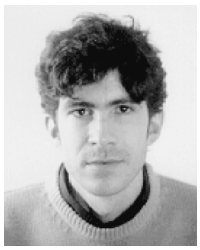

Jesús Angulo was born in Cuenca, Spain, in 1975. He received a degree in telecommunications engineering from the Polytechnical University of Valencia, Spain, in 1999, with a M.S. thesis on image and video processing, and the Ph.D. degree in mathematical morphology and image processing from the Ecole des Mines de Paris, France, in 2003, under the guidance of Prof. J. Serra.

He is currently a permanent researcher at the Center of Mathematical Morphology, MINES ParisTech. His research interests are in the areas of multivariate image processing (color, hyper/multispectral, temporal series, tensor imaging) and mathematical morphology (filtering, segmentation, shape and texture analysis, stochastic approaches, geometry), and their applications to biomedicine and biotechnology.

13.9 Publication IX : R. Verdú, J. Angulo, J. Serra. "Anisotropic morphological filters with spatially-variant structuring elements based on image-dependent gradient fields". *IEEE Trans. on Image Processing*, Vol. 20, No. 1, 200–212, 2011.

Anisotropic Morphological Filters With Spatially-Variant Structuring Elements Based on Image-Dependent Gradient Fields

Rafael Verdú-Monedero, Jesús Angulo, and Jean Serra

***Abstract*—This paper deals with the theory and applications of spatially-variant discrete mathematical morphology. We review and formalize the definition of spatially variant dilation/erosion and opening/closing for binary and gray-level images using exclusively the structuring function, without resorting to complement. This theoretical framework allows to build morphological operators whose structuring elements can locally adapt their shape and orientation across the dominant direction of the structures in the image. The shape and orientation of the structuring element at each pixel are extracted from the image under study: the orientation is given by means of a diffusion process of the average square gradient field, which regularizes and extends the orientation information from the edges of the objects to the homogeneous areas of the image; and the shape of the orientated structuring elements can be linear or it can be given by the distance to relevant edges of the objects. The proposed filters are used on binary and gray-level images for enhancement of anisotropic features such as coherent, flow-like structures. Results of spatially-variant erosions/dilations and openings/closings-based filters prove the validity of this theoretical sound and novel approach.**

***Index Terms*—Directional field regularization, mathematical morphology, nonlinear anisotropic filtering, spatially-variant operators.**

I. Introduction

MATHEMATICAL morphology is a nonlinear image processing methodology based upon lattice theory [1], [2]. The more often, it is used in a translation invariant approach, where the basic operation of a dilation (resp. erosion) consists in shifting a probe set B, called structuring element, to each pixel of the image for computing a supremum (resp. infimum). But the theory lends itself, as well, to structuring elements which vary over the space [2]–[6].

Matheron stated in [7] the kernel representation (i.e., the set of structuring elements that characterizes the operators) of spatially-invariant and increasing morphological elementary operations (i.e., morphological erosions and dilations) and their minimal basis representation was developed by Maragos and Schafer [8]–[11]. Afterwards, Serra extends in [2] the representation to spatially-variant operations as the union of erosions in a complete lattice, and Banon and Barrera proposed in [12] their kernel representation as well as Charif-Chefchaouni and Schonfeld did in the Euclidean space [13].

Spatially-variant morphological erosions and dilation were tackled by Charif-Chefchaouni and Schonfeld in [14], where they provided a kernel representation of increasing operators and established the existence of a unique minimal basis representation in the Euclidean space of increasing upper semicontinuous operators for the hit-or-miss topology in terms of spatially-variant morphological erosions and dilations. A minimal basis representation of increasing operators has been also pursued in [12] and [15].

The expression "spatially variant" encompasses both ideas of 1) the two level structure of a space E, and of all subsets $\mathcal{P}(E)$ and functions on E, and of 2) some variable processing over space E. Concerning mathematical morphology, the two founding texts about point 1) are [2, Ch. 2, 3, and 9] and [4], [5]. In [2, Ch. 2], devoted to the set case, Serra introduces the structuring function, with the derived four basic operations of dilation, erosion, and their two products, and the three dualities (adjunction, reciprocal, and complement); it is shown that a compact structuring function may have a reciprocal version infinite everywhere. In [2, Ch. 3], Matheron gives topological conditions for limiting such an expansion. [2, Ch. 9] is a first introduction to the function case, which is actually treated for the first time in [4]. In particular, Heijmans and Ronse developed the key approach by pulses sup-generators. More recent advances, due to Bouaynaya and Schonfeld can be found in [16], [17], due to Soille in [18], and concerning Roerdink group morphology in [19]. Other papers focus specifically on efficient implementations of spatially variant morphological operators, such as those of Dokladal and Dokladalova [20], [21] or Cuisenaire [22] based upon distance transformations.

Point 2) involves two branches. All examples in the founding papers refer to some geometrical deformation of the Euclidean space, by perspective [2, Ch. 4], or by rotation invariance [4]. The perspective case corresponds to an actual application to traffic control, by Beucher *et al.* [23]. But one can imagine another mode of variability, not given by a geometrical law, but by the images under study themselves. In [24], for example, in the description of a forest fire, the structuring elements are discs

Manuscript received July 29, 2009; revised December 11, 2009; accepted June 27, 2010. Date of publication July 08, 2010; date of current version December 17, 2010. This work was supported in part by the Ministerio de Ciencia e Innovación under Grant TEC2009-12675/TEC. The associate editor coordinating the review of this manuscript and approving it for publication was Dr. Jenq-Neng Wang.

R. Verdú-Monedero is with the Department of Tecnologías de la Información y las Comunicaciones, Universidad Politécnica de Cartagena, 32202 Cartagena, Spain (e-mail: rafael.verdu@upct.es).

J. Angulo is with CMM-Centre de Morphologie Mathématique, Mathématiques et Systèmes, MINES Paristech, 77300 Fontainebleau Cedex, France(e-mail: jesus.angulo@ensmp.fr; jesus.angulo@mines-paristech.fr).

J. Serra is with Laboratoire A2SI – ESIEE, 93162 Noisy-le-Grand, France (e-mail: serraj@esiee.fr).

Digital Object Identifier 10.1109/TIP.2010.2056377

whose variable radii are drawn from a so-called spread map, and they act on another image, that of the fuel map. In [25], Lerallut *et al.* introduced the notion of morphological amoebas, which are locally adaptive structuring elements obtained as geodesic balls according to edge information. As well as in [26], where the structuring elements are automatically adjusted to the gray-scale values in a range image to extract features of known sizes. A similar adaptability of the structuring element is studied by Debayle and Pinoli in [27].

Rather often, spatially variant morphology is associated with the search of directions. For example, fast implementation of morphological filters along discrete lines at arbitrary angles have been reported by Soille and Talbot in [28]. Other more sophisticated algorithms for morphological operators on thin structures are the path openings of Heijmans [29].

Close in terms of the obtained results but mathematically different to our study, continuous anisotropic morphological operations can be obtained as solutions of partial differential equations (PDEs) [30]–[33]. Breuß *et al.* developed in [34] continuous-scale morphology introducing a space-variant anisotropic behavior directly into the PDEs of dilation and erosion. They multiply the image gradient by a space-variant matrix using information from local structure tensors [35], [36], therefore, achieving that the speed of the evolution is locally adapted to the data. In the work by Tankyevych *et al.* [37], the orientation information is computed from Hessian matrix (i.e., second-order derivatives) and the curvilinear operators, such as the morphological closing, are computed by means of reciprocal structuring functions.

In this paper we focus on discrete morphology where orientated structuring elements vary over the space according to a vector field. A short version of this paper has been published in [38] and, in [39], preliminary results on binary images and linear structuring elements can be found. We draw robust information on the structuring elements from a dense and regular direction field obtained from the image under study itself. The discrete morphological processing is, thus, regularly and locally adapted to some features that already exist in the image, but that this processing aims to emphasize. The originality of our approach is that the spatially-variant anisotropic numerical openings/closings are computed from their direct geometric definitions. Evolved filters (based upon successive openings and closings) can be then used for enhancement of anisotropic images features such as coherent, flow-like structures. It is also important to remark that the orientation field is computed once from the original image, and then, for operators involving sequential openings/closings the same orientation field is used. This is coherent with the more recent theoretical results on adaptive mathematical morphology [40].

The paper is organized as follows. Section II is devoted to the mathematical background that set up the morphological operators with spatially-variant structuring elements. In Section III, we build and describe the directional vector field from which a structuring function is generated. With this tool in hand, we perform experiments on a series of binary and numerical images in Section IV, measurements that are followed by the conclusions in Section V.

II. Spatially-Variant Morphology

In mathematical morphology, many usual notions are dual from each other under complement. When the variation of a structuring function follows a geometrical law, then the complement of the dilation and of the adjoint opening can be theoretically calculated. But that is no longer true for data based variation, and this drawback obliges us to express the four basic operations by means of the structuring function exclusively, without resorting to complement, or equivalently, to reciprocal dilation.

The results on binary morphology presented in this section were mainly introduced in [2], [4], and [5] and more recently completed in [16]. However, this reminder is important to justify our extension to numerical functions. Note that our formulation is conceptually similar to the previous theoretical approach introduced in [17], but in our case, we use the notion of pulse functions and cylinder functions. In addition, the original discussion on the troubles with reciprocal functions will illustrate the real difficulties for the implementation of spatially variant structuring elements using the duality-based formulation of operators.

Notation

The images under study are modelled by sets, i.e., by subparts of a framework space E. Though we take $\mathbb{Z}^2$ for space E in the applications developed in Section IV, no condition on E is required by the theory itself. It is only when dealing with Minkowski type operators that a translation is introduced. When not, E is completely arbitrary, and can be any graph, or any continuous space. The points of E are given in bold small letters (e.g., $\mathbf{x} \in E$), and their coordinates are represented by small letters (e.g., $\mathbf{x} = (x, y)$). The subsets of E are given in capital letters (e.g., $X \subseteq E$), and the set of all these subsets (including the empty set $\emptyset$) is denoted by $\mathcal{P}(E)$. The points $\mathbf{x}$ of E, considered as elements $\{\mathbf{x}\}$ of $\mathcal{P}(E)$, are called singletons and form the subclass $\mathcal{S}(E)$ of $\mathcal{P}(E)$. A structuring function $\delta : E \to \mathcal{P}(E)$, or equivalently from $\mathcal{S}(E)$ into $\mathcal{P}(E)$, is an arbitrary family $\{\delta(\mathbf{x})\}$ of sets indexed by the points of E. One also writes $\delta(\mathbf{x}) = B(\mathbf{x})$, for emphasizing that the transform of a point is a set. When all these B are identical, up to a translation, then B is called a structuring element, and one puts $B(\mathbf{x}) = B_{\mathbf{x}}$.

The numerical axis $\mathcal{T}$ is an arbitrary family closed sequence of nonnegative numbers between two extreme bounds, 0 and M say, including these bounds. It can be $[0, +\infty]$, or the integers $[0, 255]$, etc.. The family of all numerical functions $f : E \to \mathcal{T}$ is denoted by $\mathcal{F}(E, \mathcal{T})$. Both sets $\mathcal{P}(E)$ and $\mathcal{F}(E, \mathcal{T})$ are complete lattices, i.e., posets whose any family of elements admits a supremum (a smaller upperbound) and an infimum (a larger lowerbound) [2], [4]. In the case of $\mathcal{P}(E)$, they are union and intersection, and for $\mathcal{F}(E, \mathcal{T})$ the pointwise sup and inf.

A. Dilation and Erosion

Since supremum and infimum do characterize a lattice, the two basic operations that map lattice $\mathcal{P}(E)$ into itself are those which preserve either union or intersection. In mathematical

morphology, they are called dilation and erosion, and are denoted by δ and ε, respectively

$$\delta(\cup X_i) = \cup\delta(X_i); \quad \varepsilon(\cap X_i) = \cap\varepsilon(X_i) \quad X_i \in \mathcal{P}(E). \quad (1)$$

Both operations are increasing. The two families of dilations and erosions on $\mathcal{P}(E)$ correspond to each other by the Galois's relation of an adjunction, namely

$$\delta(X) \subseteq Y \Leftrightarrow X \subseteq \varepsilon(Y). \quad (2)$$

Indeed, given a dilation δ, there always exists one and only one erosion ε that satisfies Equivalence (2) [4]. Moreover, though erosion ε usually admits many inverses, the composition product

$$\gamma(X) = \delta\varepsilon(X) \quad (3)$$

results in the smallest inverse of $\varepsilon(X)$.

Since a set X is the union of its singletons, i.e.,

$$X = \cup\{\{\mathbf{x}\} \,|\{\mathbf{x}\} \subseteq X\}$$

and since dilation commutes under union, this operation should admit a more analytical representation involving the singletons. Indeed, the dilation of (1) is generated by its restriction $\delta : \mathcal{S}(E) \rightarrow \mathcal{P}(E)$ which associates the structuring function $\delta(\mathbf{x})$ with each singleton $\{\mathbf{x}\}$ (or equivalently with each point $\mathbf{x}$ of E). One also writes $\delta(\mathbf{x}) = B(\mathbf{x})$, for emphasizing that the transform of a point is a set. The dilation of (1) becomes

$$\begin{aligned}\delta(X) &= \cup\{\delta\{\mathbf{x}\}|\{\mathbf{x}\}\subseteq X\} = \cup\{\delta(\mathbf{x})|\, \mathbf{x} \in X\} = \\ &= \cup\{B(\mathbf{x})|\, \mathbf{x} \in X\}. \end{aligned} \quad (4)$$

We then draw from adjunction (2) the expression of the erosion, namely

$$\varepsilon(X) = \{\mathbf{z} \mid B(\mathbf{z}) \subseteq X\}. \quad (5)$$

These two relations (4) and (5) show that the family $\{B(\mathbf{x}) = \delta(\mathbf{x})|\, \mathbf{x} \in E\}$ is the necessary and sufficient piece of information for generating a dilation and its adjoint erosion. Note that in spite of the name, a dilation may not be extensive (i.e., $\delta(X) \supseteq X$). Extensivity is obtained iff for all $\mathbf{x} \in E$ we have $\mathbf{x} \in B(\mathbf{x})$. Then the adjoint erosion ε is antiextensive.

B. Reciprocal Operations

The reciprocal duality between dilations plays an important role. With each structuring function δ, the reciprocal structuring function ζ is associated by writing

$$\mathbf{y} \in \zeta(\mathbf{x}), \qquad \text{iff} \qquad \mathbf{x} \in \delta(\mathbf{y}) \qquad \mathbf{x}, \mathbf{y} \in \mathbb{R}^d. \quad (6)$$

The algorithm that expresses ζ in function of δ is, therefore

$$\zeta(\mathbf{x}) = \cup\{\mathbf{y} : \mathbf{x} \in \delta(\mathbf{y})\}. \quad (7)$$

The derived dilation ζ on $\mathcal{P}(\mathbb{R}^d)$ is said to be reciprocal of δ. It satisfies the equivalence

$$\mathbf{x} \in \delta(X) \Leftrightarrow \zeta(\mathbf{x}) \text{ hits } X \quad (8)$$

which provides dilation with a new interpretation: the dilate $\delta(X)$ turns out to be the locus of those points $\mathbf{x}$ where $\zeta(\mathbf{x})$ hits X.

In addition, the notion of a reciprocal function allows us to interpret the duality for the complement. Dilation δ, viewed as acting on the background, induces an erosion ε^* since, according to (4), dilating the complement set X^c comes back to eroding X. More formally, we have that

$$\varepsilon^*(X) = [\delta(X^c)]^c.$$

Now, (8) tells us that $\delta(X^c) = \cup\{\mathbf{z} : \zeta(\mathbf{x}) \cap X^c \neq \varnothing\}$, hence

$$\varepsilon^*(X) = \cup\{\mathbf{z} : \zeta(\mathbf{x}) \subseteq X\} \quad (9)$$

i.e., the dual for complement of dilation δ is the erosion by the reciprocal structuring function ζ.

C. Opening and Closing

Let us come back to the product of operators $\gamma = \delta\varepsilon$ introduced in (3). This product γ is increasing ($X \subseteq Y \Rightarrow \gamma(X) \subseteq \gamma(Y)$), antiextensive ($\gamma(X) \subseteq X$) and idempotent ($\gamma\gamma(X) = \gamma(X)$). In algebra, these three features define an opening. Similarly, by inverting δ and ε, we obtain the closing $\varphi = \varepsilon\delta$, which is increasing, extensive, and idempotent.

The analytical representation of dilation δ by means of the structuring function $\mathbf{x} \rightarrow B(\mathbf{x})$ extends to the associated opening and closing. We directly draw from Relations (4) and (5) that

$$\delta\varepsilon(X) = \cup\{B(\mathbf{x})|B(\mathbf{x})\subseteq X\} \quad (10)$$

$$\varepsilon\delta(X) = \cup\{\mathbf{x}\,|B(\mathbf{x})\subseteq \cup[B(\mathbf{x})|\, \mathbf{x} \in X]\}. \quad (11)$$

The geometrical meaning of the first relation is clear: $\delta\varepsilon(X)$ is the region of the space swept by all structuring sets $B(\mathbf{x})$ that are included in X.

Finally, relations (4), (5), (10), and (11) are completely determined by the datum of the structuring function $\mathbf{x} \rightarrow B(\mathbf{x})$ and do not involve any reciprocal function. In particular, opening $\gamma = \delta\varepsilon$ and closing $\varphi = \varepsilon\delta$ are not dual of each other for the complement.

D. Translation Invariant Case

When E is equipped with a translation and when δ and ε commute under this translation, then we get the very classical Minkowski formalism.

Let δ_B be a translation invariant dilation, where $B = \delta_B(0)$ stands for the transform of the origin. For $\mathbf{x} \in E$, the translation of B by vector $\overrightarrow{0\mathbf{x}}$ is denoted by $B_{\mathbf{x}}$. We draw from Definition (1) and from translation invariance that

$$\delta_B(X) = \bigcup_{\mathbf{x}\in X} B_{\mathbf{x}} = \{\mathbf{b} + \mathbf{x}, \mathbf{x} \in X, \mathbf{b} \in B\} = \bigcup_{\mathbf{b}\in B} X_{\mathbf{b}}$$

which is nothing but the classical Minkowski sum $X \oplus B$, i.e.,

$$\delta_B(X) = X \oplus B = B \oplus X.$$

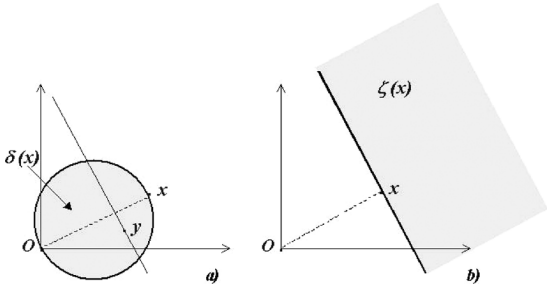

Fig. 1. (a) Point x and its structuring function δ. (b) Transposed function $\zeta(x)$.

The adjoint erosion ε_B derives from Equivalence (2) and has an expression

$$\varepsilon_B(X) = X \ominus B = \{\mathbf{z} : B_\mathbf{z} \subseteq X\} = \bigcap_{\mathbf{b}\in\check{B}} X_\mathbf{b}$$

where $\check{B} = \{-\mathbf{b}, \mathbf{b} \in B\}$ is called the transposed set of B. As before, the duality by adjunction involved here is not that of the complement. The latter should yield erosion ε^*

$$\varepsilon^*(X) = (X^c \oplus B)^c = \bigcap_{\mathbf{b}\in B} X_\mathbf{b} = \{\mathbf{z} : \check{B}_\mathbf{z} \subseteq X\} = X \ominus \check{B}. \tag{12}$$

By comparing relations (9) and (12) we see that the reciprocal structuring function $\zeta(\mathbf{x})$ at point $\mathbf{x}$ is nothing but the translate $\check{B}_\mathbf{x}$ at point $\mathbf{x}$ of the transposed set $\check{B}$. Therefore, the dilation δ^* adjoint to ε^* is written as

$$\delta^* = X \oplus \check{B} = \{\mathbf{z} \in E, X \cap B_\mathbf{z} \neq \emptyset\}.$$

When the structuring element B is symmetrical w.r.t. the origin, i.e., when $B = \check{B}$, then the two dual erosions ε and ε^* coincide, as well as the two dilations δ and δ^*. That occurs when B is a disc, an ellipse, a square, a hexagon, a segment, etc. centered at the origin, i.e., in the most popular cases.

E. Troubles With Reciprocal Functions

However, the nice identifications $\delta = \delta^*$ and $\varepsilon = \varepsilon^*$ vanish as soon as translation invariance is dropped, even when the $B(\mathbf{x})$'s are symmetrical.

The situation is even worse if there is no theoretical model for the variation of $\delta(\{\mathbf{x}\}) = B(\mathbf{x})$ over the space, because there is no ways for getting the reciprocal $\zeta(\{\mathbf{x}\})$, except by computing it numerically at each point by using (7). But that may have some surprises in store, even with just compact discs. For example, let us define as structuring function $\delta(\mathbf{x})$ the disc of diameter $O\mathbf{x}, \mathbf{x} \in \mathbb{R}^2$, (see Fig. 1). By reasoning geometrically, we see that $\mathbf{x}$ is inside the circle with diameter $O\mathbf{y}$ if and only if $\mathbf{y}$ belongs to the half-plane bounded by the perpendicular to $O\mathbf{x}$ at point $\mathbf{x}$. Function $\zeta(\mathbf{x})$, thus, consists of the half-plane, and is never bounded, even though the function $\delta(\mathbf{x})$ is always bounded. Furthermore, when $\mathbf{x}$ is moved along the $O\mathbf{x}$ axis towards the origin, the function $\delta(\mathbf{x})$ decreases but $\zeta(\mathbf{x})$ increases.

The following proposition overcomes the trouble with Fig. 1 by imposing some conditions to δ, as shown in the following definition.

Definition 1: When a structuring function $\delta : \mathcal{S}(\mathbb{R}^d) \longmapsto \mathcal{P}(\mathbb{R}^d)$ is compact in the following sense:

1) it is upper semicontinuous from $\mathcal{S}$ into $\mathcal{K}$;
2) the union $\cup\{\delta_{-x}(x), x \in \mathbb{R}^d\}$ has a compact closure δ

$$\overline{\delta} = \overline{\cup\{\delta_{-x}(x), x \in \mathbb{R}^d\}}$$

then the reciprocal structuring function ζ is in turn compact.

All the linear/elliptic dilations introduced in the following are compact. Nevertheless, computing their reciprocal forms should be rather complicated. Indeed, a lesson we can draw from Fig. 1 is to refuse any formulation, any algorithm, that involves ζ, except when the δ varies according to a specific (and easy) law, such as translation invariance, or perspective reduction, for example. That is the very reason for which the four basic relations (4), (5), (10), and (11) we gave for δ, ε, and γ, φ, exclusively depend upon the structuring function $\mathbf{x} \to B(\mathbf{x})$, and do not bring any complement into play.

F. Dilation for Numerical Functions

Note that the duality under complement works for sets only, whereas adjunction duality applies to any complete lattice, such as that $\mathcal{F}(E, \mathcal{T})$ of the numerical functions that we now consider. Associated with the numerical function $f : E \to \mathcal{T}$ under study and the set structuring function $\mathbf{x} \to B(\mathbf{x})$, we introduce the following pulse function $i_{\mathbf{x},t}$ of level t at point $\mathbf{x}$

$$i_{\mathbf{x},t}(\mathbf{x}) = t; \quad i_{\mathbf{x},t}(\mathbf{y}) = 0, \qquad \text{when } \mathbf{y} \neq \mathbf{x}.$$

Dilating $i_{\mathbf{x},\mathbf{t}}$ by the structuring function B results in the cylinder $C_{B(\mathbf{x}),t}$ of base $B(\mathbf{x})$ and height t. Now, function f can be decomposed into the supremum of its pulses, i.e.,

$$f = \vee\{i_{\mathbf{x},f(\mathbf{x})}, \mathbf{x} \in E\}.$$

Since dilation commutes under supremum, the dilate of f by δ, of structuring function B is given by the supremum of the dilates of its pulses, namely

$$\delta(f) = \vee\{C_{B(\mathbf{x}),f(\mathbf{x})}, \mathbf{x} \in E\}. \tag{13}$$

Similarly, the eroded $\varepsilon(f)$ is the supremum of those pulses whose dilated cylinders are smaller than f, i.e.,

$$\varepsilon(f) = \vee\{i_{\mathbf{x},t} \mid C_{B(\mathbf{x}),t} \leq f, \mathbf{x} \in E\}. \tag{14}$$

These two operations satisfy the equalities $\delta(\vee f_i) = \vee\delta(f_i)$ and $\varepsilon(\wedge f_i) = \wedge\varepsilon(f_i)$, $f_i \in \mathcal{F}$, and Galois equivalence (2) in the lattice $\mathcal{F}(E, \mathcal{T})$ of the numerical functions. Moreover, the cross sections of $\delta(f)$ (resp. $\varepsilon(f)$) are the dilated (resp. the eroded) versions of the cross sections of f by the same structuring function. For this reason they are called "flat operations." Just as in the set case, the duality under adjunction does not coincide with that under the involution $f \to M - f$, which plays a role similar to a complement. The operation

$$\varepsilon^* = M - \delta(M - f)$$

turns out to still be an erosion, but ε^* is different from the ε of (14).

The two products $\gamma = \delta\varepsilon$ and $\varphi = \varepsilon\delta$ are opening and closing on $\mathcal{F}(E, \mathcal{T})$, and, as δ and ε, they commute under cross sectioning. Opening γ, for example, admits the following expression:

$$\gamma(f) = \vee\{C_{B(\mathbf{x}),t} \leq f, \mathbf{x} \in E\}. \tag{15}$$

In the product space $E \times \mathcal{T}$ the subgraph of the opening $\gamma(f)$ is generated by the zone swept by all cylinders $C_{B(\mathbf{x}),t}$ smaller than f. Again, the closing $\varphi = \varepsilon\delta$ does not coincide with that, $M - \gamma(M - f)$, obtained by replacing f by $M - f$ in (15).

In case of translation invariance, (i.e., τ-invariance), one introduces the structuring element B associated with the origin in E. The previously mentioned operations δ and ε reduce to

$$(\delta_B f)(\mathbf{x}) = \vee\{f(\mathbf{x} - h), h \in B\} = (f \oplus B)(\mathbf{x})$$
$$(\varepsilon_B f)(\mathbf{x}) = \wedge\{f(\mathbf{x} + h), h \in B\} = (f \ominus B)(\mathbf{x}).$$

The corresponding opening and closing are defined, respectively, as $\gamma_B(f) = \delta_B(\varepsilon_B(f))$ and $\varphi_B(f) = \varepsilon_B(\delta_B(f))$.

III. Directional Field Computation

This section describes the method for estimating the orientation of the structures contained in a binary or gray-level image. This vector field is obtained by using the average squared gradient (ASG) and then applying a regularization process. Once the orientation is regularized and extended to the whole image, this information is used to indicate the orientation of the structuring element at each pixel of the image. Thus, there is not any pixel without orientation information. Note that the aim of this regularization process is neither smooth nor restore the original image with anisotropic diffusion [41]–[43], but avoid that a pixel does not have orientation information due to it is far from any edge [39]. Afterwards, given that all pixels in the image have information about the direction of the data, subsequent discrete morphological operations can be performed using spatially variant structuring elements.

A. ASG

The ASG method provides the directional field by squaring and averaging the gradient vectors [44], [45]. Given an image $f(x, y)$, ASG uses the following definition of gradient:

$$\mathbf{g} = \begin{bmatrix} g_1(x,y) \\ g_2(x,y) \end{bmatrix} = \operatorname{sign}\left(\frac{\partial f(x,y)}{\partial x}\right) \begin{bmatrix} \frac{\partial f(x,y)}{\partial x} \\ \frac{\partial f(x,y)}{\partial y} \end{bmatrix}. \tag{16}$$

This definition provides a gradient vector whose first component is always positive (the reason is that we are interested in the orientation of the directional field and not in the direction). Then the gradient is squared (i.e., doubling its angle and squaring its magnitude) and averaged in some neighborhood using the window W

$$\overline{\mathbf{g}_s} = \begin{bmatrix} \overline{g_{s,1}}(x,y) \\ \overline{g_{s,2}}(x,y) \end{bmatrix} = \begin{bmatrix} \sum\limits_W \left(g_1^2(x,y) - g_2^2(x,y)\right) \\ \sum\limits_W \left(2\, g_1(x,y)\, g_2(x,y)\right) \end{bmatrix}. \tag{17}$$

As a consequence, opposite gradients will point in the same direction reinforcing each other, while perpendicular vectors will cancel. The directional field ASG is $\mathbf{d} = [d_1(x, y),\, d_2(x, y)]^\top$, where its angle is obtained as

$$\angle\mathbf{d} = \frac{\Phi}{2} - \operatorname{sign}(\Phi)\frac{\pi}{2} \tag{18}$$

which is in the range $[-\pi/2,\, \pi/2]$, being $\Phi = \angle\overline{\mathbf{g}_s}$; and the magnitude of $\mathbf{d}$, $\|\mathbf{d}\|$, can be left as the magnitude of $\overline{\mathbf{g}_s}$, or the squared root of $\overline{\mathbf{g}_s}$ or, in some applications (see, e.g., [39] and [46]), it can be set to unity.

B. Regularization of the ASG: Average Squared Gradient Vector Flow (ASGVF)

The vectors of the ASG field are generally different from zero only near the edges and, in homogeneous regions, where the gradient is nearly zero, the ASG is also zero. In order to extend the orientation information to pixels where the gradient is nearly zero a regularization is performed (see, e.g., [47]). This process diffuses the orientation like gradient vector flow [48], [49], providing the ASGVF. The ASGVF is the vector field $\mathbf{v} = [v_1(x, y),\, v_2(x, y)]^\top$ that minimizes the energy functional

$$\mathcal{E}(\mathbf{v}) = \mathcal{D}(\mathbf{v}) + \alpha\mathcal{S}(\mathbf{v}) \tag{19}$$

where $\mathcal{D}$ represents a distance measure given by the square difference between the original and the regularized average square gradient, weighted by the squared value of the first one

$$\mathcal{D}(\mathbf{v}) = \frac{1}{2}\sum_{l=1}^{2}\int_E \|\mathbf{d}\|^2 \|v_l - d_l\|^2\, dx\, dy \tag{20}$$

where E is the image support and $l = 1, 2$ is the component index. The energy term $\mathcal{S}$ is the regularization term, it determines the smoothness of the directional field and represents the energy of the second-order derivatives of the signal

$$\mathcal{S}(\mathbf{v}) = \frac{1}{2}\sum_{l=1}^{2}\int_E \|\Delta v_l\|^2\, dx\, dy \tag{21}$$

where $\Delta = \partial^2/\partial x^2 + \partial^2/\partial y^2$ is the Laplacian operator. The positive parameter α governs the trade off between the fit to the data $\mathbf{d}$ and the smoothness of the solution $\mathbf{v}$ (see, e.g., [50]). According to the calculus of variations, a directional field $\mathbf{v}$ minimizing (19) is necessarily a solution of the Euler-Lagrange equations

$$(\mathbf{v} - \mathbf{d})|\mathbf{d}|^2 + \alpha\Delta^2\mathbf{v} = \mathbf{0}. \tag{22}$$

These equations can be solved by adding an artificial time and computing the steady-state solution

$$\frac{\partial}{\partial t}\mathbf{v} + (\mathbf{v} - \mathbf{d})|\mathbf{d}|^2 + \alpha\Delta^2\mathbf{v} = \mathbf{0}. \tag{23}$$

To set up the iterative solution, let the indices i, j, and n correspond to the discretization of x, y and t axes, respectively, and let the spacing between pixels be Δ_x and Δ_y, and the time step for each iteration be Δ_t. Replacing partial derivatives with its discrete approximations and considering discrete images ($\Delta_x =$

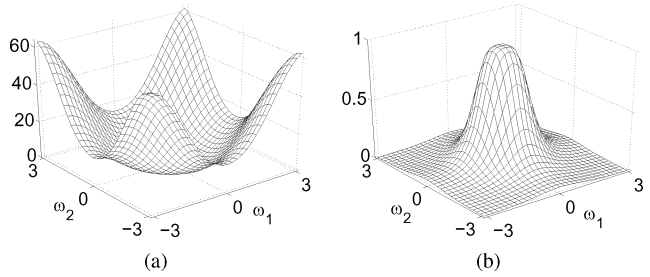

(a) (b)

Fig. 2. Spectra of filters (a) $K(\omega_1, \omega_2)$ and (b) $H(\omega_1, \omega_2)$ using $\eta = 1$.

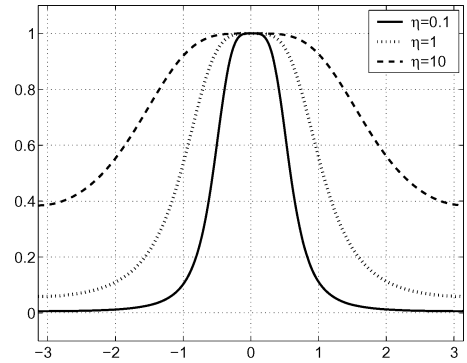

Fig. 3. Spectrum of filter $H(\omega) = \eta/(\eta + K(\omega))$ using $\eta = 0.1$ (in solid line), $\eta = 1$ (in dotted line) and $\eta = 10$ (in dashed line).

$\Delta_y = 1$) gives our iterative solution to ASGF, via a time-marching algorithm, as follows:

$$\mathbf{v}_l^n = \mathbf{v}_l^{n-1} + \Delta_t \, \mathbf{f}_l^{n-1} - \frac{1}{\eta} \, \mathbf{k} * \mathbf{v}_l^n \tag{24}$$

where $f_{i,j}^{l,n-1} = (d_{i,j}^l - v_{i,j}^{l,n-1})|\mathbf{d}_{i,j}|^2$, n is the iteration index, $\eta = (\alpha\Delta_t)^{-1}$, $\mathbf{k}$ stands for a kernel operator performing the discrete approximation of spatial derivatives of Δ^2 (see Appendix A), and $*$ denotes discrete convolution. The iteration is implemented more efficiently in the frequency domain, using the 2-D discrete Fourier transform (DFT) [51]

$$V_l^n = V_l^{n-1} + \Delta_t \, F_l^{n-1} - \frac{1}{\eta} \, K \, V_l^n \tag{25}$$

where V_l^n, V_l^{n-1}, F_l^{n-1} are the 2-D DFTs of their respective signals in the spatial domain, convolution has become a pointwise product of the spectra [52], K is the sampling of spectrum $K(\omega_1, \omega_2)$ which contains the frequency representation of the discrete derivatives in the spatial domain and is given by [53]

$$K(\omega_1, \omega_2) = 4(2 - \cos\omega_1 - \cos\omega_2)^2. \tag{26}$$

Finally, (25) can be rewritten as

$$V_l^n = H\,(V_l^{n-1} + \Delta_t \, F_l^{n-1}) \tag{27}$$

where H is a low-pass filter whose values are less than or equal to one and is defined as

$$H(\omega_1, \omega_2) = \frac{\eta}{\eta + K(\omega_1, \omega_2)}. \tag{28}$$

Fig. 2 depicts the frequency spectra of filters $H(\omega_1, \omega_2)$ and $K(\omega_1, \omega_2)$.

This method based upon the DFT considers the input image as a periodic image. This is not a problem if the data in the images is within a uniform background (e.g., when dealing with medical images) or it can be overcame by using a folded algorithm which extends the image symmetrically about its borders (see e.g., [54]).

IV. Applications

In the applications shown in the following, we shall use the regularized vector field $\mathbf{v}$ as a base for generating the structuring function $\{\delta(\mathbf{x}), \mathbf{x} \in E\}$, where the set $\delta(\mathbf{x})$ varies with the location of point $\mathbf{x}$. Before presenting the applications, we have to contemplate a theoretical question: are we sure that a family $\{\delta(\mathbf{x}), \mathbf{x} \in E\}$, which is derived from the function f under study, is able to perform a variable dilation [in the sense of (4)] on the very function f? Yes and no, indeed, according to what we decide to consider as fixed. For illustrating this point, let us take two functions f and f^*, and their supremum $f^{**} = f \vee f^*$, whose respective vector fields $\mathbf{v}, \mathbf{v}^*$, and $\mathbf{v}^{**}$, generate the three structuring functions δ, δ^*, and δ^{**}, respectively. Since the equality

$$\delta(f) \vee \delta(f^*) = \delta^{**}(f \vee f^*)$$

has no particular reason to be true, the mapping $f \to \delta(f)$ is not a dilation.

On the other hand, let us suppose now that, having constructed the vector field $\mathbf{v}_0$ of some given function f_0, we keep the family $\{\delta_0(\mathbf{x}), \mathbf{x} \in E\}$ generated by f_0, as a universal reference for dilating all numerical functions. This time, we find the framework of (4), and δ_0 is a dilation, i.e., we have

$$\vee\delta_0(f_i) = \delta_0(\vee f_i)$$

for every family f_i of numerical functions. Therefore, the adjoint operator ε of (5) is an erosion, and the two products $\gamma = \delta\varepsilon$ and $\varphi = \varepsilon\delta$ are opening and closing, respectively. The antiextensivity of γ and the extensivity of φ allow us to use the two residuals, or top-hats

$$th^+(f) = f - \gamma(f) \tag{29}$$

$$th^-(f) = \varphi(f) - f. \tag{30}$$

Both composition products $\gamma\varphi$ and $\varphi\gamma$ are idempotent and they are called alternate morphological filters. Most of the examples shown in the following involve these last six operations.

The situation becomes more ticklish with sequential alternate filters such as $M_2 = \varphi_2\gamma_2\varphi_1\gamma_1$, because in this expression, $\varphi_1\gamma_1$ and $\varphi_2\gamma_2$ are supposed to derive from two distinct structuring functions (if not we should have by idempotence $\varphi_1\gamma_1\varphi_1\gamma_1 = \varphi_1\gamma_1$). But remembering the geometrical meaning of the opening $\gamma(f) = \delta\varepsilon(f)$, namely the zone under the graph of function f swept by all horizontal $\delta(\mathbf{x})$, then, when dealing with two ordered structuring functions δ_1 and $\delta_2 \geq \delta_1$, then $\delta_2(\mathbf{x}) \subseteq X_t(f)$ implies that $\delta_1(\mathbf{x}) \subseteq X_t(f)$ for all horizontal

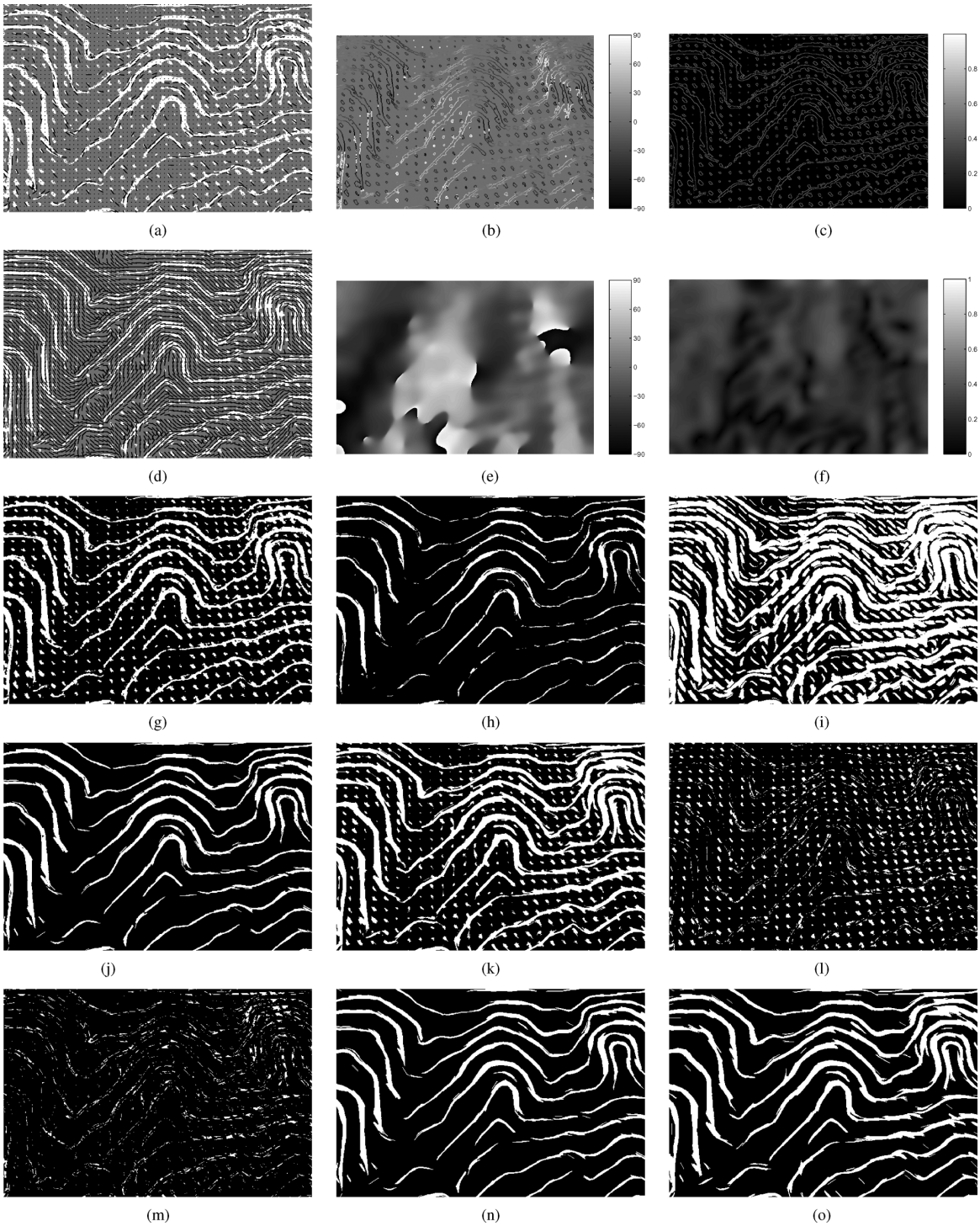

Fig. 4. (a)-(c) ASG using a flat squared averaging window of size 15×15. (d)-(f) ASGVF using $\eta = 10^{-2}$ and $\Delta_t = 1$. (g) Original binary image $f(\mathbf{x})$ 404×599. (h) Spatially-variant linear erosion of length 15 pixels. (i) Spatially-variant linear dilation of length 15 pixels. (j) Spatially-variant linear opening of length 15 pixels. (k) Spatially-variant linear closing of length 15 pixels. (l) Top-hat. (m) Dual top-hat. (n) Spatially-variant linear alternate filter (opening followed by closing) of size 15. (o) Spatially-variant linear alternate filter (closing followed by opening) of size 15. (a) ASG $\mathbf{d}$. (b) $\angle\mathbf{d}$. (c) $|\mathbf{d}|$. (d) ASGVF, $\mathbf{v}$. (e) $\angle\mathbf{v}$. (f) $|\mathbf{v}|$. (g) $f(\mathbf{x})$. (h) $\varepsilon_{L_{15}^{\theta(\mathbf{x})}}(f)(\mathbf{x})$. (i) $\delta_{L_{15}^{\theta(\mathbf{x})}}(f)(\mathbf{x})$. (j) $\gamma_{L_{15}^{\theta(\mathbf{x})}}(f)(\mathbf{x})$. (k) $\varphi_{L_{15}^{\theta(\mathbf{x})}}(f)(\mathbf{x})$. (l) $th^{+}(f)(\mathbf{x})$. (m) $th^{-}(f)(\mathbf{x})$. (n) $\varphi_{L_{15}^{\theta(\mathbf{x})}}\gamma_{L_{15}^{\theta(\mathbf{x})}}(f)(\mathbf{x})$. (o) $\gamma_{L_{15}^{\theta(\mathbf{x})}}\varphi_{L_{15}^{\theta(\mathbf{x})}}(f)(\mathbf{x})$.

cross sections of f, i.e., $\gamma_1 \geq \gamma_2$, or equivalently $\gamma_1\gamma_2 = \gamma_2\gamma_1 = \gamma_2$, and by duality $\varphi_1 \leq \varphi_2$, and $\varphi_1\varphi_2 = \varphi_2\varphi_1 = \varphi_2$. We immediately derive that M_2 is idempotent and $M_2M_1 = M_2$ (where $M_1 = \varphi_1\gamma_1$), which provides the alternate filter M_2 with a strong robustness. An example is given in Fig. 6.

In the following scenarios, a linear or rectangular structuring element is used according to the structuring function

$$\delta_L(\mathbf{x}) \equiv L^{[\theta,\lambda,w](\mathbf{x})} \tag{31}$$

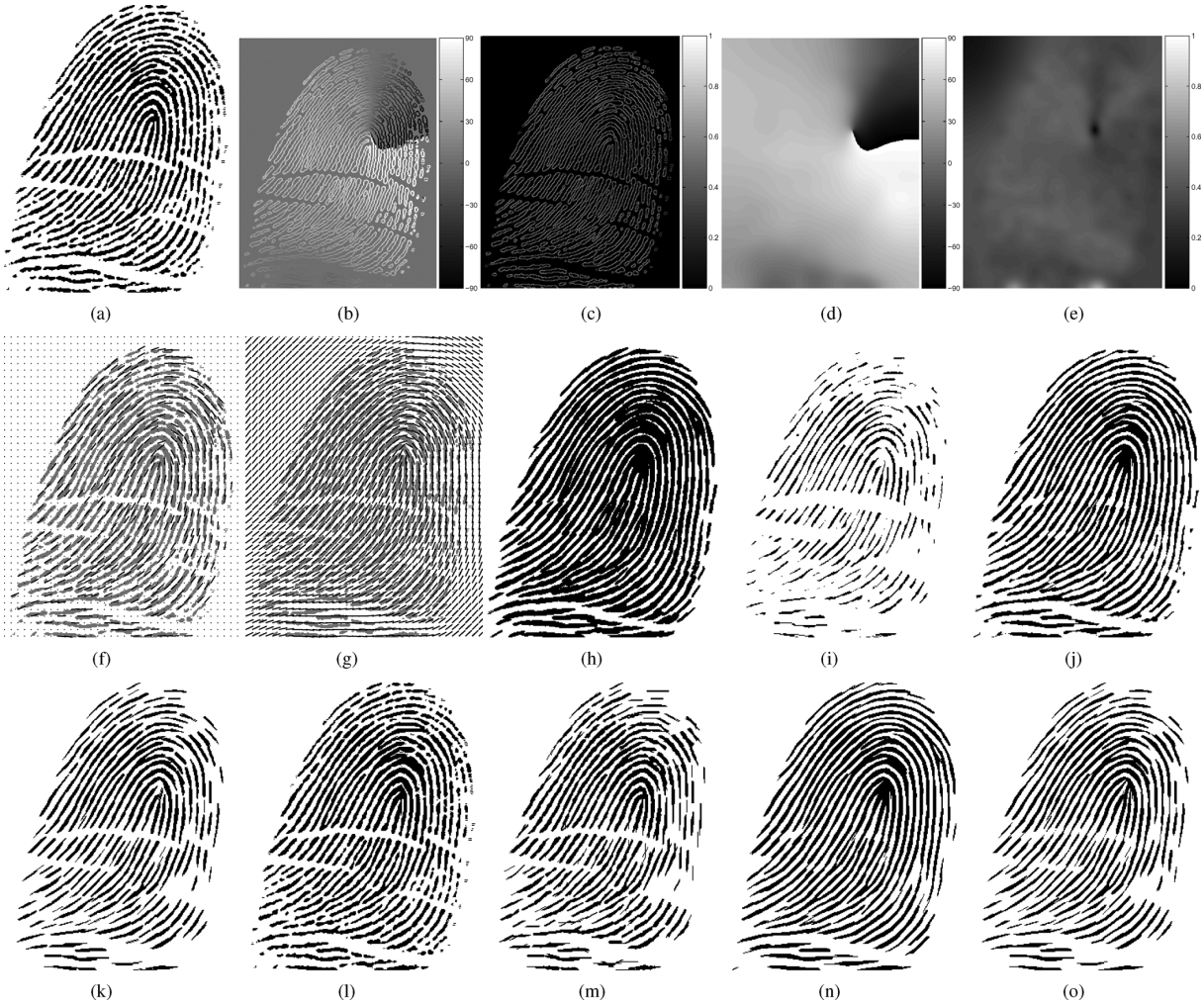

Fig. 5. (a) Original binary image $f(\mathbf{x})$ 362×285. (b) and (c) ASG using a 35×35 flat averaging window. (d) and (e) ASGVF using $\eta = 10^{-2}$ and $\Delta_t = 1$. (f) ASG $\mathbf{d}$. (g) ASGVF $\mathbf{v}$. (h) Spatially-variant linear erosion of length 15 pixels. (i) Spatially-variant linear dilation of length 15 pixels. (j) Spatially-variant linear opening of length 15 pixels. (k) Spatially-variant linear closing of length 15 pixels. (l) Classical spatially-invariant linear opening of length 15 pixels (using eight directions). (m) Classical spatially-invariant linear closing of length 15 pixels (using eight directions). (n) Spatially-variant linear alternate filter (opening followed by closing) of size 15. (o) Spatially-variant linear alternate filter (closing followed by opening) of size 15. (a) $f(\mathbf{x})$. (b) $\angle\mathbf{d}$. (c) $|\mathbf{d}|$. (d) $\angle\mathbf{v}$. (e) $|\mathbf{v}|$. (f) ASG. (g) ASGVF. (h) $\varepsilon_{L_{15}^{\theta(\mathbf{x})}}(f)(\mathbf{x})$. (i) $\delta_{L_{15}^{\theta(\mathbf{x})}}(f)(\mathbf{x})$. (j) $\gamma_{L_{15}^{\theta(\mathbf{x})}}(f)(\mathbf{x})$. (k) $\varphi_{L_{15}^{\theta(\mathbf{x})}}(f)(\mathbf{x})$. (l) $\gamma_{L_{15}^{lines}}(f)(\mathbf{x})$. (m) $\varphi_{L_{15}^{lines}}(f)(\mathbf{x})$. (n) $\varphi_{L_{15}^{\theta(\mathbf{x})}}\gamma_{L_{15}^{\theta(\mathbf{x})}}(f)(\mathbf{x})$. (o) $\gamma_{L_{15}^{\theta(\mathbf{x})}}\varphi_{L_{15}^{\theta(\mathbf{x})}}(f)(\mathbf{x})$.

where θ, λ and w are, respectively, the angle, the length, and width of the structuring element at point $\mathbf{x}$ from the regularized vector field $\mathbf{v}$.

A. Regularized Vector Field – Orientation and Magnitude

In order to illustrate the regularization of the vector field, Fig. 4(a) shows a quiver plot of the ASG of a binary image as well as its angle and the absolute value of its elements, Fig. 4(b) and (c), respectively. Fig. 4(d) illustrates the ASGVF and Fig. 4(e)-(f) show the angle and magnitude of the regularized field. In this example, ASG has been obtained using a flat averaging window of 15×15 pixels, and the parameters of ASGVF are $\eta = 10^{-2}$ and $\Delta_t = 1$.

One point to consider is the size of the averaging window W in ASG due to this window smooths the squared gradient. The size of the window must be chosen in order to preserve the orientation of the main structures we are interested in. Structures (lines, circles, dots, etc.) with size smaller than the window hardly will affect the ASG. This fact has to be taken into account when there are important details in the image whose size is comparable to the size of the window. For example, the size of the averaging window will limit the maximum curvature (high spatial frequencies) allowed for a line.

In the regularization process, the parameter η is related to the bandwidth of a low-pass filter (see Fig. 3) which filters the increments of ASGVF in (27). When the gradient of the image has homogeneous areas and abrupt transitions a higher value is necessary to allow abrupt transitions (spatial high frequencies) exist. On the other hand, when the gradient has not abrupt transitions a low value of η gets the appropriate smoothness in the regularized vector field.

The length of the structuring element is another aspect to take into consideration. A tradeoff between size and angular resolution must be reached. Small structuring elements allows get into small details of the objects but offers few directions. Bigger structuring elements can not deal with these small details but

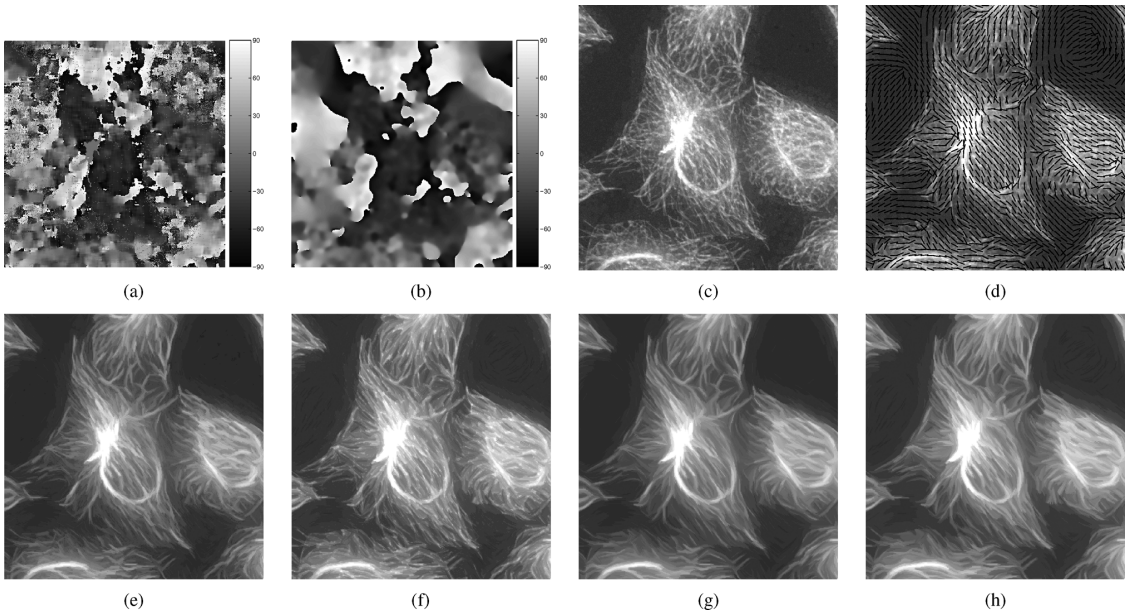

Fig. 6. (a) Phase angles of ASG using a 11×11 flat averaging window. (b) Phase angles of ASGVF using $\eta = 10^{-1}$ and $\Delta_t = 1$. (c) Original gray-level image $f(\mathbf{x})$ 348×341. (d) ASGVF $\mathbf{v}$. (e) Spatially-variant linear opening of length 11 pixels. (f) Spatially-variant linear closing of length 11 pixels. (g) Spatially-variant linear alternate filter (opening followed by closing) of sizes 11 and 17. (h) Spatially-variant linear alternate filter (closing followed by opening) of sizes 11 and 17. (a) $\angle \mathbf{d}$. (b) $\angle \mathbf{v}$. (c) $f(\mathbf{x})$. (d) ASGVF. (e) $\gamma_{L_{11}^{\theta(\mathbf{x})}}(f)(\mathbf{x})$. (f) $\varphi_{L_{11}^{\theta(\mathbf{x})}}(f)(\mathbf{x})$. (g) $\varphi_{L_{17}^{\theta(\mathbf{x})}}\gamma_{L_{17}^{\theta(\mathbf{x})}}\varphi_{L_{11}^{\theta(\mathbf{x})}}\gamma_{L_{11}^{\theta(\mathbf{x})}}(f)(\mathbf{x})$. (h) $\gamma_{L_{17}^{\theta(\mathbf{x})}}\varphi_{L_{17}^{\theta(\mathbf{x})}}\gamma_{L_{11}^{\theta(\mathbf{x})}}\varphi_{L_{11}^{\theta(\mathbf{x})}}(f)(\mathbf{x})$.

offer many directions. As detailed in [39], if the structuring element is l pixel long, the angular resolution is $\Delta_\theta = 90/(l-1)$ degrees, the discretized angles being $\theta_i = i\,\Delta_\theta$, $i \in [0, 2(l-1)-1]$.

B. Anisotropic Filtering of Binary Images Using a Linear Structuring Element

Fig. 4(g)–(o) shows the application of spatially-variant morphological operators on a binary image. The original binary image, Fig. 4(g), contains some curvilinear lines and a regular grid of superimposed stains. Morphological operators use as structuring element a line of length 15 pixels. Results reflect the appropriateness of very simple morphological filters for closing interrupted line structures and for the isolation of the regular grid of stains, which have a size of less than 15 pixels.

Next application is concerned with the enhancement of a binary fingerprint image. Fig. 5(a) shows the original 362×285 image which contains broken fingerprint ridges. The ASG [Fig. 5(b)-(c)] is obtained using a flat averaging window of size 35×35, and the regularized field has been calculated using $\eta = 10^{-2}$ and $\Delta_t = 1$, Fig. 5(d)-(e). Fig. 5(h)–(o) shows the results of applying morphological filters on the binary image using a linear structuring element of length 15 pixels. We can also compare the new spatially-variant linear opening/closing with their counterpart classical spatially-invariant linear opening/closing, Fig. 5(l) and (m), using eight directions. The standard translation invariant linear openings/closings are built according to the property that the supremum (resp. infimum) of openings (resp. closings) is an opening (resp. closing) as well.

C. Anisotropic Filtering of Gray Level Images Using a Linear Structuring Element

Fig. 6 contains the results of applying spatially-variant filters to a gray-level image of microtubules. Fig. 6(a) and (b) shows the angle of the ASG field and the angle of the regularized field, respectively. ASG uses a 11×11 flat window, whereas the regularized field is obtained using $\eta = 0.1$ and $\Delta_t = 1$. The structuring element of the morphological filters is an orientated line of 11 pixels. Results show how the proposed anisotropic filtering is able to preserve main structures in the image as well as to preserve sharp jump discontinuities.

Fig. 7 depicts another example of morphological anisotropic filtering of a fingerprint, in this case, in gray levels. For this case, the window used in ASG is 25×25 pixels, and the parameters for obtaining the regularized vector field are $\eta = 0.01$ and $\Delta_t = 1$. As well as spatially-variant linear opening and spatially-variant linear closing, a pair of spatially-variant linear alternate filters are compared with the average images of both operators. As we can observe, the average image Fig. 7(h) is a good tradeoff between these two morphological anisotropic filters and the result is quite regular but preserves the significant linear structures, improving the clarity of fingerprint image ridges and valleys.

Fig. 8 shows a 353×280 version of Vincent van Gogh's painting *The Starry Night*. The parameters for calculating ASG and ASGVF are: a 7×7 flat window, $\eta = 1$ and $\Delta_t = 1$. Fig. 8(b)-(c) contain spatially-variant alternate filters using a linear structuring element of length 7 pixels. Fig. 8(d) shows the average image of previous operators, which smooths original image in an anisotropic manner, allowing for removing the grain while preserving thin structures.

D. Anisotropic Filtering of Gray Level Images Using a Rectangular Structuring Element

In the last application shown in Fig. 9, the morphological filters use firstly a linear structuring element, and later, the structuring element is a rectangle whose length and width are related

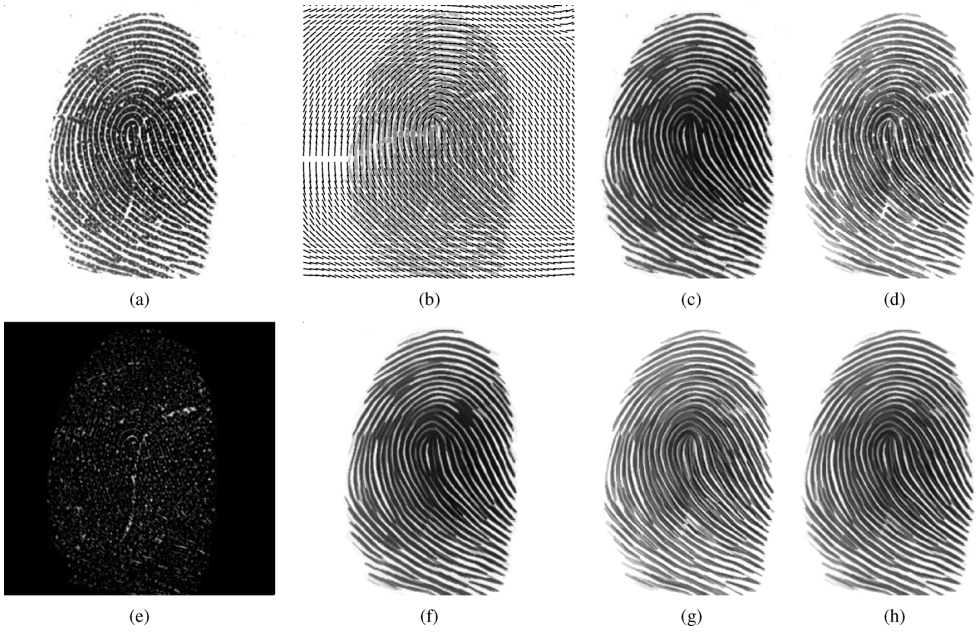

Fig. 7. (a) Original gray-level image $f(\mathbf{x})$ 348×348. (b) ASGV field using $\eta = 0.01$. (c) Spatially-variant linear opening of length 15 pixels. (d) spatially-variant linear closing of length 15 pixels. (e) Top-hat. (f) Spatially-variant linear alternate filter (opening followed by closing) of size 15. (g) Spatially-variant linear alternate filter (closing followed by opening) of size 15. (h) Average image between previous spatially-variant linear alternate filters. (a) $f(\mathbf{x})$. (b) ASGVF. (c) $\gamma_{L_{15}^{\theta(\mathbf{x})}}(f)(\mathbf{x})$. (d) $\varphi_{L_{15}^{\theta(\mathbf{x})}}(f)(\mathbf{x})$. (e) $th^{+}(f)(\mathbf{x})$. (f) $f_{\gamma\varphi}(\mathbf{x}) = \varphi_{L_{15}^{\theta(\mathbf{x})}}\gamma_{L_{15}^{\theta(\mathbf{x})}}(f)(\mathbf{x})$. (g) $f_{\varphi\gamma}(\mathbf{x}) = \gamma_{L_{15}^{\theta(\mathbf{x})}}\varphi_{L_{15}^{\theta(\mathbf{x})}}(f)(\mathbf{x})$. (h) $(f_{\varphi\gamma}(\mathbf{x}) + f_{\gamma\varphi}(\mathbf{x}))/2$.

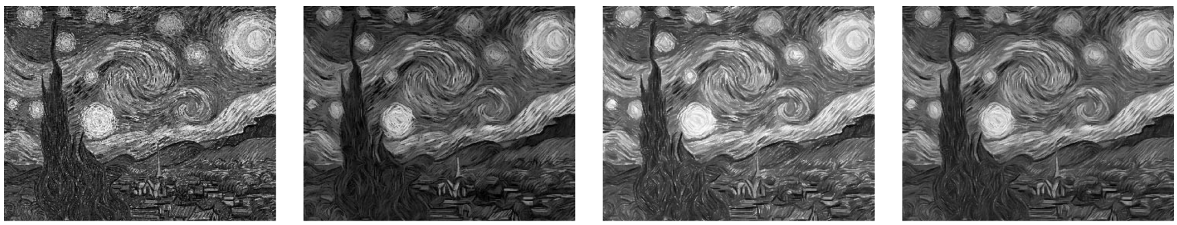

Fig. 8. (a) Original gray-level image $f(\mathbf{x})$ 353×280. (b) Spatially-variant linear alternate filter (opening followed by closing) of size 7. (c) Spatially-variant linear alternate filter (closing followed by opening) of size 7. (d) Average image between previous spatially-variant linear alternate filters. (a) $f(\mathbf{x})$. (b) $f_{\gamma\varphi}(\mathbf{x}) = \varphi_{L_7^{\theta(\mathbf{x})}}\gamma_{L_7^{\theta(\mathbf{x})}}(f)(\mathbf{x})$. (c) $f_{\varphi\gamma}(\mathbf{x}) = \gamma_{L_7^{\theta(\mathbf{x})}}\varphi_{L_7^{\theta(\mathbf{x})}}(f)(\mathbf{x})$. (d) $(f_{\varphi\gamma}(\mathbf{x}) + f_{\gamma\varphi}(\mathbf{x}))/2$.

to the distance to the edges of the objects. Fig. 9(a) shows a 256×256 gray-level image of a tree bark with an orientation of 60 degrees (real image extracted from [55]). The ASG field is obtained using a flat 15×15 averaging window, the ASGVF has been calculated using $\eta = 1$ and $\Delta_t = 1$. Fig. 9(e)-(h) show spatially-variant filtering with linear structuring element of length 15 pixels.

Fig. 9(i)–(l) contains the results of applying spatially-variant operators where the shape of the structuring element is given by the distance to the edges (in this case, the edge detector used is the Canny's method [56]). Then, the shape of the structuring element is, regardless the orientation given by the angle of ASGVF, 15×1 in the edges and a neighborhood of two pixels, 9×3 near the edges (between three and four pixel far) and 5×5 in homogeneous areas (more than five pixels far from the edges), as depicted in Fig. 9(d). Spatially-variant opening, closing, and alternate filters, Fig. 9(i)–(l) respectively, show the ability of these filters for enhancing main cracks of the bark, smoothing pieces of the bark while preserving the edges and important structures in the image.

V. Conclusion and Perspectives

We have clarified and solved some difficulties in the definition of spatially variant dilation/erosion and opening/closing for gray-level images. Then, we have proposed an algorithm for a reliable extraction of orientation information, which is finally used to build anisotropic morphological filters. The performance of derived operators has been illustrated for enhancement of anisotropic image features such as coherent, flow-like structures.

In ongoing research, we would like to address the theory of spatially-variant geodesic operators. From a practical viewpoint, we are working on a full exploitation on the directional field, including the information of magnitude and angular coherence in order to propose more general anisotropic structuring elements. The extension to 3-D and more generally to n-D spaces and the application to 3-D images (e.g., denoising MRI data, enhancement of fiber networks, etc.) will be also explored in future work.

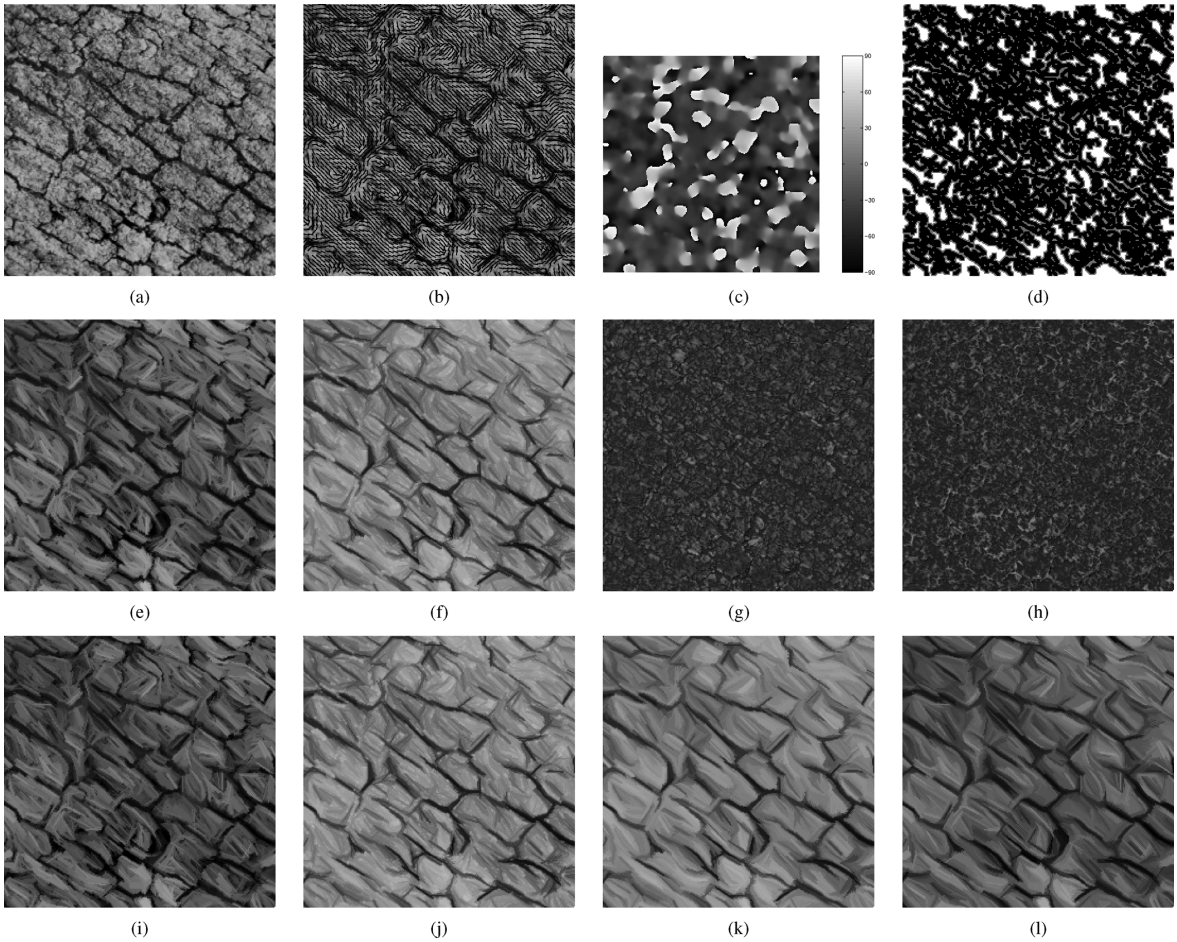

Fig. 9. (a) Original gray-level image $f(\mathbf{x})$ 256×256. (b) and (c) ASGVF using $\eta = 1$ and $\Delta_t = 1$. (d) distribution of the shape of the structuring element at each pixel $[\theta, w](\mathbf{x})$: 1×15 (black pixels), 3×9 (gray pixels) and 5×5 (white pixels). (e) Spatially-variant linear opening of length 15 pixels. (f) Spatially-variant linear closing of length 15 pixels. (g) Top-hat. (h) Dual top-hat. (i) Spatially-variant opening using as structuring element an orientated rectangle whose shape depends upon the distance to the edges and is given in (d). (j) Spatially-variant closing. (k) Spatially-variant alternate filter (closing followed by opening). (l) Spatially-variant alternate filter (opening followed by closing). (a) $f(\mathbf{x})$. (b) ASGVF $\mathbf{v}$. (c) $\angle\mathbf{v}$. (d) $w(\mathbf{x})$. (e) $\gamma_{L_{15}^{\theta(\mathbf{x})}}(f)(\mathbf{x})$. (f) $\varphi_{L_{15}^{\theta(\mathbf{x})}}(f)(\mathbf{x})$. (g) $th^{+}(f)(\mathbf{x})$. (h) $th^{-}(f)(\mathbf{x})$. (i) $\gamma_{L[\theta,w](\mathbf{x})}(f)(\mathbf{x})$. (j) $\varphi_{L[\theta,w](\mathbf{x})}(f)(\mathbf{x})$. (k) $\gamma_{L[\theta,w](\mathbf{x})}\varphi_{L[\theta,w](\mathbf{x})}(f)(\mathbf{x})$. (l) $\varphi_{L[\theta,w](\mathbf{x})}\gamma_{L[\theta,w](\mathbf{x})}(f)(\mathbf{x})$.

APPENDIX
SPECTRUM OF THE DISCRETE APPROXIMATION OF Δ^2

The partial differential operator is described by the following equation:

$$\Delta^2\mathbf{v}(\mathbf{x}) = \left(\left(\partial_{xx} + \partial_{yy}\right)^2 v_l(\mathbf{x})\right)_{l=1,2} \in \mathbb{R}^2. \tag{32}$$

The discrete approximations of second-order spatial derivatives are given by

$$\partial_{xx} v_l(\mathbf{x}) \approx \mathrm{d}^2[n_1] * v_l[\mathbf{n}] \tag{33}$$
$$\partial_{yy} v_l(\mathbf{x}) \approx \mathrm{d}^2[n_2] * v_l[\mathbf{n}] \tag{34}$$

where $\mathbf{n} = [n_1, n_2]$ is the discrete spatial index, $*$ denotes linear convolution and the discrete difference operators are defined as

$$\mathrm{d}^-[n] := \delta[n] - \delta[n-1] \tag{35}$$
$$\mathrm{d}^+[n] := \delta[n+1] - \delta[n] \tag{36}$$
$$\mathrm{d}^2[n] := \mathrm{d}^-[n] * \mathrm{d}^+[n]. \tag{37}$$

The operators d^-, d^+ and d^2 perform the backward difference, forward difference, and second-order difference, respectively, and $\delta[n]$ is the Kronecker's delta.

Then, using finite difference approximations of partial derivatives, (32) can be written as

$$\Delta^2\mathbf{v}(\mathbf{x}) \approx (\mathrm{k}[\mathbf{n}] * v_l[\mathbf{n}])_{l=1,2} \in \mathbb{R}^2. \tag{38}$$

where

$$\mathbf{k}[\mathbf{n}] = \mathrm{d}^2[n_1] * \mathrm{d}^2[n_1] + 2\mathrm{d}^2[n_1] * \mathrm{d}^2[n_2] + \mathrm{d}^2[n_2] * \mathrm{d}^2[n_2]. \tag{39}$$

Previous approximations along with the fact that the Fourier transform of the spatial sequence $y[n] = \delta[n - n_0]$ is $\tilde{y}(\omega) = e^{-j\omega n_0}$ [57], provides the expressions of the operators in the frequency domain

$$\mathrm{D}^-(\omega) = 1 - e^{-j\omega} \tag{40}$$
$$\mathrm{D}^+(\omega) = e^{j\omega} - 1 \tag{41}$$
$$\mathrm{D}^2(\omega) = -2(1 - \cos(\omega)). \tag{42}$$

Finally, the spectrum $K(\omega_1, \omega_2)$ with the frequency counterpart of the approximations of the spatial derivatives can be obtained as

$$K(\omega_1, \omega_2) = 4\ (2 - \cos\omega_1 - cos\omega_2)^2 . \qquad (43)$$

REFERENCES

[1] J. Serra, *Image Analysis and Mathematical Morphology*. New York: Academic, 1982, vol. I.

[2] J. Serra, *Image Analysis and Mathematical Morphology: Theoretical Advances*. New York: Academic, 1988, vol. II.

[3] J. Roerdink and H. Heijmans, "Mathematical morphology for structures without translation symmetry," *Signal Process.*, vol. 15, pp. 271–277, 1988.

[4] H. J. A. M. Heijmans and C. Ronse, "The algebraic basis of mathematical morphology – Part I: Dilations and erosions," *Comput. Vis. Graph. Image Process: Image Understand.*, vol. 50, no. 3, pp. 245–295, 1990.

[5] C. Ronse and H. J. A. M. Heijmans, "The algebraic basis of mathematical morphology – Part II: Openings and closings," *Comput. Vis. Graph. Image Process: Image Understand.*, vol. 54, pp. 74–97, 1991.

[6] P. Maragos, "Affine morphology and affine signal models," in *Proc. SPIE Image Algebra Morpholog. Image Process.*, 1990, vol. 1350, pp. 31–43.

[7] G. Matheron, *Random Sets and Integral Geometry*. Hoboken, NJ: Wiley, 1975.

[8] P. Maragos and R. W. Schafer, "Morphological filters – Part I: Their set-theoretic analysis and relations to linear shift-invariant filters," *IEEE Trans. Acoust., Speech, Signal Process.*, vol. ASSP–35, no. 8, pp. 1153–1169, Aug. 1987.

[9] P. Maragos and R. W. Schafer, "Morphological filters – Part II: Their relation to median, order-statistics and stack filters," *IEEE Trans. Acoust., Speech, Signal Process.*, vol. ASSP–35, no. 8, pp. 1170–1184, Aug. 1987.

[10] P. Maragos, "A unified theory of translation-invariant systems with applications to morphological analysis and coding of images," Ph.D. dissertation, Georgia Inst. Tech., Atlanta, GA, 1985.

[11] P. Maragos, "A representation theory for morphological image and signal processing," *IEEE Trans. Pattern Anal. Mach. Intell.*, vol. 11, no. 6, pp. 586–599, Jun. 1989.

[12] G. J. F. Banon and J. Barrera, "Decomposition of mappings between complete lattices by mathematical morphology – Part I: General lattices," *Signal Process.*, vol. 30, no. 3, pp. 299–327, 1993.

[13] M. Charif-Chefchaouni and D. Schonfeld, "Spatially-variant mathematical morphology," in *Proc. IEEE Int. Conf. Image Process.*, 1994, vol. 2, pp. 555–559.

[14] M. Charif-Chefchaouni and D. Schonfeld, "Spatially-variant mathematical morphology: Minimal basis representation," in *Mathematical Morphology and its Applications to Image and Signal Processing*, P. A. Maragos, R. W. Schafer, and M. A. Butt, Eds. Norwell, MA: Kluwer, 1996, pp. 49–56.

[15] H. Heijmans, *Morphological Image Operators*. New York: Academic, 1994.

[16] N. Bouaynaya, M. Charif-Chefchaouni, and D. Schonfeld, "Theoretical foundations of spatially-variant mathematical morphology – Part I: Binary images," *IEEE Trans. Pattern Anal. Mach. Intell.*, vol. 30, no. 5, pp. 823–836, May 2008.

[17] N. Bouaynaya and D. Schonfeld, "Theoretical foundations of spatially-variant mathematical morphology – Part II: Gray-level images," *IEEE Trans. Pattern Anal. Mach. Intell.*, vol. 30, no. 5, pp. 837–850, May 2008.

[18] P. Soille, *Morphological Image Analysis*. New York: Springer-Verlag, 1999.

[19] J. Roerdink, "Group morphology," *Pattern Recognit.*, vol. 33, no. 6, pp. 877–895, 2000.

[20] P. Dokládal and E. Dokládalová, "Grey-scale morphology with spatially-variant rectangles in linear time," *Adv. Concepts Intell. Vis. Syst.*, vol. 5259, pp. 674–685, 2008.

[21] H. Hedberg, P. Dokladal, and V. Owall, "Binary morphology with spatially variant structuring elements: Algorithm and architecture," *IEEE Trans. Image Process.*, vol. 18, no. 3, pp. 562–572, Mar. 2009.

[22] O. Cuisenaire, "Locally adaptable mathematical morphology using distance transformations," *Pattern Recognit.*, vol. 39, no. 3, pp. 405–416, Mar. 2006.

[23] J. Blosseville, C. Krafft, F. Lenoir, V. Motyka, and S. Beucher, "Titan: A traffic measurement system using image processing techniques," in *Proc. 2nd Int. Conf.Road Traffic Monitoring*, 1989, pp. 84–88.

[24] J. Serra, M. Suliman, and M. Mahmud, B. S. Daya Sagar, Ed., "Prediction and simulation of malaysian forest by random spread," in *Proc. Seminar on Spatial Inf. Retrieval Anal. Reasoning Model.*, Bangalore, India, Mar. 2009, pp. 13–32.

[25] R. Lerallut, E. Decenciere, and F. Meyer, "Image filtering using morphological amoebas," *Image Vis. Comput.*, vol. 25, no. 4, pp. 395–404, 2007.

[26] J. Verly and R. Delanoy, "Adaptive mathematical morphology for range imagery," *IEEE Trans. Image Process.*, vol. 2, no. 2, pp. 272–275, Apr. 1993.

[27] J. Debayle and J. Pinoli, "Spatially adaptive morphological image filtering using intrinsic structuring elements," *Image Anal. Sterol.*, vol. 24, pp. 145–158, 2005.

[28] P. Soille and H. Talbot, "Directional morphological filtering," *IEEE Trans. Pattern Anal. Mach. Intell.*, vol. 23, no. 11, pp. 1313–1329, Nov. 2001.

[29] H. Heijmans, M. Buckley, and H. Talbot, "Path openings and closings," *J. Math. Imag. Vis.*, vol. 22, no. 2-3, pp. 107–119, 2005.

[30] R. Brockett and P. Maragos, "Evolution equations for continuous-scale morphology," in *Proc. IEEE Int. Conf. Acoust., Speech, Signal Process.*, 1992, vol. 3, pp. 125–128.

[31] G. Sapiro, R. Kimmel, D. Shaked, B. B. Kimia, and A. M. Bruckstein, "Implementing continuous-scale morphology via curve evolution," *Pattern Recognit.*, vol. 26, no. 9, pp. 1363–1372, 1993.

[32] R. van den Boomgaard and A. Smeulders, "The morphological structure of images: The differential equations of morphological scale-space," *IEEE Trans. Pattern Anal. Mach. Intell.*, vol. 16, no. 11, pp. 1101–1113, Nov. 1994.

[33] P. Maragos, "Differential morphology and image processing," *IEEE Trans. Image Process.*, vol. 5, no. 6, pp. 922–937, Jun. 1996.

[34] M. Breuß, B. Burgeth, and J. Weickert, "Anisotropic continuous-scale morphology," in *Proc. 3rd Iberian Conf. Pattern Recognit. Image Anal.*, 2007, vol. 4478, no. II, pp. 515–522.

[35] A. Rao and B. Schunck, "Computing oriented texture fields," in *Proc. Comput. Vis. Pattern Recognit.*, Jun. 1989, pp. 61–68.

[36] J. Bigün, G. Granlund, and J. Wiklund, "Multidimensional orientation estimation with applications to texture analysis and optical flow," *IEEE Trans. Pattern Anal. Mach. Intell.*, vol. 13, no. 8, pp. 775–790, Aug. 1991.

[37] O. Tankyevych, H. Talbot, and P. Dokladal, "Curvilinear morpho-hessian filter," in *Proc. 5th IEEE Int. Symp. Biomed. Imag.: From Nano to Macro* , May 2008, pp. 1011–1014.

[38] R. Verdú-Monedero, J. Angulo, and J. Serra, "Spatially-variant anisotropic morphological filters driven by gradient fields," in *Proc. 9th Int. Symp. Math. Morphol.*, 2009, pp. 115–125.

[39] R. Verdú-Monedero and J. Angulo, "Spatially-variant directional mathematical morphology operators based on a diffused average squared gradient field," *Adv. Concepts Intell. Vis. Syst.*, vol. 5259, pp. 542–553, 2008.

[40] J. Roerdink, "Adaptivity and group invariance in mathematical morphology," in *Proc. IEEE Int. Conf. Image Process.*, 2009, pp. 2253–2256.

[41] J. Weickert, Anisotropic Diffusion in Image Processing Teubner-Verlag, Stuttgart, Germany, 1998, ECMI Series [Online]. Available: http://www.mia.uni-saarland.de/weickert/Papers/book.pdf

[42] J. Weickert, B. Romeny, and M. Viergever, "Efficient and reliable schemes for nonlinear diffusion filtering," *IEEE Trans. Image Process.*, vol. 7, no. 3, pp. 398–410, Mar. 1998.

[43] B. Burgeth, M. Breuß, S. Didas, and J. Weickert, "PDE-based morphology for matrix fields: Numerical solution schemes," in *Tensors in Image Processing and Computer Vision*. New York: Springer-Verlag, 2009.

[44] M. Kass and A. Witkin, "Analyzing oriented patterns," *Comput. Vis. Graph. Image Process.*, vol. 37, no. 3, pp. 362–385, 1987.

[45] A. M. Bazen and S. H. Gerez, "Systematic methods for the computation of the directional fields and singular points of fingerprints," *IEEE Trans. Pattern Anal. Mach. Intell.*, vol. 24, no. 7, pp. 905–919, Jul. 2002.

[46] P. Perona, "Orientation diffusions," *IEEE Trans. Image Process.*, vol. 7, no. 3, pp. 457–467, Mar. 1998.

[47] D. Tschumperle and R. Deriche, "Vector-valued image regularization with PDE's: A common framework for different applications," *IEEE Trans. Pattern Anal. Mach. Intell.*, vol. 27, no. 4, pp. 506–517, Apr. 2005.

[48] C. Xu and J. L. Prince, "Generalized gradient vector flow external forces for active contours," *Signal Process.*, vol. 71, no. 2, pp. 131–139, 1998.
[49] C. Xu and J. L. Prince, "Snakes, shapes, and gradient vector flow," *IEEE Trans. Image Process.*, vol. 7, no. 3, pp. 359–369, Mar. 1998.
[50] H. Engl, M. Hanke, and A. Neubauer, *Regularization of Inverse Problems*. New York: Springer-Verlag, 2000, vol. 375, Mathematics and Its Applications.
[51] R. Verdu-Monedero, J. Larrey-Ruiz, and J. Morales-Sanchez, "Frequency implementation of the Euler-Lagrange equations for variational image registration," *IEEE Signal Process. Lett.*, vol. 15, pp. 321–324, 2008.
[52] P. J. Davis, *Circulant Matrices*. Hoboken, NJ: Wiley, 1979.
[53] J. Larrey-Ruiz, R. Verdú-Monedero, and J. Morales-Sánchez, "A Fourier domain framework for variational image registration," *J. Math. Imag. Vis.*, vol. 32, no. 1, pp. 57–72, 2008.
[54] J. Bai and X.-C. Feng, "Fractional-order anisotropic diffusion for image denoising," *IEEE Trans. Image Process.*, vol. 16, no. 10, pp. 2492–2502, Oct. 2007.
[55] SIPI Image Database Univ. Southern California. Los Angeles, CA [Online]. Available: http://sipi.usc.edu/database/
[56] J. Canny, "A computational approach to edge detection," *IEEE Trans. Pattern Anal. Mach. Intell.*, vol. PAMI–8, no. 6, pp. 679–698, Nov. 1986.
[57] A. Oppenheim and R. Schafer, *Discrete-Time Signal Processing*, 2nd ed. Upper Saddle River, NJ: Prentice-Hall, 1999.

Rafael Verdú-Monedero received the M.S. degree in telecommunications engineering from the Universidad Politécnica de Valencia (UPV), Valencia, Spain, in 2000, and the Ph.D. degree in active contours and image processing from the Universidad Politécnica de Cartagena (UPCT), Cartagena, Spain, in 2005.

He is currently a Researcher and Assistant Teacher in signal and communications theory at UPCT. His technical interests are image registration formulated in the frequency domain, modeling, and inverse problems in image analysis.

Jesús Angulo was born in Cuenca, Spain, in 1975. He received the degree in telecommunications engineering from the Universidad Politécnica de Valencia (UPV), Spain, in 1999, with a M.S. thesis on image and video processing, and the Ph.D. degree in mathematical morphology and image processing from the Ecole des Mines de Paris, Paris, France, in 2003, under the guidance of Prof. Jean Serra.

He is currently a permanent researcher in the Center of Mathematical Morphology of the MINES ParisTech. His research interests are in the areas of multivariate image processing (color, hyper/multispectral, temporal series, tensor imaging) and mathematical morphology (filtering, segmentation, shape and texture analysis, stochastic approaches, geometry), and their applications to biomedicine and biotechnology.

Jean Serra In 1965 Jean Serra founded, with G. Matheron, the theory of Mathematical Morphology. The initial, and still valid, purpose was to link physical properties with textures. Then the activity of Mathematical Morphology extended progressively to other fields, such as medical imagery, remote sensing, robot vision, or video image processing.

The basic theoretical results of J. Serra and of his school may be found in "Image Analysis and Mathematical Morphology", Ac. Press, Vol. I, 1982 and Vol. II, 1988. He is the author or co-author of about two hundred scientific papers and of ten books. In the last twenty years, his three major contributions to mathematics and physics are morphological filtering, the formulation of mathematical morphology in the convenient framework of complete lattices and a new concept for connectivity that is the core curriculum for the connective segmentation theory (i.e., delineation of significant objects) and for a comprehensive class of filters. He is currently involved in multi-spectral imagery.

13.10 Publication X : J. Angulo and S. Velasco-Forero. "Sparse Mathematical Morphology using Non-Negative Matrix Factorization". In *Proc. of ISMM'11 (2011 International Symposium on Mathematical Morphology)*, LNCS 6671, Springer-Verlag Berlin Heidelberg, p. 1–12, Intra (Lake Maggiore), Italy, July 2011.

Sparse Mathematical Morphology Using Non-negative Matrix Factorization

Jesús Angulo and Santiago Velasco-Forero

CMM-Centre de Morphologie Mathématique, Mathématiques et Systèmes, MINES ParisTech; 35, rue Saint Honoré, 77305 Fontainebleau Cedex, France
{jesus.angulo,santiago.velasco}@mines-paristech.fr

Abstract. Sparse modelling involves constructing a succinct representation of initial data as a linear combination of a few typical atoms of a dictionary. This paper deals with the use of sparse representations to introduce new nonlinear operators which efficiently approximate the dilation/erosion. Non-negative matrix factorization (NMF) is a dimensional reduction (i.e., dictionary learning) paradigm particularly adapted to the nature of morphological processing. Sparse NMF representations are studied to introduce pseudo-morphological binary dilations/erosions. The basic idea consists in processing exclusively the image dictionary and then, the result of processing each image is approximated by multiplying the processed dictionary by the coefficient weights of the current image. These operators are then extended to grey-level images by means of the level-set decomposition. The performance of the present method is illustrated using families of binary shapes and face images.

1 Introduction

Mathematical morphology [11,4] is a nonlinear image processing methodology based on the application of lattice theory to spatial structures. Morphological filters and transformations are useful for various image processing tasks [12], such as denoising, contrast enhancement, multi-scale decomposition, feature extraction and object segmentation. In addition, morphological operators are defined using very intuitive geometrical notions which allows us the perceptual development and interpretation of complex algorithms by combination of various operators.

Let E be a space of points, which is considered here as a finite digital space of the pixels of the image, i.e., $E \subset \mathbf{Z}^2$ such that $N = |E|$ is the number of pixels. Image intensities are numerical values, which ranges in a closed subset $\mathcal{T}$ of $\overline{\mathbf{R}} = \mathbf{R} \cup \{-\infty, +\infty\}$; for example, for an image of discrete L values, it can be assumed $\mathcal{T} = \{t_1, t_2, \cdots, t_L\}$. Then, a binary image X is modelled as a subset of E, i.e., $X \in \mathcal{P}(E)$; a grey-level image $f(p_i)$, where $p_i \in E$ are the pixel coordinates, is a numerical function $E \to \mathcal{T}$, i.e., $f \in \mathcal{F}(E, \mathcal{T})$. In mathematical morphology, an operator ψ is a map transforming an image into an image. There are thus operators on binary images, i.e., maps $\mathcal{P}(E) \to \mathcal{P}(E)$; or on grey-level images, i.e., maps $\mathcal{F}(E, \mathcal{T}) \to \mathcal{F}(E, \mathcal{T})$.

P. Soille, M. Pesaresi, and G.K. Ouzounis (Eds.): ISMM 2011, LNCS 6671, pp. 1–12, 2011.

Sparse coding and dictionary learning, where data is assumed to be well represented as a linear combination of a few elements from a dictionary, is an active research topic which leads to state-of-the-art results in image processing applications, such as image denoising, inpainting or demosaicking [3,9,14]. Inspired by these studies, the aim of this paper is to explore how image sparse representations can be useful to efficiently calculate morphological operators.

Motivation and outline of the approach. In many practical situations, a collection of M binary or grey-level images (each image having N pixels) should be analysed by applying the same morphological operator (or a series of operators) to each image. If one considers that the content of the various images is relatively similar, we can expect that the initial collection can be efficiently projected into a dimensionality reduced image space. Then, the morphological operator (or an equivalent operator) can be applied to the reduced set of images of the projective space, in such a way that the original processed image is approximately obtained by projecting back to the initial space. Typical examples of image families which can be fit in this framework are: i) collection of shapes or a database of face images, ii) the spectral bands of a hyperspectral image, iii) the set of patches of a large image. The rationale behind this kind of approach is the hypothesis that the intrinsic dimension of the image collection is lower than $N \times M$. Usually the subspace representation involves deriving a set of basis components (or dictionary composed of atoms) using linear techniques like PCA or ICA. The projection coefficients for the linear combinations in the above methods can be either positive or negative, and such linear combinations generally involve complex cancellations between positive and negative numbers. Therefore, these representations lack the intuitive meaning of "adding parts to form a whole". This property is particularly problematic in the case of mathematical morphology since the basic binary operator, the dilation of a set, is defined as the operator which commutes with the union of parts of the set. Non-negative matrix factorization (NMF) [6] imposes the non-negativity constraints in learning basis images: the pixels values of resulting images as well as the coefficients for the reconstruction are all non-negative. This ensures that NMF is a procedure for learning a parts-based representation [6]. In addition, sparse modelling involves for the construction of a succinct representation of some data as a combination of a few typical patterns (few atoms of the dictionary) learned from the data itself. Hence, the notion of sparse mathematical morphology introduced for the first time in this paper is based on sparse NMF.

Paper organisation. This paper is structured as follows. Section 2 reviews the notion of NMF and the various algorithms proposed in the state-of-the-art, including the sparse variants. The use of NMF representations for implementing sparse pseudo-morphological binary dilations/erosions is introduced in Section 3. Using the level set decomposition of numerical functions, the extension to grey-level images of this morphological sparse processing is tackled in Section 4. Conclusions and perspectives are finally given in Section 5.

2 Non-negative Matrix Factorization and Variants

Definition. Let us assume that our data consists of M vectors of N non-negative scalar variables. Denoting the column vector $\mathbf{v}_j$, $j = 1, \cdots, M$, the matrix of data is obtained as $\mathbf{V} = (\mathbf{v}_1, \cdots, \mathbf{v}_M)$ (each $\mathbf{v}_j$ is the j-th column of $\mathbf{V}$), with $|\mathbf{v}_j| = N$. If we analyze M images of N pixels, these images can be stored in linearized form, so that each image will be a column vector of the matrix.

Given the non-negative matrix $\mathbf{V} \in \mathbb{R}^{N \times M}$, $\mathbf{V}_{i,j} \geq 0$, NMF is a linear non-negative approximate data decomposition into the two matrices $\mathbf{W} \in \mathbb{R}^{N \times R}$ and $\mathbf{H} \in \mathbb{R}^{R \times M}$ such that

$$\mathbf{V} \approx \mathbf{WH}, \quad \text{s.t. } \mathbf{W}_{i,k}, \mathbf{H}_{k,j} \geq 0, \tag{1}$$

where usually $R \ll M$ (dimensionality reduction). Each of the R columns of $\mathbf{W}$ contains a basis vector $\mathbf{w}_k$ and each row of $\mathbf{H}$ contains the coefficient vector (weights) $\mathbf{h}_j$ corresponding to vector $\mathbf{v}_j$: $\mathbf{v}_j = \sum_{k=1}^{R} \mathbf{w}_k \mathbf{H}_{k,j} = \mathbf{W}\mathbf{h}_j$. Using the modern terminology, the matrix $\mathbf{W}$ contains the dictionary and $\mathbf{H}$ the encoding.

A theoretical study of the properties of NMF representation has been achieved in [2] using geometric notions: NMF is interpreted as the problem of finding a simplicial cone which contains the data points in the positive orthant, or in other words, NMF is a conical coordinate transformation.

Algorithms for computing NMF. The factorization $\mathbf{V} \approx \mathbf{WH}$ is not necessarily unique, and the optimal choice of matrices $\mathbf{W}$ and $\mathbf{H}$ depends on the cost function that minimizes the reconstruction error. The most widely used is the Euclidean distance: minimize $\|\mathbf{V} - \mathbf{WH}\|_2^2 = \sum_{i,j} (\mathbf{V}_{i,j} - (\mathbf{WH})_{i,j})^2$ with respect to $\mathbf{W}$ and $\mathbf{H}$, subject to the constraints $\mathbf{W}, \mathbf{H} > 0$. Although the minimization problem is convex in $\mathbf{W}$ and $\mathbf{H}$ separately, it is not convex in both simultaneously. In [7] is proposed a multiplicative good performance algorithm to implement this optimization problem. They proved that the cost function is nonincreasing at the iteration and the algorithm converges at least to a local optimal solution. More precisely, the update rules for both matrices are:

$$\mathbf{H}_{k,j} \leftarrow \mathbf{H}_{k,j} \frac{(\mathbf{W}^T\mathbf{V})_{k,j}}{(\mathbf{W}^T\mathbf{WH})_{k,j}}; \quad \mathbf{W}_{i,k} \leftarrow \mathbf{W}_{i,k} \frac{(\mathbf{VH}^T)_{i,k}}{(\mathbf{WHH}^T)_{k,j}}$$

Another useful cost function, also considered in [7], is the Kullback-Leibler (KL) divergence, which leads also quite simple multiplicative update rules. In [8], it was proposed a variant of KL divergence NMF, which is named Local NMF (LNMF), aiming at learning spatially localized components (by minimizing the number of basis R to represent $\mathbf{V}$ and by maximizing the energy of each retained components) as well as imposing that different bases should be as orthogonal as possible (in order to minimize redundancy between the different bases). The multiplicative update rules for LNMF are given by

$$\mathbf{H}_{k,j} \leftarrow \sqrt{\mathbf{H}_{k,j} \sum_i \mathbf{V}_{i,j} \frac{\mathbf{W}_{i,k}}{(\mathbf{WH})_{i,k}}}; \quad \mathbf{W}_{i,k} \leftarrow \mathbf{W}_{i,k} \frac{\sum_j \mathbf{V}_{i,j} \frac{\mathbf{H}_{k,j}}{(\mathbf{WH})_{i,j}}}{\sum_j H_{k,j}}; \quad \mathbf{W}_{i,k} \leftarrow \frac{\mathbf{W}_{i,k}}{\sum_i \mathbf{W}_{i,k}}$$

NMF with sparseness constraints. A very powerful framework to add a degree of sparseness in the basis vectors $\mathbf{W}$ and/or the coefficients $\mathbf{H}$ was introduced in [5]. The sparseness measure σ of a vector $\mathbf{v} \in \mathbb{R}^{N\times 1}$ used in [5] is based on the relationship between the L_1 norm and the L_2 norm: $\sigma(\mathbf{v}) = \frac{\sqrt{N}-\|\mathbf{v}\|_1/\|\mathbf{v}\|_2}{\sqrt{N}-1}$. This function is maximal at 1 iff $\mathbf{v}$ contains only a single non-zero component, and takes a value of 0 iff all components are equal (up to signs). Then, matrix $\mathbf{W}$ and $\mathbf{H}$ are solved by the problem (1) under additional constraints $\sigma(\mathbf{w}_k) = S_w$ and $\sigma(\mathbf{h}_j) = S_h$, where S_w and S_h are respectively the desired sparseness of $\mathbf{W}$ and $\mathbf{H}$. The algorithm introduced in [5] is a projected gradient descent algorithm (additive update rule), which takes a step in the direction of the negative gradient, and subsequently projects onto the constraint space. The most sophisticated step finds, for a given vector $\mathbf{v}$, the closest non-negative vector $\mathbf{u}$ with a given L_1 norm and a given L_2 norm, see technical details in [5]. Sparseness is controlled explicitly with a pair of parameters that is easily interpreted; in addition, the number of required iterations grows very slowly with the dimensionality of the problem. In fact, for all the empirical tests considered in this paper, we have used the MATLAB code for performing NMF and its various extensions (LNMF, sparse NMF) provided by P. Hoyer [5].

Besides the spareness parameters (S_w, S_h), a crucial parameter to be chosen in any NMF algorithm is the value of R, that is, the number of basis of projective reduced space. Any dimensionality reduction technique, such as PCA, requires also to fix the number of components. In PCA, the components are ranked according to the second-order statistical importance of the components and each one has associated a value of the represented variance; whereas in NMF the selection R can be evaluated only *a posteriori*, by evaluating the error of reconstruction.

3 Sparse Binary Pseudo-dilations and Pseudo-erosions

Let $\mathcal{X} = \{X_1, \cdots, X_M\}$ be a collection of M binary shapes, i.e., $X_j \in \mathcal{P}(E)$. For each shape X_j, let $\mathbf{x}_j(i) : I \to \{0, 1\}$, with $i \in I = \{1, 2, \cdots, N\}$ and $N = |E|$, be its *characteristic vector*: $\forall X_j \in \mathcal{P}(E)$, we have $\mathbf{x}_j(i) = 1$ if $p_i \in X_j$ and $\mathbf{x}_j(i) = 0$ if $p_i \in X_j^c$. Then the shape family $\mathcal{X}$ has associated a data matrix $\mathbf{V} \in \{0, 1\}^{N\times M}$, where each characteristic vector corresponds to one column, i.e., $\mathbf{V}_{i,j} = \mathbf{x}_j(i)$.

Sparse NMF approximations to binary sets. After computing NMF optimization on data $\mathbf{V}$, for a given dimensionality R, an approximation to $\mathbf{V}$ is obtained. More precisely, if we denote by $\phi_k(p_i) : E \to \mathbb{R}^+$ the basis images associated to the basis matrix $\mathbf{W}$, i.e., $\phi_k(p_i) = \mathbf{W}_{i,k}$, the following image is obtained as

$$a_{X_j}(p_i) = \sum_{k=1}^{R} \phi_k(p_i)\mathbf{H}_{k,j} \tag{2}$$

It is obvious that without any additional constrains, function $a_X(p_i)$ is neither a binary image not even strictly defined in interval $[0, 1]$ (the value can be slightly

> 1). Hence, a thresholding operation at value α is required to impose a binary approximate set $\widetilde{X}_j$ to each initial shape X_j, i.e.,

$$X_j \xrightarrow{NMF} \widetilde{X}_j : \quad p_i \in \widetilde{X}_j \quad \text{if} \quad a_X(p_i) > \alpha \tag{3}$$

We propose to fix, for all the examples of the paper, the threshold value to $\alpha = 0.4$, in order to favor the reconstruction of X_j against its complement.

Let us consider a practical example of binary image collection $\mathcal{X}$, using $M = 100$ images of the Fish shape database ($N = 400 \times 200$). Fig. 1 depicts the corresponding basis images for various NMF algorithms: we have fixed $R = 10$ for all the cases (relatively strong dimensionality reduction). We observe that standard NMF produces a partial part-based representation, which includes also almost complete objects for outlier shapes (basis 2-upper-center and 5-center-center). As expected, LNMF produces more local decompositions, however the orthogonality constraints involves also an atomization of some common parts. A similar problem arises for Sparse-NMF when $S_w \neq 0$ (constraint of sparsity in basis matrix $\mathbf{W}$). When the sparsity constraint is limited to S_h, with a typical value around 0.6, the obtained dictionary of shapes is less local, but in exchange, this constraint involves that each binary shapes is reconstructed using a limited number of atoms. The various groups of fish shapes are therefore better approximated by the latter case than using the other NMF algorithms. The comparison of Fig. 2 illustrates the better performance of Sparse-NMF ($S_w = 0$, $S_h = 0.6$) with respect to the others.

Sparse max-approximation to binary dilation. The two fundamental morphological operators are the dilation and the erosion, which are defined respectively as the operators which preserve the union and the intersection. Given a *structuring element* $B \subseteq E$, i.e., a set defined at the origin which introduces the shape/size of the operator, the *dilation of a binary image* X by B and the *erosion of a binary image* X by B are defined respectively by by [11,4,1]

$$\delta_B(X) = \cup \{B(p_i) |\, p_i \in X\}\,, \tag{4}$$

and

$$\varepsilon_B(X) = \{p_i \in E |\, B(p_i) \subseteq X\}\,, \tag{5}$$

where $B(p_i)$ is the structuring element centered at pixel p_i. In the case of numerical functions $f \in \mathcal{F}(E, \mathcal{T})$, which are considered in detail in next section, the *dilation of a grey-level image* is defined by [4,12,1]

$$\delta_B(f)(p_i) = \left\{ f(p_m) |\, f(p_m) = \sup\left[f(p_n)\right], p_n \in \check{B}(p_i) \right\}, \tag{6}$$

and the dual *grey-level erosion* is given by [4,12,1]

$$\varepsilon_B(f)(p_i) = \left\{ f(p_m) |\, f(p_m) = \inf\left[f(p_n)\right], p_n \in B(p_i) \right\}. \tag{7}$$

where $\check{B}(p_i)$ is the transposed structuring element centered at pixel p_i. If B is symmetric with respect to the origin $\check{B} = B$.

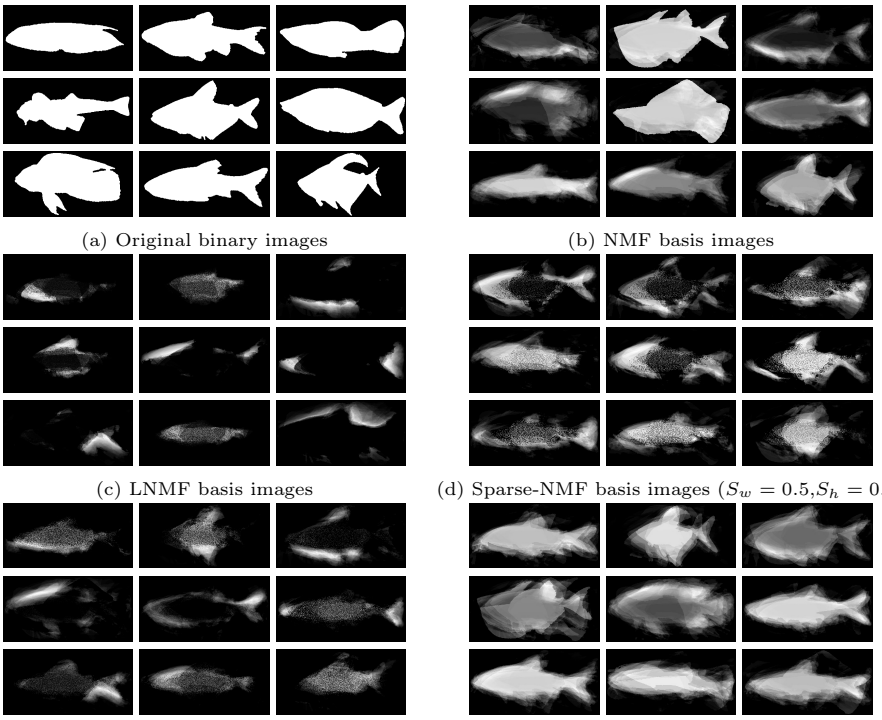

(a) Original binary images (b) NMF basis images

(c) LNMF basis images (d) Sparse-NMF basis images ($S_w = 0.5$,$S_h = 0.5$)

(e) Sparse-NMF basis images ($S_w = 0.6$,$S_h = 0$) (f) Sparse-NMF basis images ($S_w = 0$,$S_h = 0.6$)

Fig. 1. Non-negative representation of binary shapes. A collection of $M = 100$ shapes has been used in the NMF experiments (in (a) is given only a selection of 9 shapes), where the number of reduced dimensions has been fixed to $R = 10$ (in the examples are given the first 9 basis images).

The *characteristic function* of set X, denoted $\xi_X : E \to \{0, 1\}$, is defined by

$$\forall X \in \mathcal{P}(E),\ \forall p_i \in E,\ \ \xi_X(p_i) = \begin{cases} 1 \text{ if } p_i \in X \\ 0 \text{ if } p_i \in X^c \end{cases} \tag{8}$$

For a function $f : E \to \mathcal{T}$, the *thresholded set* at value $t \in \mathcal{T}$ is a mapping from $\mathcal{F}(E, \mathcal{T})$ to $\mathcal{P}(E)$ given by [11]

$$\varpi_t(f) = \{p_i \in E |\ f(p_i) \geq t\}\,. \tag{9}$$

Using these transformations it is obvious that the binary dilation (5) can be computed using the numerical operator (6), i.e.,

$$\delta_B(X) = \varpi_1\left(\delta_B(\xi_X)(p_i)\right). \tag{10}$$

We know that given a set defined as the union of a family of sets, i.e., $X = \cup_{k\in K} X_k$, the corresponding dilation is

$$\delta_B(X) = \delta_B\left(\cup_{k\in K} X_k\right) = \cup_{k\in K}\delta_B(X_k). \tag{11}$$

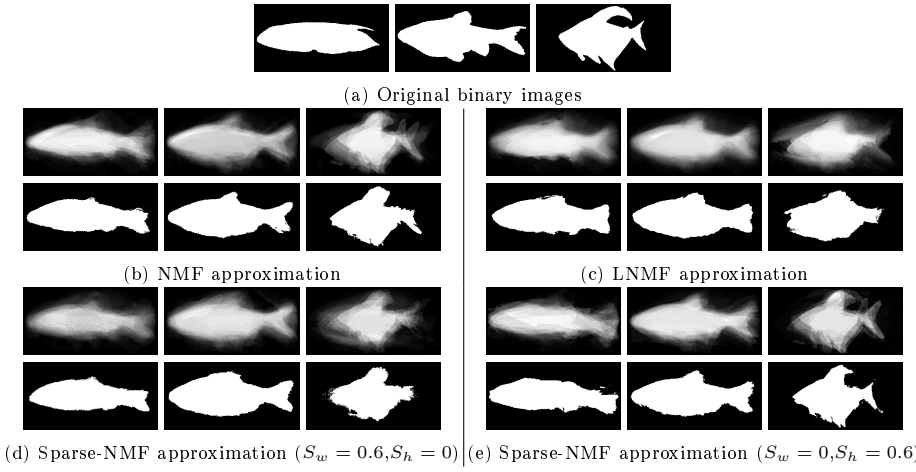

Fig. 2. Sparse NMF approximations to binary sets: (a) three original shapes X_j; (b)-(e) Top, reconstructed function a_{X_j} and Bottom, approximate set $\widetilde{X}_j$

It is also easy to see that

$$\delta_B(X) = \varpi_1 \left(\delta_B \left(\min \left\{ 1, \sum_{k \in K} \xi_{X_k}(p_i) \right\} \right) \right) = \varpi_1 \left(\sum_{k \in K} \delta_B \left(\xi_{X_k}(p_i) \right) \right). \quad (12)$$

In fact, the justification for using NMF in sparse mathematical morphology arises from equations (11) and (12).

Coming back to the NMF reconstruction, expressions (2) and (3), we can now write

$$X_j \approx \widetilde{X}_j = \varpi_\alpha \left(\sum_{k=1}^{R} \phi_k(p_i) \mathbf{H}_{k,j} \right). \quad (13)$$

Hence, we propose to introduce the following nonlinear operator, named *sparse max-approximation to binary dilation*,

$$D_B(X_j) = \varpi_\alpha \left(\sum_{k=1}^{R} \delta_B \left(\phi_k \right) (p_i) \mathbf{H}_{k,j} \right). \quad (14)$$

Note that by the positivity of $\mathbf{H}_{k,j}$, we have $\delta_B \left(\phi_k(p_i) \mathbf{H}_{k,j} \right) = \delta_B \left(\phi_k \right) (p_i) \mathbf{H}_{k,j}$. We can say that $\delta_B(X_j) \approx D_B(X_j)$, however neither the increasiness nor the extensitivity of $D_B(X_j)$ w.r.t. X_j can be guaranteed and consequently, this operator is not a morphological dilation. In other terms, in order to approximate the dilation by B of any of the M sets X_j, we only need to calculate the dilation of the R basis images. In addition, the sparsity of $\mathbf{H}$ involves that only a limited number of dilated atoms are required for each X_j.

Dual sparse max-approximation to binary erosion. One of the most interesting properties of mathematical morphology is the duality by the complement

of pair of operators. Hence, the binary erosion of set X by B can be defined as the dual operator to the dilation: $\varepsilon_{\check{B}}(X) = (\delta_B(X^c))^c$. Using this property, we propose to define the *sparse max-approximation to binary erosion* as

$$E_B(X_j) = \varpi_\alpha \left(\sum_{k=1}^{R} \complement \left[\delta_B \left(\complement[\phi_k] \right) (p_i) \right] \mathbf{H}_{k,j} \right), \tag{15}$$

where the complement basis images are defined by $\complement[\phi_k(p_i)] = \max(\mathbf{W}_{i,k}) - \phi_k(p_i) + \min(\mathbf{W}_{i,k})$.

The results of $D_B(X_j)$ and $E_B(X_j)$ for three examples of the Fish shapes, compared with respect to the standard binary dilation and erosion, are given in Fig. 3. We have compared in particular the sparse max-approximation for the standard NMF and for the Sparse-NMF.

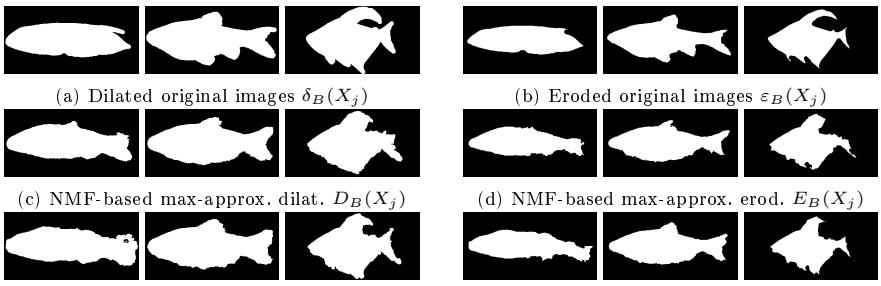

(a) Dilated original images $\delta_B(X_j)$ (b) Eroded original images $\varepsilon_B(X_j)$

(c) NMF-based max-approx. dilat. $D_B(X_j)$ (d) NMF-based max-approx. erod. $E_B(X_j)$

(e) Sparse NMF-based max-approx. dilat. $D_B(X_j)$ (f) Sparse NMF-based max-approx. erod. $E_B(X_j)$

Fig. 3. Comparison of dilation/erosion (a)/(b) vs. sparse pseudo operators for three examples of the Fish shapes. It is compared in particular the sparse max-approximation to dilation/erosion for the standard NMF (c)/(d) and for the Sparse-NMF (e)/(f), with ($S_w = 0$,$S_h = 0.6$). The structuring element B is a square of 5×5 pixels.

4 Extension to Grey-Level Images

We deal in this section with families of discrete grey-level images, i.e., $\mathcal{F} = \{f_1(p_i), \cdots, f_M(p_i)\}$, with $f_j(p_i) \in \mathcal{F}(E, \mathcal{T})$, $\mathcal{T} = \{t_1, t_2, \cdots, t_L\}$ with $(t_{l+1} - t_l) = \Delta t$. The thresholded set of f_j at each t_l, i.e., $X_j^{t_l} = \varpi_{t_l}(f_j)$, is called the cross-section or level-set at t_l. The set of cross-sections constitutes a family of decreasing sets: $t_\lambda \geq t_\mu \Rightarrow X^{t_\lambda} \subseteq X^{t_\mu}$ and $X^{t_\lambda} = \cap\{X^{t_\mu}, \mu < \lambda\}$. Any image f_j can be viewed as an unique stack of its cross-sections, which leads to the following reconstruction property:

$$f_j(p_i) = \sup\{t_l |\, p_i \in X_j^{t_l}\}, \quad t_l \in \mathcal{T}. \tag{16}$$

We prefer here to consider the alternative reconstruction [13,10] using a numerical sum of the characteristic function of cross sections:

$$f_j(p_i) = \Delta t \sum_{l=1}^{L} \xi_{X_j^{t_l}}(p_i). \tag{17}$$

It is well known in mathematical morphology that any binary increasing operator, such as the dilation and erosion, can be generalised to grey-level images by applying the binary operator to each cross-section, and then by reconstructing the corresponding grey-level image [11,10], i.e.,

$$\delta_B(f_j)(p_i) = \Delta t \sum_{l=1}^{L} \xi_{\delta_B\left(X_j^{t_l}\right)}(p_i), \quad \text{and} \quad \varepsilon_B(f_j)(p_i) = \Delta t \sum_{l=1}^{L} \xi_{\varepsilon_B\left(X_j^{t_l}\right)}(p_i). \quad (18)$$

Consider now that each image of the initial grey-level family $\mathcal{F}$ of M images is decomposed into its L cross-sections. Hence, we have

$$\mathcal{F} = \{f_1, \cdots, f_M\} \mapsto \mathcal{X} = \{X_1^{t_1}, X_1^{t_2} \cdots, X_1^{t_L}, \cdots, X_{M-1}^{t_L}, X_M^{t_1}, \cdots, X_M^{t_L}\},$$

where $\mathcal{X}$ is a family of $M' = M \times L$ binary images. Therefore, we can use NMF algorithms, for a given dimension R, to approximate each set $X_j^{t_l}$ and then approximate the corresponding function $f_j(p_i)$. Using the results of the previous section, we are able now to introduce the following definition for the *sparse max-approximation to grey-level dilation and erosion* given respectively by:

$$D_B(f_j)(p_i) = \Delta t \sum_{l=1}^{L} \xi_{D_B\left(X_j^{t_l}\right)}(p_i), \quad (19)$$

and

$$E_B(f_j)(p_i) = \Delta t \sum_{l=1}^{L} \xi_{E_B\left(X_j^{t_l}\right)}(p_i). \quad (20)$$

with

$$D_B\left(X_j^{t_l}\right) = \varpi_\alpha \left(\sum_{k=1}^{R} \delta\left(\phi_k\right)(p_i) \mathbf{H}_{k,j+l} \right);$$

$$E_B\left(X_j^{t_l}\right) = \varpi_\alpha \left(\sum_{k=1}^{R} \complement \left[\delta_B\left(\complement[\phi_k] \right)(p_i) \right] \mathbf{H}_{k,j+l} \right).$$

We must point out again that these approximate nonlinear operators do not satisfy the standard properties of grey-level dilation and erosion. The precise properties of $D_B(f_j)$ and $E_B(f_j)$ will be studied in detail in a subsequent paper.

Fig. 4 illustrates the behaviour of sparse max-approximation to grey-level dilation and erosion. This preliminary experiment deals with images from the ORL face database. In this particular case, the results obtained using the standard NMF are significantly better than those obtained using any Sparse-NMF version.

In fact, as we can observe, the quality of the sparse max-approximation to dilation and to erosion, for a particular image, depends on the quality of the initial NMF reconstruction of the image. For instance, the first face (man with glasses) is not very well approximated with the learned NMF basis and hence, its approximated dilation and erosion are also unsatisfactory. On the contrary, in the case of the last image (woman), the results are more appropriate.

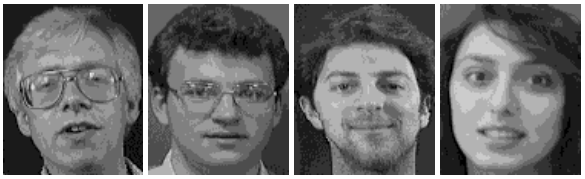

(a) Original images $f_j(p_i)$

(b) NMF approximation $\widetilde{f}_j(p_i)$

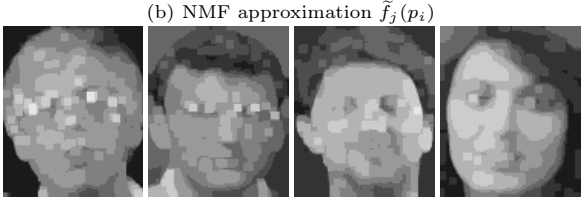

(c) Dilated images $\delta_B(f_j)(p_i)$

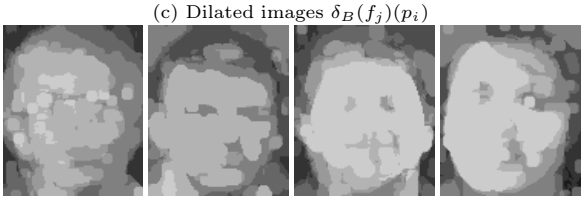

(d) Sparse max-approximation dilat. $D_B(f_j)(p_i)$

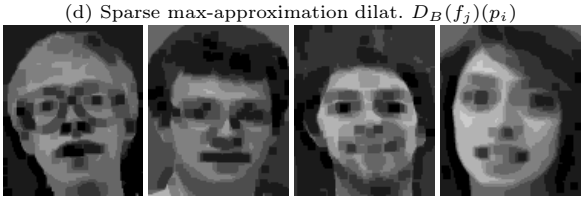

(e) Eroded images $\varepsilon_B(f_j)(p_i)$

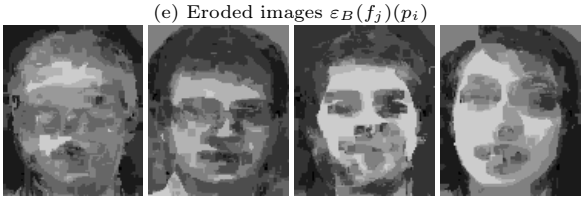

(f) Sparse max-approximation erod. $E_B(f_j)(p_i)$

Fig. 4. Four examples of the ORL face database (a) (quantized in $L = 10$ grey-levels) and corresponding approximated image using standard NMF. Comparison of dilation/erosion (c)/(d) vs. sparse max-approximation to dilation/erosion for the standard NMF (e)/(f). A collection of $M = 20$ faces has been used in the NMF experiments where the number of reduced dimensions for the binary matrix $\mathbf{V}$ has been fixed to $R = 75$ (note that $M' = 20 \times 10 = 200$ dimensions). The structuring element B is a square of size 3×3 pixels.

In any case, this is only a first experiment and a more concise investigation of the effect of variations of the parameters would be studied in ongoing research. Typically, we need to evaluate quantitatively, for a given operator, the approximation power for different sizes of structuring element as well as the approximation power of the morphological operators with respect to the degree of approximation of the initial image. In addition, the influence on the approximated morphological operators of dimensionality R and of the parameters S_w and S_h from Sparse NMF should be also evaluated. It will be also probably useful a direct comparison to another dimensionality reduction technique, typically PCA, in order to have a better judgment of the potential of the presented approach.

5 Conclusions and Perspectives

We have introduced the notion of sparse binary and grey-level pseudo-dilations and erosions using NMF sparse representation. The first results are relatively encouraging and they open a new avenue to study how the current paradigm of sparse modelling (based mainly on linear operations) can be particularised to the nonlinear morphological framework.

Besides a deeper experimental quantitative analysis, as discussed above, in ongoing research, we will focus, on the one hand, on NMF representations which produces binary basis images, see for instance [15], which is still a quite open problem. On the other hand, we will study in deep the properties of the sparse max-approximation to dilation/erosion, as well as consider alternative extensions to the grey-level case. Finally, the construction of more complex operators than dilation/erosion, and eventually the introduction of new ones, and their possible applications for inverse problems (regularisation, debluring, etc.) will be also foreseen.

References

1. Bloch, I., Heijmans, H., Ronse, C.: Mathematical Morphology. In: Aiello, M., Pratt-Hartmann, I., van Benthem, J. (eds.) Handbook of Spatial Logics, ch. 14, pp. 857–944. Springer, Heidelberg (2007)
2. Donoho, D., Stodden, V.: When does non-negative matrix factorization give a correct decomposition into parts? In: Advances in Neural Information Processing 16 (Proc. NIPS 2003). MIT Press, Cambridge (2004)
3. Elad, M., Aharon, M.: Image denoising via sparse and redundant representations over learned dictionaries. IEEE Trans. on Image Proc. 15(12), 3736–3745 (2006)
4. Heijmans, H.J.A.M.: Morphological Image Operators. Academic Press, Boston (1994)
5. Hoyer, P.: Non-negative Matrix Factorization with Sparseness Constraints. J. Mach. Learn. Res. 5, 1457–1469 (2004)
6. Lee, D.D., Seung, H.S.: Learning the parts of objects by non-negative matrix factorization. Nature 401(6755), 788–791 (1999)

7. Lee, D.D., Seung, H.S.: Algorithms for non-negative matrix factorization. In: Advances in Neural Information Processing 13 (Proc. NIPS 2000). MIT Press, Cambridge (2001)
8. Li, S.Z., Hou, X., Zhang, H., Cheng, Q.: Learning spatially localized parts-based representations. In: Proc. IEEE Conf. on Computer Vision and Pattern Recognition (CVPR), Hawaii, USA, vol. I, pp. 207–212 (2001)
9. Mairal, J., Elad, M., Sapiro, G.: Sparse representation for color image restoration. IEEE Trans. on Image Proc. 17(1), 53–69 (2008)
10. Ronse, C.: Bounded variation in posets, with applications in morphological image processing. In: Passare, M. (ed.) Proceedings of the Kiselmanfest 2006, Acta Universitatis Upsaliensis, vol. 86, pp. 249–281 (2009)
11. Serra, J.: Image Analysis and Mathematical Morphology. Image Analysis and Mathematical Morphology, vol. I. Theoretical Advances, vol. II. Academic Press, London (1982) (1988)
12. Soille, P.: Morphological Image Analysis. Springer, Berlin (1999)
13. Wendt, P.D., Coyle, E.J., Gallagher, N.C.: Stack Filters. IEEE Trans. on Acoustics, Speech, and Signal Processing 34(4), 898–911 (1986)
14. Yu, G., Sapiro, G., Mallat, S.: Solving Inverse Problems with Piecewise Linear Estimators: From Gaussian Mixture Models to Structured Sparsity. IEEE Trans. on Image Processing (2011)
15. Yuan, Y., Li, X., Pang, Y., Lu, X., Tao, D.: Binary Sparse Nonnegative Matrix Factorization. IEEE Trans. on Circuits and Systems for Video Technology 19(5), 772–777 (2009)